arXiv:2208.05756v1 [astro-ph.SR] 11 Aug 2022

Physics And Chemistry Of Star Forming Region And Protoplanetary Disk

Thesis submitted for the degree of
Doctor of Philosophy (Science)
in Physics (Theoretical)

by

Mr. Milan Sil

Department of Physics

University of Calcutta

2021

Dedicated to my beloved family.

ABSTRACT

My thesis work aims to study the inter-relation between various physical and chemical conditions in a wide range of astrophysical environments. Our studied regions range from the super-hot regions (i.e., nebular, photon-dominated, or photodissociation regions, diffuse area, through which the lights of the background stars can reach us) to the super-cold regions (i.e., dense molecular clouds, proto-planetary disks, etc. where interstellar dust particles absorb all background visible and ultraviolet lights). The chemical complexity of the interstellar cloud gradually evolves due to the evolution in physical conditions. The dense molecular clouds are the birth sites of star-formation, where a wide variety of complex organic molecules are observed. Dust particles play an essential role in the formation of these complex organic molecules. During the warm-up stage of a star-forming region, the molecules formed during the cold phase start to return to the gas phase by various thermal and non-thermal evaporation processes. These complex molecules again freeze out to the outer part of the proto-planetary disk during the further evolved stage according to their condensation temperature and form the so-called snow-lines. The binding energies of these molecules with the prevailing dust particles play a crucial role in determining the structural information of this disk. Thus the binding energy of the molecules is vital to understand several critical aspects of the star and planet formation processes. In this thesis, I will discuss the chemical complexity obtained in a wide range of the star-forming region and whether this chemical complexity lead to biomolecules in space.

Chapter 1 introduces the essential background of the research work (astrochemistry-related study) presented in this dissertation. The recent developments of this subject are also highlighted in this Chapter.

Features of the interstellar ice are investigated in Chapter 2. Systematic quantum chemical calculations have been performed to compute physisorption energies of several interstellar adsorbed species by considering different types of substrates mimicking interstellar dusts or grains or icy mantle layers. Assuming the binding energy values as appropriate for H_2 substrate, we check the encounter desorption effect on the enrichment of surface species. The presence of impurities in water ice affects the spectroscopic features of water itself. For this reason, a series of laboratory experiments and an extensive computational investigation are carried out to

evaluate the effects of different amounts of representative impurities on the band strengths and absorption band profiles of interstellar ice.

Chapter 3 deals with radiation-dominated environments such as the Crab nebula and diffuse cloud regions using a spectral synthesis code CLOUDY. This Chapter attempts to model the chemistry of hydride and hydroxyl cations of the three most common noble gas atoms: argon, neon, and helium. Their various isotopologs are also considered to check the chemical evolution in space where the radiation is extreme.

Chapter 4 discusses the chemical treatment of some prebiotic molecules such as the aldimines, amines, three nitrogen-bearing species containing peptide-like bonds, and some phosphorous-bearing species in various star-forming regions of ISM, mainly where the radiation is highly attenuated and proposes the possibility to observe some of them in space.

Finally, the concluding remarks of the works presented in this thesis are made in Chapter 5 along with my possible future research plan.

ACKNOWLEDGMENTS

Ph.D. is not about getting a certificate. It is about maturing to undertake Life and Science in unknown territories. It is becoming an adult scientist, still keeping the curiosity of a child within you. It is about keeping your vision and goals not fogged by day-to-day stupidies of politics in life. It is about dreaming beyond and working to leave knowledge behind for future generations. And finally, you are an adult in Knowledge Pursuit!

Sometimes the exploration is challenging in isolation. Voyage is beautiful when it is companied by wonderful people, and I am fortunate enough to have a bunch of such heads in this beautiful journey. There are numerous people I would like to personally acknowledge and thank for their assistance, encouragement, and support throughout the journey.

First of all, I would like to thank the whole research group "Astrochemistry / Astrobiology" at Indian Centre for Space Physics (ICSP), Kolkata, for an amicable, informal emancipated working atmosphere that formed day-by-day an enjoyable period of residence. Minor issues like having stimulating lunch discussions or going out into a restaurant, friendly people could be found herein to balance scientific work. Moreover, I am thankful for enabling travels to conferences and meetings. This level of expanding mindsets is priceless and crucial, both on a scientific and a personal level. However, a couple of people deserve a mentioning by name to express my deep gratitude.

I owe my sincere gratitude and appreciation to my Ph.D. supervisor, Dr. Ankan Das, for all the support and encouragement he gave me throughout my Ph.D. work. To me, it was an ideal degree of balancing inspiration, guidance, support, and "letting me do my things". I am forever indebted for his appearances as an elder brother and advice like a guardian. He has always been there to guide me in the proper direction, whether academic or personal. This journey into the world of Astrochemistry was a multidisciplinary, collaborative science product, to which he introduced me so well! His belief humbles me in allowing me to be a part of his group, and I have tried my best to fulfill the expectations. Interactions have felt barrierless, more like a friendship than a strict professor-student relationship. This kind of freedom is the spore

of scientific success! Thanks, Ankan da, for this hardly describable atmosphere. I am looking forward to the future!

I am very grateful to my Ph.D. joint-supervisor, Prof. Sandip K. Chakrabarti, for his essential scientific and grammatical suggestions, beautiful notions, and cosmic concepts. In addition, creative ideas regarding visualization, graphs, etc., helped me a lot during various studies. Without his guidance and constant feedback, the outcomes would not have been successful.

This research was performed in collaboration with other scientists all over the world. My thanks go to Professor Paola Caselli, Dr. Sergio Ioppolo, Dr. Jean-Christophe Loison, Professor Cristina Puzzarini, Professor Vicenzo Barone, Dr. Takashi Shimonishi, Dr. Naoki Nakatani, Dr. Kenji Furuya, Dr. Bhalamurugan Sivaraman, and Dr. Amit Pathak. They were always so helpful and provided me with their support and collaboration throughout my dissertation.

I would also like to thank my departmental group mates Dipen da, Prasanta da, Bratati, Suman Mondal da, Rana for their endless help, fruitful discussion, and contribution to this research as teamwork. A special thanks indeed go to Dr. Gorai, from whom I learned so many things in Astrochemistry. Your presence in the lab was something difficult to forget. We have shared many good times. I am highly grateful for your availability whenever I had problems or questions. I am happy to collaborate with my friend Satyam from Banaras Hindu University, Varanasi also contributed to my work. I would also like to thank Emmanuel E. Etim for his fruitful contribution to this research.

I am delighted to work at my institute, ICSP, where the atmosphere is precisely family-like, and thanks for that. All the academic and non-academic staff and faculty members, colleagues, and friends are like family members. I learn many things from Dr. Dipak Debnath, Dr. Ritabrata Sarkar, and Dr. Sudipta Sasmal, and thanks for all their support and cooperation. My knowledge in Astrophysics and Astronomy was initiated from the class taken by Ankan da, Dipak da, Rito da during my post-graduation days at Narendrapur. I heartily thank and express my love to all the past and present members of ICSP - Suman Ray da, Sourav da, Santanu da, Partha da, Sujay da, Arka da, Dusmanta da, Suman Chakraborty da, Tamal da, Shreeram da, Aslam da, Dipen da, Argha da, Prasanta da, Debjit da, Soujan da,

Suman Mondal da, Bratati, Rana, Kaushik, Sujoy, Riya, Subrata, Swati, Abhijit, Abhrajit, Binayak, Rupnath, Sagar, Ashim, Shyam, and Pabitra. I feel melancholy thinking that my journey with you all is going to end here. I will miss our tea group at ICSP. I want to thank Rajkumar da, Ram da, Pavel da, Uttam da, Debashis da, Hriday da, Susanta da, Arnab da for every kind of help regarding administrative, official, and technical issues. On many occasions, we gathered, shared, and celebrated together.

I am lucky to get a chance to visit NASA's JPL and Caltech at Pasadena, California, and SOFIA Observatory, based at NASA's Armstrong Flight Research Center at Palmdale Regional Airport, California, during the 42nd COSPAR Scientific Assembly, July 2018, USA. While staying abroad with the ICSP gang at Saga Motor Hotel, we enjoyed ourselves immensely, especially the breakfast and swimming pool. It was my first visit abroad and a very precious moment of my life.

I want to thank all my friends during my school, graduate, and post-graduate studies, especially Apurba, Subhajit (Gopi), Saptarshi, Joy, Arnidam, Souvik, Debarghya, Abinash, Biswajit, Chandralina, Tania, Tamal, Monoj, Atanu, Satyajit, Tanumoy, Sumit, Sumana. Animesh, Snehashis, Surajit, Sujoy, Subhankar (Bappa), Hemanta, Soumen are my village locality friends since childhood. We played Cricket, Football, Carrom, Cards, etc., together. A special thanks to my Ph.D. time room/flatmates, Ram da, Debjit da, Kaushik, and Sujoy. We have shared many memorable moments like cooking, bike riding, restaurant hoping, outing, gossip, fun, birthday party, music, etc., to cherish forever.

I am fortunate to have many good teachers throughout my academic journey, starting from primary school to post-graduation studies. So my warm regards go to Koushik sir during my primary school days at Ichapur Prathamic Vidyalaya, Kaikala, Hooghly. We were the first batch in class three when he joined our school. I can cherish the memory when I was ill and could not go to school; he came to see me in our house. Haripal Gurudayal Institution is a place very close to me, and still today, I enjoy remembering every possible moment that I spent there. The love that I got from all the teachers there was something special. It is tough to name all of them, but I must call a few. Rabin babu (Dr. Rabindranath Chattopadhyay), Swadesh babu, Uttam babu, Ujwal babu, Sougata babu, Pradip babu, Sourav babu, Biswajit Bag babu, Sanjit Kayal babu, Ritu di, Kakon di, Susanta sir (private teacher) are exceptional teachers during my high school days. My love for Chemistry

starts building solely due to Dhruba sir and my Physics background today is for Rabin babu and Debdas sir. Swadesh babu is always been my favorite Mathematics teacher. I delivered seminar lectures two times in my high school 'Satabarshiki Hall' only for Rabin babu. He always inspires me for any scientific purpose. AKM sir, TD sir, GSM sir, PS sir, SD sir, AB sir, DPG sir, KP sir, RB sir during my graduation days at Serampore College made my knowledge in Physics day-by-days. Especially the theoretical and practical/experimental knowledge of TD sir inspires me a lot. DJ sir (Prof. Debnarayan Jana) always encouraged and motivated me during the post-graduation days at Ramakrishna Mission Residential College, Narendrapur. All they are the builders of my academic root.

I am thankful to all my family members and relatives, especially my parents, for their unwavering support, no matter which path in life I chose to follow. I must express my sincere love and gratitude from the deepest of my heart to my maa, Mrs. Binapani Sil, and baba (bapi), Mr. Mridul Sil, for their endless unconditional love, prayers, care, sacrifices, and support. My maa taught me even during my high school days when I have no private teacher. Thank you for supporting me during all ups and downs of my career. Bapi worked overnight during our hard times. My didi, Mrs. Tithi Sil, and my brother-in-law Mr. Tapas Das helped our family and me immensely. Without their assistance, I could not be able to do my Ph.D. today. My dearest "vagna" Shivam *was born (on 11th May 2016) during my Ph.D. days. He always keeps my family full of happiness and joy. I have shared so many beautiful, memorable, and adorable moments with* Shivam*. I will miss my loving uncle Late Sanat Sil whose sudden disappearance from the Earth (due to the deadly disease DLBCL cancer) during my Ph.D. shocked me severely. I always pray for your soul to rest in peace. Mentioning everyone in my family is difficult, but I thank you all for being there.*

Finally, I would especially like to thank my adored wife, Sudipta*, for all of her sacrifices, devotion, mental support, and love since the end of my graduate studies. Thank you also for supporting me when having had hard times in my life. After seven years of relationship, we have got married on 2nd February 2021.*

I want to acknowledge the Department of Science and Technology (DST), the Government of India, for providing financial assistance through the DST-INSPIRE (Innovation in Science Pursuit for Inspired Research) Fellowship [IF160109] scheme to carry out my research during my Ph.D. I also thank DST-SERB (Science and En-

gineering Research Board) for the grant that I received under the International Travel Support (ITS) scheme to attend the overseas conference, 42nd COSPAR Scientific Assembly, July 2018, USA. This research was possible in part due to a grant-in-aid from the Higher Education Department of the Government of West Bengal. Acknowledges are also due to Indian Centre for Space Physics and the University of Calcutta for allowing me to do a Ph.D. I would also like to thank all the reviewers whose extensive comments helped improve the quality of the papers presented in this dissertation.

A special appreciation indeed goes to the complementary contributions of the internet, GOOGLE*, and my desktop and laptop, which have accelerated my work. Last but by no means least, I would like to thank all those people I inadvertently forgot to mention, but whose help nevertheless was very much appreciated. Finally, it is worth noting the global pandemic situation due to Coronavirus COVID-19 affected the work severely. In the end, I wish to say that this roller-coaster journey could not be so decorative and gorgeous without all these supports.*

Cheers!

Milan Sil
August 2021, Kolkata.

Scientific contributions

Publications

List of Publications in Peer Reviewed Journals

1. **Adsorption energies of H and H_2: A Quantum Chemical Study**, **Milan Sil**, Prasanta Gorai, Ankan Das, & Sandip K. Chakrabarti, 2017, *The European Physical Journal D*, 71, 45. **(Journal Impact Factor 2020: 1.425)**

2. **Chemical Modeling for Predicting the Abundances of Certain Aldimines and Amines in Hot Cores**, **Milan Sil**, Prasanta Gorai, Ankan Das, Bratati Bhat, & Sandip, K, Chakrabarti, 2018, *The Astrophysical Journal*, 853, 2. **(Journal Impact Factor 2020: 5.874)**

3. **An Approach to Estimate the Binding Energy of Interstellar Species**, Ankan Das, **Milan Sil**, Prasanta Gorai, Sandip K. Chakrabarti, & J. C. Loison, 2018, *The Astrophysical Journal Supplement Series*, 237, 9. **(Journal Impact Factor 2020: 8.136)**

4. **Identification of Pre-biotic Molecules Containing Peptide-like Bond in a Hot Molecular Core, G10.47+0.03**, Prasanta Gorai, Bratati Bhat, **Milan Sil**, Suman K. Mondal, Rana Ghosh, Sandip K. Chakrabarti, & Ankan Das, 2020, *The Astrophysical Journal*, 895, 86. **(Journal Impact Factor 2020: 5.874)**

5. **Systematic Study on the Absorption Features of Interstellar Ices in the Presence of Impurities**, Prasanta Gorai, **Milan Sil**, Ankan Das, Bhalamurugan Sivaraman, Sandip K. Chakrabarti, Sergio Ioppolo, Cristina Puzzarini, Zuzana Kanuchova, Anita Dawes, Marco Mendolicchio, Giordano Mancini, Vicenzo Barone, Naoki Nakatani, Takashi Shimonishi, & Nigel Mason, 2020, *ACS Earth and Space Chemistry*, 4, 920. **(Journal Impact Factor**

2020: 3.475)

6. **Exploring the Possibility of Identifying Hydride and Hydroxyl Cations of Noble Gas Species in the Crab Nebula Filament**, Ankan Das, **Milan Sil**, Bratati Bhat, Prasanta Gorai, Sandip K. Chakrabarti, & Paola Caselli, 2020, *The Astrophysical Journal*, 902, 131. **(Journal Impact Factor 2020: 5.874)**

7. **Effect of binding energies on the encounter desorption**, Ankan Das, **Milan Sil**, Rana Ghosh, Prasanta Gorai, & Sandip K. Chakrabarti, 2021, *Frontiers in Astronomy and Space Sciences*, 8, 78.

8. **Chemical complexity of phosphorous bearing species in various regions of the Interstellar medium**, **Milan Sil**, Satyam Srivastav, Bratati Bhat, Suman Kumar Mondal, Prasanta Gorai, Rana Ghosh, Takashi Shimonishi, Sandip K. Chakrabarti, Bhalamurugan Sivaraman, Amit Pathak, Naoki Nakatani, Kenji Furuya, Ankan Das, 2021, *The Astronomical Journal*, 162, 119. **(Journal Impact Factor 2020: 6.263)**

9. **Is there any linkage between interstellar aldehyde and alcohol?** Suman Kumar Mondal, Prasanta Gorai, **Milan Sil**, Rana Ghosh, Ankan Das, Emmanuel E. Etim, Sandip K. Chakrabarti, Takashi Shimonishi, Naoki Nakatani, Kenji Furuya, Jonathan C. Tan, Ankan Das, 2021, *The Astrophysical Journal*. **(Journal Impact Factor 2020: 5.874)**

Publication in Proceedings

1. **Binding Energy and Isomerism: Two Important Aspects of Astrochemistry**, **Milan Sil**, 2018, Exploring the Universe: From Near Space to Extra-Galactic, 491-501, Astrophysics and Space Science Proceedings, vol 53. Springer, Cham., Online ISBN:978-3-319-94607-8.

Oral presentations

1. Astrochemistry in the THz domain, October 2017, Chennai, India

   Title: "Systematic study on the presence of impurities on interstellar ices"

2. 42nd COSPAR Scientific Assembly, July 2018, USA

   Title: "Binding energy a key to defining interstellar volatile species"

   Title: "A Systematic Study of Pre-biotic Aldimines and Amines in Hot Cores"

   Title: "A Theoretical Prediction of Interstellar Bio-Molecule abundances"

3. Exploring the Universe: Near Earth Space Science to Extra-Galactic Astronomy, November 2018, Kolkata, India

   Title: "A New Set of Binding Energies for Astrochemical Modeling"

4. 43rd COSPAR Scientific Assembly (COSPAR-2021-Hybrid), 28 January - 4 February 2021, Sydney Australia.

   Title: "Fate of identifying noble gas related species in the Crab nebula environment"

Poster presentations

1. International Conference on Infrared Astronomy and Astrophysical Dust, October 2019, IUCAA Pune, India

   Title: "Complex Organic Molecules in the Star Forming Region"

2. 43rd COSPAR Scientific Assembly (COSPAR-2021-Hybrid), 28 January - 4 February 2021, Sydney Australia.

   Title: "Estimating realistic values of binding energy of species for astrochemical modeling"

Contents

1 Introduction **1**

1.1 Birth of stars and and the planetary systems 5

1.2 The interstellar ingredients 8

1.3 Current state-of-the-art of the astrochemistry 17

1.3.1 Astronomical observations 18

1.3.2 Theory and astrochemical models 19

1.3.3 Laboratory experiments 22

1.4 Some astrochemical tools for modelers 23

1.4.1 Quantum chemical calculations 23

1.4.2 Modeling radiation-dominated region 24

1.4.3 Modeling radiation-shielded region 32

1.4.4 Radiative transfer modeling 34

2 Interstellar Ice Features **36**

2.1 Binding energy: a key in defining interstellar chemistry 37

2.1.1 Study of binding energies of H and H_2 38

2.1.2 Study of binding energies of several interstellar species 48

2.1.3 Effect of binding energies on the encounter desorption 68

2.2 Absorption features of interstellar ices in the presence of impurities . 92

2.2.1 Methodology 92

2.2.2 Experimental methods 101

2.2.3 Results and Discussion 101

2.2.4 Summary 143

3 Radiation Dominated Region **145**

3.1 Physical conditions 148

3.1.1 Radiative Transfer Model 152

3.2 Chemical pathways 156

3.2.1 Cosmic-ray ionization rate 156

3.2.2 Ion-neutral reaction rate 160

3.2.3 Radiative association . . . 161
3.2.4 X-ray ionization rate . . . 162
3.2.5 Electronic and dissociative recombination . . . 163
3.2.6 Photodissociation . . . 163
3.3 Results and discussions on chemical modeling . . . 164
3.3.1 Diffuse interstellar medium . . . 164
3.3.2 The Crab nebula filament . . . 168
3.3.3 Time scales of molecule formation . . . 194
3.4 Spectroscopic information . . . 197
3.5 Summary . . . 198

4 Interstellar Prebiotic Molecules in Radiation Shielded Region 200
4.1 Aldimines and amines: the building-block of amino acids . . . 202
4.1.1 Computational details and methodology . . . 203
4.1.2 Results and discussion . . . 213
4.1.3 Astrophysical implications . . . 229
4.1.4 Summary . . . 236
4.2 Prebiotic molecules containing peptide-like bonds . . . 237
4.2.1 Chemical Modeling . . . 238
4.2.2 Modeling results . . . 244
4.2.3 Summary . . . 252
4.3 Phosphorous-bearing species: precursor of biomolecules . . . 253
4.3.1 The chemical network of phosphorus . . . 255
4.3.2 The binding energy of P-bearing species . . . 261
4.3.3 Chemical model . . . 262
4.3.4 An outline of our modeling results and a comparison with the earlier results . . . 281
4.3.5 IR spectroscopy of PH_3 . . . 286
4.3.6 Summary . . . 290

5 Summary, Conclusions and Future Plans 291
5.1 Summary and Conclusions . . . 291
5.2 Future Research Plans . . . 293

A X-ray ionization **295**

A.1 Direct X-ray ionization 295

A.2 Secondary X-ray ionization 296

A.3 Electron-impact X-ray ionization 297

B Glossary **299**

B.1 Units and constants 299

B.2 Acronyms 300

List of Figures

1.1 Key classes of COMs detected in the ISM, which are primarily formed on ice-coated interstellar grains. 3

1.2 Cartoon depiction of different stages characterizing low-mass (Solar-like) star and planet formation (Courtesy: Öberg & Bergin, 2021). . . 5

1.3 The low-mass stellar life cycle from diffuse clouds and the beginning of the star formation up to the death of the star. The length scale of each stage is shown (Courtesy: Öberg, 2009). 6

1.4 Left: atomic abundances of the 10 most common elements in the Universe besides H and He. Right: atomic abundances of the most common elements in the Earth's mantle (Courtesy: Fortenberry, 2020). 8

1.5 The median composition of interstellar icy grain mantles normalized to the most abundant ice species, water (Boogert et al., 2015) indicated with the minimum and maximum abundance relative to water ice detected in that line of sight (Courtesy: Öberg, 2016). 11

1.6 Approaches in astrochemistry: observations, laboratory studies, and models are carried out to explain physico-chemical processes in astronomical environments (Courtesy: Barone et al., 2015a). 17

1.7 Graphical representation of the microwave, millimeter (mm), submillimeter (Submm), and IR ranges of the electromagnetic spectrum (Courtesy: Widicus Weaver, 2019). 19

1.8 Idealized structure of an H II region and PDR (Courtesy: https://cloud9.pa.uky.edu/\protect\unhbox\voidb@x\protect\penalty\@M\{}gary/cloudy/CloudySummerSchool/2015_Pune/2_Thermal_equilibrium.pdf). 25

1.9 Common geometry of the cloud considered for a PDR model calculations. The surface of any plane-parallel or spherical cloud is illuminated either a) uni-directionally or b) isotropically. (Courtesy: Röllig et al., 2007). 26

1.10 A schematic view of a PDR structure. The PDR is illuminated from the left by a strong far-UV field (Courtesy: Hollenbach & Tielens, 1997). 27

1.11 Radiation fields that enter in the calculations (Courtesy: Part 1 of Hazy; Ferland et al., 2017). 30
1.12 Examples of types of geometry of the cloud which can be considered in the calculations (Courtesy: Part 1 of Hazy; Ferland et al., 2017). . 30
1.13 Several components of the radiation field that enter in the calculations (Courtesy: Part 1 of Hazy; Ferland et al., 2017). 32

2.1 Three favourable positions, c, h and b are shown (Sil et al., 2017). c position corresponds to the top of a carbon atom, h (hollow) position is at the center of the hexagon, and b (bridge) position is at the mid-point between two adjacent carbon atoms. 40
2.2 Benzene as a representative grain surface (Sil et al., 2017). 42
2.3 Silica cluster as a representative grain surface (Sil et al., 2017). 43
2.4 Water cluster (c-hexamer chair configuration) as a grain surface (Sil et al., 2017). 44
2.5 Efficiency window for various sets of BE shown in Table 2.5 (Sil et al., 2017). 46
2.6 Configurations of water molecule(s) used (Das et al., 2018). 49
2.7 Percentage deviations of BEs of 16 stable species with increasing numbers of water clusters acting as the grain surface (Das et al., 2018). . 53
2.8 (a) Average absolute percentage deviation and (b) fractional RMS deviation of our calculated values from experiments (Das et al., 2018). 54
2.9 Percentage deviation from experimental BE values of 16 stable species using the water c-hexamer (chair) cluster (Das et al., 2018). 54
2.10 Optimized geometries with the c-hexamer (chair) configuration (Das et al., 2018). 60
2.11 Optimized geometries with the c-pentamer configuration (Das et al., 2018). 61
2.12 Optimized geometries with the c-tetramer configuration (Das et al., 2018). 62
2.13 Optimized geometries with the c-tetramer configuration (Das et al., 2018). 63
2.14 Optimized geometries with the c-tetramer configuration (Das et al., 2018). 64

2.15 Optimized geometries with the c-tetramer configuration (Das et al., 2018). 65

2.16 Optimized geometries with the c-tetramer configuration (Das et al., 2018). 66

2.17 A comparison between the cases obtained in Hincelin et al. (2015) and Das et al. (2021). Figure 2 of Hincelin et al. (2015) is extracted using the online tool of Rohatgi (2020). Three distinct cases are shown: (A) no encounter desorption is considered with $E_d(H_2, H_2O) = 440$ K, (B) no encounter desorption is considered with $E_d(H_2, H_2) = 23$ K, and (C) encounter desorption of H_2 was considered with $E_d(H_2, H_2O) = 440$ K and $E_d(H_2, H_2) = 23$ K. An excellent match between the our calculated (solid curves) steady-state abundance of H_2 on grain surface and that obtained in Hincelin et al. (2015) (dashed curves) is noticed. 81

2.18 Time evolution of the abundances of gH_2 with $n_H = 10^7$ cm^{-3} and $T = 10$ K are shown for $R = 0.35$, 0.5, and 0.8 (Das et al., 2021). The dash-dotted purple curve shows time evolution of gH_2 abundance without encounter desorption [with $E_d(H, H_2O) = 450$ K]. gH_2 abundance remains roughly constant with the changes in R. However when encounter desorption is introduced, gH_2 abundance increases with the R. The time evolution of the gH_2 abundance with $E_d(H_2, H_2) = 23$ K and $E_d(H, H_20) = 450$ K is shown with the green dashed line when the method of Hincelin et al. (2015) is used and blue dotted line when the method of Chang et al. (2021) is used. gH_2 abundances obtained with our estimated BE value [i.e., $E_d(H_2, H_2) = 67$ K] are shown with a solid yellow line. For this case, we have used $E_d(H, H_2O) = 450$ K and the method used in Chang et al. (2021). The black dash-dotted line shows the time evolution of gH_2 abundance with $E_d(H, H_2O) = 650$ K and using the method of Chang et al. (2021). A significant difference is obtained when we use different energy barriers and different methods (Hincelin et al., 2015; Chang et al., 2021). Obtained values of gH_2 are further noted in Table 2.13 for better understanding. . . . 82

2.19 The ratio between the final abundances of gH_2 obtained with the no encounter (NE) desorption and encounter desorption (EN) is shown (Das et al., 2021). From left to right, it shows the variation of this ratio with R, n_H, and temperature, respectively. 84

2.20 Time evolution of gH_2 with $R = 0.35$ and various n_H (10^4, 10^5, 10^6, and 10^7 cm^{-3}) are shown (Das et al., 2021). The effect of encounter desorption increases with the increase in density. 85

2.21 Time evolution of gH_2 with $R = 0.35$, $n_H = 10^7$ cm^{-3} and various temperatures (5, 10, 15, and 20 K) are shown (Das et al., 2021). The effect of encounter desorption decreases with the increase in temperature. 85

2.22 Time evolution of the abundances of H, H_2, D, HD, and N obtained from our simulation (Das et al., 2021) is shown. Solid curves depict the cases by considering the encounter desorption [with $E_d(H_2, H_2) = 67$ K] of H_2 and no encounter desorption (dashed curves) with $E_d(H, H_2O) = 650$ K, $n_H = 10^7$ cm^{-3}, $T = 10$ K, and $R = 0.35$. 87

2.23 Time evolution of the abundances of ice-phase water (first panel), methanol (second panel) and ammonia (third panel) is shown for $n_H = 10^7$ cm^{-3}, $T = 10$ K, and $R = 0.35$ (Das et al., 2021). A considerabale difference between the consideration of encounter desorption (solid green line for H_2, solid red line for H, and solid blue line for N) and without encounter desorption (black line) is shown. The encounter desorption of H, N, H_2, D, and HD are considered (brown dotted line) and depict that it marginally deviates from the encounter desorption of H_2. 88

2.24 Temperature variation of the abundances of ice-phase water (first panel), methanol (second panel), and ammonia (third panel) is shown for $n_H = 10^7$ cm^{-3} and $R = 0.35$ (Das et al., 2021). A significant variation between the consideration of encounter desorption and without encounter desorption (black line) is shown. The encounter desorption of H, N, H_2, D, and HD are collectively considered, and as like Figure 2.23, it marginally varies from the encounter desorption of H_2. . . . 89

2.25 Optimized structures for (a) pure water and for the 4 : 4 concentration ratio: (b) $H_2O - HCOOH$, (c) $H_2O - NH_3$, (d) $H_2O - CH_3OH$, (e) $H_2O - CO$, (f) $H_2O - CO_2$, (g) $H_2O - H_2CO$, (h) $H_2O - CH_4$, (i) $H_2O - OCS$, (j) $H_2O - N_2$, and (k) $H_2O - O_2$ clusters (Gorai et al., 2020a). 95

2.26 **Left:** four-water system; the single QM water molecule is depicted in a ball- and-stick representation and the 3 MM molecules in a licorice representation; $O-H$ distances are indicated too. It is to be noted that the four H_2O can be considered equivalent. **Right:** innermost water molecules described at the QM level (ball and stick) and surrounding molecules described at the MM level (lines) for the $20H_2O$ system. (a) Configuration 1. (b) Configuration 2 (Gorai et al., 2020a). 97

2.27 Deviation of computed band positions (left panel) and band strengths (right panel) from experiments (Gorai et al., 2020a). 106

2.28 (a) IR spectra for different $HCOOH : H_2O$ ice mixtures deposited at $T = 20$ K. (b) IR spectra for different $NH_3 : H_2O$ ice mixtures deposited at $T = 20$ K. (c) IR spectra for different $CH_3OH : H_2O$ ice mixtures deposited at $T = 30$ K. The color legend is explained in the insets. All IR spectra are normalized with respect to the $O-H$ stretching band (Gorai et al., 2020a). 122

2.29 Absorption spectra of the four modes for water ice for the five measured compositions, ranging from pure water ice (top) to $4:4$ $H_2O-HCOOH$ mixture (bottom). The black line represents the absorbance spectra of various concentration of $H_2O-HCOOH$, where HCOOH is used as a hydrogen bond donor, and for the red line, HCOOH is used as a hydrogen bond acceptor (Gorai et al., 2020a). 123

2.30 Band strengths of the four fundamental vibration modes of water for (a) $H_2O-HCOOH$, (b) H_2O-NH_3, (c) H_2O-CH_3OH, (d) H_2O-CO, (e) H_2O-CO_2, (f) H_2O-H_2CO, (g) H_2O-CH_4, (h) H_2O-OCS, (i) H_2O-N_2, and (j) H_2O-O_2 clusters with various concentrations. The water c-tetramer configuration was used for pure water (Gorai et al., 2020a). 124

2.31 Absorption spectra of the four modes for water ice for the five measured compositions, ranging from pure water ice (top) to $4:4$ H_2O-NH_3 mixture (bottom) (Gorai et al., 2020a). 125

2.32 Comparison of computed and experimental IR spectra ($0-4000$ cm^{-1}) for pure water as well as water with HCOOH and NH_3 as impurities. We have used harmonic frequencies for the computed spectra, and the intensity is scaled with a factor 1000 to have the best match with the experimental one (Gorai et al., 2020a). 125

2.33 Comparison between the calculated and experimental band strength profiles with various concentration of HCOOH and NH_3 (Gorai et al., 2020a). 126

2.34 Band strength for $H_2O - HCOOH$ mixtures: (a) HCOOH as an H-bond donor and (b) HCOOH as an H-bond acceptor (Gorai et al., 2020a). 126

2.35 Filled circles are the data points where we considered harmonic frequencies and the corresponding fitted profiles are the solid lines. Solid filled squares represent the data sets where we considered anharmonic frequencies and the corresponding fitted results are the dotted lines (Gorai et al., 2020a). 127

2.36 Absorption spectra of the four modes for water ice for the five measured compositions, ranging from pure water ice (top) to $4:4$ $H_2O - CH_3OH$ mixture (bottom). The black line represents the absorbance spectra of various concentrations of H_2O-CH_3OH, where CH_3OH is used as a hydrogen bond donor, and for the red line, CH_3OH is used as a hydrogen bond acceptor (Gorai et al., 2020a). 128

2.37 Comparison between calculated and experimentally fitted band strength profiles as a function of CH_3OH concentration. Stars represent the experimental data points (Gorai et al., 2020a). 129

2.38 Band strength for $H_2O - CH_3OH$ mixtures: (a) CH_3OH as a hydrogen bond donor and (b) CH_3OH as a hydrogen bond acceptor (Gorai et al., 2020a). 129

2.39 Absorption spectra of the four modes for water ice for the five measured compositions, ranging from pure water ice (top) to $4:4$ $H_2O - CO$ mixture (bottom) (Gorai et al., 2020a). 131

2.40 Comparison of the band strengths of the four fundamental modes of water for various mixtures of (a) $H_2O - CO$, (b) $H_2O - CH_4$, (c) $H_2O - N_2$, and (d) $H_2O - O_2$ by considering or not the dispersion effect (Gorai et al., 2020a). 132

2.41 Absorption spectra of the four modes for water ice for the five measured compositions, ranging from pure water ice (top) to $4:4$ $H_2O - CO_2$ mixture (bottom) (Gorai et al., 2020a). 133

2.42 Absorption spectra of the four modes for water ice for the five measured compositions, ranging from pure water ice (top) to $4:4$ $H_2O - H_2CO$ mixture (bottom) (Gorai et al., 2020a). 134

2.43 Absorption spectra of the four modes for water ice for the five measured compositions, ranging from pure water ice (top) to 4 : 4 $H_2O - CH_4$ mixture (bottom) (Gorai et al., 2020a). 135

2.44 Absorption spectra of the four modes for water ice for the five measured compositions, ranging from pure water ice (top) to 4 : 4 $H_2O - OCS$ mixture (bottom) (Gorai et al., 2020a). 136

2.45 Absorption spectra of the four modes for water ice for the five measured compositions, ranging from pure water ice (top) to 4 : 4 $H_2O - N_2$ mixture (bottom) (Gorai et al., 2020a). 137

2.46 Absorption spectra of the four modes for water ice for the five measured compositions, ranging from pure water ice (top) to 4 : 4 $H_2O - O_2$ mixture (bottom) (Gorai et al., 2020a). 138

2.47 Top panel: effect of impurities on the four fundamental vibrational modes of water. Bottom panel: comparison of the band strengths for the four fundamental vibrational modes as affected by impurities (Gorai et al., 2020a). 139

2.48 Optimized structures of (a) pure water, (b) $H_2O - HCOOH$, (c) $H_2O - NH_3$, (d) $H_2O - CH_3OH$, (e) $H_2O - CO$, (f) $H_2O - CO_2$, (g) $H_2O - H_2CO$, (h) $H_2O - CH_4$, (i) $H_2O - OCS$, (j) $H_2O - N_2$, and (k) $H_2O - O_2$ clusters with a 6 : 1 concentration ratio (Gorai et al., 2020a). 140

2.49 Band strengths of the four fundamental vibration modes of water for (a) $H_2O - HCOOH$, (b) $H_2O - NH_3$, (c) $H_2O - CH_3OH$, (d) $H_2O - CO$, (e) $H_2O - CO_2$, (f) $H_2O - H_2CO$, (g) $H_2O - CH_4$, (h) $H_2O - OCS$, (i) $H_2O - N_2$, and (j) $H_2O - O_2$ clusters with various concentrations. The water c-hexamer (chair) configuration gas been used for pure water (Gorai et al., 2020a). 141

2.50 Structure of water clusters containing $20H_2O$ molecules with HCOOH as impurity in different concentration ratio: (a) pure water, (b) $H_2O : HCOOH = 20 : 1$, (c) $H_2O : HCOOH = 10 : 1$, (d) $H_2O : HCOOH = 6.67 : 1$, (e) $H_2O : HCOOH = 5 : 1$ (Gorai et al., 2020a). 142

2.51 Comparison of the band strength of the four fundamental vibrational modes for water clusters containing $20H_2O$, $6H_2O$, and $4H_2O$ molecules with HCOOH as an impurity in different concentrations. Solid lines represent the band strength profiles for $20H_2O$ cluster, dotted lines for the water c-hexamer (chair) ($6H_2O$), and dashed lines for water c-tetramer ($4H_2O$) (Gorai et al., 2020a). 142

2.52 Effect of the cluster size on the band strength profile (Gorai et al., 2020a). 143

3.1 Shape and intensity of the resulting incident SED (Das et al., 2020). The three panels of this figure show the modifications of the SED sequentially. The SED obtained from Hester (2008) is shown in panel (a), panel (b) shows the SED after the inclusion of the Galactic background radiation field of 31 Draine units, and finally, panel (c) shows the resulting complete SED after the inclusion of the X-ray spectrum from Figure 1 of Priestley et al. (2017). 149

3.2 Shape and intensity of the incident SED (Davidson & Fesen, 1985) considered for Model B are shown with the solid line. The incident SED considered for the diffuse ISM case is shown with the dashed line (Das et al., 2020). 150

3.3 Surface brightness (SB) ratio between the $2-1$ and $1-0$ transitions of $^{36}ArH^+$ by considering a column density of 1.7×10^{12} cm^{-2} (Das et al., 2020). The upper four panels show the cases with fixed temperatures (T = 10, 100, 1000, and 3000 K respectively) whereas the lower four panels show the cases with fixed H_2 density ($n_{H_2} = 10^{-2}$, 1, 10^2, and 10^4 cm^{-3} respectively). The contours are highlighted near the observed SB ratio (of ~ 2). 153

3.4 Variation of abundances for simple species with a diffuse ISM model shown in the upper panel. The right side of the upper panel, the electron temperature variation is shown. In the lower panel, the variation of isotopic abundances for noble gas species is shown. The abundances of $^{36}ArOH^+$, $^{20}NeOH^+$, and $HeOH^+$ considering the upper limit of their formation rate by radiative association reactions ($\sim 10^{-10}$ cm^3 s^{-1}), are noted [XOH^+ (10^{-10})]. The abundance profiles of $^{20}NeH^+$ and $^{20}NeOH^+$ are also shown when reaction 5a of the Ne network is off (Das et al., 2020). 165

3.5 Abundances of various ionized states of noble gas (X = ^{36}Ar, ^{20}Ne, and He) along with their respective hydride and hydroxyl cations as a function of A_V considering Crab Model A with n_H = 1900 cm^{-3} and $\zeta_{H_2} = \zeta_0 = 1.3 \times 10^{-17}$ s^{-1} (Das et al., 2020). The dashed pink lines denote the abundance of XOH$^+$ considering the upper limit of forming XOH$^+$ ($\sim 10^{-10}$ cm^3 s^{-1}; see Section 3.2.3 for the justification). Abundances of NeH$^+$ and NeOH$^+$ are shown in dotted blue and dotted magenta lines respectively when Ne network reaction 5a is switched off. 169

3.6 Fractional abundance variation of the simple species with A_V by considering n_H = 1900 cm^{-3} and $\zeta_{H_2} = \zeta_0 = 1.3 \times 10^{-17}$ s^{-1} (Model A; Das et al., 2020). The right side of the lower panel shows the electron temperature variation. 171

3.7 Parameter space for the intrinsic line surface brightness (SB) of the $1-0$ and $2-1$ transitions of ArH$^+$, the 971 GHz/308 μm transition of OH$^+$, and the 2.12 μm transition of H_2 considering Model A (Das et al., 2020). The right panel is marked with color-coded values of the intrinsic line SB (in units erg cm^{-2} s^{-1} sr^{-1}). The contours are highlighted in the range of observational limits noted in Table 3.6 (Column 2). 175

3.8 Intrinsic line surface brightness (SB) ratio of various molecular and atomic transition fluxes considering Model A (Das et al., 2020). The right side of each panel is marked with color-coded values of the intrinsic line SB ratio. The contours are highlighted around the previously observed or estimated SB ratios noted in Table 3.7 (Column 2). . . . 176

3.9 Abundance variation of simple species with A_V considering n_H = 2.00×10^4 cm^{-3} and $\zeta/\zeta_0 = 9.07 \times 10^6$ (Model A1; Das et al., 2020). . 177

3.10 Abundance variation of all the hydride and hydroxyl cations considered in this work by considering n_H = 2.00×10^4 cm^{-3} and ζ/ζ_0 = 9.07×10^6 (Model A1; Das et al., 2020). In the upper panel (a) Ar-related species are shown, and in the lower panel (b) the cases of Ne and He are shown. The abundance variation of OH$^+$ is shown in both the panels for comparison. The abundances of ^{36}ArOH$^+$, ^{20}NeOH$^+$, and HeOH$^+$ by considering the upper limit of their formation rate ($\sim 10^{-10}$ cm^3 s^{-1}) are noted [XOH$^+$ (10^{-10})]. The abundance profile of ^{20}NeH$^+$ is also shown when reaction 5a of the Ne network is off. . . 178

3.11 Emissivity of some of the strongest transitions that fall in the range of the frequency limit of Herschel's SPIRE and PACS spectrometer, and SOFIA with respect to the depth into the filament by considering $n_H = 2.00 \times 10^4$ cm^{-3} and $\zeta/\zeta_0 = 9.07 \times 10^6$ (Model A1; Das et al., 2020). 182

3.12 Calculated emissivity of various XOH^+ transitions (X=^{36}Ar, ^{20}Ne, He) noted in Table 3.9 lying in the frequency limit of Herschel's SPIRE and PACS spectrometer, SOFIA, ALMA, VLA, IRAM 30m, and NOEMA by considering $n_H = 2.00 \times 10^4$ cm^{-3} and $\zeta/\zeta_0 = 9.07 \times 10^6$ (Model A1; Das et al., 2020). The upper panel (a) shows the emissivity considering the formation rates following Bates (1983) mentioned in Section 3.2.3, whereas the lower panel (b) considers the upper limit of $\sim 10^{-10}$ cm^3 s^{-1}. 183

3.13 A comparison between the observed surface brightness of the 308 μm transition of OH^+ and the transitions of (a) $^{36}ArH^+$, (b) $^{20}NeH^+$, and (c) HeH^+ is shown (Das et al., 2020). The atmospheric transmission for each transition is shown to check the fate of their identification. . 185

3.14 Parameter space for the intrinsic line surface brightness (SB) of $1-0$ and $2-1$ transitions of ArH^+, the 971 GHz/308 μm transition of OH^+, and 2.12 μm transition of H_2 considering Model B (Das et al., 2020). Extreme right panel is marked with color coded values of the intrinsic line SB (in units erg cm^{-2} s^{-1} sr^{-1}). The contours are highlighted in the range of observational limits noted in Table 3.6 (Column 2). . . . 188

3.15 Intrinsic line surface brightness (SB) ratio of various molecular and atomic transition fluxes considering Model B (Das et al., 2020). Contours are highlighted around the observed or previously estimated values shown in Table 3.7. 189

3.16 Abundance variation of simple species with A_V considering Model B (Das et al., 2020). 190

3.17 Abundance variation of all the hydride and hydroxyl cations considered in this work by considering Model B (Das et al., 2020). In the upper panel (a) Ar related ions are shown whereas in the lower panel (b) the cases of Ne and He are shown both along with OH^+ for comparison. 191

3.18 Emissivity of some of the strongest transitions which are falling in the frequency limit of Herschel's SPIRE and PACS spectrometer, and SOFIA with respect to the depth into the filament by considering Model B (Das et al., 2020). 192

3.19 Calculated emissivity of various XOH^+ transitions (X=^{36}Ar, ^{20}Ne, and He) lying in the frequency limit of Herschel's SPIRE and PACS spectrometer, SOFIA, ALMA, VLA, IRAM 30m, and NOEMA by considering Model B (Das et al., 2020). (a) Upper panel shows the emissivity considering the formation rates following Bates (1983) mentioned in Section 3.2.3, whereas (b) lower panel considering upper limit of $\sim 10^{-10}$ cm^3 s^{-1}. 193

4.1 CH_3N isomers (Sil et al., 2018). 214

4.2 Chemical evolution of the aldimines and amines in the isothermal stage for $a_{fac} = 0.03$ (solid) and 0 (dashed) (Sil et al., 2018). 216

4.3 Chemical evolution of the aldimines and amines in the warm-up stage. Solid lines represent the gas-phase species, whereas corresponding dashed lines represent the ice-phase species (Sil et al., 2018). 216

4.4 CH_5N isomer (Sil et al., 2018). 217

4.5 C_2H_5N isomers (Sil et al., 2018). 219

4.6 Enthalpy of formation of the C_2H_5N isomeric group. Molecules already observed are marked as green circles, and those yet to be observed are marked as red circles (Sil et al., 2018). 220

4.7 Expected intensity ratio of the C_2H_5N isomeric group by considering three components of the dipole moment and effective dipole moment of all the species (Sil et al., 2018). 220

4.8 C_2H_7N isomers (Sil et al., 2018). 223

4.9 Enthalpy of formation of the C_2H_7N isomeric group (Sil et al., 2018). 223

4.10 Expected intensity ratio of the C_2H_7N isomeric group by considering three components of the dipole moment and effective dipole moment of all the species (Sil et al., 2018). 223

4.11 C_3H_7N isomers (Sil et al., 2018). 224

4.12 Enthalpy of formation of the C_3H_7N isomeric group (Sil et al., 2018). 226

4.13 Expected intensity ratio of the C_3H_7N isomeric group by considering three components of the dipole moment and the effective dipole moment of all the species (Sil et al., 2018). 226

4.14 C_3H_9N isomers (Sil et al., 2018). 227

4.15 Enthalpy of formation of the C_3H_9N isomeric group (Sil et al., 2018). 228

4.16 Expected intensity ratio of the C_3H_9N isomeric group by considering three components of the dipole moment and effective dipole moment of all the species (Sil et al., 2018). 228

4.17 Density variation of the intensity of various transitions of ethylamine by considering a non-LTE approximation (Sil et al., 2018). 234

4.18 Density variation of the intensity of various transitions of propanimine by considering a non-LTE approximation (Sil et al., 2018). 234

4.19 Chemical evolution of the peptide-bond-related molecule HNCO and corresponding isomers. This is shown for $\rho_{max} = 1.0 \times 10^7$ cm^{-3} and $T_{ice} = 20$ K by considering the best-fitted parameters with Model A. Red shaded lines represent the observed abundances obtained in G10 (Gorai et al., 2020b). 247

4.20 Chemical evolution of the peptide-bond-related molecule NH_2CHO. This is shown for $\rho_{max} = 1.0 \times 10^7$ cm^{-3} and $T_{ice} = 20$ K by considering the best-fitted parameters with Model A. Red shaded lines represent the observed abundances obtained in G10 (Gorai et al., 2020b). 247

4.21 Chemical evolution of the peptide-bond-related molecule CH_3NCO and corresponding isomers. This is shown for $\rho_{max} = 1.0 \times 10^7$ cm^{-3} and $T_{ice} = 20$ K by considering the best-fitted parameters with Model A. Red shaded lines represent the observed abundances obtained in G10 (Gorai et al., 2020b). 248

4.22 Chemical evolution of HNCO, CH_3NCO, and NH_2CHO during the three stages by considering the best-fit parameters of Model A. The best-fitted time zone is also highlighted. Abundance variation by avoiding Haupa et al. (2019) pathways in the gas phase is also shown (Gorai et al., 2020b). 248

4.23 Parameter space obtained with Model A by considering the best-fitted parameters noted in Table 4.14 at an age position of 1.12×10^6 years. Color coding in the right side of the each panel represents the abundance with respect to H_2 (Gorai et al., 2020b). 249

4.24 Abundances of HNCO, CH_3NCO, and NH_2CHO by considering different T_{coll} and ρ_{max} with Model B (Gorai et al., 2020b). 249

4.25 Abundances of HNCO, CH_3NCO, and NH_2CHO by considering $\rho_{max} = 10^7$ cm^{-3}, and different T_{max} and T_{coll} with Model B (Gorai et al., 2020b). 249

4.26 Chemical linkage between the three N-bearing molecules (Gorai et al., 2020b). 250

4.27 Parameter space of the abundances of CO, CN, CS, and HNC for A_V = 1, 2, 3, 4, 5 mag for the diffuse cloud model obtained with the CLOUDY code (Sil et al., 2021). The right side of each panel is marked with color-coded values of abundance concerning total hydrogen nuclei. The contours are highlighted around the previously observed abundance limit (Chantzos et al., 2020) toward the cloud with $v_{LSR} = -17$ km s^{-1}, including the inferred uncertainties. 264

4.28 Parameter space of the temperature for A_V = 1, 2, 3 mag for the diffuse cloud model obtained with the CLOUDY code (Sil et al., 2021). The right side of each panel is marked with color-coded values of temperature. 265

4.29 Chemical evolution of the abundances of CO, CN, CS, and HNC for the diffuse cloud model ($n_H = 300$ cm^{-3} and $\zeta = 1.7 \times 10^{-16}$ s^{-1}) with the CLOUDY code. The colored horizontal bands correspond to the observed abundances (Chantzos et al., 2020) toward the cloud with $v_{LSR} = -17$ km s^{-1}, including the inferred uncertainties (Sil et al., 2021). Here, the vertical dashed line indicates the visual extinction parameter of best agreement between observation and model results. . 266

4.30 Chemical evolution of the abundances of neutral P-bearing species (left panel) and their corresponding cations (right panel) for the diffuse cloud model ($n_H = 300$ cm^{-3} and $\zeta = 1.7 \times 10^{-16}$ s^{-1}) with the CLOUDY code (Sil et al., 2021). Here, the vertical dashed line indicates the visual extinction parameter of the best agreement between observation and model results. 266

4.31 Abundance profiles of H, H^+, H_2, H_2^+, H_3^+, e^-, and N and temperature profile for the diffuse cloud model (n_H = 300 cm^{-3} and $\zeta = 1.7 \times 10^{-16}$ s^{-1}) with the CLOUDY code (Sil et al., 2021). The vertical dashed line indicates the visual extinction parameter of best agreement between observation and model results. 268

4.32 Chemical evolution of the abundances of important P-bearing species with the CLOUDY code considering Röllig et al. (2007) F4 PDR model (Sil et al., 2021). 269

4.33 Abundance profiles of H, H^+, H_2, H_2^+, H_3^+, e^-, N, and temperature profile with the CLOUDY code considering the Röllig et al. (2007) F4 PDR model (Sil et al., 2021). 269

4.34 Time evolution of the abundances of CO, CN, CS, and HNC with the CMMC code for diffuse cloud. Observed abundances are also highlighted for better understanding. The solid curves represent the case with $n_H = 100$ cm^{-3} and dashed curves represent the case with $n_H = 500$ cm^{-3} (Sil et al., 2021). 272

4.35 Chemical evolution of the P-bearing molecules for $A_V = 2$ mag, n_H = 300 cm^{-3}, $T_{gas} = 40$ K, and $T_{dust} = 20$ K with the CMMC code for diffuse cloud is shown. The evolution of the neutrals and radicals is shown in the left panel, whereas ions are shown in the right panel. Derived abundances of all the species are found to be $< 10^{-10}$ for such conditions (Sil et al., 2021). 272

4.36 The final abundances of P^+, P, PO, and PN are shown with A_V with the CMMC code for diffuse cloud. The conversion of P^+ to P takes place in the range $A_V = 2 - 3$ mag. Beyond $A_V = 4$ mag no changes in the abundances of P^+ and P are obtained. The abundance ratio of PO and PN is found to be always < 1 (Sil et al., 2021). 273

4.37 The observed abundances of PO and PN in the high-mass star-forming region W51 and W3(OH) (Rivilla et al., 2016) are shown along with our modeled peak abundances (taken beyond the isothermal stage) with hot-core (left panel) and hot-corino (right panel) cases using CMMC code (Sil et al., 2021). The peak abundance variation of the PH_3 is also shown with the initial abundance of P^+. PH_3 is yet to be observed in hot-core/corino. The obtained peak abundance of PH_3 is far below the observed limit of PH_3 in C-star envelope IRC +10216 (Agúndez et al., 2008; Agúndez et al., 2014). Peak abundances of PO, PN, and PH_3 are also shown with the dashed lines when the BE of the P-bearing species is considered from the tetramer configuration noted in Table 4.16. The solid green curve shows the peak abundance of PH_3 in the absence of its destruction by H and OH. We obtained a significantly higher peak abundance of PH_3 with the lack of these destruction pathways. 275

4.38 Abundance variation of PO, PN, and PO/PN ratio obtained using CMMC code by considering the initial elemental abundance of P^+ as 1.8×10^{-9} for hot-core and 5.6×10^{-9} for the hot-corino case (Sil et al., 2021). Solid lines represent the cases with the BEs from KIDA, and the dashed lines represent the values with the tetramer configuration of water. During the warm-up and post-warm-up stages, we have a good correlation with our results. 276

4.39 Abundance variations of most of the P-bearing neutral and ionic species are shown using CMMC code considering initial elemental abundance of P^+ as 1.8×10^{-9} and for the hot-core region (Sil et al., 2021). In the absence of the destruction of PH_3 by H and OH, PH_3 is highly abundant. 277

4.40 Four distinct stages considered for the simulation using CMMC code (Sil et al., 2021). In the first stage, the cloud remains in the diffuse stage for 10^7 years. It starts to collapse in the next step, which continues for 10^5 years. The collapsing stage is followed by a warm-up and post-warm-up stage, which continues for another 1.5×10^5 years. 279

4.41 Time evolution of H, H_2, C^+, C, CO, CO_2, NH_3, H_2O, and CH_3OH obtained using CMMC code is shown (Sil et al., 2021). During the lifetime of the diffuse cloud H converts into H_2 and C^+ converts into C. During the collapsing stage, C atom is heavily depleted and converts into CO. 280

4.42 Time evolution of the abundances (concerning total hydrogen nuclei in all forms) of major P-bearing species using CMMC code is shown (Sil et al., 2021). 280

4.43 Ice-phase IR absorption spectra of PH_3 including the harmonic fundamental bands and anharmonic overtones and combination bands (Sil et al., 2021). 287

4.44 Comparison of ice-phase IR absorption spectra of pure PH_3 and mixture of PH_3 with other volatiles (CH_4, CO_2, CO, NH_3, H_2S, and SO_2) considering the harmonic fundamental bands (Sil et al., 2021). 289

4.45 Gas-phase IR absorption spectra of PH_3 with increasing concentration of H_2O (Sil et al., 2021). 289

List of Tables

1.1 Known interstellar molecules ($\sim$ 251 molecules; last updated: June 2021). 4

1.2 Solar elemental abundances (Asplund et al., 2009). 9

2.1 BE of H and H_2 (Sil et al., 2017) using the method used in Avgul et al. (1957). 41

2.2 BE of H and H_2 on the benzene surface (Sil et al., 2017). 42

2.3 BE of H and H_2 on silica surface (Sil et al., 2017). 43

2.4 BE of H and H_2 on water surface (Sil et al., 2017). 44

2.5 Different sets of existing BE (in Kelvin) of H and H_2 (Sil et al., 2017). 45

2.6 Calculated BEs of 16 stable species (Das et al., 2018). 51

2.7 Comparison of calculated BEs using water monomer (adsorbent) with experimentally used BEs (Das et al., 2018). 52

2.8 Calculated BEs using water hexamer (adsorbent) to check the effect of basis set superposition error (BSSE) using the counterpoise (CP) method (Das et al., 2018). 55

2.9 Calculated BEs using water tetramer (adsorbent) to check the influence of the higher-order quantum chemical level of theory (Das et al., 2018). 56

2.10 Calculated and available list of BEs of various species (Das et al., 2018). 57

2.11 Calculated BE (with MP2/aug-cc-pVDZ level of theory) of various species with H_2 monomer surface (Das et al., 2021). 70

2.12 Initial elemental abundances considered in this study (Das et al., 2021). 78

2.13 The obtained abundance of gH_2, gH, gH_2O and gCH_3OH for the effect of encounter desorption of H_2 under various situation with $R = 0.35$, $n_H = 10^7$ cm^{-3}, and $T = 10$ K (Das et al., 2021). 83

2.14 Integration bounds for the four fundamental modes of vibration (Gorai et al., 2020a). 94

2.15 Ice mixture composition details (Gorai et al., 2020a). 94

2.16 Harmonic IR frequencies and intensities of the H_2O^{QM} + 3 H_2O^{MM} complex (Figure 2, left panel) (Gorai et al., 2020a). 98

2.17 Harmonic IR frequencies and intensities of the first 4 H_2O^{QM}+16 H_2O^{MM} complex (see Figure 2.26(a), right panel, Configuration 1) evaluated at the B3LYP/6-31g(d) level (Gorai et al., 2020a). 99

2.18 Harmonic IR frequencies and intensities of the first 4 H_2O^{QM}+16 H_2O^{MM} complex (Figure 2.26(b), right panel, Configuration 2) evaluated at the B3LYP/6-31g(d) level (Gorai et al., 2020a). 100

2.19 Absorption band strengths and band positions (within parentheses) of pure water ice[a] (Gorai et al., 2020a). 102

2.20 Comparison of band positions and band intensities as obtained by different quantum-chemical level of theories (Gorai et al., 2020a). . . 103

2.21 Frequencies, integral absorbance coefficients, and normal modes of vibration of $H_2O - X$ (X = HCOOH, NH_3, CH_3OH, CO, CO_2, H_2CO, CH_4, OCS, N_2, and O_2) (Gorai et al., 2020a). 107

2.22 Harmonic IR frequencies and intensities of the complex $4H_2O$ evaluated at the B2PLYP/maug-cc-pVTZ level (Gorai et al., 2020a). . . . 111

2.23 Harmonic IR frequencies and intensities of the complex $4H_2O$/HCOOH evaluated at the B2PLYP/maug-cc-pVTZ level (Gorai et al., 2020a). 112

2.24 Harmonic IR frequencies and intensities of the complex $4H_2O$/2HCOOH evaluated at the B2PLYP/maug-cc-pVTZ level (Gorai et al., 2020a). 113

2.25 Harmonic IR frequencies and intensities of the complex $4H_2O$/3HCOOH evaluated at the B2PLYP/maug-cc-pVTZ level (Gorai et al., 2020a). 114

2.26 Harmonic IR frequencies and intensities of the complex $4H_2O$/4HCOOH evaluated at the B2PLYP/maug-cc-pVTZ level (Gorai et al., 2020a). 115

2.27 Linear fit coefficients for the $H_2O - X$ (X = HCOOH, NH_3, CH_3OH, CO, CO_2, H_2CO, CH_4, OCS, N_2, and O_2) mixtures[a] (Gorai et al., 2020a). 116

2.28 Harmonic IR frequencies and intensities of the complex $4H_2O/NH_3$ evaluated at the B2PLYP/maug-cc-pVTZ level (Gorai et al., 2020a). 117

2.29 Harmonic IR frequencies and intensities of the complex $4H_2O/2NH_3$ evaluated at the B2PLYP/maug-cc-pVTZ level (Gorai et al., 2020a). 118

2.30 Harmonic IR frequencies and intensities of the complex $4H_2O/3NH_3$ evaluated at the B2PLYP/maug-cc-pVTZ level (Gorai et al., 2020a). 119

2.31 Harmonic IR frequencies and intensities of the complex $4H_2O/4NH_3$ evaluated at the B2PLYP/maug-cc-pVTZ level (Gorai et al., 2020a). 120

3.1 Adopted physical parameters for the Crab filament (Das et al., 2020). 151
3.2 Initial gas-phase elemental abundances with respect to total hydrogen nuclei in all forms for the Crab filament (Das et al., 2020). 151
3.3 Reaction pathways for the formation and destruction of some noble gas ions (Das et al., 2020). 157
3.4 Gas-phase elemental abundances of species with respect to total hydrogen nuclei in all forms for the modeling of diffuse ISM using CLOUDY (Das et al., 2020). 164
3.5 Comparison between the obtained column densities of some atomic and molecular ions with the observation of diffuse cloud toward W51 (Indriolo et al., 2012; Das et al., 2020). 167
3.6 Summary of the previously observed surface brightness (SB) values in erg cm^{-2} s^{-1} sr^{-1} (Das et al., 2020). 173
3.7 Summary of the previously observed or estimated line surface brightness (SB) ratios (Das et al., 2020). 174
3.8 Comparison between the observed and our modeling results (Das et al., 2020). 179
3.9 Strongest transitions falling in the range of Herschel's SPIRE and PACS spectrometer, SOFIA, ALMA, VLA, IRAM 30m, and NOEMA considering $n_H = 2.00 \times 10^4$ cm^{-3} and $\zeta/\zeta_0 = 9.07 \times 10^6$ (Model A1; Das et al., 2020). 180
3.10 H_2 vibrational line surface brightnesses (SB) relative to the 1-0 S(1) line for Knot 51 from Loh et al. (2012) and for our final models (Das et al., 2020). 187
3.11 Ground vibrational and equilibrium rotational constants and asymmetrically reduced quartic centrifugal distortion constants of $ArOH^+$, $NeOH^+$, and $HeOH^+$ with the DFT-B3LYP/6-311++G(d,p) level of theory (Das et al., 2020). 196

4.1 Ice-phase formation pathways (Sil et al., 2018). 204
4.2 Enthalpy of formation and electronic energy (E_0) with zero-point vibrational energy (ZPE) and relative energy (in bracket) with G4 composite method (Sil et al., 2018). 206
4.3 Calculated dipole moment components with HF/6-31G(3df) level of theory (Sil et al., 2018). 207

4.4 Calculated rotational constants and rotational partition functions at 200 K with the MP2/6-311++G(d,p) level of theory (Sil et al., 2018). 208

4.5 Gas-phase formation and destruction pathways (Sil et al., 2018). . . 210

4.6 Line parameters of trans-ethylamine in the millimeter and submillimeter regime using ALMA (LTE) (Sil et al., 2018). 230

4.7 Line parameters of (1Z)-1-propanimine in the millimeter and submillimeter regime using ALMA (LTE) (Sil et al., 2018). 231

4.8 Non-LTE modeling line parameters of trans-ethylamine (Sil et al., 2018). 232

4.9 Non-LTE modeling line parameters of (1Z)-1-propanimine (Sil et al., 2018). 233

4.10 Initial abundances with respect to total hydrogen nuclei (Gorai et al., 2020b). 239

4.11 Computed BEs (Gorai et al., 2020b). 240

4.12 Calculated reaction enthalpies, type of reactions, and activation barriers (with ZPVE correction) of various reactions (Gorai et al., 2020b). 242

4.13 Estimated rotational temperatures, column densities, and fractional abundances of the observed species (Gorai et al., 2020b). 245

4.14 Key differences between the Model A and Model B (Gorai et al., 2020b). 246

4.15 Reaction pathways for P-chemistry (Sil et al., 2021). 256

4.16 Calculated BE (with MP2/aug-cc-pVDZ level of theory) and enthalpy of formation [with DFT-B3LYP/6-31G(d,p) level of theory] of P-bearing species (Sil et al., 2021). 260

4.17 Initial elemental abundance for the diffuse cloud and PDR model considered in the CLOUDY code (Sil et al., 2021). 263

4.18 Estimated column density and optical depth of the observed molecules for the diffuse cloud model obtained with the CLOUDY code (Sil et al., 2021). 267

4.19 Initial elemental abundance for the diffuse cloud model considered in the CMMC code (Chantzos et al., 2020; Sil et al., 2021). 271

4.20 Initial elemental abundance for the hot-core/corino model considered in the CMMC code (Wakelam & Herbst, 2008; Sil et al., 2021). . . . 274

4.21 Peak abundances of the P-bearing species under various physical conditions (Sil et al., 2021). 283
4.22 Summary of the obtained abundance ratio between PO and PN in different astrophysical environments (Sil et al., 2021). 285
4.23 Experimental and calculated IR data for PH_3 (Sil et al., 2021). . . . 288

A.1 The parameters taken from Verner & Yakovlev (1995) for calculating ionization cross sections σ_i(E) (Das et al., 2020). 298
A.2 The parameters taken from Lennon et al. (1988) to calculate the rate coefficients $\langle \sigma v \rangle$ (Das et al., 2020). 298
A.3 Calculated values of X-ray ionization rates (Das et al., 2020). 298

Chapter 1

Introduction

Astrochemistry is a flourishing field of science intending to understand the evolution of the universe toward molecular complexity. It brings us closer to understanding our origins. Molecular astrophysics are often used as synonyms for astrochemistry to define an interdisciplinary field involving chemistry and astronomy, astrophysics, and a flavor of biology and geology. It is long anticipated that the seeds of life on the Earth might have originated from space through the infall of asteroids, comets, or meteorites (Chyba et al., 1990; Chyba & Sagan, 1992). We are far from confident if one or both exogenous delivery and endogenous synthesis is correct. Space is not empty. It is full of various simple and complex molecular species. Therefore, our observable universe may be called a molecular universe (Tielens, 2013). We can diagnose different aspects of this universe by observing various types of molecules. These molecules can be utilized as tracers to determine the physical and chemical conditions of different evolutionary stages of star formation. The chemical model of a molecular cloud serves as a critical link in understanding the complexity of the star-forming region (Herbst, 2014). The "interstellar medium" (ISM) is a highly tenuous medium between the stars in a galaxy. It is filled with ordinary matter, relativistic charged particles known as cosmic rays, and magnetic fields. The ISM contributes to transport the elements synthesized in the interior of stars or outer layers of stars, in the form of atoms and molecules or of dust grains, to regions that are distant from the stellar birthplace and distribute them more uniformly through Supernovae explosions. The ISM is enriched by diverse chemical processes that give rise to complex organic molecules (COMs). It stands for interstellar molecules with a different connotation, e.g., organic chemistry or biochemistry. A carbon- (hydrogen, oxygen, and nitrogen are optional) bearing molecule containing six or more atoms is known as a COM. Methanol (CH_3OH) is the prototypically most straightforward COM (Herbst & van Dishoeck, 2009). These COMs, or at least some segments of these molecules, are produced on dusts. The hydrogenation in the cold stage and radical chemistry in the warm-up stage plays a crucial role in shaping this. The icy covered grain mantles are further exposed to interstellar radiation field (ISRF) and other dissociative radiation sources to form more extensive and

more complex molecules. ISRF has a substantial far-ultraviolet (far-UV) or vacuum-ultraviolet (VUV) component that readily dissociates most molecules. Both far-UV and VUV emission are categorized as UV emission with shorter wavelengths than 200 nm. The resulting COMs take part in the star and planet formation process and may eventually transfer the seeds of life on nascent planets. In addition, the study of prebiotic molecules is always fascinating as they are involved in forming amino acids, proteins, nucleobases, and the basic building blocks of life (Chakrabarti & Chakrabarti, 2000a,b; Chakrabarti et al., 2015; Majumdar et al., 2012, 2013, 2015; Garrod, 2013). However, the abundance of these complex prebiotic molecules is often below the observing limit of the present astronomical observation. Thus it is customary to observe their precursors to tentatively constrain the parameters that form the prebiotic species in space (Sil et al., 2018).

Merely a hundred years ago, Sir Arthur Eddington was doubtful about the existence of molecules in the vast interstellar space. He pointed out that "it is difficult to admit the existence of molecules in interstellar space because when once a molecule becomes dissociated there seems no chance of the atoms joining up again" (Bakerian lecture; Eddington, 1926). As of July 2021, about 250 different gas-phase molecules are identified in the ISM (mainly in dense interstellar clouds) and circumstellar envelopes (CSEs, formed due to strong mass loss of stars in their later stages). These molecules are listed in Table 1.1. These statistics are obtained by avoiding the isotopomers. The rate of discovery continues at a rapid pace. Most of the molecules were observed in the gas phase by their rotational transitions in the centimeter, millimeter, and submillimeter portions of the electromagnetic spectrum. Modern radio telescopes like Atacama Large Millimeter/submillimeter Array (ALMA) offer unique opportunities to include more species in the catalog. The dust particles and their icy mantles in colder regions can be probed against absorption under background radiation by vibrational spectroscopy. Among the observed complex species, about one-third of them are COMs, though we are far from having a complete inventory of the interstellar molecules. An up-to-date census by McGuire (2018) reported a summary of the first detection of each molecular species, including the observational facility, wavelength range, transitions, enabling laboratory spectroscopic work, and listing tentative and disputed detections. The ongoing web-based resources are of particular importance concerning the list of interstellar and circumstellar detections: the Astrochymist's *A Bibliography of Astromolecules*[1] maintained by David Woon or the Cologne Database for Molecular Spectroscopy's *List of Molecules in Space*[2]

[1] http://www.astrochymist.org/astrochymist_ism.html
[2] https://www.astro.uni-koeln.de/cdms/molecules

(CDMS; Müller et al., 2001, 2005; Endres et al., 2016), or community-supported Wikipedia's *List of interstellar and circumstellar molecules*[3]. Six key classes of COMs, namely, aldehydes (HCOR), ketones (RCOR′), carboxylic acids (RCOOH), esters (RCOOR′), amides ($RCONH_2$), nitriles (RCN), and isocyanates (RNCO), with R and R′ being an alkyl group, detected in the ISM are shown in Figure 1.1. A substantial fraction ($\sim 33\%$) of known molecules have now been seen in external galaxies, while the numbers of molecules known in protoplanetary disks (23), interstellar ices (6), and exoplanet atmospheres (5) are much smaller due to observational challenges.

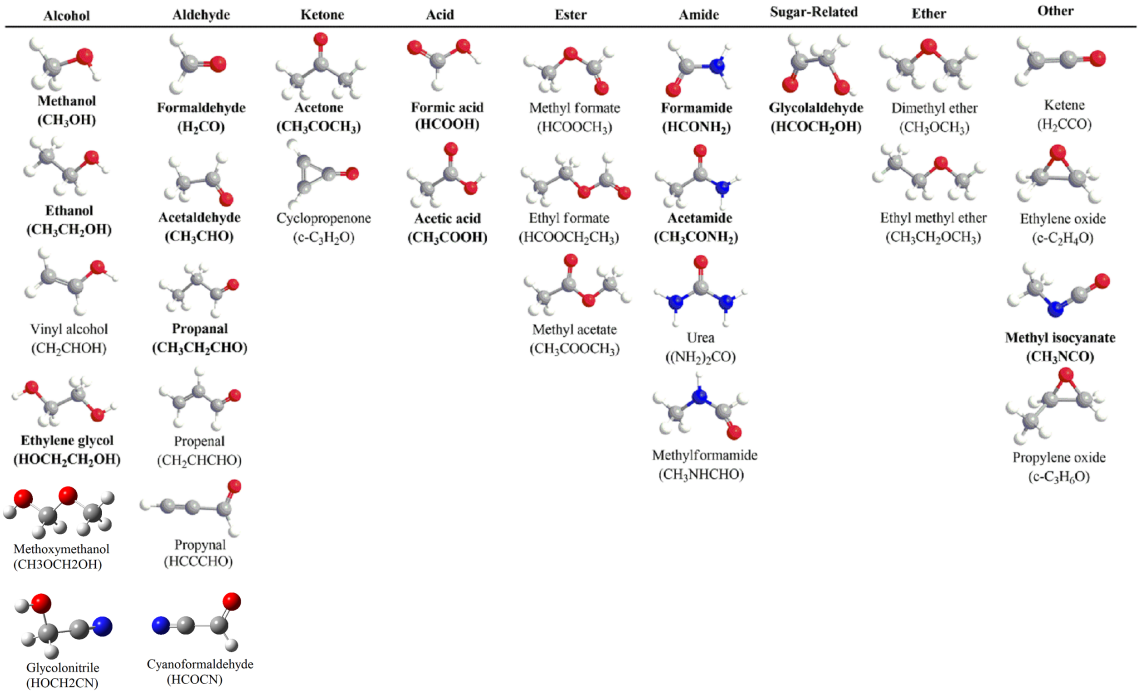

Figure 1.1: Key classes of COMs detected in the ISM, which are primarily formed on ice-coated interstellar grains.

[3] https://en.wikipedia.org/wiki/List_of_interstellar_and_circumstellar_molecules

Table 1.1: Known interstellar molecules ($\sim$ 251 molecules; last updated: June 2021).

2 atoms (45)		**3 atoms (45)**		**4 atoms (31)**		**5 atoms (32)**		**6 atoms (24)**	**7 atoms (16)**	**8 atoms (16)**	**9 atoms (15)**	
H_2	SiS	C_3	NH_2	$c-C_3H$ [a]	$c-SiC_3$ [a]	C_5	C_4H^-	C_5H	C_6H	CH_3C_3N	CH_3C_4H	C_3H_6
AlF	CS	C_2H	H_3^+	$l-C_3H$ [b]	CH_3	C_4H	HC(O)CN	$l-H_2C_4$ [b]	CH_2CHCN	HC(O)OCH_3	CH_3CH_2CN	CH_3CH_2SH
AlCl	HF	C_2O	SiCN	C_3N	C_3N^-	C_4Si	HNCNH	C_2H_4	CH_3C_2H	CH_3COOH	$(CH_3)_2O$	CH_3NHCHO
C_2	HD	C_2S	AlNC	C_3O	PH_3	$l-C_3H_2$ [b]	CH_3O	CH_3CN	HC_5N	C_7H	CH_3CH_2OH	HC_7O
CH	FeO	CH_2	SiNC	C_3S	HCNO	$c-C_3H_2$ [a]	NH_4^+	CH_3NC	CH_3CHO	C_6H_2	HC_7N	H_2C_3HCCH
CH^+	O_2	HCN	HCP	C_2H_2	HOCN	H_2CCN	H_2NCO^+	CH_3OH	CH_3NH_2	CH_2OHCHO	C_8H	HC_3HCHCN
CN	CF^+	HCO	CCP	NH_3	HSCN	CH_4	$NCCNH^+$	CH_3SH	$c-C_2H_4O$ [a]	$l-HC_6H$ [b]	$CH_3C(O)NH_2$	H_2CCHC_3N
CO	SiH	HCO^+	AlOH	HCCN	H_2O_2	HC_3N	CH_3Cl	HC_3NH^+	H_2CCHOH	CH_2CHCHO	C_8H^-	
CO^+	PO	HCS^+	H_2O^+	$HCNH^+$	C_3H^+	HC_2NC	MgC_3N	HC_2CHO	C_6H^-	CH_2CCHCN	**10 atoms (6)**	**11 atoms (7)**
CP	AlO	HOC^+	H_2Cl^+	HNCO	HMgNC	HCOOH	NH_2OH	NH_2CHO	CH_3NCO	H_2NCH_2CN	CH_3COCH_3	HC_9N
SiC	OH^+	H_2O	KCN	HNCS	HCCO	H_2CNH	HC_3O^+	C_5N	HC_5O	CH_3CHNH	$HOCH_2CH_2OH$	CH_3C_6H
HCl	CN^-	H_2S	FeCN	$HOCO^+$	CNCN	H_2C_2O	HC_3S^+	$l-HC_4H$ [b]	$HOCH_2CN$	CH_3SiH_3	CH_3CH_2CHO	C_2H_5OCHO
KCl	SH^+	HNC	HO_2	H_2CO	HONO	H_2NCN	H_2CCS	$l-HC_4N$ [b]	HC_4NC	$(NH_2)_2CO$	CH_3C_5N	$CH_3OC(O)CH_3$
NH	SH	HNO	TiO_2	H_2CN	MgCCH	HNC_3	C_4S	$c-H_2C_3O$ [a]	HC_3HNH	$HCCCH_2CN$	CH_3CHCH_2O	CH_3COCH_2OH
NO	HCl^+	MgCN	C_2N	H_2CS	HCCS	SiH_4	HC(O)SH	H_2CCNH	$c-C_3HCCH$ [a]	HC_5NH^+	CH_3OCH_2OH	$c-C_5H_6$ [a]
NS	TiO	MgNC	Si_2C	H_3O^+		H_2COH^+	HC(S)CN	C_5N^-	$l-H_2C_5$ [b]	CH_2CHCCH		$NH_2CH_2CH_2OH$
NaCl	ArH^+	N_2H^+	HS_2					HNCHCN			**12 atoms (6)**	**>12 atoms (8)**
OH	N_2	N_2O	NCO					SiH_3CN			$c-C_6H_6$ [a]	$HC_{11}N$
PN	NO^+	NaCN	HSC					C_5S			$C_2H_5OCH_3$	$c-C_6H_5CN$ [a]
SO	NS^+	OCS	HCS					MgC_4H			$n-C_3H_7CN$	$1-C_{10}H_7CN$
SO^+	VO	SO_2	CaNC					CH_3CO^+			$i-C_3H_7CN$	$2-C_{10}H_7CN$
SiN	HeH^+	$c-SiC_2$ [a]	NCS					C_3H_3			$1-c-C_5H_5CN$ [a]	$c-C_9H_8$ [a]
SiO		CO_2						H_2C_3S			$2-c-C_5H_5CN$ [a]	C_{60}
								HCCCHS				C_{60}^+
												C_{70}

Notes: Total number of molecules for each category is provided in the parentheses. These statistics are obtained by avoiding the isotopomers. Deuterium isotopic species are given separately only if their method of detection is intrinsically different from that of pure hydrogen ones.

[a] The 'c' refers to cyclic form.

[b] The 'l' refers to cyclic form.

1.1 Birth of stars and and the planetary systems

Astrochemistry and its linkage to star formation have been the subject of several reviews (van Dishoeck & Blake, 1998b; Caselli & Ceccarelli, 2012; Ceccarelli et al., 2014; Tielens, 2013; van Dishoeck et al., 2014; Öberg, 2016; Jørgensen et al., 2020; Öberg & Bergin, 2021). Stars span a large range of masses. The initial cloud mass is important beyond collapse to finally form a star. Low-mass stars are the most relevant for determining planetary compositions. They constitute the vast majority of stars, and their long lifetimes are likely a requirement for the origin and sustainance of life. Several excellent reviews (Shu et al., 1987; McKee & Ostriker, 2007; Luhman, 2012) discuss the low-mass star formation, illustrated in Figures 1.2 and 1.3.

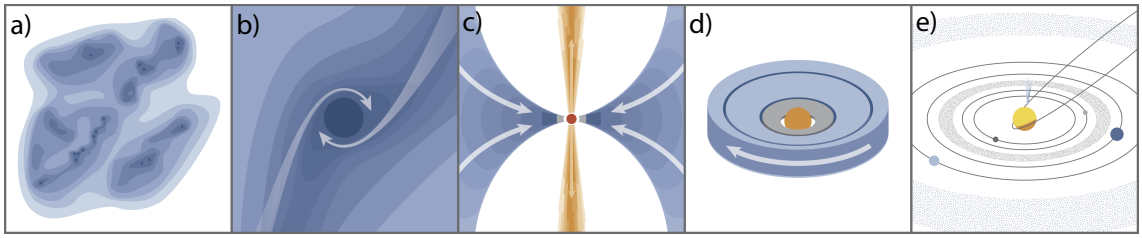

Figure 1.2: Cartoon depiction of different stages characterizing low-mass (Solar-like) star and planet formation (Courtesy: Öberg & Bergin, 2021).

Stars form in over-dense regions in inhomogeneous interstellar molecular clouds (Figure 1.2a), mainly associated with dense molecular clouds (Heyer & Dame, 2015), where densities are $> 10^5$ molecules cm^{-3}. However, denser sub-structures having sizes of the order of a tenth of a parsec within the dense clouds are referred to as the dense cores. They are characterized by orders of magnitude higher densities ($\sim 10^2 - 10^6$) and lower temperatures ($\sim$ 10 K) (Benson & Myers, 1989; Bergin & Tafalla, 2007).

Some cores are dense and massive enough (fulfilling the Jeans mass criteria) that they can begin to collapse due to self-gravity (Shu, 1977), overcoming turbulence, thermal and magnetic pressure. Cores fated to collapse are referred to as the pre-stellar, as they will eventually form a star. This collapse is initially isothermal, keeping the core cool by molecules radiating away the heat produced by the collapse. The collapse is not spherically symmetric due to the conservation of cloud angular momentum (Figure 1.2b).

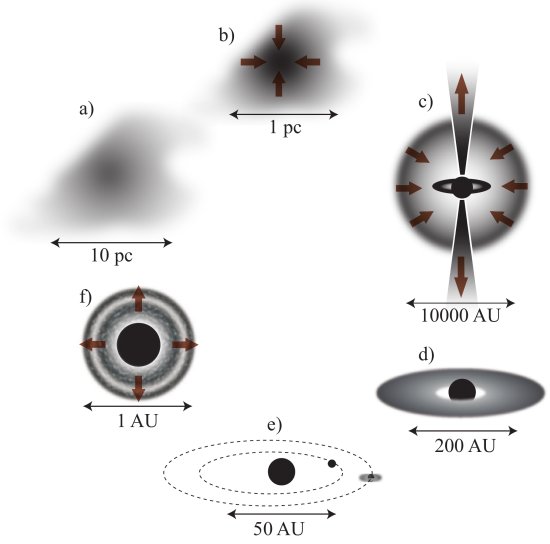

Figure 1.3: The low-mass stellar life cycle from diffuse clouds and the beginning of the star formation up to the death of the star. The length scale of each stage is shown (Courtesy: Öberg, 2009).

As the collapse proceeds, at the center of the collapsing core, a dense condensation forms, and the collapse turns adiabatic due to its higher optical thickness. The condensation eventually heats up and begins to form a young star, a stage known as a protostar (Figure 1.2c). During the protostellar stage, the central protostar consumes matter from the surrounding cloud core (i.e., protostellar envelope). Within the envelope, the temperature and density increase toward the center due to stellar heating. When the collapsing gas reaches a temperature of $100 - 300$ K, we refer to the material as a 'hot corino', or, if it is of high mass, the term 'hot core' is used. Some of the accreting material spreads out into a disk to conserve angular momentum, which simultaneously serves to funnel matter onto the star. Angular momentum is also removed from the system through the launch or ejection of a fraction of matter violently outward in the form of highly supersonic collimated jets and molecular outflows (Figure 1.2c). When the outflowing material encounters the quiescent gas of the envelope and the molecular cloud, it creates shocks, where the grain mantles and refractory grains are (partially) sputtered and vaporized. Subsequently, this stage is characterized by gas-phase chemistry, as grains flow toward the protostar. Once in the gas phase, molecules can be observed via their rotational lines.

As the protostellar system evolves, more and more mass is found in the star and disk than in the remnant envelope. The envelope is finally dispersed on time scales of ∼1 Myr, leaving a pre-main sequence star and a Keplerian disk (Figure 1.2d). The change of name from protostar to pre-main sequence star points to the fact that the central star became hot enough for fusion reaction to take place inside. The circumstellar disk is often referred to as a proto-planetary or planet-forming disk to indicate that these disks are the formation sites of planets (Williams & Cieza, 2011). However, recent observations suggest that planet formation may begin much earlier, already at the protostellar stage (ALMA Partnership et al., 2015; Harsono et al., 2018).

The protoplanetary disk stage lasts for $\sim 1-10$ Myrs depending on disk in stellar clusters. During this time, the disk material is accreted onto the star, onto planets, and dispersed through interactions with stellar photo-evaporative winds (Ercolano & Koepferl, 2014). Thus, what is left behind is a nascent planetary system (Figure 1.2e) that continues to evolve for hundreds of millions of years due to collisions between remaining the planets and planetesimals.

Understanding how the properties of protoplanetary disks link to planet formation is currently an active field of research. For example, it is theorized that "snow lines", which are regions far enough from the star to allow the freeze-out of gas-phase species (Kennedy & Kenyon, 2008), are essential to the formation of planets around a new-born star. As life exists in our Solar System, detailed knowledge of many different processes taking place at various locations in a protoplanetary disk is crucial to know. A better understanding of the role of snow lines in the chemical composition of a disk and in the planet formation process itself may ultimately show how the building blocks of life arrived on Earth. For example, through impacting comets, which are small icy bodies and remnants of the protoplanetary material, carry the chemical memory of the processes in diffuse and dense clouds (Chyba & Sagan, 1997; Altwegg et al., 2019).

Over time, the star will grow out of the main sequence stage as it becomes depleted of hydrogen, essentially burning up its adjacent shells. After several stages involving drastic temperature and pressure changes, for Sun-like stars, its outer layers are enhanced with heavy elements. It will eventually be ejected into the diffuse ISM. The ejected materials again collapse under the influence of gravity to form dense interstellar clouds, containing more overgrown and dark parts known as the cold cores. The cycle starts over again, though more enriched in heavy elements than the previous cycle.

1.2 The interstellar ingredients

Astronomers have a somewhat restricted "periodic table" than chemists. It is known as the "astronomer's periodic table". It only contains 11 elements, which are the most abundant in the Universe (McCall, 2006). The left panel of the pie graph (see Figure 1.4) shows that after hydrogen (90.8% by number and 70.4% by mass) and helium (9.1% by number and 28.1% by mass), the most abundant elements are oxygen, carbon, neon, nitrogen, etc. Except hydrogen and helium, all other elements are classified as "metals", even if they are not metal in a chemical sense. The abundances summarized in Table 1.2 were derived for the solar photosphere by Asplund et al. (2009). These abundances are believed to be applicable to the ISM as well, with a possibility of minor variations (Przybilla et al., 2008). Before the formation of stars, the entire periodic table was based on hydrogen, little helium, trace amount of lithium (fittingly a metal). In contrast, the elemental abundances of the Earth's mantle, shown on the right panel of Figure 1.4, include roughly half of the oxygen, with the rest mostly made up of magnesium, silicon, iron, and some aluminum with other trace elements.

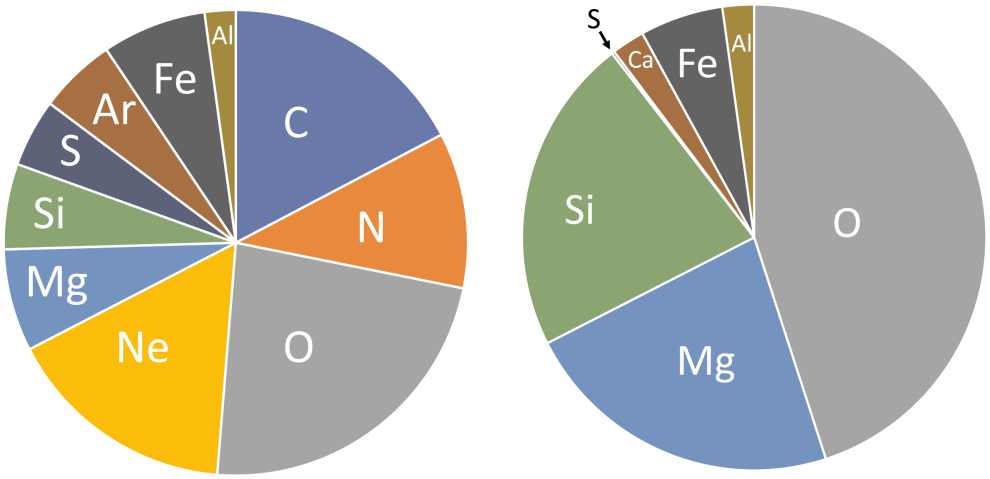

Figure 1.4: Left: atomic abundances of the 10 most common elements in the Universe besides H and He. Right: atomic abundances of the most common elements in the Earth's mantle (Courtesy: Fortenberry, 2020).

The physical conditions of ISM are different from occurring naturally on the Earth, and they are challenging to recreate in laboratory experiments. The ISM is highly heterogeneous with a broad range of temperatures, densities, and extinction

Table 1.2: Solar elemental abundances (Asplund et al., 2009).

Element	**Abundance**	**Element**	**Abundance**
H	1.00	Mg	4.0×10^{-5}
He	0.085	Al	2.8×10^{-6}
C	2.7×10^{-4}	Si	3.2×10^{-5}
N	6.8×10^{-5}	S	1.3×10^{-5}
O	4.9×10^{-4}	P	2.6×10^{-7}
Na	1.7×10^{-6}	Fe	3.2×10^{-5}

parameters. It is concentrated into regions of relatively dense gas and tiny dust particles known as the interstellar clouds, with the dust-to-gas ratio of 0.01 by mass and $\approx 3 \times 10^{-12}$ by number. Depending on several parameters, interstellar clouds are often classified as diffuse atomic, diffuse molecular, translucent, and dense (Snow & McCall, 2006). An ISM contains gas with temperatures ranging from more than 10^6 K down to 10 K and total hydrogen number density $n_H = 10^{-4}$ cm^{-3} in diffuse regions to 10^8 cm^{-3} in dense clouds. The latter is more tenuous than a typical ultra-high vacuum laboratory experiment on Earth. Considering an average $n_H = 10^2$ cm^{-3}, molecules get a scope to collide every 1.5 years in space, whereas in the Earth's atmosphere has a particle number density $\sim 10^{19}$ cm^{-3}, a collision occurs every 0.2×10^{-9} seconds. Thus, the interstellar space is a unique environment that can be studied under extreme conditions, which is totally different from the terrestrial conditions.

Interstellar dust grains

Interstellar grains or dust have size distributions from a few nanometers to a micrometer depending on the environment. For example, there may be small grains in diffuse clouds (Weingartner & Draine, 2001); more evolved, aggregated grains in dense clouds (Köhler et al., 2012); and more extensive, porous, and complex grains of μm to cm-size in protoplanetary disks (Blum, 2018). Classical dust grains are characterized by a radius of 1000 Å, a density of 3 g cm^{-3}, and 10^6 surface sites for adsorption (Hasegawa et al., 1992). They include various components such as polycyclic aromatic hydrocarbons (PAH), particles of carbon (graphite, amorphous carbon, organic refractory material), silicate (olivine), or/and a mixture of both. The olivine minerals are silicate structures having the general formula M_2SiO_4, where M is magnesium (forsterite, Mg_2SiO_4) or iron (fayalite, Fe_2SiO_4). The interstellar grain model, which has proven to be comparatively successful in conforming with the observed interstellar extinction, reflection, IR emission, and gas-phase abundances, consists of a combination of graphite and silicate grains. The $dn/da \propto a^{-3.5}$ power-

law, truncated at $a_{min} \approx 5$ nm and $a_{max} \approx 250$ nm, was first introduced in 1977 by Mathis, Rumpl, & Nordsieck, and is often referred to as the "MRN" model. Comprehensive discussions of the observations of interstellar dusts, properties, and models are provided in Whittet (2003); Draine (2003); Tielens (2010); Draine (2011).

Dust grains are not thought to have an active role as catalysts in the chemical point of view, in which surface molecules accelerate the reaction. Instead, they provide a reservoir for the atoms and molecules, where they can react with others. Furthermore, due to the confined area, the reactions that are not possible in the gas phase can also process here. They thus enable reactions with activation barriers (minimum energy required to start a chemical reaction) that are too slow in the gas, such as the hydrogenation of atomic O, C, and N. Also, they act as a third body that absorbs the BE of a newly formed molecule, thereby stabilizing it before it can dissociate again.

Most astrochemical models (Garrod et al., 2006a; Ruaud et al., 2016; Cuppen et al., 2017; Wakelam et al., 2017) mimicking the chemical evolution in the star-forming region have now integrated the gas-grain processes. Adsorption energy or BE (E_d) and diffusion energy (E_b) control the efficiency of grain surface reactions. E_b can be estimated as a fraction of the E_d of surfaces species; the ratio of E_d to E_b often ranges from 0.3 to 1.0 (Garrod et al., 2007; Cuppen et al., 2017). Species that are in the process of formation or trapped on interstellar ice may transfer to the gas phase by various desorption mechanisms (Cuppen et al., 2017) such as non-thermal reactive desorption (efficient desorption mechanisms at low temperature; Garrod et al., 2007), thermal desorption (efficient at high temperature), and energetic processes such as direct or indirect photoevaporation by photon or cosmic-ray particles. Interestingly, all the parameters causing desorption are directly or indirectly related to the BE of the species. The non-thermal chemical desorption is a mechanism in which part of the energy liberated by the formation of the chemical bond is used to desorb the molecule. It can also be impulsive spot heating by cosmic rays. According to Minissale & Dulieu (2014), the efficiency of non-thermal chemical desorption mechanisms depends on four parameters: enthalpy of formation, degrees of freedom, BE, and mass of newly formed molecules. Quantities that govern the fraction of molecules returning to the gas phase after a collision with an icy grain surface is sticking coefficients (S_T), residence times, and reaction probabilities. The ratio of adsorbed to nonadsorbed incident atoms or molecules on a surface during a given period after a collision is represented by the sticking coefficient. The residence times represent the time that a particular adsorbate (a substance that is adsorbed by adsorbent) stays on an adsorbent (a substance that adsorb other) surface after

adsorption. Both quantities are affected by the BE of adsorbate with an adsorbent surface.

Interstellar ice composition

Icy grain mantles are the building blocks of formation of COMs in the ISM and, therefore, worth providing some details. In clouds, protostellar envelopes, and protoplanetary disks, such icy mantles constitute the main reservoir of volatiles. Although Eddington (1937) proposed the existence of interstellar ice in 1937, there was a turning point more than 40 years later, when Tielens & Hagen (1982) introduced combined gas-grain chemistry for the chemical evolution of the ISM. Recently, it has been demonstrated that pre-biotic molecules can be produced in UV-irradiated astrophysical relevant ices (Woon, 2002). For instance, Nuevo et al. (2014) experimentally showed that nucleobases could be formed by UV irradiation of pyrimidine in H_2O-rich ice mixtures containing NH_3, CH_3OH, and CH_4. Ices form by condensing atoms and molecules from the gas phase and subsequent grain surface chemistry (Tielens & Hagen, 1982). O, C, N, and H accrete on grains to form H_2O, CH_4, and NH_3 by hydrogenation.

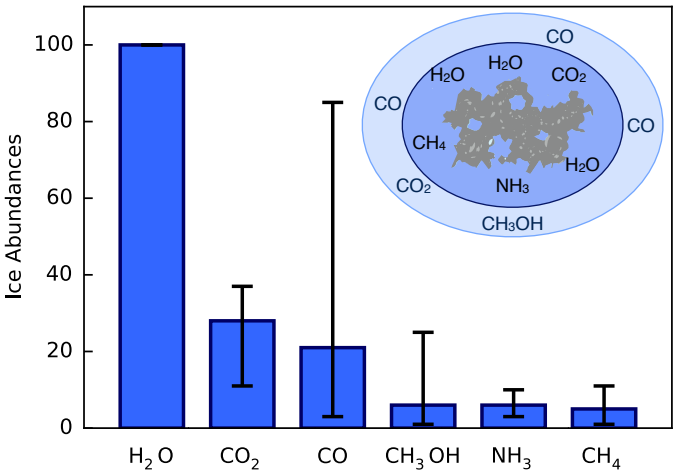

Figure 1.5: The median composition of interstellar icy grain mantles normalized to the most abundant ice species, water (Boogert et al., 2015) indicated with the minimum and maximum abundance relative to water ice detected in that line of sight (Courtesy: Öberg, 2016).

Interstellar ice compositions are primarily studied through IR absorption spectroscopy toward a background source such as a protostar (Gibb et al., 2004; Öberg et al., 2011; Boogert et al., 2015). Since the composition of grain mantles strongly depends on physical conditions (Das et al., 2008a, 2010; Das & Chakrabarti, 2011; Das et al., 2016), the observed spectra vary along different lines of sight. However, there are some general trends shown in Figure 1.5. The Figure shows the median ice abundances toward low-mass protostars, as well as the minimum and maximum abundance concerning water ice, observed for each of the other five species. Water ice is the most abundant ice constituent in dense molecular clouds (Gibb et al., 2004), accounting for $\sim 60 - 70\%$ of the icy mantels (Whittet, 2003). CO and CO2 follow it at $\sim 20 - 30\%$ each relative to water. CH_4, NH_3, and CH_3OH are also detected in many lines of sight at typical abundances of $\sim 5\%$ concerning water ice.

Water ice was first detected by comparing ground-based IR observations of its O-H stretching band at 3278.69 cm^{-1} (3.05 μm) toward Orion-KL (Gillett & Forrest, 1973) and laboratory work by Irvine & Pollack (1968). Since then, several ground-based observations were made to identify the signatures of water ice in different astrophysical environments, with further laboratory studies supporting such observations (Merrill et al., 1976; Leger et al., 1979; Hagen et al., 1979).

Only a few species are unambiguously detected in interstellar ices due to difficulties in observing them in the mid-IR. It is hard to detect interstellar atomic or molecular spectral signatures in the IR regions using ground-based observation. Most of the signals are attenuated by the Earth's atmosphere when they pass through it. A background illuminating source such as a protostar or a field star is needed for absorption. The energy required to excite a transition into emission is likely to cause the molecule to desorb into the gas phase. Furthermore, peak positions, intensities of molecular ice features, and line widths which are required to compare with laboratory spectra, further depend on ice temperature, the crystal structure of the ice, and mixing or layering with other species (Ehrenfreund et al., 1997; Schutte et al., 1999; Cooke et al., 2016). However, CO is routinely observed, showing both polar and apolar band profiles in absorbance. The CO ice-phase abundance may vary from 3% to 20% of the water-ice. Based on laboratory work (Mantz et al., 1975), the fundamental vibrational band of CO at 4.61 μm (2169.20 cm^{-1}) in absorption toward W33A was reported (Soifer et al., 1979). The corresponding band profile includes a broad (polar) component and a narrow (non-polar) component (Chiar et al., 1995, 1998). CO_2 absorption feature was observed toward several IRAS sources based on laboratory work (D'Hendecourt & Jourdain de Muizon, 1989). The ubiquitous nature of CO_2 in ice mantles was found toward several astrophysical objects (de

Graauw et al., 1996; Guertler et al., 1996; Gerakines et al., 1999) after the launch of ISO (Dartois, 2005). Ice-phase abundance of CH_3OH varies between 5% and 30% relative to H_2O (Baas et al., 1988; Grim et al., 1991; Allamandola et al., 1992). Schutte et al. (1996) first attempted the observation of H_2CO observation toward the GL 2136 protostellar source and estimated the abundance to be $\sim 7\%$ relative to H_2O. Kessler et al. (1996); Keane et al. (2001); Kessler et al. (2003) estimated the H_2CO abundance between 1% and 3%. HCOOH was observed both in the solid and gas phase (Schutte et al., 1999; van Dishoeck et al., 1995; Ikeda et al., 2001). Both gas and ice-phase CH_4 were simultaneously detected toward NGC 7538 IRS 9 (Lacy et al., 1991). Öberg et al. (2008) observed and derived CH_4 ice-phase abundance between 2% and 8%, except for a few sources where it is $11 - 13\%$. Knacke et al. (1982) claimed the first identification of NH_3 in interstellar grains; a detection later proved to be wrong (Knacke & McCorkle, 1987). Eventually, the detection of NH_3 was reported toward NGC 7538 IRS 9 (Lacy et al., 1998). Palumbo et al. (1995, 1997) identified OCS mixed with CH_3OH toward several sources based on laboratory work.

An abundant O_2 was discovered by the Rosetta Orbiter Spectrometer for Ion and Neutral Analysis (ROSINA) mass spectrometer onboard the European Space Agency's (ESA) Rosetta spacecraft in the comet 67P/Churyumov-Gerasimenko (hereafter 67P/C-G) coma. The derived ratio was $O_2/H_2O = 3.80 \pm 0.85\%$ (Bieler et al., 2015).

Neutral mass spectrometer data obtained during the ESA's Giotto flyby are consistent with abundant amounts of O_2 in the comet 1P/Halley coma, the O_2/H_2O ratio being evaluated to be $3.70 \pm 1.7\%$ (Rubin et al., 2015). In the ISM, O_2 and N_2 are depleted on grains in the solid form and are nearly absent in the gas phase (van Dishoeck et al., 1993). Therefore, N_2 and O_2 cannot be detected using radio observations due to the absence of dipole moment. However, they might be seen by their weak IR active fundamental transition in the solid phase (Sandford et al., 2001; Ehrenfreund et al., 1997).

Analysis of spectral profiles of the observed ice reveals that interstellar ices are not perfectly mixed but rather, present in at least two phases, water-rich, and water-poor. The water-rich phase is observed to form first and contains mostly water, CO_2, NH_3, and CH_4 ice. A second CO-rich ice has the remaining CO_2 ice and probably most of the CH_3OH (Figure 1.5). Theoretically, these two separate phases form because ice formation is dominated by the hydrogenation of atoms at early times and by reactions involving CO at late times.

To date, IR observations suggest that the ice mantles in molecular clouds are positively composed of the few molecules mentioned earlier (Herbst & van Dishoeck, 2009). However, more complex species, such as COMs, are also expected to be frozen on ice grains in dense cores. The low sensitivity or low resolution of available observations combined with spectral confusion in the IR region can cause weak features due to solid COMs hidden by more abundant ice species. The upcoming NASA's JWST[4] space mission set to explore the molecular nature of the Universe and the habitability of planetary systems promises to be a giant leap forward in our quest to understand the origin of molecules in space. The high resolution of spectrometers onboard the JWST will enable the search for new COMs in interstellar ices and shed light on different ice morphologies, thermal histories, and mixing environments. JWST will map the sky and see right through and deep into massive clouds of gas and dust opaque in the visible window. However, the large amount of spectral data provided by JWST could be analyzed when extensive spectral laboratory and modeling data sets are available to interpret such data.

Binding energy

The binding energy (BE) or adsorption energy is an essential input parameter and thus crucial to improve the BE values in the models to better reproduce the astrophysical abundances. A gas-phase species approaching a surface will feel at a large distance a weak attraction due to van der Waals forces. These are due to mutually induced dipole moments in the electron shells of the gas-phase species and the atoms on the surface. At short ranges, forces associated with the overlap of the wave functions of the approaching species and the surface atoms lead to much stronger binding. BEs depend on the nature of the volatile species, the chemical and morphological composition of the surface, and its coverage. Several studies have reviewed known BE on various surfaces and more especially water ices (Fraser et al., 2001; Collings et al., 2004; Noble et al., 2012; Hama & Watanabe, 2013; He et al., 2016b; Penteado et al., 2017; Wakelam et al., 2017; Sameera et al., 2017; Shimonishi et al., 2018; Sil et al., 2017; Das et al., 2018; Sameera & Maseras, 2018; Molpeceres & Kästner, 2020a; Molpeceres et al., 2020b; Duflot et al., 2021; Sil et al., 2021).

Most of the experimentally obtained BE values for stable molecules were obtained from Temperature-Programmed Desorption (TPD) experiments (Fraser et al., 2001; Öberg et al., 2005; Bolina et al., 2005; Acharyya et al., 2007; Burke & Brown, 2010; Hama & Watanabe, 2013). In TPD experiments, the surface temperature is

[4] https://jwst.stsci.edu

increased rapidly, and the desorbing particles are collected. Since the 1990s, the TPD technique has been used to determine the BE values experimentally. The thermal desorption process of interstellar COMs is possible to simulate in the laboratory through TPD analysis, deriving essential parameters such as the thermal desorption temperatures (T_d) and desorption energies (E_d). Although TPD measures the desorption energy, this energy essentially is the BE of the species if there are no activated processes. Molecules can interact on the grain surface through van der Waals-like forces and dipole-dipole interactions, as it has been routinely demonstrated through vibrational spectroscopic methods such as IR and Raman spectroscopy. Moreover, molecules can diffuse inside the grains when the submicron interstellar grains begin to accrete into hundreds of microns fluffy dust. Up to now, TPD experiments are carried out mainly from graphite and amorphous water ice surfaces (e.g., Collings et al., 2004; Hama et al., 2011; Shi et al., 2015; Chaabouni et al., 2018). Collings et al. (2004) presented an extensive TPD study for a collection of 16 astrophysically relevant molecular species. The interaction and auto-ionization of HCl on low-temperature (80−140 K) water ice surfaces are studied by Olanrewaju et al. (2011) using low-energy (5−250 eV) electron-stimulated desorption (ESD) and TPD. Ward et al. (2012) used TPD experiments coupled with time-of-flight mass spectrometry to determine the yield of OCS and additionally yields a value for the computation of desorption energies of O atoms and OCS. Noble et al. (2012) presented an experimental study of CO, O_2, and CO_2 desorption from three different surfaces: non-porous amorphous solid water (ASW), crystalline ice, and amorphous olivine-type silicates. Dulieu et al. (2013) also performed TPD experiments to derive the BE of different species on the silicate substrate. Corazzi et al. (2021), for the first time, have performed TPD experiments of acetonitrile (CH_3CN) and acetaldehyde (CH_3COH). They consider both pure and mixed with water from micrometric grains of silicate olivine [$(Mg, Fe)_2SiO_4$] used as dust analog on which the icy mixtures are condensed at 17 K.

Experimentally determined BE values depend on the nature of the substrate from which the species desorb and on the properties of the deposited ices (i.e., pure, mixed, or layered), which impact the obtained BE values from TPD experiments. Furthermore, TPD is not appropriate for reactive atoms or radicals since they may spontaneously recombine to form stable molecules at the surface before thermal desorption. Consequently, the BEs of atoms or radicals are less documented. Nevertheless, estimating the BE of these radicals is essential to map the chemical composition in the intermediate temperature (40 − 80 K). To this effect, computational studies can provide faster information as compared to experimental studies. Before the era

of TPD experiments, some estimated values of BE were used in gas-grain chemical models (Tielens & Hagen, 1982; Hasegawa & Herbst, 1993; Charnley, 1997) based on the polarizability of molecules or atoms, determining the strength of van der Waals interaction with a bare grain surface.

For species with undefined BEs, as a rule of thumb, can be very crudely estimated by an additive law, i.e., the BE of an unknown species being the sum of the BEs of the reactants. However, this approximation of the BE may lead to very misleading results (Cuppen et al., 2017).

Penteado et al. (2017) have estimated the BEs based on the results presented in Collings et al. (2004) for the deposition of each species on an H_2O substrate as,

$$E_{bind,X} = \frac{T_{des,X}}{T_{des,H_2O}} \times E_{bind,H_2O}, \tag{1.1}$$

where $T_{des,X}$ is the desorption temperature of a species X deposited on a H_2O film, T_{des,H_2O} is the desorption temperature of H_2O, and E_{bind,H_2O} is the BE of H_2O.

The BEs of species are evaluated theoretically using high-performance computers. A suitable computational model with reliable approximations is indispensable in practical simulations for interstellar chemistry. For example, Al-Halabi & van Dishoeck (2007) simulated the adsorption of H atoms to ASW using classical trajectory (CT) calculations, and the off-lattice kinetic MC approach was used by Karssemeijer & Cuppen (2014) to estimate the BE of CO and CO_2. Hornekær et al. (2005) used CT calculations to simulate the adsorption of H_2 with ASW and crystalline ice. Wakelam et al. (2017) has proposed a proportional law relating the interaction energy between the given species and one water molecule and its BE on ASW. Hybrid QM/MM (Quantum Mechanics/Molecular Mechanics) approaches, such as the ONIOM method (Chung et al., 2015), recently used by Sameera et al. (2017); Sameera & Maseras (2018) on crystalline water ices and by Duflot et al. (2021) on both hexagonal crystalline and amorphous ices, represented by a cluster of about 150 water molecules via classical MD and electronic structure methods. Molpeceres et al. (2020b) reported the MD simulations of the adsorption dynamics of the nitrogen atoms on ASW. They used extensive sampling on ab-initio accuracy. In addition, Shimonishi et al. (2018) has reported the BE of carbon, nitrogen, and oxygen atom on the low-temperature ASW based on quantum chemistry calculations and the experimental value found by Minissale et al. (2016). Molpeceres et al. (2020b) compared their findings with these studies. Molpeceres et al. (2021b) recently have studied the interaction of H_2 with crystalline and amorphous CO ice computationally, employing *ab initio* MD simulations and providing BEs and sticking coefficients

for this pair. Molpeceres & Kästner (2021a) have theoretically determined the BE distribution of the reactants, reaction energies, and (when applicable) activation energies of the chemical reactions involving P-hydrogenation sequence (P to PH_3) on top of a H_2O ice mantle.

In Chapter 2, we (Sil et al., 2017; Das et al., 2018, 2021) present quantum chemical approaches to determine the BE of several important species with astrophysical relevant surfaces.

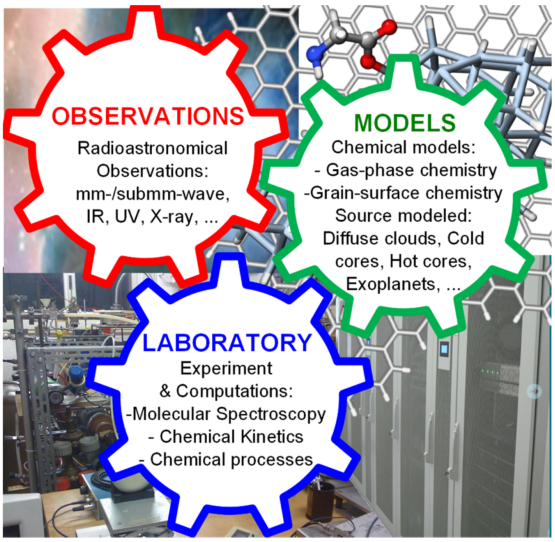

Figure 1.6: Approaches in astrochemistry: observations, laboratory studies, and models are carried out to explain physico-chemical processes in astronomical environments (Courtesy: Barone et al., 2015a).

1.3 Current state-of-the-art of the astrochemistry

The beginning of the astrochemistry community and its development history is well described by van Dishoeck (2019); Puzzarini (2020); Fortenberry (2020). Presently, it has become a broad research field that can not be addressed in isolation. It spans astronomical observations, modeling, and theoretical or experimental laboratory-based investigations (Herbst & Yates, 2013; Brown, 2014) outlined in Figure 1.6. It represents an example of how astrochemistry is developed nowadays, with such incredible research articles published in recent years, bringing new molecules, new ideas, and new paths for future research. The removal of any limb of the astrochemical tripod would collapse the structure. The progress of observational

studies revealed chemical diversity in space, the source-to-source variation in chemical composition through a synergic interplay of radio astronomical observations and laboratory spectroscopy (Müller et al., 2005; McGuire, 2018; van Dishoeck, 2019; Puzzarini, 2020; Qasim et al., 2020). The laboratory astrochemistry aims to simulate processes that occur over millions of years in space within a few hours in the laboratory. Abundances are extracted from the intensity of the observed/assigned molecular lines. The interpretation of these abundances requires a comparison with model predictions (Garrod et al., 2008; Das et al., 2015a, 2016, 2019, 2020; Gorai et al., 2017a, 2020b; Sil et al., 2018, 2021). Thus a strong interaction between different communities (such as, experimentalists, theoreticians, and observer) are involved in understanding the unknown universe.

1.3.1 Astronomical observations

Detectable emission lines are arising from electronic, vibrational, torsional, and rotational states of hundreds of species, which together can be used to probe the physical and chemical characteristics of specific regions of ISM. In principle, astrochemical observations are possible at all wavelengths where molecules emit and absorb photons at discreet energies, i.e., from UV to radio wavelengths. However, in practice, the vast majority of astrochemical observations are carried out at longer wavelengths, at infrared (IR), far-IR or terahertz (THz), submillimeter and millimeter, and radio wavelengths (see Figure 1.7). The electronic transitions (frequencies ranged from the visible to the UV region of the spectrum) are typically the most energetic and can stimulate photodissociation processes. Vibrational transitions within the same electronic state are usually observed in the near- to mid-IR ($< 20\mu$m) wavelength range. Rotational transitions within a given electronic and vibrational state, which are the weakest in energy, approximately range from the submillimeter to centimeter range of the electromagnetic spectrum.

In the present situation, the field is driven by brand new significant astronomical facilities and technology (Jørgensen et al., 2020). These include powerful ground-based telescopes and space-based telescopes. Hubble Space Telescope (HST), X-ray Multi-Mirror Mission (XMM), Chandra, X-Ray Imaging and Spectroscopy Mission (XRISM, forthcoming) are examples of UV and X-ray spectroscopy instruments perform from space. Far-IR region is studied with Spitzer Space Telescope, Herschel Space Observatory, and the Stratospheric Observatory for Infrared Astronomy (SOFIA). The submillimeter telescopes in the Atacama desert include the Atacama Pathfinder Experiment (APEX), the Atacama Submillimeter Telescope Experiment

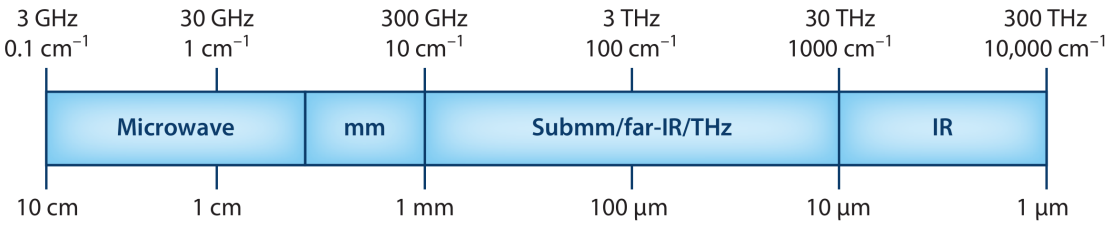

Figure 1.7: Graphical representation of the microwave, millimeter (mm), submillimeter (Submm), and IR ranges of the electromagnetic spectrum (Courtesy: Widicus Weaver, 2019).

(ASTE), and the Atacama Large Millimeter/submillimeter Array (ALMA). All these together support observational astrochemistry. With James Webb Space Telescope (JWST), Atmospheric Remote-sensing Infrared Exoplanet Large-survey (Ariel), Extremely Large Telescope (ELT), and many other future missions on the horizon would provide increasingly sharp and sensitive data to the community. Along with the advances in the detection of molecules, efficient codes like RADEX[5], which is a one-dimensional non-local thermodynamic equilibrium (non-LTE) radiative transfer code (van der Tak et al., 2007), have also been developed to infer the physical (excitation temperatures) and chemical (e.g., molecular abundances) conditions from observations. Spectroscopic databases such as CDMS[6] (Müller et al., 2005; Endres et al., 2016), Jet Propulsion Laboratory (JPL)[7] (Pickett et al., 1998), SPLATALOGUE[8], HITRAN[9] (Rothman et al., 2009; Rothman, 2021), EXOMOL[10] line lists (Tennyson et al., 2016), and Lovas/NIST[11] (Lovas, 2004) are invaluable resources for identifying lines.

1.3.2 Theory and astrochemical models

Considerable progress in computational accuracy and pace continues in the theoretical understanding of astrochemical processes that rely on a range of modeling techniques (Chakrabarti & Chakrabarti, 2000a,b; Chakrabarti et al., 2006a,b; Cup-

[5] https://home.strw.leidenuniv.nl/~moldata/radex.html
[6] http://www.astro.uni-koeln.de/cdms/
[7] http://spec.jpl.nasa.gov/home.html
[8] https://splatalogue.online//
[9] http://www.cfa.harvard.edu/hitran
[10] https://www.exomol.com/
[11] http://physics.nist.gov/PhysRefData/Micro/Html/contents.html

pen et al., 2013; Garrod & Widicus Weaver, 2013b; Das et al., 2015a,b, 2016, 2019, 2021; Gorai et al., 2017a,b, 2020b; Sil et al., 2018, 2021). The most computational expensive models are *ab initio* quantum mechanical calculations that are employed in astrochemistry to calculate collisional excitation coefficients, photodissociation cross-sections, reaction potentials, and some molecule-grain surface interactions. Collisional rate coefficients are needed to determine the excitation of interstellar molecules. State-to-state collisional rate coefficients with H_2 for pure rotational transitions of some speices like, H_2O, H_2, CO, HCN, HNC, CN, CS, SO, SO_2, CH, CH_2, HF, HCl, OH^+, NH_2D, HC_3N, CH_3CN, and CH_3OH were computed. There are also available rate coefficients with He for species like PN, SiH^+, ArH^+. Collisions with electrons are also crucial for ions and molecules with large dipole moments such as HF, CH^+, and ArH^+. The rate coefficients for vibration-rotation transitions also bring attention (for example, new data are provided for CO with H_2 and H; Song et al., 2015) driven by IR spectra from ISO and Spitzer, and with JWST on the horizon. The BASECOL[12] (Dubernet et al., 2013) and LAMDA[13] (Schöier et al., 2005; van der Tak et al., 2007) databases are there to access the available collisional data. A new revision of LAMDA, including its current status, recent updates, and plans are described in van der Tak et al. (2020).

Within astrochemistry, molecular dynamics (MD) simulations are used to uncover ice reaction mechanisms that can be parametrically incorporated into higher-level modeling efforts. More extended simulations require reaction probabilities parameterized, which is done through the so-called microscopic or kinetic Monte Carlo (KMC) models (Chang et al., 2005; Herbst & Cuppen, 2006; Chakrabarti et al., 2006a,b; Chang et al., 2007; Cuppen & Herbst, 2007; Das et al., 2008a, 2010; Das & Chakrabarti, 2011; Muralidharan et al., 2008; Cuppen et al., 2009; Chang & Herbst, 2012; Vasyunin & Herbst, 2013). Macroscopic stochastic or deterministic rate equation models are routinely employed to carry out comprehensive gas-phase and solid-state interstellar chemistry models. For example, in macroscopic Monte Carlo (MC) models, the master equation for the combined gas-phase and surface chemistry is solved using the MC technique (Gillespie, 1976; Charnley, 1998, 2001; Acharyya et al., 2005; Cuppen & Herbst, 2007; Vasyunin et al., 2009). The theory and astrochemical applications of microscopic and macroscopic MC methods in astrochemistry were recently reviewed by Cuppen et al. (2013). In terms of the number of species and reactions, the most comprehensive astrochemical models exclusively use the rate equation approach or its modified version to consider the corrections

[12] https://basecol.vamdc.eu/

[13] https://home.strw.leidenuniv.nl/~moldata/

obtained with the macroscopic MC methods (Chakrabarti et al., 2006a,b; Cuppen & Herbst, 2007; Das et al., 2008a; Garrod et al., 2008; Das et al., 2008a, 2010; Das & Chakrabarti, 2011; Das et al., 2016, 2021; Sahu et al., 2015; Gorai et al., 2017a,b, 2020b; Sil et al., 2018, 2021). The application of the rate equation approach to ice photochemistry under the astrophysical environments was recently reviewed by Garrod & Widicus Weaver (2013b). The treatment of ice surfaces separate from ice layers (Hasegawa & Herbst, 1993) and so-called three-phase models (ice mantle, ice surface, and gas-phase) are now standard (Vasyunin & Herbst, 2013; Garrod, 2013). Besides, there is another class of chemical models labeled as thermochemical models (Öberg & Bergin, 2021) applied to the general ISM, dense clouds exposed to enhanced radiation fields, and protoplanetary disks.

The rate coefficients and activation energy barrier for gas-phase and ice-phase chemical reactions are derived from experiments and theory. Typically, chemical models of the ISM in use employ databases of mainly 2-body (sometimes 3-body) chemical reactions; these contain long lists of gas and ice-phase chemical reactions. Reducing the degree of uncertainty for all the reactions would require an unfeasibly large number of laboratory experiments. Yet, chemical models entirely rely on the databases, making their accuracy a prime problem for astrochemistry. Gas-phase reactions are the backbone of chemical networks as they are the primary routes for the formation and destructions of most molecules. Gas-phase networks of COMs are incomplete (Chakrabarti & Chakrabarti, 2000a; Balucani et al., 2015; Barone et al., 2015) and astrochemical models have been struggling to explain the observed abundances of COMs. Dust grain chemistry also plays a pivotal role in forming vital abundant species observed routinely in the ISM. A couple of public databases are UMIST Database for Astrochemistry[14] (UDfA, which includes a total of 6173 gas-phase reactions involving 467 chemical species; McElroy et al., 2013) and KInetic Database for Astrochemistry[15] (KIDA, consists of a total of 7509 reactions involving 489 species; Wakelam et al., 2015), which continue to be updated with new results from the chemical physics literature. KIDA also provides astrochemical codes, such as the Nautilus gas-grain code[16]. The latest version of Nautilus allows simulating the chemical evolution of the ISM considering three phases, i.e., gas, grain surface, and grain mantles (Iqbal & Wakelam, 2018). The gas chemistry uses the KIDA network (Wakelam et al., 2015), whereas the grain chemical network is that presented in Garrod et al. (2007); Ruaud et al. (2015). Such types of codes

[14] http://udfa.ajmarkwick.net/
[15] http://kida.astrophy.u-bordeaux.fr/
[16] http://kida.astrophy.u-bordeaux.fr/codes.html

and chemical models find essential applications in sources like cold cores, which in conjunction with submillimeter observations might explain the desorption and formation of COMs in icy mantles (Vasyunin et al., 2017). Heays et al. (2017) have provided the wavelength-dependent photodissociation and photoionization cross sections for 102 astrophysically essential species. The cross-section and calculated rate of these species are available from the Leiden Observatory database of "photodissociation and photoionization of astrophysically relevant molecules"[17].

1.3.3 Laboratory experiments

Laboratory experiments serve as the bridge between astrochemical models and observations. For example, through the calculations of spectra of interstellar and circumstellar molecules, molecular and atomic excitations, etc. Laboratory measurements of molecular spectra across the electromagnetic spectrum are base for astrochemical purposes (Widicus Weaver, 2019). Laboratory facilities across the world include large synchrotron and advanced light sources and the most powerful computers. There are innovative laboratory setups like cavity ringdown and CHIRP spectroscopy, helium droplets, crossed beam experiments, and UHV surface science techniques. An overview of rotational spectroscopy and its relationship with observational astronomy, as well as an overview of laboratory spectroscopic techniques focusing on both historical approaches and new advancements, are elaborated in Widicus Weaver (2019). Smith (2011) summarizes different experimental methods developed to obtain collisional excitation data, gas-phase reaction rates, and product branching ratios. Two significant developments of the past few decades are the so-called Selected Ion Flow Tube (SIFT; Martinez et al., 2008), CRESU (Sims et al., 1993; Chastaing et al., 2001), or crossed molecular beams (Morales et al., 2011) method enables the measurements of gas-phase reaction rates. Ice-phase reactions are characterized using surface-science apparatuses designed to mimic the high vacuum and range of temperatures (down to 4 K) characteristic of interstellar environments. The Reflection Absorption Infra-Red Spectroscopy (RAIRS) is an IR technique that allows the identification of adsorbates from their vibrational frequencies and determines the orientation of the adsorbed species. TPD experiments (Collings et al., 2004) now routinely probe thermal desorption of both pure and mixed ices. They provide binding energies (BEs) that can be used in models. Öberg et al. (2011) reviewed ice photochemistry experiments and discussed the qualitative and quantitative kinetic and mechanistic constraints.

[17] http://www.strw.leidenuniv.nl/~ewine/photo

1.4 Some astrochemical tools for modelers

1.4.1 Quantum chemical calculations

A technique called *ab initio* quantum chemistry allows scientists to start from pure quantum mechanics. This theory describes behavior of the subatomic particles to calculate properties of a molecule based on the motions of the protons, neutrons, and electrons in the atoms that comprise it. On a super-computer or a server based computer, scientists can run repeated simulations for a specific molecule, each time slightly adjusting its structure and the arrangement of its particles, and watch the results to find the optimal geometry of a compound. But with quantum chemistry, we are limited by the size of the molecules. As a result, we need large amounts of computational power to do the calculations. In this thesis, the IR absorption spectra, rotational parameters, kinetic data, reaction data, etc. are mostly calculated quantum chemically using GAUSSIAN 09 (G09) computational chemistry program (Frisch et al., 2013) to study various features of species and include some of these physical parameters into our chemical model to study the evolution.

The GAUSSIAN *09 suite of programs*

GAUSSIAN 09 is a Gaussian series of programs. It provides state-of-the-art capabilities for a wide-ranging suite of the most advanced electronic structure modeling. GaussView is a graphical user interface (GUI) designed to prepare input for submission to GAUSSIAN and to examine the output graphically that GAUSSIAN produces. The various types of applications of the GAUSSIAN 09 software for our astrochemical approach are briefly well documented in Gorai (2019). There are different *ab initio* methods available such as Hartree-Fock (HF), Møller-Plesset perturbation (MPn, n=2, 4), Coupled Cluster (CC), and Configuration Interaction (CI). A most popular method of Density Functional Theory like B3LYP and composite methods like Gaussian-4 (G4) are widely used in our calculations. There are various basis sets available. For example, minimal (STO-3G), split valence (people, can be modified with polarization and diffuse functions) and correlation consistent (cc-pVXZ, X = D for double, T for the triple, Q for quadruple, 5, 6, 7, can be modified with diffuse functions using prefix aug-), which can be modified to obtain better approximations to describe a system. GAUSSIAN 09 is a powerful software that can perform a multitude of calculations for a given molecule, starting from the fundamental laws of quantum mechanics. Geometry optimization, single-point energy, frequen-

cies, and thermochemistry, potential energy surface (PES), solvation effect are the most valuable types of jobs to calculate molecular properties. Atomic coordinates of the target molecule such as optimized atomic distances and angles, Mulliken atomic charges, dipole moments, electron affinities, molecular orbitals, single-point energy, harmonic frequencies, IR intensities, UV/visible spectra, temperature, pressure, isotopes used, molecular mass, thermal energy, free energy (sum of electronic and thermal free energies), enthalpy (sum of electronic and thermal enthalpies), polarizability, susceptibility are the most crucial information we get out of these calculations.

1.4.2 Modeling radiation-dominated region

Diffuse and translucent clouds

Diffuse atomic clouds represent the regime in the ISM that is fully exposed to the ISRF, and consequently, nearly all molecules are quickly destroyed by photodissociation. It typically has a fairly low density of $\sim 10-100$ cm^{-3} and temperatures of $30-100$ K. There is an intermediate physical structure between diffuse and dense clouds; this structure is called a translucent cloud and has a density of $10^2 - 10^3$ cm^{-3} and a visual extinction of ≈ 3. Several earlier models (Glassgold & Langer, 1974; Black & Dalgarno, 1977; Black et al., 1978b; van Dishoeck & Black, 1986; Jannuzi et al., 1988; van Dishoeck & Black, 1988, 1989; Viala, 1986; Viala et al., 1988; Heck et al., 1993; Le Petit et al., 2004; Shaw et al., 2006) have been performed to study the diffuse and translucent clouds.

H II and photon-dominated regions

H II regions are created when the extreme UV radiation from a star ionizes (H to H^+) and heats the surrounding gas. The gas in these regions is ionized and has a temperature of about 10^4 K. Densities range from 10^3 to 10^4 cm^{-3} for compact (~ 0.5 pc) H II regions such as the Orion Nebula to ~ 10 cm^{-3} for more diffuse and extended nebulae such as the North America Nebula (~ 10 pc). H II regions are formed by young massive stars with spectral type earlier than about B1 ($T_{eff} > 25000$ K), which emit copious amounts of photons beyond the Lyman limit ($h\nu > 13.6$ eV) and ionize and heat their surrounding clouds. All molecules are dissociated into atoms and ionized to form a high-temperature plasma. An idealized structure of an H II region is indicated in Figure 1.8.

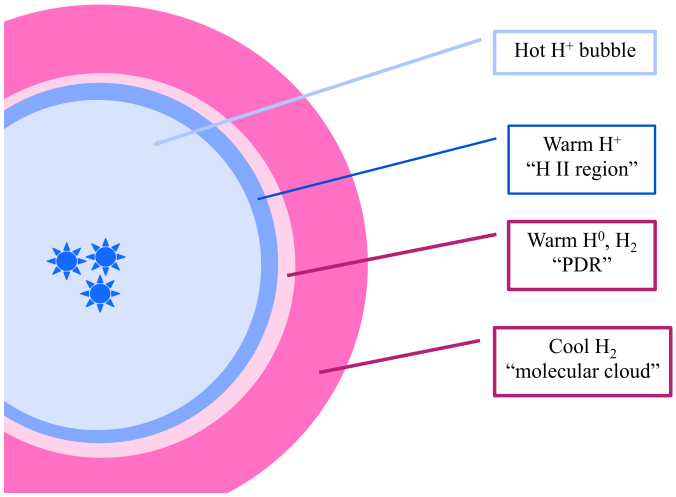

Figure 1.8: Idealized structure of an H II region and PDR (Courtesy: https://cloud9.pa.uky.edu/~gary/cloudy/CloudySummerSchool/2015_Pune/2_Thermal_equilibrium.pdf).

Photon-dominated or photodissociation regions (PDRs) are parts of the interstellar clouds that separate ionized H II region and cold molecular clouds (see Figure 1.8) near bright luminous O and B stars (Hollenbach & Tielens, 1999) and so are exposed to intense UV radiation enhanced by a factor of 10^5 concerning average ISRF and warmed by high levels of photons (Hollenbach & Tielens, 1997), which controls both the physical and chemical state of the gas. Here, the gas is heated by the far-UV radiation ($6 < h\nu < 13.6$ eV, from the ambient UV field and hot stars) and cooled via the emission of spectral line radiation of atomic and molecular species and continuum emission by dust.

At the edge of the cloud, the gas temperature becomes so high (~ 1000 K) that endothermic processes and reactions with energy barriers can proceed. PDR's are ubiquitous in the ISM. The Orion Bar PDR and the Horsehead nebula in the same constellation Orion are prototype examples of well-studied dense PDRs.

The standard PDR model is a one-dimensional system in which slabs of differing temperature and density are considered, starting from the outside with low densities and high temperatures and proceeding to the inside with lowering temperatures and increasing densities. The excitation by electrons rather than H_2 or H can become significant in PDRs. Two typical geometrical setups of model PDRs are shown in Figure 1.9. Most PDR models consider a plane-parallel geometry, illuminated either from one side or both sides suggesting a directed illumination perpendicular to the

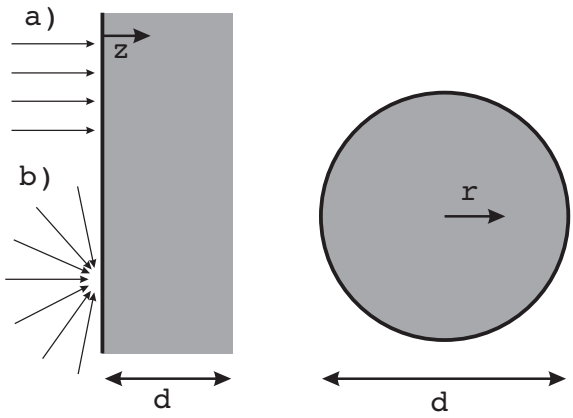

Figure 1.9: Common geometry of the cloud considered for a PDR model calculations. The surface of any plane-parallel or spherical cloud is illuminated either a) unidirectionally or b) isotropically. (Courtesy: Röllig et al., 2007).

cloud surface. Since most plane-parallel PDR models are infinite perpendicular to the cloud depth z it is also straightforward to account for an isotropic far-UV irradiation within the pure 1-D formalism. For a spherical geometry, one can exploit the model symmetry only for an far-UV field isotropically striking onto the cloud. The ambient far-UV is provided in units of Draine χ (Draine, 1978) or Habing G_0 (Habing, 1968) fields.

PDRs play an essential role in interstellar chemistry. They are responsible for the emission characteristics of ISM and dominate the IR and submillimeter spectra of star-forming regions and galaxies. Several earlier literature (Hollenbach & Salpeter, 1971; Jura, 1974; Glassgold & Langer, 1975; Black & Dalgarno, 1977; Tielens & Hollenbach, 1985; van Dishoeck & Black, 1988; Hollenbach et al., 1991; Fuente et al., 1993; Le Bourlot et al., 1993; Sternberg, 1995; Jansen et al., 1995; Bertoldi & Draine, 1996; Lee et al., 1996; Bakes & Tielens, 1998; Hollenbach & Tielens, 1999; Walmsley et al., 1999; Röllig et al., 2002; Savage & Ziurys, 2004; Teyssier et al., 2004; Fuente et al., 2005; Meijerink & Spaans, 2005) have discussed numerous aspects of PDR chemistry in detail and provided a comprehensive overview of the field. PDR host the critical $H^+/H/H_2$ and $C^+/C/CO$ transition layers of the ISM. As one traverses inward, the dominant species change once the chemistry is evolved (see, Figure 1.10). For example, if we consider the major forms of carbon: the outer layers are dominated by C^+, the innermost layers by CO, and some intermediate layers have significant amounts of neutral atomic carbon. Hydrogen is atomic in the outer layers, but within a short distance inside an efficient conversion to the molecular

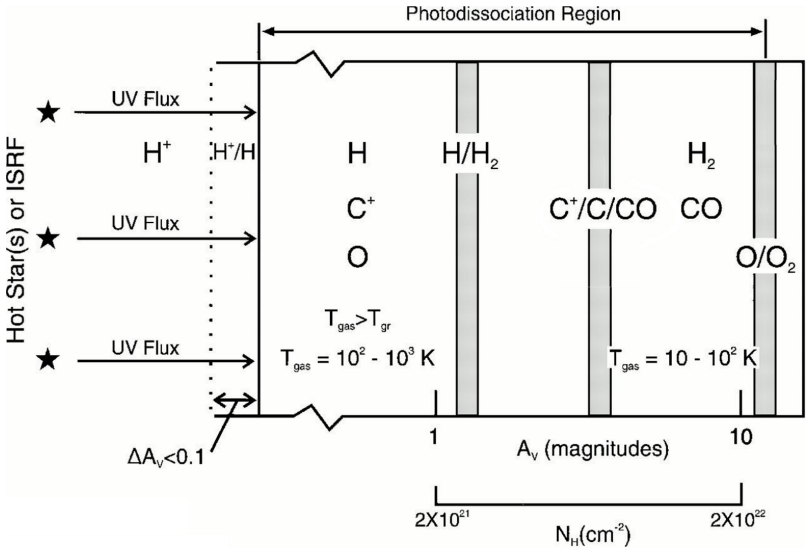

Figure 1.10: A schematic view of a PDR structure. The PDR is illuminated from the left by a strong far-UV field (Courtesy: Hollenbach & Tielens, 1997).

form is witnessed. Röllig et al. (2007) have benchmarked the physical and chemical structure of PDRs using several codes and compared among them.

Supernova remnants

Supernova remnants (SNRs) are formed when the material ejected in the explosion of an aged high-mass star surrounding ISM material terminating the life of the star. SNRs emit radiation in all electromagnetic wavelengths. The Crab Nebula is a compact SNR.

The spectral synthesis code

CLOUDY is a photo-ionization microphysics code, which simulates matter under a broad range of interstellar conditions. It is for general use under an open-source license[18]. CLOUDY is designed (by numerical simulations) to understand complex physical environments starting from the first principles. The equations of statistical equilibrium, charge conservation, and energy conservation are solved (Osterbrock & Ferland, 2006). CLOUDY code deals with the range of temperatures that extends

[18] https://gitlab.nublado.org/cloudy/cloudy/-/wikis/home

from the CMB temperature (2.7 K) up to 1.001×10^{10} K, and the physical state ranges from fully molecular to bare nuclei. It determines the physical conditions within a non-equilibrium gas, possibly exposed to an external source of radiation, and determines the level of ionization, the particle density, the kinetic gas temperature, chemical state of a cloud, populations of levels within atoms, and then predicts the resulting full-spectrum (which often includes hundreds of thousands of lines) and many observed quantities self-consistently by specifying only the minimum number of free parameters (i.e., the properties of the cloud and the radiation field exposed on it). The level of ionization is calculated by balancing all ionization (photo, Auger, and collisional ionization and charge transfer) and recombination processes (low-temperature dielectronic, high-temperature dielectronic, three-body recombination, charge transfer, and radiative). The free electrons are assumed to belong to a predominantly Maxwellian velocity distribution with a kinetic temperature, which is determined by the balance between heating (mechanical, photoelectric, cosmic-ray, etc.) and cooling (mainly inelastic collisions between the electrons and other particles) processes. The associated continuum and line radiative transfer is solved simultaneously.

The CLOUDY code was first developed in August 1978 at the Institute of Astronomy, Cambridge. Like all programs, CLOUDY goes through versions as it is developed through computing and compiling all the atomic data (line positions, oscillator strengths, collisional and photoionization cross sections, recombination rate coefficients) that enter the program (Ferland et al., 1998, 2013, 2017). We use the latest version, 17.02, last reviewed by Ferland et al. (2017) for our models presented in this dissertation.

Here I describe some important aspects in the following subsections.

What must be specified?

CLOUDY needs the following input parameters before it can predict conditions within a cloud:

1. The shape and intensity/luminosity of the external ISRF striking a cloud.
2. The total hydrogen density.
3. The chemical composition of the gas and whether grains are present.
4. The geometry of the cloud, including its radial extent (thickness).

In general, the radiation field striking the cloud can be specified either of the two ways: In the luminosity case the total luminosity emitted by the central object and the inner radius of the cloud is needed, whereas, in the intensity case, only

the flux of radiation striking the cloud is specified. Up to 100 different radiation fields can be included in the total field striking the cloud. However, there must be the same number of shapes and intensity (luminosity) specifications. The program considers the lightest 30 elements in detail. Abundances are specified by number relative to hydrogen. Grains are not part of the default composition but can be included. All stages of ionization are treated, and all published charge exchange, radiative recombination, and dielectronic recombination processes are included as recombination mechanisms. In addition, photoionization from the valence and inner shells is considered. Many excited states and collisional ionization by both thermal and supra-thermal electrons, and charge transfer, are included as ionization mechanisms. The geometry is always considered to be one Dimensional and spherically symmetric but can be made effectively plane parallel by making the inner radius much larger than the thickness of the cloud. The default is for the gas to have constant density and to fill its volume fully.

Radiation fields

Figure 1.11 shows several of the radiation fields (incident, diffuse, transmitted, and reflected) computed in the calculation. The side of the cloud facing the source of the external radiation field is the illuminated face of the cloud. The opposite side, in shadow, is the shielded face of the cloud. The luminous face is generally hotter and more highly ionized than the covered face. The external radiation field emitted by the central object that strikes the illuminated face of the cloud is the incident radiation field, which is often the only energy source for the cloud. It is diminished by extinction as transmitted through the cloud. The spectral energy distribution (SED) of the incident radiation field is specified between the energies of 3.040×10^{-9} Ryd ($\lambda \approx 29.98$ m) and 100 MeV $\approx 7.354 \times 10^{6}$ Ryd. The radiation field emitted by gas and grains within the nebula is known as the diffuse radiation field (often referred to as the diffuse fields, e.g., the Lyman, Balmer, or two-photon continua emitted by hydrogen). These fields are very nearly isotropic and can be significant sources of ionizing radiation under some circumstances. The transmitted radiation field is considered as the net emission emergent from the shielded face of the cloud. Therefore, both the attenuated incident field and the diffuse radiation field are included. On the other hand, the reflected radiation field is considered the emission from the illuminated face of the cloud into the direction towards (i.e., within 2π sr of) the source of the external field. Thus, the reflected field results from both backscattered incident radiation and diffuse emission emitted from the cloud

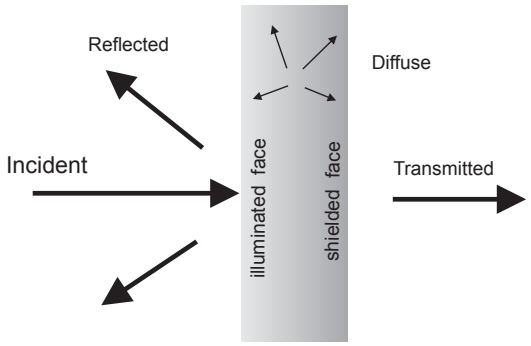

Figure 1.11: Radiation fields that enter in the calculations (Courtesy: Part 1 of HAZY; Ferland et al., 2017).

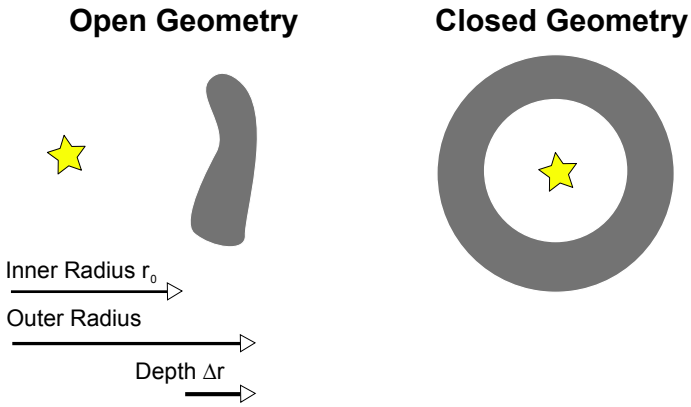

Figure 1.12: Examples of types of geometry of the cloud which can be considered in the calculations (Courtesy: Part 1 of HAZY; Ferland et al., 2017).

toward the source of ionizing radiation.

Geometry

Figure 1.12 shows two possible geometries and some terminologies used to describe them. This radius is the distance from the center of symmetry, usually the center of the central object, to a given point. The depth is the distance between the illuminated face of the cloud and a point within the cloud. The inner radius is r_0, and the thickness or depth is Δr, and the current radius is r. Figure 1.12 shows examples of the assumed two limiting cases, referred to as open and closed geometry, having a different influence upon the calculations. To know the terms better,

we first need to understand what the covering factor is. The covering factor is the fraction of 4πsr covered by the gas, as viewed from the central source of radiation. It is usually written as $\Omega/4\pi$, has the limits $0 \leq \Omega/4\pi \leq 1$, and is the fraction of the radiation field emitted by the central object strikes nebular gas. An open geometry is one in which the covering factor of the gas is negligible. Thus, all radiation that escapes from the illuminated face towards the continuous radiation source escapes from the system without further interaction with gas. Emission-line gas covers $\sim 4\pi$ sr as seen by the central object in a closed geometry. The central object is small relative to the nebula, then all diffuse fields that escape from the illuminated face of the cloud in the direction towards the central object will strike the far side of the nebula. In Figure 1.12, the source of ionizing radiation is denoted by a star and the shaded area represents the cloud. The inner radius (r_0) and thickness or depth (Δr) of the cloud determine whether the geometry is plane parallel ($\Delta r/r_0 < 0.1$), a thick shell ($\Delta r/r_0 < 3$), or spherical ($\Delta r/r_0 \geq 3$).

Intensity and luminosity cases

The external radiation field is usually specified with two different commands. One defines the shape of the incident radiation field. The second command sets the brightness of the light. The illumination of the radiation field striking the cloud can be specified as intensity or luminosity.

In the case when intensity is considered as the input, the energy flux (erg cm^{-2} s^{-1}) or photon flux (cm^{-2} s^{-1}) striking a unit area of cloud is set. The inner radius does not need to be specified, although it is possible to do so. If the starting radius is not specified, then an inner radius of 10^{30} cm is assumed. Usually it results in a plane-parallel geometry. If the starting radius is specified, then the resulting geometry may be spherical, plane-parallel, or a thick shell, depending on the thickness (depth) ratio to inner radii. The emission per unit area (erg cm^{-2} s^{-1}) is predicted.

In the case when the luminosity is used as the input, the total luminosity of the central source of radiation is specified. The inner or starting radius of the cloud must be set so that the flux of photons can be derived. Finally, the luminosities of emission lines (erg s^{-1}) are predicted.

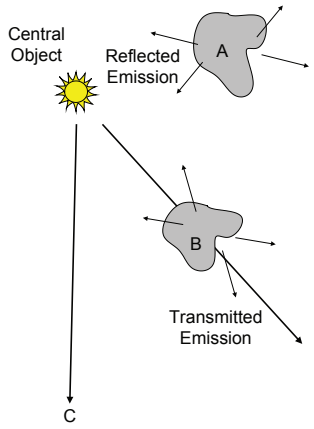

Figure 1.13: Several components of the radiation field that enter in the calculations (Courtesy: Part 1 of HAZY; Ferland et al., 2017).

From the observation perspective

Two lines of sight to the central object and two clouds are shown in Figure 1.13. Each cloud produces both a reflected and transmitted emission component. Three possible geometries, indicated by the letter on the Figure, occur depending on how the central source and the clouds are viewed: (A) the central object cannot be directly observed, although it can be seen by reflection from the illuminated face of a cloud, (B) the transmitted continuum and the outward emission from the emitting cloud are observed, and (C) the unattenuated continuum directly without absorption is observed.

1.4.3 Modeling radiation-shielded region

The protostars and hot core/corino stage

The dense and warmer places of high-mass star-forming regions are known as hot molecular cores (HMCs), and their low mass analogs are known as the hot corinos. The most recent studies contain up to three stages to explain the chemical treatment of hot cores and corinos. The initial (cold) stage occurs as the cold core ages and undergoes isothermal collapse. At this time, an icy mantle is built up around the

granular cores of silicates and carbon. The following (warm-up) stage occurs during the passive warm-up of the inner envelope of the protostar to temperatures of $100-300$ K and the subsequent sublimation of the ice mantles. Finally, the last (hot-core) stage occurs at the temperature of the hot core or corino. During the cold, warm-up, and hot-core stages, the individual chemistries produce zeroth-generation, first-generation, and second-generation organic molecules, respectively (Herbst & van Dishoeck, 2009).

Zeroth-generation species are large molecules formed in the gas and granular icy mantles during the cold core ages. An example is methanol (CH_3OH), produced by the surface hydrogenation of gas-phase carbon monoxide that accretes onto the cold mantle. During the warm-up stage, a cold core becomes a young stellar object (YSO). First-generation species are formed at least partially in and on granular mantles. Here photodissociation of zeroth-generation species such as methanol and formaldehyde produces radicals such as CH_3O and HCO. The radicals can diffuse readily and associate to form larger molecules such as methyl formate ($HCOOCH_3$) at surface temperatures significantly above 10 K. Once the core become a hot core or corino, the second-generation species are formed. In this stage, the temperature becomes $100-300$ K, which is high enough to evaporate the icy mantles completely. The gas-phase chemistry dominates via both ion $-$ molecule and neutral $-$ neutral reactions. Because the ices on the grain mantles sublimate during the warm-up stage, the only chemistry that can occur in the next, or hot-core, stage is the gas-phase chemistry. Because the temperature is much larger than that of cold cores, many more reactions, including endothermic processes and exothermic processes with barriers, can occur efficiently. Eventually, complex molecules are destroyed by the gas-phase chemistry unless incorporated into disks. Thus, this three-stage approach represents the most straightforward way of accounting for the history of hot cores/corinos, an accounting in which physical conditions are time-dependent but not heterogeneous.

The chemical model for molecular cloud code

Assuming the gas and grains coupled through accretion, thermal, and non- thermal desorption processes, we developed the chemical model for molecular cloud (hereafter, CMMC) code (Sil et al., 2018, 2021; Das et al., 2019, 2021; Gorai et al., 2020b; Shimonishi et al., 2020). The gas-phase chemical network of the CMMC code mainly adopted from the UMIST database (McElroy et al., 2013). A cosmic-ray rate of 1.3×10^{-17} s^{-1} is considered in all our models. For the grain surface reaction net-

work, we mainly followed Hasegawa et al. (1992); Cuppen & Herbst (2007); Ruaud et al. (2015); Das et al. (2015b); Gorai et al. (2020b). The BE of the surface species is mostly considered from KIDA (Wakelam et al., 2017), and sometimes from our own quantum chemical calculations (Das et al., 2018, 2021; Sil et al., 2021).

1.4.4 Radiative transfer modeling

Radiative transfer calculation is a handy technique for extracting physical conditions from observed line profiles or generating synthetic spectra. From the radiative transfer calculation, we can get the molecular abundances from the telescopic data in IR and submillimeter wavelength. The level of accuracy needed for radiative transfer calculation depends on the amount and nature of the available data like collisional rate coefficients discussed in subsection 1.3.2. van der Tak (2011) reviewed the radiative transfer calculations in detail.

LTE model

The most straightforward approach to continue the radiative transfer modeling calculation is to consider the Boltzmann distribution to estimate the level population taking the excitation temperature (T_{ex}) equal to the kinetic temperature (T_{kin}). This approximation is called local thermodynamic equilibrium (LTE). But often this approximation does not work. Nevertheless, this condition holds well around the high-density region where collision determines the excitation. T_{ex} is determined from a range of energy levels where several lines are observed for a molecule, the relative intensities of lines are plotted as a function of upper-level energy. From the slope of the graph, we can determine T_{ex}, and the diagram is called the "rotation diagram" (Goldsmith & Langer, 1999) for rotational energy levels.

Non-LTE model

In the low-density region, the number of molecules in each energy level is not well-described by a Boltzmann distribution as the gas density lower than the density required to thermalize the population. In that case, both the radiative (emission or absorption) processes and collisional (thermal) processes take place. As a result, T_{ex} becomes less than T_{kin} of the colliding gas. This is known as the non-LTE formalism. So a detailed calculation is required to take accounts of the radiative and collisional processes and balance between the excitation and de-excitation processes.

An overview of non-LTE radiative transfer methods is given by van Zadelhoff et al. (2002).

Radiative transfer codes

RADEX (van der Tak et al., 2007) is a one-dimensional non-LTE radiative transfer code that uses the escape probability formulation to assume an isothermal and homogeneous medium without large-scale velocity fields. It is publicly available as a part of LAMDA[19]. In addition, this code provides an online version[20] for quick access. It is a helpful way to analyze a large set of rapidly observational data, providing constraints on some physical parameters density and kinetic temperature. It provides an alternative to the widely used rotation diagram method, which relies upon the availability of many optically thin emission lines and is applicable only in roughly constraining the excitation temperature in addition to the column density.

RATRAN (Hogerheijde & van der Tak, 2000) is another radiative transfer code to calculate the excitation of molecular lines. The code can be implemented to all atoms or molecules for which collisional rate data is available and any axially symmetric source model. Thus, it is a valuable tool in analyzing data from present and future IR and submillimeter telescopes. Furthermore, this code can treat both spherically symmetric (1D) and cylindrically symmetric (2D) source geometries.

LIME (Brinch & Hogerheijde, 2011) is a molecular excitation and non-LTE spectral line radiative transfer code for 3D models for arbitrary geometries. LIME can predict line strengths and profiles of molecular transitions and the intensity of the thermal continuum. It can model disks around young stellar objects, proto-stellar envelopes, giant molecular clouds, outflows, and similar environments. Öberg et al. (2015); Parfenov et al. (2016); Quénard et al. (2018b) have used this 3D non-LTE radiative transfer calculation for modeling different astrophysical regions and spectral line emission properties from various species.

RADMC-3D[21] is a radiative transfer code for dust and lines. It calculates for a geometrical distribution of gas and dust what its images and spectra would look like when viewed from a certain angle. Thus, it allows comparing their models with observed data. It can be applied to dusty molecular clouds, protoplanetary disks, CSEs, dusty tori near AGN (active galactic nuclei) and models of galaxies.

[19] http://home.strw.leidenuniv.nl/~moldata
[20] http://var.sron.nl/radex/radex.php
[21] http://www.ita.uni-heidelberg.de/dullemond/software/radmc-3d

Chapter 2

Interstellar Ice Features

Overview

The interstellar clouds belong to four different classes: diffuse atomic, diffuse molecular, translucent, and dense molecular (Snow & McCall, 2006). The size of these clouds vary from a few to hundreds of light-years and are composed of gas ($\sim$ 99% by mass) and a tiny fraction of dust ($\sim$ 1% by mass) particles. These clouds are the birthplaces of stars. Our Sun is one of this kind, which was formed by this generic process and finally hosted the planets like our living home the Earth. The colder regions of stellar outflows and supernova ejecta produce molecules and grains. Interstellar dust grains are composed of crystalline and amorphous magnesium-rich silicates (e.g., olivine, pyroxene, etc.). Carbonaceous compounds such as graphite and amorphous silicon carbide (SiC), and titanium carbide (TiC) clusters are also the constituents of dust grains. At low dust temperatures ($\sim$ 10 K), the atoms and molecules freeze out on dust grains, forming an icy layer or mantle. Freeze-out of the gas-phase elements onto cold grains builds up ice mantles (H_2O, CO_2, CO, CH_3OH are the major constituents). Ices are the essential repository of the elements in dense regions of ISM. In the broader astrophysical context, ices play crucial roles. It speeds up the grain coagulation process. When the grain is heated up, these molecules sublime back into the gas. This process is called thermal desorption process and it is controlled by the BEs or adsorption energies.

Thus, the determinations of BEs of ices, either as pure or mixed ices, are essential for understanding the observations of star- and planet-forming regions. In this Chapter, we focus on two crucial directions of interstellar ices:

1. Binding energy: a key defining interstellar chemistry (Sil et al., 2017; Das et al., 2018, 2021), and

2. Absorption features of interstellar ices in the presence of impurities (Gorai et al., 2020a).

2.1 Binding energy: a key in defining interstellar chemistry

One of the major obstacles to accurately modeling interstellar chemistry is an inadequate knowledge of the BE of interstellar species. Abundances are governed by adsorption and desorption on grains. The chemical composition of the interstellar grain mantle is dependent mainly on the BEs of the surface species. The BE of the interstellar species regulates the chemical complexity of the interstellar grain mantle. Since hydrogen is widespread either in atomic or molecular form, we first review the variation of the BEs of H and H_2 depending on the nature of the adsorbents. Choice of adsorbents is based on the relative abundances of interstellar materials. The abundance of interstellar ice constituents is generally expressed in terms of the water ice. At the low temperature, the hydrogenation of oxygen is very active, and H_2O molecules predominantly cover a significant part of the interstellar grain surface. Therefore, the usage of BEs with bare grains is not useful in such scenarios. So, the BE of surface species with the water is provided and is widely used in astrochemical modeling. Thus the interaction of gas-phase species with water ice is essential to trace realistic physical and chemical processes. We consider different clusters of water molecules to calculate the BE of several atoms, molecules, and radicals of astrochemical interest. Systematic studies are carried out to develop a relatively more accurate BE of astrophysically relevant species on water ice. The calculated BEs are compared with the available experimental or theoretically obtained BE values. H_2 is also the dominant molecular species in the vast majority of interstellar environments. Thus, its accretion rate on a grain is much higher in comparison to the other species. In more dense regions, gas-phase H_2 easily accretes on the grain and mostly gets back to the gas phase due to their low sticking probability and lower BEs. But some H_2 could be trapped under some accreting species. For example, one H_2 may accrete on another H_2 before it is desorbed. In this situation, the "encounter desorption" mechanism is proven to be an essential means of transportation of H_2 to the gas phase (Hincelin et al., 2015). Usually, in the literature, only the encounter desorption of H_2 is considered due to its wide presence in the dense ISM. However, recently, Chang et al. (2021) considered the encounter desorption of the H atom as well. So, we calculate the BE of several species considering H_2 molecule as a substrate to examine the effect of encounter desorption on the availability of species on interstellar grain. High-level quantum chemical calculations are performed to estimate the BEs of several relevant interstellar species. The obtained BEs are used in astrochemical models.

2.1.1 Study of binding energies of H and H_2

Hydrogen is known as the most ubiquitous element in the Universe. The spectral characteristics of molecular clouds in the far-UV and near-IR region are strongly dominated by molecular hydrogen (H_2) due to its very high abundance (Tielens, 2010). The H_2 formation process through gas-phase interactions between hydrogen atoms (H) or ions is too slow compared to the observed formation rate (Tielens, 2010). Therefore it is commonly believed that there must be other processes causing rapid H_2 formation. H_2 are formed by taking two H atoms and putting them together. Since the possibility of one single H atom finding a larger grain surface is much higher than finding another H atom in the gas phase, calculation of BE of H and H_2 with appropriate grain surfaces is essential to understand their synthesis in the gas phase as well as interstellar icy grain mantle. A larger grain surface may accrete many simple species (atoms or molecules). There are two types of adsorption: (a) physisorption/molecular adsorption and (b) chemisorption/dissociative adsorption. Interstellar grains play an essential role in molecule formation at low-temperature regimes (Mayo Greenberg, 2002), and physisorption is always favored at low temperatures. Incoming H atoms can stick with grain surfaces and form molecules via different acceptable mechanisms like (a) Langmuir-Hinshelwood (LH), where two species can adsorb and react on neighboring sites (Langmuir, 1922), (ii) Eley-Rideal (ER), where formations can happen by direct impingement of incoming species on an adsorbed species (Eley & Rideal, 1940; Eley, 1941) and (iii) Hot-atom, where the incoming species with large impact parameters may be trapped and react with other adsorbed species (Harris & Kasemo, 1981). Formation of H_2 on the grain surface has already been studied (Gould & Salpeter, 1963; Hollenbach & Salpeter, 1970, 1971; Acharyya et al., 2005; Chakrabarti et al., 2006a,b; Tielens, 2010; Sahu et al., 2015). Details of such formation provide valued information about the physical and chemical evolution of the space environments. H_2 is believed to be a precursor of many complex molecules. One of its protonated forms, H_3^+, acts as an essential coolant and saves itself along with other species from incoming radiation fields (Wakelam et al., 2010).

Here, we perform *ab initio* calculations for the adsorbed species (H and H_2) on benzene, silicate cluster, and water cluster systems to investigate the physisorption BE of H and H_2 and see their trend.

Computational details and methodology

The GAUSSIAN 09 suite of programs (Frisch et al., 2013) is utilized for all the BE quantum chemical calculations performed in our study. In a periodic treatment of surface adsorption phenomena, the BE is related to the interaction energy (ΔE), as:

$$BE = -\Delta E \tag{2.1}$$

For a bounded adsorbate, the BE is a positive quantity and is defined as:

$$BE = (E_{surface} + E_{species}) - E_{ss}, \tag{2.2}$$

where E_{ss} is the optimized energy for the complex system where a species is placed at a suitable distance from the grain surface through a weak bond so that a van der Waals interaction occurs during the optimization. $E_{surface}$ and $E_{species}$ are the optimized energies of the grain surface and species, respectively.

To find the optimized energy of all structures, we use a Second-order Møller-Plesset perturbation theory (MP2) level (Møller & Plesset, 1934) in conjunction with an aug-cc-pVDZ basis set. 'Aug' prefix is used to add diffusion function, and cc-pVDZ is the Dunning's correlation consistent basis set (Dunning, 1989) having double zeta function. A fully optimized ground-state structure is verified to be a stationary point (having non-imaginary frequency) by harmonic vibrational frequency analysis. Most of the calculations are performed without the inclusion of zero-point vibrational energy (ZPVE) and basis set superposition error (BSSE; Jansen & Ros, 1969; Liu & McLean, 1973) corrections. Calculations are also performed by excluding BSSE using the counterpoise (CP) method (Boys & Bernardi, 1970), though the usage of CP corrections is highly debated. CP correction is a method to limit an error that results when studying an intermolecular reaction using an incomplete basis set. In studies of weakly bound clusters, a BSSE can occur. As monomer A approaches monomer B, the dimer (A ---B) can be artificially stabilized as the monomer A utilizes the extra basis functions from the monomer B to describe its electron distribution and vice versa. BSSEs are more pronounced for smaller basis sets. One way to correct this is to use a larger basis set. However, it is not always possible to use a larger basis set because it is too computationally expensive. Alternatively, one can calculate a CP correction, which approximates the bias to the quality of the calculation that results in the intermediate range.

We take the last iteration CP corrected energy of the dimer system $E_{CP-corrected}$ from the GAUSSIAN output file and calculate the BE, including CP correction with

the usual formula:

$$BE_{CP} = (E_{surface} + E_{species}) - E_{CP-corrected}, \tag{2.3}$$

Avgul et al. (1957, 1960) discussed a general scheme for calculating the adsorption energy of non-polar molecules on a graphite surface. We also employ their relation for an educated estimation of the BEs of H and H_2. As the input parameters, polarizability and diamagnetic susceptibility of H and H_2 are supplied by using quantum chemical calculations using the GAUSSIAN 09 suite of programs with B3LYP/6-311g(d,p) level of theory. For the placement of the adsorbed species on the lattice of graphite, we use three different positions, as mentioned in Barrer (1937). First, over the carbon atom (position c); second, over the mid-point between two neighboring carbon atoms (position b); and finally, over the center of the hexagon of carbon atoms (position h). A schematic arrangement of H atoms on a simple unit of PAH molecule (benzene) for these three different positions is shown in Figure 2.1.

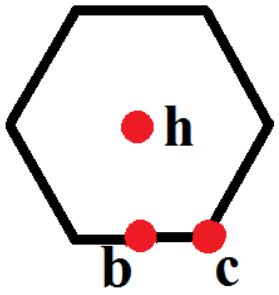

Figure 2.1: Three favourable positions, c, h and b are shown (Sil et al., 2017). c position corresponds to the top of a carbon atom, h (hollow) position is at the center of the hexagon, and b (bridge) position is at the mid-point between two adjacent carbon atoms.

Avgul et al. (1957, 1960) considered that H and H_2 are sticking with the graphite as an adsorbent. They calculated the adsorption energy (Φ_i'') of a segment of i of adsorbate atom by,

$$\Phi_i''(z) = -C_{i1}p_1 z^{-q_1} - C_{i2}p_2 z^{-q_2} - C_{i3}p_3 z^{-q_3} + B_i'' p_m z^{-q_m} \tag{2.4}$$

Table 2.1: BE of H and H_2 (Sil et al., 2017) using the method used in Avgul et al. (1957).

Species	**Binding energy (in Kelvin) for**		
	h position	**b position**	**c position**
H	268	171	157
H_2	944	594	545

where B_i'' is the constant associated with the repulsion, z is the distance from the i^{th} segment, p_1, q_1, p_2, q_2, p_3, q_3, p_m, q_m are the constants available from the logarithmic graphs of Avgul et al. (1957, 1960) and C_{i1}, C_{i2} and C_{i3} are the constants. For the computation of C_{i1}, C_{i2}, and C_{i3}, polarizability and diamagnetic susceptibility of the adsorbate and adsorbent are required. Since we choose graphite as the adsorbent, we use the values given in Barrer (1937) for the individual carbon atom (polarizability $= 0.937 \times 10^{-24}$ cm^3 and diamagnetic susceptibility $= -10.54 \times 10^{-30}$ cm^3). For the adsorbates, the polarizability and diamagnetic susceptibility are calculated quantum chemically. We obtain the values of mean polarizability 8.742887×10^{-26} cm^3 for H atom and 4.48999×10^{-25} cm^3 for H_2 molecule and diamagnetic susceptibility of $-4.07199302 \times 10^{-30}$ cm^3 for H atom and -6.0225×10^{-30} cm^3 for H_2 molecule.

We calculate the BEs of H and H_2 on graphite grain surfaces for various positions using the method mentioned above. From Table 2.1, it is clear that the most favorable adsorption occurs at the hollow (h) site, which Avgul et al. (1960) had discussed earlier. We perform additional calculations using the method presented by these authors to compare with our calculated results.

Results and discussion

Adsorption of species on the grain surface is the primary process for any molecular formation mechanism. H and H_2 being the most abundant, it is essential to know their BEs for various substrates. Since BEs of the surface species mainly control surface chemistry, an inaccurate estimation may cause wrong results. This Section reports the results of our high-level quantum chemical calculations for the BEs of H and H_2. Here, we use three types of substrates as the grain materials: (1) benzene surface, (2) silica cluster, and (3) water cluster.

1. Benzene surface

   The hydrogen-graphite and hydrogen-PAH systems are considered to investigate H_2 formation on realistic grain surfaces. We consider benzene as a representative of graphite, graphene, or PAHs. Although the coronene surface

Table 2.2: BE of H and H_2 on the benzene surface (Sil et al., 2017).

Species	Binding energy (in Kelvin) for		
	h site	b site	c site
H	217 (336[a])	117	105
H_2	315 (1006[a])		

Note: [a] without CP.

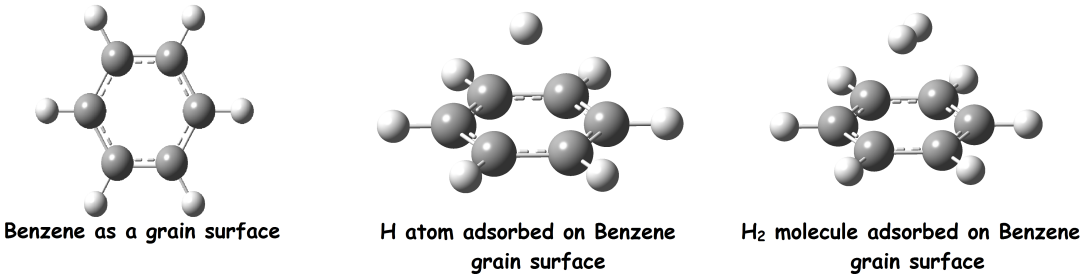

Figure 2.2: Benzene as a representative grain surface (Sil et al., 2017).

is more suited to mimic the interstellar carbonaceous grain, we use a benzene surface to save computational time. Benzene is a vital organic compound having the chemical formula C_6H_6. Bonfanti et al. (2007) found that the CP corrected BE of H is 18.8 meV with the most favorable hollow site of benzene surface using MP2/aug-cc-pVDZ level of theory. They also calculated the CP corrected BE of H to be 18.7 meV using the higher-level coupled-cluster single-double and perturbative triple excitation [CCSD(T)] method, taking the same basis set. The resulting differences between the MP2 and CCSD(T) methods were negligible in the broader astrophysical aspects. Thus to save computational time, we also employ the MP2/aug-cc-pVDZ level of theory for our BE calculations for H and H_2. The standard quantum chemical method is used for a hydrogen − benzene system to determine physisorption BEs over the high-symmetry sites accurately. Here, the BE of the H atom is calculated for three suitable positions of the benzene surface. For the calculations, CP correction is employed to minimize the BSSE. Calculated BEs at three positions considered in Figure 2.1 are presented in Table 2.2. It is clear from Table 2.2 that the hollow site is the most favorable location because it has a higher BE. We find the CP corrected BE of H is 217 K (18.7 meV) with hollow site of benzene surface. The value is very similar to that obtained by Bonfanti et al. (2007). In the case of H_2, only the most favorable position (h site) is employed. BE values with CP corrections and without CP corrections (shown in the parentheses)

Table 2.3: BE of H and H_2 on silica surface (Sil et al., 2017).

Species	Binding energy (in Kelvin)
H	580
H_2	1090

are listed in Table 2.2. Figure 2.2 shows the structure of benzene, along with the adsorption of H and H_2 in the hollow site. The BEs computed on benzene surfaces follow a similar trend as theoretically calculated values presented in Table 2.1.

2. Silica cluster

   To calculate the BEs of H and H_2 on bare silicate grain (a compound containing silicon), we consider three silica molecules together. For better accuracy, it is required to increase the size of the cluster. However, it would take a substantial computational time to converge. Thus we restrict ourselves by considering $(SiO_2)_3$ to mimic the silicate nature of the grain surface. Figure 2.3 depicts the silica cluster and the position of adsorbed species (H and H_2) with the silica cluster. In Table 2.3, the calculated BE values are shown. Here also, we find that BE of H_2 is higher than that of H.

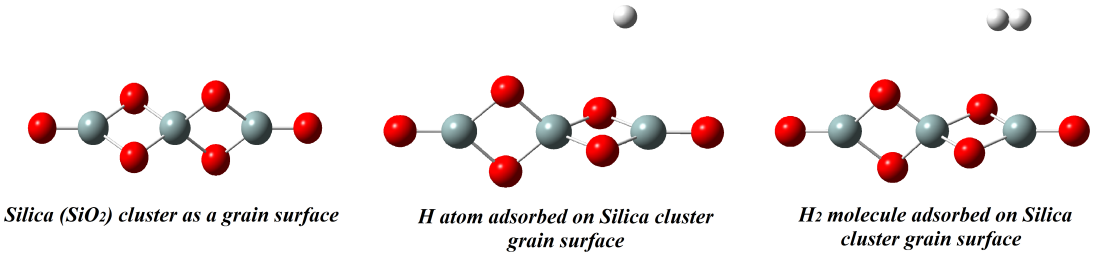

Figure 2.3: Silica cluster as a representative grain surface (Sil et al., 2017).

3. Water cluster

   To calculate the BE of H and H_2, here we use the water cluster (six water molecules as a grain surface) to mimic the water ice grain mantle. Ohno et al. (2005) calculated various geometries of water clusters $[(H_2O)_n$, for $n = 1 - 8]$. They found that the most stable structure of the water hexamer is the chair configuration. Thus, we consider the hexamer structure (chair) of the water molecule as a substrate here. A significant portion ($\sim$ 70% by mass) of the interstellar grain mantle is covered with water molecules around the dense

Table 2.4: BE of H and H_2 on water surface (Sil et al., 2017).

Species	Binding energy (in Kelvin)
H	181
H_2	545

cloud region of ISM (Keane et al., 2001; Whittet, 2003; Gibb et al., 2004; Das et al., 2010; Das & Chakrabarti, 2011; Das et al., 2016). Thus the incoming gas species may be directly adsorbed onto the water ice. So, knowing the BEs of the adsorbed species with water ice is essential to estimate better the composition of interstellar grain mantle in dense cloud regions. Figure 2.4 shows the structure of the water cluster (c-hexamer chair configuration) along with the adsorbed configuration of H and H_2. Table 2.4 shows the calculated BEs (no CP correction is considered here) with the water cluster. As in other substrates, the water cluster also yields a similar trend between the BEs of H and H_2. However, we find an exciting trend for the BEs obtained with the size of the water cluster ($n = 1 - 6$). As we increase the cluster size of the water molecules, we obtain higher values of BEs. For example, the BEs of H and H_2 are 30 K and 361 K with the water monomer, 125 K and 528 K with the water c-tetramer, and 181 K and 545 K with the water c-hexamer chair configuration. However, this trend is valid up to six water molecules clusters studied here. Beyond this, a saturation with experimental values of BE is expected.

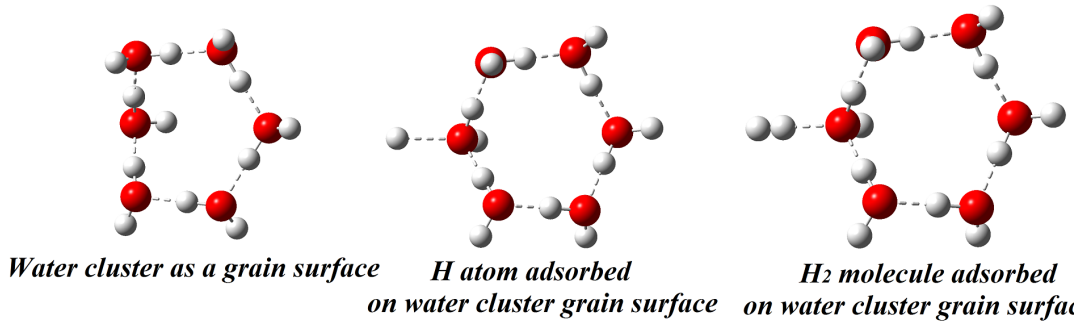

Figure 2.4: Water cluster (c-hexamer chair configuration) as a grain surface (Sil et al., 2017).

Table 2.5: Different sets of existing BE (in Kelvin) of H and H_2 (Sil et al., 2017).

Species	**Set 1** (Allen & Robinson, 1977)	**Set 2 for olivine** (Katz et al., 1999)	**Set 3 for amorphous carbon** (Katz et al., 1999)	**Set 4** (Vidali et al., 1991)
H	350	373	658	499 ± 3
H_2	450	314	542	660 ± 6

Binding energy of H and H_2 already available from the earlier studies

Table 2.5 presents different sets of available theoretical and experimental values of BEs of H and H_2. Set 1 corresponds to the theoretical values obtained by Allen & Robinson (1977). For olivine grain (Set 2), they determined 373 K and 314 K BE values for H and H_2, respectively. The desorption energies of H and H_2 were experimentally determined by Katz et al. (1999); Pirronello et al. (1999) for amorphous carbon with values of 658 K for H and 542 K for H_2 (Set 3). Ghio et al. (1980) calculated the van der Waals interaction between graphite and H with energy 503 ± 6 K. This value fully supports the experimental data given by Vidali et al. (1991), where the best estimate was given as 499 ± 3 K. Han & Lee (2004) used the density functional theory (DFT) method to calculate a value of 400 K for H_2 interacting with carbonaceous material (carbon nanotube), while Vidali et al. (1991) gave the best estimate of 660 ± 6 K for H_2 − graphite system. The estimated values of Vidali et al. (1991) are shown in Table 2.5 as Set 4. Dulieu et al. (2005) found a large distribution of energies for H_2 using TPD experiments. According to their study, the mean value of the BE of H_2 can be 520 K for the non-porous substrate, which is very close to the theoretical value of 550 K (Hollenbach & Salpeter, 1970) and experimental value of 550 ± 35 K (Sandford & Allamandola, 1993). Hornekær et al. (2005) found the value for H_2 as 440 K, which was also used by Cuppen & Hornekær (2008). For H atom on ice, there are three theoretical values for crystalline and amorphous ice: Hollenbach & Salpeter (1970); Buch & Czerminski (1991); Al-Halabi et al. (2002) determined energies of 450 K, ≈ 500 K, and 400 ± 50 K, respectively. Cuppen & Hornekær (2008) used 650 K calculated by Al-Halabi & van Dishoeck (2007) for the BE of H on amorphous ice. For sets 2 and 3, the BE of H_2 is less than H, whereas the opposite is true for sets 1 and 4. Interestingly, in all our calculations, we obtain the same trend between H and H_2. BE of H_2 is found to be always greater than that of H for all types of surfaces considered here.

Chemical modeling

H_2 formation is studied by various authors (Chakrabarti et al., 2006a,b; Biham et al., 2001; Sahu et al., 2015). Biham et al. (2001); Katz et al. (1999) discussed the steady-state conditions that may be reached by keeping the flux and temperature fixed. Here, we use the steady-state relation obtained by the earlier authors to calculate the H_2 formation efficiency window (see Figure 2.5) for various sets of BE values shown in Table 2.5. For this case, we consider a flux of 0.18×10^{-8} ML s^{-1} falling on a grain of diameter 0.1 μm. The density of the adsorption sites (s_n) is assumed to be 2×10^{14} cm^{-2} for the olivine surface (Set 1 and Set 2 of Table 2.5) and 5×10^{13} cm^{-2} for the amorphous carbon surface (Set 3). In the case of Set 4 also, we assume $s_n = 5 \times 10^{13}$ cm^{-2}.

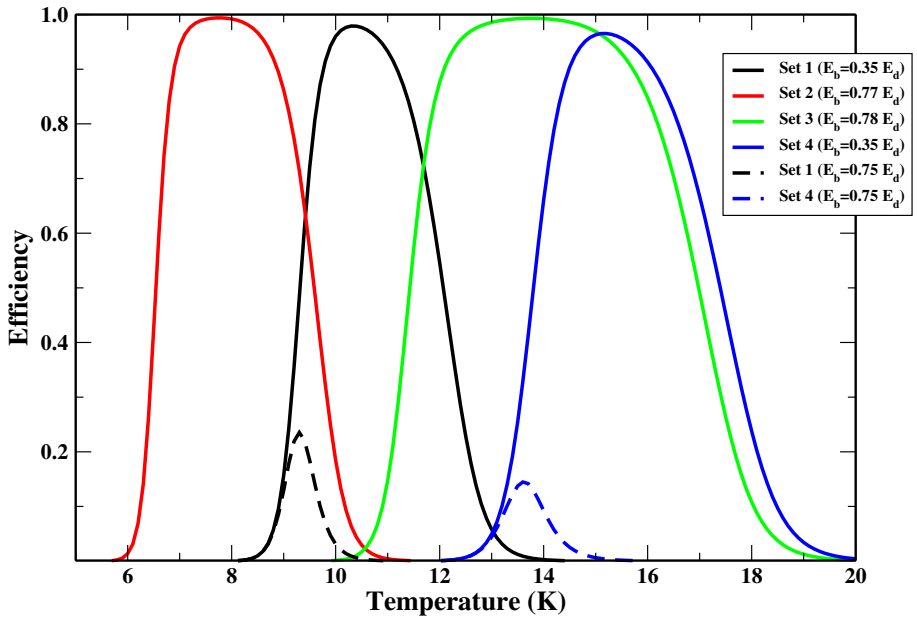

Figure 2.5: Efficiency window for various sets of BE shown in Table 2.5 (Sil et al., 2017).

In Set 2 and Set 3, diffusion energies of the H atom were available. In Set 1, obtained energy against diffusion barriers was 287 K (Pirronello et al., 1997). Thus the obtained ratio of the diffusion energy (E_b) and desorption energy (E_d) of H for Set 2 is ~ 0.77. For Set 3, this ratio is found to be ~ 0.78. This ratio is very poorly constrained in the literature, and various authors approximate their choices in the range of $0.3 - 0.8$. Since in the case of Set 1 and Set 4, no E_b was suggested, we use $E_b = 0.75E_d$ (dashed curve of Set 1 and Set 4), close to the experimentally obtained

ratio. For another case of Set 1 and Set 4, we assume $E_b = 0.35E_d$ (curves of Set 1 and Set 4). As expected, it is found that as we are increasing the mobility of the H atom (by decreasing the barrier against diffusion), the efficiency of formation increases (solid curves of Set 1 and Set 4), and H_2 molecules are efficiently forming within the much wider zone. For the olivine grain (Set 2), H_2 formation efficiency is maximum around $8-9$ K. In contrast, for the BE on amorphous carbon grains (Set 3), it is around $13-14$ K. The efficiency window obtained for the amorphous carbon grain (Set 3) is much broader than that of the olivine grain (Set 2). Considering the value obtained by Allen & Robinson (1977) (Set 1), the H_2 formation efficiency peaks around 10 K. For the Set 4 case, the peak efficiency is around 15 K.

Summary

From our calculated physisorption BEs of H atom and H_2 molecule on different grain surfaces, we find an exciting trend that BE of H_2 always remains higher than H for all the cases. However, our calculated values of the BEs of the H atom with the silica cluster and water cluster are very low compared to the experimentally obtained values. In our calculations, only one benzene, three SiO_2, and six H_2O molecules are considered to mimic the nature of the carbonaceous, silicate, and water substrate, respectively, which may not represent the actual astrophysical scenarios. However, this is the starting point to consider more complex and realistic systems. Assuming a steady-state solution to the rate equation method, we also present the H_2 formation efficiency window in various cases.

2.1.2 Study of binding energies of several interstellar species

Knowledge of the BE of the interstellar species is crucial to understand the synthesis of molecules in the gas phase and interstellar icy grain mantle. The BE depends on the volatile but also the grain surface composition. The ISM mainly consists of silicate and carbonaceous type grains. Numerous studies have been conducted in determining the composition of the interstellar grains and, more significantly, icy grain mantles (Whittet et al., 1996; van Dishoeck, 1998a; Ehrenfreund & Charnley, 2000; Ehrenfreund et al., 2003; Pontoppidan et al., 2008). These studies reveal that the denser regions of molecular clouds are predominantly composed of H_2O in the amorphous phase, with the addition of some other impurities, such as CO, CO_2, NH_3, CH_3OH, etc., in comparatively lower amounts. Early experiments (Chakarov & Kasemo, 1998) and astronomical observations (Malfait et al., 1998; Maldoni et al., 2003) suggest the presence of crystalline ice or vapor-deposited amorphous ice (ASW). It continues to attract more and more fundamental research (Dulieu et al., 2013; Hama & Watanabe, 2013) due to its occurrences in astronomical environments such as icy satellites, comets, planetary rings, interstellar grains, etc. Observations of the OH vibrational stretch in the IR absorption show that the structure of ice in the ISM is mostly amorphous (Hagen et al., 1981). Various surface processes such as adsorption, diffusion, tunneling reactions, and nuclear-spin conversion on interstellar ASW are summarized in Hama & Watanabe (2013). ASW is by far the most significant component of the icy mantles, with abundances of $\sim 10^{-4}$ concerning the total hydrogen (Williams & Herbst, 2002), equivalent to coverages of up to 100 mono-layers (MLs). The extinction threshold (A_V) for H_2O mantle is $\sim$ 3.3 mag (Whittet et al., 1988). In reality, the interstellar ices are thought to have low levels of porosity, as they are continuously exposed to external radiation (Palumbo, 2006). The ASW is known to have physical properties that are distinct from other crystalline states, e.g., a lower thermal conductivity, a larger surface area, and higher porosity (Dohnálek et al., 2003). Here, we devise a computational approach to approximate the BE for some relevant interstellar species on ASW substrate.

Computational Details and Methodology

The BE is usually seen as a local property arising from the electronic interaction between the grain surface and the species deposited on its surface (adsorbate). As mentioned earlier, a knowledge of the BE of the adsorbed species with water ice as adsorbent is essential for building a realistic astrochemical model that studies

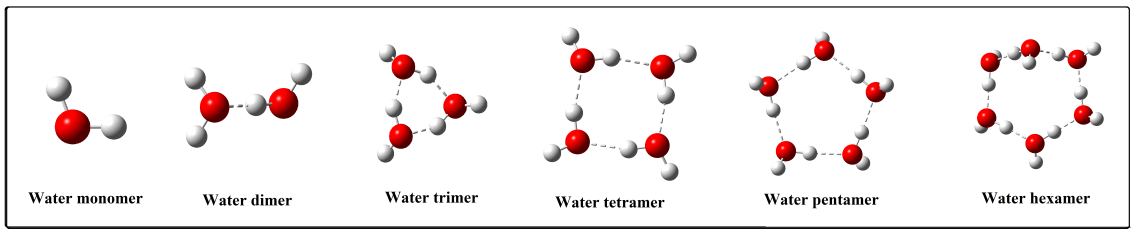

Figure 2.6: Configurations of water molecule(s) used (Das et al., 2018).

the composition of the interstellar grain mantle. Therefore, for investigation of the BEs, we use the most stable configurations of water monomer, dimer, c-trimer, c-tetramer, c-pentamer, and c-hexamer (chair) (Ohno et al., 2005) as the adsorbents (Figure 2.6).

We calculate the BE of a species on the grain surface following the formulae 2.1 and 2.2 mentioned earlier in subsection 2.1.1. We carry out calculations using the GAUSSIAN 09 suite of programs developed by Frisch et al. (2013). The MP2/aug-cc-pVDZ level of theory is mainly used for computing the optimized energy of all the species and complexes. The CCSD(T)/aug-cc-pVTZ level of theory is also used to calculate the single-point energy by taking the optimized structure obtained with the MP2 method for tetramer and hexamer (water clusters). The cc-pVDZ and cc-pVTZ are the Dunnings-correlation-consistent basis set (Dunning, 1989) with double and triple zeta functions, respectively. The dependency of our computed BE values are reviewed on the implemented method and basis set. A fully optimized ground-state structure is verified as a stationary point (having non-imaginary frequency) by the harmonic vibrational frequency analysis. Most of the calculations are performed without the corrections of ZPVE and BSSE. Calculations are also performed by including ZPVE and excluding BSSE (using the CP method, see the formula 2.3) to check their effect.

Results and discussions on the BE values

In this Section, the results of high-level quantum chemical calculations are presented and discussed in detail. Wakelam et al. (2017) selected 16 stable species to compute the BEs by considering a water monomer. Here, we employ a similar methodology and carry out calculations by increasing the cluster size of water molecule to check its consequences. Six different sets of adsorbents are used to see the effects of cluster size on the computed BEs. With the increase in cluster size, we find a trend of increasing BE for most species considered here. Most interestingly,

the calculated BEs, by considering the water pentamer and hexamer configurations, seem to be closer to the experimentally obtained values than the calculated BEs with the water monomer, dimer, trimer, or tetramer configurations. The BEs of these 16 stable species with various water cluster configurations are given in Table 2.6. For the sake of comparison, in Table 2.6, we also show the experimentally obtained values, estimated values from Wakelam et al. (2017), and BEs from the UMIST Database[1] (McElroy et al., 2013).

Figure 2.7 is subdivided into 16 blocks for 16 different species. We show the sizes of water clusters along the X-axis, and along the Y-axis, we show the percentage of deviation relative to experiments. The red horizontal line in each block denotes the zero deviation. The result clearly shows that mostly the percentage of deviation is comparatively higher (underestimated) when the water monomer is used and lower when the pentamer or hexamer configuration of the water cluster is used. However, we can see that the BEs with dimer configuration largely deviate from that obtained with the rest of the arrangements. For example, in the case of OCS, HCl, CH_3OH, NH_3, C_2H_2, CO_2, and N_2, the BEs with the dimer configuration vastly increased compared to the BEs obtained with the other water structures. On the contrary, BEs of CH_3CN, H_2O_2, H_2S, and CH_3CCH with the dimer configuration are minimal compared to the rest of the cases. The percentage deviations are noted in parentheses in Tables 2.6 and 2.7 as well. Furthermore, we calculate the average absolute percentage deviation and root mean square (RMS) fractional deviation of these species presented in Tables 2.6 and 2.7. It is interesting to note (in Table 2.6) that while we gradually increase the cluster size, the average percentage of deviations are found to be $\pm$41.6%, $\pm$29.0%, $\pm$24.6%, $\pm$18.8%, $\pm$15.8%, and $\pm$16.7%, for monomer, dimer, trimer, tetramer, pentamer, and hexamer, respectively. Similarly the fractional RMS deviations are found to be 0.435, 0.292, 0.324, 0.236, 0.205, and 0.221, respectively. These average absolute percentage deviations and fractional RMS deviations are shown in Figure 2.8(a) and (b), respectively. The large deviations from experimental BE values in case of water dimer cluster shown in Figure 2.7 are averaged out in Figure 2.8, which shows a similar trend. But in reality, it is not the case. Figure 2.9 depicts the percentage deviation from experimental BE values of each species considering water hexamer.

[1] http://udfa.ajmarkwick.net

Table 2.6: Calculated BEs of 16 stable species (Das et al., 2018).

Sl. No.	Species	Calculated BE (in Kelvin) on different water clusters using MP2/aug-cc-pVDZ						Experimental values of BE (in Kelvin) M06-2X	BE from Wakelam et al. (2017) (in Kelvin)		BE (in Kelvin) from UMIST database[k]
		Monomer	Dimer	Trimer	Tetramer	Pentamer	Hexamer		using DFT aug-cc-pVTZ	using MP2	
1	OCS	1139 (−53.1%)	2106 (−13.3%)	1905 (−21.6%)	1571 (−35.3%)	2014 (−17.1%)	1808 (−25.5%)	2430 ± 24[a]	2100 (13.5%)	—	2888 (18.8%)
2	HCl	3116 (−39.7%)	4994 (−3.4%)	3545 (−31.4%)	3924 (−24.1%)	4099 (−20.7%)	4104 (−20.6%)	5172[b]	4800 (7.1%)	5000 (−3.3%)	900 (−82.5%)
3	CH_3CN	2676 (−42.8%)	2039 (−56.4%)	4108 (−12.2%)	2838 (−39.3%)	2820 (−39.7%)	3786 (−19.1%)	4680[c]	4300 (8.1%)	4800 (2.5%)	4680 (0.00%)
4	H_2O_2	3838 (−36.0%)	5632 (−61.3%)	3942 (−34.3%)	3928 (−34.5%)	5288 (−11.8%)	5286 (−11.9%)	6000[d]	6800 (−13.3%)	6100 (1.6%)	5700 (−5.0%)
5	CH_3OH	3124 (−37.5%)	5932 (18.6%)	3924 (−21.5%)	4368 (−12.6%)	4607 (−7.8%)	4511 (−9.7%)	5000[e]	4800 (4.0%)	4850 (−3.0%)	4930 (−1.4%)
6	NH_3	3501 (−36.6%)	5684 (27.8%)	3745 (−32.3%)	3825 (−30.8%)	3751 (−32.1%)	5163 (−6.6%)	5530[c]	5600 (−1.2%)	5500 (−0.5%)	5534 (0.6%)
7	CO	595 (−54.2%)	1027 (−21.0%)	664 (−48.9%)	1263 (−2.8%)	1320 (1.5%)	1292 (−0.6%)	1300[g]	1300 (0.0%)	1100 (−15.3%)	1150 (−11.5%)
8	C_2H_2	1532 (−40.7%)	3399 (31.4%)	2581 (−0.2%)	2593 (0.2%)	2633 (1.7%)	2640 (2.0%)	2587[c]	2600 (−0.5%)	2700 (4.3%)	2587 (0.0%)
9	CO_2	1506 (−34.5%)	2719 (18.2%)	1935 (−15.9%)	2293 (−0.3%)	2287 (−0.5%)	2352 (2.2%)	2300[g]	3100 (34.7%)	2600 (13.0%)	2990 (30.0%)
10	N_2	793 (−27.9%)	1203 (9.4%)	884 (−19.6%)	900 (−18.1%)	893 (−18.8%)	1161 (5.5%)	1100[e]	1100 (0.0%)	1400 (27.2%)	790 (−28.1%)
11	NO	886 (−50.7%)	1115 (−38.0%)	568 (−68.4%)	1265 (−29.7%)	1300 (−27.7%)	1988 (10.4%)	1800[e]	1600 (11.1%)	1700 (−5.5%)	1600 (−11.1%)
12	O_2	391 (−67.4%)	572 (−52.3%)	382 (−68.2%)	940 (−21.6%)	1116 (−7.0%)	1352 (12.6%)	1200[g]	1000 (16.6%)	900 (−25.0%)	1000 (−16.6%)
13	H_2S	1727 (−37.0%)	1460 (−46.8%)	2849 (3.9%)	2556 (−6.8%)	2396 (−12.6%)	3232 (17.8%)	2743[c,k]	2700 (1.5%)	2550 (−7.0%)	2743 (0.0%)
14	CH_3CCH	2266 (−9.3%)	2115 (−15.4%)	2580 (3.2%)	2342 (−6.3%)	2673 (6.9%)	3153 (26.1%)	2500 ± 40[h]	3800 (−52.0%)	3800 (52.0%)	2470 (−1.2%)
15	HNCO	2046 (−47.5%)	2653 (−32.0%)	3973 (1.9%)	3922 (0.5%)	4097 (5.0%)	5554 (42.4%)	3900[i]	4850 (−24.3%)	...	2850 (−26.9%)
16	CH_4	469 (−51.2%)	780 (−19.0%)	1066 (10.7%)	1327 (37.7%)	1366 (41.8%)	1491 (54.8%)	963[j]	800 (16.9%)	1000 (3.8%)	1090 (13.1%)
Average absolute deviation		±41.6%	±29.0%	±24.6%	±18.8%	±15.8%	±16.7%		±12.8%	±11.7%	±15.4%
Fractional RMS deviation		0.435	0.292	0.324	0.236	0.205	0.221		0.189	0.182	0.254

Note:
Percentage deviations from experimental BE values (Column 8) are shown in parentheses for Columns 3, 4, 5, 6, 7, 8, 10, 11, and 12.
[a] Ward et al. (2012), [b] Olanrewaju et al. (2011), [c] Collings et al. (2004), [d] Dulieu et al. (2013), [e] Wakelam et al. (2017), [g] Minissale et al. (2016), [h] Kimber et al. (2014), [i] Noble et al. (2015), [j] Raut et al. (2007), [k] UMIST database (http://udfa.ajmarkwick.net).

Table 2.7: Comparison of calculated BEs using water monomer (adsorbent) with experimentally used BEs (Das et al., 2018).

Sl. No.	Species	BE (in Kelvin) using different methods and basis sets including (+) or excluding (−) ZPVE and BSSE					Experimental values of BE (in Kelvin)
		MP2/aug-cc-pVDZ − ZPVE and − BSSE	MP2/aug-cc-pVDZ + ZPVE but − BSSE	MP2/aug-cc-pVDZ − ZPVE but + BSSE	MP2/aug-cc-pVTZ − ZPVE and − BSSE	CCSD(T)/aug-cc-pVTZ − ZPVE and − BSSE	
1	OCS	1139 (−53.1%)	683 (−71.9%)	803 (−66.9%)	1074 (−55.8%)	1086 (−55.3%)	2430 ± 24[a]
2	HCl	3116 (−39.7%)	2113 (−59.1%)	2627 (−49.2%)	2975 (−42.5%)	2777 (−46.3%)	5172[b]
3	CH_3CN	2676 (−42.8%)	1970 (−57.9%)	2242 (−52.1%)	2676 (−42.8%)	2635 (−43.7%)	4680[c]
4	H_2O_2	3838 (−36.0%)	2647 (−55.9%)	3204 (−46.6%)	3775 (−37.1%)	3802 (−36.6%)	6000[d]
5	CH_3OH	3124 (−37.5%)	2149 (−57.0%)	2586 (−48.3%)	3021 (−39.6%)	2988 (−40.2%)	5000[e]
6	NH_3	3501 (−36.6%)	2368 (−57.2%)	2941 (−46.8%)	3375 (−39.0%)	3332 (−39.7%)	5530[c]
7	CO	595 (−54.2%)	236 (−81.8%)	349 (−73.2%)	565 (−56.5%)	662 (−49.1%)	1300[g]
8	C_2H_2	1532 (−40.7%)	950 (−63.3%)	1111 (−57.1%)	1519 (−41.3%)	1444 (−44.2%)	2587[c]
9	CO_2	1506 (−34.5%)	1109 (−51.8%)	1159 (−49.6%)	1417 (−38.4%)	1511 (−34.3%)	2300[g]
10	N_2	793 (−27.9%)	340 (−69.1%)	534 (−51.4%)	791 (−28.1%)	759 (−31.0%)	1100[e]
11	NO	886 (−50.7%)	353 (−80.4%)	249 (−86.2%)	876 (−51.3%)	780 (−56.7%)	1800[e]
12	O_2	391 (−67.4%)	258 (−78.5%)	191 (−84.1%)	385 (−67.9%)	419 (−65.1%)	1200[g]
13	H_2S	1727 (−37.0%)	971 (−64.6%)	1305 (−52.4%)	1662 (−39.4%)	1598 (−41.7%)	2743[c,k]
14	CH_3CCH	2266 (−9.3%)	1548 (−38.1%)	1675 (−33.0%)	2175 (−13.0%)	2083 (−16.7%)	2500 ± 40[h]
15	HNCO	2046 (−47.5%)	1376 (−64.7%)	1644 (−57.8%)	3260 (−16.4%)	2058 (−47.2%)	3900[i]
16	CH_4	469 (−51.2%)	145 (−84.9%)	265 (−72.5%)	374 (−61.2%)	401 (−58.4%)	963[j]
Average abs deviation		± 41.6 %	± 64.7 %	± 58 %	± 41.9 %	± 44.1 %	—
Frac. RMS deviation		0.435	0.659	0.597	0.443	0.456	—

Note:
Percentage deviations from experimental BE values (Column 8) are shown in parentheses for Columns 3, 4, 5, 6, and 7.
[a] Ward et al. (2012), [b] Olanrewaju et al. (2011), [c] Collings et al. (2004), [d] Dulieu et al. (2013), [e] Wakelam et al. (2017), [g] Minissale et al. (2016), [h] Kimber et al. (2014), [i] Noble et al. (2015), [j] Raut et al. (2007), [k] UMIST database (`http://udfa.ajmarkwick.net`).

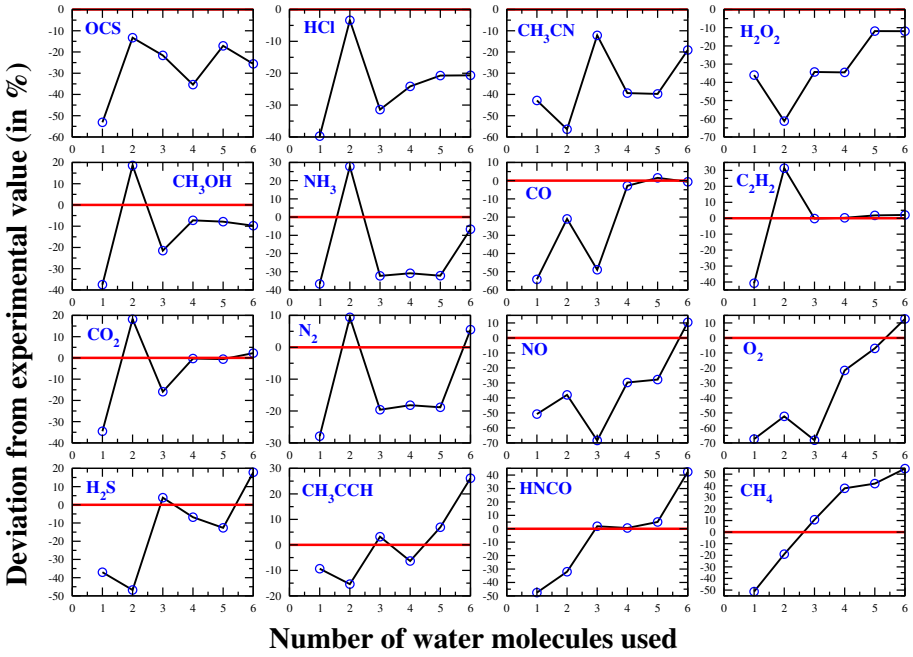

Figure 2.7: Percentage deviations of BEs of 16 stable species with increasing numbers of water clusters acting as the grain surface (Das et al., 2018).

Table 2.6 presents the average absolute percentage of deviation of calculated BE values from Wakelam et al. (2017). We see that, on an average, the predicted/scaled values of Wakelam et al. (2017) deviate from the experimental values by ±12.8% and ±11.7%, when DFT/M06-2X and MP2/aug-cc-pVTZ level of theories were used, respectively. The BE values in the UMIST database deviate from the experimental values by ±15.4%. Our calculations with pentamer and hexamer configurations produce average deviations of ±15.8% and ±16.7%, respectively, from the experimental values. No proportional law fitting (as in Wakelam et al., 2017) is required for our calculations. Since the calculations with the pentamer and hexamer configurations can roughly estimate the experimental values, it is suggested to use these configurations to evaluate the BE of species without any existing experimental values.

Table 2.7 shows a comparison between the results obtained by considering BSSE corrections using the CP method (Column 5) and without BSSE corrections (Column 3) considering water monomer as adsorbent. By considering the water hexamer structure, the same comparison is performed noted in Table 2.8. BSSE-corrected BE values are lower than those without BSSE corrections, implying that the basis set leads to significant BSSE. Table 2.7 also shows a comparison between the results obtained by including ZPVE (Column 4) and without including ZPVE (Col-

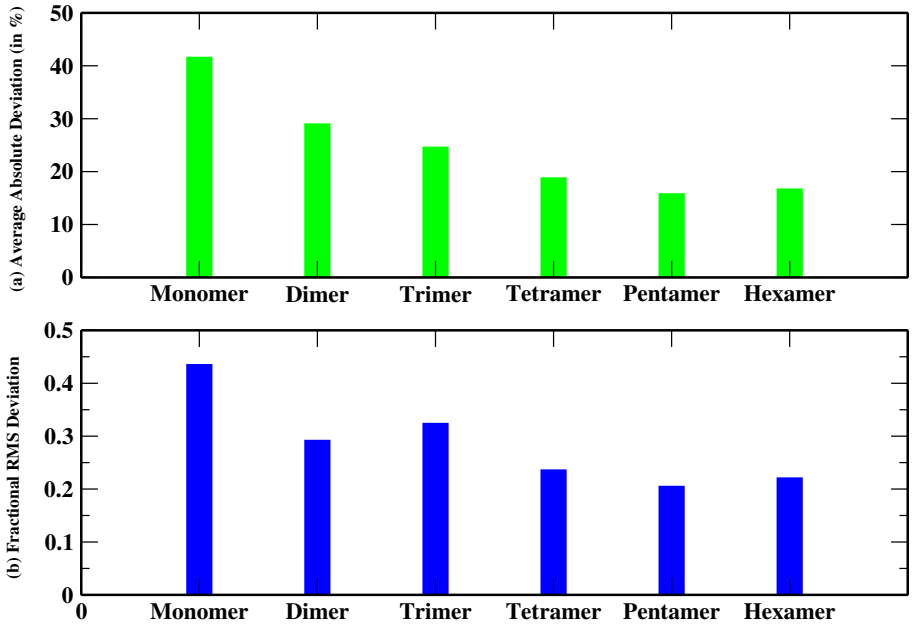

Figure 2.8: (a) Average absolute percentage deviation and (b) fractional RMS deviation of our calculated values from experiments (Das et al., 2018).

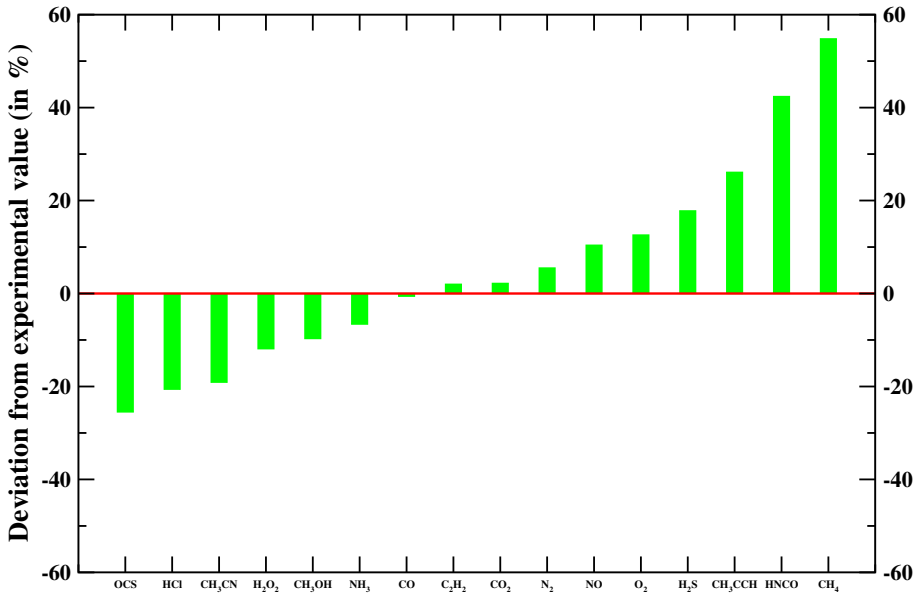

Figure 2.9: Percentage deviation from experimental BE values of 16 stable species using the water c-hexamer (chair) cluster (Das et al., 2018).

Table 2.8: Calculated BEs using water hexamer (adsorbent) to check the effect of basis set superposition error (BSSE) using the counterpoise (CP) method (Das et al., 2018).

Sl. No.	**Species**	**BE (in Kelvin) using MP2/aug-cc-pVDZ level of theory**	
		Values without BSSE correction	**BSSE corrected values**
1	OCS	1808 (−25.5%)	1294 (−46.7%)
2	HCl	4104 (−20.6%)	3777 (−26.9%)
3	CH_3CN	3786 (−19.1%)	2194 (−53.1%)
4	H_2O_2	5286 (−11.9%)	4161 (−30.6%)
5	CH_3OH	4511 (−9.7%)	3550 (−29.0%)
6	NH_3	5163 (−6.6%)	3082 (−44.2%)
7	CO	1292 (−0.6%)	840 (−35.3%)
8	C_2H_2	2640 (2.0%)	1890 (−26.9%)
9	CO_2	2352 (2.2%)	1624 (−29.3%)
10	N_2	1161 (5.5%)	568 (−48.3%)
11	NO	1988 (10.4%)	911 (−49.3%)
12	O_2	1352 (12.6%)	519 (−56.7%)
13	H_2S	3232 (17.8%)	1954 (−28.8%)
14	CH_3CCH	3153 (26.1%)	1382 (−44.7%)
15	HNCO	5554 (42.4%)	5017 (28.6%)
16	CH_4	1491 (54.8%)	653 (−32.1%)
Average absolute deviation		±16.7%	±34.6%
Fractional RMS deviation		0.221	0.395

Note: Percentage deviation from experimental BE values are shown in parentheses for Columns 3 and 4.

umn 3), considering water monomer. Notably, results obtained without ZPVE and BSSE corrections are closer to the experimental values. To check the dependency on the level of theories, BE calculations are performed using a higher-level theory (CCSD(T)/aug-cc-pVTZ) by single-point energy calculations considering water monomer. The results are shown in Column 7 of Table 2.7. The same higher-level theory is employed to evaluate BEs of some selected species (N, O, O_2, H_2O, CO, and N_2) considering water tetramer noted in Table 2.9. We notice a minor change of BE values considering BSSE, ZPVE corrections, and higher-level theory. Wakelam et al. (2017) noticed a slightly better fitting of the proportional law without including ZPVE because the ZPVE is roughly proportional to the BE. After the inclusion of the ZPVE, the parameters for the fits are not the same, but the results of the fits show similar deviations. However, we notice that the MP2 method in conjunction with the aug-cc-pVDZ basis set (without considering ZPVE and BSSE corrections) is comparatively best among all the methods and basis sets used in our computation. A lower-level theory (without considering ZPVE and BSSE corrections) results in better agreement with the experimental result than those from a higher-level theory. This is likely because effects various approximations at lower levels cancel each other. It is possibly a coincidence but is helpful as it makes it

Table 2.9: Calculated BEs using water tetramer (adsorbent) to check the influence of the higher-order quantum chemical level of theory (Das et al., 2018).

Sl. No.	Species	BE (in Kelvin) using water tetramer	
		MP2/aug-cc-pVDZ	CCSD(T)/aug-cc-pVTZ
1	N	269	273
2	O	1002	1024
3	O_2	940	853
4	H_2O	2670	2632
5	CO	1263	1196
6	N_2	900	854

easier to process many systems.

BE calculations considering water pentamer and hexamer cluster configuration (as a substrate) are computationally expensive and sometimes take a long time to converge; thus, it is not easy to apply for a large set of species. Table 2.10 provides our calculated BE values for 21 species with the hexamer configuration. Since BE values taking the water hexamer cluster configuration deviate by $\sim \pm 16.7\%$, they can be scaled by 1 ± 0.167. We also provide a large set of BE values for 100 crucial interstellar or circumstellar species considering the water tetramer configuration as a substrate. In this case, the deviation from the experimental values is $\sim \pm 18.8\%$ and can be scaled by 1 ± 0.188. Our calculations taking tetramer configuration of water cluster are an exciting alternative to complete calculations or the fitting model used by Wakelam et al. (2017). Some strange values of BE of some species are due to induced deviation from the global minimum. The mobility of atoms is significant for grain chemistry in dense molecular clouds and depends mainly on their BE with the grain surface. The BEs of some relevant atoms (such as H, He, C, N, O, Na, Mg, Si, P, and S) are also included in Table 2.10. Our calculations with the tetramer configuration likely deviate from the experimental BE values due to the long-range interactions (interactions with water molecules not close to the species, as visible from Figures 2.12−2.16), which seems crucial for cases with low BEs. Thus, using only a scale factor without offset from the tetramer configuration may likely underestimate the real BE, particularly for low BE cases.

Previously used and recently proposed BE values by the KIDA[2] (Wakelam et al., 2017) and other sources are provided in Columns 6, 7, and 8, respectively, of Table 2.10. Among the sixteen stable species shown in Tables 2.6 and 2.7, there are both polar (OCS, CH_3OH, NH_3, H_2S, CH_3CCH, CH_3CN, H_2O_2, HCl, HNCO, NO) and non-polar molecules (CO, CO_2, N_2, O_2, CH_4, C_2H_2). We notice that for the non-

[2] http://kida.obs.u-bordeaux1.fr

Table 2.10: Calculated and available list of BEs of various species (Das et al., 2018).

Sl. No.	Species	Ground state used	BE (in Kelvin) on water tetramer	BE (in Kelvin) on water hexamer	BE from KIDA		BE (in Kelvin) from other literature sources
					Old values (in Kelvin)	New values (in Kelvin)	
1	H	Doublet	125	181	450[g]	650 ± 195	650 ± 100[c]
2	H_2	Singlet	528	545	450	440 ± 132	500 ± 100[c]
3	He	Singlet	113		100		100 ± 50[c]
4	C	Triplet	660		800	10000 ± 3000	715 ± 360[c], 14100 ± 420[k]
5	N	Quartet	269	619	800	720 ± 216	715 ± 358[c], 400 ± 30[k]
6	O	Triplet	1002	660	1660 ± 60[a]	1600 ± 480	1660 ± 60[c], 1504 ± 12[j], 1440 ± 160[k]
7	Na	Doublet	2214		11800		10600 ± 500[c]
8	Mg	Singlet	654		5300		4750 ± 500[c]
9	Si	Triplet	6956		2700	11600 ± 3480	2400 ± 500[c]
10	P	Quartet	616		1100		750 ± 375
11	S	Triplet	1428		1100	2600 ± 780	985 ± 495[c]
12	NH	Triplet	1947		2378	2600 ± 780	542 ± 270[c]
13	OH	Doublet	3183		2850[g]	4600 ± 1380	3210 ± 1550[c]
14	PH	Triplet	944				800 ± 400
15	C_2	Triplet	9248		1600		1085 ± 500[c]
16	HF	Singlet	5540				500 ± 250
17	HCl	Singlet	3924	4104	5174 ± 1[b]	5172 ± 1551.6	900 ± 450
18	CN	Doublet	1736		1600		1355 ± 500[c]
19	N_2	Singlet	900	1161	1000[g]	1100 ± 330	990 ± 100[c], 1000[f]
20	CO	Singlet	1263	1292	1150[g]	1300 ± 390	1100 ± 250[c], 1300[e]
21	SiH	Doublet	8988		3150	13000 ± 3900	2620 ± 500[c]
22	NO	Doublet	1265	1988	1600	1600 ± 480	1085 ± 500[c]
23	O_2	Triplet	940	1352	1000	1200 ± 360	898 ± 30[c], 1200[e], 1000[f]
24	HS	Doublet	2221		1450	2700 ± 810	1350 ± 500[c]
25	SiC	Triplet	5850		3500		3150 ± 500[c]
26	CP	Doublet	1699		1900		1050 ± 500
27	CS	Singlet	2217		1900	3200 ± 960	1800 ± 500[c]
28	NS	Doublet	2774		1900		1800 ± 500[c]
29	SO	Triplet	2128		2600	2800 ± 840	1800 ± 500[c]
30	S_2	Triplet	1644		2200		2000 ± 500[c]
31	CH_2	Triplet	1473		1050	1400 ± 420	860 ± 430[c]
32	NH_2	Doublet	3240		3956	3200 ± 960	770 ± 385[c]
33	H_2O	Singlet	2670	4166	5700[g]	5600 ± 1680	4800 ± 100[c]
34	PH_2	Doublet	1226		2000		850 ± 425
35	C_2H	Doublet	2791		2137	3000 ± 900	1330 ± 500[c]
36	N_2H	Doublet	3697		1450		
37	O_2H	Doublet	5778		3650	5000 ± 1500	1510 ± 500[c]
38	HS_2	Doublet	4014		2650		2300 ± 500[c]
39	HCN	Singlet	2352		2050	3700 ± 1110	1580 ± 500[c]
40	HNC	Singlet	5225		2050	3800 ± 1140	1510 ± 500[c]
41	HCO	Doublet	1857		1600[g]	2400 ± 720	1355 ± 500[c]
42	HOC	Doublet	5692				
43	HCS	Doublet	2713		2350	2900 ± 870	2000 ± 500[c]
44	HNO	Singlet	2988		2050	3000 ± 900	1510 ± 500[c]
45	H_2S	Singlet	2556	3232	2743[f]	2700 ± 810	2290 ± 90[c]
46	C_3	Singlet	2863		2400	2500 ± 750	2010 ± 500[c]
47	O_3	Singlet	2545		1800	2100 ± 630	2100 ± 100[c]
48	C_2N	Doublet	1281		2400		2010 ± 500[c]
49	C_2S	Triplet	2477		2700		2500 ± 500[c]
50	OCN	Doublet	3085		2400		1805 ± 500[c]
51	CO_2	Singlet	2293	2352	2575	2600 ± 780	2267 ± 70[c], 2300[e]
52	OCS	Singlet	1571	1808	2888	2400 ± 720	2325 ± 95[c]
53	SO_2	Singlet	3745		3405	3400 ± 1020	3010 ± 110[c]
54	CH_3	Doublet	1322		1175	1600 ± 480	1040 ± 500[c]
55	NH_3	Singlet	3825	5163	5534	5500 ± 1650	2715 ± 105[c], 5530[f]

Sl. No.	Species	Ground state used	BE (in Kelvin) on water tetramer	BE (in Kelvin) on water hexamer	BE from KIDA		BE (in Kelvin) from other literature sources
					Old values (in Kelvin)	New values (in Kelvin)	
56	SiH_3	Doublet	1269		4050		3440 ± 500[c]
57	C_2H_2	Singlet	2593	2640	2587[f]	2587 ± 776.1	2090 ± 85[c]
58	N_2H_2	Singlet	3183				
59	H_2O_2	Singlet	3928	4248	5700	6000 ± 1800	6000 ± 100[c], 5410[l]
60	H_2S_2	Singlet	4368		3100		2600 ± 500[c]
61	H_2CN	Doublet	2984		2400		2400 ± 500[c]
62	CHNH	Doublet	3742				
63	H_2CO	Singlet	3242		2050[g]	4500 ± 1350	3260 ± 60[c]
64	CHOH	Triplet	4800				
65	HC_2N	Triplet	3289				2270 ± 500[c]
66	HC_2O	Doublet	2914		2400		2010 ± 500[c]
67	HNCO	Singlet	3922	5554	2850	4400 ± 1320	2270 ± 500[c], 3900[h]
68	H_2CS	Singlet	3110		2700	4400 ± 1320	2025 ± 500[c]
69	C_3O	Singlet	3542		2750		2520 ± 500[c]
70	CH_4	Singlet	1327	2321	1300[g]	960 ± 288	1250 ± 120[c]
71	SiH_4	Singlet	1527		4500		3690 ± 500[c]
72	C_2H_3	Doublet	2600		3037	2800 ± 840	1760 ± 500[c]
73	$CHNH_2$	Singlet	7069				
74	CH_2NH	Singlet	4352		5534		1560 ± 500[c]
75	CH_3N	Triplet	2194				
76	c-C_3H_2	Singlet	3892		3387	5900 ± 1770	2110 ± 500[c]
77	H_2CCN	Doublet	3730		4230		2470 ± 500[c]
78	H_2CCO	Singlet	2847		2200	2800 ± 840	2520 ± 500[c]
79	HCOOH	Singlet	3483		5570[g]		4532 ± 150[c]
80	CH_2OH	Doublet	4772		5084	4400 ± 1320	2170 ± 500[c]
81	NH_2OH	Singlet	4799				2770 ± 500[c]
82	C_4H	Doublet	2946		3737		2670 ± 500[c]
83	HC_3N	Singlet	2925		4580		2685 ± 500[c]
84	HC_3O	Doublet	2619				
85	C_5	Singlet	2403		4000		3220 ± 500[c]
86	C_2H_4	Singlet	2052		3487	2500 ± 750	2010 ± 500[c]
87	CH_2NH_2	Doublet	3831		5534[d]		
88	CH_3NH	Doublet	3414				1760 ± 500[c]
89	CH_3OH	Singlet	4368	4511	5534	5000 ± 1500	3820 ± 135[c], 5530[f]
90	CH_2CCH	Doublet	2726		3837	3300 ± 990	3840 ± 500[c]
91	CH_3CN	Singlet	2838	3786	4680[f]	4680 ± 1404	3790 ± 130[c]
92	H_2C_3N	Doublet	2637				
93	H_2C_3O	Singlet	3006				
94	C_6	Quintet	3226		4800		3620 ± 500[c]
95	CH_3NH_2	Singlet	4434		6584		5130 ± 500[c], 4269[m]
96	C_2H_5	Doublet	1752		3937	3100 ± 930	2110 ± 500[c]
97	CH_3CCH	Singlet	2342	3153	4287	3800 ± 1140	4290 ± 500[c], 2500 ± 40[i]
98	CH_2CCH_2	Singlet	2775			3000 ± 900	4290 ± 500[c]
99	CH_3CHO	Singlet	3849		2450	5400 ± 1620	2870 ± 500[c]
100	C_7	Singlet	4178		5600		4430 ± 500[c]

Note:
The average deviations from experiments for the cases of tetramer (Column 4) and hexamer (Column 5) are ∼ ±18.8% and ∼ ±16.7% respectively.
[a]He et al. (2015), [b]Olanrewaju et al. (2011), [c]Penteado et al. (2017), [d]Ruaud et al. (2015), [e]Minissale et al. (2016), [f]Collings et al. (2004), [g]Garrod & Herbst (2006b), [h]Noble et al. (2015), [i]Kimber et al. (2014), [j]Ward et al. (2012), [k]Shimonishi et al. (2018), [l]Lamberts & Kästner (2017). [m]Chaabouni et al. (2018).

polar species, BE calculation sometimes overestimates the attractive interaction if we choose the position of the species at the center of a water cluster. The species (like HCl, CH_3OH, etc.) leading to hydrogen bonds with H_2O are localized on one water molecule with H-bonding. In most such cases, the interaction is well reproduced by our calculations. The case with the oxygen atom is found as an intermediate one. The BEs of the oxygen atom are found to be 1002 K and 660 K (given in Table 2.10) for the tetramer and hexamer configurations, respectively. In contrast, the current value is 1660 ± 60 K in KIDA (Wakelam et al., 2017) desorption energy on an ASW surface. This is because the complex containing water hexamer with an oxygen atom is significantly modified, so the interaction with water is weaker. It seems that the interaction with the oxygen atom does not compensate for this. However, the values are more accurate in the complex containing water tetramer with an oxygen atom. The likely cause could be that water interaction is not so perturbed in that case. The BE of hydrogen atom is found to be 125 K with tetramer and 181 K with hexamer (see Table 2.10). Strangely, it leads to a much smaller interaction compared to the average value ($\sim$ 650 K) computed by Al-Halabi & van Dishoeck (2007). Thus, though a very good approximation (on an average) is found by using the pentamer and hexamer configurations, we should keep in mind that using only one adsorption site geometry may induce significant errors in BE values. For a targeted species, it is recommended to consider different adsorption sites and corresponding optimized geometries and then take an average to come up with a more accurate approximation. In our case, when various binding sites are found, we try to choose the one with the closest available experimental values. We provide the complex geometries used to determine the BEs as supplementary materials (Das et al., 2018). Figures 2.10−2.16 provide the optimized geometries for the species considered here with hexamer, pentamer, and tetramer configurations, respectively. The BEs are very much sensitive to the chosen ground state spin multiplicity. Therefore, the ground states used for each species are also provided in Column 3 of Table 2.10. The ground state spin multiplicities of each species are calculated using the GAUSSIAN 09 suite of programs. For this purpose, separate calculations (job type "opt+freq") are performed, each with different spin multiplicities, and then compare. The lowest energy electronic state solution of the chosen spin multiplicity is the ground state noted for the species in Table 2.10.

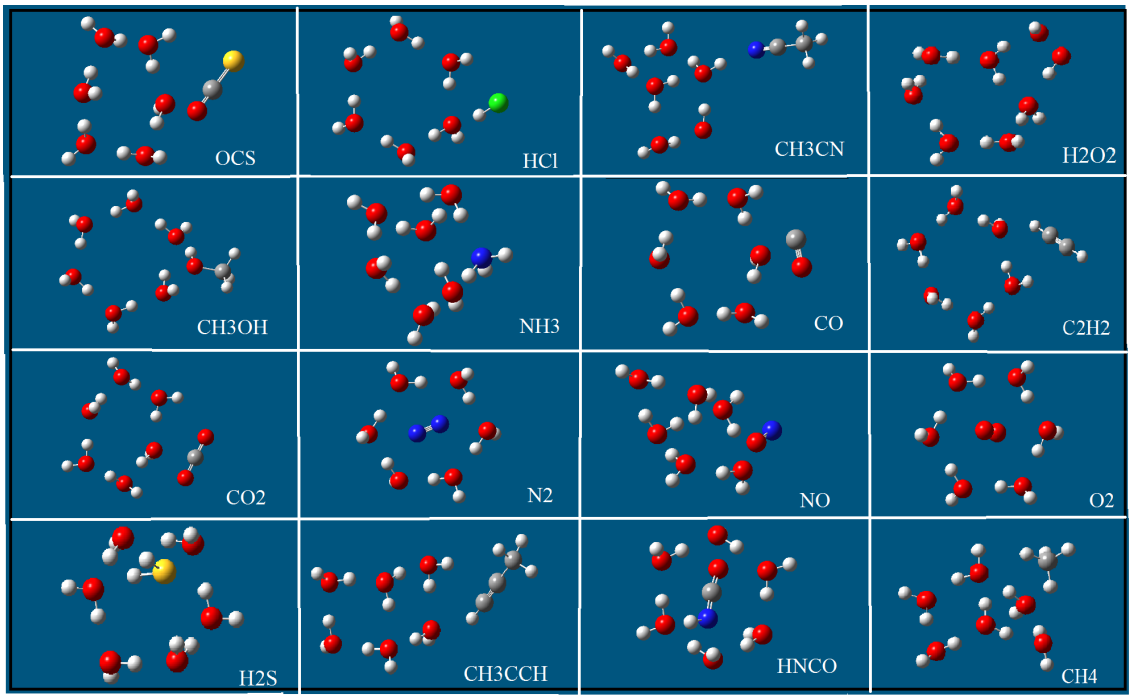

Figure 2.10: Optimized geometries with the c-hexamer (chair) configuration (Das et al., 2018).

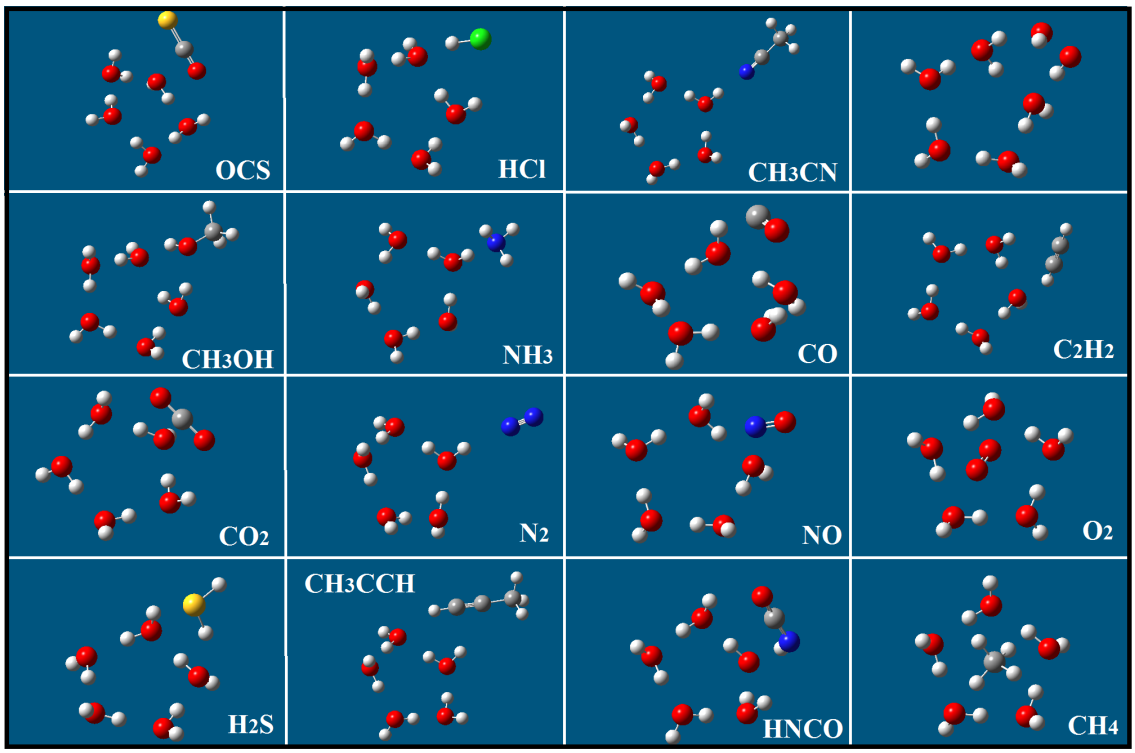

Figure 2.11: Optimized geometries with the c-pentamer configuration (Das et al., 2018).

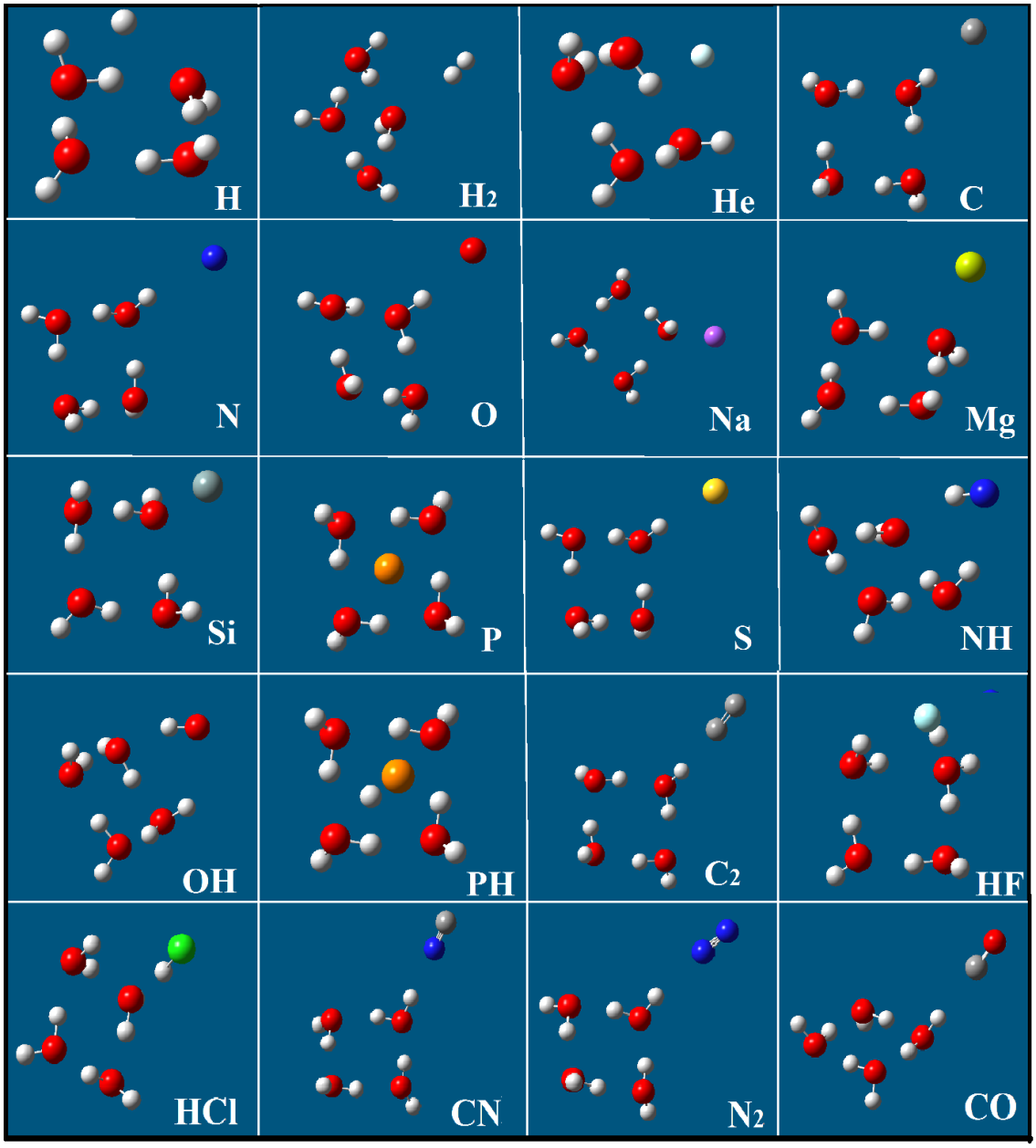

Figure 2.12: Optimized geometries with the c-tetramer configuration (Das et al., 2018).

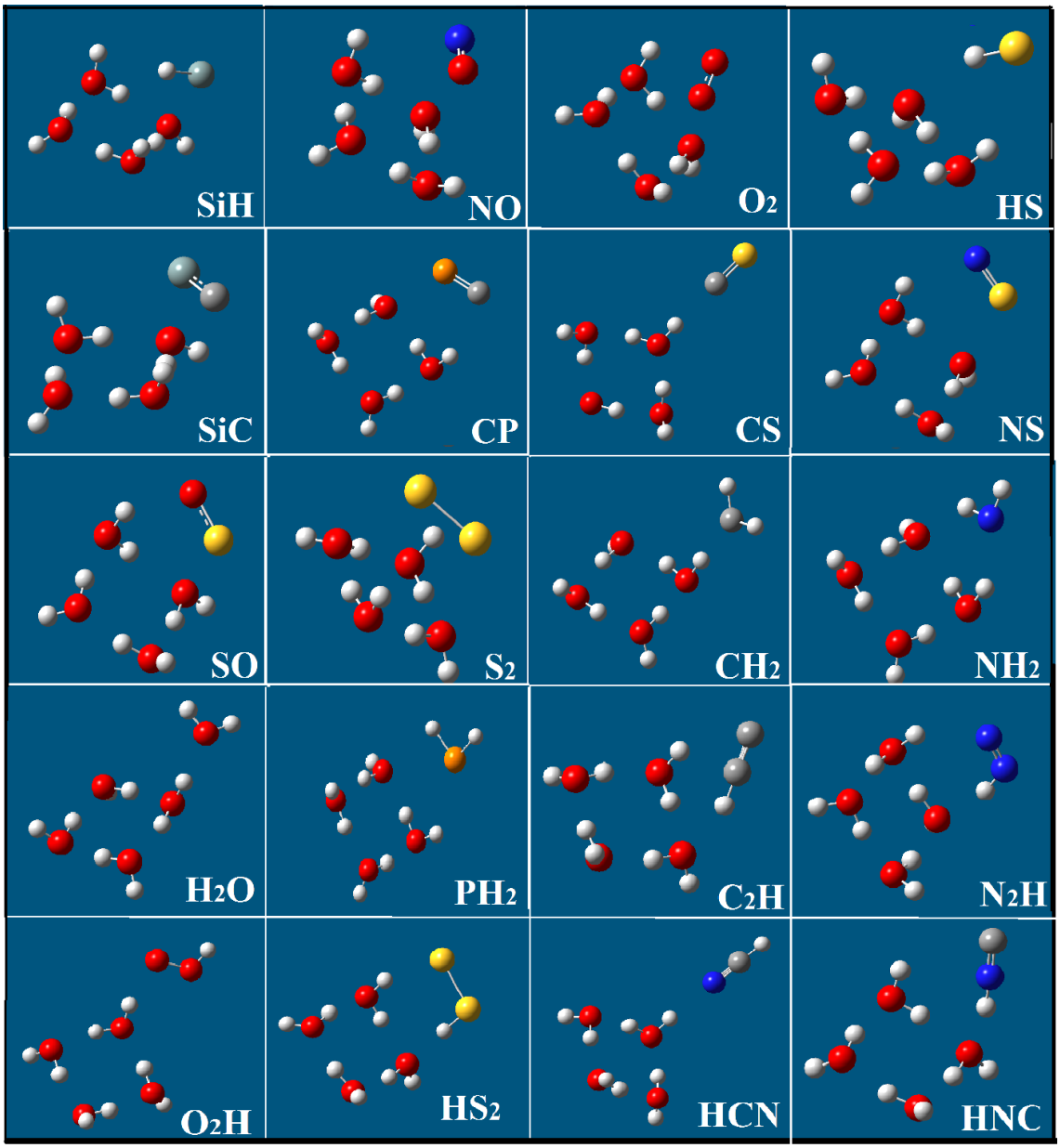

Figure 2.13: Optimized geometries with the c-tetramer configuration (Das et al., 2018).

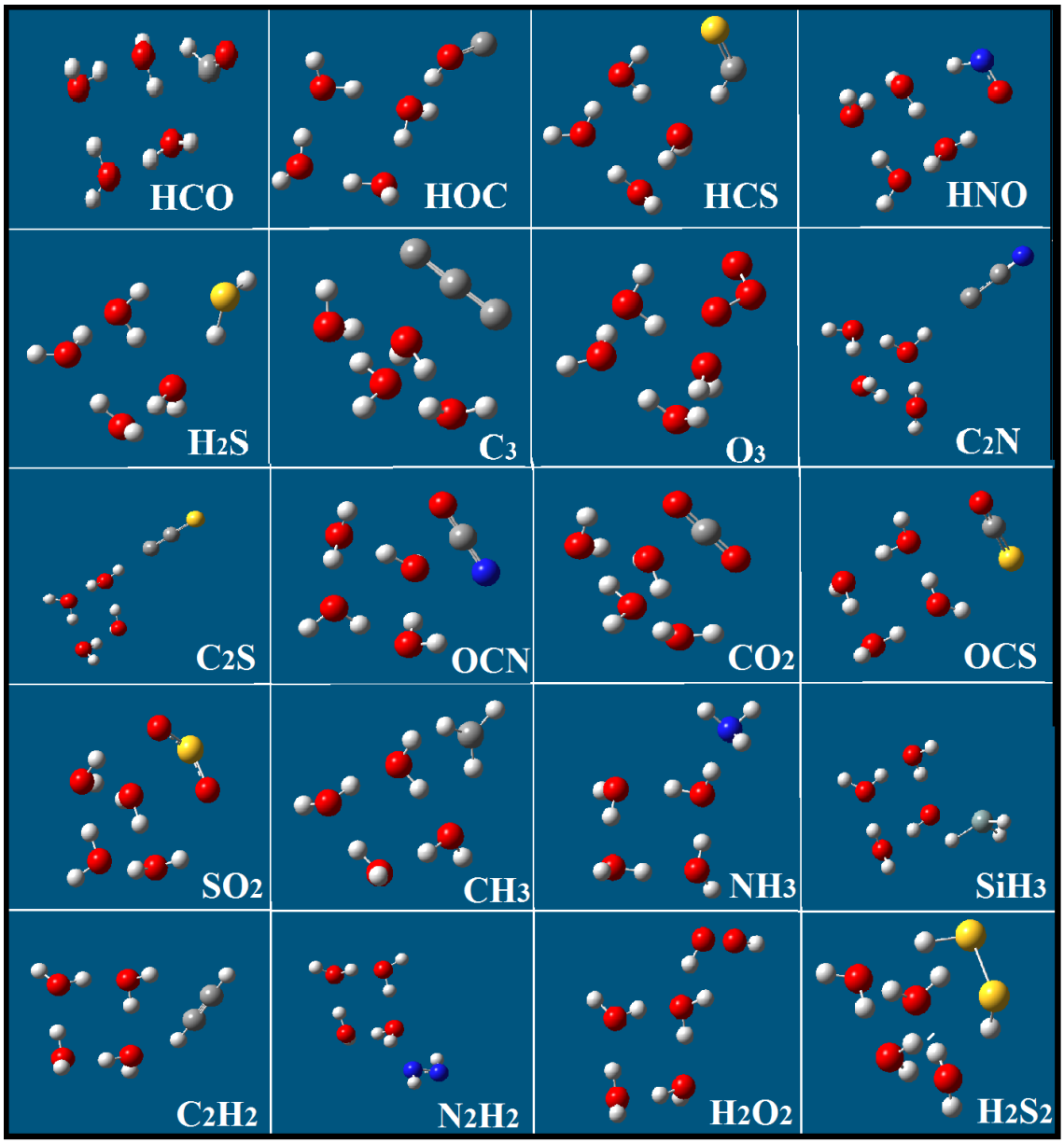

Figure 2.14: Optimized geometries with the c-tetramer configuration (Das et al., 2018).

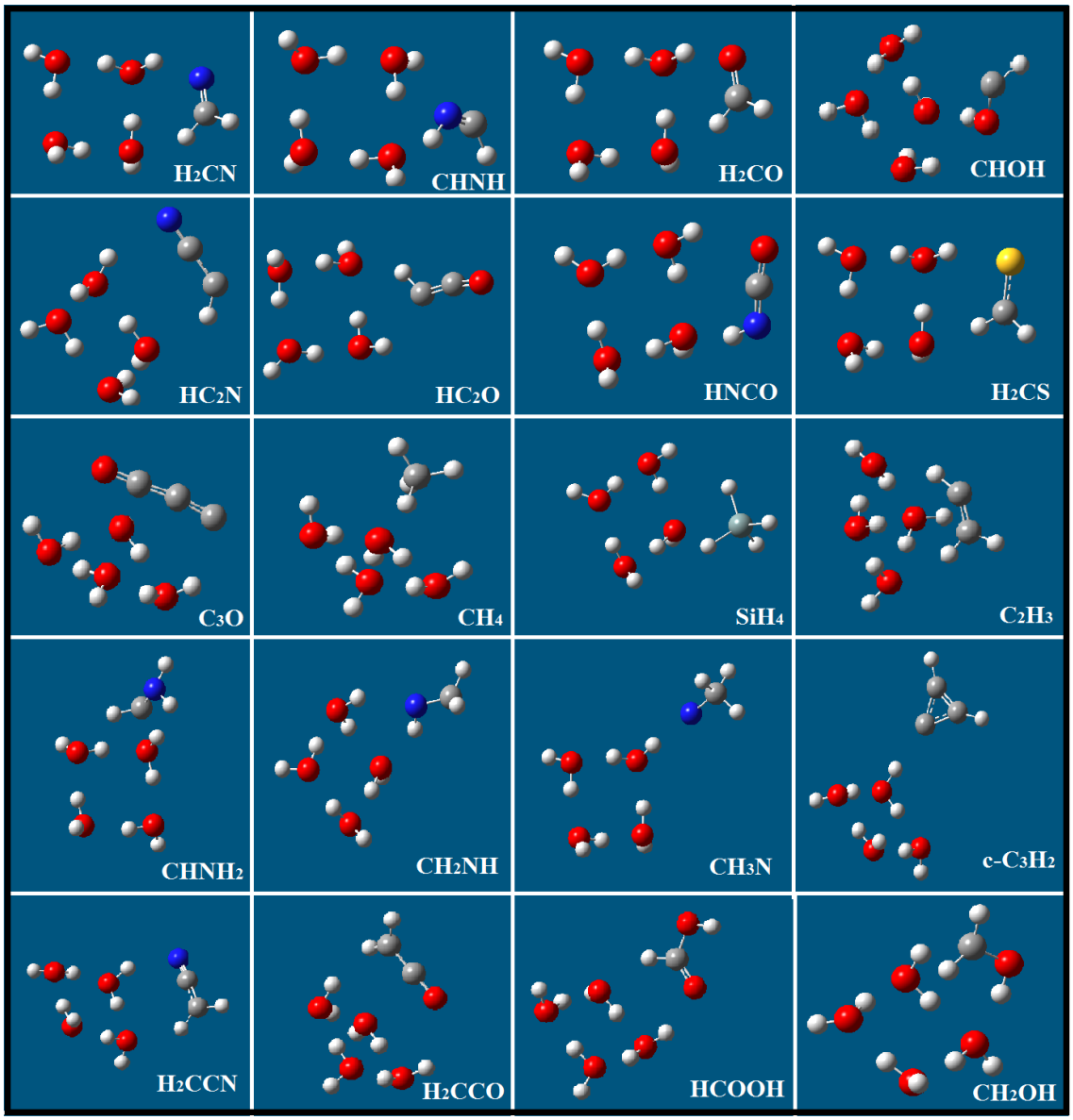

Figure 2.15: Optimized geometries with the c-tetramer configuration (Das et al., 2018).

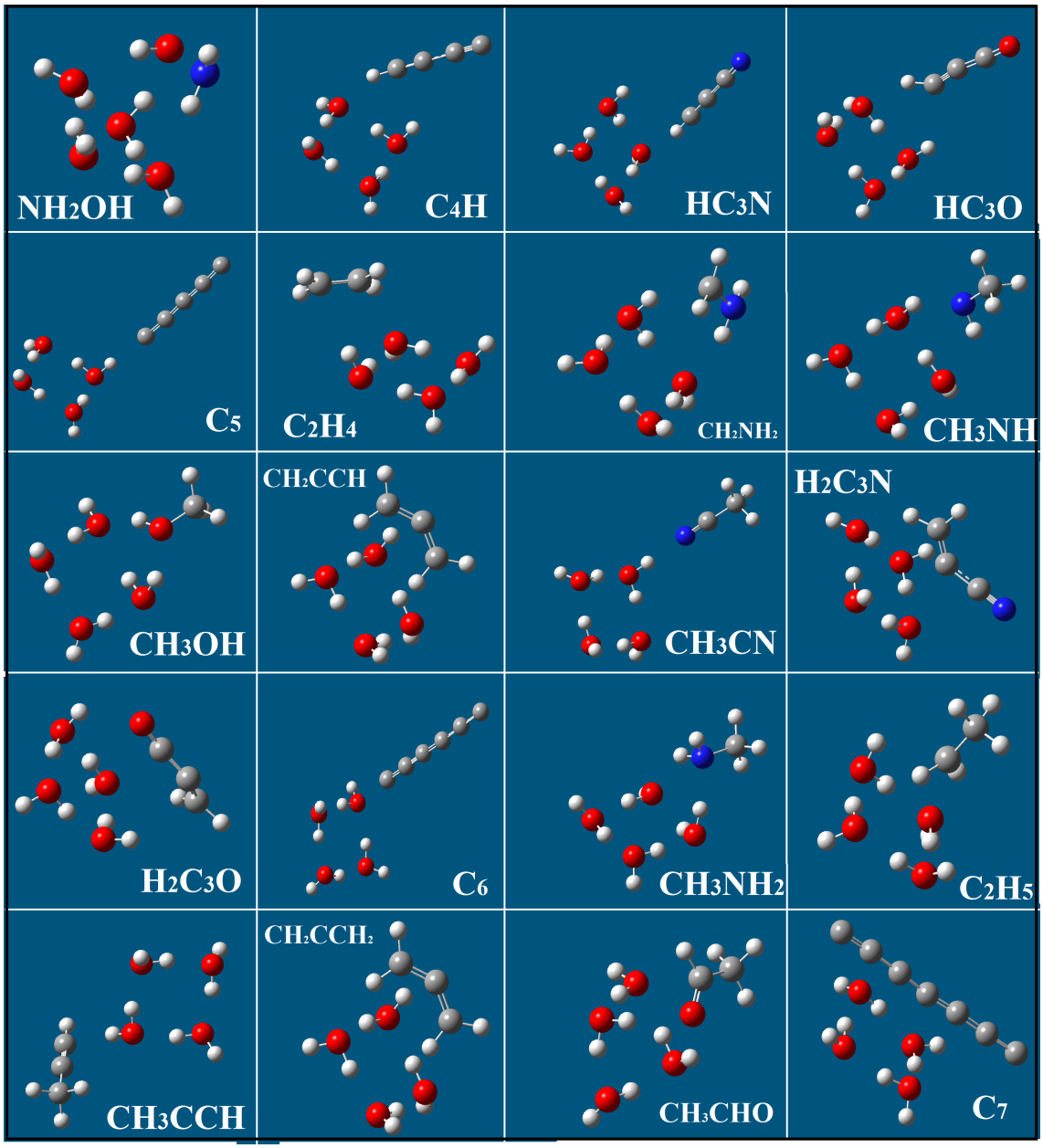

Figure 2.16: Optimized geometries with the c-tetramer configuration (Das et al., 2018).

Summary

A series of quantum chemical calculations are performed systematically to compute physisorption BE of various interstellar adsorbed species by considering the monomer, dimer, c-trimer, c-tetramer, c-pentamer, and c-hexamer (chair) configurations of water clusters as substrates. The benefit of using two or more water molecules is that one can consider the H-bonding donor and acceptor behavior of some species. We note that our computed BEs approach gradually to the experimental values when the size of the cluster is increased. More specifically, when the c-pentamer and c-hexamer (chair) configurations are considered, our computed BE values deviate from experimental values on average of $\sim \pm 15.8\%$ and $\sim \pm 16.7\%$, respectively. It is worth mentioning that the computed BE would be saturated to the experimental values upon considering a sufficient number of binding sites. For a broad set of interstellar or circumstellar species, we provide the BE values that deviate, on an average, $\sim \pm 18.8\%$ with the c-tetramer configuration. The comparisons show that we can safely use our procedure to compute the BEs of any such molecules with a reasonable accuracy.

2.1.3 Effect of binding energies on the encounter desorption

The encounter desorption mechanism was initially introduced by Hincelin et al. (2015) to eliminate the overestimation of the abundance of H_2 on the grain. The desorption process occurs during surface diffusion and is induced by the presence of repulsive inter-H_2 forces, effectively reducing the BE of H_2. They considered $gH_2 + gH_2 \rightarrow H_2 + gH_2$, where "g" denotes the surface species. They obtained a striking match between the microscopic MC and rate equation approach when this unique approach was implemented. The MC method is best suited for monitoring the chemical composition of a grain mantle. However, it is a time-consuming (Chakrabarti et al., 2006a,b; Das et al., 2008a, 2010; Das & Chakrabarti, 2011; Das et al., 2016; Cuppen & Herbst, 2007). Recently, Chang et al. (2021) considered a similar process and included desorption of H by a similar mechanism. They considered $gH + gH_2 \rightarrow H + gH_2$, which means that the surface H desorbs with a certain probability whenever the surface H meets one surface H_2. They reported a significant deviation between the formation of some key surface species with the inclusion of this treatment.

The encounter desorption effect is important mainly during the cold prestellar phase. Classifying the various evolutionary phases of star formation is one of the essential intricacies of astronomy and astrophysics. A thorough understanding of the star formation process is yet to be fully established. Briefly, stars are formed by a long condensation process (Pagani et al., 2013). In the beginning, warm diffuse material ($\sim$ 8000 K) converts into a cold neutral atomic gas ($\sim$ 100 K and $\sim 10-100$ cm^{-3}). Later, it transforms into a more dense region ($10^2 - 10^4$ cm^{-3} and $\sim 10 - 20$ K). In the absence of the other heating sources, a dense core ($> 10^4$ cm^{-3}) develops in some places, which further evolves into prestellar cores ($> 10^5$ cm^{-3}) (Bergin & Tafalla, 2007; Keto & Caselli, 2008). It further evolves to form a protostar. The gas-phase abundance in the colder and denser regions decreases due to their depletion. On the contrary, ice mantles develop. In the low-temperature regime, the hydrogenation reaction mainly controls the chemical complexity. The chemical composition of the bulk ice varies with the evolutionary stages of the star formation. Thus, it is expected that the ice composition would be very different in various places. However, from the IR observations, it appears that significant repositories of interstellar hydrogen, oxygen, carbon, and nitrogen are water (H_2O), methanol (CH_3OH), carbon monoxide (CO), carbon dioxide (CO_2), formaldehyde (H_2CO), methane (CH_4), and ammonia (NH_3) (Boogert et al., 2015).

BE values are mainly obtained from the TPD studies on various model substrates

like graphite, diamond-like carbon, amorphous or crystalline silica, silicates, water, and other ice surfaces (Collings et al., 2004; Acharyya et al., 2007; Ward et al., 2012; Noble et al., 2012; Dulieu et al., 2013). But, adequate information regarding BE of the species with H_2 substrate is lacking. Vidali et al. (1991) estimated the BE of H atom on H_2 substrate $\sim$ 45 K. Cuppen & Herbst (2007) estimated the BEs of several species (e.g., O, OH, H_2, O_2, H_2O, O_3, O_2H, and H_2O_2) on H_2 substrate by scaling its obtained BE on H_2O substrate with the ratio of BE between H on H_2 and on H_2O substrates. Thus, a vital impediment in examining the encounter desorption with other species is the shortage of information about the BE of these species with H_2 molecule. Here, we employ the quantum chemical calculations to determine the BE of 95 interstellar species considering H_2 substrate. Obtained BEs are used in our chemical model (Das et al., 2021).

Computational details and methodology

Quantum chemical calculations

We calculate the BE of a species on the grain surface following Equations 2.1 and 2.2 mentioned earlier in subsection 2.1.1. The optimized energy of all structures is obtained using the MP2/aug-cc-pVDZ level of theory (Dunning, 1989). For this computation, a monomer configuration of the H_2 molecule is considered an adsorbent. Each adsorbate noted in Table 2.11 is placed with a weak bond to sustain a van der Waals interaction during the optimization process. The optimized geometries are furnished in Table 2.11 and supplementary information[3] as well. It is to be noted that the interstellar species considered in this study are often larger than the H_2. The estimated BEs depend on the adsorption sites. This may be misleading. Thus, it is necessary to consider the average of the BEs obtained with various binding sites. Following the BE calculations carried out by Das et al. (2018) (see Tables 2.7 and 2.8), here, we do not consider the ZPVE and BSSE corrections for our BE calculations. All the obtained BE values considering H_2 substrate are presented in Table 2.11. Interestingly, except for phosphorous, the calculated BEs of most of the abundant atoms (H, C, N, O, and S) are < 100 K.

The BE values reported here are obtained by considering a free-standing H_2 interacting with a species. But in reality, this H_2 would be pre-adsorbed and can fill the surface. Thus, it would yield a different BE than the previous case. To check the

[3]The supplementary material of this article is available online at: https://www.frontiersin.org/articles/10.3389/fspas.2021.671622/full#supplementary-material

Table 2.11: Calculated BE (with MP2/aug-cc-pVDZ level of theory) of various species with H_2 monomer surface (Das et al., 2021).

Sl. No.	Species	Optimized Structures	Ground State	Binding Energy	
				in K	in kJ/mol
1	H	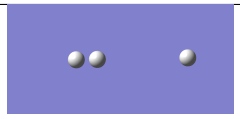	Doublet	23 (25^a), 45^c	0.189 (0.210^a)
2	H_2	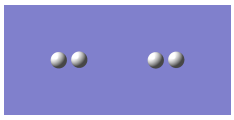	Singlet	67 (79^a), 23^c, 100^d	0.549 (0.659^a)
3	He	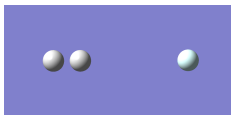	Singlet	27	0.226
4	C	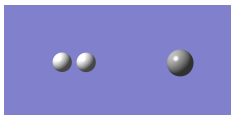	Triplet	50	0.417
5	N	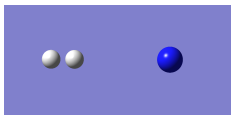	Quartet	83 (78^a)	0.690 (0.651^a)
6	O	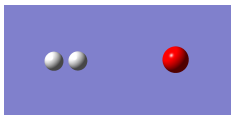	Triplet	46, 55^c	0.386
7	Na	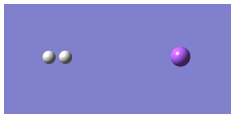	Doublet	22	0.184
8	Mg	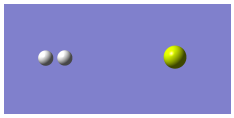	Singlet	62	0.514
9	Si	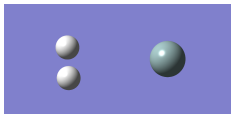	Triplet	642	5.343
10	P	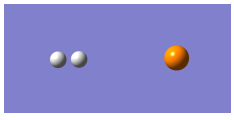	Quartet	107	0.887
11	S	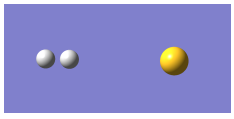	Triplet	88	0.732
12	NH	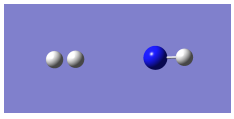	Triplet	286	2.381

Sl. No.	Species	Optimized Structures	Ground State	Binding Energy	
				in K	in kJ/mol
13	OH	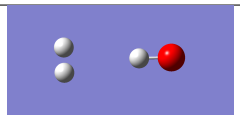	Doublet	380, 240[c]	3.158
		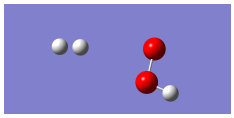		380[b]	3.158[b]
14	PH	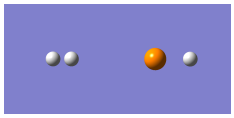	Triplet	151	1.258
15	C_2	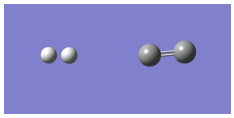	Triplet	204	1.696
16	HF	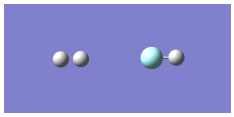	Singlet	287	2.386
17	HCl	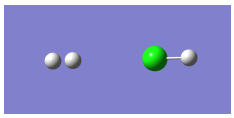	Singlet	162	1.350
18	CN	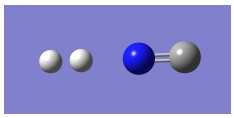	Doublet	4695	39.041
19	N_2	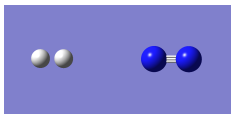	Singlet	198	1.649
20	CO	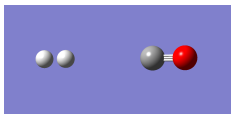	Singlet	215	1.788
21	SiH	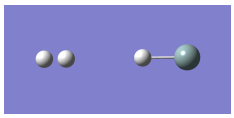	Doublet	188	1.562
22	NO	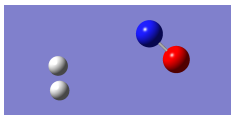	Doublet	159	1.321
23	O_2	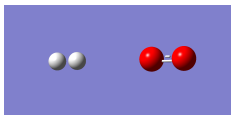	Triplet	159, 69[c]	1.321
24	HS	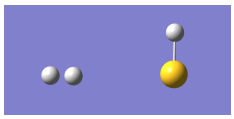	Doublet	222	1.848
25	SiC	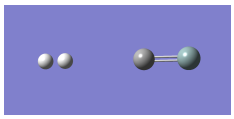	Triplet	212	1.759

Sl. No.	Species	Optimized Structures	Ground State	Binding Energy	
				in K	in kJ/mol
26	CP	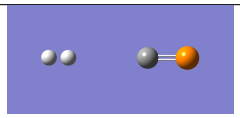	Doublet	165	1.373
27	CS	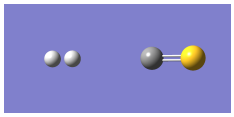	Singlet	337	2.804
28	NS	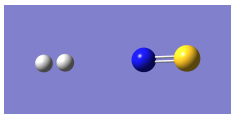	Doublet	353	2.938
		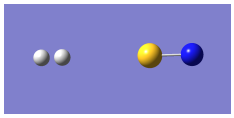		171[b]	1.423[b]
29	SO	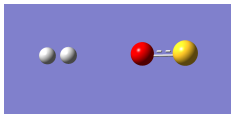	Triplet	337	2.801
30	S_2	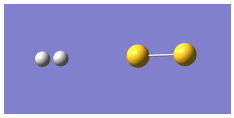	Triplet	187	1.552
31	CH_2	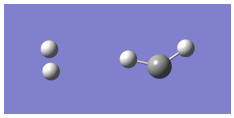	Triplet	165	1.376
32	NH_2	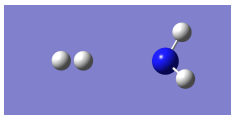	Doublet	347	2.888
33	H_2O	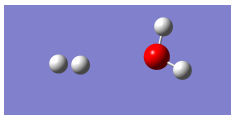	Singlet	360, 390[c]	2.993
		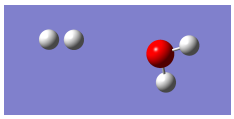		360[b]	2.993[b]
34	PH_2	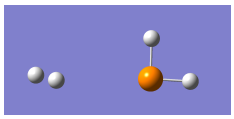	Doublet	178	1.483
35	C_2H	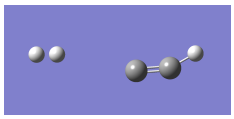	Doublet	242	2.014
36	N_2H	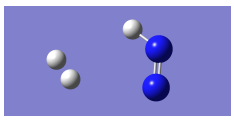	Doublet	432	3.589

Sl. No.	Species	Optimized Structures	Ground State	Binding Energy	
				in K	in kJ/mol
37	O_2H	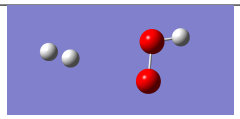	Doublet	339, 300[c]	2.819
		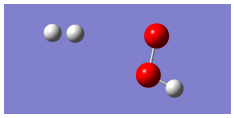		339[b]	2.819[b]
38	HS_2	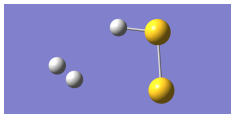	Doublet	660	5.487
39	HCN	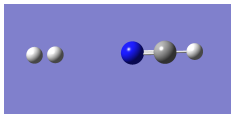	Singlet	395	3.282
40	HNC	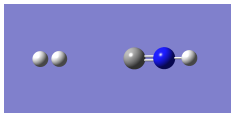	Singlet	338	2.814
41	HCO	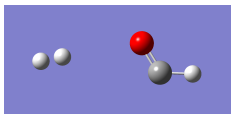	Doublet	243	2.019
42	HOC	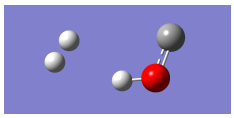	Doublet	769	6.396
43	HCS	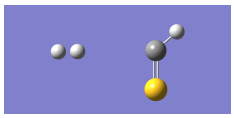	Doublet	334	2.780
		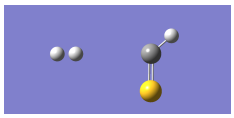		334[b]	2.780[b]
44	HNO	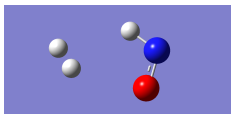	Singlet	574	4.773
45	H_2S	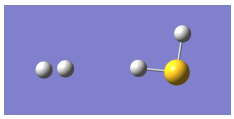	Singlet	99	0.824
46	C_3	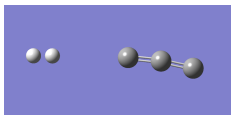	Singlet	295	2.455
47	O_3	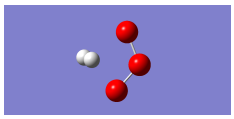	Singlet	381, 120[c]	3.169
		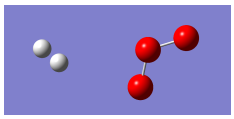			

Sl. No.	Species	Optimized Structures	Ground State	Binding Energy	
				in K	in kJ/mol
48	C_2N	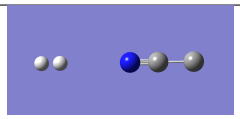	Doublet	339	2.817
49	C_2S	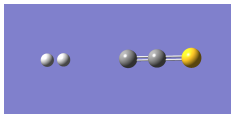	Triplet	355	2.951
50	OCN	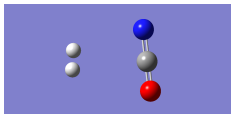	Doublet	422	3.510
51	CO_2	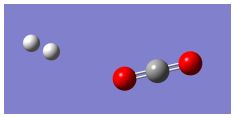	Singlet	241	2.003
52	OCS	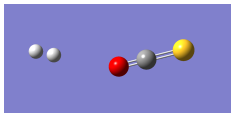	Singlet	257	2.137
53	SO_2	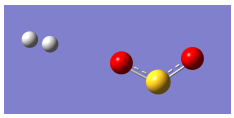	Singlet	324	2.691
54	CH_3	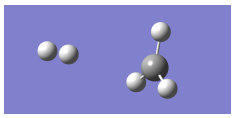	Doublet	198	1.644
55	NH_3	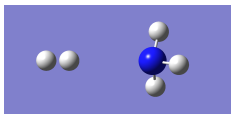	Singlet	455	3.781
56	SiH_3	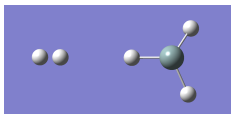	Doublet	159	1.321
57	C_2H_2	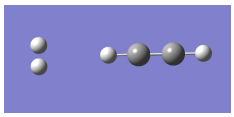	Singlet	337	2.799
58	N_2H_2	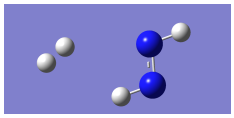	Singlet	608	5.059
59	H_2O_2	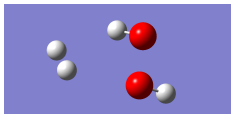	Singlet	628, 340[c]	5.222
60	H_2S_2	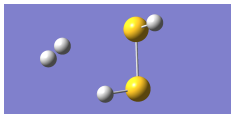	Singlet	573	4.763
61	H_2CN	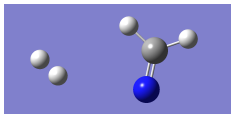	Doublet	376	3.130

Sl. No.	Species	Optimized Structures	Ground State	Binding Energy	
				in K	in kJ/mol
62	H_2CO	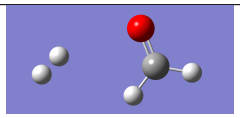	Singlet	507	4.219
63	HC_2N	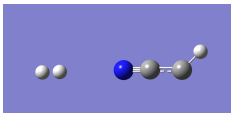	Triplet	413	3.434
64	HC_2O	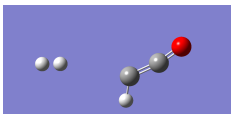	Doublet	326	2.712
65	HNCO	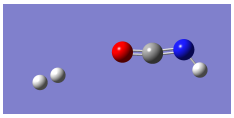	Singlet	289	2.405
66	H_2CS	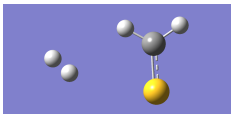	Singlet	545	4.532
67	C_3O	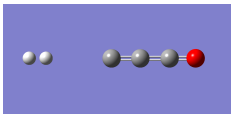	Singlet	414	3.442
68	CH_4	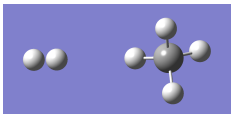	Singlet	138	1.150
69	SiH_4	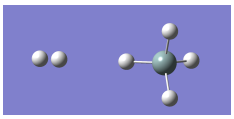	Singlet	165	1.370
70	C_2H_3	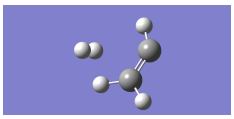	Doublet	265	2.200
71	$CHNH_2$	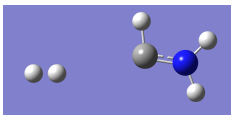	Singlet	858	7.133
		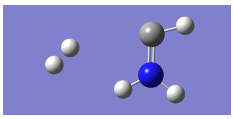		463[b]	3.846[b]
72	CH_2NH	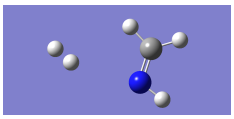	Singlet	602	5.007
73	c-C_3H_2	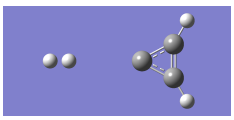	Singlet	472	3.925

Sl. No.	Species	Optimized Structures	Ground State	Binding Energy	
				in K	in kJ/mol
74	CH_2CN	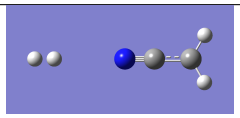	Doublet	440	3.662
75	CH_2CO	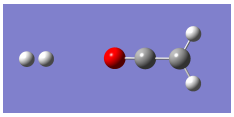	Singlet	276	2.297
76	HCOOH	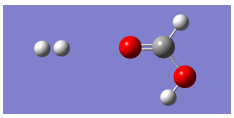	Singlet	369	3.066
77	CH_2OH	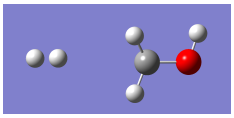	Doublet	272	2.263
78	NH_2OH	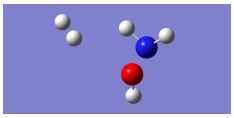	Singlet	2770	23.028
79	HC_3N	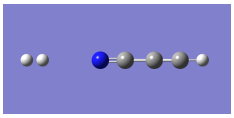	Singlet	427	3.555
80	C_5	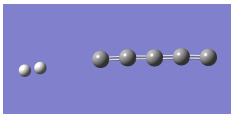	Singlet	379	3.156
81	C_2H_4	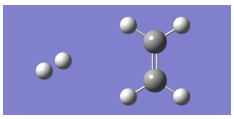	Singlet	250	2.079
82	CH_2NH_2	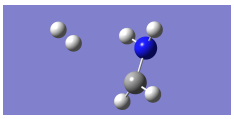	Doublet	428	3.560
83	CH_3OH	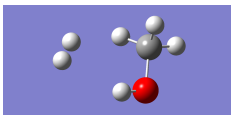	Singlet	414	3.445
		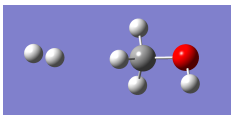		258^b	2.145^b
84	CH_2CCH	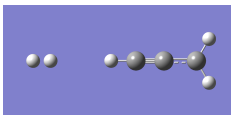	Doublet	105	0.872
85	CH_3CN	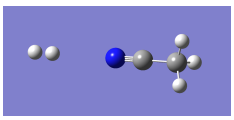	Singlet	453	3.765

Sl. No.	Species	Optimized Structures	Ground State	Binding Energy	
				in K	in kJ/mol
86	CH_3NH_2	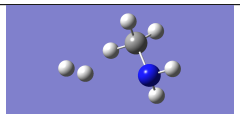	Singlet	610	5.072
87	C_2H_5	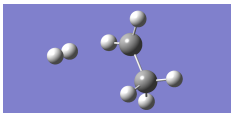	Doublet	327	2.720
88	CH_3CCH	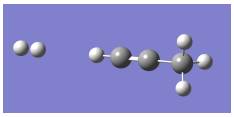	Singlet	125	1.040
89	CH_2CCH_2	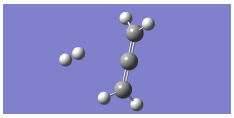	Singlet	489	4.070
90	CH_3CHO	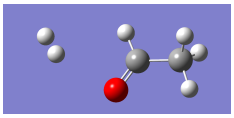	Singlet	573	4.765
91	PN	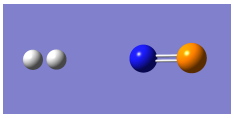	Singlet	399	3.324
92	PO	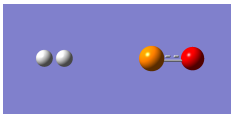	Doublet	509	4.230
93	SiN	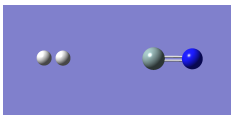	Doublet	154	1.281
94	F	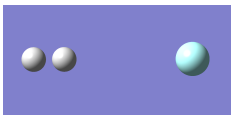	Doublet	24	0.202
95	C_2H_5OH	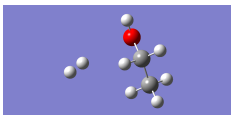	Singlet	590	4.906

[a] The BE values for the adsorbates H, H_2, and N with the adsorbent as H_2 considering IEFPCM model are noted in parentheses.
[b] Alternative BE values are for different binding sites.
[c] Cuppen & Herbst (2007).
[d] Sandford & Allamandola (1993).

Table 2.12: Initial elemental abundances considered in this study (Das et al., 2021).

Species	Abundances
H_2	5.00×10^{-1}
He	9.00×10^{-2}
N	7.60×10^{-5}
O	2.56×10^{-4}
C^+	1.20×10^{-4}
S^+	8.00×10^{-8}
Si^+	8.00×10^{-9}
Fe^+	3.00×10^{-9}
Na^+	2.00×10^{-9}
Mg^+	7.00×10^{-9}
Cl^+	2.00×10^{-10}
HD	1.60×10^{-5}

influence of condensed H_2O, we carry out our computation by considering the species embedded in the continuum solvation field. The local impacts and the Integral Equation Formalism variant of the Polarizable Continuum Model (IEFPCM) are examined (Cancès et al., 1997; Tomasi et al., 2005) with water as a solvent. The obtained values for H, H_2, N with the IEFPCM model are noted in Table 2.11 (in parentheses). However, the two calculations significantly differ. For example, the BE of H, H_2, and N are obtained $\sim$ 23 K, 67 K, and 83 K, respectively, with the free-standing H_2, whereas with the IEFPCM model, we obtain $\sim$ 25 K, 79 K, and 78 K, respectively. So, the free-standing H_2 underestimates the BE of H and H_2 by 2 K and 12 K, respectively. In contrast, it overestimates BE of N by $\sim$ 5 K. We also provide the BEs from literature (Cuppen & Herbst, 2007; Sandford & Allamandola, 1993) in Table 2.11 (if available) for the comparison.

The BEs of the 16 stable interstellar species considering the various configurations of water molecules are provided in Table 2.6 (Das et al., 2018). Table 2.11 shows their BEs with the H_2 monomer. The corresponding ground state spin multiplicities are also noted. We notice that the computed BEs with H_2 monomer substrate are much smaller than the BE with the water configurations.

Astrochemical model

We include the encounter desorption phenomenon in our CMMC code (Das et al., 2021) to study its effect. The surface chemistry network of our model is mainly adopted from Ruaud et al. (2015); Das et al. (2015b); Gorai et al. (2020b). The gas-phase network of the CMMC code is mainly adopted from the UMIST database (McElroy et al., 2013). Additionally, we also include the deuterated gas-phase chem-

ical network from the UMIST. A cosmic-ray rate of 1.3×10^{-17} s^{-1} is considered in all our models. In addition, cosmic ray-induced desorption and non-thermal desorption rate with a fiducial parameter of 0.01 are considered. We adopt a photodesorption rate of 1×10^{-4} per incident UV photon (Ruaud et al., 2015) for all the surface species. Except for H and H_2, a sticking coefficient of 1.0 is considered for all the neutral species. The sticking coefficients of H and H_2 are considered by following the relation proposed by Chaabouni et al. (2012). Following Garrod & Pauly (2011), here, we implement the competition between diffusion, desorption, and reaction. For the diffusion energy (E_b), we consider R × desorption energy (E_d). Here, the scaling factor, R, can vary between 0.35 and 0.8 (Garrod et al., 2007). The BE of the surface species is mainly considered from Wakelam et al. (2017), and a few from Das et al. (2018). Table 2.12 refers to the adopted initial abundances concerning the total hydrogen nuclei in all forms. Except for the value of HD in Table 2.12, elemental abundances are taken from Semenov et al. (2010). We consider the initial abundances of HD from Roberts & Millar (2000).

The effect of encounter desorption was first introduced by Hincelin et al. (2015). The rate of encounter desorption of H_2 on the surface of H_2 is defined as:

$$En_{H_2} = \frac{1}{2}\ k_{H_2,H_2}\ gH_2\ gH_2\ P(H_2,H_2), \tag{2.5}$$

where gH_2 is the surface concentration of H_2 molecules in cm^{-3}, $P(H_2,H_2)$ represents the probability of desorption over the diffusion, and k_{H_2,H_2} is the diffusion rate coefficient over the H_2O substrate. k_{H_2,H_2} is defined as follows (Hasegawa et al., 1992):

$$k_{H_2,H_2} = \kappa(R_{diffH_2} + R_{diffH_2})/n_d \ \ cm^3 s^{-1}. \tag{2.6}$$

In the above equation, n_d is the dust-grain number density, κ is the probability of the occurrence of the reaction (unity for the exothermic reaction without activation energy), and R_{diff} is the diffusion of the species. $P(H_2,H_2)$ in Equation 2.5 is defined as:

$$P(H_2,H_2) = \frac{Desorption\ rate\ of\ H_2\ on\ H_2\ substrate}{Desorption\ rate\ of\ H_2\ on\ H_2\ substrate\ +\ Diffusion\ of\ H_2\ on\ H_2\ substrate}. \tag{2.7}$$

There would be various desorption factors (thermal, reactive, cosmic-ray etc.). The thermal desorption is defined as: $\nu\ exp(-E_d(H_2,H_2)/T)$ s^{-1}, where T is the temperature of the dust. Similarly, there would be various diffusion processes, but the thermal diffusion would be the dominating. It is defined as: $\nu\ exp(-E_b(H_2,H_2)/T)/S$ (s^{-1}) = *thermal hopping rate / number of sites* (s^{-1}). Recently, Chang et al. (2021) extended this work considering the encounter desorption of H atom. They

defined the encounter desorption of H_2, (in Equation 2.7) by the hopping rate of H_2 on H_2 substrate instead of the diffusion rate of H_2 on H_2 substrate. Following the prescription defined in Chang et al. (2021), the encounter desorption of species X is defined as:

$$En_{X,H_2} = \frac{h_{X,H_2}}{S} gX\ gH_2\ P(X,H_2)\ P_X, \tag{2.8}$$

where h_{X,H_2} is the hopping rate over H_2O surface, $P(X,H_2)$ is the desorption probability of gX while encountering gH_2, and P_X denotes the probability of gX for migrating at the location of gH_2 over the H_2O substrate. $P(X,H_2)$ and P_X are defined as,

$$P(X,H_2) = \frac{Desorption\ rate\ of\ X\ on\ H_2\ substrate}{Desorption\ rate\ of\ X\ on\ H_2\ substrate\ +\ Hopping\ rate\ of\ X\ on\ H_2\ substrate}, \tag{2.9}$$

$$P_X = \frac{Hopping\ rate\ of\ X\ on\ H_2O\ substrate}{Hopping\ rate\ of\ X\ on\ H_2O\ substrate\ +\ Hopping\ rate\ of\ H_2\ on\ H_2O\ substrate}. \tag{2.10}$$

Results and discussions

Encounter desorption of H_2

We benchmark our model with Hincelin et al. (2015). In Figure 2.17, we compare our results with those obtained in Hincelin et al. (2015). For this comparison, following Hincelin et al. (2015), we use $T = 10$ K, $E_d(H_2,H_2O) = 440$ K, $E_d(H,H_2O) = 450$ K, $E_d(H_2,H_2) = 23$ K, and $R = 0.5$. Solid curves in Figure 2.17 represent our (Das et al., 2021) obtained cases, and the rest are extracted from Hincelin et al. (2015) using the online tool of Rohatgi (2020). Our results considering and avoiding encounter desorption show an excellent match with Hincelin et al. (2015). Presently in the KIDA, more updated BE values are listed (Wakelam et al., 2017). It suggests that $E_d(H,H_2O) = 650$ K. The results obtained from our quantum chemical calculations shown in Table 2.11 represent the estimated BE values with the H_2 substrate. We use these updated BE values, and the effects of their changes are discussed.

gH_2

Figure 2.18 shows the time evolution of gH_2 by considering $n_H = 10^7$ cm^{-3}, $T = 10$ K and $R = 0.35 - 0.80$. Interestingly the abundance of gH_2 seems to be constant with the changes of R, whereas it strongly depends on R in encounter desorption. This is because lower value of R means a quicker hopping, whereas a higher value represents a delayed hopping rate. With the increase in R, gH_2 abundance

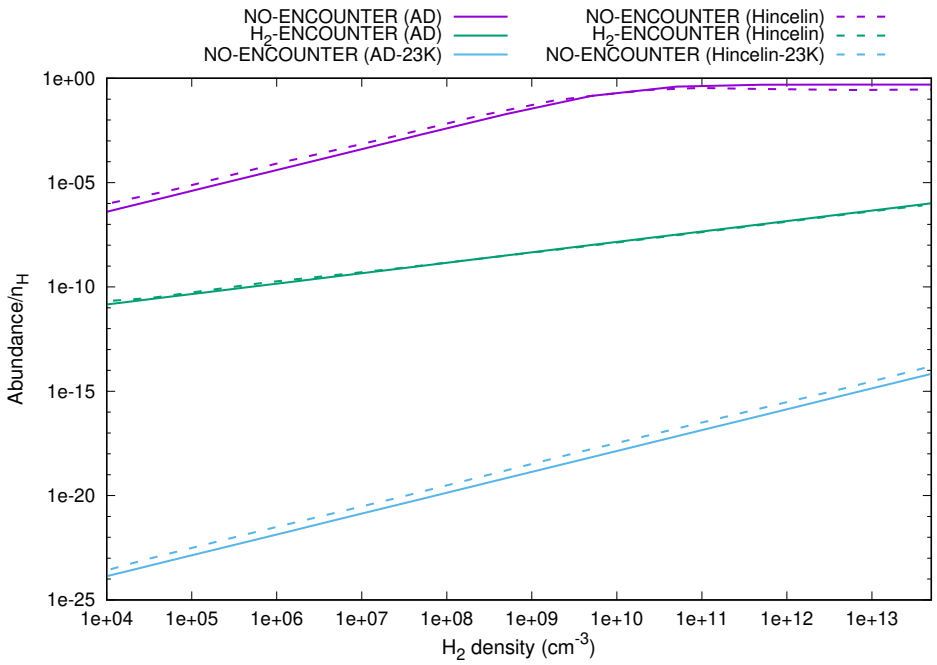

Figure 2.17: A comparison between the cases obtained in Hincelin et al. (2015) and Das et al. (2021). Figure 2 of Hincelin et al. (2015) is extracted using the online tool of Rohatgi (2020). Three distinct cases are shown: (A) no encounter desorption is considered with $E_d(H_2, H_2O) = 440$ K, (B) no encounter desorption is considered with $E_d(H_2, H_2) = 23$ K, and (C) encounter desorption of H_2 was considered with $E_d(H_2, H_2O) = 440$ K and $E_d(H_2, H_2) = 23$ K. An excellent match between the our calculated (solid curves) steady-state abundance of H_2 on grain surface and that obtained in Hincelin et al. (2015) (dashed curves) is noticed.

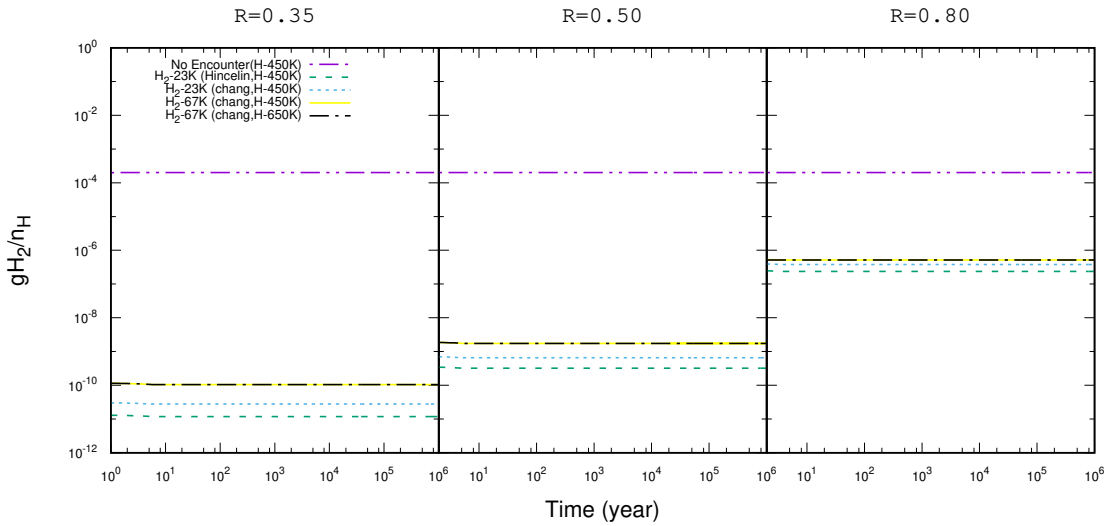

Figure 2.18: Time evolution of the abundances of gH_2 with $n_H = 10^7$ cm^{-3} and $T =$ 10 K are shown for $R = 0.35$, 0.5, and 0.8 (Das et al., 2021). The dash-dotted purple curve shows time evolution of gH_2 abundance without encounter desorption [with $E_d(H, H_2O) = 450$ K]. gH_2 abundance remains roughly constant with the changes in R. However when encounter desorption is introduced, gH_2 abundance increases with the R. The time evolution of the gH_2 abundance with $E_d(H_2, H_2) = 23$ K and $E_d(H, H_20) = 450$ K is shown with the green dashed line when the method of Hincelin et al. (2015) is used and blue dotted line when the method of Chang et al. (2021) is used. gH_2 abundances obtained with our estimated BE value [i.e., $E_d(H_2, H_2) = 67$ K] are shown with a solid yellow line. For this case, we have used $E_d(H, H_2O) = 450$ K and the method used in Chang et al. (2021). The black dash-dotted line shows the time evolution of gH_2 abundance with $E_d(H, H_2O) = 650$ K and using the method of Chang et al. (2021). A significant difference is obtained when we use different energy barriers and different methods (Hincelin et al., 2015; Chang et al., 2021). Obtained values of gH_2 are further noted in Table 2.13 for better understanding.

Table 2.13: The obtained abundance of gH_2, gH, gH_2O and gCH_3OH for the effect of encounter desorption of H_2 under various situation with $R = 0.35$, $n_H = 10^7$ cm^{-3}, and $T = 10$ K (Das et al., 2021).

Case No.	Case specification	Abundance at 10^6 years with $n_H = 10^7$ cm^{-3}			
		gH_2	gH	gH_2O (% increase)	gCH_3OH (% increase)
	$E_d(H, H_2O) = 450$ K				
1	No encounter desorption	2.0011749×10^{-4}	2.311976×10^{-24}	8.8375039×10^{-5} (0.00)	8.8416179×10^{-6} (0.00)
2	$E_d(H_2, H_2) = 23$ K (Hincelin et al., 2015)	1.183836×10^{-11}	$3.2799079 \times 10^{-24}$	8.927643×10^{-5} (1.02)	6.3629209×10^{-6} (−28.03)
3	$E_d(H_2, H_2) = 23$ K (Chang et al., 2021)	$2.7660509 \times 10^{-11}$	3.253898×10^{-24}	8.9327989×10^{-5} (1.08)	6.4358829×10^{-6} (−27.21)
4	$E_d(H_2, H_2) = 67$ K (Chang et al., 2021)	1.051303×10^{-10}	2.25004×10^{-24}	1.02707×10^{-4} (16.22)	6.119676×10^{-6} (−30.79)
5	$E_d(H_2, H_2) = 79$ K (Chang et al., 2021)	$1.5474109 \times 10^{-10}$	$2.2527589 \times 10^{-24}$	1.028505×10^{-4} (16.38)	6.2066129×10^{-6} (−29.8)
	$E_d(H, H_2O) = 650$ K				
6	No encounter desorption	2.00117×10^{-4}	1.467684×10^{-21}	9.434889×10^{-5} (0.00)	5.799469×10^{-6} (0.00)
7	$E_d(H_2, H_2) = 67$ K (Chang et al., 2021)	1.051293×10^{-10}	$2.0551489 \times 10^{-21}$	9.361905×10^{-5} (−0.77)	4.559358×10^{-6} (−29.80)

raises for the encounter desorption case. However, it means that as we raise the value of R, the encounter desorption effect depreciates. The left panel of Figure 2.19 exposes that with the increase in R, a steady decrease in the ratio between gH_2 abundance with no encounter desorption case (NE) and with the encounter desorption case (EN) is noticed. The probability of the encounter desorption is found to be inversely proportional to the rate of diffusion (Equation 2.7) or hopping (Equation 2.9). Since the increase in R induces faster diffusion and hopping, it lowers the encounter desorption probability of H_2 as expected. Figure 2.20 shows the time evolution of gH_2 with the NE and EN for $R = 0.35$, $T = 10$ K and $n_H = 10^4 - 10^7$ cm^{-3}. In both cases, the abundances of gH_2 increase with the density. The middle panel of Figure 2.19 shows that the gH_2 abundance ratio between NE and EN with density. It shows that the effect of encounter desorption is more pronounced for the higher density. Figure 2.21 shows that the gH_2 abundances when we use $n_H = 10^7$, $R = 0.35$, and $T = 5 - 20$ K. In the right panel of Figure 2.19, we show the gH_2 abundance ratio obtained between NE and EN with the temperature changes. The figures show that the effect of encounter desorption is maximum toward the lower temperature ($\sim$ 10 K). It ceases around 20 K. This is similar to the H_2 formation efficiency discussed in Chakrabarti et al. (2006a,b) for olivine grain. As the temperature decrease, mobility of H atoms decreases. Thus, the formation rate decreases. Conversely, with the increase in temperature, the hopping rate increases, increasing the formation efficiency, but simultaneously, the residence time of H atoms decreases, affecting the H_2 formation efficiency. As a result, the H_2 formation efficiency is maximum at around $\sim$ 10 K, and the effect of the encounter desorption is pronounced

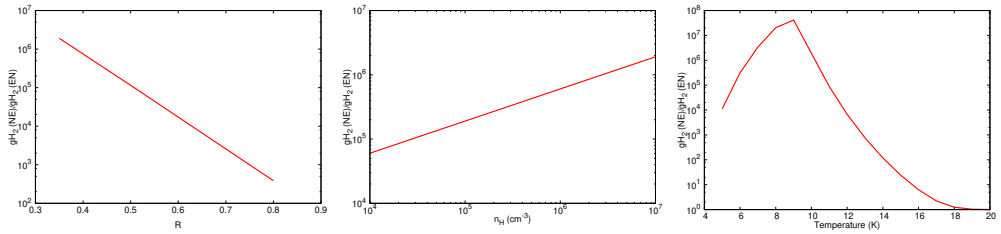

Figure 2.19: The ratio between the final abundances of gH_2 obtained with the no encounter (NE) desorption and encounter desorption (EN) is shown (Das et al., 2021). From left to right, it shows the variation of this ratio with R, n_H, and temperature, respectively.

at the peak hydrogen formation efficiency.

For a better understanding, the obtained abundances with $R = 0.35$, $T = 10$ K, and $n_H = 10^7$ cm^{-3} are noted in Table 2.13 at the end of the total simulation time ($\sim 10^6$ years). Chang et al. (2021) considered the competition between hopping rate and desorption rate of H_2 (Equation 2.9), whereas Hincelin et al. (2015) considered the battle between the diffusion and desorption rate of H_2 (Equation 2.7). This difference in consideration resulting $\sim$ two times higher abundance of gH_2 with the consideration of Chang et al. (2021) compared to Hincelin et al. (2015) (see cases 2 and 3 of Table 2.13 and Figure 2.18). Our quantum chemical calculation yields $E_d(H_2, H_2) = 67$ K, which is higher than it was used in the earlier literature value of 23 K (Cuppen & Herbst, 2007; Hincelin et al., 2015; Chang et al., 2021). The computed BE is further increased to 79 K when we consider the IEFPCM model. Table 2.13 shows that an increase in the BE ($E_d(H_2, H_2) = 67$ K, and 79 K, for cases 4 and 5 of Table 2.13) results in sequentially higher surface coverage of gH_2 than it was with $E_d(H_2, H_2) = 23$ K (case 3 of Table 2.13). In case 5 of Table 2.13, we note the abundance of gH_2 in the absence of the encounter desorption effect, but a higher BE of H atom is used ($E_d(H, H_2O) = 650$ K). Case 6 of Table 2.13 also considers this BE of H atom along with $E_d(H_2, H_2) = 67$ K, and the method of Chang et al. (2021) is used. A comparison between the abundance of gH_2 obtained with cases 4 and 6 (BEs of gH are different) shows a marginal decrease in the abundance of gH_2 when a higher BE of gH is used.

gH

The abundance of gH is noted in Table 2.13. Its abundance is marginally decreased in Chang et al. (2021) compared to Hincelin et al. (2015). The use of higher

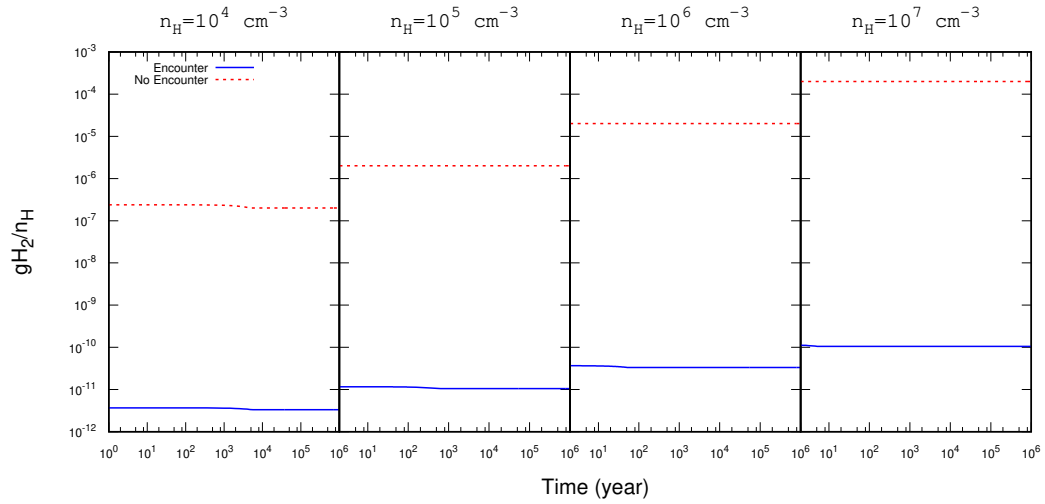

Figure 2.20: Time evolution of gH_2 with $R = 0.35$ and various n_H (10^4, 10^5, 10^6, and 10^7 cm^{-3}) are shown (Das et al., 2021). The effect of encounter desorption increases with the increase in density.

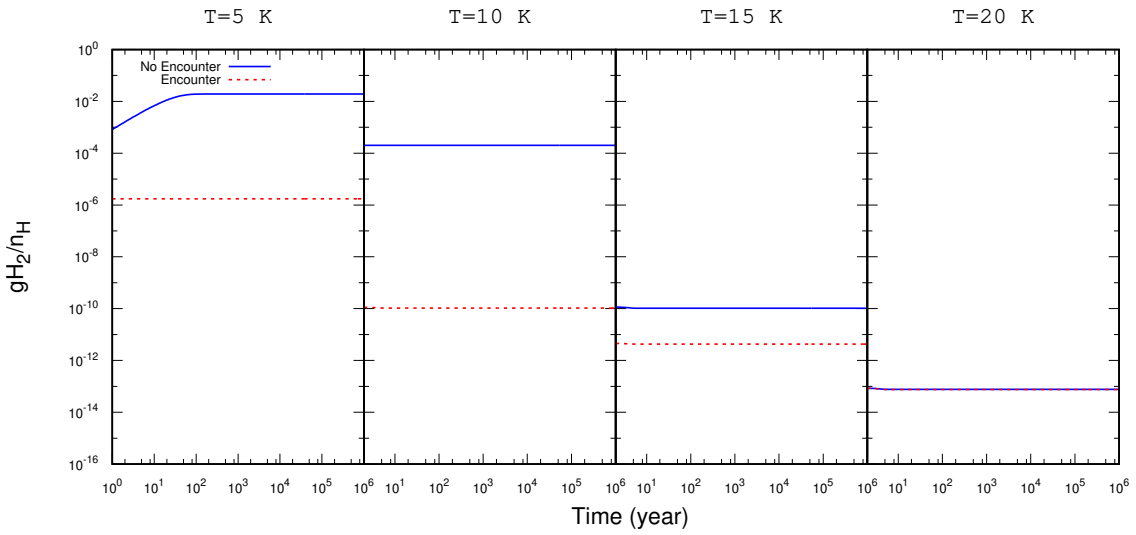

Figure 2.21: Time evolution of gH_2 with $R = 0.35$, $n_H = 10^7$ cm^{-3} and various temperatures (5, 10, 15, and 20 K) are shown (Das et al., 2021). The effect of encounter desorption decreases with the increase in temperature.

$E_d(H_2, H_2)$ ($\sim$ 67 K and 79 K) lowers the abundance of gH (compared to case 2). However, $E_d(H) = 650$ K can increase the gH abundance by a couple of orders of magnitude (see case 7 of Table 2.13).

gH_2O, gCH_3OH

The encounter desorption effect on the other principal surface species (gH_2O and gCH_3OH) is also shown in Table 2.13. The increase (percentage) in their abundances from the case where no encounter desorption is considered [for $E_d(H, H_2O) =$ 450 K and 650 K, respectively] are noted in the bracketed term. Table 2.13 shows that the consideration of encounter desorption of H_2 can significantly change (decrease by $\sim 27 - 30\%$) the methanol abundance (cases 3 and 7) from cases 1 and 6 (i.e., no encounter desorption). However, the percentage changes in the surface abundance of water are minimal ($\sim \pm 1\%$) for the addition of the encounter desorption of H_2. These (increase or decrease) are highly dependent on the BE of H, temperature, density, and the value of R ($\sim$ 0.35 noted in Table 2.13). The $E_d(H_2, H_2)$ from 23 K to 67 K can alter the methanol and water abundance on the grain. For example, Table 2.13 shows that there is a significant increase ($\sim$ 15%) in the abundance of gH_2O when higher BE ($E_d(H_2, H_2) = 67$ K) is used (case 3 and case 4). However, this higher BE can marginally under-produce the methanol on the grain. In brief, from Table 2.13, the encounter desorption may influence the chemical composition of the grain surfaces. These changes are highly dependent on the adopted BE with the water and H_2 ice and adopted physical parameters (n_H, R, T).

Encounter desorption of other species

The notion of encounter desorption (Hincelin et al., 2015) primarily arose to eliminate the enhanced surface coverage of H_2 in the relatively denser and colder medium. Because H_2 has lower BE with the water surface ($\sim$ 440 K), it could move fast on the surface and occupy a position on the top of another H_2 molecule. Comparatively, the chances of this occurrence enhance in the colder and denser region. Furthermore, since the H_2 molecule on H_2 has negligible BE (23 K used in Cuppen & Herbst, 2007; Hincelin et al., 2015), it could easily desorb to the gas phase. All the other surface species can, of course, meet with H_2. Still, implementing this encounter desorption is essential when the species can occupy a position on the top of the H_2 molecule. For example, a carbon (C) atom has a BE of 10000 K (Wakelam et al., 2017). H_2 could quickly meet one C atom on the grain surface,

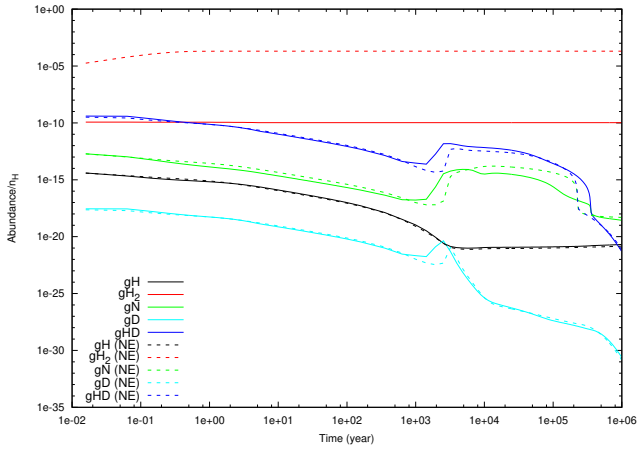

Figure 2.22: Time evolution of the abundances of H, H_2, D, HD, and N obtained from our simulation (Das et al., 2021) is shown. Solid curves depict the cases by considering the encounter desorption [with $E_d(H_2, H_2) = 67$ K] of H_2 and no encounter desorption (dashed curves) with $E_d(H, H_2O) = 650$ K, $n_H = 10^7$ cm^{-3}, $T = 10$ K, and $R = 0.35$.

but due to the lower mobility of the C atom at a low temperature, H_2 will be on the top of the C atom every time. Since the whole $C - H_2$ system is linked to the water substrate, this will not meet the encounter desorption probability. Among the other key elements considered in this study, gH, gN, and gF have the BE of 650 K (Wakelam et al., 2017), 720 K (Wakelam et al., 2017), and 800 K (listed in the original gas-grain code of Eric Herbst group in 2006 of OSU), respectively, with the water ice. Thus, it yields a reasonable timescale for hopping at a low grain temperature ($\sim$ 10 K). However, since the initial elemental abundance of F is very small, we can ignore its contribution. The time scale of hopping is heavily dependent on the considered R. For example, with $R = 0.35$, at 10 K, the hopping timescale for gH and gN is 1.12×10^4 years [with $E_d(H, H_2O) = 650$ K] and 4.61×10^{-3} years [with $E_d(N, H_2O) = 720$ K], respectively. It changes to 1.9 and 226 years for H and N atoms, respectively, with $R = 0.5$. Since the usual lifetime of a dark cloud is $\sim 10^6$ years, the encounter desorption criterion is often satisfied. Among the di-atomic species, H_2 only has a faster-swapping rate (having BE 440 K, which corresponds to a hopping time scale of $\sim 1.24 \times 10^{-7}$ and 9×10^{-5} years, respectively, with $R = 0.35$ and $R = 0.5$). Considering the faster hopping rate and their abundances on the grain surface, we consider the encounter desorption of these species. We consider $gX + gH_2 \rightarrow X + gH_2$, where X refers to gas-phase H_2, H, and N.

In Figure 2.22, we show the time evolution of the abundances of gH, gH_2, gN,

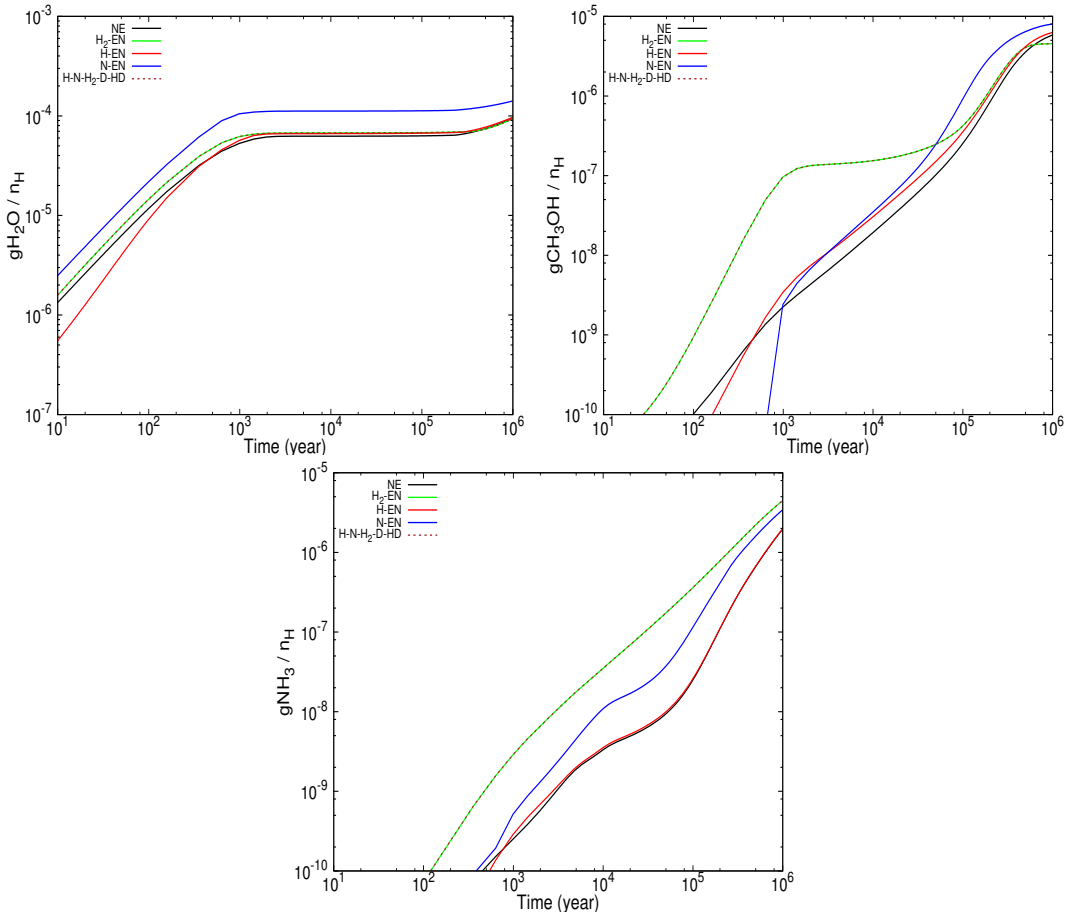

Figure 2.23: Time evolution of the abundances of ice-phase water (first panel), methanol (second panel) and ammonia (third panel) is shown for $n_H = 10^7$ cm^{-3}, $T = 10$ K, and $R = 0.35$ (Das et al., 2021). A considerabale difference between the consideration of encounter desorption (solid green line for H_2, solid red line for H, and solid blue line for N) and without encounter desorption (black line) is shown. The encounter desorption of H, N, H_2, D, and HD are considered (brown dotted line) and depict that it marginally deviates from the encounter desorption of H_2.

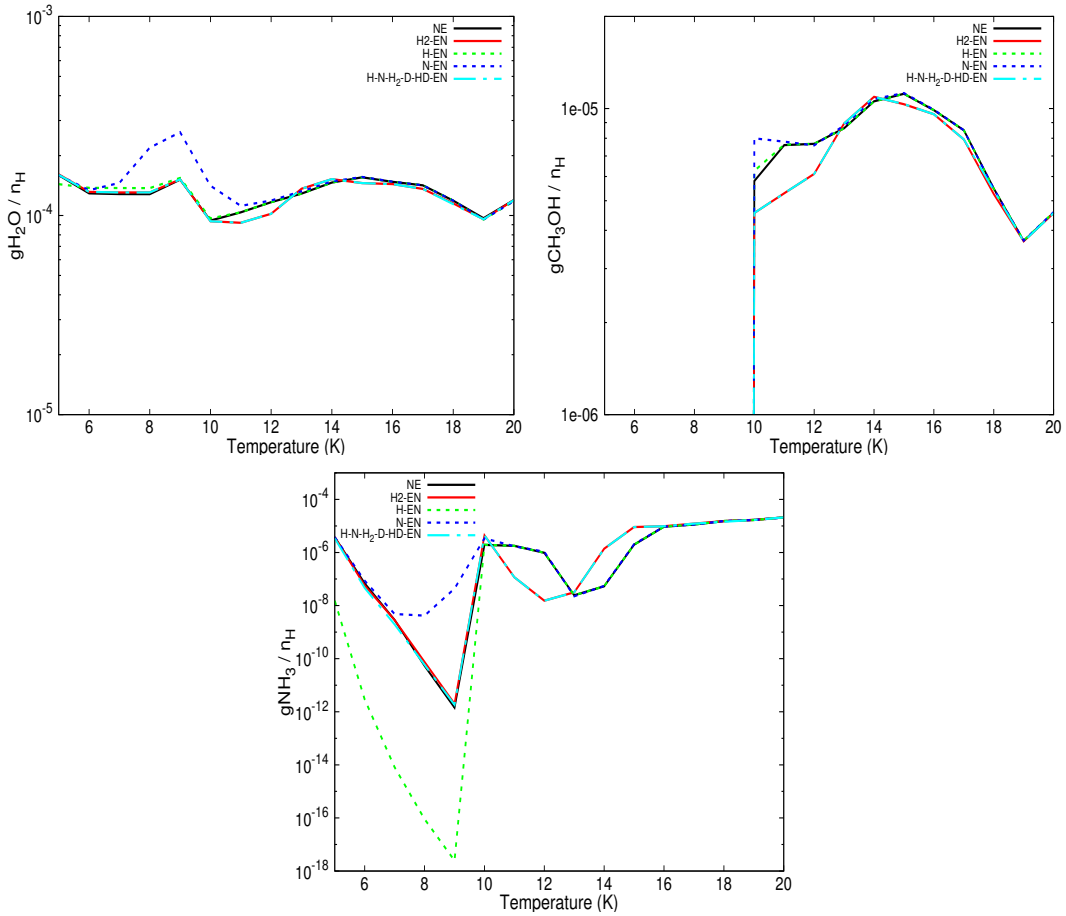

Figure 2.24: Temperature variation of the abundances of ice-phase water (first panel), methanol (second panel), and ammonia (third panel) is shown for $n_H = 10^7$ cm^{-3} and $R = 0.35$ (Das et al., 2021). A significant variation between the consideration of encounter desorption and without encounter desorption (black line) is shown. The encounter desorption of H, N, H_2, D, and HD are collectively considered, and as like Figure 2.23, it marginally varies from the encounter desorption of H_2.

gD, and gHD with $n_H = 10^7$ cm^{-3}, $T = 10$ K, and $R = 0.35$. The encounter desorption of H_2 and without the encounter desorption effect are shown to show the differences. Figure 2.22 depicts that the abundances of gN, gH, and gH_2, have a reasonably high surface coverage. Since these species have a considerable hopping rate at a low temperature, desorption of these species needs to be considered. Here, we include the encounter desorption of these species sequentially to check their influence on some key surface species (gH_2O, gCH_3OH, and gNH_3). To check the effect of the other species, we gradually include the encounter desorption of H_2, H, and N. Figure 2.23 shows the time evolution of the encounter desorption of gH_2O, gCH_3OH, and gNH_3. We have already noted the encounter desorption of gH_2 in Section 2.1.3. Figure 2.23 shows that when we include the encounter desorption of the H and N atoms, the time evolution of the abundances shows considerable changes in the abundance. It depicts that the encounter desorption of N atom can substantially increase the abundances of gH_2O, gCH_3OH, and gNH_3 for the physical condition considered here ($n_H = 10^7$ cm^{-3}, $T = 10$ K, and $R = 0.35$). We further consider the encounter desorption of D and HD by considering the same BE as it obtained for H and H_2 with the H_2 substrate. The cumulative effect (considering the encounter desorption of H, H_2, N, D, and HD together) is shown with the dotted curve. We notice that the abundance profile with the cumulative effect shows a notable difference from the absence of the encounter desorption. But the cumulative effect minutely differs from the encounter desorption effect of H_2. Figure 2.24 shows the temperature variation of the final abundances of water, methanol, and ammonia to total hydrogen nuclei in all forms. It shows that the ice-phase abundances of methanol, water, and ammonia can strongly deviate from the no encounter desorption case. As in Figure 2.23, we also see that the cumulative effect of the encounter desorption deviates from the encounter desorption of H_2. Around 20 K, a great match between the cumulative encounter desorption case (dash-dotted cyan curve), H_2 encounter desorption case (solid red line), and no encounter desorption case (solid black line) is obtained. The right panel of Figure 2.19 shows that for a temperature beyond 10 K, the effect of the encounter desorption of H_2 starts to decline. Around 20 K, it roughly vanishes. Since the cumulative effect reflects the nature of H_2 encounter desorption, it also matches the no encounter desorption case at ~ 20 K.

Summary

We provide realistic BEs of several interstellar species considering H_2 monomer as a substrate. Furthermore, our quantum chemical calculation finds a lower BE value considering H_2 monomer as a substrate than it obtained earlier with the monomer (on average $\sim$ 7 times), tetramer (on average $\sim$ 9 times), and hexamer (on average $\sim$ 11 times) water cluster as a substrate (Das et al., 2018). $E_d(H_2, H_2) = 23$ K (Cuppen & Herbst, 2007; Hincelin et al., 2015; Chang et al., 2021) and $E_d(H, H_2) = 45$ K (Cuppen & Herbst, 2007; Chang et al., 2021) are used earlier in the literature. Our quantum chemical computations find an opposite trend with $E_d(H_2, H_2) = 67$ K and $E_d(H, H_2) = 23$ K, i.e., the BE of the H_2 molecule always remains higher than that of the H atom, supporting our earlier work (Sil et al., 2017). Supported with these reported BE values, we further implement our CMMC code to check the encounter desorption effect of H_2, H, and N on the interstellar ices. The consideration of these updated BEs shows a significant deviation in the abundances of the grain surface species. It suggests that the inclusion of the encounter desorption of the H, H_2, and N may influence the abundances of the principal surface constituents such as water, methanol, and ammonia. The cumulative effect almost resembles a similar abundance with that obtained considering the encounter desorption of H_2 only. The encounter desorption effect of H_2 diminishes for a bit higher temperature ($\sim$ 20 K). Then, the encounter desorption of the cumulative cases matches precisely with the no encounter desorption case.

2.2 Absorption features of interstellar ices in the presence of impurities

Spectroscopic studies play a crucial role in identifying and analyzing interstellar ices and their structure. IR spectroscopy is used for identifying interstellar species, particularly in condensed phases. However, it requires that vibrations are IR-active. The criterion is fulfilled when the dipole moment changes during vibration. The IR feature of a water cluster is one of the primary tools to analyze the features of the aggregation processes in a water matrix (Ohno et al., 2005; Bouwman et al., 2007; Öberg et al., 2007). The four vibrational modes of water (libration, bending, bulk stretching, and free OH stretching) are crucial to extract relevant information about the water cluster itself in various astrophysical environments (Gerakines et al., 1995; Ohno et al., 2005; Bouwman et al., 2007; Öberg et al., 2007). Many molecules are identified within the interstellar ices either as pure, mixed, or layered structures. Since water is the principal component of the interstellar ice matrix, the latter is considered composed of water molecules, with the other species being impurities or pollutants. Absorption band features of water ice can significantly change with the presence of different types of impurities (e.g., CO, CO_2, CH_3OH, H_2CO, etc.). Many studies have been devoted to vibrational spectra of dilute aqueous solutions corresponding to the polar impurities. However, the intention is usually focused on the vibrational properties of the solute and not on the solvent (Choi & Cho, 2011; Cappelli et al., 2011; Błasiak et al., 2013). In a broader context, some IR studies are available for the whole solubility range of some species (Max & Chapados, 2003, 2004).

2.2.1 Methodology

There are three established structures of water ice (with a local density of 0.94 g cm^{-3}) formed by vapor deposition at low pressure. Two of them are crystalline (hexagonal and cubic), and one is a low-density amorphous form (Jenniskens & Blake, 1994). High-density amorphous water ice (with a local density 1.07 g cm^{-3}) also exists and can be formed by the vapor deposition at low temperatures (Jenniskens & Blake, 1994). Pradzynski et al. (2012) experimentally analyzed the number of water molecules needed to generate the smallest ice crystal. According to that study, the appearance of crystallization is first observed for 275 ± 25 and 475 ± 25 water molecules, these aggregates showing the well-known band of crystalline ice around 3200 cm^{-1} (in the OH-stretching region). Jenniskens & Blake (1994) found

experimentally that the onset of crystallization occurs at 148 K. Since we aim to validate our calculations for the low-temperature and low-pressure regime, we focus on the amorphous ices showing a peak in the IR spectrum at around 3400 cm^{-1}. However, since it is not clear how many water molecules are necessary to mimic the amorphous nature of water ice, we consider pure water clusters of different sizes and study their absorption spectra. For this purpose, we optimize water clusters of increasing size at different levels of theory. The water clusters considered are $2H_2O$ (dimer), $4H_2O$ (tetramer), $6H_2O$ (hexamer), $8H_2O$ (octamer), and $20H_2O$, with their structures being optimized with three different methods (B3LYP, B2PLYP, and QM/MM) as explained in the next computational details Section. The specific choice of these cluster models is based on experimental outcomes. Experimentally, it has been demonstrated that the water dimer has a nearly linear hydrogen-bonded structure (Odutola & Dyke, 1980). The water clusters with $4H_2O$ molecules are cyclic in the gas phase (Viant et al., 1997). For the $6H_2O$ cluster, different structures are available: a three-dimensional cage in the gas phase (Liu et al., 1997) and cyclic (chair) in the liquid helium droplet (Nauta & Miller, 2000). For $8H_2O$, an octamer cube is found in gaseous states (Ohno et al., 2005). Finally, the $20H_2O$ cluster is considered to check the direct effect of the environment, with more details being provided in the computational detail Section.

The harmonic frequencies are computed by using the optimized structures of the series of clusters above. The band strengths of the four fundamental modes are calculated by assuming the integration bounds, as shown in Table 2.14. Similar integration bounds (except for free OH stretching mode) were considered in Bouwman et al. (2007) and Öberg et al. (2007). Similar absorption profiles of four fundamental modes of pure water are obtained from our calculations. Their intensity, band positions, and strengths vary for the different cluster sizes and levels of theory used. It is thus essential to find the best compromise between accuracy and computational cost. It means understanding which is the smallest cluster and the cheapest level of theory to provide a reliable description of water ice. To this aim, we compare the band positions and the corresponding band strengths of the four vibrational fundamental modes of water obtained with different cluster sizes and different methodologies to experimental work.

While the outcome of this comparison will be discussed later in the text, here, we anticipate that the $4H_2O$ cluster in the c-tetramer configuration will be chosen as a water ice unit. To investigate the effect of impurities, we consider several impurity molecules that are added to obtain the desired ratio, as shown in Table 2.15. For example, to get a 2 : 1 ratio of water: impurity(x), we consider four water molecules

Table 2.14: Integration bounds for the four fundamental modes of vibration (Gorai et al., 2020a).

Species	Assignment	Integration bounds	
		Lower (cm^{-1})	Upper (cm^{-1})
H_2O	$\nu_{libration}$	500	1100
	$\nu_{bending}$	1100	1900
	$\nu_{bulk-stretching}$	3000	3600
	$\nu_{freeOH-stretching}$	3600	4000

Table 2.15: Ice mixture composition details (Gorai et al., 2020a).

H_2O:X	Total no. of molecules	No. of water molecules	No. of pollutant molecules
1:0.25	5	4 (80.0%)	1 (20.0%)
1:0.50	6	4 (66.7%)	2 (33.3%)
1:0.75	7	4 (57.1%)	3 (42.9%)
1:1.00	8	4 (50.0%)	4 (50.0%)

Note: Contributions in percentage are provided in the parentheses.

hooked up with two "x" molecules. However, for some systems, we needed to consider more water molecules to have more realistic features of the water cluster. Since it is known that the water ice clusters containing six H_2O molecules are the form of all-natural snow and ice on Earth (Abascal et al., 2005), we also present a case with six H_2O molecules together as a unit. The cyclic hexamer (chair) configuration of the water cluster containing six H_2O is the most stable (Ohno et al., 2005) and considered in our calculations.

In Figure 2.25a, we present the optimized water clusters for the c-tetramer configuration. The same structure was considered by Ohno et al. (2005) and others (Sil et al., 2017; Das et al., 2018; Nguyen et al., 2019). Since four H atoms are available for interacting with the impurities through hydrogen bonds, in our calculations, we can reach a $1:1$ ratio between the water and the impurity (i.e., we can reach up to 50% concentration of the impurity in the ice mixture).

To understand the effect of impurities on the band strengths of the four fundamental bands considered, we calculate the area under the curve for each band for different mixtures of pure water and pollutants. The band strength is derived using the following relation (introduced by Bouwman et al., 2007; Öberg et al., 2007)

$$A^{band}_{H_2O:x=1:y} = \int_{band} I_{H_2O:x=1:y} \times \frac{A^{H_2O}_{band}}{\int_{band} I_{H_2O}}, \tag{2.11}$$

where $A^{band}_{H_2O:x}$ is the calculated band strength of the vibrational water mode in the $1:y$ mixture, $I_{H_2O:x=1:y}$ is its integrated area, $A^{H_2O}_{band}$ is the band strength of the water

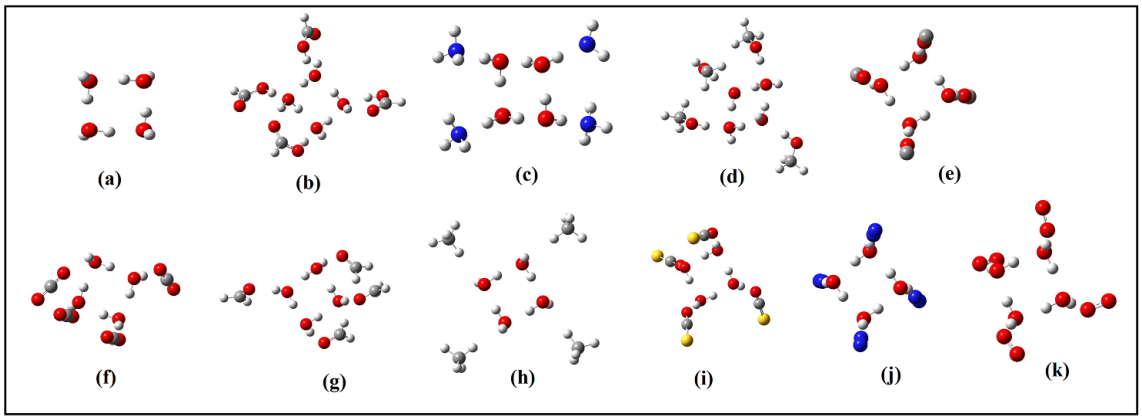

Figure 2.25: Optimized structures for (a) pure water and for the 4 : 4 concentration ratio: (b) $H_2O - HCOOH$, (c) $H_2O - NH_3$, (d) $H_2O - CH_3OH$, (e) $H_2O - CO$, (f) $H_2O - CO_2$, (g) $H_2O - H_2CO$, (h) $H_2O - CH_4$, (i) $H_2O - OCS$, (j) $H_2O - N_2$, and (k) $H_2O - O_2$ clusters (Gorai et al., 2020a).

modes available from the literature, and $\int_{band} I_{H_2O}$ is the integrated area under the vibrational mode for pure water ice. The experimental absorption band strengths of the three modes of pure water ice are taken from Gerakines et al. (1995), who carried out measurements with amorphous water at 14 K. The adopted values are 2×10^{-16}, 1.2×10^{-17}, and 3.1×10^{-17} cm molecule^{-1}, for the bulk stretching (3280 cm^{-1}), bending (1660 cm^{-1}), and libration mode (760 cm^{-1}), respectively. Our ab initio calculations refer to the temperature at 0 K. To calculate the band strengths, we consider the strongest feature of that band. Since for the free OH stretching mode, no experimental values exist, we consider the result $A^{H_2O}_{freeOH} = 2.09 \times 10^{-17}$ and 2.52×10^{-17} cm molecule^{-1} for the c-tetramer and hexamer water clusters, respectively.

Computational details

As already mentioned, quantum chemical calculations are performed to evaluate the changes of the absorption features of four different fundamental modes, namely, (i) libration, (ii) bending, (iii) bulk stretching, and (iv) free OH stretching of water in the presence of impurities (CO, CO_2, CH_3OH, H_2CO, HCOOH, CH_4, NH_3, OCS, N_2, and O_2). High-level quantum chemical calculations (such as CCSD(T) method and hybrid force field method) are proven to be the best suited for reproducing the experimental data (Puzzarini et al., 2014a; Barone et al., 2015a). However, due to the dimensions of our targeted species, these levels of theory are hardly applicable.

As already anticipated, different DFT functionals are tested. Most computations are carried out using the B3LYP hybrid functional (Becke, 1988; Lee et al., 1988) in conjunction with the 6-31G(d) basis set (GAUSSIAN 09 package; Frisch et al., 2013). Some test computations are also performed by using the B2PLYP double-hybrid functional (Grimme, 2006) in conjunction with the m-aug-cc-pVTZ basis set (Papajak et al., 2009) in which the d functions are removed on hydrogen atoms (m-aug-cc-pVTZ-dH). In this case, harmonic force fields are obtained employing analytic first and second derivatives (Biczysko et al., 2010) available in the GAUSSIAN 16 suite of programs (Frisch et al., 2016). The reliability and effectiveness of this computational model in the evaluation of vibrational frequencies and intensities are documented in several studies (see, for example, Barone et al., 2015). We also perform the anharmonic calculations (with the B3LYP/6-31G(d) level) for the $H_2O - CO$ and $H_2O - NH_3$ systems to check the impact of anharmonicity on the band strength profiles of the four water fundamental modes.

The spectral features of the astrophysical ices can alter active (direct) and passive (bulk) ways. Following a consolidated practice (Sandford et al., 2020), to include the passive contribution of the bulk ice on the spectral properties of ice mixtures, we embed our explicit cluster in a continuum solvation field to represent local effects on the ice mixture. To this end, we resort to the IEF variant of the PCM (Tomasi et al., 2005). The solute cavity has been built by using a set of interlocking spheres centered on the atoms with the following radii (in Å): 1.443 for hydrogen, 1.925 for carbon, 1.830 for nitrogen, and 1.750 for oxygen, each of them scaled by a factor of 1.1, which is the default value in GAUSSIAN. For the ice dielectric constant, bulk water ($\varepsilon = 78.355$) is used, although any dielectric constant larger than ~ 30 would lead to very similar results.

In addition, we also perform QM/MM geometry optimizations of a pure water cluster containing $4H_2O$ molecules in which all but one molecule at the square vertexes are placed in the MM layer (see Figure 2.26, left panel). A pure water cluster system containing $20H_2O$ molecules has also been considered. For this, we start from the coordinates of the full quantum mechanical (QM) optimization and select two alternative sets of four innermost molecules at the center of the cluster with a complete hydrogen bond network (determined with a geometric criterion; Pagliai et al., 2017) with the first neighbor water molecules. The remaining 16 molecules are described at the MM level (see Figure 2.26, right panel).

It is difficult and highly time-consuming and disk/memory-consuming to accurately calculate the structure and properties of large and complex molecular systems using pure quantum mechanical (QM) methods. Among many efforts made to make

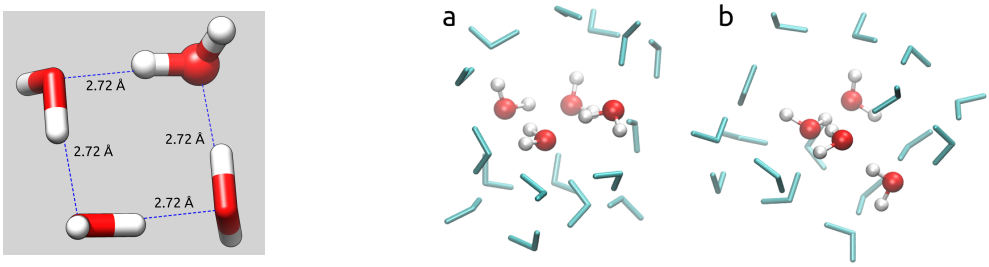

Figure 2.26: **Left:** four-water system; the single QM water molecule is depicted in a ball- and-stick representation and the 3 MM molecules in a licorice representation; $O-H$ distances are indicated too. It is to be noted that the four H_2O can be considered equivalent. **Right:** innermost water molecules described at the QM level (ball and stick) and surrounding molecules described at the MM level (lines) for the $20H_2O$ system. (a) Configuration 1. (b) Configuration 2 (Gorai et al., 2020a).

such calculations feasible, one is the hybrid method, otherwise known as a multiscale method. In this method, a large molecule is divided into multiple fragments. Various theoretical methods, ranging from very expensive and accurate methods to less expensive and accurate methods, are then applied to the different fragments. Thus, combining expensive QM and inexpensive classical molecular mechanics (MM) force fields was initiated (Honig & Karplus, 1971) and formalized in a "generic" QM/MM scheme (Warshel & Levitt, 1976), often called an "additive" scheme (Senn & Thiel, 2009). In this formalism, the entire molecular system is divided into two parts: the model and environment systems. The small "model" part is the key chemically important layer. It is treated with the accurate and expensive QM method. The remaining environment ("env") part is treated with the less accurate but more efficient MM method. In this scheme, as shown in Equation 2.12, the total energy of the whole system ($E_{QM/MM}$) is a sum of the energy of the model system by the QM method (E_{QM}), the energy of the environment system by the MM method (E_{MM}), and the interactions (E_{QM-MM}) between the QM model system and the MM environment system.

$$E_{QM/MM} = E_{QM} + E_{MM} + E_{QM-MM} \tag{2.12}$$

All QM/MM (Chung et al., 2015) calculations are carried out with the GAUSSIAN 16 (Frisch et al., 2016) code (rev. C01) using the hybrid B3LYP functional in conjunction with the 6-31 G(d) basis set. Atom types and force field parameters for water molecules in the MM layer are assigned according to the SPC-Fw flexible water model (Wu et al., 2006). The choice is driven by (i) the necessity for a flexible, three-body classical water model and (ii) the accuracy with which the selected

Table 2.16: Harmonic IR frequencies and intensities of the H_2O^{QM} + 3 H_2O^{MM} complex (Figure 2, left panel) (Gorai et al., 2020a).

NM	ω **[cm^{-1}]**	**IR Int. [km/mol]**
1	39.0097	3.5702
2	70.0478	0.9941
3	107.4593	248.8304
4	114.6669	81.5288
5	134.1712	121.9418
6	251.1220	19.7407
7	253.1088	18.8069
8	270.4875	7.7664
9	286.0773	10.8931
10	331.3394	156.5948
11	417.2017	11.4416
12	483.9590	107.2607
13^t	502.7496	211.3432
14^t	539.1224	59.4593
15^t	620.5928	2.9662
16^t	670.5374	209.1029
17^t	734.0061	476.6369
18^t	870.1429	201.9038
19^b	1407.2265	191.4554
20^b	1422.8362	445.8394
21^b	1456.6860	64.4541
22^b	1764.1323	143.3391
23^s	3399.8219	161.5281
24^s	3533.5836	119.6470
25^s	3561.1437	374.8984
26^s	3579.9423	110.7922
27^f	3643.1130	84.3280
28^f	3647.6874	450.2363
29^f	3651.3875	90.6885
30^f	3797.0095	37.5965

Note: ^{t}OH torsion; ^{b}OH scissoring; ^{s}OH stretching; ^{f}free OH

model reproduces ice I_h properties. The solvent effects are considered by using PCM (Cancès et al., 1997). The vibrational analysis results from QM/MM calculations are provided in Tables 2.16, 2.17, and 2.18.

Table 2.17: Harmonic IR frequencies and intensities of the first 4 H_2O^{QM}+16 H_2O^{MM} complex (see Figure 2.26(a), right panel, Configuration 1) evaluated at the B3LYP/6-31g(d) level (Gorai et al., 2020a).

NM	ω [cm^{-1}]	IR Int. [km/mol]	NM	ω [cm^{-1}]	IR Int. [km/mol]	NM	ω [cm^{-1}]	IR Int. [km/mol]
1	28.5053	1.6212	59	334.6995	4.4240	117^b	1406.8655	454.2350
2	32.4112	0.3452	60	347.3954	4.9640	118^b	1412.4834	218.9410
3	40.5682	1.9422	61	387.1876	8.8358	119^b	1415.0050	217.1485
4	42.6937	0.9658	62	426.8869	78.1914	120^b	1416.7673	553.3807
5	45.5125	2.8291	63	432.7664	47.4011	121^b	1423.8136	320.7421
6	47.0457	2.4796	64	449.0251	78.8810	122^b	1427.0557	239.2493
7	51.1545	1.5206	65	455.8202	9.0749	123^b	1431.3527	280.4839
8	53.0040	0.4852	66	458.4089	52.9014	124^b	1433.6066	107.3301
9	57.4113	4.9283	67	461.3395	7.1542	125^b	1436.1459	143.6834
10	58.9090	1.5004	68	468.0311	44.1926	126^b	1442.3811	59.3969
11	62.8440	3.3091	69	476.0688	5.2943	127^b	1456.0330	69.7821
12	64.6577	0.5053	70	483.8486	73.9300	128^b	1465.8850	261.4679
13	67.1132	0.4600	71	500.1090	30.3953	129^b	1481.4184	129.4706
14	71.0670	1.0092	72	500.9839	36.5412	130^b	1490.6689	54.4350
15	72.1009	5.5430	73	508.1366	20.0694	131^b	1759.3916	113.0751
16	78.5377	1.2279	74	512.3840	13.9454	132^b	1781.9431	109.2325
17	79.5809	2.8592	75	532.3995	46.0624	133^b	1805.1440	185.2649
18	84.0856	0.3164	76	535.4481	4.4789	134^b	1821.5031	81.3961
19	88.1866	0.5336	77	543.6866	60.5730	135^s	3277.1620	1061.3522
20	91.6244	1.1620	78	545.4049	57.7011	136^s	3379.4017	1450.1515
21	95.9146	1.9115	79	557.0745	41.0189	137^s	3415.3773	260.6407
22	131.1634	139.0258	80	560.6706	18.2338	138^s	3441.1055	54.0971
23	147.4509	6.2284	81	581.7986	25.4989	139^s	3501.0930	137.3189
24	155.1556	1.5936	82	585.3805	214.1458	140^s	3510.2084	280.1448
25	157.0881	12.4196	83	588.1325	72.1128	141^s	3515.4119	164.7163
26	163.8254	4.8492	84^t	593.3498	6.1937	142^s	3527.1563	98.4213
27	169.5773	3.8618	85^t	598.2759	204.0196	143^s	3532.0223	374.1860
28	173.1802	11.6779	86^t	620.7530	378.5822	144^s	3535.9755	331.7897
29	177.8697	22.1882	87^t	623.3143	58.9759	145^s	3539.5696	667.4359
30	179.4412	3.0508	88^t	629.3486	219.1103	146^s	3541.9090	42.2047
31	189.5523	12.2882	89^t	639.6399	56.7824	147^s	3546.9082	185.0747
32	193.8849	18.7990	90^t	642.7590	240.6043	148^s	3549.9374	209.7596
33	199.5633	30.2086	91^t	648.3193	65.9335	149^s	3555.5498	189.4891
34	203.7815	44.7590	92^t	658.9772	36.8759	150^s	3558.8959	76.1871
35	205.2272	29.8834	93^t	676.8776	176.4931	151^s	3563.2840	189.8014
36	210.7469	42.9633	94^t	679.7026	594.2500	152^s	3568.4433	217.3753
37	212.8473	18.5861	95^t	685.0436	47.0063	153^s	3575.4761	97.1563
38	215.6034	104.3096	96^t	690.6345	554.1850	154^s	3576.5391	86.9267
39	219.2947	9.1183	97^t	695.3495	353.6124	155^s	3579.7822	19.6952
40	221.2358	136.0590	98^t	699.7148	156.7689	156^s	3589.8658	38.6004
41	223.7398	14.6743	99^t	704.2320	32.3584	157^s	3590.2134	57.5165
42	226.9991	92.7095	100^t	721.7785	334.5258	158^s	3603.0421	149.2000
43	229.4667	11.8754	101^t	725.6449	111.7286	159^s	3618.1897	266.3486
44	231.1955	180.5173	102^t	728.6757	454.3782	160^s	3620.8200	224.9253
45	235.9253	6.3462	103^t	747.1205	168.5362	161^s	3622.0658	233.3283
46	239.8566	146.4113	104^t	753.5614	192.6962	162^s	3623.0520	397.9328
47	249.2394	2.9212	105^t	765.5413	275.9737	163^s	3624.0959	35.3011
48	254.8166	52.0837	106^t	766.1653	425.8765	164^s	3626.6346	276.1415
49	260.4354	12.2059	107^t	772.0067	356.3800	165^s	3630.3037	955.2942
50	270.0093	13.8498	108^t	803.0436	327.2798	166^s	3631.8424	16.4537
51	280.9175	13.8528	109^t	818.6290	277.6746	167^s	3633.8572	248.7481
52	284.5581	1.3055	110^t	839.8062	313.0187	168^f	3646.1348	108.4691
53	286.3104	31.7468	111^t	850.6360	671.1597	169^f	3650.9996	175.2420
54	307.5132	4.0551	112^t	929.4103	415.2180	170^f	3652.3329	128.0414
55	308.3710	4.8097	113^t	955.5738	180.7041	171^f	3652.8838	205.0487
56	314.4016	25.2868	114^t	966.2260	55.4464	172^f	3653.3844	33.2033
57	319.3857	8.4817	115^b	1401.1608	328.9992	173^f	3653.8800	205.2072
58	330.7679	1.3826	116^b	1404.9892	279.6521	174^f	3654.0193	86.2440

Note: ^{t}OH torsion; ^{b}OH scissoring; ^{s}OH stretching; ^{f}free OH.

Table 2.18: Harmonic IR frequencies and intensities of the first 4 H_2O^{QM}+16 H_2O^{MM} complex (Figure 2.26(b), right panel, Configuration 2) evaluated at the B3LYP/6-31g(d) level (Gorai et al., 2020a).

NM	ω [cm^{-1}]	IR Int. [km/mol]	NM	ω [cm^{-1}]	IR Int. [km/mol]	NM	ω [cm^{-1}]	IR Int. [km/mol]
1	29.4016	1.2924	59	338.1423	9.0936	117^b	1404.8169	265.9060
2	34.4375	0.6290	60	366.0320	9.0877	118^b	1411.9292	63.9287
3	40.5656	1.6279	61	381.8881	2.8750	119^b	1414.1855	237.2331
4	44.5388	1.2326	62	425.0003	72.9104	120^b	1414.6760	480.1803
5	47.5478	0.5182	63	433.1753	46.5032	121^b	1424.0139	304.7906
6	49.2499	4.4372	64	449.7627	54.6515	122^b	1426.0145	322.1644
7	52.7161	1.1206	65	453.1267	32.8363	123^b	1430.3473	297.6835
8	53.7670	0.7604	66	454.2652	31.3116	124^b	1434.2284	77.0402
9	58.1400	3.8023	67	457.6722	30.6715	125^b	1442.9373	116.7008
10	62.8023	2.1220	68	461.6648	46.8946	126^b	1444.1623	105.5626
11	65.0382	1.4900	69	472.4824	9.8892	127^b	1459.2322	55.3003
12	65.4195	1.0334	70	485.9271	79.1355	128^b	1465.8496	252.0918
13	68.9622	1.6328	71	489.0285	21.2511	129^b	1482.2478	140.3077
14	71.1636	2.8146	72	504.9767	27.4262	130^b	1505.1507	42.7361
15	75.3263	4.0105	73	512.8253	6.2202	131^b	1775.8533	82.3784
16	77.6513	1.4318	74	520.2208	42.0235	132^b	1780.7273	68.7098
17	79.5630	1.9564	75	531.5264	37.2553	133^b	1801.6979	332.8605
18	86.9075	2.3428	76	534.9918	6.2757	134^b	1807.9136	66.8586
19	88.7674	0.0132	77	548.5225	54.6906	135^s	3312.7170	920.6313
20	92.6829	0.4316	78	551.0483	47.1921	136^s	3377.7305	741.7304
21	97.2538	2.3252	79	557.6667	22.4631	137^s	3421.1305	761.8361
22	132.9698	136.0213	80	567.0486	44.8651	138^s	3445.3287	168.4186
23	144.3282	7.0450	81	577.5475	247.0326	139^s	3485.4299	175.0443
24	150.9225	8.8323	82	582.7791	105.7169	140^s	3509.6340	116.0370
25	160.4446	11.5643	83	589.4278	39.6372	141^s	3525.2414	27.1764
26	163.9774	15.3603	84^t	593.7719	63.8280	142^s	3527.9472	11.8392
27	166.9931	18.7482	85^t	602.0192	207.8189	143^s	3529.5426	406.7703
28	174.8622	3.9430	86^t	607.5690	235.3652	144^s	3536.2221	608.4735
29	178.6797	9.5964	87^t	620.9062	128.9013	145^s	3539.1759	168.8773
30	186.2172	5.2561	88^t	630.0995	226.7652	146^s	3542.1608	517.6770
31	189.8802	22.8351	89^t	642.3136	46.5019	147^s	3544.0015	105.2415
32	196.0450	18.6789	90^t	646.4580	155.7202	148^s	3551.6796	422.3966
33	200.1828	70.0050	91^t	656.2139	245.2327	149^s	3556.2138	104.4402
34	201.5062	8.6800	92^t	659.7475	92.3092	150^s	3559.4252	140.9715
35	202.0414	8.0519	93^t	668.0591	88.0836	151^s	3562.5905	344.5012
36	208.0234	21.2606	94^t	678.1031	752.6557	152^s	3566.5079	71.2504
37	211.9547	44.9818	95^t	687.1452	86.4196	153^s	3568.8607	31.6257
38	216.4440	154.2248	96^t	702.2325	266.3036	154^s	3577.3367	111.0585
39	217.8326	186.4806	97^t	704.8812	97.3595	155^s	3577.8583	220.6935
40	218.1099	26.3216	98^t	711.5869	144.5530	156^s	3583.4466	183.5092
41	221.6619	28.3099	99^t	715.1892	66.1333	157^s	3590.2972	17.7387
42	224.3879	13.6861	100^t	725.8863	598.8691	158^s	3591.3690	14.5938
43	227.4102	2.3297	101^t	726.0798	18.1883	159^s	3611.7321	8.8719
44	229.1919	70.6417	102^t	730.7761	246.5783	160^s	3618.8579	235.6198
45	230.9956	94.8355	103^t	736.1656	277.1486	161^s	3623.1189	386.5676
46	243.1731	117.8833	104^t	744.0336	554.7832	162^s	3624.3597	98.4237
47	249.4187	0.5086	105^t	761.4750	271.4461	163^s	3627.3709	210.1150
48	253.8914	22.9344	106^t	775.7715	563.7792	164^s	3628.9811	88.7231
49	257.2356	35.1484	107^t	786.5512	479.5887	165^s	3630.5375	639.2414
50	267.5344	24.9850	108^t	805.5061	212.9173	166^s	3631.3807	548.9593
51	280.0676	6.8173	109^t	826.6848	229.7506	167^s	3632.6677	305.9009
52	285.7365	23.7669	110^t	845.7629	191.2681	168^f	3646.2015	105.3221
53	296.6659	17.1441	111^t	887.6214	524.4212	169^f	3651.1285	183.1653
54	304.8541	3.0164	112^t	923.2407	210.8728	170^f	3652.3160	143.6466
55	308.4159	0.7582	113^t	950.0147	288.1648	171^f	3652.6720	169.0597
56	314.4300	7.5522	114^t	1014.9949	128.1520	172^f	3653.3819	24.7682
57	317.0437	9.2531	115^b	1401.2013	312.9877	173^f	3653.5148	97.5307
58	327.0967	1.0243	116^b	1403.0314	627.4395	174^f	3654.0199	236.1947

Note: ^{t}OH torsion; ^{b}OH scissoring; ^{s}OH stretching; ^{f}free OH.

2.2.2 Experimental methods

Laboratory data are used from the literature whenever possible to constrain simulations (Bouwman et al., 2007; Öberg et al., 2007). In the cases of formic acid, ammonia, and methanol in water ice, new experiments are performed using the high-vacuum (HV) portable astrochemistry chamber (PAC) at the Open University (OU) in the United Kingdom. A detailed description of the system is described elsewhere (Dawes et al., 2016). Briefly, the main chamber is a commercial conflat flange cube (Kimball Physics Inc.) connected to a molecular turbopump (300 L/s), a custom-made stainless steel dosing line through an all-metal leak valve, a cold finger of a closed-cycle He cryostat (Sumitomo Cryogenics), and two ZnSe windows suitable for IR spectroscopy. During operation, the base pressure in the chamber is in the 10^{-9} mbar range, and the base temperature of the cold finger is 20 K. In thermal contact with the cryostat, the substrate is a ZnSe window (20 mm $\times$ 2 mm). A DT-670 silicon diode temperature sensor (LakeShore Cryotronics) is connected to the substrate to measure its temperature, while a Kapton flexible heater (Omegalux) is used to change its temperature. The diode and heater are both connected to an external temperature controller (Oxford Instruments).

Gaseous samples are prepared and mixed in a pre-chamber (dosing line) before being dosed into the main chamber through an all-metal leak valve. A mass-independent pressure transducer is used to control the amount of gas components mixed in the pre-chamber. Chemicals are purchased at Sigma-Aldrich with the highest purity available [HCOOH ($>$ 95%), NH_3 (99.95%), and CH_3OH (99.8%)]. Ices are grown in situ by direct vapor deposition onto the substrate at normal incidence via a 3 mm nozzle 20 mm away from the sample. IR spectroscopy is performed in transmission mode using a Fourier transform infrared (FTIR; Nicolet Nexus 670) spectrometer with an external mercury cadmium telluride (MCT) detector. A background spectrum comprising 512 co-added scans are acquired before deposition at 20 K and used as a reference spectrum for all the spectra collected after deposition to remove all the IR signatures along the beam pathway that did not originate from the ice sample. Each IR spectrum is a collection of 256 co-added scans. The IR path is purged with dry compressed air to remove water vapor.

2.2.3 Results and Discussion

In this Section, firstly, the pure water ice will be addressed to establish the best compromise between accuracy and computational cost to describe the water ice unit

Table 2.19: Absorption band strengths and band positions (within parentheses) of pure water ice[a] (Gorai et al., 2020a).

Vibration mode	**Experiment** Gerakines et al. (1995)	**Dimer** **B3LYP-631G(d)**	**c-Tetramer** **B3LYP-631G(d)**	**c-Hexamar (chair)** **B3LYP-631G(d)**	**Octamer (cube)** **B3LYP-631G(d)**
Libration	3.1×10^{-17} (760)	2.70×10^{-17}(670)	2.40×10^{-17}(733)	1.17×10^{-16}(870)	1.27×10^{-17}(848)
Bending	1.2×10^{-17} (1660)	2.23×10^{-17}(1710)	4.18×10^{-17}(1714)	4.62×10^{-17}(1730)	6.85×10^{-17}(1717)
Stretching	2.0×10^{-16} (3280)	8.27×10^{-17}(3540)	3.11×10^{-16}(3298)	5.53×10^{-16}(3220)	3.89×10^{-16}(3320)
Free-OH	–	1.35×10^{-17}(3810)	2.10×10^{-17}(3775)	2.52×10^{-17}(3780)	1.52×10^{-17}(3788)
Vibration mode	Experiment Gerakines et al. (1995)	**c-Tetramer** **B2PLYP/m-aug-cc-pVTZ**	**$1H_2O$(QM)+$3H_2O$(MM)** **B3LYP-631G(d)**		**$4H_2O$(QM)+$16H_2O$(MM)** **B3LYP-631G(d)**
Libration	3.1×10^{-17} (760)	3.94×10^{-17}(714)	7.91×10^{-17}(669)		4.9×10^{-17}(720)
Bending	1.2×10^{-17} (1660)	2.93×10^{-17}(1635)	2.37×10^{-17}(1431)		1.88×10^{-17}(1426)
Stretching	2.0×10^{-16} (3280)	2.97×10^{-16}(3477)	2.68×10^{-17}(3593)		1.76×10^{-16}(3565)
Free-OH	...	2.40×10^{-17}(3865)	6.24×10^{-18}(3797)		2.52×10^{-17}(3636)

Note: [a] Computed values in cm molecule^{-1} and band position in cm^{-1}.

cell. To this aim, we will resort to the comparison with the experiment. Then, we will move to the ice containing impurities. To further proceed with the validation of our protocol, water ice containing HCOOH, NH_3, CH_3OH, CO, and CO_2 as impurities will be investigated, thus exploiting the comparison between experiment and computations. This will also involve, as mentioned above, new measurements. Finally, in the last part, our protocol will be extended to the study of water ices with H_2CO, CH_4, N_2, and O_2 as impurities.

Part 1. Validation

Band strength of pure water

In Table 2.19, the water band positions obtained with different methods and different sizes of the water cluster are compared with experimental data. Our computations provide several frequencies corresponding to a single mode of vibration. For the comparison, we report the computed frequencies of the four fundamental modes after convolving them with a Gaussian function with an adequate width (Licari et al., 2015) (all transition frequencies are collected in Table 2.20). The comparison of Table 2.19 is graphically summarized in Figure 2.27. The left panel shows the average deviation of the band position of three fundamental modes of water (libration, bending, and stretching) from the experimental counterpart (Gerakines et al., 1995). Interestingly, the band positions obtained using the tetramer configuration and the B3LYP/6-31G(d) level of theory provide the best agreement. The right panel shows the average deviation of the band strengths from experiments. QM/MM calculations for the 20 water molecule clusters (described in the computational details Section above) show the minimum deviation from experimental data. The results obtained for the tetramer configuration, both at the B3LYP and B2PLYP levels, also pro-

Table 2.20: Comparison of band positions and band intensities as obtained by different quantum-chemical level of theories (Gorai et al., 2020a).

Assignment	$4H_2O$+PCM, B3PLYP/6-31G(d)		$4H_2O$+PCM, B2PLYP/m-aug-cc-pVTZ		$1H_2O$(QM)+$3H_2O$(MM) +PCM, B3PLYP/6-31G(d)		$4H_2O$(QM)+$16H_2O$(MM) +PCM, B3PLYP/6-31G(d)	
	Wavenumber (cm^{-1})	Intensity (km/mol)	Wavenumber (cm^{-1})	Intensity (km/mol)	Wavenumber (cm^{-1})	Intensity (km/mol)	Wavenumber (cm^{-1})	Intensity (km/mol)
1							28.5053	1.6212
2							32.4112	0.3452
3			39.3404	0.0000	39.0097	3.5702	40.5682	1.9422
4	42.31	0.000					42.6937	0.9658
5							45.5125	2.8291
6							47.0457	2.4796
7							51.1545	1.5206
8							53.0040	0.4852
9							57.4113	4.9283
10							58.9090	1.5004
11							62.8440	3.3091
12							64.6577	0.5053
13							67.1132	0.4600
14					70.0478	0.9941	71.0670	1.0092
15							72.1009	5.5430
16							78.5377	1.2279
17							79.5809	2.8592
18			85.5169	4.1241			84.0856	0.3164
19							88.1866	0.5336
20							91.6244	1.1620
21	101.53	0.5953			107.4593	248.8304	95.9146	1.9115
22					114.669	81.5288	131.1634	139.0258
23					134.1712	121.9418	147.4509	6.2284
24							155.1556	1.5936
25							157.0881	12.4196
26							163.8254	4.8492
27							169.5773	3.8618
28							173.1802	11.6779
29							177.8697	22.1882
30							179.4412	3.0508
31							189.5523	12.2882
32							193.8849	18.7990
33							199.5633	30.2086
34			202.1393	0.0000			203.7815	44.7590
35							205.2272	29.8834
36							210.7469	42.9633
37							212.8473	18.5861
38							215.6034	104.3096
39							219.2947	9.1183
40			222.9069	104.7500			221.2358	136.0590
41			22.29069	104.7500			223.7398	14.6743
42							226.9991	92.7095
43							229.4667	11.8754
44			231.0105	94.8938			231.1955	180.5173
45							235.9253	6.3462
46	243.67	0.000	240.0832	0.6734			239.8566	146.4113
47			246.4688	287.8694	251.1220	19.7407	249.2394	2.9212
48			246.4688	287.8694	253.1088	18.8069	254.8166	52.0837
49							260.4354	12.2059
50	277.10	206.9799	274.1815	0.000	270.4875	7.7664	270.0093	13.8498
51	277.10	206.9799			286.0773	10.8931	280.9175	13.8528
52	281.08	0.3532					284.5581	1.3055
53							286.3104	31.7468
54	301.85	0.1654					307.5132	4.0551
55	307.74	298.2083					308.3710	4.8097
56	307.74	298.2083					314.4016	25.2868
57							319.3857	8.4817
58	327.52	0.0000			331.3394	156.5948	330.7679	1.3826
59							334.6995	4.4240
60							347.3954	4.9640

Assignment	$4H_2O$+PCM, B3PLYP/6-31G(d)		$4H_2O$+PCM, B2PLYP/m-aug-cc-pVTZ		$1H_2O$(QM)+$3H_2O$(MM) +PCM, B3PLYP/6-31G(d)		$4H_2O$(QM)+$16H_2O$(MM) +PCM, B3PLYP/6-31G(d)	
	Wavenumber (cm^{-1})	Intensity (km/mol)	Wavenumber (cm^{-1})	Intensity (km/mol)	Wavenumber (cm^{-1})	Intensity (km/mol)	Wavenumber (cm^{-1})	Intensity (km/mol)
61			398.6011	0.000			387.1876	8.8358
62			427.5608	44.2017	417.2017	11.4416	426.8869	78.1914
63							432.7664	47.4011
64			443.1204	79.6160			449.0251	78.8810
65			443.1204	79.6160			455.8202	9.0749
66							458.4089	52.9014
67							461.3395	7.1542
68							468.0311	44.1926
69	473.37	0.000					476.0688	5.2943
70					483.9590	107.2607	483.8486	73.9300
71							500.1090	30.3953
72					502.7496^t	211.3432	500.9839	36.5412
73							508.1366	20.0694
74							512.3840	13.9454
75	523.50	58.1147					532.3995	46.0624
76	523.76	0.9980			539.1224^t	59.4593	535.4481	4.4789
77	523.76	0.9980					543.6866	60.5730
78							545.4049	57.7011
79							557.0745	41.0189
80							560.6706	18.2338
81							581.7986	25.4989
82							585.3805	214.1458
83							588.1325	72.1128
84^t							593.3498	6.1937
85^t							598.2759	204.0196
86^t					620.5928^t	2.9662	620.7530	378.5822
87^t							623.3143	58.9759
88^t							629.3486	219.1103
89^t							639.6399	56.7824
90^t							642.7590	240.6043
91^t							648.3193	65.9335
92^t							658.9772	36.8759
93^t					670.5374^t	209.1029	676.8776	176.4931
94^t							679.7026	594.2500
95^t			683.4168	312.1539			685.0436	47.0063
96^t							690.6345	554.1850
97^t							695.3495	353.6124
98^t							699.7148	156.7689
99^t							704.2320	32.3584
100^t							721.7785	334.5258
101^t	737.11^t	144.3682			734.0061^t	476.6369	725.6449	111.7286
102^t							728.6757	454.3782
103^t							747.1205	168.5362
104^t							753.5614	192.6962
105^t							765.5413	275.9737
106^t			778.3957^t	237.5051			766.1653	425.8765
107^t			778.3957^t	237.5051			772.0067	356.3800
108^t							803.0436	327.2798
109^t							818.6290	277.6746
110^t							839.8062	313.0187
111^t	894.95^t	342.8199			870.1429^t	201.9038	850.6360	671.1597
112^t	894.95^t	342.8199	934.3601^t	0.000			929.4103	415.2180
113^t							955.5738	180.7041
114^t	1127.57^t	0.000					966.2260	55.4464
115^b							1401.1608	328.9992
116^b							1404.9892	279.6521
117^b					1407.2265^b	191.4554	1406.8655	454.2350
118^b							1412.4834	218.9410
119^b							1415.0050	217.1485
120^b							1416.7673	553.3807

Assignment	$4H_2O$+PCM, B3PLYP/6-31G(d)		$4H_2O$+PCM, B2PLYP/m-aug-cc-pVTZ		$1H_2O$(QM)+$3H_2O$(MM) +PCM, B3PLYP/6-31G(d)		$4H_2O$(QM)+$16H_2O$(MM) +PCM, B3PLYP/6-31G(d)	
	Wavenumber (cm^{-1})	Intensity (km/mol)	Wavenumber (cm^{-1})	Intensity (km/mol)	Wavenumber (cm^{-1})	Intensity (km/mol)	Wavenumber (cm^{-1})	Intensity (km/mol)
121^b					1422.8362^b	445.8394	1423.8136	320.7421
122^b							1427.0557	239.2493
123^b							1431.3527	280.4839
124^b							1433.6066	107.3301
125^b							1436.1459	143.6834
126^b							1442.3811	59.3969
127^b					1456.6860^b	64.4541	1456.0330	69.7821
128^b							1465.8850	261.4679
129^b							1481.4184	129.4706
130^b							1490.6689	54.4350
131^b	1711.28^b	251.8157	1630.3695^b	176.7723	1764.1323^b	143.3391	1759.3916	113.0751
132^b	1723.10^b	82.9912	1647.3535^b	74.0296			1781.9431	109.2325
133^b	1723.10^b	82.9911	1647.3536^b	74.0296			1805.1440	185.2649
134^b	1741.00^b	0.0000	1672.6698^b	0.000			1821.5031	81.3961
135^s	3182.21^s	0.0000					3277.1620	1061.3522
136^s	3297.07^s	1871.6907					3379.4017	1450.1515
137^s	3297.07^s	1871.6907	3411.5900^s	0.000	3399.8219^s	161.5281	3415.3773	260.6407
138^s	3366.39^s	50.2255	3477.3996^s	1793.2478			3441.1055	54.0971
139^s			3477.3996^s	1793.2478			3501.0930	137.3189
140^s							3510.2084	280.1448
141^s							3515.4119	164.7163
142^s			3522.3300^s	2.0149			3527.1563	98.4213
143^s					3533.5836^s	119.6470	3532.0223	374.1860
144^s							3535.9755	331.7897
145^s							3539.5696	667.4359
146^s							3541.9090	42.2047
147^s							3546.9082	185.0747
148^s							3549.9374	209.7596
149^s							3555.5498	189.4891
150^s							3558.8959	76.1871
151^s					3561.1437^s	374.8984	3563.2840	189.8014
152^s							3568.4433	217.3753
153^s							3575.4761	97.1563
154^s							3576.5391	86.9267
155^s					3579.9423^s	110.7922	3579.7822	19.6952
156^s							3589.8658	38.6004
157^s							3590.2134	57.5165
158^s							3603.0421	149.2000
159^s							3618.1897	266.3486
160^s							3620.8200	224.9253
161^s							3622.0658	233.3283
162^s							3623.0520	397.9328
163^s							3624.0959	35.3011
164^s							3626.6346	276.1415
165^s							3630.3037	955.2942
166^s							3631.8424	16.4537
167^s							3633.8572	248.7481
168^f					3643.1130^f	84.3280	3646.1348	108.4691
169^f					3647.6874^f	450.2363	3650.9996	175.2420
170^f					3651.3875^f	90.6885	3652.3329	128.0414
171^f	3778.38^f	126.4545	3864.6871^f	144.7620			3652.8838	205.0487
172^f	3779.79^f	52.8022	3865.9912^f	138.6232			3653.3844	33.2033
173^f	3779.79^f	52.8022	3865.9912^f	138.6232			3653.8800	205.2072
174^f	3781.36^f	0.0000	3867.1847^f	0.0000	3797.0095^f	37.5965	3654.0193	86.2440

Note:

^{t}OH torsion; ^{b}OH scissoring; ^{s}OH stretching; ^{f}free OH.

For the conversion of km/mol to cm molecule^{-1}, intensity values need to be multiplied by a factor 1.6603×10^{-19}.

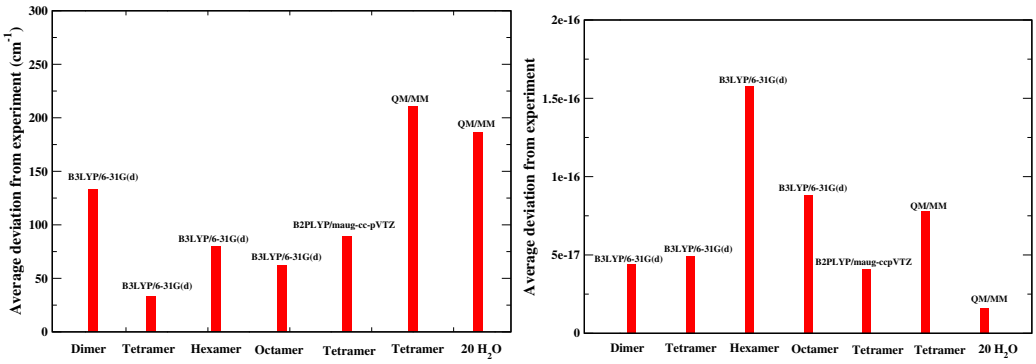

Figure 2.27: Deviation of computed band positions (left panel) and band strengths (right panel) from experiments (Gorai et al., 2020a).

vide minor variations. Based on the comparison results, the B3LYP/6-31G(d) level of theory and the tetramer configuration are suitable combinations to describe the water cluster with a little computational cost.

In the following sections, the results for water ice with HCOOH and NH_3 as impurities are first reported and discussed, thereby exploiting the outcomes of new experiments. Then, we move to the $CH_3OH - H_2O$ ice, for which new experimental results are obtained. Finally, for the last two cases addressed, namely $CO - H_2O$ and $CO_2 - H_2O$, the experimental data for the comparison are taken from the literature. Unless otherwise stated, we use the c-tetramer configuration for the rest of our calculations.

HCOOH ice

IR spectra are measured for various mixtures of H_2O and HCOOH ice deposited at 20 K, as explained in the experimental details Section (see Section 2.2.2). These, normalized to the $O - H$ stretch, are shown in Figure 2.28a. Minor contamination due to CO_2 is detected in some experiments. However, in all experiments, the amount of CO_2 deposited in the ice is 1000 and more than 100 times less abundant than H_2O and HCOOH, respectively. Therefore, we do not expect that the CO_2 contamination affects the recorded IR spectra profiles.

The mixture ratios are determined from the fit of the spectrum of a selected mixture, measurement of the area of the water band at 3333.33 cm^{-1} (3.00 μm), and comparing with the pure water counterparts. For HCOOH, the absorption area is measured at 1700 cm^{-1}. In fact, HCOOH has the strongest mode at 1694.92 cm^{-1} (5.90 μm), which corresponds to its $C = O$ stretching mode. However, the

Table 2.21: Frequencies, integral absorbance coefficients, and normal modes of vibration of $H_2O - X$ (X = HCOOH, NH_3, CH_3OH, CO, CO_2, H_2CO, CH_4, OCS, N_2, and O_2) (Gorai et al., 2020a).

H_2O : X	Frequency at peak in cm^{-1} (μm)	Integral absorbance coefficient in cm $molecule^{-1}$	Modes of vibration
	HCOOH		
1:0.25	875.47 (11.42)	5.98×10^{-17}	OH torsion
	1698.42 (5.89)	5.24×10^{-17}	H_2O scissoring
	3326.84 (3.00)	1.88×10^{-16}	OH stretching
	3635.02 (2.75)	4.11×10^{-17}	free OH
1:0.50	859.72 (11.63)	6.18×10^{-17}	OH torsion
	1696.3 (5.90)	5.37×10^{-17}	H_2O scissoring
	3341.67 (2.99)	2.08×10^{-16}	OH stretching
	3632.99 (2.75)	4.19×10^{-17}	free OH
1:0.75	878.28 (11.38)	4.91×10^{-17}	OH torsion
	1688.62 (5.92)	6.27×10^{-17}	H_2O scissoring
	3260.11 (3.07)	2.46×10^{-16}	OH stretching
	3611.81 (2.77)	6.46×10^{-17}	free OH
1:1.00	747.49 (13.38)	9.21×10^{-17}	OH torsion
	1685.24 (5.93)	7.56×10^{-17}	H_2O scissoring
	3343.53 (2.99)	2.08×10^{-16}	OH stretching
	3608.22 (2.77)	7.15×10^{-17}	free OH
	NH_3		
1:0.25	886.69 (11.28)	7.31×10^{-17}	OH torsion
	1717.36 (5.82)	3.58×10^{-17}	H_2O scissoring
	3055.07 (3.27)	2.20×10^{-16}	OH stretching
	3778.71 (2.65)	1.16×10^{-17}	free OH
1:0.50	877.63 (11.39)	8.92×10^{-17}	OH torsion
	1725.39 (5.80)	3.28×10^{-17}	H_2O scissoring
	3127.37 (3.20)	4.38×10^{-16}	OH stretching
	3737.41 (2.65)	7.02×10^{-18}	free OH
1:0.75	859.21 (11.64)	4.99×10^{-17}	OH torsion
	1730.52 (5.78)	2.47×10^{-17}	H_2O scissoring
	3264.44 (3.06)	4.27×10^{-16}	OH stretching
	3777.53 (2.65)	5.89×10^{-18}	free OH
1:1.00	938.38 (10.66)	9.35×10^{-17}	OH torsion
	1751.53 (5.71)	4.43×10^{-17}	H_2O scissoring
	3270.01 (3.06)	4.90×10^{-16}	OH stretching
	–	–	free OH
	CH_3OH		
1:0.25	751.68 (13.30)	5.60×10^{-17}	OH torsion
	1703.98 (5.87)	3.85×10^{-17}	H_2O scissoring
	3252.5 (3.07)	2.33×10^{-16}	OH stretching
	3774.67 (2.65)	1.73×10^{-17}	free OH
1:0.50	719.11 (13.91)	7.67×10^{-17}	OH torsion
	1654.59 (6.04)	3.62×10^{-17}	H_2O scissoring
	3207.15 (3.12)	4.57×10^{-16}	OH stretching
	3843.18 (2.60)	2.26×10^{-17}	free OH
1:0.75	702.71 (14.23)	5.49×10^{-17}	OH torsion
	1690.03 (5.92)	2.92×10^{-17}	H_2O scissoring
	3351.12 (2.96)	2.25×10^{-16}	OH stretching
	3783.4 (2.64)	1.72×10^{-17}	free OH
1:1.00	906.29 (11.03)	6.61×10^{-17}	OH torsion
	1693.39 (5.90)	2.96×10^{-17}	H_2O scissoring
	3295.67 (3.03)	3.97×10^{-16}	OH stretching
	3774.54 (2.65)	2.03×10^{-17}	free OH
	CO		
1:0.25	895.46 (11.17)	5.70×10^{-17}	OH torsion
	1711.46 (5.84)	4.14×10^{-17}	H_2O scissoring
	3290.66 (3.04)	3.14×10^{-16}	OH stretching
	3791.25 (2.64)	2.39×10^{-17}	free OH
1:0.50	898.71 (11.13)	5.64×10^{-17}	OH torsion
	1711.73 (5.84)	4.19×10^{-17}	H_2O scissoring
	3285.68 (3.04)	3.22×10^{-16}	OH stretching
	3791.07 (2.64)	2.42×10^{-17}	free OH
1:0.75	898.22 (11.13)	5.71×10^{-17}	OH torsion
	1713.47 (5.84)	4.18×10^{-17}	H_2O scissoring
	3290.55 (3.04)	3.16×10^{-16}	OH stretching
	3789.19 (2.64)	4.93×10^{-17}	free OH
1:1.00	899.44 (11.12)	5.89×10^{-17}	OH torsion
	1715.94 (5.83)	4.22×10^{-17}	H_2O scissoring
	3293.09 (3.04)	3.13×10^{-16}	OH stretching
	3789.31 (2.64)	6.92×10^{-17}	free OH

H_2O : X	**Frequency at peak in cm^{-1} (μm)**	**Integral absorbance coefficient in cm $molecule^{-1}$**	**Modes of vibration**
		CO_2	
1:0.25	893.79 (11.19)	5.63×10^{-17}	OH torsion
	1710.62 (5.84)	4.23×10^{-17}	H_2O scissoring
	3288.08 (3.04)	3.10×10^{-16}	OH stretching
	3766.88 (2.65)	3.85×10^{-17}	free OH
1:0.50	890.45 (11.23)	5.72×10^{-17}	OH torsion
	1713.11 (5.84)	4.22×10^{-17}	H_2O scissoring
	3278.84 (3.05)	3.26×10^{-16}	OH stretching
	3767.04 (2.65)	4.21×10^{-17}	free OH
1:0.75	891.90 (11.21)	5.98×10^{-17}	OH torsion
	1709.11 (5.85)	4.20×10^{-17}	H_2O scissoring
	3294.04 (3.04)	3.17×10^{-16}	OH stretching
	3766.76 (2.65)	5.31×10^{-17}	free OH
1:1.00	896.53 (11.15)	5.61×10^{-17}	OH torsion
	1709.45 (5.85)	4.41×10^{-17}	H_2O scissoring
	3296.79 (3.03)	3.05×10^{-16}	OH stretching
	3765.50 (2.66)	7.28×10^{-17}	free OH
		H_2CO	
1:0.25	890.85 (11.22)	6.00×10^{-17}	OH torsion
	1712.86 (5.84)	3.97×10^{-17}	H_2O scissoring
	3274.97 (3.05)	3.06×10^{-16}	OH stretching
	3607.83 (2.77)	8.46×10^{-17}	free OH
1:0.50	886.56 (11.28)	5.44×10^{-17}	OH torsion
	1710.12 (5.85)	4.17×10^{-17}	H_2O scissoring
	3246.10 (3.08)	3.27×10^{-16}	OH stretching
	3601.67 (2.78)	9.12×10^{-17}	free OH
1:0.75	937.07 (10.67)	5.41×10^{-17}	OH torsion
	1767.86 (5.66)	2.81×10^{-17}	H_2O scissoring
	3279.19 (3.05)	3.23×10^{-16}	OH stretching
	3607.45 (2.77)	1.35×10^{-17}	free OH
1:1.00	904.32 (11.06)	5.51×10^{-17}	OH torsion
	1713.74 (5.84)	3.51×10^{-17}	H_2O scissoring
	3338.99 (2.99)	2.96×10^{-16}	OH stretching
	3612.36 (2.77)	9.67×10^{-17}	free OH
		CH_4	
1:0.25	903.11 (11.07)	5.96×10^{-17}	OH torsion
	1710.29 (5.85)	4.14×10^{-17}	H_2O scissoring
	3287.91 (3.04)	3.06×10^{-16}	OH stretching
	3777.98 (2.65)	2.03×10^{-17}	free OH
1:0.50	910.32 (10.98)	5.97×10^{-17}	OH torsion
	1706.49 (5.86)	4.14×10^{-17}	H_2O scissoring
	3280.67 (3.05)	3.30×10^{-16}	OH stretching
	3778.16 (2.65)	2.16×10^{-17}	free OH
1:0.75	905.03 (11.05)	6.05×10^{-17}	OH torsion
	1706.58 (5.86)	4.10×10^{-17}	H_2O scissoring
	3296.35 (3.03)	3.22×10^{-16}	OH stretching
	3778.86 (2.65)	2.18×10^{-17}	free OH
1:1.00	893.41 (11.19)	6.23×10^{-17}	OH torsion
	1705.91 (5.86)	4.11×10^{-17}	H_2O scissoring
	3312.78 (3.02)	3.41×10^{-16}	OH stretching
	3777.04 (2.65)	2.40×10^{-17}	free OH
		OCS	
1:0.25	897.72 (11.14)	5.74×10^{-17}	OH torsion
	1711.96 (5.84)	4.11×10^{-17}	H_2O scissoring
	3288.8 (3.04)	3.10×10^{-16}	OH stretching
	3772.38 (2.65)	4.82×10^{-17}	free OH
1:0.50	889.91 (11.24)	5.80×10^{-17}	OH torsion
	1712.15 (5.84)	4.30×10^{-17}	H_2O scissoring
	3281.28 (3.05)	3.27×10^{-16}	OH stretching
	3772.57 (2.65)	6.60×10^{-17}	free OH
1:0.75	901.72 (11.09)	5.77×10^{-17}	OH torsion
	1713.88 (5.83)	4.40×10^{-17}	H_2O scissoring
	3290.61 (3.04)	3.26×10^{-16}	OH stretching
	3771.53 (2.65)	9.02×10^{-17}	free OH
1:1.00	897.75 (11.14)	5.75×10^{-17}	OH torsion
	1713.97 (5.83)	4.47×10^{-17}	H_2O scissoring
	3299.75 (3.03)	3.29×10^{-16}	OH stretching
	3770.63 (2.65)	1.11×10^{-16}	free OH

H_2O : X	**Frequency at peak in cm^{-1} (μm)**	**Integral absorbance coefficient in cm $molecule^{-1}$**	**Modes of vibration**
		N_2	
1:0.25	894.31 (11.18)	5.63×10^{-17}	OH torsion
	1709.81 (5.85)	4.16×10^{-17}	H_2O scissoring
	3292.23 (3.04)	3.16×10^{-16}	OH stretching
	3778.08 (2.65)	2.34×10^{-17}	free OH
1:0.50	889.34 (11.24)	5.98×10^{-17}	OH torsion
	1716.33 (5.83)	4.54×10^{-17}	H_2O scissoring
	3290.41 (3.04)	3.10×10^{-16}	OH stretching
	3778.76 (2.65)	2.36×10^{-17}	free OH
1:0.75	892.07 (11.21)	5.98×10^{-17}	OH torsion
	1716.67 (5.82)	4.69×10^{-17}	H_2O scissoring
	3295.86 (3.03)	3.05×10^{-16}	OH stretching
	3784.28 (2.64)	5.14×10^{-17}	free OH
1:1.00	899.90 (11.11)	5.73×10^{-17}	OH torsion
	1714.47 (5.83)	4.52×10^{-17}	H_2O scissoring
	3297.32 (3.03)	3.15×10^{-16}	OH stretching
	3780.99 (2.64)	7.59×10^{-17}	free OH
		O_2	
1:0.25	893.78 (11.19)	5.65×10^{-17}	OH torsion
	1711.86 (5.84)	4.11×10^{-17}	H_2O scissoring
	3286.24 (3.04)	3.10×10^{-16}	OH stretching
	3729.93 (2.68)	4.41×10^{-17}	free OH
1:0.50	934.71 (10.70)	6.49×10^{-17}	OH torsion
	1700.17 (5.88)	3.78×10^{-17}	H_2O scissoring
	3225.04 (3.10)	4.51×10^{-16}	OH stretching
	3774.84 (2.65)	2.77×10^{-17}	free OH
1:0.75	892.96 (11.20)	5.75×10^{-17}	OH torsion
	1717.35 (5.82)	4.04×10^{-17}	H_2O scissoring
	3286.59 (3.04)	3.12×10^{-16}	OH stretching
	3729.19 (2.68)	8.72×10^{-17}	free OH
1:1.00	900.52 (11.10)	5.67×10^{-17}	OH torsion
	1718.90 (5.82)	4.18×10^{-17}	H_2O scissoring
	3299.52 (3.03)	3.19×10^{-16}	OH stretching
	3727.75 (2.68)	1.08×10^{-16}	free OH

feature overlaps with the OH bending mode of solid water at 1666.67 cm^{-1} (6.00 μm). Therefore, the water bending mode contribution at $\sim$1700 cm^{-1} has been subtracted from the total area before the band strength mentioned above being used to calculate the amount of HCOOH in the ice mixture. The band strengths used here are 2.0×10^{-16} for H_2O (Gerakines et al., 1995) and 6.7×10^{-17} for HCOOH (Marechal, 1987; Schutte et al., 1999). Another relatively weaker mode of HCOOH at 1388.89 cm^{-1} (7.20 μm) is also considered because the corresponding region is free from interfering transitions (Schutte et al., 1999). As seen in Figure 2.28a, the HCOOH:H_2O ratios cover the 0.05 to 3.46 range. It is worth noting that abundances of solid-phase HCOOH in the interstellar ices vary between 1% and 5% relative to the H_2O ice (Bisschop et al., 2007).

Figure 2.25b shows how the HCOOH molecules are bonded to the water molecules to form the $4:4$ $H_2O-HCOOH$ mixture used in our calculations. The absorption band profiles of the $H_2O-HCOOH$ clusters with different impurity concentrations are shown in Figure 2.29. The transition frequencies and the corresponding most vital intensity values, obtained at the B3LYP/6-31G(d) level, are given in Table 2.21. Calculations are also carried out using the B2PLYP functional. The results are summarized in Tables 2.22−2.26.

The data are fitted with a linear function $A_{eff} = a[X]+b$ (where X = HCOOH, NH_3, CH_3OH, CO, CO_2, H_2CO, CH_4, OCS, N_2, and O_2) to investigate the variation of the band strength with impurity concentrations. The coefficient a provides the information whether the band strength increases or decreases by increasing the concentration of X, $[X]$. The coefficient b indicates the band strength of the vibration mode in the absence of impurities. The fitting coefficients for all impurities considered are provided in Table 2.27. In Figure 2.30a, the band strength profile as a function of the concentration of HCOOH is shown.

NH_3 ice

Most of the intense modes of ammonia overlap with the dominant features due to water and silicates. However, when ammonia is mixed with H_2O ice, it forms hydrates showing an intense mode at 2881.84 cm^{-1} (3.47 μm) (Dartois, 2005). Another characteristic feature of ammonia is the umbrella mode at 1111.11 cm^{-1} (9.00 μm), which is relatively intense. Still, it often overlaps with the CH_3 rocking mode of methanol, thus leading to an overestimation of the abundance of ammonia.

In this work, IR spectra are recorded for various mixing ratios of H_2O-NH_3 ice deposited at 20 K. IR spectra, normalized to the most intense band (i.e., the O − H

Table 2.22: Harmonic IR frequencies and intensities of the complex $4H_2O$ evaluated at the B2PLYP/maug-cc-pVTZ level (Gorai et al., 2020a).

NM	ω **[cm^{-1}]**	**IR Int. [km/mol]**
1	39.3404	0.0000
2	85.5169	4.1241
3	202.1393	0.0000
4	222.9069	104.7500
5	222.9069	104.7500
6	231.0105	94.8938
7	240.0832	0.6734
8	246.4688	287.8694
9	246.4688	287.8694
10	274.1815	0.0000
11	398.6011	0.0000
12	427.5608	44.2017
13	443.1204	79.6160
14	443.1204	79.6160
15	683.4168	312.1539
16^t	778.3957	237.5051
17^t	778.3957	237.5051
18^t	934.3601	0.0000
19^b	1630.3695	176.7723
20^b	1647.3535	74.0296
21^b	1647.3536	74.0296
22^b	1672.6698	0.0000
23^s	3411.5900	0.0000
24^s	3477.3996	1793.2478
25^s	3477.3996	1793.2478
26^s	3522.3300	2.0149
27^f	3864.6871	144.7620
28^f	3865.9912	138.6232
29^f	3865.9912	138.6232
30^f	3867.1847	0.0000

Note: ^{t}OH torsion; ^{b}OH scissoring; ^{s}OH stretching; ^{f}free OH.

Table 2.23: Harmonic IR frequencies and intensities of the complex $4H_2O$/HCOOH evaluated at the B2PLYP/maug-cc-pVTZ level (Gorai et al., 2020a).

NM	ω **[cm^{-1}]**	**IR Int. [km/mol]**
1	7.4652	2.8797
2	21.6554	0.4836
3	31.8296	0.8007
4	45.1056	0.3993
5	61.0883	3.2003
6	99.9662	7.7802
7	176.7899	26.3202
8	190.2330	26.8829
9	212.6031	80.9785
10	214.8008	65.5508
11	229.1782	167.5034
12	238.5224	82.0767
13	255.2508	249.2937
14	283.6779	26.8213
15	291.4533	55.7068
16	356.4031	83.8068
17	417.6885	49.4695
18	428.1868	57.7373
19	460.8606	57.1370
20	508.1693	55.1486
21	660.2176	284.6155
22	690.3556	83.8851
23^t	754.6078	231.9718
24^t	824.4685	178.7024
25^{t*}	939.4045	72.3782
26^{t*}	992.4637	143.3107
27	1085.0300	25.7493
28	1202.3494	398.5316
29	1404.3401	4.1326
30	1450.6121	11.3947
31^b	1630.0596	190.6522
32^b	1643.5475	74.8871
33^b	1650.3969	67.4629
34^b	1671.1011	2.8373
35	1727.4428	643.7374
36	3082.2813	261.4632
37^{s*}	3180.6017	2093.2108
38^{s*}	3305.3198	591.1162
39^s	3439.5143	1097.5194
40^s	3501.1192	960.3923
41^s	3594.2178	538.8467
42^f	3844.3939	126.6809
43^f	3864.5499	125.4762
44^f	3865.8634	156.4890
45^f	3866.9802	55.7713

Note: ^{t}OH torsion; ^{b}OH scissoring; ^{s}OH stretching; ^{f}free OH; *vibrations contaminated by HCOOH modes.

Table 2.24: Harmonic IR frequencies and intensities of the complex $4H_2O/2HCOOH$ evaluated at the B2PLYP/maug-cc-pVTZ level (Gorai et al., 2020a).

NM	ω **[cm^{-1}]**	**IR Int. [km/mol]**
1	4.6054	0.4281
2	13.0063	2.9178
3	16.5189	0.8051
4	19.0314	2.3774
5	20.9593	2.6393
6	33.4976	0.4467
7	36.7713	1.8500
8	42.5055	1.8790
9	57.0477	3.6453
10	87.6438	1.4306
11	98.3938	9.9521
12	109.3757	0.0813
13	179.0412	24.1400
14	190.5090	28.2740
15	214.0975	84.9229
16	218.8524	55.4812
17	230.2931	171.1476
18	238.6575	89.3090
19	267.3732	231.1914
20	283.3954	21.6224
21	299.6074	70.4602
22	358.3291	97.5174
23	418.1841	53.6749
24	433.0143	50.5761
25	453.3466	44.2133
26	511.7339	57.2963
27	626.1257	81.2731
28	663.5082	202.0801
29	664.5570	266.9661
30	690.0285	82.0272
31^t	746.7845	238.4794
32^t	832.5630	181.3816
33^{t*}	936.5175	‘ 69.8256
34^{t*}	992.1307	142.3809
35	1086.4569	25.8243
36	1100.7355	4.5531
37	1117.2066	421.1594
38	1202.1232	398.7897
39	1301.5992	19.3272
40	1403.7379	3.7351
41	1441.6206	5.0048
42	1449.0432	11.3813
43^b	1630.1114	189.4041
44^b	1643.0592	75.7767
45^b	1650.4443	71.8600
46^b	1671.6065	3.7550
47	1727.3571	640.6790
48	1740.9364	573.8795
49	3082.1544	256.8737
50^{s*}	3108.5982	9.0680
51^{s*}	3182.8047	2058.2321
52^{s*}	3311.8175	593.5776
53^s	3443.5223	1123.8585
54^s	3495.5861	975.1779
55^s	3593.0205	538.1736
56	3722.9218	111.6916
57^f	3843.8168	126.4406
58^f	3860.4740	132.4083
59^f	3863.8070	104.3051
60^f	3865.7512	106.7733

Note: ^{t}OH torsion; ^{b}OH scissoring; ^{s}OH stretching; ^{f}free OH; *vibrations contaminated by HCOOH modes.

Table 2.25: Harmonic IR frequencies and intensities of the complex $4H_2O/3HCOOH$ evaluated at the B2PLYP/maug-cc-pVTZ level (Gorai et al., 2020a).

NM	ω [**cm**$^{-1}$]	**IR Int. [km/mol]**	**NM**	ω [**cm**$^{-1}$]	**IR Int. [km/mol]**
1	4.8748	0.5689	51	1400.7389	2.9534
2	8.5054	0.7327	52	1440.0730	5.2611
3	10.9091	1.7844	53	1445.8193	12.3688
4	14.1204	2.2282	54	1445.9512	8.9357
5	16.8372	1.6310	55^b	1630.5379	192.0093
6	19.1432	3.8603	56^b	1645.2809	74.7331
7	22.9673	0.5549	57^b	1649.3090	90.0689
8	28.0702	2.8070	58^b	1670.3929	1.3964
9	34.3674	0.6429	59	1729.0788	813.5933
10	40.7401	1.8661	60	1729.3363	445.0961
11	45.9916	0.3401	61	1741.9079	575.8421
12	54.8514	5.3280	62	3085.0941	261.1337
13	66.6228	5.5016	63	3085.5154	98.0625
14	89.0988	1.1463	64	3110.4187	7.6777
15	99.3575	2.6618	65^{s*}	3215.3096	2288.1686
16	110.9935	9.9385	66^{s*}	3232.6395	1833.2038
17	174.0921	44.5063	67^{s*}	3306.6741	311.8714
18	177.9118	30.6049	68^s	3451.6305	978.9670
19	188.6541	24.0948	69^s	3473.6093	894.3564
20	209.4056	83.4103	70^s	3609.3777	516.6451
21	212.1508	55.0788	71	3723.4615	111.6932
22	234.2838	28.4231	72^f	3838.2715	172.2543
23	245.2791	210.0525	73^f	3841.3048	97.0635
24	261.2989	35.4759	74^f	3857.9521	119.5655
25	284.3732	27.8615	75^f	3865.5487	121.3331
26	314.1459	145.9808			
27	352.7412	77.0879			
28	410.7784	41.6288			
29	418.4381	142.3769			
30	451.8321	62.9268			
31	486.2526	26.6238			
32	515.8604	43.5007			
33	626.3452	78.8764			
34	658.3748	265.4010			
35	664.0178	196.3924			
36	686.9044	88.1977			
37	687.6686	73.9457			
38^{t*}	798.2680	156.7957			
39^t	803.7700	211.1567			
40^{t*}	926.7114	95.5456			
41	949.5463	177.0601			
42	1005.8276	134.0566			
43	1083.1613	20.4516			
44	1083.9241	23.7748			
45	1098.4056	4.7221			
46	1118.0234	421.3278			
47	1198.2543	380.9330			
48	1198.3514	418.6655			
49	1303.1561	18.8667			
50	1400.6093	4.0266			

Note: ^{t}OH torsion; ^{b}OH scissoring; ^{s}OH stretching; ^{f}free OH; *vibrations contaminated by HCOOH modes.

Table 2.26: Harmonic IR frequencies and intensities of the complex $4H_2O/4HCOOH$ evaluated at the B2PLYP/maug-cc-pVTZ level (Gorai et al., 2020a).

NM	ω **[cm^{-1}]**	**IR Int. [km/mol]**	**NM**	ω **[cm^{-1}]**	**IR Int. [km/mol]**
1	5.2521	0.5902	51	1082.2723	15.9752
2	6.6193	1.2706	52	1082.8090	29.1817
3	8.8369	0.8598	53	1083.2383	8.1740
4	9.6756	1.0009	54	1096.9310	4.7996
5	14.2363	3.0419	55	1118.5677	421.7245
6	15.7986	1.1225	56	1194.7613	402.1943
7	18.3559	3.0357	57	1196.6655	678.8383
8	19.2707	2.7650	58	1196.9390	124.3700
9	22.1555	0.9922	59	1303.5269	19.2431
10	27.4779	3.1848	60	1398.1664	2.8858
11	30.7377	0.4104	61	1399.8325	2.3693
12	36.6940	0.3940	62	1400.1243	3.6218
13	42.5989	1.4605	63	1438.1358	3.4116
14	50.4443	2.9039	64	1443.1291	10.6650
15	56.1885	2.0333	65	1444.6815	8.9685
16	67.8597	3.6648	66	1445.0393	12.6099
17	79.8514	11.6336	67^b	1633.0557	204.1450
18	88.6848	0.8582	68^b	1645.9171	94.0994
19	101.4052	1.0586	69^b	1651.0001	68.5795
20	120.4063	2.7295	70^b	1672.8271	2.1359
21	173.0431	53.0876	71	1729.8409	773.0317
22	174.6165	79.9014	72	1729.9568	580.0062
23	181.6174	16.9912	73	1730.9646	527.5802
24	193.2247	8.7228	74	1742.3118	572.3800
25	207.4059	98.2327	75	3086.2791	171.0952
26	209.4436	56.3457	76	3087.0204	182.6391
27	214.9922	15.9518	77	3087.9488	105.7546
28	251.9141	48.3664	78	3114.3577	6.5557
29	260.0519	27.0848	79^{s*}	3235.8092	2226.0999
30	277.2414	21.6313	80	3251.6769	2145.0628
31	294.7764	138.3103	81^{s*}	3269.8018	1271.6200
32	370.6813	53.2423	82^{s*}	3338.7804	329.7573
33	411.5523	157.3717	83^s	3451.7939	830.3998
34	426.8010	160.0370	84^s	3506.2315	849.9293
35	432.4841	46.3694	85^s	3580.2425	496.8387
36	474.7455	4.1043	86	3723.2687	112.7727
37	500.7327	25.1590	87^f	3837.0764	199.2805
38	506.2341	58.6370	88^f	3839.9016	135.3088
39	626.8822	79.1196	89^f	3841.2858	85.4332
40	662.8116	197.7640	90^f	3859.2614	129.2712
41^{t*}	680.2702	165.0245			
42^{t*}	685.5338	74.2193			
43^{t*}	685.8711	129.0114			
44^t	703.1086	134.5453			
45^t	777.4948	157.2018			
46^{t*}	836.4350	145.9547			
47	918.5370	51.5171			
48	934.3780	130.8642			
49	940.6167	399.9756			
50	1005.3540	55.4131			

Note: ^{t}OH torsion; ^{b}OH scissoring; ^{s}OH stretching; ^{f}free OH; *vibrations contaminated by HCOOH modes.

Table 2.27: Linear fit coefficients for the $H_2O - X$ (X = HCOOH, NH_3, CH_3OH, CO, CO_2, H_2CO, CH_4, OCS, N_2, and O_2) mixtures[a] (Gorai et al., 2020a).

Mixture	Vibrational mode	Linear coefficients	
		Constant [10^{-16} cm molecule^{-1}]	Slope [10^{-19} cm molecule^{-1}]
$H_2O - HCOOH$	$\nu_{libration}$	2.45 (0.26)[b]	132.73 (0.90)[b]
	$\nu_{bending}$	0.58 (0.05)[b]	184.25 (14.40)[b]
	$\nu_{stretching}$	1.80 (1.90)[b]	48.60 (-7.30)[b]
	ν_{freeOH}	0.20 (0.16)[b]	9.80 (-0.40)[b]
$H_2O - NH_3$	$\nu_{libration}$	0.27 (0.34)[b]	6.11 (5.00)[b]
	$\nu_{bending}$	0.09 (0.12)[b]	5.48 (2.20)[b]
	$\nu_{stretching}$	1.90 (2.38)[b]	0.41 (-14.4)[b]
	ν_{freeOH}	0.21 (0.12)[b]	-4.21 (-2.1)[b]
$H_2O - CH_3OH$	$\nu_{libration}$	0.25	10.0
	$\nu_{bending}$	0.12	2.00
	$\nu_{stretching}$	1.92	32.00
	ν_{freeOH}	0.26	2.65
$H_2O - CO$	$\nu_{libration}$	0.30 (0.30±0.02)[c]	-0.32 (-2.1±0.4)[c]
	$\nu_{bending}$	0.12 (0.13±0.02)[c]	-0.016 (-1.0 ±0.3)[c]
	$\nu_{stretching}$	1.98 (2.0±0.1)[c]	-3.2 (-16±3)[c]
	ν_{freeOH}	0.18 (0.0)[c]	5.69 (1.2 ±0.1)[c]
$H_2O - CO_2$	$\nu_{libration}$	0.3 (0.32±0.02)[d]	2.07 (-3.2±0.4)[d]
	$\nu_{bending}$	0.11 (0.14±0.01)[d]	0.12 (-0.5±0.2)[d]
	$\nu_{stretching}$	2.02 (2.1±0.1)[d]	-0.22 (-22±2)[d]
	ν_{freeOH}	0.19 (0.0)[d]	10.02 (1.62±0.07)[d]
$H_2O - H_2CO$	$\nu_{libration}$	0.26	5.73
	$\nu_{bending}$	0.10	4.59
	$\nu_{stretching}$	1.92	0.10
	ν_{freeOH}	0.13	16.53
$H_2O - CH_4$	$\nu_{libration}$	0.31	0.53
	$\nu_{bending}$	0.11	1.18
	$\nu_{stretching}$	2.01	3.39
	ν_{freeOH}	0.20	0.52
$H_2O - OCS$	$\nu_{libration}$	0.30	0.42
	$\nu_{bending}$	0.11	0.23
	$\nu_{stretching}$	1.96	2.18
	ν_{freeOH}	0.17	0.13
$H_2O - N_2$	$\nu_{libration}$	0.31	-0.30
	$\nu_{bending}$	0.12	0.17
	$\nu_{stretching}$	0.12	0.11
	ν_{freeOH}	0.17	7.75
$H_2O - O_2$	$\nu_{libration}$	0.31	-0.23
	$\nu_{bending}$	0.12	-0.13
	$\nu_{stretching}$	2.02	4.71
	ν_{freeOH}	0.13	13.80

Note:
[a] Experimental values are provided in the parentheses.
[b] This work.
[c] Bouwman et al. (2007).
[d] Öberg et al. (2007).

Table 2.28: Harmonic IR frequencies and intensities of the complex $4H_2O/NH_3$ evaluated at the B2PLYP/maug-cc-pVTZ level (Gorai et al., 2020a).

NM	ω **[cm^{-1}]**	**IR Int. [km/mol]**
1	17.4723	1.6404
2	24.2573	2.7053
3	42.9718	9.2433
4	56.2828	14.2890
5	77.4675	5.3857
6	176.7386	14.5514
7	205.9991	61.5386
8	210.2974	51.1840
9	220.3754	138.5385
10	234.6966	41.4586
11	240.2432	175.3537
12	253.5984	22.5694
13	262.9908	199.8180
14	269.0541	36.5738
15	288.0112	25.8883
16	411.0477	10.8123
17	438.1929	57.2835
18	462.1627	115.4840
19	649.2280	90.3859
20^t	673.7378	245.4033
21^t	761.0067	286.3846
22^t	785.5912	213.8984
23^t	855.6009	110.1452
24	973.8257	54.6453
25	1133.1043	207.9712
26^b	1635.5747	161.1828
27^b	1648.9602	81.2871
28^{b*}	1654.1532	68.4123
29	1659.8070	23.9527
30^{b*}	1664.0270	13.9746
31^{b*}	1687.1189	4.9894
32^s	3278.5997	1998.0299
33^s	3358.0759	412.2786
34^s	3442.1676	1170.0672
35	3483.9230	0.6553
36^s	3499.4250	959.9493
37^s	3600.3604	714.2057
38	3600.7264	13.1052
39	3601.5192	18.8438
40^f	3865.2764	131.5539
41^f	3866.4890	96.2050
42^f	3867.7812	62.0566

Note: ^{t}OH torsion; ^{b}OH scissoring; ^{s}OH stretching; ^{f}free OH; *vibrations contaminated by NH_3 modes.

Table 2.29: Harmonic IR frequencies and intensities of the complex $4H_2O/2NH_3$ evaluated at the B2PLYP/maug-cc-pVTZ level (Gorai et al., 2020a).

NM	ω **[cm^{-1}]**	**IR Int. [km/mol]**
1	13.2137	3.5154
2	35.8031	4.5193
3	37.7152	15.3999
4	42.6399	0.6394
5	44.0908	1.0833
6	50.2282	25.2398
7	62.5104	1.7351
8	74.8511	7.5826
9	174.7854	0.3931
10	184.1028	49.5918
11	202.3520	59.3483
12	215.2501	3.8987
13	233.8400	170.4567
14	236.8583	13.8898
15	250.5424	28.2234
16	252.5110	43.5646
17	263.8678	24.6139
18	264.6765	198.4026
19	280.7045	30.8723
20	288.8026	34.1641
21	434.2362	2.5448
22	465.8322	178.0575
23	636.4757	5.8561
24	665.1100	92.9446
25^t	688.2585	220.0675
26^t	740.4480	369.3099
27^t	786.8028	188.6747
28^t	823.9109	101.1914
29^t	894.7322	182.6960
30^t	973.9338	41.1551
31	1131.1976	200.1314
32	1131.3535	216.3485
33^b	1643.5894	150.8608
34^b	1651.7575	100.8326
35^{b*}	1656.3567	54.5510
36^{b*}	1659.4699	6.3334
37	1660.0271	21.6415
38	1660.6689	23.4365
39^{b*}	1680.0902	25.5517
40^{b*}	1690.1602	1.1013
41^s	3300.1629	879.2415
42^s	3307.6453	2808.4413
43^s	3377.2024	646.7542
44^s	3391.5768	729.5638
45	3483.7965	0.9990
46	3483.9555	1.0499
47^s	3578.8775	1603.7262
48^s	3582.2181	63.0838
49	3600.8734	18.3990
50	3600.9540	18.6472
51	3601.2568	18.6290
52	3601.5982	18.6555
53^f	3866.9165	77.0140
54^f	3867.0372	90.8323

Note: ^{t}OH torsion; ^{b}OH scissoring; ^{s}OH stretching; ^{f}free OH; *vibrations contaminated by NH_3 modes.

Table 2.30: Harmonic IR frequencies and intensities of the complex $4H_2O/3NH_3$ evaluated at the B2PLYP/maug-cc-pVTZ level (Gorai et al., 2020a).

NM	ω [**cm**$^{-1}$]	**IR Int. [km/mol]**	**NM**	ω [**cm**$^{-1}$]	**IR Int. [km/mol]**
1	12.5470	2.6010	51^{s}	3360.1503	1320.9055
2	23.2847	18.0759	52^{s}	3374.8469	2291.7299
3	28.7571	23.4249	53^{s}	3393.0086	199.4039
4	35.7710	0.3934	54^{s*}	3478.9512	630.0948
5	38.9667	0.0081	55	3483.7372	1.4326
6	40.5045	3.8999	56	3483.7543	6.5600
7	44.8244	0.2126	57^{s*}	3484.7724	142.9342
8	46.5267	10.5312	58^{s}	3520.0887	1009.6190
9	50.6992	8.8616	59^{s}	3596.2284	723.7876
10	69.7890	5.0744	60	3600.8160	17.3429
11	72.6524	9.5767	61	3600.9676	17.3826
12	166.7922	5.9217	62	3601.0701	18.0350
13	180.8039	37.7349	63	3601.4302	17.6940
14	191.1116	39.0754	64	3601.4607	18.0960
15	207.3981	10.9113	65	3601.5560	18.1230
16	226.1385	96.0046	66^{f}	3867.3234	81.2889
17	239.4714	55.1417			
18	245.0773	9.5193			
19	245.6175	62.3353			
20	248.1708	26.4263			
21	249.2122	68.1865			
22	258.4416	35.6050			
23	269.5283	80.6776			
24	272.4683	30.5828			
25	285.7225	20.2189			
26	453.0415	74.3332			
27	625.3188	29.7964			
28	647.1033	149.3482			
29	670.2563	144.8666			
30	705.1954	132.9061			
31^{t}	747.2466	332.8596			
32^{t}	768.5970	229.7125			
33^{t}	809.9923	25.6758			
34^{t}	842.7130	230.7932			
35^{t}	871.0453	187.0537			
36^{t}	977.2613	31.3718			
37	1126.3891	215.3444			
38	1128.4031	174.0675			
39	1128.4565	237.3456			
40^{b}	1645.9709	133.6692			
41^{b*}	1654.7182	86.0037			
42^{b*}	1655.6708	67.1056			
43^{b*}	1658.8667	1.5603			
44	1659.6806	25.9239			
45	1660.1304	26.0074			
46	1660.3043	24.5183			
47^{b*}	1672.4596	26.6593			
48^{b*}	1678.8129	23.6462			
49^{b}	1693.1435	0.5825			
50^{s}	3302.1390	1539.8513			

Note: ^{t}OH torsion; ^{b}OH scissoring; ^{s}OH stretching; ^{f}free OH; *vibrations contaminated by NH_3 modes.

Table 2.31: Harmonic IR frequencies and intensities of the complex $4H_2O/4NH_3$ evaluated at the B2PLYP/maug-cc-pVTZ level (Gorai et al., 2020a).

NM	ω **[cm^{-1}]**	**IR Int. [km/mol]**	**NM**	ω **[cm^{-1}]**	**IR Int. [km/mol]**
1	4.9193	4.9769	51	1659.5005	30.4815
2	9.0775	2.0942	52	1659.5303	21.8453
3	17.7847	11.5017	53	1660.0190	25.0784
4	19.1211	1.0599	54	1660.1436	28.1216
5	22.4392	0.6988	55^{b*}	1673.3466	67.4843
6	25.9838	0.4032	56^{b*}	1674.2718	0.3138
7	27.6254	26.7443	57^{b}	1688.6077	33.8790
8	35.4482	23.6215	58^{b}	1691.9499	0.0133
9	39.7909	2.7928	59^{s}	3369.6234	0.2819
10	42.1429	0.1113	60^{s}	3385.6965	2574.9240
11	46.9852	0.0030	61^{s}	3387.6855	2801.0441
12	62.8166	0.0005	62^{s}	3394.0812	0.7615
13	72.1392	0.0251	63^{s*}	3473.3538	0.1108
14	74.9466	18.9444	64	3483.3149	13.0568
15	158.5797	0.0024	65	3483.4935	11.1778
16	174.6287	36.1323	66	3483.6384	2.6130
17	178.2147	35.4550	67^{s*}	3484.6015	0.0846
18	201.4197	0.0105	68^{s}	3507.3380	1567.4274
19	233.9639	3.4824	69^{s}	3510.2809	1820.7051
20	235.9429	83.2509	70^{s}	3536.4083	0.1714
21	237.2040	33.3809	71	3600.7487	17.4948
22	239.2784	72.0949	72	3600.7879	17.3727
23	239.6302	3.0360	73	3600.9757	17.5063
24	242.2423	80.4390	74	3601.0932	17.3475
25	243.0833	36.6777	75	3601.1747	17.5682
26	246.3526	2.0432	76	3601.2866	17.5694
27	261.6961	0.8343	77	3601.4175	17.2943
28	266.9875	0.6015	78	3601.5786	17.6734
29	269.0885	42.6136			
30	273.9278	71.7557			
31^{t}	613.8454	0.0116			
32	630.4192	212.2155			
33	666.2987	0.0041			
34	670.4647	0.0071			
35	700.3570	199.6747			
36	744.5970	379.8388			
37^{t}	755.9618	361.3020			
38^{t}	799.7584	0.0050			
39^{t}	815.2370	0.3721			
40^{t}	825.5015	342.7098			
41^{t}	846.8651	297.2880			
42^{t}	946.2925	0.0017			
43	1125.1644	153.1328			
44	1125.2155	143.7533			
45	1125.4081	503.2784			
46	1125.4766	35.6108			
47^{b*}	1654.5148	120.1771			
48^{b*}	1654.8637	41.6854			
49^{b*}	1657.2551	58.5445			
50^{b*}	1657.8279	12.4900			

Note: ^{t}OH torsion; ^{b}OH scissoring; ^{s}OH stretching; ^{f}free OH; *vibrations contaminated by NH_3 modes.

stretching mode) are shown in Figure 2.28b. Mixing ratios are derived by measuring the areas of the selected bands for the H_2O band (at 2220 cm^{-1}) (Mastrapa et al., 2009) and for NH_3 (umbrella mode band at 1070 cm^{-1}) (D'Hendecourt, 1986), with a procedure analogous to that introduced in the previous Section for HCOOH.

Figure 2.25c shows the optimized geometry of the $H_2O - NH_3$ system with a 4 : 4 ratio as obtained from our quantum chemical calculations. Figure 2.31 depicts the absorption band profiles of $H_2O - NH_3$ mixtures with various concentrations. The transition frequencies and the corresponding intensity values are provided in Table 2.21 as well. The vibrational analysis is also carried out at a higher-level theory, thereby using the B2PLYP functional. The results are reported in Tables 2.28−2.31. Figure 2.30b shows the band strengths as a function of the impurity concentration under consideration, i.e., NH_3.

Comparison between experiment and simulations

In Figure 2.32, the comparison between experimentally obtained spectra and our computed spectra for pure water, the $H_2O - HCOOH$ mixture, and $H_2CO - NH_3$ mixture is shown. We note a good agreement between experimental and theoretical absorption spectra. Figure 2.33 shows the comparison between the experimental (dotted lines) and theoretical (solid and dashed lines) band strengths of the four water bands as a function of the concentration of HCOOH and NH_3. From Figure 2.33, it is evident that the experimental strength of the libration and bending modes increases by increasing the concentration of HCOOH. On the contrary, the strength of the stretching and free OH modes shows a decreasing trend. These behaviors should be compared with the B2PLYP/mug-cc-pVTZ (dashed) and B3PLYP/6-31G(d) (solid) trends. For the libration and bending band strength profiles, there is a qualitative agreement with experiments. However, in the stretching and free OH modes, theoretical band strength profiles deviate from experimental work. The lack of experimental data in the 3600−4000 cm^{-1} range (see Figure 2.28a) may contribute to this disagreement. By comparing the two levels of theory, it is noted that there is a rather good agreement. In the $H_2O - HCOOH$ mixture, HCOOH can act as both an H-bond donor and an H-bond acceptor. We consider both interactions. We note that if we consider HCOOH as an H-bond acceptor, the band strengths of the three modes (libration, bending, and stretching) are lower relative to the case where HCOOH is treated as the H-bond donor. However, in the free OH mode, the band strength slope increases (See Figure 2.34).

Moving to ammonia, the experimental data of Figure 2.33 show that the band

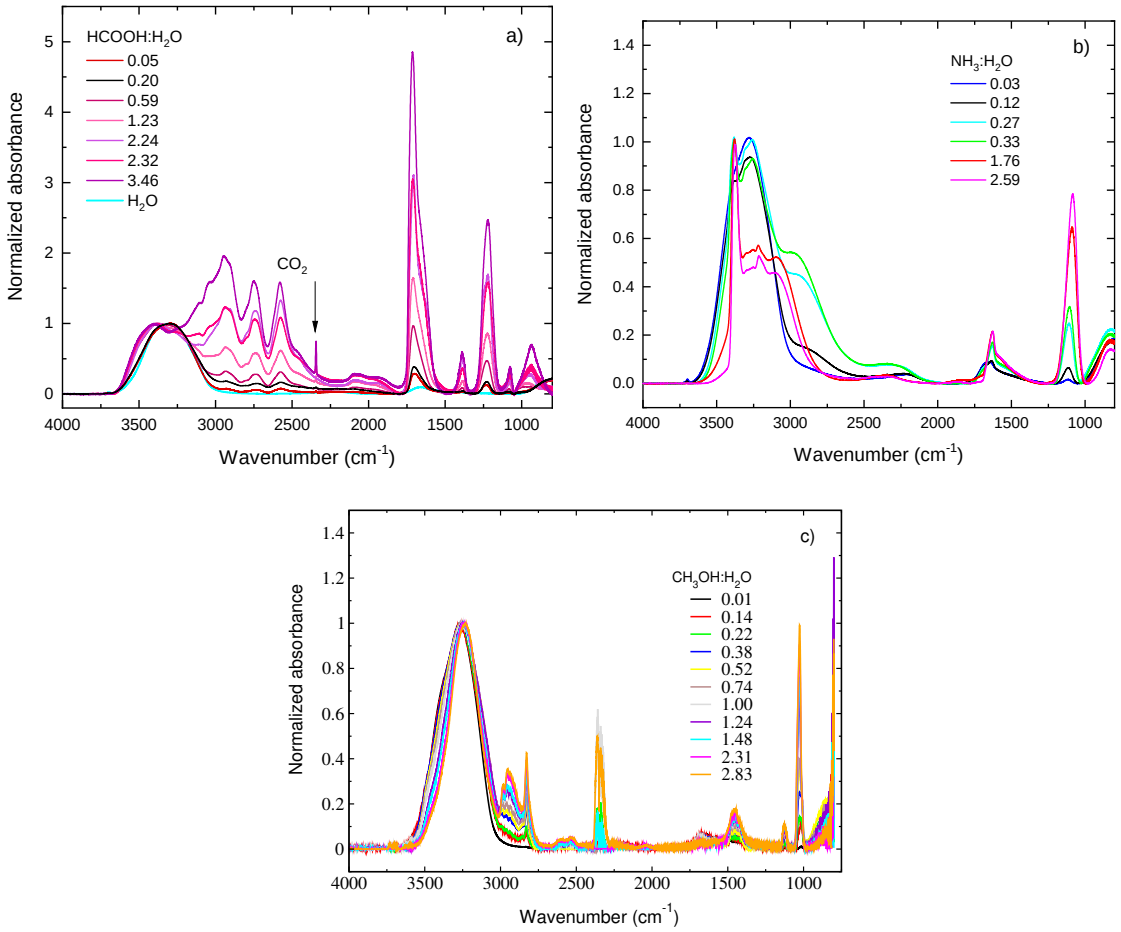

Figure 2.28: (a) IR spectra for different $HCOOH : H_2O$ ice mixtures deposited at $T = 20$ K. (b) IR spectra for different $NH_3 : H_2O$ ice mixtures deposited at $T = 20$ K. (c) IR spectra for different $CH_3OH : H_2O$ ice mixtures deposited at $T = 30$ K. The color legend is explained in the insets. All IR spectra are normalized with respect to the $O - H$ stretching band (Gorai et al., 2020a).

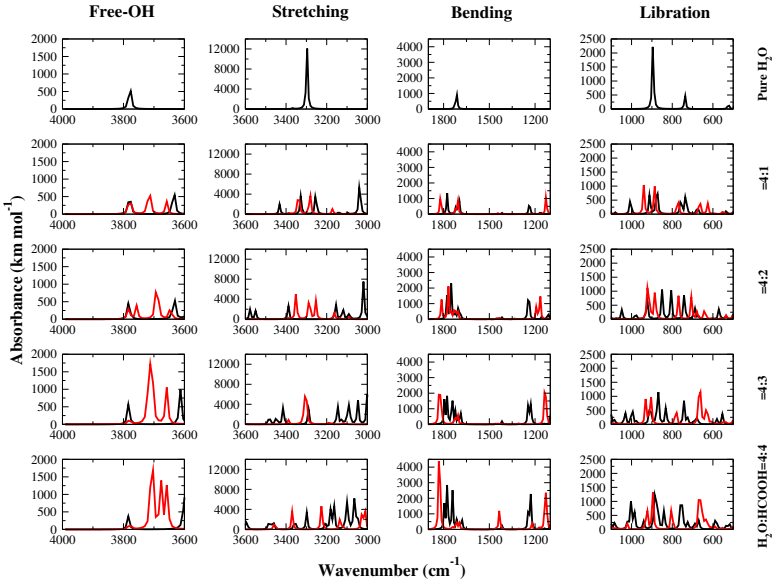

Figure 2.29: Absorption spectra of the four modes for water ice for the five measured compositions, ranging from pure water ice (top) to 4 : 4 $H_2O - HCOOH$ mixture (bottom). The black line represents the absorbance spectra of various concentration of $H_2O - HCOOH$, where HCOOH is used as a hydrogen bond donor, and for the red line, HCOOH is used as a hydrogen bond acceptor (Gorai et al., 2020a).

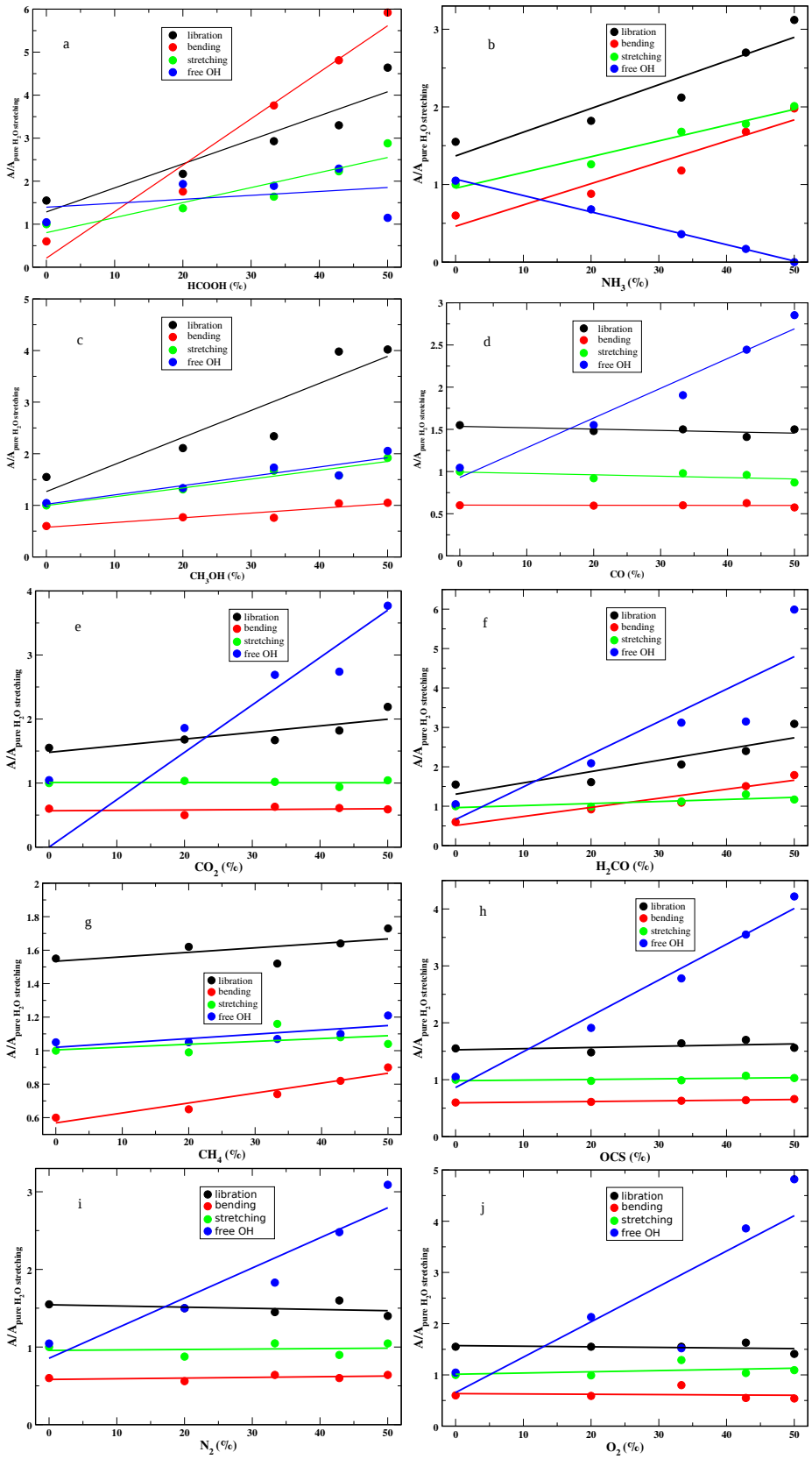

Figure 2.30: Band strengths of the four fundamental vibration modes of water for (a) H_2O – HCOOH, (b) H_2O – NH_3, (c) H_2O – CH_3OH, (d) H_2O – CO, (e) H_2O – CO_2, (f) H_2O – H_2CO, (g) H_2O – CH_4, (h) H_2O – OCS, (i) H_2O – N_2, and (j) H_2O – O_2 clusters with various concentrations. The water c-tetramer configuration was used for pure water (Gorai et al., 2020a).

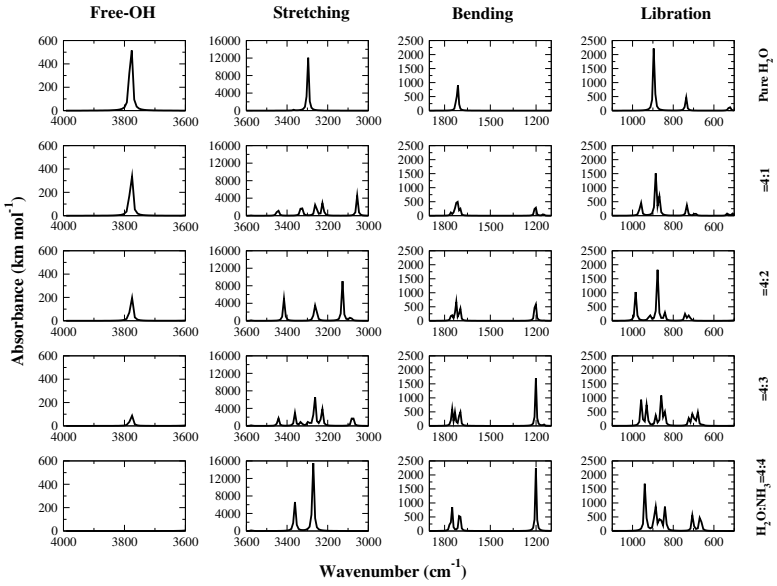

Figure 2.31: Absorption spectra of the four modes for water ice for the five measured compositions, ranging from pure water ice (top) to $4:4$ $H_2O - NH_3$ mixture (bottom) (Gorai et al., 2020a).

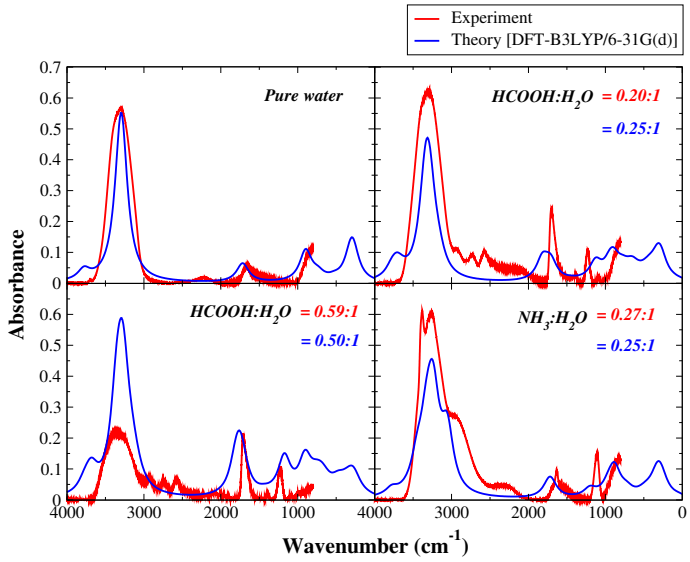

Figure 2.32: Comparison of computed and experimental IR spectra ($0 - 4000$ cm^{-1}) for pure water as well as water with HCOOH and NH_3 as impurities. We have used harmonic frequencies for the computed spectra, and the intensity is scaled with a factor 1000 to have the best match with the experimental one (Gorai et al., 2020a).

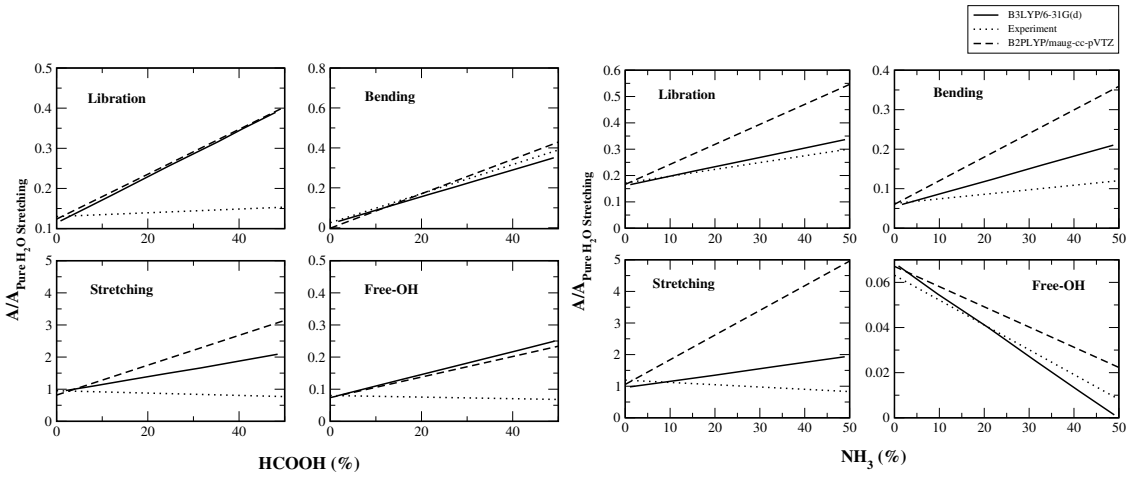

Figure 2.33: Comparison between the calculated and experimental band strength profiles with various concentration of HCOOH and NH_3 (Gorai et al., 2020a).

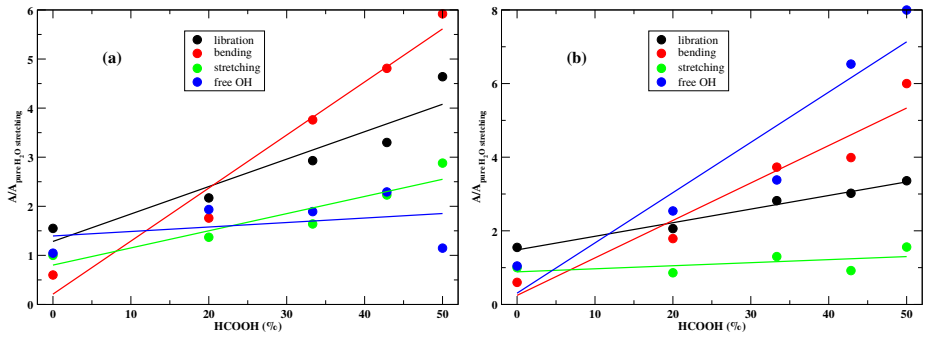

Figure 2.34: Band strength for H_2O – HCOOH mixtures: (a) HCOOH as an H-bond donor and (b) HCOOH as an H-bond acceptor (Gorai et al., 2020a).

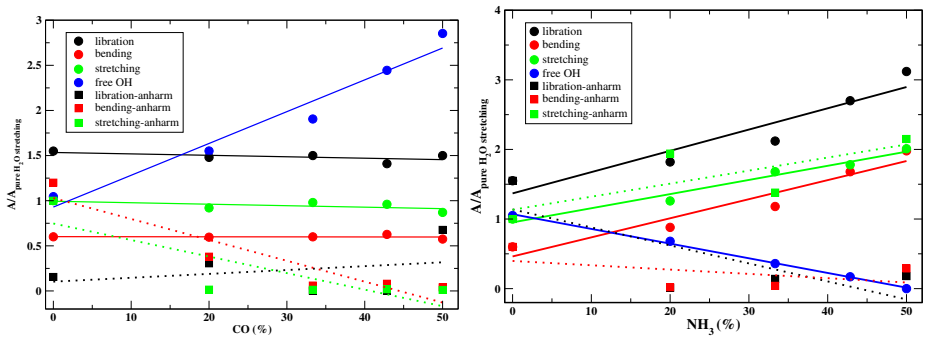

Figure 2.35: Filled circles are the data points where we considered harmonic frequencies and the corresponding fitted profiles are the solid lines. Solid filled squares represent the data sets where we considered anharmonic frequencies and the corresponding fitted results are the dotted lines (Gorai et al., 2020a).

strength of the free OH stretching mode nearly vanishes when a 50% concentration of the impurity (NH_3) is reached. This feature interestingly supports our calculated spectra shown in the last panel of Figure 2.31. Instead, libration and bending modes have an opposite trend, with the band strength increasing by increasing the concentration of NH_3. The band strength of the stretching mode shows a slightly decreasing trend with the concentration of NH_3. From the inspection of Figure 2.33, it is evident that both sets of theoretical results (B3LYP and B2PLYP) are in reasonably good agreement with experimental data for the libration, bending, and free OH modes. Interestingly, the results obtained using the lower level of theory are in better agreement with experiments. In Figure 2.35, the comparison of band strengths evaluated using (a) harmonic and (b) anharmonic calculations is shown. We only consider fundamental bands in the 0 to 3600 cm^{-1} frequency range to investigate the effect of anharmonicity on the band strengths. From our experimental study on the $H_2O - NH_3$ system, as already mentioned, we obtain an increasing trend of the band strength for the libration, bending, and stretching modes with the increase in the concentration of NH_3. In contrast, the band strength decreases for the free OH mode and becomes zero with a 50% concentration of NH_3. We find similar trends to those obtained from the experiment using harmonic calculations for all four fundamental modes. However, if we consider anharmonic estimates, only the behavior of the stretching mode is well reproduced. All other modes deviate from the experimental results. While we are not claiming that harmonic calculations are better than the anharmonic ones, this comparison suggests that the former show a better error compensation. A similar outcome is obtained for the $H_2O - CO$ system

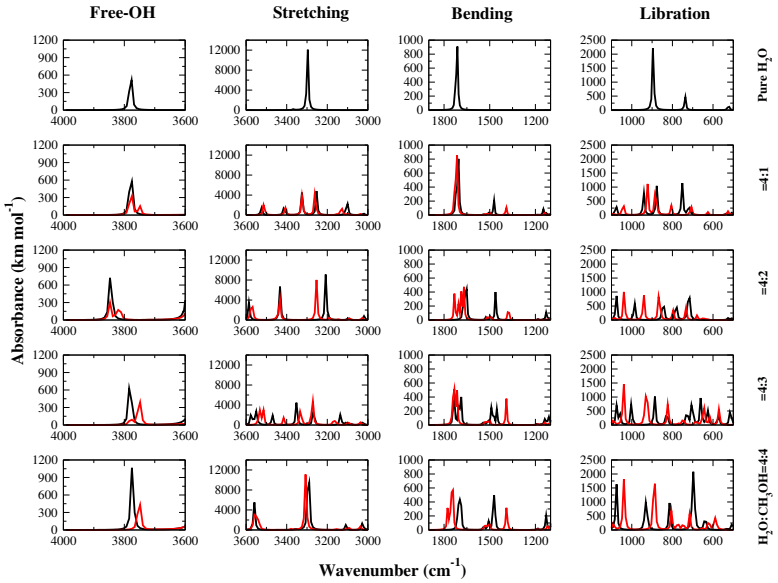

Figure 2.36: Absorption spectra of the four modes for water ice for the five measured compositions, ranging from pure water ice (top) to 4 : 4 $H_2O - CH_3OH$ mixture (bottom). The black line represents the absorbance spectra of various concentrations of H_2O-CH_3OH, where CH_3OH is used as a hydrogen bond donor, and for the red line, CH_3OH is used as a hydrogen bond acceptor (Gorai et al., 2020a).

and will be briefly addressed later in the text.

Based on the comparisons discussed above, the B3LYP/6-31G(d) level of theory provides reliable results. Therefore, it is employed in the following investigations. First of all, we compare the computed band strengths with the experiments for the $H_2O - CH_3OH$, $CO - H_2O$, and $CO_2 - H_2O$ mixtures to support their suitability.

CH_3OH ice

The effect of the CH_3OH concentration on the band profiles of water ice has been experimentally investigated. In the case of methanol, CO_2 gas is still present in the system (i.e., outside the vacuum chamber) in quantities that vary in time, causing negative and/or positive contributions to CO_2 gas-phase absorption features concerning the background spectrum, as is evident in Figure 2.28c at $\sim$2340 cm^{-1}. Such contamination is most likely due to the dosing line, but its negligible amount should not affect the final results. Figure 2.28c shows the experimental absorption spectra for various $CH_3OH - H_2O$ ice mixtures deposited at $T = 30$ K. The spectra are normalized to 1 with respect to the maximum of the $O - H$ stretch band.

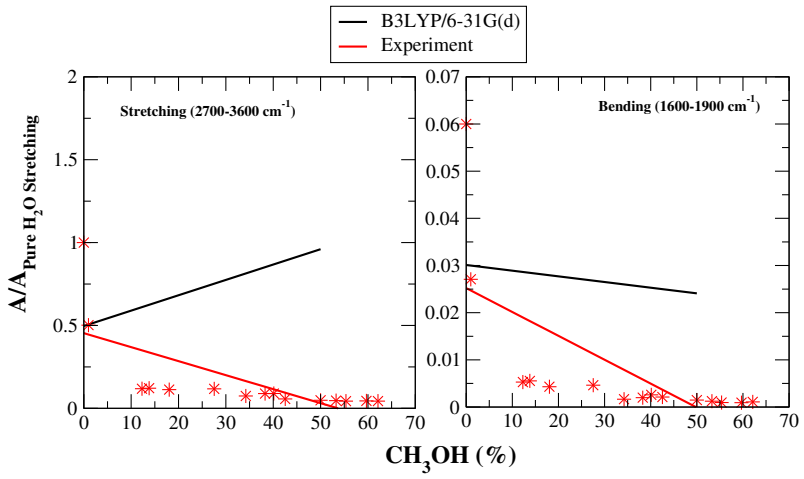

Figure 2.37: Comparison between calculated and experimentally fitted band strength profiles as a function of CH_3OH concentration. Stars represent the experimental data points (Gorai et al., 2020a).

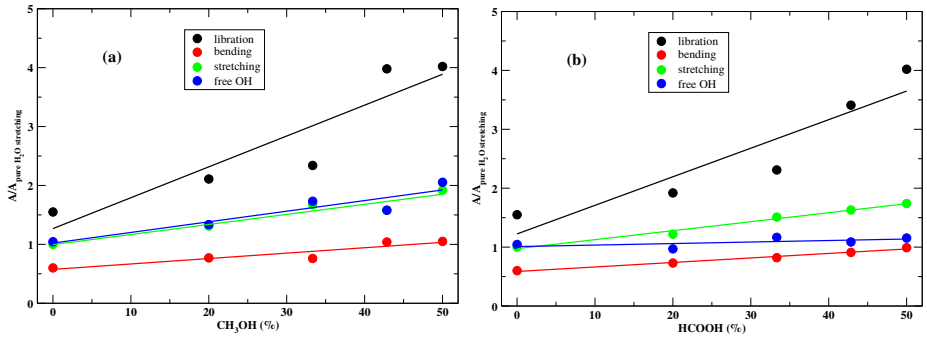

Figure 2.38: Band strength for $H_2O - CH_3OH$ mixtures: (a) CH_3OH as a hydrogen bond donor and (b) CH_3OH as a hydrogen bond acceptor (Gorai et al., 2020a).

Figure 2.25d shows the optimized structure of the $H_2O - CH_3OH$ mixture with a 4 : 4 concentration ratio. It is noted that a weak hydrogen bond is expected to be formed. The simulated IR spectra for different concentrations are shown in Figure 2.36. Peak positions, integral absorption coefficients, and band assignments for various H_2O-CH_3OH mixtures are collected in Table 2.21. The computed band strengths as a function of different concentrations are shown in Figure 2.30c. The calculated strength of the bending mode gradually increases with CH_3OH concentration (see Figure 2.37; right panel), which is in qualitative agreement with the experimental results Dawes et al. (2016). In the stretching mode, computationally, a slightly increasing trend of the band strength is noted, whereas experimental results show an opposite trend (see Figure 2.37; left panel). Because of the lack of experimental spectra, we cannot compare the band strength of the libration and free OH modes. In $H_2O - CH_3OH$ mixtures, methanol can act as an H-bond donor and an H-bond acceptor. We consider both possibilities and find that if we consider methanol as an H-bond donor, the band strength of all four modes shows an increasing trend. On the other hand, if we consider methanol as an H-bond acceptor, the band strengths of three modes, namely, libration, bending, and stretching, present trends similar to the previous case (where methanol acts as an H-bond donor), while the free OH band shows a less pronounced behavior (see Figure 2.38).

CO ice

Figure 2.25e depicts the $H_2O - CO$ optimized structure with a 4 : 4 concentration ratio: the four CO molecules interact with the H atoms of the H_2O molecules not involved in the H-bond (interaction of the O atom of CO with the H atom of H_2O). However, for the $H_2O - CO$ system, the interaction can occur through both O and C atoms of CO with the H atom of H_2O (Zamirri et al., 2018). Therefore, we consider both types of interaction and evaluated their effects on the band strengths. However, we do not find any considerable difference. Thus, we only discuss the band strength of the $H_2O - CO$ mixture with the interaction on the O side of CO. For completeness, it should be mentioned that there is also another type of interaction, which occurs between the π bond of CO and one water−hydrogen, and it gives rise to a T-shaped complex (Collings et al., 2014). However, according to a computational study by Collings et al. (2014), this has a negligible effect on IR vibrational bands. As a consequence, we do not investigate in detail this kind of complex. The simulated IR absorption spectra of the four fundamental vibrational modes for various compositions are shown in Figure 2.39. The four fundamental frequencies of water

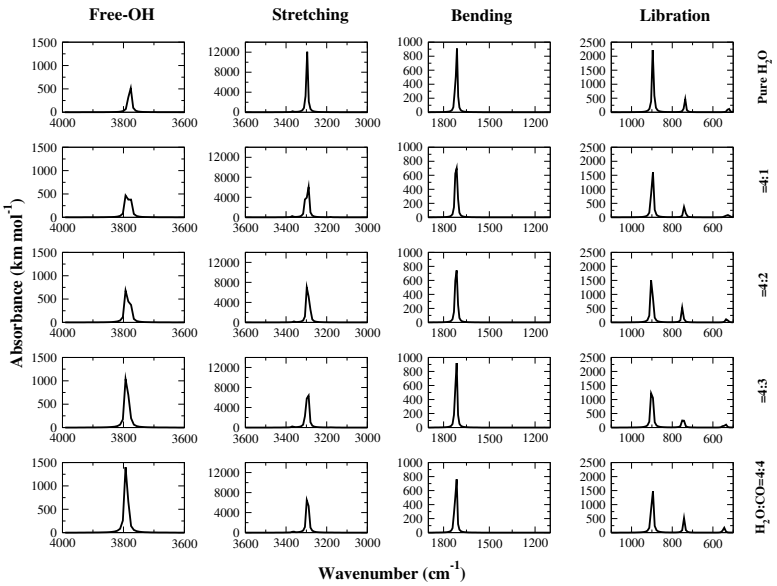

Figure 2.39: Absorption spectra of the four modes for water ice for the five measured compositions, ranging from pure water ice (top) to 4 : 4 $H_2O - CO$ mixture (bottom) (Gorai et al., 2020a).

ice change significantly by increasing the concentration of CO. The most intense peak positions and the corresponding integral abundance coefficients for different $H_2O - CO$ mixtures are provided in Table 2.21. In Figure 2.30d, the integrated intensities of water vibrational modes are plotted as a function of the CO concentration. It is noted that the strength of the libration, bending, and stretching modes decreases with the concentration of CO. However, the free OH mode shows a sharp increase in the band strength with increasing CO concentration. In Table 2.27, the resulting linear fit coefficients are collected together with the available experimental values for $H_2O - CO$ mixtures deposited at 15 K (Bouwman et al., 2007). It is noted that theoretical band strength slopes are in relatively good agreement with experimental results (Bouwman et al., 2007). For the $H_2O - CO$ system, anharmonic calculations are also carried out. While the band strengths of the bending and stretching modes have a similar trend to experimental data, a deviation is noted for the libration mode (see Figure 2.35).

To check the influence of dispersion, B3LYP-D3/6-31G(d) calculations are performed, with D3 denoting the correction for dispersion effects (Grimme et al., 2010). B3LYP-D3 calculations are carried out for $H_2O - CO$, $H_2O - CH_4$, $H_2O - N_2$, and $H_2O - O_2$ systems. Figure 2.40a shows the comparison of the band strengths of

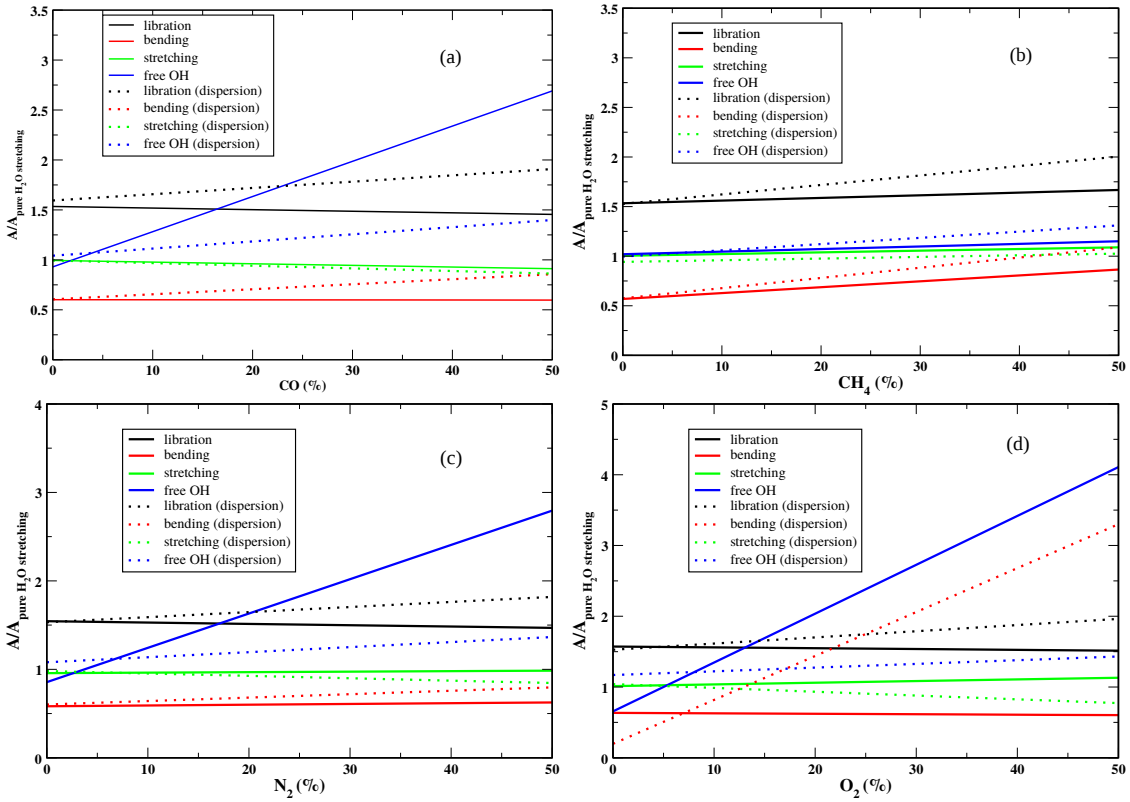

Figure 2.40: Comparison of the band strengths of the four fundamental modes of water for various mixtures of (a) $H_2O - CO$, (b) $H_2O - CH_4$, (c) $H_2O - N_2$, and (d) $H_2O - O_2$ by considering or not the dispersion effect (Gorai et al., 2020a).

different vibrational modes of water with and without the dispersion correction for the $H_2O - CO$ system. The overall conclusion is that there is a good agreement with the experimental band strengths when the dispersion effect is not considered. On the contrary, our computed band strength profile shows a different trend when the dispersion correction is included. The libration and bending modes present a positive slope with the increase in impurity concentration, whereas experimental results show a negative slope. For the free OH mode, a slightly increasing trend of the band strength is obtained, whereas the experimental band strength presents a sharp increase with CO concentration. The band strength of the stretching mode has similar behavior to dispersion and without dispersion and agrees with the experimental result (Bouwman et al., 2007, see Figure 3). Thus, in summary, while we are not claiming that the dispersion effects are not important for the systems investigated, we note that by neglecting them, we obtain a consistent description of the experimental behavior (probably due to a fortuitous error compensation).

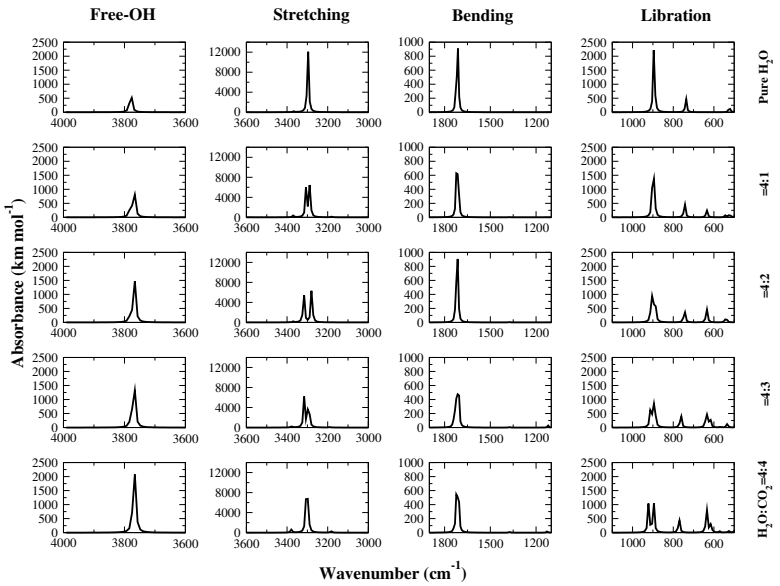

Figure 2.41: Absorption spectra of the four modes for water ice for the five measured compositions, ranging from pure water ice (top) to $4:4$ H_2O-CO_2 mixture (bottom) (Gorai et al., 2020a).

CO_2 ice

Figure 2.25f shows the optimized geometry of the $4:4$ mixture of H_2O-CO_2 system. The absorption features of water ice for different CO_2 concentrations are shown in Figure 2.41. The most intense frequencies for the various H_2O-CO_2 mixtures are also summarized in Table 2.21. The trend of the band strength as a function of CO_2 concentrations is shown in Figure 2.30e. For the free OH mode, a rapid increase with CO_2 concentration is noted, which agrees with the experimental results by Öberg et al. (2007). Computed band strengths of the libration and bending modes also increase by increasing the CO_2 concentration, which is, however, in contrast with the available experimental data (Öberg et al., 2007). The band strength of the bulk stretching mode decreases instead with CO_2 concentration, in reasonably good agreement with the available experiments (Öberg et al., 2007). FTIR spectroscopy of the matrix-isolated molecular complex H_2O-CO_2 shows that CO_2 does not form a weak hydrogen bond with H_2O (Tso & Lee, 1985), but instead, CO_2 destroys the bulk hydrogen bond network. This may cause a significant decrease in the band strength of the bulk stretching mode, while the intermolecular $O-H$ bond strength increases with the CO_2 concentration. Therefore, the disagreement between calculated and experimental band strengths could

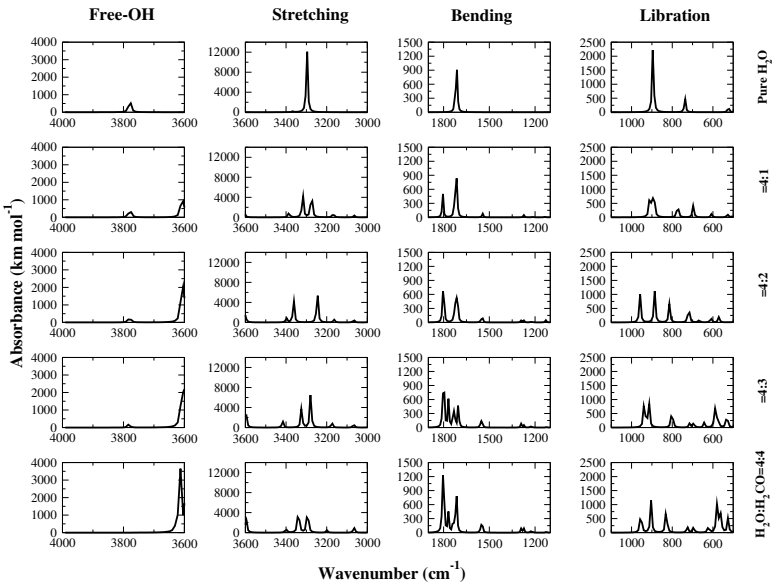

Figure 2.42: Absorption spectra of the four modes for water ice for the five measured compositions, ranging from pure water ice (top) to 4 : 4 $H_2O - H_2CO$ mixture (bottom) (Gorai et al., 2020a).

be due to the cluster size of water molecules. In Table 2.27, the resulting linear fit coefficients are reported, together with the available experimental values for the $H_2O - CO_2$ mixture deposited at 15 K (Öberg et al., 2007).

Part 2. Applications

The results discussed in previous Sections suggest that the water c-tetramer structure and harmonic B3LYP/6-31G(d) calculations can predict the experimental results presented here and the literature data. Thus, to study the effect of other impurities (H_2CO, CH_4, OCS, N_2, and O_2) on pure water ice, we further exploit this methodology. Additionally, the effect of impurities on the band strengths of the four fundamental bands is also studied by considering the c-hexamer (chair) structure.

H_2CO ice

The strongest modes of formaldehyde (H_2CO) lie at 1724.14 cm^{-1} (5.80 μm) and 1497.01 cm^{-1} (6.68 μm). Figure 2.25g depicts the optimized structure of the 4 : 4 $H_2O - H_2CO$ mixture. The desired ratio is attained upon forming the H-bond between the O atom of H_2CO and the dangling H atoms of H_2O. The effect

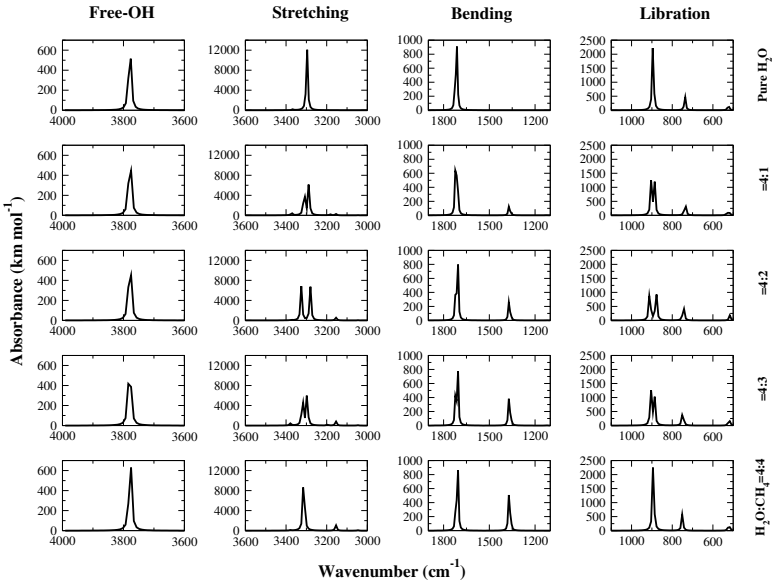

Figure 2.43: Absorption spectra of the four modes for water ice for the five measured compositions, ranging from pure water ice (top) to $4:4$ H_2O-CH_4 mixture (bottom) (Gorai et al., 2020a).

of formaldehyde on the water IR spectrum is shown in Figure 2.42. Frequencies, integral absorption coefficients, and mode assignments are also reported in Table 2.21. The band strength profiles as a function of the concentration of H_2O are shown in Figure 2.30f. Like the methanol – water mixture, all band strengths increase with the concentration of formaldehyde, the free OH stretching mode being the most affected.

CH_4 ice

CH_4 cannot be observed through rotational spectroscopy since it has no permanent dipole moment. The optimized structure of the H_2O-CH_4 system with a $4:4$ ratio is shown in Figure 2.25h. The absorption IR spectra for different H_2O-CH_4 mixtures are depicted in Figure 2.43. Peak positions, integral absorption coefficients, and band assignments are also provided in Table 2.21. Figure 2.30g shows the band strength variations with the concentration of CH_4. All band strengths marginally increase with the CH_4 concentration. Figure 2.40b shows the comparison of the band strengths with and without incorporating corrections for accounting for dispersion effects. For all the four fundamental modes, differences are minor.

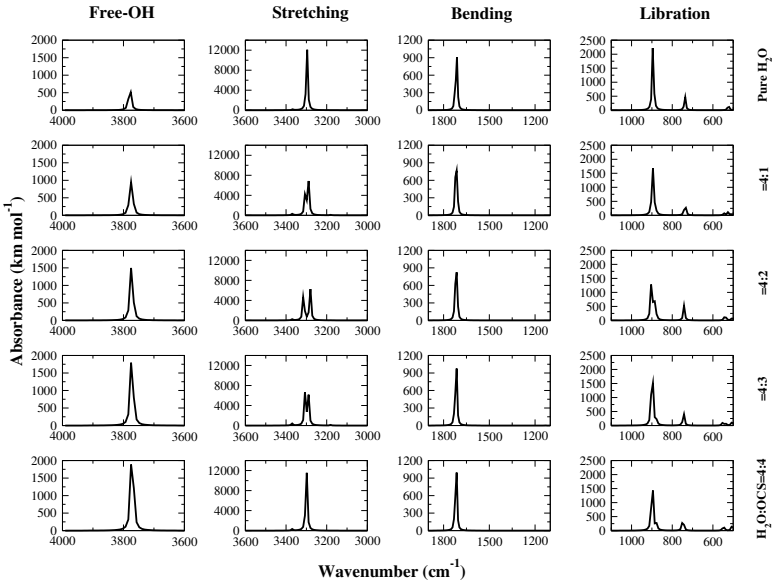

Figure 2.44: Absorption spectra of the four modes for water ice for the five measured compositions, ranging from pure water ice (top) to $4:4$ H_2O-OCS mixture (bottom) (Gorai et al., 2020a).

OCS ice

Garozzo et al. (2010) proposed that carbonyl sulfide (OCS) is a key ingredient of the grain surface. Its abundance in the ice phase may vary between 0.05% and 0.15% (Dartois, 2005). Figure 2.25i shows the optimized structure of the $4:4$ H_2O-OCS. Since oxygen is more electronegative than sulfur, the O atom of the OCS molecule is H-bonded to the water-free hydrogens. Figure 2.44 shows the absorption IR band spectra for H_2O-OCS clusters with various concentrations. Figure 2.30h depicts the band strengths as a function of the concentration of OCS. Here, the free OH mode is the most affected, and its band strength increases with the concentration of OCS. All other modes roughly remain unaffected by varying the amount of impurity.

N_2 ice

N_2 is a stable homonuclear molecule, and due to its symmetry, it is IR-inactive. However, when embedded in an ice matrix, the crystal field breaks the symmetry, and an IR transition is activated around 2325.58 cm^{-1} (4.30 μm). Figure 2.25j shows the optimized geometry of the H_2O-N_2 system with a $4:4$ ratio. The IR absorption spectra of water ice containing different amounts of N_2 are shown in

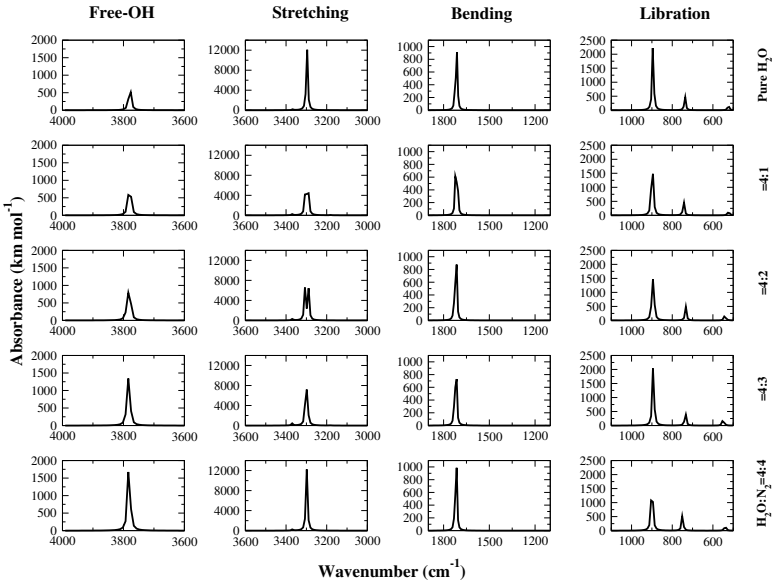

Figure 2.45: Absorption spectra of the four modes for water ice for the five measured compositions, ranging from pure water ice (top) to 4 : 4 $H_2O - N_2$ mixture (bottom) (Gorai et al., 2020a).

Figure 2.45. The corresponding peak frequencies and intensities are also provided in Table 2.21. The dependence of the band strengths on the N_2 concentration is depicted in Figure 2.30i. It is noticed that the slope of the band strength of the libration mode decreases, whereas the bending, stretching, and free OH modes show an increasing trend with the concentration of N_2. The linear fitting coefficients are provided in Table 2.27. Figure 2.40c shows the comparison of band strengths with and without considering the dispersion effects. It is noted that the inclusion of the dispersion effect leads to minor changes.

O_2 ice

Analogous to N_2, O_2 is a homonuclear molecule, which is IR-inactive except when it is embedded in an ice matrix (Ehrenfreund et al., 1992; Ehrenfreund & van Dishoeck, 1998), thus giving rise to an absorption band around 1550.39 cm^{-1} (6.45 μm). O_2 ice is not very abundant because the largest part of the oxygen budget in the dense molecular clouds is locked in the form of CO_2, CO, water ice, and silicates. The optimized geometry of the 4 : 4 $H_2O - O_2$ ratio is shown in Figure 2.25k. IR spectra for different concentrations and the corresponding peak frequencies and intensities are provided in Figure 2.46 and Table 2.21, respectively.

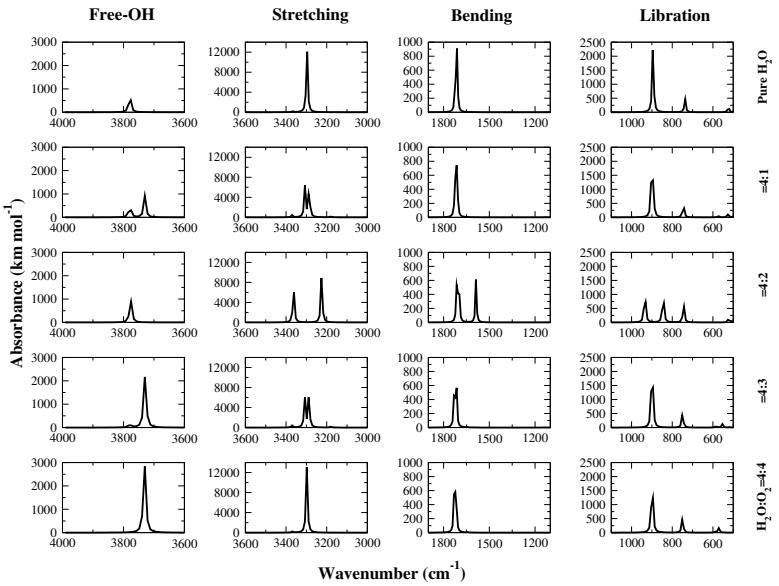

Figure 2.46: Absorption spectra of the four modes for water ice for the five measured compositions, ranging from pure water ice (top) to 4 : 4 $H_2O - O_2$ mixture (bottom) (Gorai et al., 2020a).

The dependence of band strengths upon O_2 concentration is shown in Figure 2.30j. Similar to the N_2 – water case, the free OH mode is the most affected. The slope of the band strength of the libration and bending modes decreases. In contrast, the stretching and free OH modes show an increasing trend with the concentration of O_2. The fitting coefficients for different $H_2O - N_2$ mixtures are provided in Table 2.27.

Figure 2.40d depicts the comparison of the band strengths with and without the inclusion of dispersion effects for the $H_2O - O_2$ system. It is evident that the trend of the band strength with the impurity concentration slightly increases for the libration mode. In contrast, it slightly decreases for the stretching mode when corrections for dispersion effects are present. The band strength rapidly increases in the bending mode, whereas it rapidly decreases for the free OH mode.

Comparison between various mixtures

To compare the effect of all impurities considered in this study on the band strength, we plot the band profiles of the four fundamental modes of water ice as a function of the concentration of impurities, the results being shown in Figure 2.47, top panel. For all basic modes, band strengths increase with the concentration of

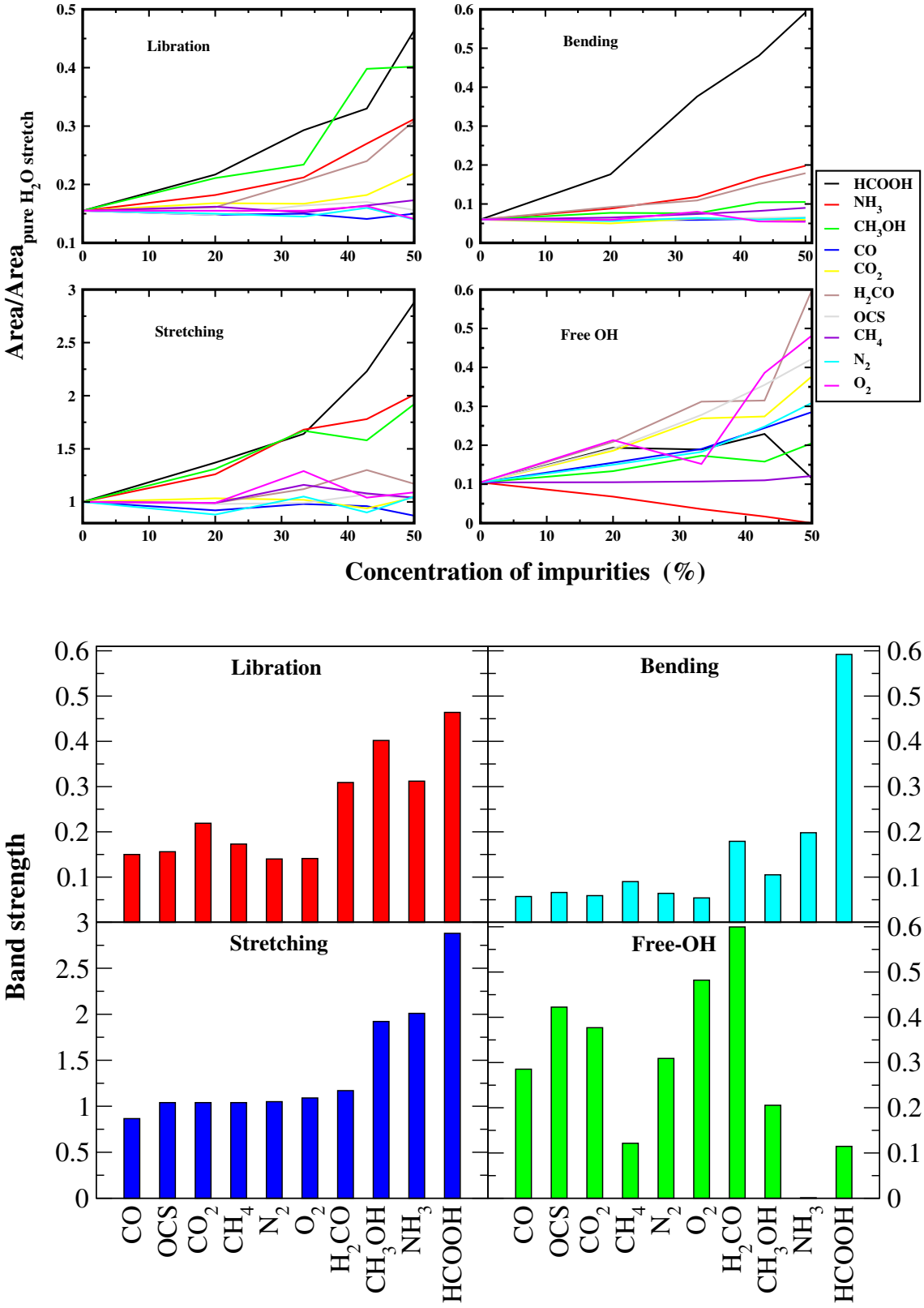

Figure 2.47: Top panel: effect of impurities on the four fundamental vibrational modes of water. Bottom panel: comparison of the band strengths for the four fundamental vibrational modes as affected by impurities (Gorai et al., 2020a).

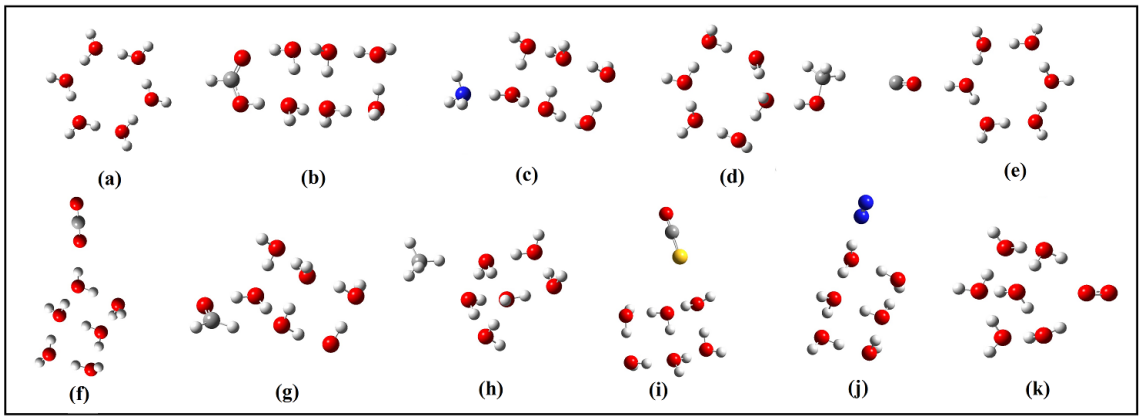

Figure 2.48: Optimized structures of (a) pure water, (b) $H_2O - HCOOH$, (c) $H_2O - NH_3$, (d) $H_2O - CH_3OH$, (e) $H_2O - CO$, (f) $H_2O - CO_2$, (g) $H_2O - H_2CO$, (h) $H_2O - CH_4$, (i) $H_2O - OCS$, (j) $H_2O - N_2$, and (k) $H_2O - O_2$ clusters with a 6 : 1 concentration ratio (Gorai et al., 2020a).

CH_3OH, H_2CO, HCOOH, CH_4. In Figure 2.47, bottom panel, we report the relative band strengths for the 4 : 4 ratio mixtures to better understand their effect. From this, it is clear that the libration, bending, and stretching modes are affected mainly by formic acid, while the free OH mode is mainly affected by formaldehyde. An interesting feature is found for the free OH mode for the $NH_3 - H_2O$ system. By increasing the NH_3 concentration to that of pure water, the band strength of the free OH mode decreases and disappears when the 4 : 4 concentration ratio is reached.

Figure 2.48 depicts the optimized structures of the pure water c-hexamer (chair) configuration along with those obtained for a 6 : 1 concentration ratio. Figure 2.49, analogous to Figure 2.30, collects the results for the band strength variations where c-hexamer (chair) water cluster configuration is considered. The geometries of water clusters containing 20 water molecules with HCOOH as an impurity in various concentrations are shown in Figure 2.50. The corresponding variations of the band strengths with increasing concentration of HCOOH are depicted in Figure 2.51. This figure also reports the comparison of band strength profiles for different water clusters. The structures of the 20-water-molecule clusters are taken from Shimonishi et al. (2018). The structures as a model of the ASW surface were obtained by MD-annealing calculations using classical force fields. The comparison shown in Figure 2.51 demonstrates that the $4H_2O$ model provides results similar to those obtained with 6 and 20 water molecules. This furthermore confirms the validity of our approach.

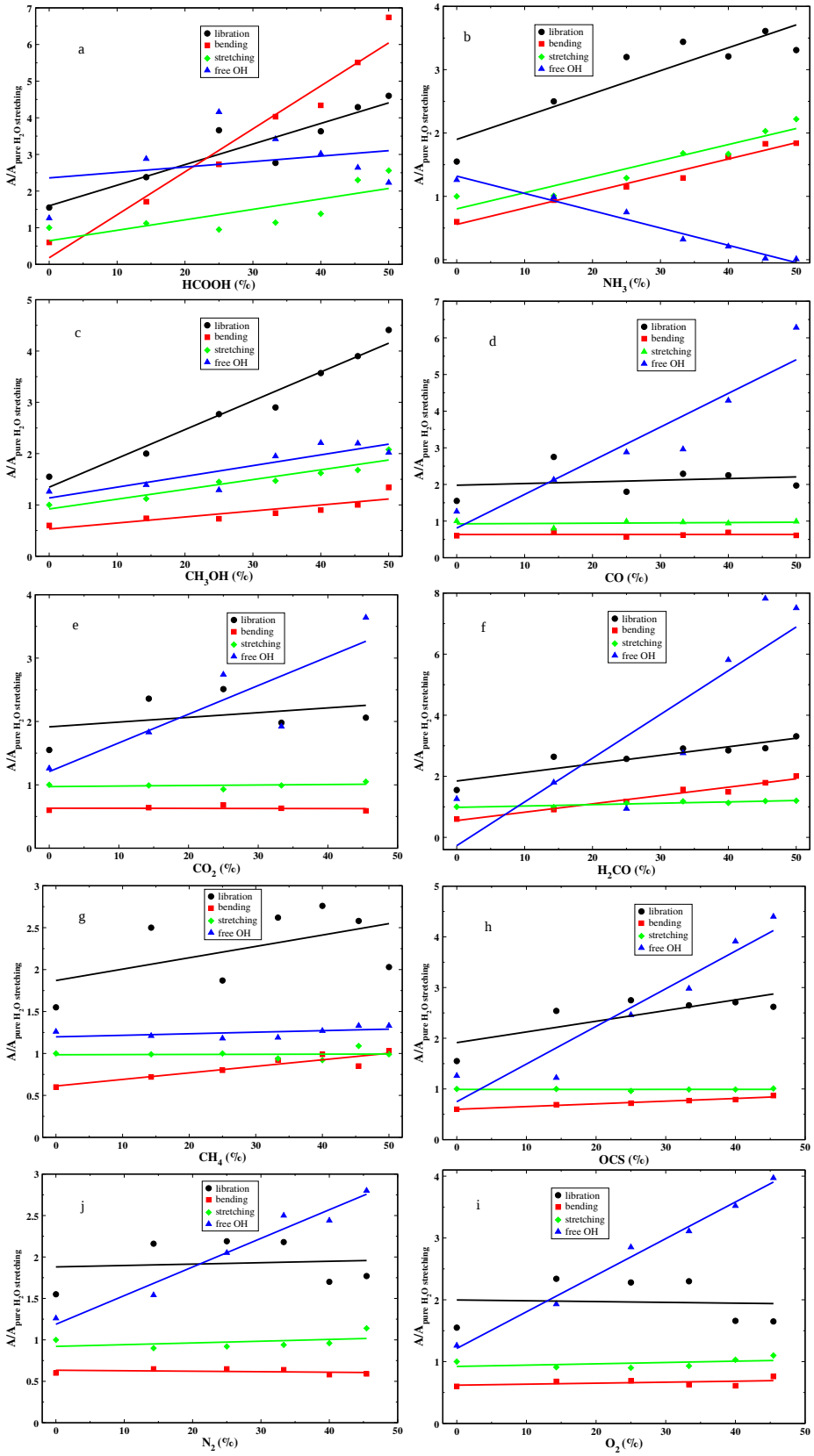

Figure 2.49: Band strengths of the four fundamental vibration modes of water for (a) $H_2O - HCOOH$, (b) $H_2O - NH_3$, (c) $H_2O - CH_3OH$, (d) $H_2O - CO$, (e) $H_2O - CO_2$, (f) $H_2O - H_2CO$, (g) $H_2O - CH_4$, (h) $H_2O - OCS$, (i) $H_2O - N_2$, and (j) $H_2O - O_2$ clusters with various concentrations. The water c-hexamer (chair) configuration gas been used for pure water (Gorai et al., 2020a).

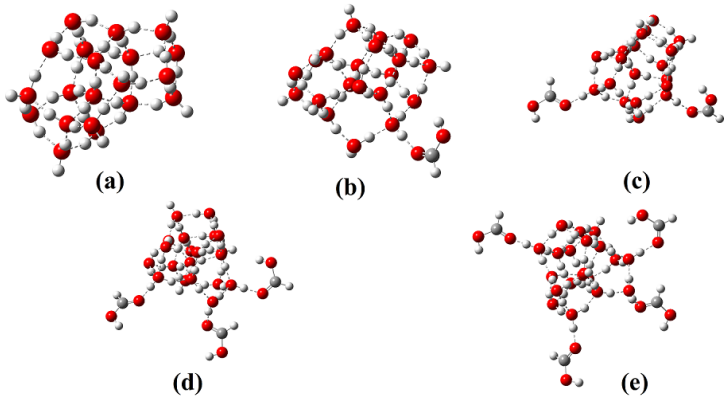

Figure 2.50: Structure of water clusters containing $20H_2O$ molecules with HCOOH as impurity in different concentration ratio: (a) pure water, (b) H_2O : HCOOH = 20 : 1, (c) H_2O : HCOOH = 10 : 1, (d) H_2O : HCOOH = 6.67 : 1, (e) H_2O : HCOOH = 5 : 1 (Gorai et al., 2020a).

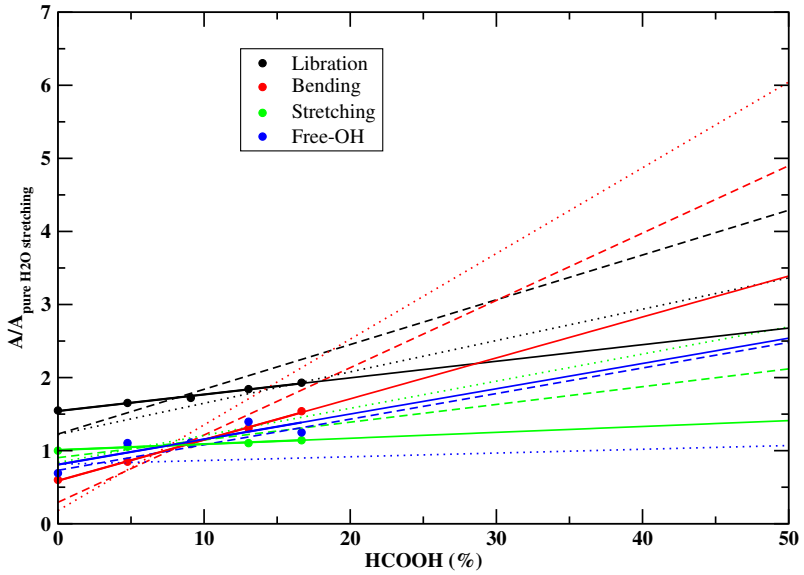

Figure 2.51: Comparison of the band strength of the four fundamental vibrational modes for water clusters containing $20H_2O$, $6H_2O$, and $4H_2O$ molecules with HCOOH as an impurity in different concentrations. Solid lines represent the band strength profiles for $20H_2O$ cluster, dotted lines for the water c-hexamer (chair) ($6H_2O$), and dashed lines for water c-tetramer ($4H_2O$) (Gorai et al., 2020a).

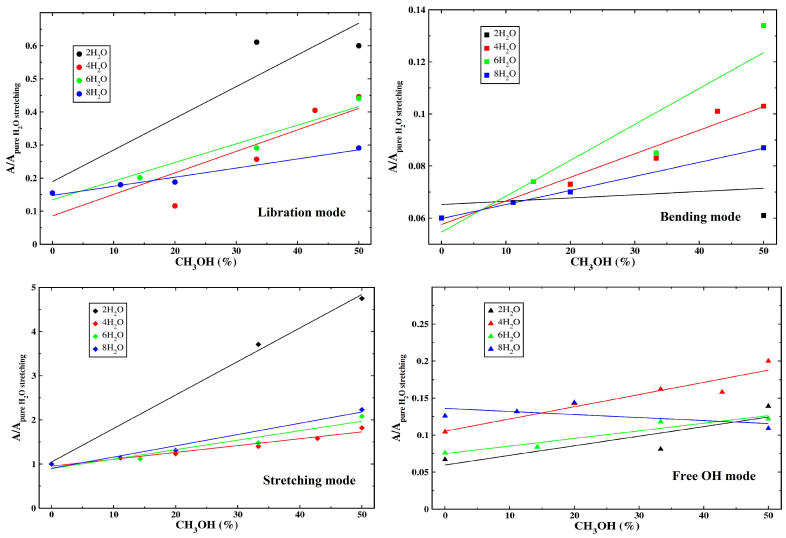

Figure 2.52: Effect of the cluster size on the band strength profile (Gorai et al., 2020a).

2.2.4 Summary

Water ice is known to be the major constituent of interstellar icy grain mantles. Interestingly, there are several astronomical observations (Boogert et al., 2000; Keane et al., 2001) of the OH stretching and HOH bending modes at 3278.69 cm^{-1} (3.05 μm) and 1666.67 cm^{-1} (6.00 μm), respectively. However, it is noteworthy that the intensity ratio of these two bands is very different from that obtained in laboratory experiments for pure water ice. This suggests that the presence of impurities in water ice affects the spectroscopic features of water itself. For this reason, a series of laboratory experiments are carried out to explain the discrepancy between observations and experiments. Furthermore, these observations have prompted us to perform an extensive computational investigation to evaluate the effect of different amounts of representative impurities on the band strengths and absorption band profiles of interstellar ice.

A systematic study of the four fundamental vibrational modes of water in various molecular species with different concentration ratios is carried out. We select the most abundant interstellar ice impurities (HCOOH, NH_3, CH_3OH, CO, CO_2, H_2CO, CH_4, OCS, N_2, and O_2) and study their impact on four fundamental vibrational bands of pure water ice by employing different cluster models. Specifically, we examine the effect on the libration, bending, bulk stretching, and free OH stretching modes. The theoretical calculations are supported and complemented by

some IR spectroscopy experiments to verify the effect of HCOOH, NH_3, and CH_3OH on the band profiles of pure H_2O ice. Indeed, both the experimental and theoretical peak positions might differ from the astronomical observations. This is because the grain shape, size, constituents, surrounding physical conditions, and impurities play a crucial role in tuning the ice spectroscopic features.

Although most of the computations are performed for a cluster containing only four water molecules as a model system (to find a trend in the absorption band strength), we demonstrate that increasing the size of the cluster would change the band strength profile only marginally. From the band strength profiles shown in Figure 2.52, it is apparent that the stretching mode is the most affected, and the bending mode is the least affected by the presence of impurities. Libration, bending, and bulk stretching modes are the most affected by HCOOH impurity, followed by CH_3OH and H_2CO. Another interesting point to be noted is that the band strength of the free OH stretching mode decreases with the increasing concentration of NH_3 and completely vanishes when the concentration of NH_3 becomes 50%. Interestingly, the experimental free OH band profile shows a decreasing trend when water is mixed with NH_3 (Figure 2.33, right panel), similar to that obtained computationally.

Finally, the work presented here aims at gaining information on the effect of intermolecular interactions in interstellar relevant ices, thus providing some valuable new laboratory and computed absorption spectra of water-rich ices. These will be useful for interpreting future detailed space-borne observations using the upcoming JWST mission (Gibb et al., 2004) in the mid-IR spectral region.

Chapter 3

Radiation Dominated Region

Overview

Two noble gas molecular cations, argonium (ArH^+) and hydro-helium or helenium (HeH^+), are discovered toward the two radiation-dominated environments in space: the Crab Nebula SNR and the planetary nebula (NGC 7027), respectively. Though the elemental abundance of neon is lower than helium, it is higher than that of the Argon. However, neonium cation (NeH^+) remains undetected in space to date. Hydroxyl radicals ($-OH$) are very abundant in neutral and cationic forms. Consequently, they are found predominantly in radiation-dominated regions. Still, hydroxyl cations of such noble gases (i.e., $ArOH^+$, $NeOH^+$, and $HeOH^+$) are yet to be detected in space. This Chapter attempts to model the noble gas chemistry containing hydride and hydroxyl cations (ArH^+, NeH^+, HeH^+, $ArOH^+$, $NeOH^+$, and $HeOH^+$). We also consider various isotopologs of these hydride and hydroxide cations (^{36}Ar, ^{38}Ar, ^{40}Ar, ^{20}Ne, and ^{22}Ne). The chemical evolution of these species under the diffuse and exotic environment (the Crab Nebula filamentary region) is studied (Das et al., 2020). The intrinsic line surface brightness (SB) is calculated to find a favorable parameter space that can explain the observational features for the condition suitable in the Crab filamentary region.

The Crab Nebula (M1 = NGC 1952) is the freely expanding remnant of the historical core-collapse supernova of AD 1054 (SN 1054). It is too young to be polluted by interstellar or circumstellar material. The Crab pulsar is situated at a distance of 3.37 kpc (Fraser & Boubert, 2019) from the Sun with RA and DEC $05^h\ 34^m\ 31.935^s$ and $+22°\ 0'\ 52''.19$ respectively (Kaplan et al., 2008). The Crab, laying about 200 pc away from the Galactic plane in a low-density region, contains both atomic and molecular hydrogen, electrons, and an area of enhanced ionized argon emission.

Loh et al. (2010, 2011) identified numerous strong H_2-emitting (2.12 μm) knots in the Crab, and Richardson et al. (2013) modeled emission features of H_2-emitting gas in the Crab knot 51 filamentary region. The kinetic gas and dust temperature around the knots of the Crab is around $\sim 2000 - 3000$ K (Loh et al., 2012; Richardson et al., 2013) and $\sim 28 - 63$ K (Gomez et al., 2012), respectively. The strong radiation in the Crab enhances the abundance of the electrons, which can readily convert H atoms into H^- by radiative attachment reaction ($H + e^- \rightarrow H^- + \gamma$), and H^- eventually react with H atoms again to form the H_2 molecules by associative detachment reaction ($H^- + H \rightarrow H_2 + e^-$). There can be some physisorption and chemisorption (Cazaux & Tielens, 2004) pathways that may lead to the formation of H_2. The majority of the H_2 molecules are formed inside the cleanest knot (knot 51) of the Crab by associative detachment reaction rather than by the usual grain catalysis ($2H + \text{grain} \rightarrow H_2 + \text{grain}$) method (Richardson et al., 2013).

In the atmosphere of the Earth, Argon is the third most abundant element, having an isotopic ratio of $^{40}Ar/^{38}Ar/^{36}Ar$ is 1584/1.00/5.30 (Lee et al., 2006). ^{40}Ar isotope is mainly produced from the decay of potassium-40 in the Earth's crust. Strikingly, the ratio obtained in the Jupiter family comet, 67P/C-G, by ROSINA mass spectrometer is similar of about $^{36}Ar/^{38}Ar \sim 5.4 \pm 1.4$ (Altwegg et al., 2016). In the solar wind, the ratio of $^{40}Ar/^{38}Ar/^{36}Ar$ has been measured to 0.00/1.00/5.50 (Meshik et al., 2007), whereas, in the ISM, the ^{36}Ar isotope is the most abundant ($\sim 84.6\%$), followed by ^{38}Ar ($\sim 15.4\%$) and traces of ^{40}Ar ($\sim 0.025\%$; Wieler, 2002). The ^{36}Ar isotope is mainly produced during the core collapse of supernovae events by the explosive nucleosynthesis reactions in massive stars. Using the observed data from the Spectral and Photometric Image REceiver (SPIRE) of the Herschel satellite, Barlow et al. (2013) reported $J = 1 \rightarrow 0$ (617.5 GHz) and $J = 2 \rightarrow 1$ (1234.6 GHz) emission of $^{36}ArH^+$ along with the strongest fine-structure component of the OH^+ ion (971.8 GHz) toward the Crab. They predicted the limits of the abundance ratios to be $^{36}ArH^+/^{38}ArH^+ > 2$ and $^{36}ArH^+/^{40}ArH^+ > 4-5$. Molecular excitations mainly occur due to the collision with electrons in the Crab region with a density

of about $\sim 10^2$ cm^{-3}. ArH^+ can be used as a unique tracer of H_2 (by anticorrelation) as well as atomic gas (by correlation) in specific environments (Barlow et al., 2013; Schilke et al., 2014; Neufeld & Wolfire, 2016). Schilke et al. (2014) assigned $J = 1 \rightarrow 0$ transition of both the isotopologs of ArH^+ ($^{36}ArH^+$ and $^{38}ArH^+$) in absorption. These transitions were observed with the Heterodyne Instrument for the Far Infrared (HIFI) on board the Herschel satellite toward Sagittarius (Sgr) B2(M) and only the primary isotopolog ($^{36}ArH^+$) toward numerous prominent continuum sources, e.g., Sgr B2(N), W51e, W49N, W31C, and G34.26+0.15. Their Herschel survey also covered the $J = 1 \rightarrow 0$ NeH^+ transition at 1039.3 GHz but failed to report any detection despite neon being much more abundant than Argon. Müller et al. (2015) also detected $^{36}ArH^+$ and $^{38}ArH^+$ in the absorption of a foreground galaxy at $z = 0.89$ along with two different lines of sight toward PKS $1830 - 211$ with band 7 of the ALMA interferometer. Hamilton et al. (2016) described the excitation of ArH^+ in the Crab by collisions with electrons through radiative transfer calculations. They found that the $2 \rightarrow 1$ and $1 \rightarrow 0$ emissions ratio is consistent with an ArH^+ column density of 1.7×10^{12} cm^{-2}. Priestley et al. (2017) performed a combined photoionization and photodissociation study for the emission of ArH^+, HeH^+, and OH^+ in the Crab filament. This filamentary region is subjected to synchrotron radiation and a high flux of charged particles. Their model successfully reproduced the observation of Barlow et al. (2013) when they considered total hydrogen densities between 1900 and 2×10^4 cm^{-3}. Though they predicted HeH^+ emission above detection thresholds, the formation time-scale for this molecule is much longer than the age of the Crab.

Helium is the second most abundant species (after hydrogen) in the universe, having an abundance of 1/10 relative to hydrogen nuclei. Because Argon, neon, and helium are noble gases, they do not usually form stable molecules, but they can form stable ions. After a few hundred thousand years of the Big Bang, when the universe cools sufficiently under 4000 K, helium was the first neutral element produced in the universe due to its highest ionization potential. Shortly after the first helium atom formed, the first chemical bond in the universe formed through the radiative association reaction between the neutral helium atom and a proton during the Age of Recombination. It developed HeH^+ by photon emission, which is believed to be a major conduit of photons for the observable cosmic microwave background (CMB) radiation. The radiative association between He and He^+ was also possible to form He^{2+}. But the constant presence of H^+ when most of the helium was neutralized keeps the population of HeH^+ relatively higher than He^{2+}. Due to this fact, HeH^+ is considered to be the first molecular ion formed in the

universe, and its bond is regarded as the first chemical bond of the universe (Lepp et al., 2002; Galli & Palla, 2013; Fortenberry, 2019). The helium hydride ion, HeH^+, was first observed in the laboratory nearly a century ago in 1925 (Hogness & Lunn, 1925), and parts of its vibrational spectrum were first speculated in the mid-1970s (Black, 1978). Despite these early measurements and predictions, recently, Güsten et al. (2019) reported the first astrophysical identification of HeH^+ based on the advances in terahertz spectroscopy and high-altitude observation. They used the German REceiver for Astronomy at Terahertz Frequencies (GREAT) on board the SOFIA. They were successful in identifying HeH^+ by its rotational ground-state transition at a wavelength of 149.137 μm (2010.184 GHz) in a young and dense planetary nebula (NGC 7027) located in the Cygnus constellation. Very recently, Neufeld et al. (2020) identified the $v = 1-0$ P(1) at 3.51629 μm and $v = 1-0$ P(2) at 3.60776 μm) of HeH^+ in emission. They detected these transitions toward the planetary nebula NGC 7027 using the iSHELL spectrograph on NASA's Infrared Telescope Facility (IRTF) situated at Maunakea. They further confirmed the early discovery of this species reported in Güsten et al. (2019).

3.1 Physical conditions

Because the physical and chemical processes are inter-linked, it is customary to use appropriate physical parameters to constrain the abundances of the noble gas species. Here, we construct two models for the Crab Nebula filamentary region: Model A and Model B, to explain the various aspects of the Crab using the CLOUDY code[1] (version 17.02, last described by Ferland et al., 2017).

Earlier, Owen & Barlow (2015) modeled the properties of dust and gas densities by fitting the predicted SED to the multi-wavelength observations. Based on their results, amorphous carbon grain is used to mimic the dust pertaining inside the Crab. For this purpose, the optical constants are taken from Zubko et al. (1996), and a mass density of 1.85 g cm^{-3} is adopted. We modify the default grain size distribution of CLOUDY and assume that it would maintain a power-law distribution $n(a) \propto a^{-\alpha}$ with $\alpha = 2.7$, $a_{min} = 0.005$ μm, and $a_{max} = 0.5$ μm following the clumpy model VI of Owen & Barlow (2015). We use a higher dust-to-gas mass ratio ($\frac{M_d}{M_g} = 0.027$; Owen & Barlow, 2015) suitable for the Crab. The $A_V/N(H)$ ratio is self-consistently calculated based on the dust-to-gas mass ratio in the CLOUDY code. We obtain $A_V/N(H) \sim 2.094 \times 10^{-20}$ mag cm^2. Priestley et al. (2017) used a

[1] https://gitlab.nublado.org/cloudy/cloudy/-/wikis/home

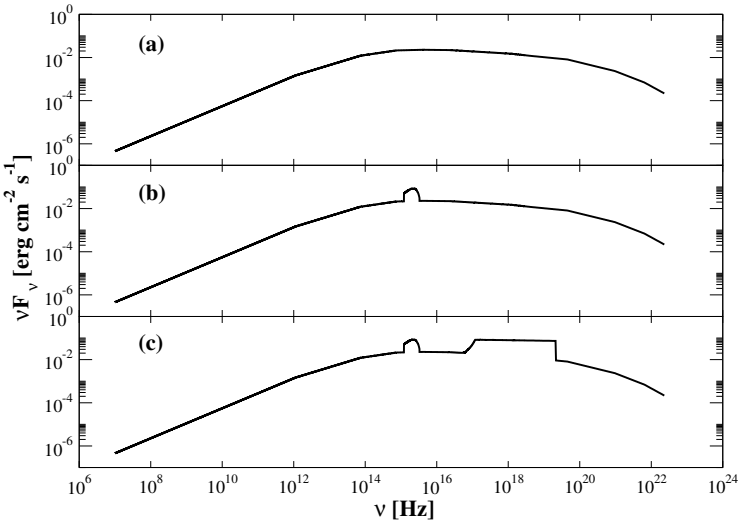

Figure 3.1: Shape and intensity of the resulting incident SED (Das et al., 2020). The three panels of this figure show the modifications of the SED sequentially. The SED obtained from Hester (2008) is shown in panel (a), panel (b) shows the SED after the inclusion of the Galactic background radiation field of 31 Draine units, and finally, panel (c) shows the resulting complete SED after the inclusion of the X-ray spectrum from Figure 1 of Priestley et al. (2017).

similar dust-to-gas mass ratio in their model, but they kept their extinction-to-gas ratio $A_V/N(H)$ at the standard interstellar value (6.289×10^{-22} mag cm^2), which is about two orders of magnitude lower than the (more realistic) value used here. We assume a shell of matter having a thickness (dr) of 3.5×10^{16} cm located at 2.5 pc from the central point source (i.e., inner radius, $r_{in} = 2.5$ pc; Priestley et al., 2017). Because we consider $r_{in} >> dr$, in principle, a plane-parallel geometry is assumed. Following Shaw et al. (2005), the extensive model for the H_2 is considered. We include the physics of PAHs in our model. Also, the photoelectric heating and collisional processes are included.

We adopt the shape of the SED mentioned in Hester (2008). We consider the luminosity (L) $\sim 1.3 \times 10^{38}$ erg s^{-1} as the synchrotron emission from the pulsar at the center of the Crab has a spin-down luminosity $\sim 10^5$ times that of the Sun (Hester, 2008). Because our object is located 2.5 pc away from the central source, the intensity of the external radiation field striking a unit surface area of the cloud ($\frac{L}{4\pi r_{in}^2}$) is $\sim$ 0.174 erg cm^{-2} s^{-1}. The obtained shape and intensity of the SED are shown in Figure 3.1a. The Galactic background radiation field proposed by

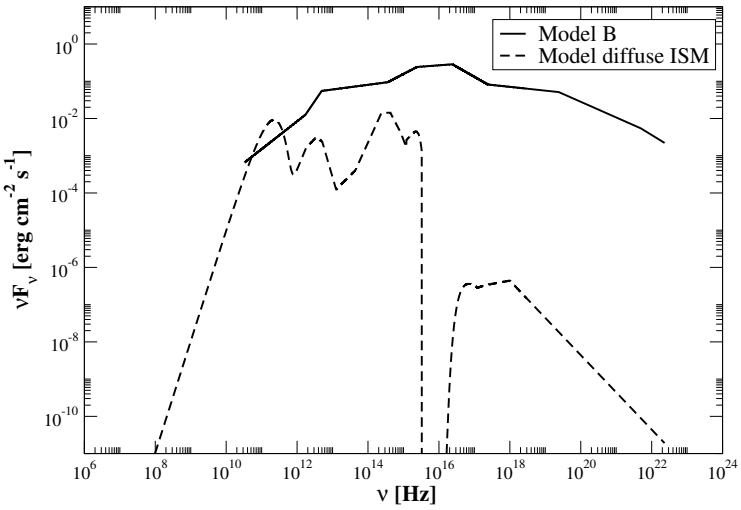

Figure 3.2: Shape and intensity of the incident SED (Davidson & Fesen, 1985) considered for Model B are shown with the solid line. The incident SED considered for the diffuse ISM case is shown with the dashed line (Das et al., 2020).

Bertoldi & Draine (1996) is also included to modify our SED. This radiation field is only defined over a narrow wavelength range. The strength of this radiation field is 31 Draine units (i.e., 31× the ISRF in Draine's units $\approx 31 \times 2.7 \times 10^{-3}$ erg s^{-1} cm^{-2}, Draine, 1978). The resulting SED with the Galactic background radiation field included is shown in Figure 3.1b. We digitally extract (using the online tool of Rohatgi, 2020) the output X-ray spectrum (i.e., Figure 1) of Priestley et al. (2017) and include an X-ray flux of 0.35 erg cm^{-2} s^{-1} from 0.1 to 100 in our SED (Figure 3.1c). The shape and intensity of the final SED used in the case of the Crab are shown in Figure 3.1c. All of the parameters discussed here are considered as the physical input parameters of Model A.

Richardson et al. (2013) studied the nature of the H_2-emitting gas in knot 51 of the Crab. They mentioned that Davidson's SED (Davidson & Fesen, 1985) is an excellent fit to reproduce observations. In Figure 3.2, the SED of Davidson & Fesen (1985) is shown with a solid curve for the ionizing particle model (Model B) following Richardson et al. (2013). Additionally, for diffuse ISM case, a SED is considered shown in Figure 3.2 with a dashed curve. Details about this SED and modeling results are discussed in Section 3.3.1.

The physical parameters are summarized in Table 3.1, and the gas-phase elemental abundances are listed in Table 3.2. Tables 3.1 and 3.2 contain input parameters

Table 3.1: Adopted physical parameters for the Crab filament (Das et al., 2020).

Physical parameters	**Adopted values**
Model A (adopted from Priestley et al., 2017)	
Inner radius (r_{in})	2.5 pc = 7.715×10^{18} cm
Shell thickness (dr)	3.5×10^{16} cm
Luminosity (L)	1.3×10^{38} erg s^{-1}
ISRF	31 Draine units
SED	Hester (2008) + X-ray from Figure 1 of Priestley et al. (2017)
Type of grain	Amorphous carbon
Dust-to-gas mass ratio	0.027 (Owen & Barlow, 2015)
Model B (adopted from Richardson et al., 2013)	
Incident ionizing photon flux on the slab (Φ(H))	$10^{10.06}$ $cm^{-2}s^{-1}$
Thickness	$10^{16.5}$ cm
Additional heating	$\zeta_H/\zeta_0 = 10^{5.3}$
$n_{H(min)}$	10^3 cm^{-3}
$n_{H(core)}$	$10^{5.25}$ cm^{-3}
SED	Davidson & Fesen (1985)
Type of grain	Mix of graphite and silicate
Dust-to-gas mass ratio	0.003

Table 3.2: Initial gas-phase elemental abundances with respect to total hydrogen nuclei in all forms for the Crab filament (Das et al., 2020).

Element	**Abundance**	**Element**	**Abundance**
Model A (adopted from Owen & Barlow, 2015)			
H	1.00	^{36}Ar	1.00×10^{-5}
He	1.85	^{38}Ar	1.82×10^{-6}
C	1.02×10^{-2}	^{40}Ar	2.90×10^{-9}
N	2.50×10^{-4}	^{20}Ne	4.90×10^{-3}
O	6.20×10^{-3}	^{22}Ne	3.60×10^{-4}
Model B (adopted from Richardson et al., 2013)			
H	1.00	Si	8.91×10^{-6}
He	2.95×10^{-1}	S	1.95×10^{-5}
C	3.98×10^{-4}	Cl	4.68×10^{-8}
N	5.62×10^{-5}	^{36}Ar	4.79×10^{-6}
O	5.25×10^{-4}	^{38}Ar	8.70×10^{-7}
^{20}Ne	1.82×10^{-4}	^{40}Ar	1.39×10^{-9}
^{22}Ne	1.34×10^{-5}	Fe	2.45×10^{-5}
Mg	2.00×10^{-5}		

Note: For the initial isotopic ratio of argon and neon, we have used ^{36}Ar/^{38}Ar/^{40}Ar = 84.5946/15.3808/0.0246 and ^{20}Ne/^{21}Ne/^{22}Ne = 92.9431/0.2228/6.8341, following Wieler (2002).

for the two models, Model A and Model B. In Model A, we consider the physical parameters from Priestley et al. (2017) and initial elemental abundances from the clumpy model VI of Owen & Barlow (2015). In Model B, we consider the initial elemental abundances and physical input parameters for the ionizing particle model that Richardson et al. (2013) considered. Some significant differences between the physical parameters of Model A and Model B are that Model A is a constant-density model. In contrast, we consider a dense core ($n_{H(core)} \sim 10^{5.25}$ cm^{-3}) by introducing a varying density profile in Model B, and the grain type in both models is different. For the initial isotopic ratio of argon and neon, we use $^{36}Ar/^{38}Ar/^{40}Ar$ = 84.5946/15.3808/0.0246 and $^{20}Ne/^{21}Ne/^{22}Ne$ = 92.9431/0.2228/6.8341, following Wieler (2002).

3.1.1 Radiative Transfer Model

The $J = 1$ and $J = 2$ levels of $^{36}ArH^+$ are at 29.6 K and 88.9 K, respectively. The measured electron temperature (7500 − 15000 K; Davidson & Fesen, 1985) for the ionized gas and measured excitation temperature of H_2 (2000 − 3000 K; Loh et al., 2011) in the Crab region is much higher than that at these energy levels. If the region where ArH^+ transitions were observed has the density of the colliding partner exceeding the critical density and temperature > 100 K, the level populations would be in Boltzmann equilibrium and yield a $2 - 1/1 - 0$ ratio of ~ 30. Because the observed ratio is ~ 2, it is expected that the density of the colliding partner is much lower than their critical densities. Barlow et al. (2013) also attributed this difference to the density of the collisional partners being below the critical density of the ArH^+ rotational levels. They used a radiative transfer model to determine the densities of H_2 and e^- from the observational ratio. They obtained a critical density of electrons of $\sim 10^4$ cm^{-3} and $H_2 \sim 10^8$ cm^{-3}.

ArH^+ favors regions where H_2/H is small. If there are any significant H_2 densities, then the reactive collision with ArH^+ may be high enough to affect the excitation. By including the reactive collision rate with H_2, it might be possible to compare models and observed fluxes to limit the H_2/H ratio in the emitting region. However, with the public version of RADEX, it is not possible to study this feature. Moreover, around the Crab filamentary region, where ArH^+ was identified, the abundance of H atoms and electrons is $> 10^4 - 10^5$ times higher than that of H_2 (see Figure 16 of Priestley et al., 2017, and Figures 3.9 and 3.16 in the latter part of this Chapter). It suggests that a nonreactive collision might be the primary source of excitation of ArH^+.

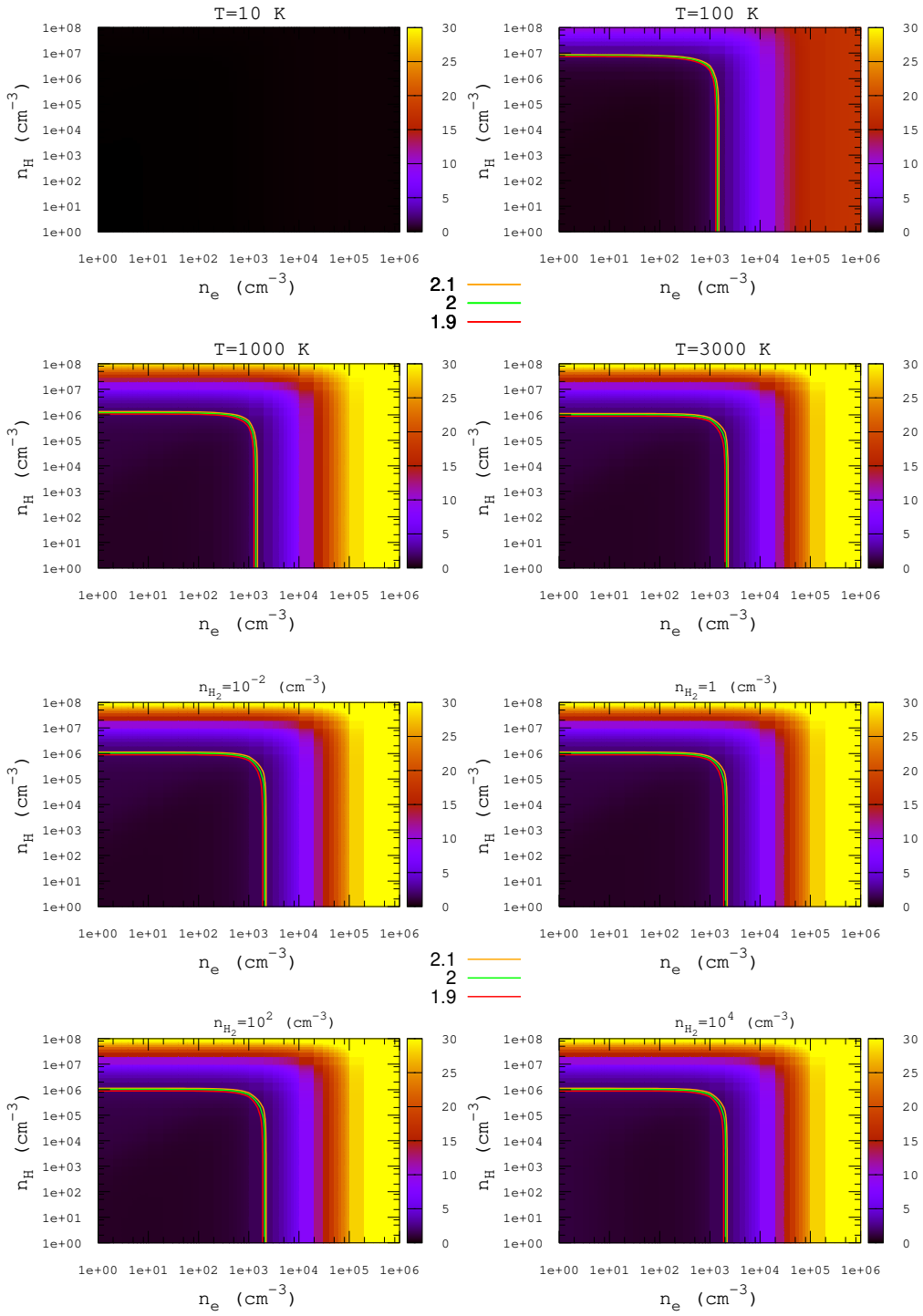

Figure 3.3: Surface brightness (SB) ratio between the $2-1$ and $1-0$ transitions of $^{36}ArH^+$ by considering a column density of 1.7×10^{12} cm^{-2} (Das et al., 2020). The upper four panels show the cases with fixed temperatures ($T = 10,\ 100,\ 1000$, and 3000 K respectively) whereas the lower four panels show the cases with fixed H_2 density ($n_{H_2} = 10^{-2}$, 1, 10^2, and 10^4 cm^{-3} respectively). The contours are highlighted near the observed SB ratio (of ~ 2).

Barlow et al. (2013) used the MADEX code (Cernicharo, 2012), where they used H_2 and electron as the collision partner. Due to the unavailability of the collisional rate parameters, they used the collisional deexcitation rate of $SiH^+ + He$ and $CH^+ + e^-$ in place of the interaction of H_2 and e^- with ArH^+, respectively. Because the electron-impact rate coefficient for the dipolar transitions is roughly $10^4 - 10^5$ times larger than the neutrals (H and H_2), Hamilton et al. (2016) used electrons as the only colliding partner. Because reactive collisions are not implemented in the public version of RADEX, we only take the nonreactive collisions into account. We assume that due to the low abundance of H_2 in the ArH^+ formation region and high electron-impact rate, reactive collision with H_2 would have minimal effect in this condition. Here, we consider three colliders, H, H_2, and electrons, in RADEX. Collisional rates with H and H_2 are scaled (Schöier et al., 2005) from the available collisional rates of $ArH^+ - He$ obtained from García-Vázquez et al. (2019), and collisional rates with electrons are taken from Hamilton et al. (2016).

Here, we use the RADEX code (van der Tak et al., 2007) for non-LTE computation to explain the observational results. We prepare this collisional data file using the spectroscopic parameters available in the JPL[2] (Pickett et al., 1998) or CDMS[3] (Müller et al., 2001, 2005; Endres et al., 2016) database and include the electron-impact excitation rates from Hamilton et al. (2016). Collisional data files for the other hydride/hydroxyl cations are unavailable in the CLOUDY code as well. We use our approximated data files to calculate the SB and emissivity discussed in the latter part of this Chapter. We consider Figure 3.1c as the input of the background radiation field in the radiative transfer calculations reported here. We prepare the self-made background radiation field in the format prescribed in `https://personal.sron.nl/~vdtak/radex/index.shtml`. This file contains three columns. The first column is the wavenumber (in cm^{-1}), the second is the intensity (in Jy nsr^{-1}), and the third is the dilution factor which varies between 0 and 1. Here, for the estimation, we use an average dilution factor of 0.5. We do not find a significant difference while considering a different dilution factor in our calculations.

We draw a parameter space with a wide range of H densities ($1 - 10^8$ cm^{-3}), H_2 densities ($10^{-2} - 10^4$ cm^{-3}), electron number densities ($1 - 10^6$ cm^{-3}), and excitation temperatures ($10 - 3000$ K). Figure 3.3 shows the SB ratio between $2 \rightarrow 1$ and $1 \rightarrow 0$ transitions of $^{36}ArH^+$. For this computation, we consider the column density of $^{36}ArH^+ \sim 1.7 \times 10^{12}$ cm^{-2} as obtained from Hamilton et al. (2016), and a line width (FWHM) of 5 km s^{-1}. For the upper four panels, we consider the H_2 density

[2] `https://spec.jpl.nasa.gov`
[3] `https://cdms.astro.uni-koeln.de`

of 1 cm^{-3} and temperature fixed at 10 K, 100 K, 1000 K, and 3000 K, respectively. Some contours near the observed SB ratio (~ 2) are highlighted in all the panels. The top-left panel of Figure 3.3 shows that at 10 K, the SB ratio between these two transitions is ~ 0. This is because the excitation temperature is below the upstate energy of these two transitions. Thus, for the higher temperature, energy levels are gradually populated, and the ratio increases. The upper four panels of Figure 3.3 depict how the observed ratio is obtained with an electron density of $1000 - 3000$ cm^{-3} when the number density of H atoms is $< 10^6 - 10^7$ cm^{-3}, and the temperature is beyond the upstate energy of $2 \rightarrow 1$ and $1 \rightarrow 0$. For the case with a temperature of 100 K, when H density is below $\sim 10^7$ cm^{-3}, the observed ratio is obtained with an electron density of ~ 1000 cm^{-3}. For $n_H \sim 10^7$ cm^{-3}, the observed ratio is obtained with $n_e = 1 - 1000$ cm^{-3}. As we gradually increase the temperature, the observed ratio is obtained at a lower H density (for example, at 1000 K, it is $\sim$ a few times $\times 10^6$ cm^{-3}) and a little higher electron density range ($1 - 2000$ cm^{-3}). If the temperature is further increased from here (i.e., at 3000 K), a minimal decrease of n_H, and a slight increase in n_e range are required to reproduce the observed ratio. For the higher temperature (~ 3000 K) and higher electron density ($> 10^5$), the highest value of the ratio ~ 30 is achieved. This value is also obtained when the H density is around 10^8 cm^{-3}. Thus, the critical density of electrons and hydrogen atoms are 10^5 cm^{-3} and 10^8 cm^{-3}, respectively. In the lower four panels of Figure 3.3, we keep the temperature fixed at 2700 K and the H_2 density set at 10^{-2} cm^{-3}, 1 cm^{-3}, 10^2 cm^{-3}, and 10^4 cm^{-3}, respectively. All four panels give a similar result, implying that the excitation is independent of the H_2 collision. The upper four panels of Figure 3.3 remain unchanged when the H_2 is omitted as a collider. The right four panels show that it is independent of the collision of H_2 when the H_2 density is $< 10^4$ cm^{-3}. However, the reactive collisions with H_2 may show differences that are not considered here due to the limitations of the public version of the RADEX code. In brief, we find that it is only the nonreactive collision with electrons that can successfully explain the excitation of ArH^+ when the temperature is beyond the upstate energy of these two levels discussed here. Loh et al. (2012) estimated the electron number density and total hydrogen number density ($n(H^+) + n(H) + 2n(H_2)$) in the filaments and knots to be around $1400 - 2500$ cm^{-3} and $14000 - 25000$ cm^{-3} respectively. Barlow et al. (2013) estimated the electron number density of $\sim$ a few times 100 cm^{-3}. Our results shown in the top four panels of Figure 3.3 require a n_e of $\sim 2000 - 3000$ cm^{-3} to reproduce the observed ratio around the measured excitation temperature of H_2. Only the nonreactive collision with electrons can explain the ArH^+ excitation in the Crab.

3.2 Chemical pathways

Following the reaction network of ArH^+ presented in Priestley et al. (2017), here, we prepare similar pathways for NeH^+ and HeH^+. Additionally, we prepare the pathways for the hydroxyl cations of the noble gas species ($ArOH^+$, $NeOH^+$, and $HeOH^+$) under similar environments. In Table 3.3, the reaction network adopted here to study the chemical evolution of the related hydride and hydroxyl cations is listed along with the corresponding rate coefficients. The enlisted rate coefficients are either estimated or taken from the literature as mentioned in the footnote. In the following subsections, we present an extensive discussion to prepare or adapt the rate coefficients of various kinds of reactions considered. We use the reaction rates of UMIST as the default for the other reactions. For H_2 formation on grains, we use the modified "Jura rate" (Sternberg & Neufeld, 1999) for Model A. The default "Jura rate" of H_2 formation is 3×10^{-17} cm^3 s^{-1} (Jura, 1975). In Model B, the chemical pathways are the same as discussed above, except the H_2 formation rate is through grain catalysis. This rate is taken from Cazaux & Tielens (2002) as it was considered by Richardson et al. (2013).

3.2.1 Cosmic-ray ionization rate

The cosmic-ray ionization rate affects the chemical and ionization state of the gas. The CLOUDY code deals with the cosmic-ray density. It automatically converts the given cosmic-ray ionization rates into the cosmic-ray density. It considers the cosmic-ray ionization rate to be 2×10^{-16} s^{-1} per H (ζ'_H) and 4.6×10^{-16} s^{-1} per H_2 (ζ'_{H_2}) by default. Thus, the default rate per H_2 (ζ'_{H_2}) is 2.3 times higher than that of H (ζ'_H). The factor 2.3 instead of 2 in the relation arises because of the secondary ionization. This ionization is produced when the suprathermal electrons are knocked off in the primary ionization. Here, we use the cosmic-ray ionization rate per H_2 as $\zeta_{H_2} = \zeta_0 = 1.3 \times 10^{-17}$ s^{-1} (CLOUDY scales it with respect to ζ'_H to consider the cosmic-ray density). Our standard rate is varied (in between ζ_0 and $10^8\zeta_0$) relative to it. This means our standard ζ_H is 5.65×10^{-18} s^{-1}. In Table 3.3, reaction number 1 (CR) of the Ar network represents the cosmic-ray ionization rate by ζ_H and reaction number 2 (CRPHOT) by ζ_{H_2}. For the similar cosmic-ray ionization reactions with He and Ne, we consider the same leading coefficient as Ar (Schilke et al., 2014; Priestley et al., 2017). In CLOUDY, the direct ionization by cosmic-rays is automatically considered for all the ionization stages and all elements.

Table 3.3: Reaction pathways for the formation and destruction of some noble gas ions (Das et al., 2020).

Reaction Number (Type)	Reactions	Rate coefficient	References and comments
	Ar chemistry		
1 (CR)	$Ar + CR \rightarrow Ar^+ + e^-$	$10\zeta_{H,cr}$ s^{-1}	a, d
2 (CRPHOT)	$Ar + CRPHOT \rightarrow Ar^+ + e^-$	$0.8\frac{\zeta_{H_2,cr}}{1-\omega}$ s^{-1}	a, d
3 (IN)	$Ar + H_2^+ \rightarrow ArH^+ + H$	10^{-9} cm^3 s^{-1}	a
4 (IN)	$Ar + H_3^+ \rightarrow ArH^+ + H_2$	$8 \times 10^{-10}\exp(\frac{-6019\ K}{T})$ cm^3 s^{-1}	This work
5 (IN)	$Ar^+ + H_2 \rightarrow ArH^+ + H$	$8.4 \times 10^{-10}(\frac{T}{300\ K})^{0.16}$ cm^3 s^{-1}	a
6 (IN)	$ArH^+ + H_2 \rightarrow Ar + H_3^+$	8×10^{-10} cm^3 s^{-1}	a
7 (IN)	$ArH^+ + CO \rightarrow Ar + HCO^+$	1.25×10^{-9} cm^3 s^{-1}	a
8 (IN)	$ArH^+ + O \rightarrow Ar + OH^+$	8×10^{-10} cm^3 s^{-1}	a
9 (IN)	$ArH^+ + C \rightarrow Ar + CH^+$	8×10^{-10} cm^3 s^{-1}	a
10 (IN)	$Ar^{++} + H \rightarrow Ar^+ + H^+$	10^{-15} cm^3 s^{-1}	b
11 (RA)	$Ar + OH^+ \rightarrow ArOH^+ + h\nu$	1.9×10^{-17} cm^3 s^{-1}	c, m
12 (RA)	$Ar^+ + OH \rightarrow ArOH^+ + h\nu$	1.5×10^{-17} cm^3 s^{-1}	c, m
13 (RA)	$ArH^+ + O \rightarrow ArOH^+ + h\nu$	3.0×10^{-17} cm^3 s^{-1}	c, m
14 (IN)	$Ar + N_2^+ \rightarrow Ar^+ + N_2$	3.65×10^{-10} cm^3 s^{-1}	d
15 (IN)	$Ar^+ + H_2 \rightarrow Ar + H_2^+$	2.00×10^{-12} cm^3 s^{-1}	d
16 (IN)	$Ar^+ + O_2 \rightarrow Ar + O_2^+$	3.50×10^{-11} cm^3 s^{-1}	d
17 (IN)	$Ar^+ + CH_4 \rightarrow CH_2^+ + Ar + H_2$	1.40×10^{-10} cm^3 s^{-1}	d
18 (IN)	$Ar^+ + CH_4 \rightarrow CH_3^+ + Ar + H$	7.90×10^{-10} cm^3 s^{-1}	d
19 (IN)	$Ar^+ + HCl \rightarrow Ar + HCl^+$	2.90×10^{-10} cm^3 s^{-1}	d
20 (IN)	$Ar^+ + HCl \rightarrow ArH^+ + Cl$	6.00×10^{-11} cm^3 s^{-1}	d
21 (IN)	$Ar^+ + CO \rightarrow Ar + CO^+$	2.80×10^{-11} cm^3 s^{-1}	d
22 (IN)	$Ar^+ + NH_3 \rightarrow Ar + NH_3^+$	1.60×10^{-9} cm^3 s^{-1}	d
23 (IN)	$Ar^+ + N_2 \rightarrow Ar + N_2^+$	1.20×10^{-11} cm^3 s^{-1}	d
24 (IN)	$Ar^+ + H_2O \rightarrow Ar + H_2O^+$	1.30×10^{-9} cm^3 s^{-1}	d
25 (XR)	$Ar + XR \rightarrow Ar^{++} + e^- + e^-$	ζ_{XR} s^{-1}	d, e
26 (XR)	$Ar^+ + XR \rightarrow Ar^{++} + e^-$	ζ_{XR} s^{-1}	d, e
27 (XRSEC)	$Ar + XRSEC \rightarrow Ar^+ + e^-$	$5.53\zeta_{H,XRPHOT}$ s^{-1}	d, l
28 (XRPHOT)	$Ar + XRPHOT \rightarrow Ar^+ + e^-$	$0.8\frac{\zeta_{H2,XRPHOT}}{1-\omega}$ s^{-1}	d, l
29 (ER)	$Ar^+ + e^- \rightarrow Ar + h\nu$		d
30 (ER)	$Ar^{++} + e^- \rightarrow Ar^+ + h\nu$		d
31 (DR)	$ArH^+ + e^- \rightarrow Ar + H$	10^{-11} cm^3 s^{-1}	a, k
32 (DR)	$ArOH^+ + e^- \rightarrow Ar + OH$	10^{-11} cm^3 s^{-1}	This work
33 (PH)	$ArH^+ + h\nu \rightarrow Ar^+ + H$	$4.20 \times 10^{-12}\exp(-3.27A_V)$ s^{-1}	h
34 (PH)	$ArOH^+ + h\nu \rightarrow Ar + OH^+$	$4.20 \times 10^{-12}\exp(-3.27A_V)$ s^{-1}	This work

Reaction Number (Type)	Reactions	Rate coefficient	References and comments
	Ne chemistry		
1 (CR)	$Ne + CR \rightarrow Ne^+ + e^-$	$10\zeta_{H,cr}$ s^{-1}	This work, d
2 (CRPHOT)	$Ne + CRPHOT \rightarrow Ne^+ + e^-$	$0.8\frac{\zeta_{H_2,cr}}{1-\omega}$ s^{-1}	This work, d
3 (IN)	$Ne + H_2^+ \rightarrow NeH^+ + H$	$2.58 \times 10^{-10}exp(\frac{-6717\ K}{T})$ cm^3 s^{-1}	This work
4 (IN)	$Ne + H_3^+ \rightarrow NeH^+ + H_2$	$8 \times 10^{-10}exp(\frac{-27456\ K}{T})$ cm^3 s^{-1}	This work
5a (IN)	$Ne^+ + H_2 \rightarrow NeH^+ + H$	$3.2 \times 10^{-9}(\frac{T}{300\ K})^{0.16}$ cm^3 s^{-1}	This work
5b (IN)	$Ne^+ + H_2 \rightarrow Ne + H + H^+$	$1.98 \times 10^{-14}exp(-35\ K/T)$ cm^3 s^{-1}	This work
5c (IN)	$Ne^+ + H_2 \rightarrow Ne + H_2^+$	4.84×10^{-15} cm^3 s^{-1}	This work
6 (IN)	$NeH^+ + H_2 \rightarrow Ne + H_3^+$	3.65×10^{-9} cm^3 s^{-1}	This work
7 (IN)	$NeH^+ + CO \rightarrow Ne + HCO^+$	2.26×10^{-9} cm^3 s^{-1}	This work
8 (IN)	$NeH^+ + O \rightarrow Ne + OH^+$	2.54×10^{-9} cm^3 s^{-1}	This work
9 (IN)	$NeH^+ + C \rightarrow Ne + CH^+$	1.15×10^{-9} cm^3 s^{-1}	This work
10 (IN)	$Ne^{++} + H \rightarrow Ne^+ + H^+$	1.94×10^{-15} cm^3 s^{-1}	This work
11 (RA)	$Ne + OH^+ \rightarrow NeOH^+ + h\nu$	1.4×10^{-18} cm^3 s^{-1}	c, m
12 (RA)	$Ne^+ + OH \rightarrow NeOH^+ + h\nu$	7.5×10^{-17} cm^3 s^{-1}	c, m
13 (RA)	$NeH^+ + O \rightarrow NeOH^+ + h\nu$	2.3×10^{-17} cm^3 s^{-1}	c, m
14 (IN)	$HeH^+ + Ne \rightarrow NeH^+ + He$	1.25×10^{-9} cm^3 s^{-1}	d
15 (IN)	$NeH^+ + He \rightarrow HeH^+ + Ne$	3.8×10^{-14} cm^3 s^{-1}	d
16 (IN)	$Ne^+ + CH_4 \rightarrow CH^+ + Ne + H_2 + H$	8.4×10^{-13} cm^3 s^{-1}	d
17 (IN)	$Ne^+ + CH_4 \rightarrow CH_2{}^+ + Ne + H_2$	4.2×10^{-12} cm^3 s^{-1}	d
18 (IN)	$Ne^+ + CH_4 \rightarrow CH_3{}^+ + Ne + H$	4.7×10^{-12} cm^3 s^{-1}	d
19 (IN)	$Ne^+ + CH_4 \rightarrow CH_4{}^+ + Ne$	1.1×10^{-11} cm^3 s^{-1}	d
20 (IN)	$Ne^+ + NH_3 \rightarrow NH^+ + Ne + H_2$	4.5×10^{-12} cm^3 s^{-1}	d
21 (IN)	$Ne^+ + NH_3 \rightarrow NH_2{}^+ + Ne + H$	1.9×10^{-10} cm^3 s^{-1}	d
22 (IN)	$Ne^+ + NH_3 \rightarrow NH_3{}^+ + Ne$	2.7×10^{-11} cm^3 s^{-1}	d
23 (IN)	$Ne^+ + N_2 \rightarrow N_2{}^+ + Ne$	1.1×10^{-13} cm^3 s^{-1}	d
24 (IN)	$Ne^+ + H_2O \rightarrow H_2O^+ + Ne$	8.0×10^{-10} cm^3 s^{-1}	d
25 (IN)	$Ne^+ + O_2 \rightarrow O^+ + Ne + O$	6.0×10^{-11} cm^3 s^{-1}	d
26 (XR)	$Ne + XR \rightarrow Ne^{++} + e^- + e^-$	ζ_{XR} s^{-1}	d, e
27 (XR)	$Ne^+ + XR \rightarrow Ne^{++} + e^-$	ζ_{XR} s^{-1}	d, e
28 (XRSEC)	$Ne + XRSEC \rightarrow Ne^+ + e^-$	$1.84\zeta_{H,XRPHOT}$ s^{-1}	d, l
29 (XRPHOT)	$Ne + XRPHOT \rightarrow Ne^+ + e^-$	$0.8\frac{\zeta_{H2,XRPHOT}}{1-\omega}$ s^{-1}	d, l
30 (ER)	$Ne^+ + e^- \rightarrow Ne + h\nu$		d
31 (ER)	$Ne^{++} + e^- \rightarrow Ne^+ + h\nu$		d
32 (DR)	$NeH^+ + e^- \rightarrow Ne + H$	10^{-11} cm^3 s^{-1}	This work
33 (DR)	$NeOH^+ + e^- \rightarrow Ne + OH$	10^{-11} cm^3 s^{-1}	This work
34 (PH)	$NeH^+ + h\nu \rightarrow Ne^+ + H$	$4.20 \times 10^{-12}exp(-3.27A_V)$ s^{-1}	This work
35 (PH)	$NeOH^+ + h\nu \rightarrow Ne + OH^+$	$4.20 \times 10^{-12}exp(-3.27A_V)$ s^{-1}	This work

Reaction Number (Type)	Reactions	Rate coefficient	References and comments
	He chemistry		
1 (CR)	$He + CR \rightarrow He^+ + e^-$	$10\zeta_{H,cr}$ s^{-1}	This work, d
2 (CRPHOT)	$He + CRPHOT \rightarrow He^+ + e^-$	$0.8\frac{\zeta_{H_2,cr}}{1-\omega}$ s^{-1}	This work, d
3 (IN)	$He + H_2^+ \rightarrow HeH^+ + H$	$3 \times 10^{-10}\exp(\frac{-6717\ K}{T})$ cm^3 s^{-1}	n
4 (IN)	$He + H_3^+ \rightarrow HeH^+ + H_2$	$8 \times 10^{-10}\exp(\frac{-29110\ K}{T})$ cm^3 s^{-1}	This work
5a (IN)	$He^+ + H_2 \rightarrow HeH^+ + H$		Not considered
5b (IN)	$He^+ + H_2 \rightarrow He + H + H^+$	$3.70 \times 10^{-14}\exp(-35\ K/T)$ cm^3 s^{-1}	This work, UMIST
5c (IN)	$He^+ + H_2 \rightarrow He + H_2^+$	7.20×10^{-15} cm^3 s^{-1}	This work, UMIST
6 (IN)	$HeH^+ + H_2 \rightarrow He + H_3^+$	1.26×10^{-9} cm^3 s^{-1}	j
7 (IN)	$HeH^+ + CO \rightarrow He + HCO^+$	2.33×10^{-9} cm^3 s^{-1}	This work
8 (IN)	$HeH^+ + O \rightarrow He + OH^+$	2.68×10^{-9} cm^3 s^{-1}	This work
9 (IN)	$HeH^+ + C \rightarrow He + CH^+$	1.18×10^{-9} cm^3 s^{-1}	This work
10 (IN)	$He^{++} + H \rightarrow He^+ + H^+$	2.45×10^{-15} cm^3 s^{-1}	This work
11 (RA)	$He + OH^+ \rightarrow HeOH^+ + h\nu$	2.2×10^{-18} cm^3 s^{-1}	c, m
12 (RA)	$He^+ + OH \rightarrow HeOH^+ + h\nu$	1.7×10^{-16} cm^3 s^{-1}	c, m
13 (RA)	$HeH^+ + O \rightarrow HeOH^+ + h\nu$	2.8×10^{-17} cm^3 s^{-1}	c, m
14 (IN)	$HeH^+ + H \rightarrow He + H_2^+$	1.7×10^{-9} cm^3 s^{-1}	n
15 (RA)	$He^+ + H \rightarrow HeH^+ + h\nu$	1.44×10^{-16} cm^3 s^{-1}	i, n
16 (RA)	$He + H^+ \rightarrow HeH^+ + h\nu$	$5.6 \times 10^{-21}(\frac{T}{10^4 K})^{-1.25}$ cm^3 s^{-1}	d, n
17 (XR)	$He + XR \rightarrow He^{++} + e^- + e^-$	ζ_{XR} s^{-1}	d, e
18 (XR)	$He^+ + XR \rightarrow He^{++} + e^-$	ζ_{XR} s^{-1}	d, e
19 (XRSEC)	$He + XRSEC \rightarrow He^+ + e^-$	$0.84\zeta_{H,XRPHOT}$ s^{-1}	d, l
20 (XRPHOT)	$He + XRPHOT \rightarrow He^+ + e^-$	$0.8\frac{\zeta_{H2,XRPHOT}}{1-\omega}$ s^{-1}	d, l
21 (ER)	$He^+ + e^- \rightarrow He + h\nu$		d
22 (ER)	$He^{++} + e^- \rightarrow He^+ + h\nu$		d
23 (DR)	$HeH^+ + e^- \rightarrow He + H$	$4.3 \times 10^{-10}(\frac{T}{10^4\ K})^{-0.5}$ cm^3 s^{-1}	n
24 (DR)	$HeOH^+ + e^- \rightarrow He + OH$	$4.3 \times 10^{-10}(\frac{T}{10^4\ K})^{-0.5}$ cm^3 s^{-1}	This work
25 (PH)	$HeH^+ + h\nu \rightarrow He^+ + H$		d, n
26 (PH)	$HeOH^+ + h\nu \rightarrow He + OH^+$	$4.20 \times 10^{-12}\exp(-3.27A_V)$ s^{-1}	This work
27	$He^+ + H^- \rightarrow HeH^+ + e^-$	$3.2 \times 10^{-11}(\frac{T}{10^4\ K})^{-0.34}$ cm^3 s^{-1}	n
	Additional modified chemistry		
1 (RA)	$H^+ + H \rightarrow H_2^+ + h\nu$	$2.3 \times 10^{-16}(\frac{T}{10^4\ K})^{1.5}$ cm^3 s^{-1}	d, n
2 (DR)	$H_2^+ + e^- \rightarrow H + H$	$3 \times 10^{-9}(\frac{T}{10^4\ K})^{-0.4}$ cm^3 s^{-1}	d, n
3 (IN)	$H_2^+ + H \rightarrow H_2 + H^+$	6.4×10^{-10} cm^3 s^{-1}	d, n

Note:
CR refers to cosmic-rays, CRPHOT to secondary photons produced by cosmic-rays, XR to direct X-rays, XRSEC to secondary electrons which are produced by X-rays, XRPHOT to secondary photons from X-rays, IN to ion-neutral reactions, RA to radiative association reactions, ER to electronic recombination reactions for atomic ions, DR to dissociative recombination reactions for molecular ions, PH to photodissociation reactions, $h\nu$ to a photon, ζ to cosmic-ray or X-ray ionization rates, and ω is the dust albedo.

[a] Schilke et al. (2014).
[b] Kingdon & Ferland (1996).
[c] This lower limit of the rate is calculated following Bates (1983) described in Section 3.2.3.
[d] Reaction pathways are already included or automatically calculated in Cloudy by default.
[e] Meijerink & Spaans (2005).
[h] Roueff et al. (2014).
[i] Güsten et al. (2019).
[j] Orient (1977).
[k] Priestley et al. (2017).
[l] See Appendix A for the calculation details. Here, we are not considering this rate because we are using default values in Cloudy. In the Cloudy code, these values are automatically calculated without any special actions being required.
[m] This upper limit of the rate is of $\sim 10^{-10}$ cm^3 s^{-1}. See Section 3.2.3 for a more detailed discussion regarding this upper limit.
[n] Neufeld et al. (2020) and references therein.

3.2.2 Ion-neutral reaction rate

The rate coefficients of the ion-neutral (IN) reaction of the Ar-related species were already discussed in Priestley et al. (2017). In constructing the reaction network with He and Ne, we either assume the same rate constants as used for the IN reactions of Ar or use some educated guess. We also include the reaction pathways and rate constants from Güsten et al. (2019), Neufeld et al. (2020), and Orient (1977). In Table 3.3, the IN rates are given in reaction numbers $3-10$, $14-24$ for Ar, $3-10$, $14-25$ for Ne, and $3-10$, 14 for He netwok. Reaction numbers $14-24$ of Ar, $14-25$ of Ne network were not considered in Priestley et al. (2017). However, these pathways are included in the CLOUDY default network, and thus, we use it.

For reaction 3 ($Ar + {H_2}^+ \rightarrow ArH^+ + H$) of Ar, we consider a rate coefficient of 10^{-9} cm^3 s^{-1} following Priestley et al. (2017). We also use quantum-chemical calculations (DFT B3LYP/6-311++G(d,p) level of theory) with the GAUSSIAN 09 suite of programs (Frisch et al., 2013) and find that this reaction is highly exothermic. Similar calculations for NeH^+ formation ($Ne + {H_2}^+ \rightarrow NeH^+ + H$) and HeH^+ formation ($He + {H_2}^+ \rightarrow HeH^+ + H$) show a highly endothermic nature. Neufeld et al. (2020) considered a rate coefficient of $\sim 3 \times 10^{-10} \exp(\frac{-6717\ \mathrm{K}}{\mathrm{T}})$ cm^3 s^{-1} for the HeH^+ formation by this reaction. We notice that the endothermicity of NeH^+ formation by this reaction is smaller than that of the endothermicity of HeH^+. Because no reference is available for $Ne + {H_2}^+ \rightarrow NeH^+ + H$, we scale the HeH^+ formation rate here and use $\sim 2.58 \times 10^{-10} \exp(\frac{-6717\ \mathrm{K}}{\mathrm{T}})$ cm^3 s^{-1} in our network.

In the case of reaction 4 ($X + {H_3}^+ \rightarrow XH^+ + H_2$) of Ar, an endothermicity of about 6400 K was noted by Villinger et al. (1982). We use the same empirical relation for the reaction between ${H_3}^+$ and He/Ne. From our quantum-chemical calculations, we obtain endothermicities of about 6019 K, 27456 K, and 29110 K for reaction 4 of the Ar, Ne, and He-related pathways, respectively, and use these values for the computation of the rate constant of reaction 4 shown in Table 3.3.

We calculate the enthalpies of reactions for reaction numbers $5-10$ of Table 3.3 and find all reactions are exothermic. The rate constants of some of these reactions containing Ar were already given in Priestley et al. (2017). Here, we use the same rate for our calculation. To estimate the rate constant for Ne, we derive a scaling factor depending on our computed exothermicity values. Because the earlier studies did not consider reaction 5a of the He network (Güsten et al., 2019; Neufeld et al., 2020), we are not considering this reaction here. We consider two other routes of Ne and He, having the possible product channels 5(b) $X^+ + H_2 \rightarrow X + H + H^+$ and 5(c) $X^+ + H_2 \rightarrow X + H_2^+$. In the case of X=Ne, channel 5(b) is considered because

the ionization potential of Ne (21.56 eV) is greater than the sum of the ionization potential of H and the dissociation energy of H_2, i.e. (13.60 + 4.48) eV = 18.08 eV. In the UMIST network, similar reaction channels (5b and 5c) are available for the X=He network. By calculating the enthalpies of reactions and comparing them between reactions 5b and 5c of the Ne and He networks, we again obtain scaling factors to estimate the rate coefficients of reactions 5b and 5c of the Ne network.

For the rate coefficient for the destruction of ArH^+ with H_2, we consider the same one used in Priestley et al. (2017). To destroy HeH^+ by H_2 (i.e., reaction number 6 of the He network), we use the rate coefficient measured by Orient (1977). For the NeH^+ destruction by H_2, we use a scaling technique similar to that mentioned earlier. We prepare the IN reaction network of He according to the very recent work by Neufeld et al. (2020). For the sake of completeness, they updated the reaction network developed by Güsten et al. (2019) and added several formation and destruction reactions related to He. We include the HeH^+ destruction by H (reaction 14 of the He network) with a constant rate coefficient 1.7×10^{-9} cm^3s^{-1}.

3.2.3 Radiative association

Recently, Theis & Fortenberry (2016) studied the formation of $ArOH^+$ and $NeOH^+$ quantum-chemically. They considered three channels for the formation of $NeOH^+$ (by $Ne^+ + OH$, $NeO + H^+$, and $NeH^+ + O$) and three channels for the formation of $ArOH^+$ (by $Ar^+ + OH$, $ArO + H^+$, and $ArH^+ + O$). According to their relative energy calculations, $ArOH^+$ remains in an energy state lower than the total relative energy of their reactants and products (see Figure 2 of Theis & Fortenberry, 2016), whereas $NeOH^+$ leads to a likely spontaneous dissociation into Ne and OH^+ (see Figure 1 of Theis & Fortenberry, 2016). Because the reactants have higher energy, some energy is released during its formation. These reactions could be treated as radiative association reactions (reaction numbers 11-13 of Table 3.3). We calculate the rate constant of these reactions using the method described below (Bates, 1983):

$$K = 1 \times 10^{-21} A_r \frac{(6E_0 + N - 2)^{3N-7}}{(3N-7)!}\ cm^3 s^{-1}. \tag{3.1}$$

This temperature-independent semiempirical relation provided by Bates (1983) requires the association energy (E_0) in eV, numbers of nuclei (N) in the complex, and transition probability (A_r) in s^{-1}, which is taken to be 100, as suggested by Bates (1983). The calculated rates for reactions $11 - 13$ are noted in Table 3.3. But this semiempirical relation is temperature-independent and estimated at a temperature

of $\sim$ 30 K. Here, we are dealing with Crab knots, where the temperature is much higher. Keeping this in mind, additionally, we consider an upper limit (10^{-10} cm^3 s^{-1}) to these reactions. Although Theis & Fortenberry (2016) did not consider the reaction between X (= Ar, Ne, and He) and OH^+ for the formation of XOH^+, we consider reaction number 11 of each network because we find it to be exothermic.

We adopt the value of 1.44×10^{-16} cm^3 s^{-1} as the rate coefficient of the HeH^+ formation reaction (He-related reaction number 15, i.e., $He^+ + H \rightarrow HeH^+ + h\nu$). Güsten et al. (2019) ignored $He + H^+ \rightarrow HeH^+ + h\nu$ (reaction 16 of He-related reactions) in the planetary nebula environment, which dominates HeH^+ formation in the early universe. But Neufeld et al. (2020) considered the same formation of HeH^+ through the radiative association reaction using a temperature-dependent rate of $5.6 \times 10^{-21}(\frac{T}{10^4 K})^{-1.25}$ cm^3 s^{-1}. Here also, we use the same rate coefficient for reaction 16 of the He network.

3.2.4 X-ray ionization rate

X-ray photoionization, including inner-shell ionization and Auger cascades, collisional ionization by secondary electrons coming from the inner-shell photoionization, are fully treated in CLOUDY for all basic elements without any unique action being required. However, the physical conditions adopted here demand a chemical network that takes the effect of X-ray ionization into account. We consider the three types of X-ray-induced reactions, namely (a) ionization by direct X-rays (ζ_{XR}), (b) secondary ionization by X-rays (ζ_{XRPHOT}), and (c) electron-impact X-ray ionization (ζ_{XRSEC}). The X-ray can mainly ionize the heavy elements by removing the K-shell electron. Auger transitions then fill the vacancy created by the removal of the K-shell electron. In addition, other electrons and X-ray photons are emitted by the ion during this process, resulting in multiply ionized species. Thus, x-ray ionization is an essential means to dictate the chemistry around the Crab environment. Here, we compute various X-ray ionization rates by adopting the method used in Meijerink & Spaans (2005). Though these calculated rates are not directly used in the CLOUDY model, building the noble-gas-related pathways from scratch will be very useful. Please see Appendix Chapter A for the detailed process of the estimation of the X-ray ionization rate.

3.2.5 Electronic and dissociative recombination

We consider the electronic recombination (ER) reactions of the noble gas atomic ions (X^+, X^{++} for X =Ar, Ne, He) and dissociative recombination (DR) reactions of the noble gas molecular ions (XH^+, XOH^+ for X =Ar, Ne, He). The ER reactions with numbers 29-30 for Ar, 30-31 for Ne, and 21-22 for He are treated automatically in CLOUDY to make sure that they correctly balance the inverse photoionization processes. So, we do not include them again. We list them in Table 3.3 for the sake of completeness. Priestley et al. (2017) consider a temperature-dependent rate coefficient for ER of Ar^+ (Schilke et al., 2014) and Ar^{++} (Shull & van Steenberg, 1982).

For the DR of ArH^+, Priestley et al. (2017) considered a typical rate of about 10^{-9} cm^3 s^{-1} for their initial model following Schilke et al. (2014) and a reduced rate 10^{-11} cm^3 s^{-1} for their final models. Abdoulanziz et al. (2018) presented the cross sections for DR and electron-impact vibrational excitation of ArH^+ at electron energies appropriate for the interstellar environment. They found very low values of the DR rate coefficients at temperatures below 1000 K. They concluded that DR plays a minor role. In contrast, the collisions with H_2 molecules and the photodissociation are the only significant ArH^+ destruction mechanisms in the ISM. Here, we consider a temperature-independent rate constant of 10^{-11} cm^3 s^{-1}, similar to the final models of Priestley et al. (2017) for the DR of ArH^+. In addition, we assume that the same rate constant of 10^{-11} is valid for the DR of $ArOH^+$, NeH^+, and $NeOH^+$. For HeH^+, we use the very recently updated temperature-dependent rate of $4.3 \times 10^{-10}(T/10^4\ K)^{-0.5}$ cm^3 s^{-1} following Neufeld et al. (2020). For $HeOH^+$, we consider the same DR rate as it was considered for HeH^+.

3.2.6 Photodissociation

We consider the rate coefficients of the photodissociation (PH) reactions of the hydride and hydroxyl cations following the PH reaction of ArH^+ (Roueff et al., 2014; Priestley et al., 2017). Priestley et al. (2017) did not consider the PH reaction of HeH^+ (i.e., He network reaction number 25) because their input SED has negligible flux beyond the Lyman limit relevant for the cross-section given by Roberge & Dalgarno (1982). Güsten et al. (2019) also ignored it as the reaction progresses very slowly. According to Neufeld et al. (2020), we consider this reaction, which is automatically controlled in CLOUDY default network.

Table 3.4: Gas-phase elemental abundances of species with respect to total hydrogen nuclei in all forms for the modeling of diffuse ISM using CLOUDY (Das et al., 2020).

Element	Abundance	Element	Abundance
H	1.00	^{36}Ar	2.82×10^{-6}
He	0.098	^{38}Ar	5.13×10^{-7}
C	2.51×10^{-4}	^{40}Ar	8.20×10^{-10}
N	7.94×10^{-5}	^{20}Ne	1.23×10^{-4}
O	3.19×10^{-4}	^{22}Ne	9.04×10^{-6}
Cl	1.00×10^{-7}	S	3.24×10^{-5}
Mg	1.26×10^{-5}	Fe	6.31×10^{-7}
Si	3.16×10^{-6}		

Note: For the initial isotopic ratio of argon and neon, we have used ^{36}Ar/^{38}Ar/^{40}Ar = 84.5946/15.3808/0.0246 and ^{20}Ne/^{21}Ne/^{22}Ne = 92.9431/0.2228/6.8341, following Wieler (2002).

3.3 Results and discussions on chemical modeling

Based on the reactions network described in the early Section 3.2, we study the hydride and hydroxyl cations of Ar, Ne, and He. Schilke et al. (2014) assigned absorption lines of ArH^+ to the previously unidentified absorption lines. Though we mainly focus here on the Crab environment, it will be very useful to first check our model with the model described in Schilke et al. (2014) and Priestley et al. (2017) for the diffuse ISM. It will also be useful to look at the predicted abundances of other hydride and hydroxyl cations in diffuse cloud conditions.

3.3.1 Diffuse interstellar medium

Here, we assume a cloud with the initial number density of total hydrogen nuclei (n_H) of 50 cm^{-3} and a primary cosmic-ray ionization rate for atomic hydrogen of $\zeta_H = 2 \times 10^{-16}$ s^{-1} (Schilke et al., 2014). We consider the default ISM elemental abundances of CLOUDY shown in Table 3.4. The unextinguished local ISRF is generated with the command *Table ISM* in CLOUDY. We use the mean ISRF (Draine, 1978) of 1 Draine unit, and the resultant shape of the incident SED is further modified by including the extinction due to photoelectric absorption by a cold neutral slab with a column density of $N(H) = 10^{20}$ cm^{-2} (Figure 3.2). Using the default ISM grain and the H_2 grain formation rate of 3×10^{-17} cm^{3}s^{-1} (Jura, 1975) and by considering the default PAH treatment in CLOUDY, we obtain an extinction-to-gas ratio of $A_V/N(H) = 5.412 \times 10^{-22}$ mag cm^2 for this region.

Figure 3.4 shows the abundances of some of the essential species considered in our network as a function of the visual extinction, A_V. The cloud remains in atomic

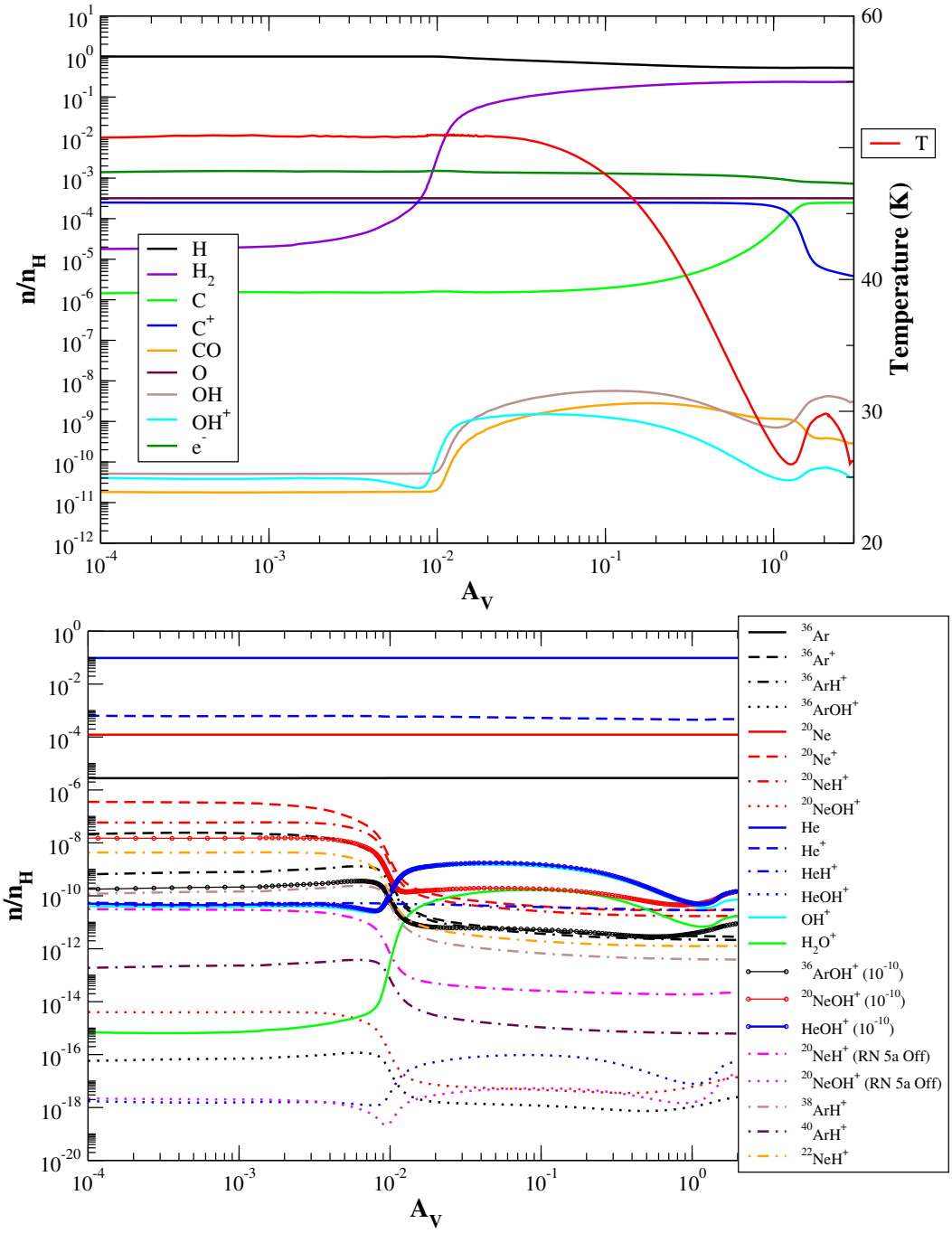

Figure 3.4: Variation of abundances for simple species with a diffuse ISM model shown in the upper panel. The right side of the upper panel, the electron temperature variation is shown. In the lower panel, the variation of isotopic abundances for noble gas species is shown. The abundances of $^{36}ArOH^+$, $^{20}NeOH^+$, and $HeOH^+$ considering the upper limit of their formation rate by radiative association reactions ($\sim 10^{-10}$ cm^3 s^{-1}), are noted [XOH^+ (10^{-10})]. The abundance profiles of $^{20}NeH^+$ and $^{20}NeOH^+$ are also shown when reaction 5a of the Ne network is off (Das et al., 2020).

form throughout the region, and the H_2 fractional abundance varies between 2×10^{-5} and 10^{-1}. The electron temperature ranges between 25 and 50 K, and electron fractional abundance remains roughly constant at $\sim 10^{-3}$. The peak abundance of ArH^+ is around 1.3×10^{-9}, decreasing with increasing A_V deep inside the cloud. ArH^+ is a unique tracer of the atomic gas, having an H_2 fractional abundance of $10^{-4} - 10^{-3}$ (Schilke et al., 2014). We find a very similar result here. Deep inside the filament, where the H_2 density is sufficiently increased, a strong anticorrelation is present between ArH^+ and H_2. The abundance profile of ArH^+ shows a strong anticorrelation with OH^+ and H_2O^+. It implies that while ArH^+ traces the region with lower H_2/H ratio, OH^+ and H_2O^+ favor the higher H_2/H ratio region. The obtained abundances of Ar^+ and ArH^+ match those measured by Schilke et al. (2014) and present a similar variation to A_V. For similar conditions, Priestley et al. (2017) found a slightly lower abundance of these species. NeH^+ also follows the similar behavior of ArH^+ and a strong anticorrelation with H_2 is observed. Moreover, we obtain a peak fractional abundance of $NeH^+ \sim 5 \times 10^{-8}$. Table 3.4 shows that Ne has a higher initial elemental abundance than Ar ($\frac{\mathrm{Ne}}{\mathrm{Ar}} = 43.6$). This is also reflected in the obtained peak abundance ratio between NeH^+ and ArH^+ (~ 38). However, the much higher initial elemental abundance of He than that of the Ar and Ne is not reflected in the obtained abundance of HeH^+. The obtained HeH^+ fractional abundance is smaller (peak abundance 5×10^{-11}) than that of ArH^+ and NeH^+. This is because ArH^+ and NeH^+ formation by $X^+ + H_2 \rightarrow XH^+ + H$ (reaction numbers 5 of Ar and 5a of the Ne network) is considered, which is avoided in HeH^+ formation here.

Theis et al. (2015) questioned the formation of NeH^+ by reaction 5a. They also found that the possible product of this reaction would be Ne and $H_2{}^+$ (i.e., reaction 5(c)). Here, for the diffuse cloud model, we find that the reaction between Ne^+ and H_2 (i.e., reaction 5a) forms the majority of NeH^+, and the abundance of NeH^+ is higher than that of ArH^+. However, NeH^+ is yet to be identified in the diffuse region. This also suggests an overestimation of the NeH^+ abundance in our model. To check the effect of reaction 5a, we consider the case where this reaction is switched off. In this case, we find that the abundance of NeH^+ significantly dropped and is consistent with its absence in the observed spectra (having a peak fractional abundance of $\sim 3 \times 10^{-11}$). The formation of the majority of NeH^+ in this case happens via reaction 14 ($HeH^+ + Ne \rightarrow NeH^+ + He$). However, in this case, we also see the anticorrelation between NeH^+ and H_2. Unless otherwise stated, the reaction 5a is on by default in all the cases reported here.

According to the recent work by Theis & Fortenberry (2016), the hydroxyl cations

Table 3.5: Comparison between the obtained column densities of some atomic and molecular ions with the observation of diffuse cloud toward W51 (Indriolo et al., 2012; Das et al., 2020).

Species	**Column density (cm^{-2})**	
	Model	**Observation**
H	3.02×10^{21}	$(1.39 \pm 0.3) \times 10^{21}$
H_2	1.26×10^{21}	$(1.06 \pm 0.52) \times 10^{21}$
H_3^+	3.52×10^{13}	$(2.89 \pm 0.37) \times 10^{14}$
OH^+	9.04×10^{11}	$(2.97 \pm 0.13) \times 10^{13}$
H_2O^+	1.43×10^{11}	$(6.09 \pm 0.96) \times 10^{12}$
C^+	5.61×10^{17}	$(4.0 \pm 0.4) \times 10^{17}$

of noble gas are the most stable small noble gas molecules analyzed, besides their respective hydride diatomic cation cousins. So, we include them in our network and plot them here to show the comparison between them. When reaction 5a of the Ne network is on, the abundance profile of $ArOH^+$ and $NeOH^+$ follows the ArH^+ and NeH^+ abundance profiles because most of them form by $ArH^+ + O$ and $NeH^+ + O$ (reaction 13 of the Ar and Ne network), respectively. The abundance profile of $HeOH^+$ follows that of OH due to the formation of the majority of $HeOH^+$ by He^+ and OH. When reaction 5a of the Ne network is off, we find a similar abundance profile of $NeOH^+$ with $HeOH^+$. Figure 3.4 also shows the abundances of $ArOH^+$, $NeOH^+$, and $HeOH^+$ by considering the upper limit of their formation rate by radiative association reactions ($\sim 10^{-10}$ cm^3 s^{-1}; see Section 3.2.3 for the justification). A significant production of hydroxyl ions is observed only when the upper limit of the rate coefficients is used. A comparison between the obtained column densities of some atomic and molecular ions with the observation of a diffuse cloud toward W51 is shown in Table 3.5. We find that our results are very close to the observed results.

We also include the ^{38}Ar, ^{40}Ar, ^{20}Ne, and ^{22}Ne isotopes in our network. $^{21}NeH^+$ is not considered here because the corresponding spectral information is absent in the CDMS/JPL database. For the initial isotopic ratio of argon and neon, we use $^{36}Ar/^{38}Ar/^{40}Ar = 84.5946/15.3808/0.0246$ and $^{20}Ne/^{22}Ne = 13.6$ (Wieler, 2002). We find that the peak fractional abundance of $^{38}ArH^+$, $^{40}ArH^+$, and $^{22}NeH^+$ is 2.2×10^{-10}, 3.8×10^{-13}, and 4.5×10^{9}, respectively. This yields a ratio of the peak abundance of $^{36}ArH^+/^{38}ArH^+/^{40}ArH^+ = 84.5946/14.32/0.0247$ and $^{20}NeH^+/^{22}NeH^+ = 11.11/1.0$ (reaction 5a of the Ne network is considered here). Because no fractionation reactions are considered in this work, initial elemental abundances are roughly reflected in the abundances of their respective hydride ions.

3.3.2 The Crab nebula filament

Physical conditions suitable for the Crab environment are already presented in Section 3.1. Figure 3.5 shows the variation of the abundances of different ionization states of the primary isotope of the noble gas ions (X = ^{36}Ar, ^{20}Ne, and He) as a function of the visual extinction (A_V) for Model A. For this case, we consider the initial model of the Crab with a total hydrogen nuclei density $n_H = 1900$ cm^{-3} and cosmic-ray ionization rate per H_2 $\zeta = \zeta_0 = 1.3 \times 10^{-17}$ s^{-1}. This ζ value is too low for an SNR; more realistic values are explored in the following sections. Here, we use this value because it is the standard value used in chemical models of molecular clouds and used in the initial model of Priestley et al. (2017). In the three blocks of Figure 3.5, we show three noble-gas-related (Ar, Ne, and He) species. We find that reaction numbers $1-2$ of all reaction sets in Table 3.3 and reaction numbers $27-28$ of Ar, $28-29$ of Ne, and $19-20$ of He are responsible for producing X^+ from X. X^+ is further converted into X^{++} by direct X-ray ionization. X^{++} can additionally be produced directly from X-ray ionization. In all blocks of Figure 3.5, we obtain a higher abundance of X^+ compared to X^{++}. Here, we use the initial elemental abundance of ^{36}Ar, ^{20}Ne, and He of 1.0×10^{-5}, 4.9×10^{-3}, and 1.85, respectively, relative to total hydrogen nuclei in all forms (see Table 3.2). This initial elemental abundance ratio between the noble gases is not maintained after forming their respective hydride ions. If they followed their initial abundances, then the abundance of the ArH^+ would have been $\sim 10^5$ times lower than that of the HeH^+ ion. Instead, from Figure 3.5, we obtain the peak abundance of ArH^+, NeH^+ (when Ne reaction 5a is off), and HeH^+ in a similar range. The reason behind this is due to (i) the lower ionization potential of ^{36}Ar (15.76 eV) compared to ^{20}Ne (21.5645 eV) and He (24.5874 eV), (ii) the high proton affinity of Ar (3.85 eV) compared to Ne (2.08 eV) and He (1.85 eV; Jolly, 1984), and (iii) the reaction pathways adopted.

In the early universe, HeH^+ formation was dominated by the reaction between He and H^+. Due to their high ionization potential, helium ions (He^+ and He^{+2}) recombined with electrons to produce the neutral helium first. Neutral helium was indeed the first neutral atom of the universe. In such a metal-free situation, He then reacted with H^+ to form the first chemical bond of the universe ($He + H^+ \rightarrow HeH^+ + h\nu$) and thus the first molecule, HeH^+. Recently, Güsten et al. (2019) identified the pure rotational ($J = 1-0$) transition of HeH^+ in the planetary nebula NGC 7027. But the formation of HeH^+ in the planetary environment progresses in a very different manner. Looking at the environment of NGC 7027 and its age, they ignored the HeH^+ formation by the reactions $He + H_2^+ \rightarrow HeH^+ + H$ and $He + H^+ \rightarrow HeH^+ + h\nu$ (re-

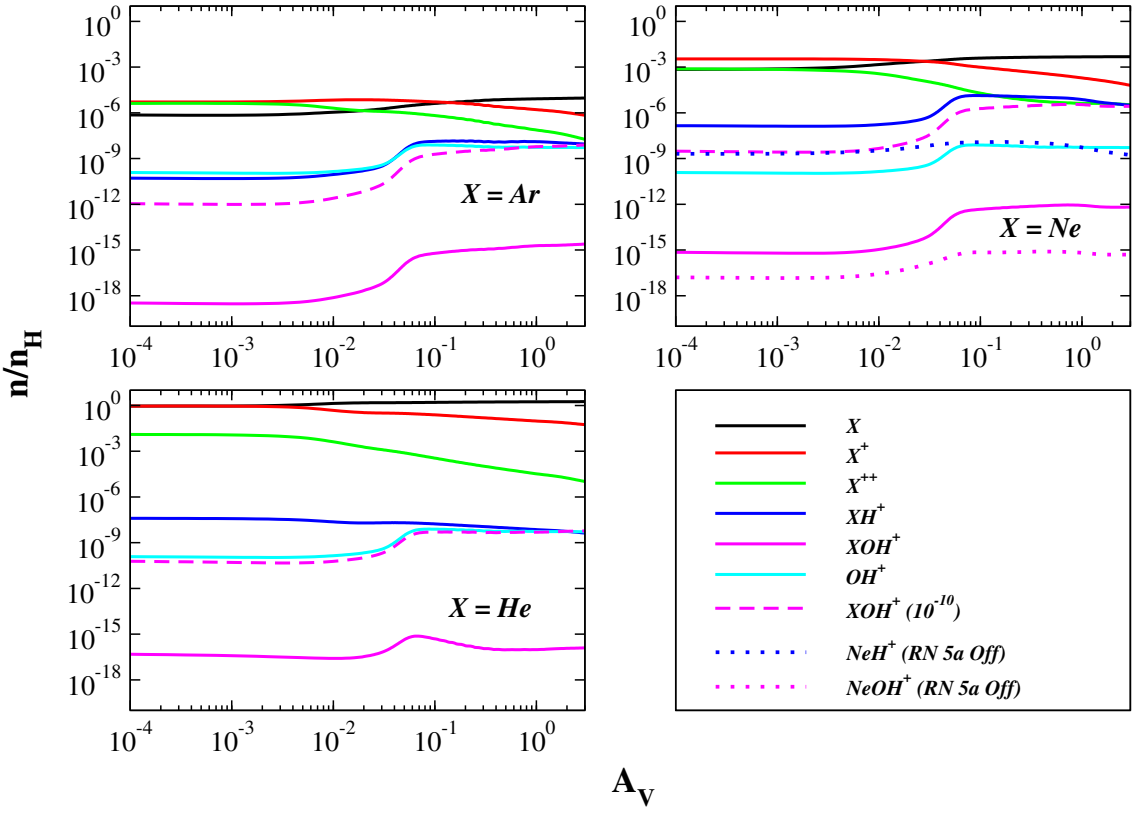

Figure 3.5: Abundances of various ionized states of noble gas (X = ^{36}Ar, ^{20}Ne, and He) along with their respective hydride and hydroxyl cations as a function of A_V considering Crab Model A with n_H = 1900 cm^{-3} and $\zeta_{H_2} = \zeta_0 = 1.3 \times 10^{-17}$ s^{-1} (Das et al., 2020). The dashed pink lines denote the abundance of XOH$^+$ considering the upper limit of forming XOH$^+$ ($\sim 10^{-10}$ cm^3 s^{-1}; see Section 3.2.3 for the justification). Abundances of NeH$^+$ and NeOH$^+$ are shown in dotted blue and dotted magenta lines respectively when Ne network reaction 5a is switched off.

action numbers 3 and 16, respectively, of the He network in Table 3.3). Neufeld et al. (2020) considered these two reactions in their network. Here, we use their adopted rate in our simulation. Additionally, we also consider $He^+ + H \rightarrow HeH^+ + h\nu$ (reaction number 15) following Güsten et al. (2019). The reaction between Ar and $H_3{}^+$ (reaction number 4) is considered by Priestley et al. (2017) in their model. We examine XH^+ formation by this reaction quantum-chemically (discussed in Section 3.2.2) and find an endothermicity of ≈ 6019 K for the formation of ArH^+. For the formation of NeH^+ and HeH^+, it is ~ 5 times higher than that of the ArH^+. It shows that the appearance of HeH^+ and NeH^+ by reaction number 4 is only possible at high temperatures (> 1000 K). The consideration of very different chemical pathways for the formation of ArH^+ compared to HeH^+ and NeH^+ thus plays a significant role in the mismatch between the initial elemental ratio considered and the ratio obtained after forming their hydride ions.

The lower limit of the detected OH^+ transition in the Crab can be used to set the lower observational limit for the noble gas ions modeled here. To show the comparison between the OH^+ abundance and the abundances of other noble-gas-related species, we plot the abundance of OH^+ in all panels of Figure 3.5. We obtain a lower peak abundance of OH^+ than Priestley et al. (2017). This is indeed required because Barlow et al. (2013) observed the ArH^+ transition to be significantly stronger than that of the OH^+. Figure 3.5 shows that ArH^+ is initially less abundant than OH^+, and finally, deep inside the filament, it shows the opposite trend.

The abundance variation for some important species is shown in Figure 3.6, considering the same physical condition as in Figure 3.5. The left panel shows the abundance variation of H, H_2, C, C^+, CO, OH, and OH^+ and the right panel shows the simple ions of H (H^+, $H_2{}^+$, and $H_3{}^+$), electrons, and the variation of the electron temperature. The left panel shows that most of the hydrogen is in atomic form, and thus, the cloud remains entirely atomic. In the outer part ($A_V < 1$ mag) of the cloud, carbon remains in the ionized form (C^+), but it is converted into the neutral form inside ($A_V > 1$ mag) the cloud. Because the cloud is mostly in diffuse atomic form, the CO fractional abundance is $\sim 10^{-10}$. Figure 3.6 shows that the abundance of H_2 is increasing deep inside the cloud. Figure 3.5 shows that the abundance of ArH^+ is also growing deep inside the cloud. Thus, the anticorrelation that has been seen between the abundance profile of ArH^+ and H_2 in Figure 3.4 is not reflected here. This might be due to the consideration of completely different physical-chemical conditions between these two cases. The right panel shows that H^+ is very abundant, and the electron abundance varies within a few times 10^{-1} (i.e., electron number density $\sim$ few times 10^2 cm^{-3} for $n_H = 1900$ cm^{-3}), which

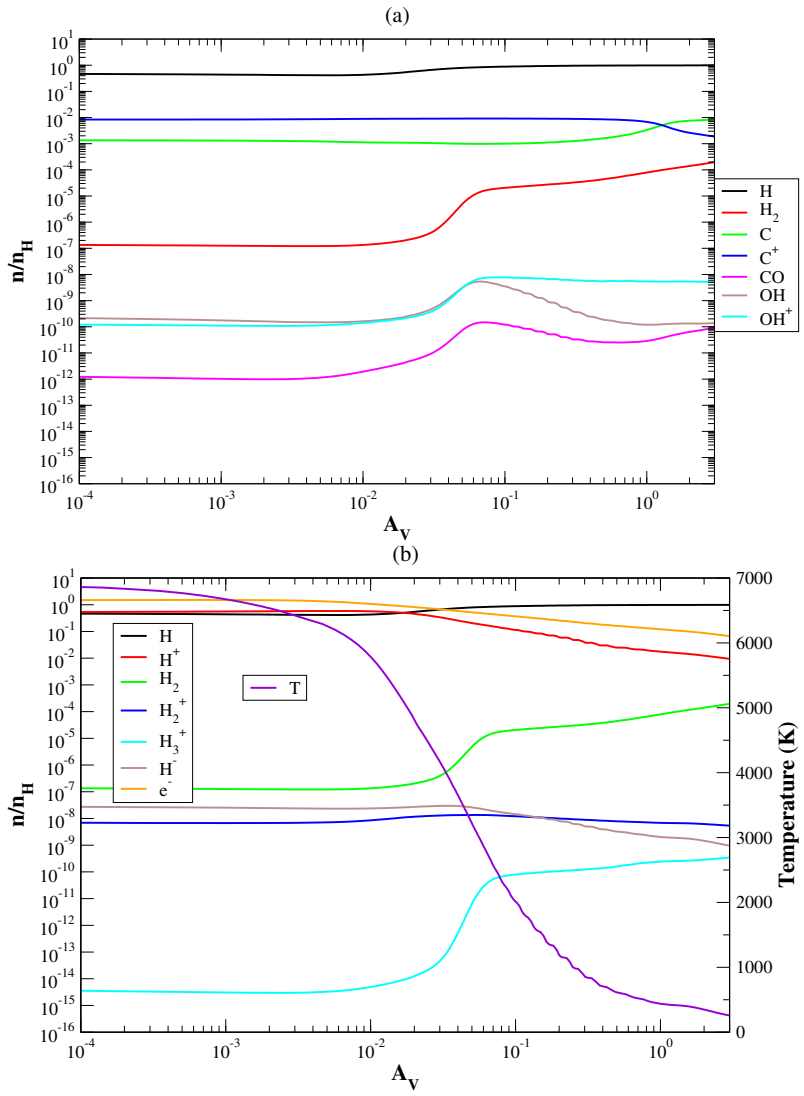

Figure 3.6: Fractional abundance variation of the simple species with A_V by considering $n_H = 1900$ cm^{-3} and $\zeta_{H_2} = \zeta_0 = 1.3 \times 10^{-17}$ s^{-1} (Model A; Das et al., 2020). The right side of the lower panel shows the electron temperature variation.

matches with that of the predicted electron number density in the knot of the Crab (Barlow et al., 2013). In this effort, it is thus essential to find out the physical conditions that can explain most of the observational results of Barlow et al. (2013).

Comparison with observations: Model A

To find a suitable favorable zone to explain the observed features, we vary the physical parameters (n_H and ζ). Our parameter space consists of n_H variation of about $10^3 - 10^7$ cm^{-3} and ζ/ζ_0 ($\zeta_0 = 1.3 \times 10^{-17}$ s^{-1}) variation of about $1 - 10^8$. In Table 3.6, we summarize the results obtained from Model A and Model B in explaining the observed absolute SB of the two transitions of ArH^+ ($2 \rightarrow 1$ and $1 \rightarrow 0$), the 308 μm (971 GHz, $J = 2 \rightarrow 1,\ F = 5/2 \rightarrow 3/2$) transition of OH^+, and the 2.12 μm transition of H_2 (Barlow et al., 2013; Loh et al., 2011). Figure 3.7 shows the absolute SB variation of various transitions with a wide range of parameter space for Model A. We obtain a reasonable match of the absolute SB of these transitions with the observation when high values of $\frac{\zeta}{\zeta_0} \sim 10^6 - 10^8$ and $n_H \sim 10^4 - 10^{5.3}$ cm^{-3} are considered. In Figure 3.14, we show the variation of the absolute SB of these transitions with respect to the variation of a wide range of parameter space (varying $\frac{\zeta}{\zeta_0}$ and the core density $n_{H(core)}$) by considering Model B.

The results obtained from Model A and Model B in explaining the observed SB ratio of several transitions are summarized in Table 3.7. Figure 3.8 shows these ratios for a wide range of parameter space for Model A. The observed ratio of $\sim 1 - 17$ (obtained by taking the minimum and maximum values from the observed two transitions of ArH^+) between the two transitions of ArH^+ and the ratio between these two ArH^+ transitions with respect to the OH^+ 971 GHz transition is best reproduced when we consider $\frac{\zeta}{\zeta_0} \sim 10^7$ with $n_H = 10^{4-6}$ cm^{-3}. Since no transitions of CO are detected, it is expected that the SB ratio of the various transitions of CO with respect to the OH^+ 971 GHz transition would be < 1. We also obtain a lower SB ratio between all the transitions of CO and the 971 GHz transition of OH^+. One of the major drawbacks of our Model A is that we cannot reproduce the lack of [C I] emissions found by Barlow et al. (2013). This mismatch is due to the high abundance of neutral carbon [C I] as compared to OH^+ in our Model A. However, our model can successfully explain the lack of CO emission, the 158 μm transition of C^+ [C II], and the relative line strengths between [O I] and [C II]. Similarly, the results obtained with Model B are shown in Figure 3.15, and the most suitable zone is highlighted in Table 3.7. With Model B, we can successfully explain most of the observed features. Even the lack of [C I] emission is well illustrated by this model.

Table 3.6: Summary of the previously observed surface brightness (SB) values in erg cm^{-2} s^{-1} sr^{-1} (Das et al., 2020).

Molecular transitions	**Observational SB limits**[a]	**Matching zone with $\frac{\zeta}{\zeta_0}$ and n_H (cm^{-3})**	
		Model A	**Model B ($n_H = n_{H(core)}$)**[b]
$ArH^+(1-0)$ (617 GHz/485 μm)	$(2.2-9.9)\times10^{-7}$	$\frac{\zeta}{\zeta_0} \sim 10^{0-5}$ for $n_H \sim 10^{3-5}$ $\frac{\zeta}{\zeta_0} \sim 10^{6-7}$ for $n_H \sim 3.16\times10^4$ $\frac{\zeta}{\zeta_0} \sim 10^{7}$ for $n_H \sim 10^5$ $\frac{\zeta}{\zeta_0} \sim 10^{5}$ for $n_H \sim 10^{6-7}$	$\frac{\zeta}{\zeta_0} \sim 10^{0-6}$ for $n_H \sim (3.16\times10^3)-10^5$ $\frac{\zeta}{\zeta_0} \sim 10^{0-7}$ for $n_H \sim (3.16\times10^5)-10^6$
$ArH^+(2-1)$ (1234 GHz/242 μm)	$(1-3.8)\times10^{-6}$	$\frac{\zeta}{\zeta_0} \sim 10^{4-7}$ for $n_H \sim 10^{4-5}$ $\frac{\zeta}{\zeta_0} \sim 10^{5-6}$ for $n_H \sim 10^{6-7}$	$\frac{\zeta}{\zeta_0} \sim 10^{0-6}$ for $n_H \sim (3.16\times10^3)-10^5$ $\frac{\zeta}{\zeta_0} \sim 10^{0-7}$ for $n_H \sim (3.16\times10^5)-10^6$
OH^+ (971 GHz/308 μm)	$(3.4-10.3)\times10^{-7}$	$\frac{\zeta}{\zeta_0} \sim 10^{0-4}$ for $n_H \sim 10^{4-7}$ $\frac{\zeta}{\zeta_0} \sim 10^{5-7}$ for $n_H \sim 10^4$ $\frac{\zeta}{\zeta_0} \sim 10^{7}$ for $n_H \sim 10^5$	$\frac{\zeta}{\zeta_0} \sim 10^{0-6}$ for $n_H \sim 3.16\times10^{3-5}$ $\frac{\zeta}{\zeta_0} \sim 10^{0-7}$ for $n_H \sim 10^6$
H_2 (2.12 μm)	$(1-4.8)\times10^{-5}$	$\frac{\zeta}{\zeta_0} \sim 10^{6}$ for $n_H \sim 10^4$ $\frac{\zeta}{\zeta_0} \sim 10^{0-5}$ for $n_H \sim 10^5$	$\frac{\zeta}{\zeta_0} \sim 3.54\times10^6$ for $n_H \sim (3.16\times10^3)-10^6$

Note: The most suitable values of n_H and $\frac{\zeta}{\zeta_0}$ to explain the observed values are also mentioned.

[a] Priestley et al. (2017) and references therein.

[b] $n_H = n_{H(core)}$ indicates the core density for Model B (see Section 3.1 for details).

From Tables 3.6-3.7 and Figures 3.7-3.8, it is challenging to arrive at the best suitable parameter for n_H and $\frac{\zeta}{\zeta_0}$ that can reproduce all the observational results simultaneously. However, from Model A, we have two favorable matching zones at $n_H \sim 10^{4-5}$ cm^{-3} and $\frac{\zeta}{\zeta_0} \sim 10^{6-7}$, and for Model B, we find that the values used by Richardson et al. (2013) for their ionizing particle model with $n_{H(core)} \sim 10^{5-6}$ cm^{-3} and $\frac{\zeta}{\zeta_0} \sim 10^{6-7}$ are favorable. So, in general, in terms of the absolute intrinsic SB and SB ratio, we find our favorable parameter space with $n_H \sim 10^{4-6}$ and higher $\frac{\zeta}{\zeta_0} = 10^{6-7}$.

In the favorable zone of Model A, we further consider $n_H = 2.00\times10^4$ cm^{-3} and $\zeta = 9.07\times10^6\zeta_0$ as Model A1 to suitably match the absolute SB of the two transitions of $^{36}ArH^+$ (242 and 485 μm) and the 308 μm transition of OH^+ simultaneously, and $n_H = 3.16\times10^4$ cm^{-3} and $\zeta = 4.55\times10^6\zeta_0$ as Model A2 to suitably match the absolute SB of H_2 of 2.12 μm separately. Unless otherwise stated, Model A1 is always used in all the cases reported throughout this Chapter. Figure 3.9 shows the abundance variation of the simple species, electron, and the electron temperature of the Crab. The Figure depicts that the temperature of the Crab region is 4000 K and the electron abundance is > 0.1, which is in line with the observation (Barlow et al., 2013). A suitably high fractional abundance of H_2 ($\sim 10^{-6}$) is observed, which can

Table 3.7: Summary of the previously observed or estimated line surface brightness (SB) ratios (Das et al., 2020).

Transition ratios	**Observed or estimated SB ratios**	**Matching zone with $\frac{\zeta}{\zeta_0}$ and n_H (cm^{-3})**	
		Model A	**Model B ($n_H = n_{H(core)}$)**[a]
$\frac{ArH^+(2-1)}{ArH^+(1-0)}$	2^b $(1-17)^c$	$\frac{\zeta}{\zeta_0} \sim 10^{6-8}$ for $n_H \sim 10^3$ $\frac{\zeta}{\zeta_0} \sim 10^{0-7}$ for $n_H \sim 10^4$ $\frac{\zeta}{\zeta_0} \sim 10^{0-5}$ for $n_H \sim 10^5$ $\frac{\zeta}{\zeta_0} \sim 10^{4-5}$ for $n_H \sim 10^{6-7}$	$\frac{\zeta}{\zeta_0} \sim 10^{0-7}$ for $n_H \sim (3.16 \times 10^3) - 10^5$ $\frac{\zeta}{\zeta_0} \sim 10^{0-6}$ for $n_H \sim (3.16 \times 10^5) - 10^6$
$\frac{ArH^+(2-1)}{OH^+(971\ GHz/308\ \mu m)}$	$1.66 - 3.9^b$ $(1-11)^c$	$\frac{\zeta}{\zeta_0} \sim 10^5$ for $n_H \sim 10^3$ $\frac{\zeta}{\zeta_0} \sim 10^{0-7}$ for $n_H \sim 10^4$ $\frac{\zeta}{\zeta_0} \sim 10^{6-8}$ for $n_H \sim 10^{5-6}$	$\frac{\zeta}{\zeta_0} \sim 10^{0-4}$ for $n_H \sim (3.16 \times 10^3) - 10^4$ $\frac{\zeta}{\zeta_0} \sim 10^{0-6}$ for $n_H \sim 10^{5-6}$
$\frac{ArH^+(1-0)}{OH^+(971\ GHz/308\ \mu m)}$	$0.56 - 0.8^b$ $(0.21 - 2.91)^c$	$\frac{\zeta}{\zeta_0} \sim 10^6$ for $n_H \sim 10^{3-4}$	$\frac{\zeta}{\zeta_0} \sim 10^7$ for $n_H \sim (3.16 \times 10^3) - 10^6$ $\frac{\zeta}{\zeta_0} \sim 10^{4-5}$ for $n_H \sim 3.16 \times 10^5$ $\frac{\zeta}{\zeta_0} \sim 10^{0-7}$ for $n_H \sim 10^6$
$\frac{CO\ (4-3, 5-4, ..., 13-12)}{OH^+(971\ GHz/308\ \mu m)}$	$<< 1^d$	$\frac{\zeta}{\zeta_0} \sim 10^{0-6}$ for $n_H \sim 10^{3-4}$ $\frac{\zeta}{\zeta_0} \sim 10^{5-8}$ for $n_H \sim 10^{5-7}$	$\frac{\zeta}{\zeta_0} \sim 10^{0-7}$ for $n_H \sim (3.16 \times 10^3) - 10^5$ $\frac{\zeta}{\zeta_0} \sim 10^{5-7}$ for $n_H \sim 10^6$
$\frac{C\ I\ (809\ GHz/370\ \mu m)}{OH^+(971\ GHz/308\ \mu m)}$	$< 1^d$	$\frac{\zeta}{\zeta_0} \sim 3.13 \times 10^2$ for $n_H \sim 10^7$	$\frac{\zeta}{\zeta_0} \sim 10^{0-6}$ for $n_H \sim (3.16 \times 10^3) - 10^6$
$\frac{C\ I\ (492\ GHz/609\ \mu m)}{OH^+(971\ GHz)/308\ \mu m}$	$< 1^d$	$\frac{\zeta}{\zeta_0} \sim 10^{3,5,7}$ for $n_H \sim 10^7$	$\frac{\zeta}{\zeta_0} \sim 10^{0-6}$ for $n_H \sim (3.16 \times 10^3) - 10^6$
$\frac{HeH^+\ (1-0,\ 2010\ GHz/149\ \mu m)}{O\ I\ (2053\ GHz/146\ \mu m)}$	$< 1^e$	$\zeta/\zeta_0 \sim 10^{0-8}$ for $n_H \sim 10^{3-7}$	$\frac{\zeta}{\zeta_0} \sim 10^{0-8}$ for $n_H \sim (3.16 \times 10^3) - 10^6$
$\frac{HeH^+\ (2-1,\ 4020GHz/74\ \mu m)}{O\ I\ (2053\ GHz/146\ \mu m)}$	$< 1^e$	$\frac{\zeta}{\zeta_0} \sim 10^{0-8}$ for $n_H \sim 10^{3-7}$	$\frac{\zeta}{\zeta_0} \sim 10^{0-8}$ for $n_H \sim (3.16 \times 10^3) - 10^6$
$\frac{HeH^+(3-2, 5985\ GHz/50\ \mu m)}{HeH^+(2-1, 4020\ GHz/74\ \mu m)}$	$\sim 0.05^e$	$\frac{\zeta}{\zeta_0} \sim 10^{4-6}$ for $n_H \sim 10^{6-7}$	$\frac{\zeta}{\zeta_0} \sim 10^5$ for $n_H \sim 3.16 \times 10^{3-4}$ $\frac{\zeta}{\zeta_0} \sim 10^{5-6}$ for $n_H \sim 10^{5-6}$
$\frac{O\ I\ (4758\ GHz/63\ \mu m)}{O\ I\ (2053\ GHz/146\ \mu m)}$	$16.4 - 38.7^f$	$\frac{\zeta}{\zeta_0} \sim 10^8$ for $n_H \sim 10^{4-5}$ $\frac{\zeta}{\zeta_0} \sim 10^{0-4}$ for $n_H \sim 10^{6-7}$	$\frac{\zeta}{\zeta_0} \sim 10^{0-8}$ for $n_H \sim (3.16 \times 10^3) - 10^6$
$\frac{O\ I\ (2053\ GHz/146\ \mu m)}{C\ II\ (1897\ GHz/158\ \mu m)}$	$0.125 - 0.323^f$	$\frac{\zeta}{\zeta_0} \sim 10^{5-8}$ for $n_H \sim 10^{3-4}$	$\frac{\zeta}{\zeta_0} \sim 10^{0-4}$ for $n_H \sim (3.16 \times 10^3) - 10^6$

Note: The most suitable values of n_H and $\frac{\zeta}{\zeta_0}$ to explain the listed SB values are also pointed out.

[a] $n_H = n_{H(core)}$ indicates the core density for Model B (see Section 3.1 for details).

[b] Priestley et al. (2017) and references therein.

[c] Taking the ratio with the observed maximum and minimum SB between the two transitions noted in Table 3.6.

[d] Priestley et al. (2017); weak enough to be consistent with the observation.

[e] Prediction from the model of Priestley et al. (2017).

[f] Gomez et al. (2012).

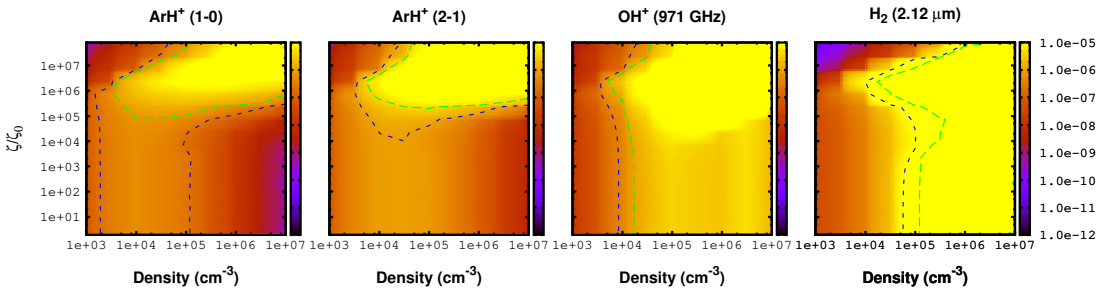

Figure 3.7: Parameter space for the intrinsic line surface brightness (SB) of the $1-0$ and $2-1$ transitions of ArH^+, the 971 GHz/308 μm transition of OH^+, and the 2.12 μm transition of H_2 considering Model A (Das et al., 2020). The right panel is marked with color-coded values of the intrinsic line SB (in units erg cm^{-2} s^{-1} sr^{-1}). The contours are highlighted in the range of observational limits noted in Table 3.6 (Column 2).

explain the H_2 SB in the knots of the Crab. Additionally, we show the abundances of H_2^+ and H_3^+. Figure 3.10a shows the abundances of Ar-related species along with their isotopologs. Figure 3.10b shows the abundances of the He- and Ne- related (and its isotopologs) species. We do not consider any fractionation reaction between the isotopologs of Ar and Ne. Due to this reason, the elemental abundance ratio is reflected in the molecular abundances of the various isotopologs. OH^+ had been identified in the emitting knots of the Crab. So, the observability of the species may be compared to the OH^+ abundance. Both the panels of Figure 3.10 show the OH^+ abundance to understand the fate of other chemical species for future identification in the Crab knots. Figure 3.10(a) and (b) depict that the abundances of $^{36}ArH^+$, $^{20}NeH^+$, and HeH^+ are higher than that of OH^+. Even in the absence of reaction 5a, we obtain a comparable abundance of $^{20}NeH^+$ with OH^+ (see Figure 3.10b). Thus $^{20}NeH^+$ and HeH^+ could have been observed in the Crab knots. However, even with the upper limit of the rate coefficient, we always obtain a lower abundance of hydroxyl cations ($^{36}ArOH^+$, $^{20}NeOH^+$, and $HeOH^+$) than OH^+.

Similarly, the abundance profiles obtained with Model B are shown in Figures 3.16 and 3.17. For this case, we obtain a much higher electron temperature ($>$ 10000 K) that can yield a better estimation for the various atomic transitions listed in Table 3.8.

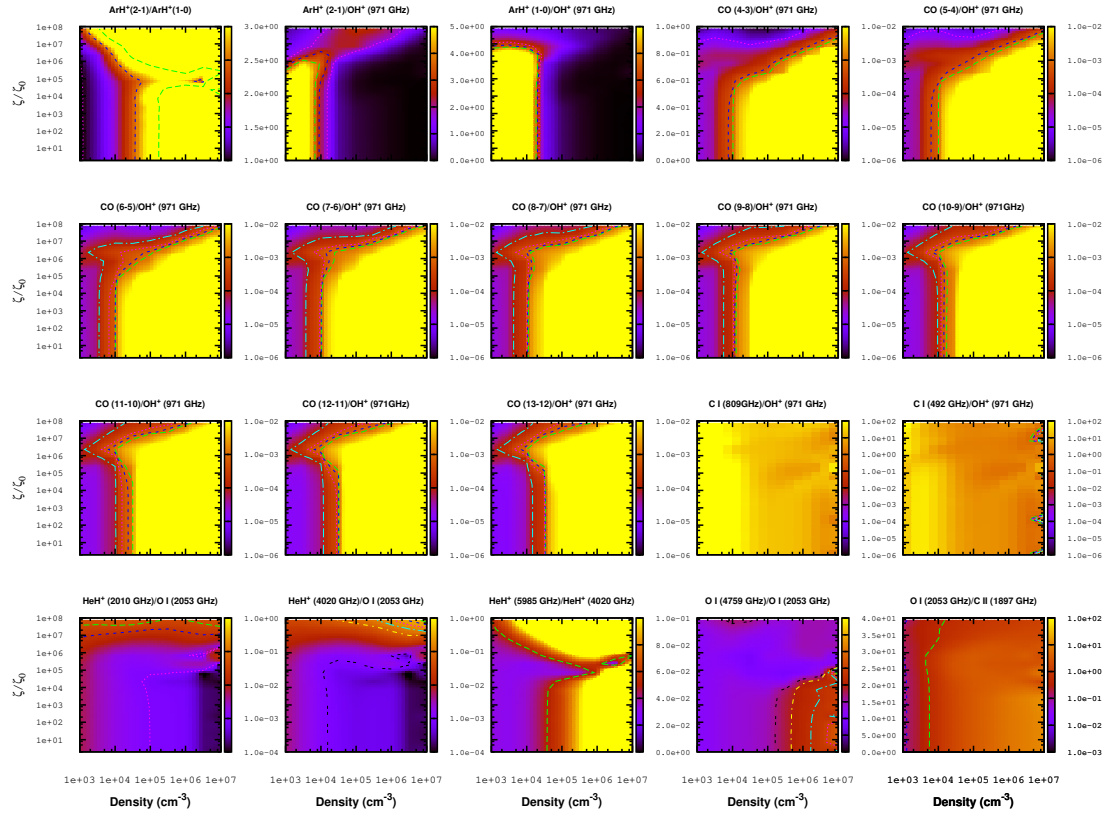

Figure 3.8: Intrinsic line surface brightness (SB) ratio of various molecular and atomic transition fluxes considering Model A (Das et al., 2020). The right side of each panel is marked with color-coded values of the intrinsic line SB ratio. The contours are highlighted around the previously observed or estimated SB ratios noted in Table 3.7 (Column 2).

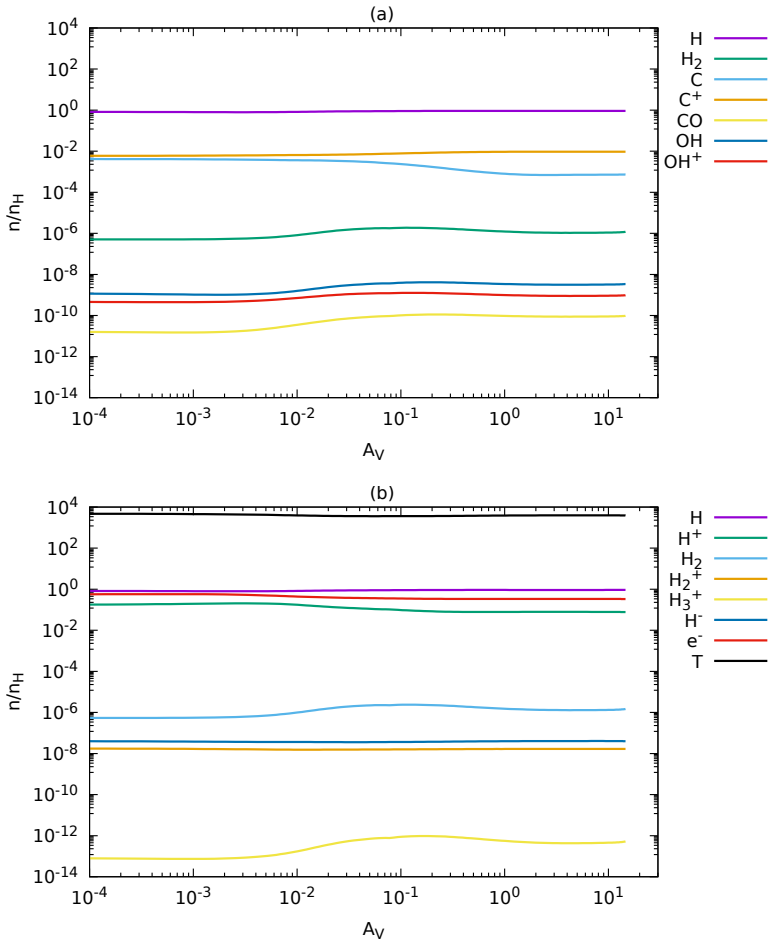

Figure 3.9: Abundance variation of simple species with A_V considering $n_H = 2.00 \times 10^4$ cm^{-3} and $\zeta/\zeta_0 = 9.07 \times 10^6$ (Model A1; Das et al., 2020).

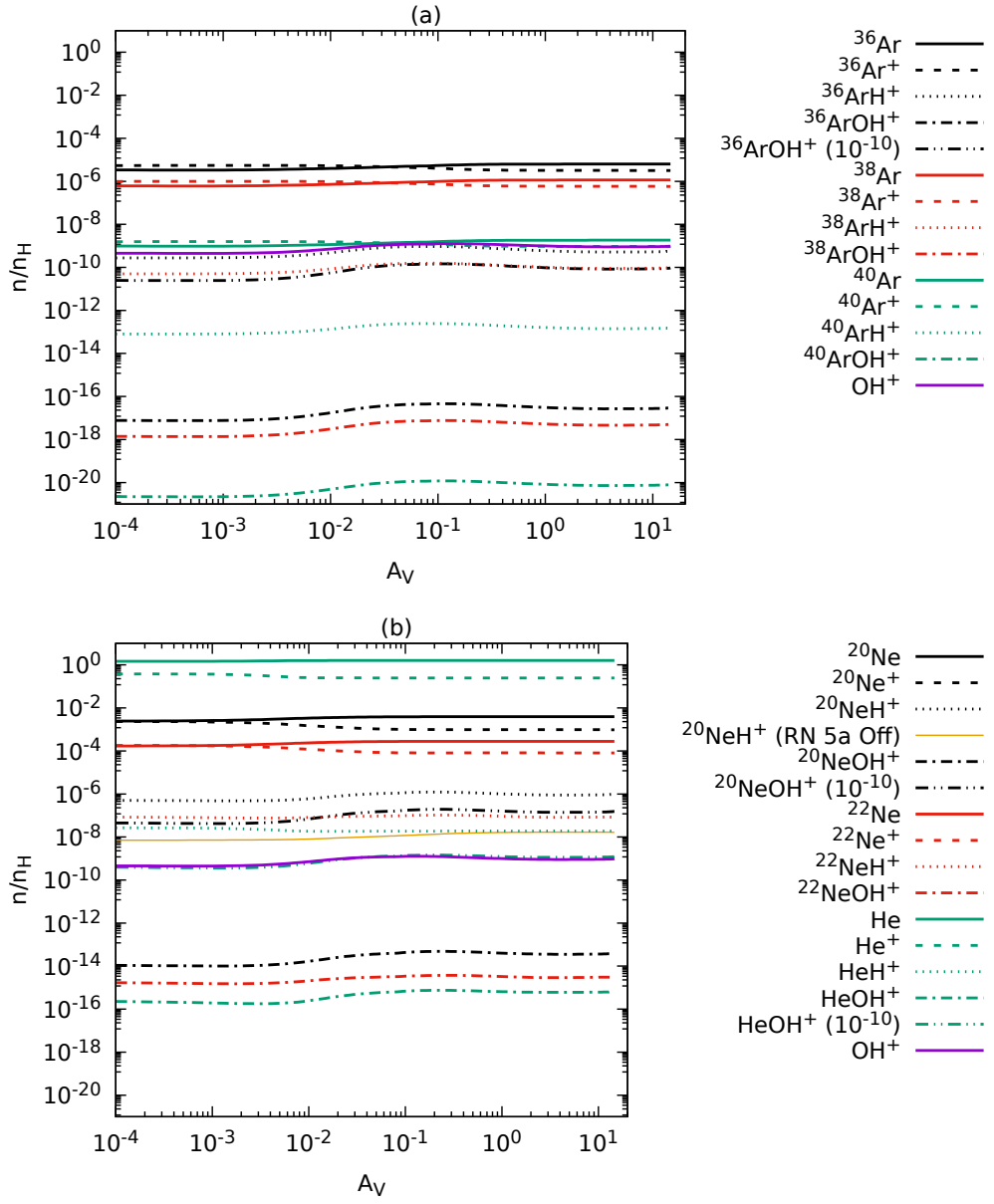

Figure 3.10: Abundance variation of all the hydride and hydroxyl cations considered in this work by considering $n_H = 2.00 \times 10^4$ cm^{-3} and $\zeta/\zeta_0 = 9.07 \times 10^6$ (Model A1; Das et al., 2020). In the upper panel (a) Ar-related species are shown, and in the lower panel (b) the cases of Ne and He are shown. The abundance variation of OH^+ is shown in both the panels for comparison. The abundances of $^{36}ArOH^+$, $^{20}NeOH^+$, and $HeOH^+$ by considering the upper limit of their formation rate ($\sim 10^{-10}$ cm^3 s^{-1}) are noted [XOH^+ (10^{-10})]. The abundance profile of $^{20}NeH^+$ is also shown when reaction 5a of the Ne network is off.

Table 3.8: Comparison between the observed and our modeling results (Das et al., 2020).

Atomic	**Flux (erg cm^{-2} s^{-1})**		**Predicted/observed**	**Predicted/observed ratio**		
lines	**Observed**	**Dereddened**	**ratio**[a]	**Model A1**	**Model A2**	**Model B**
H_2 λ2.12 μm	6.5×10^{-15a}	7.6×10^{-15a}	1.1^a	5.3×10^{-4}	0.080	0.022
...	(4.05×10^{-15b})	...	...	$(8.5 \times 10^{-4})^c$	$(0.127)^c$	$(0.036)^c$
O II λ3727	7.7×10^{-14a}	6.7×10^{-13a}	1.0^a	0.17	0.005	1.053
Ne III λ3869	1.7×10^{-14a}	1.4×10^{-13a}	1.1^a	0.004	1.7×10^{-4}	1.144
H I λ4340	4.4×10^{-15a}	2.9×10^{-14a}	2.0^a	20.728	16.056	4.330
He I λ4471	1.7×10^{-15a}	1.0×10^{-14a}	1.2^a	187.452	189.495	13.029
He II λ4686	2.9×10^{-15a}	1.7×10^{-14a}	1.2^a	1.697	0.965	1.013
H I λ4861	1.04×10^{-14a}	5.4×10^{-14a}	2.3^a	18.826	14.675	3.931
O III λ5007	7.6×10^{-14a}	3.7×10^{-13a}	1.2^a	1.8×10^{-5}	1.13×10^{-6}	0.958
N I λ5198	1.8×10^{-15a}	8.1×10^{-15a}	1.6^a	7.261	1.096	1.301
He I λ5876	6.8×10^{-15a}	2.5×10^{-14a}	1.6^a	125.885	128.481	8.751
O I λ6300	5.3×10^{-14a}	1.8×10^{-13a}	0.7^a	7.120	0.981	0.357
H I λ6563	5.0×10^{-14a}	1.6×10^{-13a}	2.5^a	11.400	9.020	2.384
N II λ6584	9.7×10^{-14a}	3.1×10^{-13a}	0.5^a	0.357	0.029	0.296
S II λ6716	9.0×10^{-14a}	2.8×10^{-13a}	0.8^a	...	...	0.468
S II λ6731	1.2×10^{-13a}	3.6×10^{-13a}	0.9^a	...	...	0.582
He I λ7065	2.6×10^{-15a}	7.6×10^{-15a}	1.3^a	204.777	200.769	10.875
Ar III λ7136	1.3×10^{-14a}	3.7×10^{-14a}	1.0^a	0.285	0.026	0.542
Fe II λ7155	2.7×10^{-15a}	7.6×10^{-15a}	2.0^a	...	...	1.608
O II λ7320	3.6×10^{-15a}	9.7×10^{-15a}	2.3^a	0.017	1.3×10^{-4}	0.849
O III (52 μm)	4.2×10^{-15d}	...	...	0.001	7.3×10^{-4}	1.629
N III (57 μm)	4.0×10^{-16d}	...	...	3.0×10^{-4}	1.1×10^{-4}	1.610
O I (63 μm)	1.7×10^{-15d}	...	...	1089.851	1651.994	109.574
O III (88 μm)	3.6×10^{-15d}	...	...	2.1×10^{-4}	1.2×10^{-4}	0.613
N II (122 μm)	1.2×10^{-16d}	...	...	9.104	4.311	1.451
O I (145 μm)	8.0×10^{-17d}	...	...	1742.984	2981.480	83.172
C II (158 μm)	2.9×10^{-16d}	...	...	742.966	877.732	16.426

Note:
[a] Richardson et al. (2013).
[b] Loh et al. (2011).
[c] Taking the ratio with the observed values of Loh et al. (2011).
[d] Gomez et al. (2012).

Table 3.9: Strongest transitions falling in the range of Herschel's SPIRE and PACS spectrometer, SOFIA, ALMA, VLA, IRAM 30m, and NOEMA considering $n_H = 2.00 \times 10^4$ cm^{-3} and $\zeta/\zeta_0 = 9.07 \times 10^6$ (Model A1; Das et al., 2020).

Species	Transitions	E_U (K)	Frequency (GHz) (μm)	Total column density (cm^{-2})	Optical depth (τ)	Surface brightness (erg cm^{-2} s^{-1} sr^{-1})
$^{36}ArH^+$	J = 1 → 0	29.64	617.52 (485.34)	3.80×10^{11}	2.557×10^{-2}	2.84×10^{-7} $((2.2 - 9.9) \times 10^{-7})^a$
$^{36}ArH^+$	J = 2 → 1	88.89	1234.60 (242.76)	3.80×10^{11}	7.547×10^{-3}	1.29×10^{-6} $((1.0 - 3.8) \times 10^{-6})^a$
$^{36}ArH^+$	J = 3 → 2	177.71	1850.78 (161.94)	3.80×10^{11}	4.258×10^{-4}	1.15×10^{-6}
$^{36}ArH^+$	J = 4 → 3	296.04	2465.62 (121.56)	3.80×10^{11}	5.405×10^{-5}	7.76×10^{-7}
$^{36}ArH^+$	J = 5 → 4	443.80	3078.68 (97.35)	3.80×10^{11}	1.287×10^{-5}	3.86×10^{-7}
$^{36}ArH^+$	J = 6 → 5	620.86	3689.50 (81.23)	3.80×10^{11}	1.203×10^{-6}	8.63×10^{-8}
$^{36}ArH^+$	J = 7 → 6	827.12	4297.65 (69.74)	3.80×10^{11}	4.792×10^{-8}	1.32×10^{-8}
$^{38}ArH^+$	J = 1 → 0	29.39	616.65 (486.03)	6.57×10^{10}	4.431×10^{-3}	4.92×10^{-8}
$^{38}ArH^+$	J = 2 → 1	88.14	1232.85 (243.10)	6.57×10^{10}	1.297×10^{-3}	2.24×10^{-7}
$^{38}ArH^+$	J = 3 → 2	176.23	1848.16 (162.17)	6.57×10^{10}	7.320×10^{-5}	2.00×10^{-7}
$^{38}ArH^+$	J = 4 → 3	293.57	2462.13 (121.73)	6.57×10^{10}	9.492×10^{-6}	1.36×10^{-7}
$^{38}ArH^+$	J = 5 → 4	440.09	3074.32 (97.49)	6.57×10^{10}	2.255×10^{-6}	6.76×10^{-8}
$^{38}ArH^+$	J = 6 → 5	615.68	3684.29 (81.35)	6.57×10^{10}	2.080×10^{-7}	1.50×10^{-8}
$^{38}ArH^+$	J = 7 → 6	820.22	4291.58 (69.84)	6.57×10^{10}	8.343×10^{-9}	2.33×10^{-9}
$^{40}ArH^+$	J = 1 → 0	29.35	615.86 (486.66)	1.04×10^{8}	7.012×10^{-6}	7.76×10^{-11}
$^{40}ArH^+$	J = 2 → 1	88.03	1231.27 (243.42)	1.04×10^{8}	2.061×10^{-6}	3.35×10^{-10}
$^{40}ArH^+$	J = 3 → 2	176.00	1845.79 (162.38)	1.04×10^{8}	1.160×10^{-7}	3.17×10^{-10}
$^{40}ArH^+$	J = 4 → 3	293.20	2458.98 (121.88)	1.04×10^{8}	1.516×10^{-8}	2.15×10^{-10}
$^{40}ArH^+$	J = 5 → 4	439.53	3070.39 (97.61)	1.04×10^{8}	3.578×10^{-9}	1.07×10^{-10}
$^{40}ArH^+$	J = 6 → 5	614.890	3679.58 (81.45)	1.04×10^{8}	3.328×10^{-10}	2.38×10^{-11}
$^{40}ArH^+$	J = 7 → 6	819.17	4286.11 (69.93)	1.04×10^{8}	1.323×10^{-11}	3.71×10^{-12}
$^{20}NeH^+$	J = 1 → 0	49.53	1039.26 (288.39)	6.51×10^{14} $(1.16 \times 10^{13})^b$	4.246×10^{1} $(2.175)^b$	4.20×10^{-4} $(3.97 \times 10^{-5})^b$
$^{20}NeH^+$	J = 2 → 1	148.50	2076.57 (144.33)	6.51×10^{14} $(1.16 \times 10^{13})^b$	4.022×10^{1} $(1.352 \times 10^{-1})^b$	2.41×10^{-3} $(6.74 \times 10^{-5})^b$
$^{20}NeH^+$	J = 3 → 2	296.72	3110.02 (96.37)	6.51×10^{14} $(1.16 \times 10^{13})^b$	4.794 $(2.352 \times 10^{-3})^b$	3.67×10^{-3} $(4.95 \times 10^{-5})^b$
$^{20}NeH^+$	J = 4 → 3	493.92	4137.67 (72.43)	6.51×10^{14} $(1.16 \times 10^{13})^b$	8.114×10^{-2} $(3.061 \times 10^{-4})^b$	2.40×10^{-3} $(3.44 \times 10^{-5})^b$
$^{20}NeH^+$	J = 5 → 4	739.73	5157.61 (58.11)	6.51×10^{14} $(1.16 \times 10^{13})^b$	4.225×10^{-3} $(8.033 \times 10^{-5})^b$	1.26×10^{-3} $(9.92 \times 10^{-6})^b$
$^{20}NeH^+$	J = 6 → 5	1033.68	6167.92 (48.59)	6.51×10^{14} $(1.16 \times 10^{13})^b$	6.559×10^{-4} $(2.499 \times 10^{-6})^b$	4.36×10^{-4} $(7.74 \times 10^{-7})^b$
$^{20}NeH^+$	J = 7 → 6	1375.24	7166.70 (41.82)	6.51×10^{14} $(1.16 \times 10^{13})^b$	3.649×10^{-5} $(4.035 \times 10^{-8})^b$	5.49×10^{-5} $(6.29 \times 10^{-8})^b$
$^{22}NeH^+$	J = 1 → 0	49.32	1034.79(289.63)	5.94×10^{13}	8.939	1.34×10^{-4}
$^{22}NeH^+$	J = 2 → 1	147.86	2067.67 (144.95)	5.94×10^{13}	1.771	4.00×10^{-4}
$^{22}NeH^+$	J = 3 → 2	295.45	3096.70 (96.78)	5.94×10^{13}	2.453×10^{-2}	3.11×10^{-4}
$^{22}NeH^+$	J = 4 → 3	491.80	4119.99 (72.74)	5.94×10^{13}	1.659×10^{-3}	2.05×10^{-4}
$^{22}NeH^+$	J = 5 → 4	736.56	5135.64 (58.36)	5.94×10^{13}	4.031×10^{-4}	8.45×10^{-5}
$^{22}NeH^+$	J = 6 → 5	1029.28	6141.73 (48.80)	5.94×10^{13}	2.677×10^{-5}	1.08×10^{-5}
$^{22}NeH^+$	J = 7 → 6	1369.39	7136.41 (41.99)	5.94×10^{13}	4.307×10^{-7}	7.22×10^{-7}
HeH^+	J= 1 → 0	95.80	2010.18 (149.10)	1.33×10^{13}	8.473×10^{-1}	7.68×10^{-5}
HeH^+	J = 2 → 1	286.86	4008.73 (74.76)	1.33×10^{13}	7.901×10^{-3}	6.51×10^{-5}
HeH^+	J = 3 → 2	572.06	5984.14 (50.08)	1.33×10^{13}	2.080×10^{-4}	6.69×10^{-6}
HeH^+	J = 4 → 3	949.76	7925.15 (37.82)	1.33×10^{13}	1.454×10^{-6}	3.18×10^{-7}
HeH^+	J = 5 → 4	1417.82	9820.88 (30.52)	1.33×10^{13}	1.289×10^{-8}	1.22×10^{-8}
HeH^+	J = 6 → 5	1973.57	11660.90 (25.70)	1.33×10^{13}	7.291×10^{-11}	2.77×10^{-9}
HeH^+	J = 7 → 6	2613.89	13435.35 (22.31)	1.33×10^{13}	1.356×10^{-12}	1.47×10^{-9}
OH^+	J = 2 → 1 (F= 5/2 → 3/2)	46.64	971.80 (308.41)	6.53×10^{11}	2.370×10^{-2}	6.17×10^{-7} $[(3.4 - 10.3) \times 10^{-7}]^a$

Species	Transitions	E_U (K)	Frequency (GHz) (μm)	Total column density (cm^{-2})	Optical depth (τ)	Surface brightness (erg cm^{-2} s^{-1} sr^{-1}0
$^{36}ArOH^+$	J = 1 → 0 (K_- = 1 → 0)	1.38	28.94 (10358)	6.19×10^{10}	6.617×10^{-10}	7.76×10^{-23}
$^{36}ArOH^+$	J = 2 → 1 (K_- = 2 → 1)	4.14	57.88 (5179)	6.19×10^{10}	2.740×10^{-9}	2.48×10^{-21}
$^{36}ArOH^+$	J = 3 → 2 (K_- = 3 → 2)	8.28	86.82 (3453)	6.19×10^{10}	6.561×10^{-9}	1.88×10^{-20}
$^{36}ArOH^+$	J = 4 → 3 (K_- = 4 → 3)	13.79	115.76 (2590)	6.19×10^{10}	1.225×10^{-8}	7.91×10^{-20}
$^{36}ArOH^+$	J = 5 → 4 (K_- = 5 → 4)	20.69	144.70 (2072)	6.19×10^{10}	2.183×10^{-8}	2.41×10^{-19}
$^{36}ArOH^+$	J = 6 → 5 (K_- = 6 → 5)	28.96	173.63 (1727)	6.19×10^{10}	3.602×10^{-8}	5.97×10^{-19}
$^{36}ArOH^+$	J = 7 → 6 (K_- = 7 → 6)	38.62	202.56 (1480)	6.19×10^{10}	5.809×10^{-8}	1.29×10^{-18}
$^{36}ArOH^+$	J = 8 → 7 (K_- = 8 → 7)	49.65	231.48 (1295)	6.19×10^{10}	5.900×10^{-8}	2.50×10^{-18}
$^{36}ArOH^+$	J = 9 → 8 (K_- = 9 → 8)	62.06	260.40 (1151)	6.19×10^{10}	1.088×10^{-7}	4.49×10^{-18}
$^{36}ArOH^+$	J = 10 → 9 (K_- = 10 → 9)	75.85	289.32 (1036)	6.19×10^{10}	1.845×10^{-7}	7.57×10^{-18}
$^{36}ArOH^+$	J = 11 → 10 (K_- = 11 → 10)	91.02	318.22 (942)	6.19×10^{10}	4.923×10^{-7}	1.21×10^{-17}
$^{20}NeOH^+$	J = 1 → 0 (K_- = 1 → 0)	1.89	39.76 (7540)	1.02×10^{14}		1.56×10^{-17}
$^{20}NeOH^+$	J = 2 → 1 (K_- = 2 → 1)	5.68	79.52 (3770)	1.02×10^{14}		4.97×10^{-16}
$^{20}NeOH^+$	J = 3 → 2 (K_- = 3 → 2)	11.37	119.27 (2514)	1.02×10^{14}	3.914×10^{-3}	3.78×10^{-15}
$^{20}NeOH^+$	J = 4 → 3 (K_- = 4 → 3)	18.95	159.01 (1885)	1.02×10^{14}	1.895×10^{-2}	1.58×10^{-14}
$^{20}NeOH^+$	J = 5 → 4 (K_- = 5 → 4)	28.42	198.75 (1508)	1.02×10^{14}	5.306×10^{-2}	4.77×10^{-14}
$^{20}NeOH^+$	J = 6 → 5 (K_- = 6 → 5)	39.78	238.47 (1257)	1.02×10^{14}	1.047×10^{-1}	1.16×10^{-13}
$^{20}NeOH^+$	J = 7 → 6 (K_- = 7 → 6)	53.04	278.18 (1078)	1.02×10^{14}	1.603×10^{-1}	2.41×10^{-13}
$^{20}NeOH^+$	J = 8 → 7 (K_- = 8 → 7)	68.19	317.88 (943)	1.02×10^{14}	1.998×10^{-1}	4.52×10^{-13}
$^{20}NeOH^+$	J = 9 → 8 (K_- = 9 → 8)	85.23	357.56 (838)	1.02×10^{14}	2.322×10^{-1}	7.46×10^{-13}
$^{20}NeOH^+$	J = 10 → 9 (K_- = 10 → 9)	104.16	397.21 (755)	1.02×10^{14}	2.176×10^{-1}	1.09×10^{-12}
$^{20}NeOH^+$	J = 11 → 10 (K_- = 11 → 10)	124.98	436.84 (686)	1.02×10^{14}	1.674×10^{-1}	1.24×10^{-12}
$HeOH^+$	J = 1 → 0 (K_- = 1 → 0)	9.62	201.89 (1485)	8.19×10^{11}		1.67×10^{-16}
$HeOH^+$	J = 2 → 1 (K_- = 2 → 1)	28.86	403.71 (742)	8.19×10^{11}	1.013×10^{-3}	5.12×10^{-15}
$HeOH^+$	J = 3 → 2 (K_- = 3 → 2)	57.71	605.39 (495)	8.19×10^{11}	2.158×10^{-3}	3.19×10^{-14}
$HeOH^+$	J = 4 → 3 (K_- = 4 → 3)	96.17	806.85 (372)	8.19×10^{11}	1.330×10^{-3}	8.53×10^{-14}
$HeOH^+$	J = 5 → 4 (K_- = 5 → 4)	144.21	1008.02 (297)	8.19×10^{11}	4.246×10^{-4}	1.23×10^{-13}
$HeOH^+$	J = 6 → 5 (K_- = 6 → 5)	201.82	1208.84 (248)	8.19×10^{11}	8.820×10^{-5}	1.09×10^{-13}
$HeOH^+$	J = 7 → 6 (K_- = 7 → 6)	268.98	1409.22 (213)	8.19×10^{11}	1.331×10^{-5}	5.30×10^{-14}

Note:
Hydride cations of noble gases and OH^+ are calculated using the lower limit of the formation rate, whereas hydroxyl cations of noble gases are calculated using the upper limit of the formation rate mentioned in Section 3.2.3. Following Bates's 1983 formation rate, the total column density of the hydroxyl cations of noble gases are $ArOH^+ = 1.97 \times 10^4$ cm^{-2}, $NeOH^+ = 2.59 \times 10^7$ cm^{-2}, and $HeOH^+ = 4.34 \times 10^5$ cm^{-2}.
[a] Barlow et al. (2013).
[b] The total column density, optical depth, and SB of $^{20}NeH^+$ transitions are also provided in the parentheses when reaction 5a of the Ne network is off.

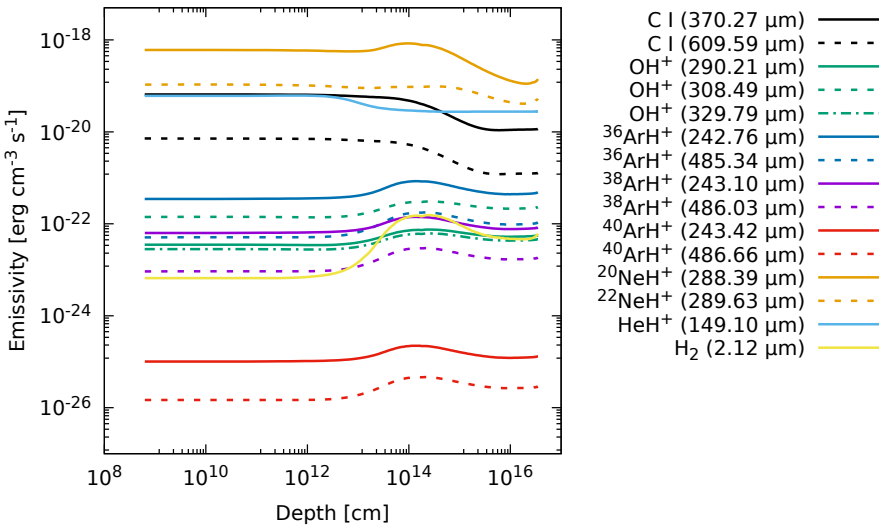

Figure 3.11: Emissivity of some of the strongest transitions that fall in the range of the frequency limit of Herschel's SPIRE and PACS spectrometer, and SOFIA with respect to the depth into the filament by considering $n_H = 2.00 \times 10^4$ cm^{-3} and $\zeta/\zeta_0 = 9.07 \times 10^6$ (Model A1; Das et al., 2020).

The emissivity of some of the prominent transitions that fall in between the frequency regime of Herschel's SPIRE and Photodetecting Array Camera and Spectrometer (PACS) and SOFIA are shown in Figure 3.11 for Model A1. Barlow et al. (2013) found that the $2-1$ and $1-0$ transitions of $^{36}ArH^+$ were significantly stronger than those of OH^+. Figure 3.11 depicts that in most regions, 971 GHz (308 μm) transition of OH^+ (the strongest transition of OH^+ in such a condition) is comparatively stronger than that of the $1-0$ transition. But it is weaker than the $2-1$ transition of $^{36}ArH^+$. This is partly consistent with the observation of Barlow et al. (2013). Barlow et al. (2013) also found the $J = 2-1$ transition of ArH^+ stronger than the $J = 1-0$ transition. We find the same trend in Figure 3.11. Barlow et al. (2013) detected only the 971 GHz (308 μm) transition, which was comparable to the $J = 1-0$ transition of $^{36}ArH^+$. Our model shows that the $1-0$ transition of $^{36}ArH^+$ is comparable to the 971 GHz transition of OH^+ deep inside the filament. The emissivity of the XOH^+ (X = Ar, Ne, and He) transitions, which fall in between the $29-1409$ GHz region, is shown in Figure 3.12. These transitions could be beneficial for the future astronomical detection of these species around similar environments, where strong OH^+ emissions had already been identified.

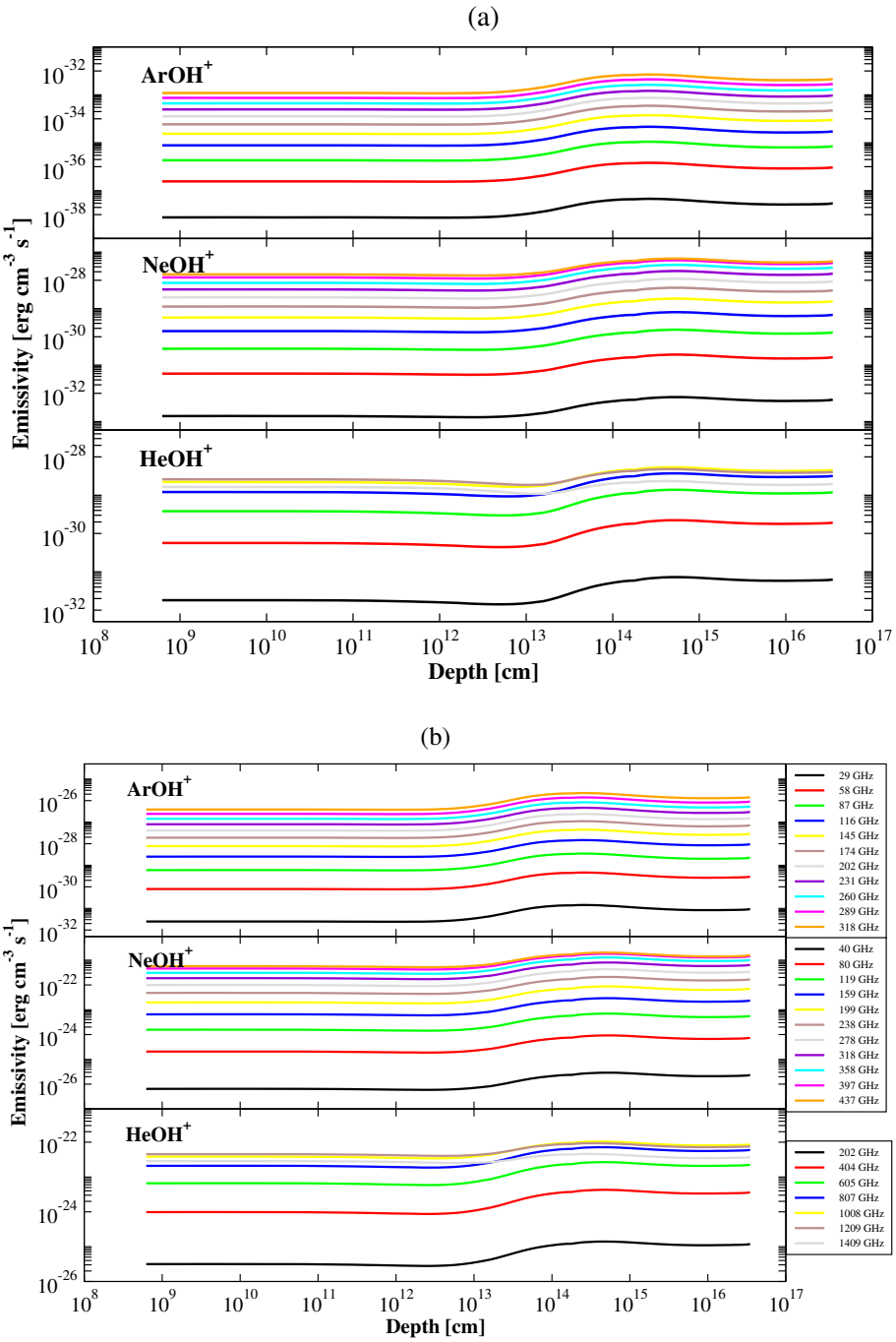

Figure 3.12: Calculated emissivity of various XOH^+ transitions (X=^{36}Ar, ^{20}Ne, He) noted in Table 3.9 lying in the frequency limit of Herschel's SPIRE and PACS spectrometer, SOFIA, ALMA, VLA, IRAM 30m, and NOEMA by considering $n_H = 2.00 \times 10^4$ cm^{-3} and $\zeta/\zeta_0 = 9.07 \times 10^6$ (Model A1; Das et al., 2020). The upper panel (a) shows the emissivity considering the formation rates following Bates (1983) mentioned in Section 3.2.3, whereas the lower panel (b) considers the upper limit of $\sim 10^{-10}$ cm^3 s^{-1}.

In Table 3.9, we list the strongest transitions that fall in the observed range of Herschel's SPIRE and PACS spectrometer and also within the range of SOFIA, ALMA, Very Large Array (VLA), Institute for Radio Astronomy in the Millimeter Range (IRAM) 30m, and Northern Extended Millimeter Array (NOEMA). The optical depth of all these transitions is also noted. For this calculation, we use the RADEX program by considering only electrons as colliding partners. We consider $n_e = 10^3$ cm^{-3} and temperature 2700 K. The radiation field shown in Figure 3.1c is considered as the background radiation field. The total column density of the species is also noted from the calculation with $n_H = 2.00 \times 10^4$ cm^{-3} and $\zeta/\zeta_0 = 9.07 \times 10^6$ (Model A1). Similarly, the emissivity obtained with Model B is shown in Figures 3.18 and 3.19.

Barlow et al. (2013) obtained an SB of $\sim (2.2 - 9.9) \times 10^{-7}$ erg cm^{-2} s^{-1} sr^{-1} for the $1 \rightarrow 0$ transition of $^{36}ArH^+$ whereas our best-fitted Model A (i.e., Model A1) finds $\sim 2.84 \times 10^{-7}$ erg cm^{-2} s^{-1} sr^{-1}. For the $2 \rightarrow 1$ transition of $^{36}ArH^+$, Barlow et al. (2013) obtained an SB of $\sim (1.0 - 3.8) \times 10^{-6}$ erg cm^{-2} s^{-1} sr^{-1}, whereas our best-fitted model finds $\sim 1.29 \times 10^{-6}$ erg cm^{-2} s^{-1} sr^{-1}. Priestley et al. (2017) checked the detectability of these transitions based on the observed SB of the 971 GHz (308 μm) transition of OH^+. Barlow et al. (2013) obtained the SB of the 971 GHz transition of $\sim (3.4 - 10.3) \times 10^{-7}$ erg cm^{-2} s^{-1} sr^{-1} whereas our best-fitted model finds it to be $\sim 6.17 \times 10^{-7}$ erg cm^{-2} s^{-1} sr^{-1}. Thus, our best-fitted model (Model A1) always predicts a comparable or stronger SB of $^{36}ArH^+$ transitions (242 and 485 μm) in comparison with the 308 μm transition of OH^+, which is consistent with the results. Now, to examine the detectability of the other transitions of $^{36}ArH^+$ and for other hydride ions along with their isotopic forms considered in this study, we check three criteria for each transition: (i) whether the SB of that transition is comparable to or stronger than the observed SB of the 308 μm transition of OH^+, (ii) the presence of atmospheric transmission (calculated by the ATRAN program of Lord, 1992) at the height of $\sim$ 41000 ft (i.e., at the height of SOFIA), and (iii) the optical depth of that transition. With the ground-based telescope, transitions falling between 30 and 650 μm are heavily affected by atmospheric transmission. For example, at the ALMA site, the amount of precipitable water vapor is typically 1.0 mm, falling below 0.25 mm up to 5% of the time. All transitions of $^{36}ArH^+$ reported here are falling in this range (69-486 μm), and thus, it is difficult to observe these transitions with any ground-based telescope. However, with a space-based telescope, it is possible to detect some more transitions of this species.

In Figure 3.13a, we show the SB of these transitions obtained from our best-fitted Model A1 along with the observed 308 μm transition of OH^+ to show the

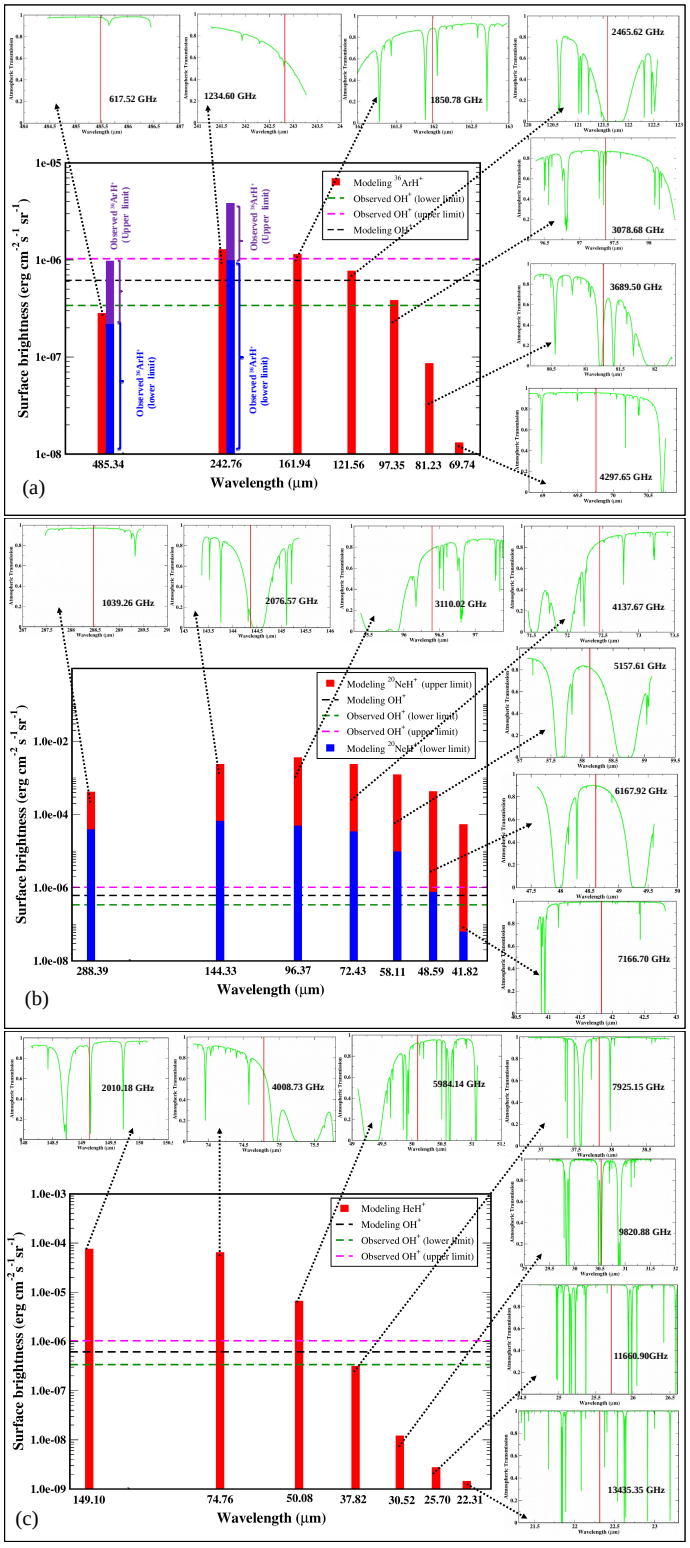

Figure 3.13: A comparison between the observed surface brightness of the 308 μm transition of OH^+ and the transitions of (a) $^{36}ArH^+$, (b) $^{20}NeH^+$, and (c) HeH^+ is shown (Das et al., 2020). The atmospheric transmission for each transition is shown to check the fate of their identification.

detectability of these transitions clearly. Table 3.9 clearly shows that all these transitions have optical depth < 1. Figure 3.13a shows that the first five transitions are stronger relative to the observed 917 GHz (308 μm) transition of OH^+. The 617 GHz (485 μm) and 1234 GHz (242 μm) transitions were already observed by Herschel, which is no longer operational. Among the other three transitions of $^{36}ArH^+$, we can see that 2465 GHz (121 μm) and 3078 GHz (97 μm) are heavily affected by the atmospheric transmission and thus challenging to observe. But the $3 \rightarrow 2$ transition at 1850 GHz (162 μm) is far from atmospheric absorption features and falls in the range of the LFA receiver of the modular heterodyne instrument GREAT of SOFIA. However, we find a long integration time required for this transition with the SOFIA instrument time estimator. We expect that with Herschel, the chance of detection would have been higher.

A similar analysis is carried out for $^{20}NeH^+$ and HeH^+. When we consider $Ne^+ + H_2 \rightarrow NeH^+ + H$ (reaction 5a) for the formation of NeH^+, we obtain a higher abundance of $^{20}NeH^+$ and called it an upper limit. In the absence of this reaction, we obtain a lower limit of the NeH^+ formation. With the upper limit of its formation, Table 3.9 shows that the 1039 GHz (288 μm), 2076 GHz (144 μm), and 3110 GHz (96 μm) transitions have an optical depth > 1. For the other four transitions, it is < 1. Figure 3.13b shows that the other four transitions at 4137 GHz (72 μm), 5157 GHz (58 μm), 6167 (48 μm), and 7166 GHz (42 μm) are showing a comparatively stronger SB than that of the observed 308 μm transition of OH^+. With the lower limit of its formation, Table 3.9 shows that the 7166 GHz (42 μm) transition is below, and the 6167 GHz (48 μm) transition is comparable to the observed 308 μm transition of OH^+. However, the optical depths of the 2076 and 3110 GHz transitions are found to be < 1 with the lower limit. But the 2076 GHz transition is very much affected by the atmospheric transmission, as shown in Figure 3.13b, which calls into question its detectability.

In the case of HeH^+, we find that the optical depths of all the transitions are < 1. But, Figure 3.13c shows that only three transitions show a stronger SB than the 308 μm transition of OH^+. Among them, the 2010 GHz (149 μm) transition is heavily affected by atmospheric transmission. The other two transitions at 4008 GHz (75 μm) and 5984 GHz (50 μm) are free from atmospheric features and produce a strong SB.

Table 3.9 shows that even with the upper limit of the formation, the SB of all the transitions of XOH^+ (X = ^{36}Ar, ^{20}Ne, and He) is less than the SB of the 308 μm transition of OH^+. So the chance of their detection in the Crab environment is challenging. Thus, we do not carry out any similar analysis for them.

Table 3.10: H_2 vibrational line surface brightnesses (SB) relative to the 1-0 S(1) line for Knot 51 from Loh et al. (2012) and for our final models (Das et al., 2020).

H_2 Lines	Wavelength (μm)	SB (erg cm^{-2} s^{-1} sr^{-1})			SB relative to the 1-0 S(1) line			Observed SB relative to the 1-0 S(1) line for Knot 51
		Model A1	Model A2	Model B	Model A1	Model A2	Model B	
1-0 S(0)	2.22269	3.13×10^{-8}	4.38×10^{-6}	1.24×10^{-6}	0.214	0.200	0.200	0.23 ± 0.04^a
1-0 S(1)	2.12125	1.46×10^{-7}	2.18×10^{-5}	6.18×10^{-6}	1.000	1.000	1.000	1 ± 0.04^a
1-0 S(2)	2.03320	7.50×10^{-8}	9.35×10^{-6}	2.69×10^{-6}	0.513	0.428	0.436	0.52 ± 0.09^a
2-1 S(1)	2.24711	1.17×10^{-7}	5.47×10^{-6}	1.49×10^{-6}	0.798	0.251	0.242	0.19 ± 0.03^a
2-1 S(2)	2.15364	6.25×10^{-8}	2.40×10^{-6}	6.64×10^{-7}	0.428	0.110	0.107	$< 0.13^a$
2-1 S(3)	2.07294	1.90×10^{-7}	7.31×10^{-6}	1.97×10^{-6}	1.300	0.335	0.319	$< 0.28^a$

Note: [a] Loh et al. (2012).

Comparison with observations: Model B

Table 3.8 compares our obtained values with the observational (Loh et al., 2011, 2012; Gomez et al., 2012; Richardson et al., 2013; Priestley et al., 2017) as well as with the previous modeling results (Richardson et al., 2013). The adopted physical parameters and the gas-phase elemental abundances relative to total hydrogen nuclei in all forms are summarized in Tables 3.1 and 3.2 for Model B. Though in Model B, we use similar parameters as used in Richardson et al. (2013), we find very little difference. This small difference is due to the changes in the associative detachment reactions between the CLOUDY version 10.00 (Ferland et al., 1998) used in Richardson et al. (2013) and version 17.02 (used in this work). In the case of Model A, we do not obtain any transition of sulfur (S) and iron (Fe) because, for this case, we do not consider any initial elemental abundance for these two elements (see Table 3.2). For Model A, we consider $n_H = 2.00 \times 10^4$ cm^{-3} and $\zeta/\zeta_0 = 9.07 \times 10^6$ (Model A1) and $n_H = 3.16 \times 10^4$ cm^{-3} and $\zeta/\zeta_0 = 4.55 \times 10^6$ (Model A2), whereas, for Model B, we consider the ionizing particle model of Richardson et al. (2013), which yields a core density $n_{H(core)} = 10^{5.25}$ cm^{-3} and $\frac{\zeta}{\zeta_0} = 7.06 \times 10^6$. The striking differences between Model A and Model B are the consideration of a very high abundance of He and a dust to gas ratio of 0.027 in Model A, whereas in Model B, by considering the initial elemental abundance pointed out in Table 3.2, we obtain (from the CLOUDY output) a dust-to-gas mass ratio ~ 8 times lower than that of Model A. Table 3.10 provides H_2 vibrational line SB relative to the 1-0 S(1) line for knot 51 for both Model A and Model B and compared with the observed values (Loh et al., 2012). We find that our Model A1 can reproduce the observed line strength ratio except for the 2-1 S(X) (X = 1, 2, 3) lines, whereas our Model A2 and Model B are efficient enough to reproduce the 2-1 S(X) lines. All the results obtained with Model B are shown in Figures 3.14-3.19.

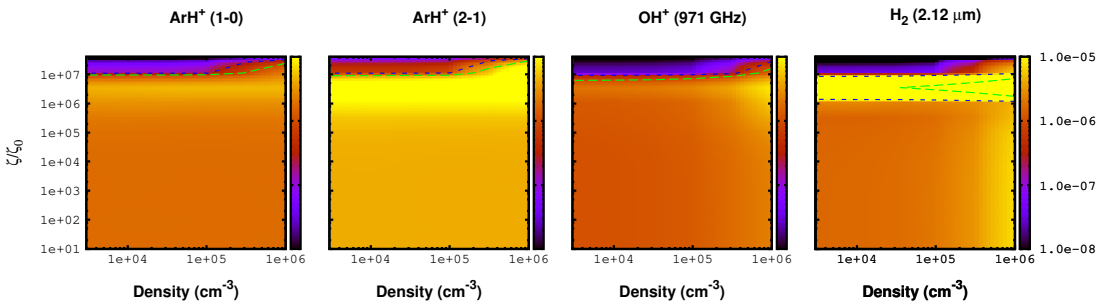

Figure 3.14: Parameter space for the intrinsic line surface brightness (SB) of $1-0$ and $2-1$ transitions of ArH^+, the 971 GHz/308 μm transition of OH^+, and 2.12 μm transition of H_2 considering Model B (Das et al., 2020). Extreme right panel is marked with color coded values of the intrinsic line SB (in units erg cm^{-2} s^{-1} sr^{-1}). The contours are highlighted in the range of observational limits noted in Table 3.6 (Column 2).

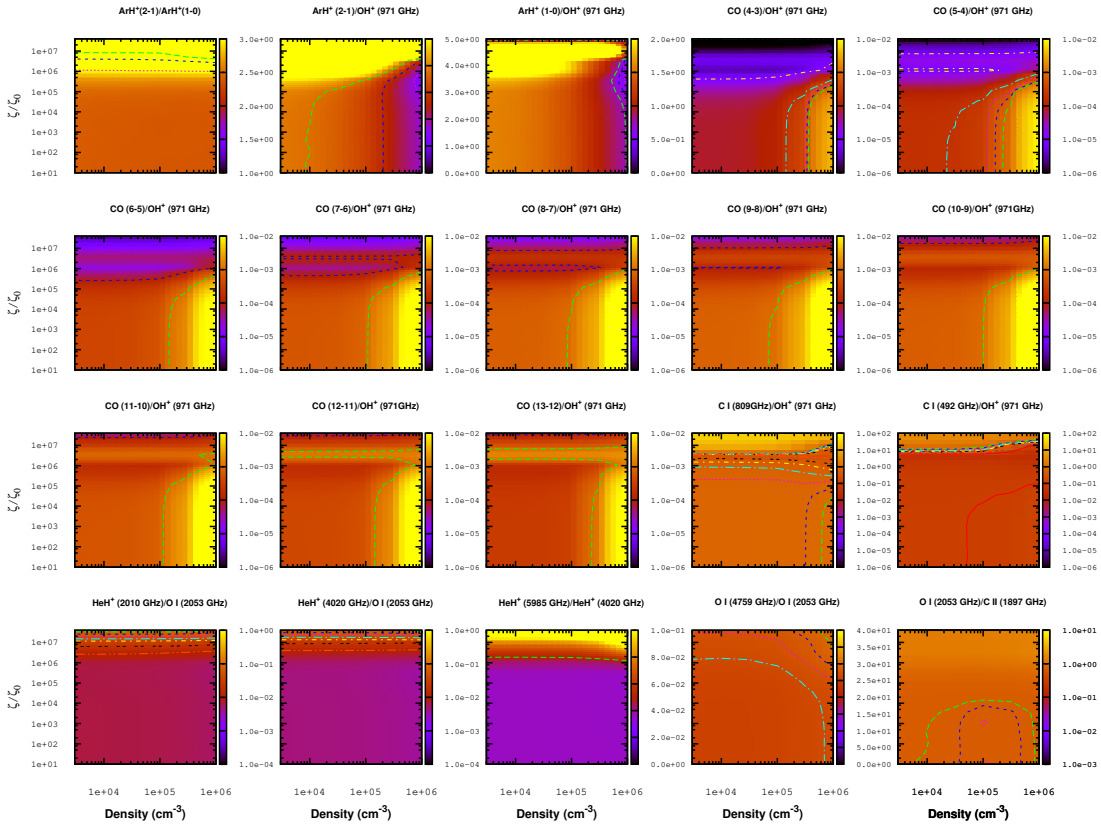

Figure 3.15: Intrinsic line surface brightness (SB) ratio of various molecular and atomic transition fluxes considering Model B (Das et al., 2020). Contours are highlighted around the observed or previously estimated values shown in Table 3.7.

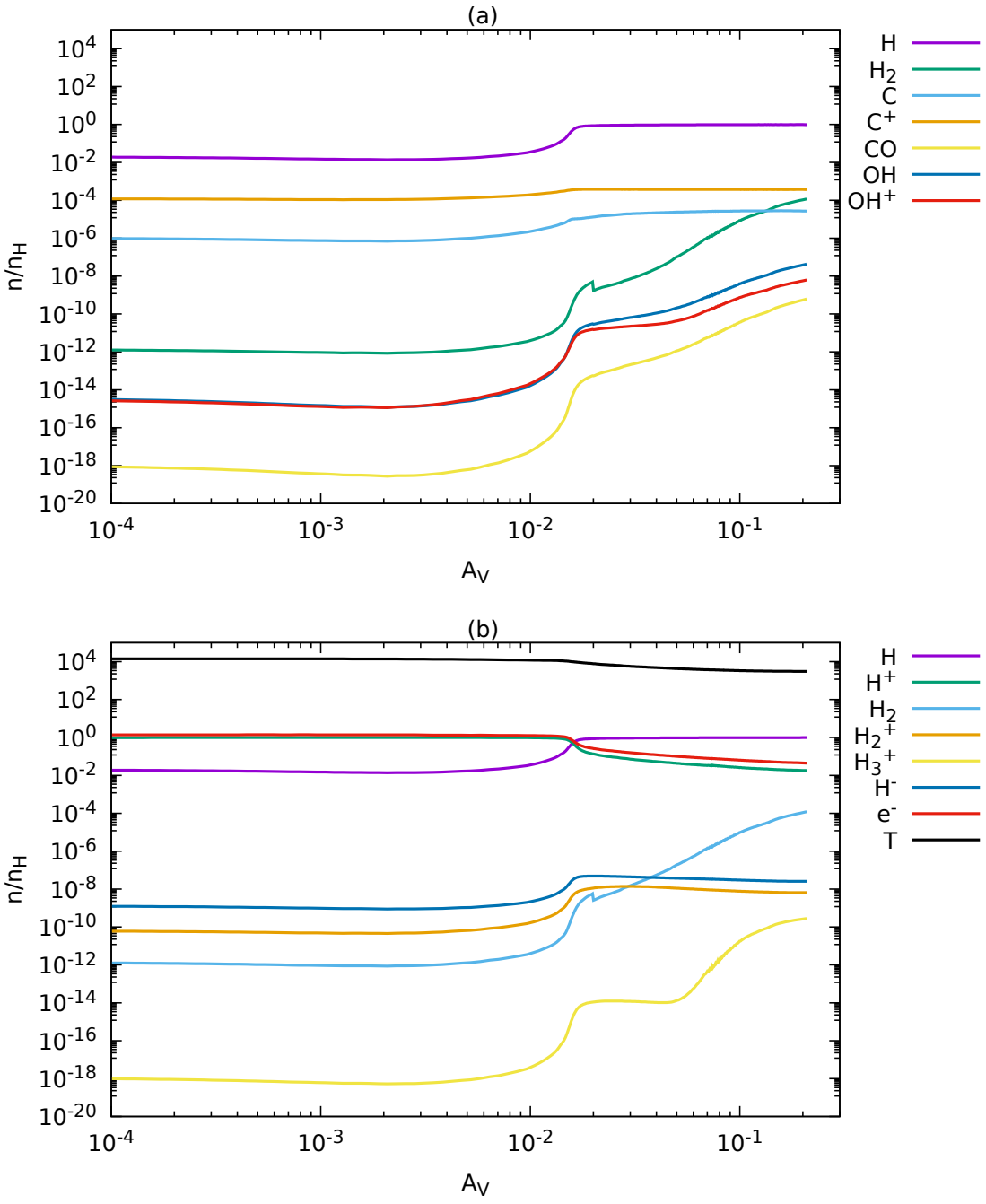

Figure 3.16: Abundance variation of simple species with A_V considering Model B (Das et al., 2020).

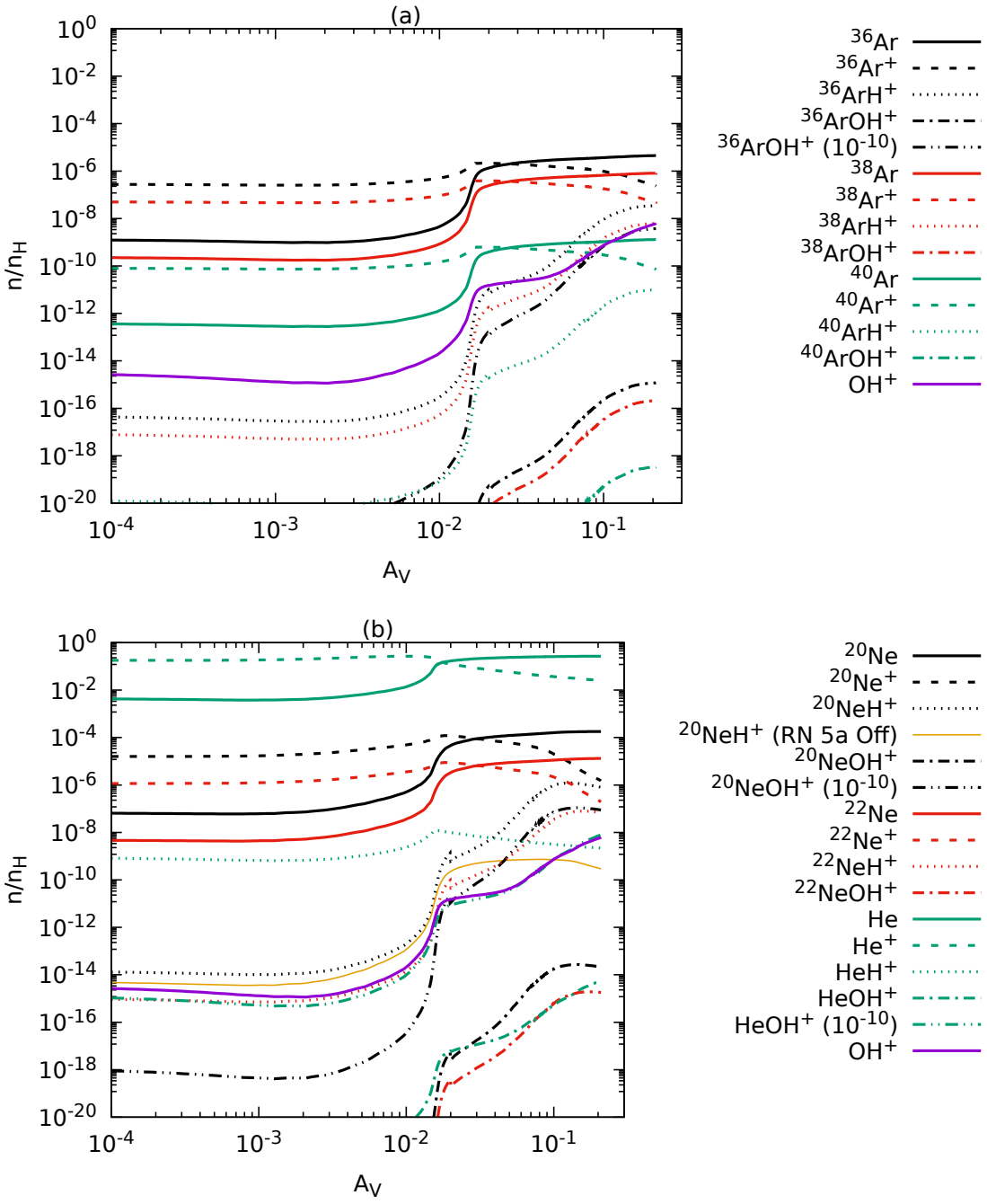

Figure 3.17: Abundance variation of all the hydride and hydroxyl cations considered in this work by considering Model B (Das et al., 2020). In the upper panel (a) Ar related ions are shown whereas in the lower panel (b) the cases of Ne and He are shown both along with OH^+ for comparison.

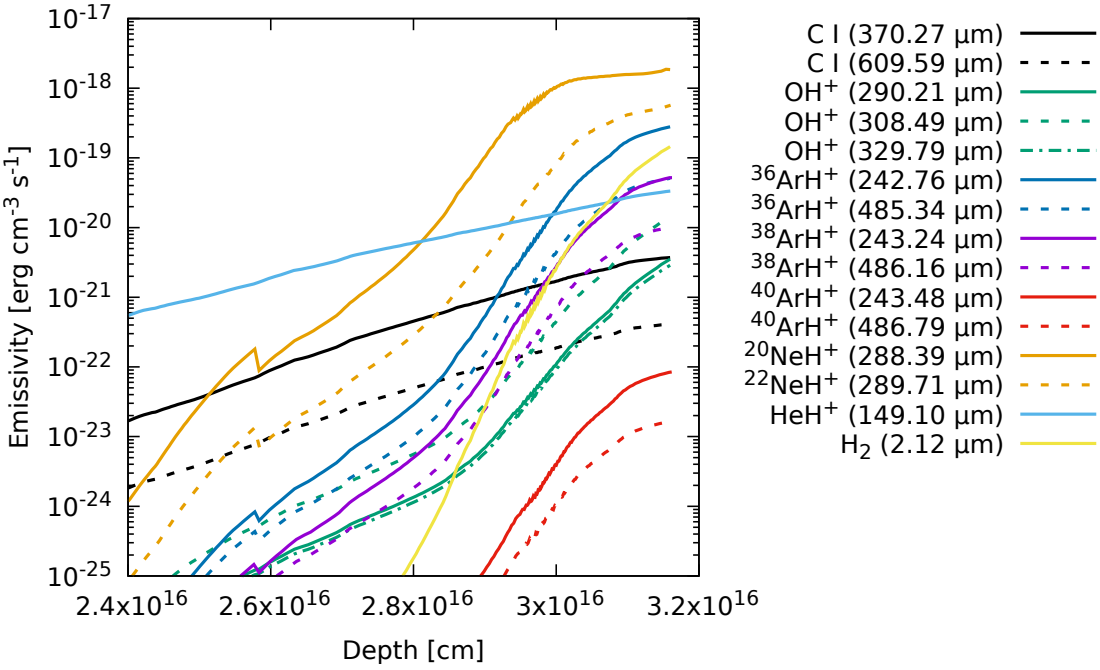

Figure 3.18: Emissivity of some of the strongest transitions which are falling in the frequency limit of Herschel's SPIRE and PACS spectrometer, and SOFIA with respect to the depth into the filament by considering Model B (Das et al., 2020).

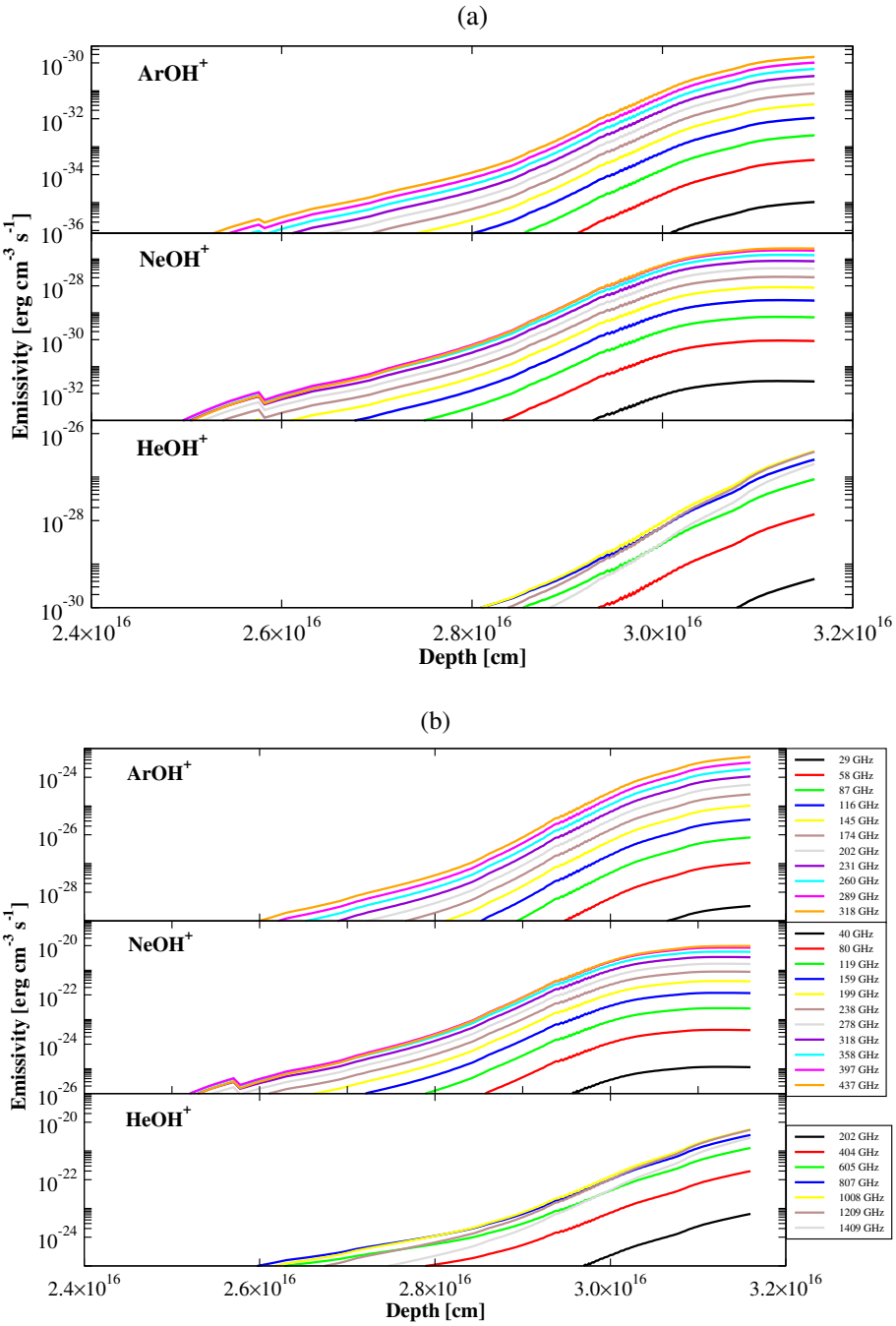

Figure 3.19: Calculated emissivity of various XOH^+ transitions (X=^{36}Ar, ^{20}Ne, and He) lying in the frequency limit of Herschel's SPIRE and PACS spectrometer, SOFIA, ALMA, VLA, IRAM 30m, and NOEMA by considering Model B (Das et al., 2020). (a) Upper panel shows the emissivity considering the formation rates following Bates (1983) mentioned in Section 3.2.3, whereas (b) lower panel considering upper limit of $\sim 10^{-10}$ cm^3 s^{-1}.

3.3.3 Time scales of molecule formation

Richardson et al. (2013) and Priestley et al. (2017) mentioned that steady-state chemistry might not be applicable because of the H_2 formation time scale and mass-loss rate of the Crab knot. Richardson et al. (2013) used CLOUDY version 10.00 for their study, and Priestley et al. (2017) used the UCL PDR code (Bell et al., 2005, 2006; Bayet et al., 2011) for their study. Here, we use CLOUDY version 17.02. To check whether the computation is time steady or not, we run our model with the '*age*' command available in the CLOUDY code. This command checks whether the microphysics is time steady or not. We find that both of our best-fitted models show that the longest time scale is below the age of the Cloud (for the best-fitted case of Model A, it is ~ 9 years, and for Model B, it is ~ 134 years). Thus, we are not overestimating the abundance of H_2 by considering the radiative attachment of H and then the associative detachment reaction. Because a time-dependent simulation is out of scope for this work, we discuss the time scale of their formation relevant to the Crab environment.

ArH^+

ArH^+ is mainly formed by the reaction between Ar^+ and H_2 (Priestley et al., 2017, also reported a similar observation) with a rate coefficient of $\sim 10^{-9}$ cm^3 s^{-1}. This yields a time of $\sim 10^9$ sec ~ 30 years (sufficiently smaller than the age of the Crab) by considering an H_2 density of ~ 1 cm^{-3}. Our best-fitted zone is also within the limit of the observed SB of H_2. In the observed region, we have an H_2 number density < 1 cm^{-3}. This rules out the overestimation of the formation of ArH^+ considered here. Our obtained intrinsic absolute line SB and line SB ratio match the observations.

NeH^+

In the case of NeH^+ formation, if we include the reaction between Ne^+ and H_2 (reaction 5a; see Table 3.3) in our network, that controls the formation. By considering an H_2 number density of ~ 1 cm^{-3}, the formation time scale is well within the Crab age, as discussed in the context of ArH^+. However, we find that its formation depends on the $HeH^+ + Ne$ route (reaction 14). The rate coefficient for the reaction is $\sim 10^{-9}$ cm^3 s^{-1}. Because the number density of Ne is ~ 1 cm^{-3}, it is very fast. However, its formation depends on the HeH^+ produced by a comparatively slower process than ArH^+.

HeH^+

In the best-fitted model, the dominant pathway for the formation of HeH^+ is the reaction between He^+ and H. Priestley et al. (2017) also found this pathway to be the dominant one in their network. The rate coefficient used for this reaction is $\sim 1.44 \times 10^{-16}$ cm^3 s^{-1} (Güsten et al., 2019, found the best fit with a rate constant of $\sim 6 \times 10^{-16}$ cm^3 s^{-1}). By considering the H density of $\sim 10^3 - 10^5$ cm^{-3} used here, the time scale for the formation of HeH^+ seems to be much shorter ($\sim 10^3$ years by considering the lowest He^+ abundance) than that of the ArH^+. Thus, it is possible to form HeH^+ within the lifetime of the Crab. The recent observation of HeH^+ in NGC 7027 (age of ~ 600 years) by Güsten et al. (2019) might be a good reason to look for HeH^+ in the Crab as well.

Based on the formation time scales of the hydride ions, it is expected that all these molecules would likely be observed in the filamentary region of the Crab.

$ArOH^+$, $NeOH^+$, and $HeOH^+$

These three noble gas hydroxyl cations are mainly formed in our network by radiative association reactions (see Section 3.2.3). The rate coefficients of these reactions are calculated using a temperature-independent semiempirical formula proposed by Bates (1983). Unfortunately, this yields a prolonged formation rate and is thus very unlikely to be formed in the Crab environment. However, the formula provided by Bates (1983) to calculate the rate coefficients is temperature-independent and approximated for ~ 30 K. This semiempirical relation might underestimate the rate in the condition relevant to the Crab (temperature $\sim 2000 - 3000$ K). Therefore, to have an educated estimation of their formation, we consider an upper limit of these rates ($\sim 10^{-10}$ cm^3 s^{-1}). In the case of $ArOH^+$ and $NeOH^+$ formation, the dominant pathway in our network is the reaction between ArH^+ and O and NeH^+ and O, respectively (reaction 13; see Table 3.3). For $HeOH^+$ formation, the reaction between He^+ and OH dominates (reaction 12). Due to this reason, the $ArOH^+$ and $NeOH^+$ abundance profiles follow the ArH^+ and NeH^+ abundance profiles, respectively, whereas $HeOH^+$ roughly follows the abundance profile of OH. We notice that only with the upper limit of the formation, the abundances of these species are significant. Otherwise, the formation time scale is much slower and very unlikely to form in the Crab environment. But the pathways proposed here are beneficial to study their formation in the other sources where they have a much longer time for their appearance.

Table 3.11: Ground vibrational and equilibrium rotational constants and asymmetrically reduced quartic centrifugal distortion constants of $ArOH^+$, $NeOH^+$, and $HeOH^+$ with the DFT-B3LYP/6-311++G(d,p) level of theory (Das et al., 2020).

Sl. No.	**Species**	**Rotational constants**	**Calculated values (in MHz)**	**Distortion constants**	**Calculated values (in MHz)**
1.	$^{36}ArOH^+$ (Singlet)	A_0	606170.618 (574419.7[a])	D_N	0.026258855
		B_0	13423.202 (14538.2[a])	D_K	2846.358531040
		C_0	12929.814 (14157.4[a])	D_{NK}	30.956851344
		A_e	568404.429 (577984.9[a])	d_N	-0.001548795
		B_e	13362.883 (14652.2[a])	d_K	7.374941060
		C_e	13055.944 (14290.0[a])		
2.	$^{38}ArOH^+$ (Singlet)	A_0	607114.959 (574400.2[a])	D_N	0.025404061
		B_0	13198.879 (14293.6[a])	D_K	2929.193961459
		C_0	12717.473 (13925.4[a])	D_{NK}	30.950234568
		A_e	568391.892 (577970.7[a])	d_N	-0.001507393
		B_e	13137.742 (14405.4[a])	d_K	7.371572618
		C_e	12840.938 (14055.1[a])		
3.	$^{40}ArOH^+$ (Singlet)	A_0	608006.144 (574382.6[a])	D_N	0.024644498
		B_0	12996.499 (14073.0[a])	D_K	3007.592807161
		C_0	12525.768 (13715.9[a])	D_{NK}	30.944237144
		A_e	568380.591 (577958.0[a])	d_N	-0.001470202
		B_e	12934.645 (14182.7[a])	d_K	7.368596645
		C_e	12646.841 (13843.0[a])		
4.	$^{20}NeOH^+$ (Singlet)	A_0	523937.941 (525452.4[a])	D_N	0.095861623
		B_0	18963.535 (19702.7[a])	D_K	1279.215533495
		C_0	18045.404 (18942.7[a])	D_{NK}	38.200509306
		A_e	525035.970 (530275.0[a])	d_N	-0.002683004
		B_e	19104.672 (20252.3[a])	d_K	9.480927416
		C_e	18433.910 (19507.3[a])		
5.	$^{22}NeOH^+$ (Singlet)	A_0	524108.356 (525436.6[a])	D_N	0.088272895
		B_0	18178.763 (18884.4[a])	D_K	1366.928818198
		C_0	17320.737 (18185.1[a])	D_{NK}	38.205763489
		A_e	525022.539 (530266.0[a])	d_N	-0.002605291
		B_e	18307.032 (19406.6[a])	d_K	9.452753621
		C_e	17690.192 (18721.4[a])		
6.	$HeOH^+$ (Singlet)	A_0	526770.350	D_N	2.987029963
		B_0	108480.244	D_K	294.469427824
		C_0	88444.204	D_{NK}	78.618941712
		A_e	530435.668	d_N	0.215953242
		B_e	110472.442	d_K	24.945899641
		C_e	91430.461		

Note: [a] Theis & Fortenberry (2016)

3.4 Spectroscopic information

Spectroscopic information of ArH^+, NeH^+, and HeH^+ is already available in the CDMS catalog. However, NeH^+ and HeH^+ are yet to be identified in the Crab environment. The $1 \rightarrow 0$ (2010.18 GHz) and $2 \rightarrow 1$ (4008.73 GHz) transitions of HeH^+ fall in the range of SOFIA and the PACS instrument of Herschel. The $1 \rightarrow 0$ transition of NeH^+ (1039.25 GHz) is well within the range of the SPIRE instrument of Herschel and SOFIA, whereas the $2 \rightarrow 1$ transition of NeH^+ (2076.57 GHz) falls in the PACS and SOFIA limit. We prepare the collisional data files for NeH^+ and HeH^+ to study the observability of their transitions. To prepare the collisional data file, we consider that electrons are the only colliding partners. Therefore, we use the electron-impact excitation of HeH^+ from Hamilton et al. (2016) for this collisional data file. No collisional rates are available for NeH^+. Thus we approximate the same by considering the collisional rates of $ArH^+ - e^-$.

One of the aims of this work is to study the emission lines of hydroxyl ions of noble gases. Recently, Theis & Fortenberry (2016) calculated rotational constants for the various isotopologs of $ArOH^+$ and $NeOH^+$. However, the spectroscopic information of $HeOH^+$ is not yet available. We carry out quantum-chemical calculations using the GAUSSIAN 09 program to find out these rotational parameters. We compute the rotational constants and asymmetrically reduced quartic centrifugal distortion constants with the DFT-B3LYP/6-311++G(d,p) level of theory, useful for providing spectral information in the THz domain. Obtained ground vibrational and equilibrium values of the rotational constants and asymmetrically reduced quartic centrifugal distortion constants along with the ground vibrational and equilibrium values calculated by Theis & Fortenberry (2016) for comparison are given in Table 3.11. Moreover, we use the SPCAT (Pickett, 1991) program to determine the rotational transitions of these species, which fall between the THz domain. The obtained spectral information files are supplied on Zenodo under a Creative Commons Attribution license: https://doi.org/10.5281/zenodo.3998450. As per the JPL catalog style, we rename the cat files of $^{36}ArOH^+$ as c053009.cat, $^{38}ArOH^+$ as c055003.cat, $^{40}ArOH^+$ as c057004.cat, $^{20}NeOH^+$ as c037006.cat, $^{22}NeOH^+$ as c039007.cat, and $HeOH^+$ as c021003.cat. To prepare the spectral information for $ArOH^+$ and $NeOH^+$, we use both the ground vibrational and equilibrium values of the rotational constants calculated by Theis & Fortenberry (2016), whereas, in the case of $HeOH^+$, we use our computed parameters. To prepare the collisional data file, we consider the interaction between their first 11 levels. This upper limit of the level is because of the absence of collisional rates of ArH^+ for the upper levels

(Hamilton et al., 2016). We do not have any first-hand approximate values for the collisional rates of all the species. Hamilton et al. (2016) provided the collision rate only for ArH^+, and we consider the same collisional rate for all these hydroxyl ions. Therefore, we assess their transitions further for the modeling. However, for the transitions of the first 12 levels, we obtain the highest frequency at 318 GHz for $ArOH^+$ and 437 GHz for $NeOH^+$. These frequencies are not in the range of SPIRE or PACS. However, these transitions fall within the observed range of the ALMA, IRAM 30m, and NOEMA. In the case of $HeOH^+$, most of the frequencies that arise fall within the range of Herschel SPIRE, SOFIA, ALMA, IRAM 30m, and NOEMA.

3.5 Summary

We model a Crab filament using the spectral synthesis code, CLOUDY to study the hydride and hydroxyl cations of some noble gas species. A wide range of parameter space is used to explain the observational aspects suitably. We check that under the Crab filamentary conditions, steady-state chemistry is justified for our best-fitted models. Our findings are highlighted below:

- A realistic chemical network is prepared to study the fate of hydride and hydroxyl cations of the various isotopes of Ar, Ne, and He. No fractionation reactions between the isotopologs are considered. We find that the abundances of $^{36}ArH^+$, $^{20}NeH^+$, and HeH^+ are comparable to the abundance of OH^+ in the Crab filament. Considering the upper limit of the formation rate, we obtain a reasonably high abundance of $^{36}ArOH^+$, $^{20}NeOH^+$, and $HeOH^+$. However, using the realistic rates of these reactions, we obtain very low abundances of these hydroxyl cations. It is thus important to accurately measure/estimate these rates.

- In the diffuse ISM, we find that the XH^+ (X=Ar, Ne, and He) fractional abundances are reasonably high and could have been identified. For example, we find a peak fractional abundance of $\sim 1.3 \times 10^{-9}$ for $^{36}ArH^+$. $^{20}NeH^+$ seems to be also highly abundant (peak abundance $\sim 5 \times 10^{-8}$) when reaction 5a ($Ne^+ + H_2 \rightarrow NeH^+ + H$) is considered. However, its peak fractional abundance significantly drops ($\sim 3 \times 10^{-11}$) in the absence of this pathway. The peak fractional abundance of $HeH^+ \sim 3 \times 10^{-11}$ is obtained.

- We find that a high value of the cosmic-ray ionization rate ($\frac{\zeta}{\zeta_0} \sim 10^6 - 10^7$) with a total hydrogen density a few times $10^4 - 10^6$ cm^{-3} can successfully

reproduce the absolute SB of the two transitions of $^{36}ArH^+$ (242 and 485 μm), the 308 μm transition of OH^+, and the 2.12 μm transition of H_2.

- With the favorable values of n_H and ζ/ζ_0, we can successfully explain the observed SB ratio between (a) the $2-1$ and $1-0$ transitions of $^{36}ArH^+$, (b) two transitions ($2-1$ and $1-0$) of $^{36}ArH^+$ and the 308 μm transition of OH^+, and (c) various transitions of CO concerning the 308 μm transition of OH^+. Our most suitable case can explain the SB ratio obtained by Priestley et al. (2017) between the transitions (a) HeH^+ and 146 μm of [O I], and (b) $3-2$ and $2-1$ of HeH^+. It can also explain the SB ratio between the transitions (a) 63 μm and 146 μm of [O I], and (b) 146 μm of [O I] and 158 μm of [C II] observed by Gomez et al. (2012) using Herschel PACS and ISO Long Wavelength Spectrometer (LWS) fluxes for IR fine-structure emission lines. However, our Model A always overproduces the SB of [C I], and even around the low A_V region, we have the fractional abundance of CO and OH $\sim 10^{-11} - 10^{-9}$. A major reason for this is the obtained electron temperature ($\sim$ 4000 K) with Model A which is low. We find that our Model B requires a much higher electron temperature ($>$ 10000 K) to explain most of the observed features in the Crab filamentary region.

- The optical depth of the most probable transitions of the XH^+ and XOH^+ (where X=Ar, Ne, and He) are calculated under the condition of the Crab nebula filamentary region. Analyzing the results, we notice that the 485 μm, 242 μm, and 162 μm transitions of $^{36}ArH^+$; 96 μm, 72μm, 58μm, and 48 μm transitions of $^{20}NeH^+$; and 75 μm and 50 μm transitions of HeH^+ are most likely would be identified with space-based observation. However, the fate of detecting XOH^+ in a similar environment with a similar facility could be challenging.

- The ground vibrational and equilibrium values of rotational constants are calculated. Also, asymmetrically reduced quartic centrifugal distortion constants for various isotopologs of $ArOH^+$ and $NeOH^+$ are computed. Moreover, we compare them with the theoretically calculated values of Theis & Fortenberry (2016). We also provide these constants for $HeOH^+$, which are not available until now. Additionally, we provide the catalog files as per JPL style for various isotopologs of $ArOH^+$, and $NeOH^+$ (with both the ground vibrational and equilibrium rotational constants of Theis & Fortenberry, 2016), and $HeOH^+$ (with our calculated ground vibrational and equilibrium values), which might enable their future astronomical detection in other sources.

Chapter 4

Interstellar Prebiotic Molecules in Radiation Shielded Region

Overview

In the last two decades, astronomers have made a great attempt to explain the evolutionary history of biomolecules in the ISM. Historically, Chakrabarti & Chakrabarti (2000a,b) first attempted to obtain the abundances of 421 species (including several biologically important amino acids) through detailed time dependent hydrochemical evolution of a collapsing molecular cloud using the largest network till date with several thousand reactions. Some unavailable reaction cross-sections were included with certain assumptions. Subsequently, Ehrenfreund & Charnley (2000) discussed the interstellar origin of amino acids and noted that the Chakrabarti & Chakrabarti (2000a) computation should be relooked as the chemical environment in ISM could be far from equilibrium. Glycine (NH_2CH_2COOH) is the simplest amino acid and an essential building block for life formation. It has been extensively searched in space (Kuan et al., 2003). Though it has been found (together with many other amino acids and nucleic bases) in some meteorites on the Earth (Kvenvolden et al., 1970) and in the coma of comets (Glavin et al., 2008; Elsila et al., 2009; Altwegg et al., 2016; Hadraoui et al., 2019), efforts to detect it in the ISM have so far unsuccessful. The rotational transitions arising out of glycine are below the detection limit of astronomical surveys (Puzzarini, 2020). The lack of its detection raises many speculations about its formation mechanism. Sahu et al. (2020) tentatively identified one of its isomer methylcarbamate in the ISM. Following the procedure clearly laid down by Chakrabarti & Chakrabarti (2000a), Das et al. (2008b, 2013b); Garrod (2013); Majumdar et al. (2012, 2013); Chakrabarti et al. (2015) studied the formation of glycine in the star-forming region, with improved rate coefficients and pathways. Various interdisciplinary studies are involved in the search for the origin of life on the Earth. Whether life evolved *ab initio* here on the Earth or came from another part of space is debatable. Still, it is believed that our single-celled ancestors formed from the raw materials present at that time

somewhere in the universe. When, where, and how the first life came to be is not straightforward to answer. However, it is necessary to explain how the building blocks of life (simple molecule → complex molecule → prebiotic → biomolecule) could be indigenously produced in the universe. In the event prebiotic molecules are below detection limits, attempts are made to observe their precursors to estimate their abundances. This Chapter discusses the chemical studies of some COMs in various parts of the star-forming region. This study includes the formation of a) aldimines and amines (Sil et al., 2018), b) three nitrogen (N)-bearing species containing peptide-like bonds (Gorai et al., 2020b), and b) phosphorous (P) bearing (Sil et al., 2021) species.

4.1 Aldimines and amines: the building-block of amino acids

Aldimines and amines are essential ingredients of amino acids (Godfrey et al., 1973; Holtom et al., 2005). Thus their discovery under astrophysical circumstances could be treated as important clues leading to the origin of life. Aldimines are seen within the reactions of Strecker-type synthesis, which prepares α-aminonitriles, which are versatile intermediates for synthesizing amino acids via hydrolysis of nitriles. However, the contribution of Strecker synthesis towards the formation of these species is less significant (Elsila et al., 2007). A total of 34 molecules from six isomeric groups (CH_3N, CH_5N, C_2H_5N, C_2H_7N, C_3H_7N, and C_3H_9N), each contains at least one aldimine or amine, are studied to determine their possibility of detection in the ISM. From the CH_3N isomeric group, methanimine (CH_2NH) was observed using Parkes 64 m telescope toward Sgr B2 (Godfrey et al., 1973). From the CH_5N isomeric group, methylamine (CH_3NH_2) was detected (Kaifu et al., 1974; Fourikis et al., 1974) in both Sgr B2 and Orion A. Glycine could have been formed by the reaction between methanimine and formic acid (Godfrey et al., 1973). Thus, methanimine could be treated as the precursor of glycine (Suzuki et al., 2016). Furthermore, Holtom et al. (2005) showed that glycine could have been formed by reacting with another precursor molecule (reaction between methylamine and CO_2 under UV irradiation on an icy grain mantle). Finally, Woon (2002) recommended that glycine could be formed by the reaction between CH_2NH_2 and the COOH radical. On the other hand, methylamine could be produced by two successive H addition reactions with methanimine. It can also be formed by four subsequent H additions to HCN on the surface of grains (Godfrey et al., 1973; Woon, 2002; Theule et al., 2011). Both these precursor molecules (methylamine and ethylamine) of glycine were observed in comet 81P/Wild, also known as Wild 2 (Glavin et al., 2008), and the coma of $67P/C-G$ (Altwegg et al., 2016). Microwave and millimeter-wave spectra of the two conformers of ethanimine (E- and Z-ethanimine) were characterized to guide the astronomical searches (Brown et al., 1980; Lovas et al., 1980). Finally, from the C_2H_5N isomeric group, ethanimine has been detected with both forms in the same sources where methanimine has already been observed (Loomis et al., 2013).

However, any species from the following C_2H_7N, C_3H_7N, and C_3H_9N isomeric groups in this sequence have yet to be detected. This prompts us to study their possibility of detection from these three isomeric groups. Ethylamine, propanimine, and trimethylamine are of particular interest from these isomeric groups because they could play a role in forming amino acids and other prebiotic molecules. Margulès et al. (2015) performed the first spectroscopic study of the propanimine molecule

and found its two conformers, E-propanimine and Z-propanimine. It is essential to know the spectroscopic details and the chemical abundances of these species to detect these species under astrophysical conditions. High-level quantum chemical calculations are employed to estimate the accurate energies of all the species. A large gas-grain chemical model is used to study the presence of these species in the ISM.

4.1.1 Computational details and methodology

Quantum chemical calculations

For the quantum chemical calculations, we use the GAUSSIAN 09 suite of programs (Frisch et al., 2013). We consider some ice-phase reactions leading to the formation of various interstellar amines and aldimines listed in Table 4.1. The reactions include radical – radical (RR), which can happen at each encounter, and neutral – radical (NR) that often possess activation barriers. The Quadratic Synchronous Transit (QST2 method) approach is employed to search for transition state (TS) structures and to determine reaction pathways using Synchronous Transit-Guided Quasi-Newton (STQN) method (Peng & Bernhard Schlegel, 1993; Peng et al., 1996). The QST2 method with DFT-B3LYP/6-311++G(d,p) level of theory is employed to calculate the activation barrier and Gibbs free energy of activation.

The Gaussian-4 (G4) theory is employed to estimate the accurate enthalpies of formation of all the species. In arriving at precise total energy for a given species, the G4 composite method performs a sequence of well-defined *ab initio* molecular calculations (Curtiss et al., 2007). A fully optimized ground-state structure is verified as a stationary point (having non-imaginary frequency) by harmonic vibrational frequency analysis. To compute the enthalpy of formation, we calculate the atomization energy of molecules. Experimental enthalpies of formation of atoms are taken from Curtiss et al. (1997). Table 4.2 summarizes the present astronomical status and enthalpy of formation ($\Delta_f H^O$) of all the considered species. Subsequently, we arrange the species according to the ascending order of the enthalpy of formation in all the tables. Some experimental enthalpy of formation values (if available) are also shown for comparison. Relative energies of each isomeric group member are also shown with the G4 level of theory. Osmont et al. (2007) found that this approach is also suitable for the computation of the enthalpies of formation. Moreover, in Table 4.2, we also include our calculated enthalpies of formation with the DFT-B3LYP/6-31G(d,p) level of theory. In our case, we find that the computed

Table 4.1: Ice-phase formation pathways (Sil et al., 2018).

Reaction number (type)	**Reaction**	**Activation barrier (K)**
R1(RR)[a]	$N + CH_3 \rightarrow CH_2NH$	0.0
R2(RR)[a]	$NH + CH_2 \rightarrow CH_2NH$	0.0
R3(RR)[a]	$NH_2 + CH \rightarrow CH_2NH$	0.0
R4(NR)[a]	$HCN + H \rightarrow H_2CN$	3647[e]
R5(NR)[a]	$HCN + H \rightarrow HCNH$	6440[e]
R6(RR)[a]	$H_2CN + H \rightarrow CH_2NH$	0.0
R7(RR)[a]	$HCNH + H \rightarrow CH_2NH$	0.0
R8(NR)[a]	$CH_2NH + H \rightarrow CH_3NH$	2134[e]
R9(NR)[a]	$CH_2NH + H \rightarrow CH_2NH_2$	3170[e]
R10(RR)[a]	$CH_3NH + H \rightarrow CH_3NH_2$	0.0
R11(RR)[a]	$CH_2NH_2 + H \rightarrow CH_3NH_2$	0.0
R12(RR)[b]	$CH_2CN + H \rightarrow CH_3CN$	0.0
R13(RR)[c]	$CH_3 + CN \rightarrow CH_3CN$	0.0
R14(NR)[d]	$CH_3CN + H \rightarrow CH_3CNH$	1400[e]
R15(RR)[d]	$CH_3CNH + H \rightarrow CH_3CHNH$	0.0
R16(RR)[d]	$CH_3 + H_2CN \rightarrow CH_3CHNH$	0.0
R17(NR)	$CH_3CHNH + H \rightarrow CH_3CH_2NH$	1846
R18(RR)	$CH_3CH_2NH + H \rightarrow CH_3CH_2NH_2$	0.0
R19(RR)	$C_2H_5 + H_2CN \rightarrow CH_3CH_2CHNH$	0.0
R20(RR)	$C_2H_5 + CN \rightarrow CH_3CH_2CN$	0.0
R21(NR)	$CH_3CH_2CN + H \rightarrow CH_3CH_2CNH$	2712
R22(RR)	$CH_3CH_2CNH + H \rightarrow CH_3CH_2CHNH$	0.0

Note:
NR refers to neutral − radical reactions, RR to radical − radical reactions.
[a] Suzuki et al. (2016).
[b] Hasegawa et al. (1992).
[c] Quan et al. (2010).
[d] Quan et al. (2016).
[e] Woon (2002).

enthalpies of formation with the DFT-B3LYP/6-31G(d,p) level of theory are closer to the experimental values than those with the G4 composite method.

Rotational spectroscopy is the most convenient and the most reliable method for identifying molecules in the ISM. Species having permanent electric dipole moments are generally detected from their rotational transitions. About 80% of all the known interstellar and circumstellar molecules are discovered by these transitions. The intensity of any rotational transition is mainly dependent on the temperature and the components (a-type, b-type, and c-type) of the dipole moment (Fortman et al., 2014; McMillan et al., 2014). The relative signs of the dipole moment components may induce the change of intensities of some transitions (Müller et al., 2016). These intensities are directly proportional to the square of the dipole moment and inversely proportional to the rotational partition function. Thus, in general, for a fixed temperature, the higher the dipole moments, the higher the intensities. All the molecules considered here have a nonzero permanent electric dipole moment. Dipole moment components along the inertial axis (μ_a, μ_b, and μ_c) are summarized in Table 4.3. For the computation of the dipole moment components, we use various levels of theory. Among them, our calculations at the HF level yielded excellent agreement with the existing experimental results. Lakard (2003) analyzed permanent electric dipole moments of some primary aliphatic amines. They used various models for comparing their calculated results with the experimentally obtained results. They found that the HF/6-31G(3df) level of theory is more reliable for the aliphatic amines. According to their calculations, on average, this level of theory can predict values of permanent electric dipole moments with a deviation of only 2.1% of its experimental values. Concerning their results, here we use the same level of theory to compute the dipole moment components. Table 4.3 shows our calculated dipole moment components along with the experimental values, whenever available. Table 4.3 shows that our estimated total dipole moments are in good agreement with the experimentally available data for most of the cases. For example, in the case of E-ethanimine, we find a maximum deviation of 11.5% between our calculated and experimental values of total dipole moments. On average, we find a 5.35% variation between our calculated and experimented values.

Accurate quantum chemical studies provide reliable spectroscopic constants to aid laboratory microwave studies and interstellar detections with confidence. We use the MP2/6-311++G(d,p) level of theory to produce spectroscopic constants close to the experimental values. Corrections for the interaction between rotational and vibrational motions, along with corrections for vibrational averaging and anharmonic corrections to the vibrational motion, are considered in our calculations. Table

Table 4.2: Enthalpy of formation and electronic energy (E_0) with zero-point vibrational energy (ZPE) and relative energy (in bracket) with G4 composite method (Sil et al., 2018).

Number	Species	Astronomical Status	E_0+ZPE in Hartree/particle (Relative Energy in kcal/mol)	Calculated $\Delta_f H^0$ using G4 composite method (using B3LYP/6-31G(d,p) method) (in kcal/mol)	Experimental $\Delta_f H^0$ (in kcal/mol)
			CH_3N Isomeric Group		
1	Methanimine	observed[b]	-94.596377 (0.00)	18.2604366 (20.0748878)	—
2	λ^1-Azanylmethane	not observed	−94.519754 (48.08)	66.3715977 (66.9874996)	—
			CH_5N Isomeric Group		
1	Methylamine	observed[c,d]	−95.802182 (0.00)	−9.00194363 (−7.3082602)	−5.37763[a]
			C_2H_5N Isomeric Group		
1	E-ethanimine	observed[e]	−133.896198 (0.00)	5.90189865 (7.9892830)	5.74[f]
2	Z-ethanimine	observed[e]	−133.895732 (0.29)	6.20797719 (8.3293932)	—
3	Ethenamine	not observed	−133.889919 (3.94)	9.8284533 (12.7953785)	—
4	N-methylmethanimine	not observed	−133.884403 (7.40)	13.275162 (15.5507728)	10.51625[f]
5	Aziridine	not observed	−133.862508 (21.14)	26.62315 (29.3566098)	30.11472[a]
			C_2H_7N Isomeric Group		
1	Ethylamine (trans)	not observed	−135.094044 (0.00)	−16.366079 (−14.5306661)	—
2	Ethylamine (gauche)	not observed	−135.09341 (0.40)	−15.955933 (−14.1008221)	−11.3528[a]
3	Dimethylamine	not observed	−135.084612 (5.92)	−10.437412 (−8.4344111)	−4.445507[a]
			C_3H_7N Isomeric Group		
1	2-Propanimine	not observed	−173.193699 (0.00)	−4.7991787 (−2.2671314)	—
2	2-Propenamine	not observed	−173.18563 (5.06)	0.18444024 (3.5818848)	—
3	(1E)-1-Propanimine	not observed	−173.183877 (6.163)	1.287921 (3.7186819)	—
4	(1Z)-1-Propen-1-amine	not observed	−173.183875 (6.164)	1.2981179 (3.7205644)	—
5	(1E)-N-Methylethanimine	not observed	−173.183821 (6.20)	1.4335242 (4.0067087)	—
6	(1Z)-1-Propanimine	not observed	−173.183423 (6.45)	1.59211071 (4.0393392)	—
7	(1E)-1-Propen-1-amine	not observed	−173.181835 (7.44)	2.6644726 (5.9243778)	—
8	N-Ethylmethanimine	not observed	−173.17536 (11.51)	6.5932994 (12.4893824)	—
9	N-Methylethenamine	not observed	−173.171735 (13.78)	9.0000089 (12.4893824)	—
10	Allylamine	not observed	−173.168277 (15.95)	11.096984 (14.2338589)	—
11	Cyclopropanamine	not observed	−173.159802 (21.27)	15.985053 (18.7632226)	18.475[a]
12	S-2-Methylaziridine	not observed	−173.157389 (22.7846)	17.531164 (20.4380455)	—
13	(2S)-2-Methylaziridine	not observed	−173.157388 (22.7853)	17.535559 (20.4405556)	—
14	2-Methylaziridine (trans)	not observed	−173.157386 (22.7865)	17.543877 (20.4393006)	—
15	2-Methylaziridine (cis)	not observed	−173.156991 (23.03)	17.7562713 (20.7574479)	—
16	Azetidine	not observed	−173.1536 (25.16)	19.607872 (22.3205741)	—
17	Methylaziridine	not observed	−173.147784 (28.81)	23.520139 (26.5719511)	—
18	N-Methylethanamine	not observed	−173.126259 (42.32)	37.837958 (41.5192279)	—
19	(Dimethyliminio)methanide	not observed	−173.112784 (50.77)	45.881231 (50.7837785)	—
			C_3H_9N Isomeric Group		
1	2-Aminopropane	not observed	−174.385779 (0.00)	−23.5149351 (−21.4656727)	−20.0048[a]
2	Propylamine	not observed	−174.381773 (2.51)	−20.9566988 (−18.7880896)	−16.7543[a]
3	Ethylmethylamine	not observed	−174.375953 (6.16)	−17.3159833 (−15.0857834)	—
4	Trimethylamine	not observed	−174.369667 (10.11)	−13.4808824 (−10.9573983)	−5.64054[a]

Note:
Additional computation of enthalpy of formation by the B3LYP/6-31G(d,p) level of theory is pointed out in parentheses.
[a] Frenkel' et al. (1994).
[b] Godfrey et al. (1973).
[c] Kaifu et al. (1974).
[d] Fourikis et al. (1974).
[e] Loomis et al. (2013).
[f] NIST Chemistry Webbook (http://webbook.nist.gov/chemistry).

Table 4.3: Calculated dipole moment components with HF/6-31G(3df) level of theory (Sil et al., 2018).

Number	Species	μ_a (D)	μ_b (D)	μ_c (D)	μ_{tot} (D)
		CH_3N Isomeric Group			
1	Methanimine	−1.5115 (−1.300[g])	−1.4556 (−1.500[g])	0.0000 (0.000[g])	2.0985 (2.000[g])
2	λ^1-azanylmethane	−1.9499	−0.0176	0.1483	1.9556
		CH_5N Isomeric Group			
1	Methylamine	0.4410	0.2771	1.1774	1.2874 (1.310[h])
		C_2H_5N Isomeric Group			
1	(E)-Ethanimine	0.2063	−2.0884	0.2912	2.1187 (1.900[h])
2	(Z)-Ethanimine	0.6062	−2.3957	0.5926	2.5412
3	Ethenamine	0.5514	1.0539	−0.7109	1.3857
4	N-Methylmethanimine	−0.2812	1.0514	1.2499	1.6573 (1.530[i])
5	Aziridine	1.6649	−0.2522	0.1768	1.6931 (1.90±0.01[h])
		C_2H_7N Isomeric Group			
1	Ethylamine (trans)	0.8802	−0.1949	0.8894	1.2664 (1.304±0.011[h])
2	Ethylamine (gauche)	−0.5839	−1.0489	−0.2731	1.2312 (1.220[h])
3	Dimethylamine	0.1499	−0.9771	−0.1444	0.9991 (1.030[h])
		C_3H_7N Isomeric Group			
1	2-Propanimine	−0.8107	1.8357	1.4047	2.4495
2	2-Propenamine	0.4017	0.4670	−1.1975	1.3467
3	(1E)-1-Propanimine	−1.0918	−1.5598	0.8831	2.0987
4	(1Z)-1-Propen-1-amine	−0.1209	1.0920	1.7882	2.0987
5	(1E)-N-Methylethanimine	−1.3457	−0.2385	0.8994	1.6360
6	(1Z)-1-Propanimine	−2.1065	1.5775	−0.0300	2.6318
7	(1E)-1-Propen-1-amine	1.0898	−0.4583	−0.2748	1.2138
8	N-Ethylmethanimine	−1.4418	−0.6595	−0.0489	1.5862
9	N-Methylethenamine	−1.2679	−0.0583	−0.0886	1.2723
10	Allylamine	−0.1645	−1.1175	−0.2388	1.1545 (≈1.2[h])
11	Cyclopropanamine	0.0564	0.9405	−0.8402	1.2624 (1.190[g])
12	S-2-Methylaziridine	1.3228	0.6207	0.7330	1.6347
13	(2S)-2-Methylaziridine	0.5335	0.4331	1.4840	1.6354
14	2-Methylaziridine (trans)	0.6744	0.0897	−1.4863	1.6346 (1.57±0.03[h])
15	2-Methylaziridine (cis)	0.6744	0.0897	−1.4863	1.6346 (1.77±0.09[h])
16	Azetidine	0.2802	0.2805	1.1993	1.2632
17	Methylaziridine	0.8549	0.1523	0.9647	1.2980
18	N-methylethanamine	−0.5108	−1.0613	0.4630	1.2655
19	(Dimethyliminio)methanide	−1.4791	−2.9791	0.3350	3.3429
		C_3H_9N Isomeric Group			
1	2-Aminopropane	−0.0991	−0.3068	1.1727	1.2162 (1.190[j])
2	Propylamine	−0.9663	0.5630	0.3766	1.1800 (1.170[h])
3	Ethylmethylamine	0.1756	0.2227	−0.8964	0.9402
4	Trimethylamine	0.1174	0.1270	−0.6598	0.6821 (0.612[h])

Note:
Experimental values are also shown in parentheses.
[g] Demaison et al. (1974).
[h] Nelson Jr et al. (1967).
[i] Sastry & Curl (1964).
[j] Mehrotra et al. (1977).

Table 4.4: Calculated rotational constants and rotational partition functions at 200 K with the MP2/6-311++G(d,p) level of theory (Sil et al., 2018).

Number	Species	A (in GHz)	B (in GHz)	C (in GHz)	Rotational Partition function at 200 K
		CH_3N Isomeric Group			
1	Methanimine	195.72173 (196.21116[k])	34.45869 (34.64252[k])	29.30013 (29.35238[k])	0.107265(+04)
2	λ^1-azanylmethane	157.58498	27.56460	27.56460	0.459337(+03)
		CH_5N Isomeric Group			
1	Methylamine	103.42705 (103.12861[o])	22.75135 (22.62234[o])	21.85872 (21.69598[o])	0.210246(+04)
		C_2H_5N Isomeric Group			
1	(E)-Ethanimine	52.91394 (52.83537[k])	9.76090 (10.07601[k])	8.68503 (8.70427[k])	0.711944(+04)
2	(Z)-Ethanimine	50.17305 (49.5815[k])	9.76932 (10.15214[k])	8.61433 (8.644814[k])	0.733810(+04)
3	Ethenamine	55.91347	9.98960	8.55386	0.689840(+04)
4	N-Methylmethanimine	51.70697 (52.52375[k])	10.71490 (10.66613[k])	9.39306 (9.37719[k])	0.660982(+04)
5	Aziridine	22.81302 (22.73612[p])	21.19888 (21.19238[p])	13.43101 (13.38307[p])	0.591642(+04)
		C_2H_7N Isomeric Group			
1	Ethylamine (trans)	31.90275 (31.75833[m])	8.75819 (8.749157[m])	7.82305 (7.798905[m])	0.101989(+05)
2	Ethylamine (gauche)	32.46287 (32.423470[n])	8.99003 (8.942086[n])	7.86715 (7.825520[n])	0.995128(+04)
3	Dimethylamine	34.22904 (34.24222[q])	9.38988 (9.33403[q])	8.26707 (8.21598[q])	0.925036(+04)
		C_3H_7N Isomeric Group			
1	2-Propanimine	9.64694	8.48897	4.78348	0.240917(+05)
2	2-Propenamine	9.54753	8.97855	4.79187	0.235267(+05)
3	(1E)-1-Propanimine	23.30832	4.33503	4.20885	0.231221(+05)
4	(1Z)-1-Propen-1-amine	23.30833	4.33547	4.20908	0.231203(+05)
5	(1E)-N-Methylethanimine	38.04146	4.07938	3.86089	0.194801(+05)
6	(1Z)-1-Propanimine	23.19882 (24.1852684[l])	4.28693 (4.2923639[l])	4.17097 (4.1567893[l])	0.234119(+05)
7	(1E)-1-Propen-1-amine	38.31516	3.85080	3.59371	0.207076(+05)
8	N-Ethylmethanimine	24.05782	4.60272	4.48201	0.214037(+05)
9	N-Methylethenamine	32.00012	4.30235	4.04446	0.202070(+05)
10	Allylamine	23.65103	4.23494	4.17205	0.233259(+05)
11	Cyclopropanamine	16.28786 (16.26995[r])	6.72692 (6.72300[r])	5.80201 (5.79533[r])	0.189118(+05)
12	S-2-Methylaziridine	16.91977	6.53608	5.76664	0.188818(+05)
13	(2S)-2-Methylaziridine	16.91889	6.53525	5.76592	0.188847(+05)
14	2-Methylaziridine (trans)	16.92200	6.53613	5.76677	0.188803(+05)
15	2-Methylaziridine (cis)	16.68599	6.56078	5.81794	0.188940(+05)
16	Azetidine	11.54225	11.36812	6.70581	0.160748(+05)
17	Methylaziridine	16.41594	7.25710	6.19112	0.175575(+05)
18	N-methylethanamine	36.98588	4.14324	3.84501	0.196438(+05)
19	(Dimethyliminio)methanide	10.15847	9.14934	5.12560	0.218464(+05)
		C_3H_9N Isomeric Group			
1	2-Aminopropane	8.37627 (8.33183[j])	7.99371 (7.97718[j])	4.67889 (4.63719[j])	0.269396(+05)
2	Propylamine	25.18613	3.74012	3.49778	0.262689(+05)
3	Ethylmethylamine	26.06033	3.92898	3.67799	0.245712(+05)
4	Trimethylamine	8.75934	8.75934	4.99056	0.812259(+04)

Note:
Experimentally obtained rotational constants are shown in parentheses.
[j] Mehrotra et al. (1977).
[k] Pearson & Lovas (1977).
[l] Margulès et al. (2015).
[m] Fischer & Botskor (1982).
[n] Fischer & Botskor (1984).
[o] Herzberg (1966).
[p] Bak & Skaarup (1971).
[q] Wollrab & Laurie (1968).
[r] Hendricksen & Harmony (1969).

4.4 summarizes our calculated theoretical values of rotational constants for all the species considered here. A comparison with the existing experimental results, whenever available, is also made. These spectroscopic constants can be used to generate catalog files of spectroscopic frequencies by using the SPCAT program (Pickett, 1991) in the JPL/CDMS format. Table 4.4 also contains the rotational partition function of a temperature relevant to the hot-core condition ($\sim$ 200 K). These partition functions are calculated quantum chemically using the "freqchk" utility, which is used to retrieve frequency and thermochemistry data from a checkpoint file, with the optional specification of an alternate temperature, pressure, scale factor, and/or isotope substitutions. Among all the species considered here, λ^1-azanylmethane is a prolate symmetric top and trimethylamine is an oblate symmetric top, and both have three rotational symmetries. The rest of the species in this study are asymmetric top having rotational symmetry 1. One can appropriate the ground vibrational state rotational partition function for the asymmetric top molecules (Cernicharo et al., 2016) with

$$Q_{rot} = 5.3311 \times 10^6 \sqrt{(T^3/ABC)}/\sigma, \tag{4.1}$$

where A, B, and C are the rotational constants for the molecule (in MHz), T is the temperature (in K), and σ is the rotational symmetry number. The rotational partition function for the prolate symmetric top molecule can be approximated with

$$Q_{rot} = 5.3311 \times 10^6 \sqrt{(T^3/B^2A)}/\sigma. \tag{4.2}$$

For the oblate symmetric top molecule, the rotational partition function can be approximated with

$$Q_{rot} = 5.3311 \times 10^6 \sqrt{(T^3/A^2C)}/\sigma. \tag{4.3}$$

Chemical modeling

Our large gas-grain chemical model (Das et al., 2015a,b; Gorai et al., 2017a,b; Sil et al., 2018) is employed for chemical modeling. Gas and grains are considered as coupled through accretion and thermal/non-thermal desorption. Unless otherwise stated, a moderate value of the non-thermal desorption factor of $\sim$ 0.03 is assumed, as mentioned in Garrod et al. (2007). A visual extinction of 150 and a cosmic-ray ionization rate of 1.3×10^{-17} s^{-1} are used. The initial condition is adopted from Leung et al. (1984). To mimic actual physical conditions of the star-forming region, we consider the warm-up method that was established by Garrod & Herbst (2006b). Initially, we assume that the cloud remains in the isothermal (T = 10 K) stage

Table 4.5: Gas-phase formation and destruction pathways (Sil et al., 2018).

Reaction number (type)	Reactions	α	β	γ	Rate coefficient at 10 K
	Formation pathways				
G1(RR)	$N + CH_3 \rightarrow CH_2NH + PHOTON$	1.00×10^{-15}	−3.0	0.0	2.70×10^{-11}
G2(RR)	$NH + CH_2 \rightarrow CH_2NH + PHOTON$	1.00×10^{-15}	−3.0	0.0	2.70×10^{-11}
G3(RR)	$NH_2 + CH \rightarrow CH_2NH + PHOTON$	1.00×10^{-15}	−3.0	0.0	2.70×10^{-11}
G4(NR)	$H + HCN \rightarrow H_2CN + PHOTON$ ($\Delta G\ddagger = 8.37^a$ kcal/mol)	—	—	-	—
G5(NR)	$H + HCN \rightarrow HCNH + PHOTON$ ($\Delta G\ddagger = 10.06^a$ kcal/mol)	—	—	—	—
G6(RR)	$H + H_2CN \rightarrow CH_2NH + PHOTON$	1.00×10^{-15}	−3.0	0.0	2.70×10^{-11}
G7(RR)	$H + HCNH \rightarrow CH_2NH + PHOTON$	1.00×10^{-15}	−3.0	0.0	2.70×10^{-11}
G8(NR)	$H + CH_2NH \rightarrow CH_3NH + PHOTON$ ($\Delta G\ddagger = 7.84^a$ kcal/mol)	—	—	—	—
G9(NR)	$H + CH_2NH \rightarrow CH_2NH_2 + PHOTON$ ($\Delta G\ddagger = 11.64^a$ kcal/mol)	—	—	—	—
G10(RR)	$H + CH_3NH \rightarrow CH_3NH_2 + PHOTON$	1.00×10^{-15}	−3.0	0.0	2.70×10^{-11}
G11(RR)	$H + CH_2NH_2 \rightarrow CH_3NH_2 + PHOTON$	1.00×10^{-15}	−3.0	0.0	2.70×10^{-11}
G12(RR)	$H + CH_2CN \rightarrow CH_3CN + PHOTON$	1.00×10^{-15}	−3.0	0.0	2.70×10^{-11}
G13(RR)	$CH_3 + CN \rightarrow CH_3CN + PHOTON$	1.00×10^{-15}	−3.0	0.0	2.70×10^{-11}
G14(NR)	$H + CH_3CN \rightarrow CH_3CNH + PHOTON$ ($\Delta G\ddagger = 10.32^a$ kcal/mol)	—	—	—	—
G15(RR)	$H + CH_3CNH \rightarrow CH_3CHNH + PHOTON$	1.00×10^{-15}	−3.0	0.0	2.70×10^{-11}
G16(RR)	$CH_3 + H_2CN \rightarrow CH_3CHNH + PHOTON$	1.00×10^{-15}	−3.0	0.0	2.70×10^{-11}
G17(NR)	$H + CH_3CHNH \rightarrow CH_3CH_2NH + PHOTON$ ($\Delta G\ddagger = 9.98^a$ kcal/mol)	—	−3.0	0.0	—
G18(RR)	$H + CH_3CH_2NH \rightarrow CH_3CH_2NH_2 + PHOTON$	1.00×10^{-15}	−3.0	0.0	2.70×10^{-11}
G19(RR)	$C_2H_5 + H_2CN \rightarrow CH_3CH_2CHNH + PHOTON$	1.00×10^{-15}	−3.0	0.0	2.70×10^{-11}
G20(RR)	$C_2H_5 + CN \rightarrow CH_3CH_2CN + PHOTON$	1.00×10^{-15}	−3.0	0.0	2.70×10^{-11}
G21(NR)	$H + CH_3CH_2CN \rightarrow CH_3CH_2CNH$ ($\Delta G\ddagger = 11.03^a$ kcal/mol)	—	−3.0	0.0	—
G22(RR)	$H + CH_3CH_2CNH \rightarrow CH_3CH_2CHNH$	1.00×10^{-15}	−3.0	0.0	2.70×10^{-11}
G23(RR)	$C_2H_5 + NH \rightarrow CH_3CHNH + H$	2.75×10^{-12}	0.0	0.0	2.75×10^{-12}
	Destruction pathways				
G24(IN)	$C^+ + CH_3CNH \rightarrow C_2H_3^+ + HNC$	8.10×10^{-10}	−0.5	0.0	4.44×10^{-9}
G25(IN)	$H^+ + CH_3CNH \rightarrow C2H_4N^+ + H$	2.50×10^{-9}	−0.5	0.0	1.37×10^{-8}
G26(IN)	$H^+ + CH_3CNH \rightarrow CH_3CN^+ + H_2$	2.50×10^{-9}	−0.5	0.0	1.37×10^{-8}
G27(IN)	$He^+ + CH_3CNH \rightarrow He + HNC^+ + CH_3$	1.80×10^{-9}	−0.5	0.0	9.86×10^{-9}
G28(IN)	$He^+ + CH_3CNH \rightarrow He + HNC + CH_3^+$	1.80×10^{-9}	−0.5	0.0	9.86×10^{-9}
G29(IN)	$H_3^+ + CH_3CNH \rightarrow C_2H_5N^+ + H_2$	1.50×10^{-9}	−0.5	0.0	8.22×10^{-9}
G30(IN)	$H_3O^+ + CH_3CNH \rightarrow C_2H_5N^+ + H_2O$	6.80×10^{-10}	−0.5	0.0	3.72×10^{-9}
G31(IN)	$HCO^+ + CH_3CNH \rightarrow C_2H_5N^+ + CO$	6.00×10^{-10}	−0.5	0.0	3.29×10^{-9}
G32(IN)	$HCO_2^+ + CH_3CNH \rightarrow C_2H_5N^+ + CO_2$	5.30×10^{-10}	−0.5	0.0	2.90×10^{-9}
G33(IN)	$C^+ + CH_3CHNH \rightarrow C_2H_4^+ + HNC$	1.70×10^{-9}	−0.5	0.0	9.31×10^{-9}
G34(IN)	$H^+ + CH_3CHNH \rightarrow C_2H_4N^+ + H_2$	5.10×10^{-9}	−0.5	0.0	2.79×10^{-8}
G35(IN)	$H^+ + CH_3CHNH \rightarrow C_2H_5N^+ + H$	5.10×10^{-9}	−0.5	0.0	2.79×10^{-8}
G36(IN)	$H_3^+ + CH_3CHNH \rightarrow C_2H_6N^+ + H_2$	3.00×10^{-9}	−0.5	0.0	1.64×10^{-8}
G37(IN)	$H_3O^+ + CH_3CHNH \rightarrow C_2H_6N^+ + H_2O$	1.40×10^{-9}	−0.5	0.0	7.67×10^{-9}
G38(IN)	$HCO^+ + CH_3CHNH \rightarrow C_2H_6N^+ + CO$	1.20×10^{-9}	−0.5	0.0	6.57×10^{-9}
G39(IN)	$HCO_2^+ + CH_3CHNH \rightarrow C_2H_6N^+ + CO_2$	1.10×10^{-9}	−0.5	0.0	6.02×10^{-9}
G40(IN)	$H^+ + CH_2NH_2 \rightarrow NH_2 + CH_3^+$	1.00×10^{-9}	0.0	0.0	1.00×10^{-9}
G41(IN)	$H^+ + CH_2NH_2 \rightarrow NH_2^+ + CH_3$	1.00×10^{-9}	0.0	0.0	1.00×10^{-9}
G42(IN)	$H_3O^+ + CH_2NH_2 \rightarrow CH_2NH_3^+ + H_2O$	1.00×10^{-9}	0.0	0.0	1.00×10^{-9}
G43(IN)	$HCO^+ + CH_2NH_2 \rightarrow CH_2NH_3^+ + CO$	1.00×10^{-9}	0.0	0.0	1.00×10^{-9}
G44(IN)	$He^+ + CH_2NH_2 \rightarrow NH + CH_3^+ + He$	1.00×10^{-9}	0.0	0.0	1.00×10^{-9}
G45(IN)	$H^+ + CH_3NH \rightarrow NH_2^+ + CH_3$	1.00×10^{-9}	0.0	0.0	1.00×10^{-9}
G46(IN)	$H^+ + CH_3NH \rightarrow NH_2 + CH_3^+$	1.00×10^{-9}	0.0	0.0	1.00×10^{-9}
G47(IN)	$H_3O^+ + CH_3NH \rightarrow CH_2NH_3^+ + H_2O$	1.00×10^{-9}	0.0	0.0	1.00×10^{-9}
G48(IN)	$HCO^+ + CH_3NH \rightarrow CH_2NH_3^+ + CO$	1.00×10^{-9}	0.0	0.0	1.00×10^{-9}
G49(IN)	$He^+ + CH_3NH \rightarrow NH + CH_3^+ + He$	1.00×10^{-9}	0.0	0.0	1.00×10^{-9}
G50(IN)	$H^+ + CH_3NH_2 \rightarrow NH_2 + CH_4^+$	1.00×10^{-9}	0.0	0.0	1.00×10^{-9}
G51(IN)	$H^+ + CH_3NH_2 \rightarrow NH_2^+ + CH_4$	1.00×10^{-9}	0.0	0.0	1.00×10^{-9}
G52(IN)	$H_3O^+ + CH_3NH_2 \rightarrow CH_3NH_3^+ + H_2O$	1.00×10^{-9}	0.0	0.0	1.00×10^{-9}
G53(IN)	$HCO^+ + CH_3NH_2 \rightarrow CH_3NH_3^+ + CO$	1.00×10^{-9}	0.0	0.0	1.00×10^{-9}
G54(IN)	$He^+ + CH_3NH_2 \rightarrow NH_2 + CH_3^+ + He$	1.00×10^{-9}	0.0	0.0	1.00×10^{-9}
G55(IN)	$C^+ + CH_3CH_2NH_2 \rightarrow C_2H_5^+ + H_2CN$	1.70×10^{-9}	−0.5	0.0	9.31×10^{-9}
G56(IN)	$H^+ + CH_3CH_2NH_2 \rightarrow CH_3CNH^+ + H_2 + H_2$	5.10×10^{-9}	−0.5	0.0	2.79×10^{-8}
G57(IN)	$H^+ + CH_3CH_2NH_2 \rightarrow C_2H_4N^+ + H_2 + H_2$	5.10×10^{-9}	−0.5	0.0	2.79×10^{-8}
G58(IN)	$H_3^+ + CH_3CH_2NH_2 \rightarrow C_2H_6N^+ + H_2 + H_2$	3.00×10^{-9}	−0.5	0.0	1.64×10^{-8}
G59(IN)	$H_3O^+ + CH_3CH_2NH_2 \rightarrow C_2H_6N^+ + H_2O + H_2$	1.40×10^{-9}	−0.5	0.0	7.67×10^{-9}
G60(IN)	$HCO^+ + CH_3CH_2NH_2 \rightarrow C_2H_6N^+ + CO + H_2$	1.20×10^{-9}	−0.5	0.0	6.57×10^{-9}

Reaction number (type)	Reaction	α	β	γ	Rate coefficient@10K
G61(IN)	$HCO_2^+ + CH_3CH_2NH_2 \rightarrow C_2H_6N^+ + CO_2 + H_2$	1.10×10^{-9}	−0.5	0.0	6.02×10^{-9}
G62(IN)	$C^+ + CH_3CH_2CN \rightarrow C_2H_5^+ + C_2N$	1.70×10^{-9}	−0.5	0.0	9.31×10^{-9}
G63(IN)	$H^+ + CH_3CH_2CN \rightarrow CH_3CNH^+ + CH_2$	5.10×10^{-9}	−0.5	0.0	2.79×10^{-8}
G64(IN)	$H^+ + CH_3CH_2CN \rightarrow C_2H_4N^+ + CH_2$	5.10×10^{-9}	−0.5	0.0	2.79×10^{-8}
G65(IN)	$H_3^+ + CH_3CH_2CN \rightarrow C_2H_6N^+ + CH_2$	3.00×10^{-9}	−0.5	0.0	1.64×10^{-8}
G66(IN)	$H_3O^+ + CH_3CH_2CN \rightarrow C_2H_6N^+ + H_2CO$	1.40×10^{-9}	−0.5	0.0	7.67×10^{-9}
G67(IN)	$HCO^+ + CH_3CH_2CN \rightarrow C_2H_6N^+ + C_2O$	1.20×10^{-9}	−0.5	0.0	6.57×10^{-9}
G68(IN)	$HCO_2^+ + CH_3CH_2CN \rightarrow C_2H_5^+ + CO_2 + HCN$	1.10×10^{-9}	−0.5	0.0	6.02×10^{-9}
G69(IN)	$C^+ + CH_3CH_2CNH \rightarrow C_2H_5^+ + C_2N + H$	1.70×10^{-9}	−0.5	0.0	9.31×10^{-9}
G70(IN)	$H^+ + CH_3CH_2CNH \rightarrow CH_3CNH^+ + CH_2 + H$	5.10×10^{-9}	−0.5	0.0	2.79×10^{-8}
G71(IN)	$H^+ + CH_3CH_2CNH \rightarrow C_2H_4N^+ + CH_3$	5.10×10^{-9}	−0.5	0.0	2.79×10^{-8}
G72(IN)	$H_3^+ + CH_3CH_2CNH \rightarrow C_2H_6N^+ + CH_3$	3.00×10^{-9}	−0.5	0.0	1.64×10^{-8}
G73(IN)	$H_3O^+ + CH_3CH_2CNH \rightarrow C_2H_6N^+ + H_2CO + H$	1.40×10^{-9}	−0.5	0.0	7.67×10^{-9}
G74(IN)	$HCO^+ + CH_3CH_2CNH \rightarrow C_2H_6N^+ + C_2O + H$	1.20×10^{-9}	−0.5	0.0	6.57×10^{-9}
G75(IN)	$HCO_2^+ + CH_3CH_2CNH \rightarrow C_2H_6N^+ + C_2O + OH$	1.10×10^{-9}	−0.5	0.0	6.02×10^{-9}
G76(IN)	$C^+ + CH_3CH_2CHNH \rightarrow C_2H_5^+ + C_2N + H_2$	1.70×10^{-9}	−0.5	0.0	9.31×10^{-9}
G77(IN)	$H^+ + CH_3CH_2CHNH \rightarrow CH_3CNH^+ + CH_3 + H$	5.10×10^{-9}	−0.5	0.0	2.79×10^{-8}
G78(IN)	$H^+ + CH_3CH_2CHNH \rightarrow C_2H_4N^+ + CH_3 + H$	5.10×10^{-9}	−0.5	0.0	2.79×10^{-8}
G79(IN)	$H_3^+ + CH_3CH_2CHNH \rightarrow C_2H_6N^+ + CH_3 + H$	3.00×10^{-9}	−0.5	0.0	1.64×10^{-8}
G80(IN)	$H_3O^+ + CH_3CH_2CHNH \rightarrow C_2H_6N^+ + H_2CO + H_2$	1.40×10^{-9}	−0.5	0.0	7.67×10^{-9}
G81(IN)	$HCO^+ + CH_3CH_2CHNH \rightarrow C_2H_6N^+ + C_2O + H_2$	1.20×10^{-9}	−0.5	0.0	6.57×10^{-9}
G82(IN)	$HCO_2^+ + CH_3CH_2CHNH \rightarrow C_2H_6N^+ + C_2O + H_2O$	1.10×10^{-9}	−0.5	0.0	6.02×10^{-9}
G83(IN)	$C^+ + CH_3CH_2NH \rightarrow C_2H_5^+ + HCN$	1.70×10^{-9}	−0.5	0.0	9.31×10^{-9}
G84(IN)	$H^+ + CH_3CH_2NH \rightarrow CH_3CNH^+ + H_2 + H$	5.10×10^{-9}	−0.5	0.0	2.79×10^{-8}
G85(IN)	$H^+ + CH_3CH_2NH \rightarrow C_2H_4N^+ + H_2 + H$	5.10×10^{-9}	−0.5	0.0	2.79×10^{-8}
G86(IN)	$H_3^+ + CH_3CH_2NH \rightarrow C_2H_6N^+ + H_2 + H$	3.00×10^{-9}	−0.5	0.0	1.64×10^{-8}
G87(IN)	$H_3O^+ + CH_3CH_2NH \rightarrow C_2H_6N^+ + H_2O + H$	1.40×10^{-9}	−0.5	0.0	7.67×10^{-9}
G88(IN)	$HCO^+ + CH_3CH_2NH \rightarrow C_2H_6N^+ + CO + H$	1.20×10^{-9}	−0.5	0.0	6.57×10^{-9}
G89(IN)	$HCO_2^+ + CH_3CH_2NH \rightarrow C_2H_6N^+ + CO_2 + H$	1.10×10^{-9}	−0.5	0.0	6.02×10^{-9}
G90(NN)	$CH_3CNH + H \rightarrow CH_3CN + H_2$	1.28×10^{-11}	0.5	0.0	2.37×10^{-12}
G91(NN)	$CH_3CHNH + H \rightarrow CH_3CNH + H_2$	1.28×10^{-11}	0.5	1050.0	2.37×10^{-12}
G92(NN)	$CH_3CNH + C \rightarrow CH_3CN + CH$	4.18×10^{-12}	0.5	0.0	7.67×10^{-13}
G93(NN)	$CH_3CHNH + C \rightarrow CH_3CNH + CH$	4.18×10^{-12}	0.5	0.0	7.67×10^{-13}
G94(NN)	$C_2H_5 + N \rightarrow CH_3CNH + H$	8.30×10^{-12}	0.0	0.0	8.30×10^{-12}
G95(DR)	$C_2H_4N^+ + e^- \rightarrow CH_3CN + H$	1.50×10^{-7}	−0.5	0.0	8.22×10^{-7}
G96(DR)	$C_2H_4N^+ + e^- \rightarrow CH_2CN + H + H$	1.50×10^{-7}	−0.5	0.0	8.22×10^{-7}
G97(DR)	$C_2H_5N^+ + e^- \rightarrow CH_3CNH + H$	1.50×10^{-7}	−0.5	0.0	8.22×10^{-7}
G98(DR)	$C_2H_5N^+ + e^- \rightarrow CH_3 + H_2CN$	1.50×10^{-7}	−0.5	0.0	8.22×10^{-7}
G99(DR)	$C_2H_6N^+ + e^- \rightarrow CH_3CHNH + H$	1.50×10^{-7}	−0.5	0.0	8.22×10^{-7}
G100(DR)	$C_2H_6N^+ + e^- \rightarrow CH_4 + H_2CN$	1.50×10^{-7}	−0.5	0.0	8.22×10^{-7}
G101(DR)	$CH_2NH_3^+ + e^- \rightarrow CH_4 + NH$	1.50×10^{-7}	−0.5	0.0	8.22×10^{-7}
G102(DR)	$CH_3NH_3^+ + e^- \rightarrow CH_4 + NH_2$	1.50×10^{-7}	−0.5	0.0	8.22×10^{-7}
G103(PH)	$CH_3CNH + PHOTON \rightarrow CH_3 + HNC$	1.00×10^{-9}	0.0	1.9	5.60×10^{-18}
G104(PH)	$CH_3CNH + PHOTON \rightarrow CH_3CN + H$	1.00×10^{-9}	0.0	1.9	5.60×10^{-18}
G105(PH)	$CH_3CHNH + PHOTON \rightarrow CH_3 + H_2CN$	1.00×10^{-9}	0.0	1.9	5.60×10^{-18}
G106(PH)	$CH_3CHNH + PHOTON \rightarrow CH_3CNH + H$	1.00×10^{-9}	0.0	1.9	5.60×10^{-18}
G107(PH)	$CH_3CH_2CN + PHOTON \rightarrow CH_3CNH + CH$	1.00×10^{-9}	0.0	1.9	5.60×10^{-18}
G108(PH)	$CH_3CH_2NH_2 + PHOTON \rightarrow CH_3NH_2 + CH_2$	1.00×10^{-9}	0.0	1.9	5.60×10^{-18}
G109(PH)	$CH_3CH_2CNH + PHOTON \rightarrow CH_3CNH + CH_2$	1.00×10^{-9}	0.0	1.9	5.60×10^{-18}
G110(PH)	$CH_3CH_2CHNH + PHOTON \rightarrow CH_3CNH + CH_3$	1.00×10^{-9}	0.0	1.9	5.60×10^{-18}
G111(PH)	$CH_2NH_2 + PHOTON \rightarrow H_2CN + H_2$	1.00×10^{-9}	0.0	1.6	3.94×10^{-16}
G112(PH)	$CH_3NH + PHOTON \rightarrow H_2CN + H_2$	1.00×10^{-9}	0.0	1.6	3.94×10^{-16}
G113(PH)	$CH_3NH_2 + PHOTON \rightarrow H_2CN + H_2 + H$	3.50×10^{-9}	0.0	1.6	3.94×10^{-16}
G114(PH)	$CH_3CH_2NH + PHOTON \rightarrow CH_3CHNH + H$	3.50×10^{-9}	0.0	1.6	3.94×10^{-16}
G115(PH)	$CH_3CH_2NH + PHOTON \rightarrow C_2H_5 + NH$	3.50×10^{-9}	0.0	1.6	3.94×10^{-16}
G116(CR)	$CH_3CNH + CRPHOT \rightarrow CH_3 + HNC$	1.30×10^{-17}	0.0	1.9	1.95×10^{-14}
G117(CR)	$CH_3CNH + CRPHOT \rightarrow CH_3CN + H$	1.30×10^{-17}	0.0	1.9	1.95×10^{-14}
G118(CR)	$CH_3CHNH + CRPHOT \rightarrow CH_3 + H_2CN$	1.30×10^{-17}	0.0	1.9	1.95×10^{-14}
G119(CR)	$CH_3CHNH + CRPHOT \rightarrow CH_3CNH + H$	1.30×10^{-17}	0.0	1.9	1.95×10^{-14}
G120(CR)	$CH_3CH_2NH_2 + CRPHOT \rightarrow CH_3NH_2 + CH_2$	1.30×10^{-17}	0.0	1.9	1.95×10^{-14}
G121(CR)	$CH_3CH_2CN + CRPHOT \rightarrow CH_3CNH + CH$	1.30×10^{-17}	0.0	1.9	1.95×10^{-14}
G122(CR)	$CH_3CH_2CNH + CRPHOT \rightarrow CH_3CNH + CH_2$	1.30×10^{-17}	0.0	1.9	1.95×10^{-14}
G123(CR)	$CH_3CH_2CHNH + CRPHOT \rightarrow CH_3CNH + CH_3$	1.30×10^{-17}	0.0	1.9	1.95×10^{-14}
G124(CR)	$CH_2NH_2 + CRPHOT \rightarrow NH + CH_3$	1.30×10^{-17}	0.0	500.0	1.95×10^{-14}
G125(CR)	$CH_3NH + CRPHOT \rightarrow NH + CH_3$	1.30×10^{-17}	0.0	500.0	1.95×10^{-14}
G126(CR)	$CH_3NH_2 + CRPHOT \rightarrow NH_2 + CH_3$	1.30×10^{-17}	0.0	500.0	1.95×10^{-14}
G127(CR)	$CH_3CH2NH + CRPHOT \rightarrow CH_3CHNH + H$	1.30×10^{-17}	0.0	1.9	1.95×10^{-14}
G128(CR)	$CH_3CH2NH + CRPHOT \rightarrow C_2H_5 + NH$	1.30×10^{-17}	0.0	1.9	1.95×10^{-14}

Note:
CR refers to cosmic-rays, IN to ion − neutral reactions, NR to neutral − radical reactions, NN to neutral − neutral reactions, RR to radical − radical reactions, DR to dissociative recombination reactions for molecular ions, PH to photodissociation reactions.
[a]This work

for 10^6 years, followed by a subsequent warm-up stage where the temperature can gradually increase up to 200 K in 10^5 years. Hence, our simulation time is restricted to 1.1×10^6 years. Furthermore, we assume that each stage has the same constant density ($n_H = 10^7$ cm^{-3}).

Our gas-phase chemical network is mainly adapted from the UMIST 2012 database (McElroy et al., 2013). For the grain surface reaction network, we primarily follow Ruaud et al. (2016). In addition to the above network, our network includes some needed reactions for the formation/destruction of interstellar amines and aldimines (see Tables 4.1 and 4.5).

For the computation of the gas-phase rate coefficients of some additional gas-phase neutral – radical (NR) reactions with a barrier, we use the transition state theory (TST), which leads to the Eyring equation (Eyring, 1935):

$$k = (k_B T/hc) \exp(-\Delta G‡/RT)\ s^{-1}, \tag{4.4}$$

where $\Delta G‡$ is the Gibbs free energy of activation and c is the concentration, set to 1. $\Delta G‡$ is calculated by the quantum chemical calculation (QST2 method with B3LYP/6-311++G(d,p) level of theory). Equation 4.4 suggests that the rate coefficient is exponentially increasing with the temperature. Thus, to avoid any unattainable rate coefficient around the high-temperature domain, we use an upper limit (10^{-10} cm^{3}s^{-1}) for Equation 4.4.

Usually, a radical – radical addition reaction with a single product can occur through the radiative association. Vasyunin & Herbst (2013) outlined the rate coefficient for the formation of larger molecules by gas-phase radiative association reactions. According to them, a larger molecule such as CH_3OCH_3 can be formed by

$$CH_3 + CH_3O \rightarrow CH_3OCH_3 + \text{Photon}.$$

They considered the following temperature-dependent rate coefficient for the above reaction:

$$k = 10^{-15}(T/300)^{-3}. \tag{4.5}$$

We also consider similar rate coefficients for the radical – radical gas-phase reactions leading to a single product. In our model, we consider the formation and destruction of these species in both phases.

To compute the rate coefficients of ice-phase reaction pathways, we use diffusive reactions with a barrier against diffusion ($\kappa \times R_{diff}$), which is based on thermal diffusion (Hasegawa et al., 1992). κ is the quantum mechanical probability of tunneling through a rectangular barrier of thickness d. κ is unity in the absence of

a barrier. For reactions with activation energy barriers (E_a), κ is defined as the quantum mechanical probability for tunneling through the rectangular barrier of thickness $d(=1)$ and is calculated by

$$\kappa = \exp[-2(d/\hbar)(2\mu E_a)^{1/2}]. \tag{4.6}$$

Chemical enrichment of interstellar grain mantles depends on the desorption energies (E_d) and barriers against diffusion (E_b) of the adsorbed species. In the low-temperature regime, the mobility of the lighter species such as H, D, N, and O mainly controls the chemical composition of the interstellar grain mantle. Here we use $E_b = 0.50E_d$ (Garrod, 2013). BEs are mostly taken from the KIDA. However, BEs of some of the newly added ice-phase species are not available in the KIDA. For these species, we add the BEs of the reactants required to form these species. A similar technique was also employed in Garrod (2013). For example, for calculating the BE of CH_3CNH, we add the BEs of CH_3CN and H.

We assume various ion – neutral (IN) and photodissociative pathways for the destruction of gaseous amines and aldimines. Different IN and photodissociative destruction pathways are already available in Quan et al. (2016) (for ethanimine) and McElroy et al. (2013) (for methanimine). We follow similar pathways and the same rate coefficients for the destructions of other amines, aldimines, and their associated species. In Table 4.5, we point out all the gas-phase formation and destruction reactions that are considered here. In analogy, we assume similar photodissociative reactions to destroy ice-phase amines, aldimines, and their associated neutrals. Rate coefficients for the photodissociative reactions are assumed to be the same in both phases. Abundances of the gas-phase species can also decrease via adsorption onto the ice. However, the reverse process (desorption) also occurs.

4.1.2 Results and discussion

Here, the results of high-level quantum chemical calculations, together with our chemical model, are presented and discussed for each isomeric group.

CH_3N *Isomeric Group*

This group contains two molecular species (see Figure 4.1), methanimine and λ^1-azanylmethane. Though the presence of methanimine (CH_2NH) in ISM has already been confirmed (Godfrey et al., 1973), λ^1-azanylmethane is yet to be ascertained. Based on the enthalpy of formation and relative energy values shown in Table 4.2,

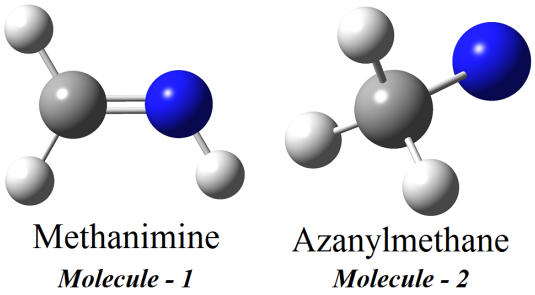

Figure 4.1: CH_3N isomers (Sil et al., 2018).

methanimine appears to be the most stable candidate of the CH_3N isomeric group. But enthalpy of formation is not only a factor to dictate the abundance of these species, specifically, when it is far away from the equilibrium. It is only the reaction pathways that can dictate the final abundance of any species in the ISM. Our calculated dipole moment components (shown in Table 4.3) of methanimine are very close to the available experimental values. From our calculated dipole moment components, it is found that for methanimine, "a" and "b" type rotational transitions are the strongest, whereas "c" type transition is absent. In the case of λ^1-azanylmethane, the strongest component of dipole moment is found to be the "a" component, whereas the "b" component is found to be the weakest. The average dipole moment component of methanimine is slightly higher than that of the λ^1-azanylmethane. Our calculated rotational constants for methanimine are shown in Table 4.4, which are very close to the overall experimental values.

It is believed that methanimine is primarily created within the ice phase. The dominated pathways are shown in the reaction range R4 − R7 of Table 4.1. CH_2NH may form through the successive H addition reaction in the ice phase, starting with the cyanide radical. Subsequent H addition may occur in two ways: H addition with HCN could result in H_2CN (R4) or HCNH (R5). Woon (2002) pointed out that reactions R4 and R5 possess activation energy barriers of about 3647 K and 6440 K, respectively. H_2CN and HCNH can further produce CH_2NH by the H addition reaction (R6 and R7, respectively). The surface network of KIDA already considers the reactions enlisted in Graninger et al. (2014), and thus HCN/HNC-related chemistry is consistent. The gas-phase pathways of Graninger et al. (2014) are also considered in our gas-phase network. Near the higher temperatures, methanimine may be produced by the decomposition of methylamine (CH_3NH_2; Johnson & Lovas, 1972). Suzuki et al. (2016) pointed out that this species could be produced on the interstellar ice by other reactions (R1 − R3) shown in Table 4.1.

For the gas-phase reactions G4 and G5 of Table 4.5, we obtain $\Delta G‡$ of 8.37 kcal/mol and 10.06 kcal/mol, respectively. The chemical evolution of methanimine within the cold isothermal stage and the subsequent warm-up stage is shown in Figures 4.2 and 4.3, respectively. Abundances are shown relative to H_2 molecules. During the isothermal stage, methanimine is significantly abundant in both phases and has a peak abundance of 5.93×10^{-08} in the gas phase and 3.49×10^{-06} in the ice phase. A strong decreasing slope of gas-phase methanimine is observed from Figure 4.2a. Figure 4.2b also depicts a decreasing slope of ice-phase methanimine (during the end of the isothermal regime) due to the production of methylamine by successive H addition reactions (R8 − R9). Dashed curves in Figure 4.2a are shown for the gas-phase abundances considering a non-thermal desorption factor, $a_{fac} = 0$. The gas-phase abundances of methanimine with $a_{fac} = 0$ (dashed line in Figure 4.2a) and $a_{fac} = 0.03$ (solid line in Figure 4.2a) differ significantly. This is because, in the isothermal stage, the gas-phase contribution of methanimine is mainly coming from the ice phase via the non-thermal desorption mechanism. Following the KIDA, the BE of methanimine is assumed to be 5534 K. It is evident from Figure 4.3 that sublimation of methanimine occurs around 110 K in the warm-up stage and the abundance of gas-phase methanimine is significantly increased owing to the efficient gas-phase formation by reactions G1 − G7. The peak abundance of gas-phase methanimine is found to be around 1.81×10^{-09}. Our obtained abundances can be compared with the hot-core observation of methanimine of $\sim 7.0 \times 10^{-08}$ in G10.47+0.03 (hereafter, G10), and 3.0×10^{-9} in NGC 6334F by Suzuki et al. (2016).

CH_5N Isomeric Group

Only methylamine (CH_3NH_2) belongs to this isomeric group (see Figure 4.4), and this was already observed long ago in Sgr B2 and Ori A (Fourikis et al., 1974; Kaifu et al., 1974). In Table 4.2, we compare our calculated enthalpies of formation with that of the current experimental value. We find that our computed value with the DFT-B3LYP/6-31G(d,p) level of theory is closer to the experimentally obtained value than computed from the G4 composite method. Takagi & Kojima (1973); Kaifu et al. (1974) found that the c-type transitions of methylamine are four times stronger than the a-type transitions. We also find a very strong c-component of dipole moment noted in Table 4.3. The calculated total dipole moment component for methylamine is 1.2874 D, whereas the experimentally obtained value is 1.31±0.03 D. Also, an excellent correlation between our calculated rotational constants and experimentally obtained values can be seen in Table 4.4.

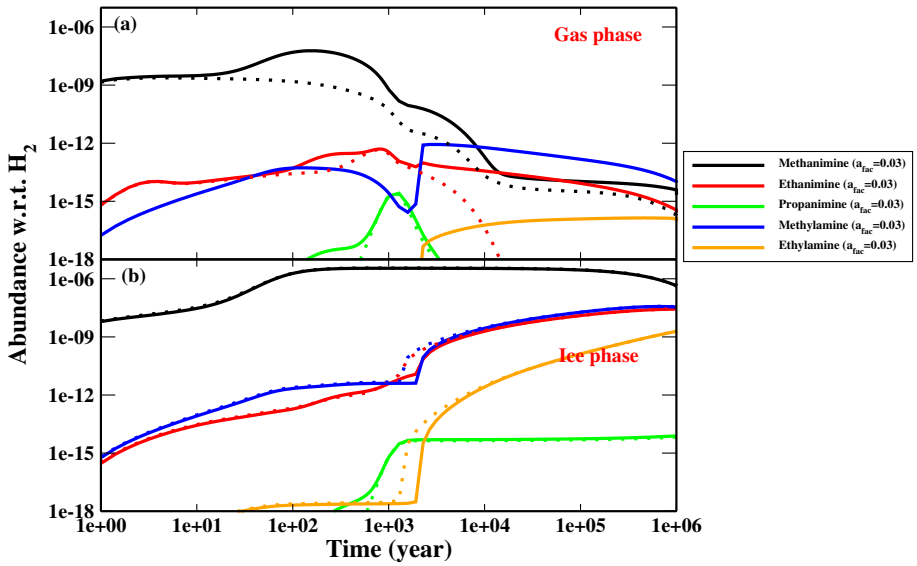

Figure 4.2: Chemical evolution of the aldimines and amines in the isothermal stage for $a_{fac} = 0.03$ (solid) and 0 (dashed) (Sil et al., 2018).

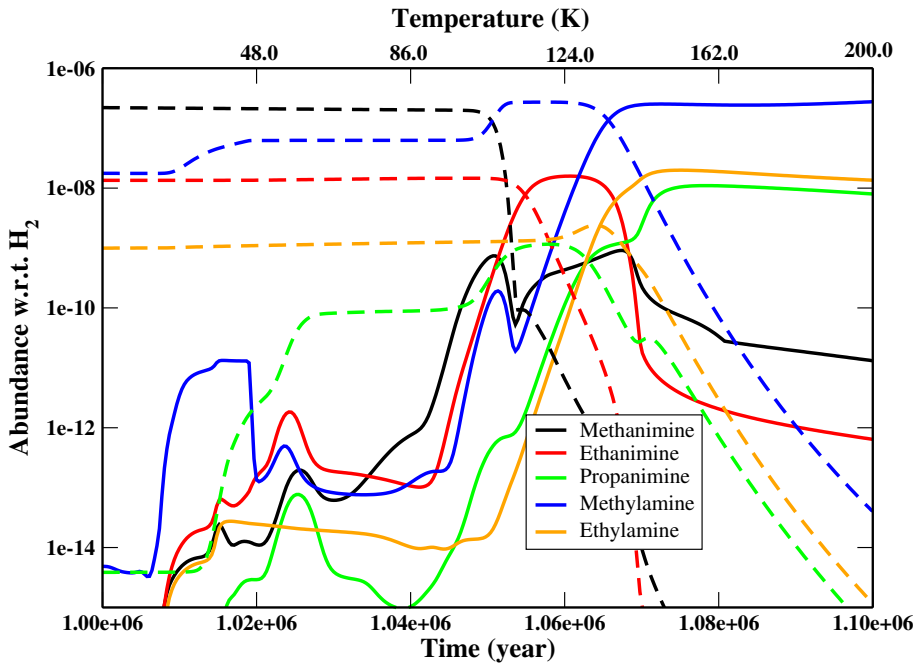

Figure 4.3: Chemical evolution of the aldimines and amines in the warm-up stage. Solid lines represent the gas-phase species, whereas corresponding dashed lines represent the ice-phase species (Sil et al., 2018).

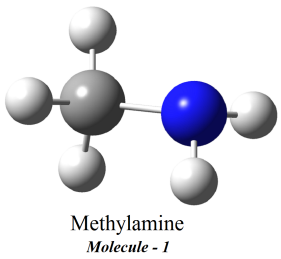

Figure 4.4: CH_5N isomer (Sil et al., 2018).

In the ISM, methylamine may be formed via two successive H addition reactions of methanimine in the ice phase (Godfrey et al., 1973; Suzuki et al., 2016). Woon (2002) determined that the primary step of this H addition reaction may proceed in two ways. First, hydrogenation of methanimine yields CH_3NH (R8) having an activation barrier of 2134 K; second, it may produce CH_2NH_2 (R9) having an activation barrier of 3170 K. Reactions R8 and R9 may also occur in the gas phase. From our TST calculation, we have $\Delta G‡ = 7.84$ kcal/mol for reaction G8 of Table 4.5. However, we do not find a suitable TS for gas-phase reaction G9 of Table 4.5. In the ice phase, R9 possesses a higher (1.485 times) activation barrier than R8. We assume that a similar trend is followed for the gas-phase reaction G9, so we consider $\Delta G‡ = 11.64$ kcal/mol for the gas-phase reaction number G9. Methylamine may further be produced by the hydrogenation reaction of these two products by reactions R10 and R11, respectively.

The reaction number G8 and G9 possess high $\Delta G‡$. Thus, during the isothermal stage, the production of gas-phase methylamine is inadequate. However, despite a high activation barrier (E_a), reactions R8 and R9 would be efficiently processed on interstellar ice by quantum mechanical tunneling and populate the gas phase by the non-thermal desorption. Mainly due to the non-thermal chemical desorption phenomenon, ice-phase methylamine populates the gas phase. It is visible from Figure 4.2a that with $a_{fac} = 0$, the gas-phase contribution of methylamine is negligible (the dashed line, which corresponds to the methylamine is absent). Hence, in the isothermal stage, the contribution for the gas-phase methylamine mainly comes from the ice phase. In the isothermal stage, methylamine attains a peak abundance of 8.46×10^{-13} in the gas phase and 3.70×10^{-08} in the ice phase. From Figure 4.3, it is observed that the ice-phase abundance initially increases owing to the increase in the mobility of the reactants. Peak ice-phase abundance of methylamine is obtained to be 5.44×10^{-07}. Near the high temperature, the production of gas-phase methylamine significantly contributed to (a) the enhancement of the

temperature-dependent rate coefficient of reactions G8 and G9 and (b) the increase in the gas-phase methanimine formation. The peak gas-phase abundance of methylamine is found to be 5.54×10^{-07}. Our obtained values may be compared with the recent observation of methylamine (Ohishi et al., 2017). They predicted methylamine abundance of $\sim 1.2 \times 10^{-08}$ in G10.

C_2H_5N Isomeric Group

Five isomers belong to this isomeric group (see Figure 4.5): E-ethanimine, Z-ethanimine, ethenamine, N-methylmethanimine, and aziridine. Out of these five isomers, both conformers (E and Z) of ethanimine (CH_3CHNH) had been detected in Sgr B2 (Loomis et al., 2013). From our quantum chemical calculation, we find that E-ethanimine is energetically more stable (4.35 kJ/mol by using MP2/6-311G++(d,p) level of theory and 1.2 kJ/mol by using the G4 composite method) than Z-ethanimine. Quan et al. (2016) and Loomis et al. (2013) obtained an energy difference of 4.60 kJ/mol and 4.24 kJ/mol, respectively, between these two conformers. We show the enthalpy of formation values for all the species in Table 4.2, along with the experimentally obtained values, where available. Our calculated enthalpies of formation using the DFT-B3LYP/6-31G(d,p) level of theory are in good agreement with the experimentally obtained values of E-ethanimine, N-methylmethanimine, and aziridine. For a better assessment, in Figure 4.6, we show the enthalpy of formation with the molecule number noted in Table 4.2 and Figure 4.5 for the C_2H_5N isomeric group. E-ethanimine has the minimum enthalpy of formation, followed by Z-ethanimine. The energy difference between these two is smaller than the other isomers of this isomeric group. Observed isomers are marked as green circles in Figures 4.6 and 4.7, and the unobserved isomers are marked as red circles.

All the dipole moment components are presented in Table 4.3. It is found that in both the cases (E and Z), the b-type transition dominates. Our calculated dipole moments are compared with the existing values (Lovas et al., 1980). The effective dipole moment of Z-ethanimine is found to be higher than that of E-ethanimine. Charnley et al. (1995) pointed out that an estimate of the antenna temperature could be made by calculating the intensity of a given rotational transition for an optically thin emission. This intensity is proportional to $\mu^2/Q(T_{rot})$, where μ is the electric dipole moment, and $Q(T_{rot})$ is the partition function at rotational temperature (T_{rot}). In Table 4.4, we point out the rotational constants and the rotational partition function for $T_{rot} = 200$ K. In Figure 4.7, we show the plot of the ex-

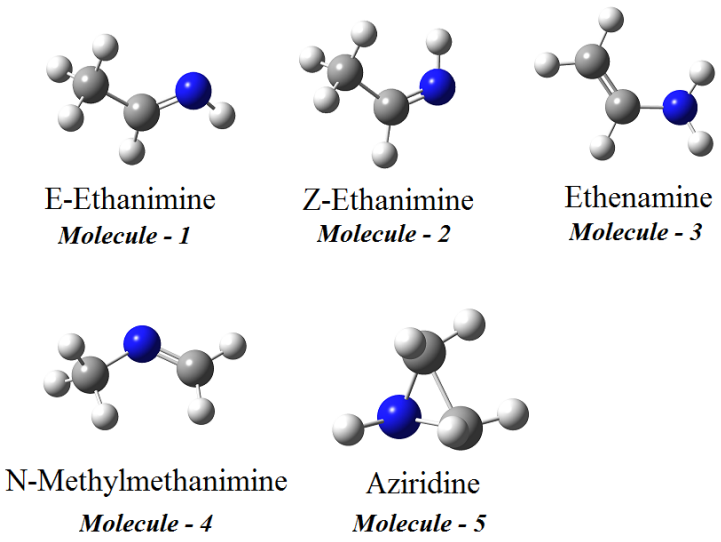

Figure 4.5: C_2H_5N isomers (Sil et al., 2018).

pected intensity ratio (assuming that all the species of this isomeric group have the same abundances) concerning the most stable isomer (E-ethanimine) of this isomeric group. Relative energy values with molecule number of all isomers of this isomeric group are noted in Table 4.2). In Figure 4.7, the expected intensity ratios for all the species of this isomeric group are shown by considering the three components of the dipole moment along with the effective dipole moments. In this isomeric group, Z-ethanimine has the largest effective dipole moment. So considering the same abundances, the probability of detecting the Z isomer of ethanimine will be more favorable than the other isomers of this isomeric group. From Figure 4.5, we can see that after E and Z isomers of ethanimine, aziridine has the most robust transition. Still, due to its higher relative energy compared to E-ethanimine, it is the less probable candidate (if reaction pathways do not influence it another way) for astronomical detection.

Loomis et al. (2013) mentioned that ethanimine might be produced via two consecutive H addition reactions with CH_3CN in the ice phase. Quan et al. (2016) recently proposed that the first step (R14) of the H addition reaction with CH_3CN has a barrier of 1400 K, and the second step (R15) is a radical − radical reaction and assumed to be barrierless. For the gas-phase reaction of G14 of Table 4.5, our calculated value of $\Delta G‡$ is 10.32 kcal/mol. Quan et al. (2016) additionally suggested that ethanimine can even be produced by the reaction between CH_3 and H_2CN in the ice phase. Among the gas-phase pathways, the reaction between C_2H_5 and NH

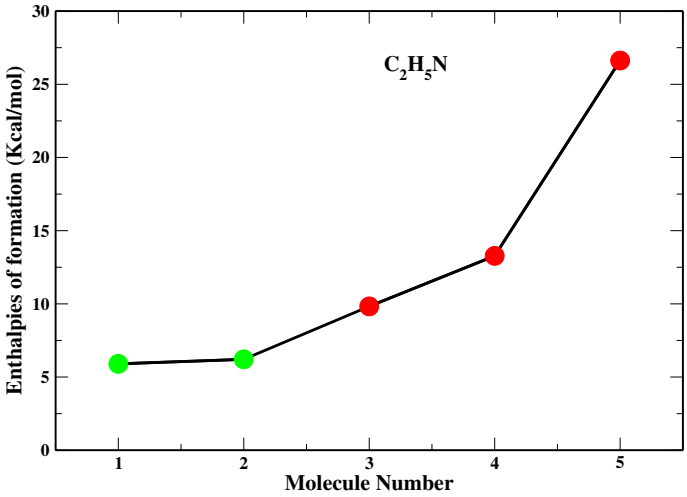

Figure 4.6: Enthalpy of formation of the C_2H_5N isomeric group. Molecules already observed are marked as green circles, and those yet to be observed are marked as red circles (Sil et al., 2018).

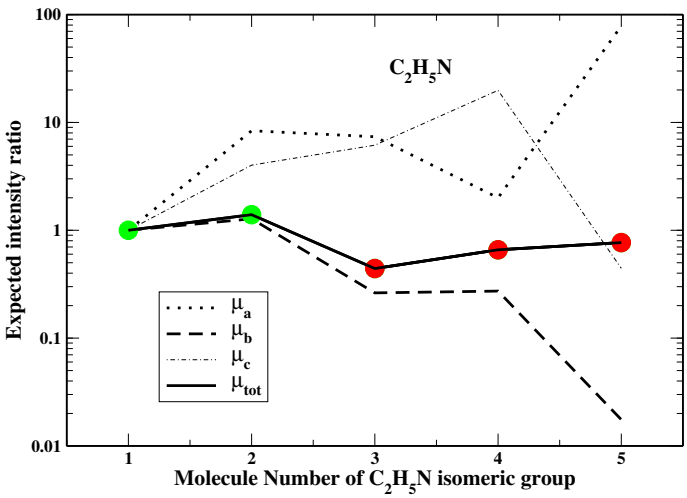

Figure 4.7: Expected intensity ratio of the C_2H_5N isomeric group by considering three components of the dipole moment and effective dipole moment of all the species (Sil et al., 2018).

(reaction G23 of Table 4.5) may lead to CH_3CHNH. In our network, we assume only one form of ethanimine (E-ethanimine) for our modeling.

In the isothermal stage (see Figure 4.2), ethanimine has a peak value of 4.99×10^{-13} in the gas phase and 2.69×10^{-08} in the ice phase. During the warm-up stage (see Figure 4.3), gas-phase ethanimine has a peak value of 3.17×10^{-08}. In the warm-up stage, gas-phase production of ethanimine is also contributing owing to the enhancement of the temperature-dependent rate coefficient of reaction G14. The abundance of ethanimine attains a peak around 125 K, and then starts to decrease due to the formation of ethylamine by the successive hydrogenation reactions (R17 − R18). Since reaction R17 has a barrier, we use Equation 4.4 for the computation of its rate coefficient. Equation 4.4 clearly says that as we are increasing the temperature, the rate coefficient rises exponentially. Thus, in the warm-up stage, the rate coefficient of reaction G17 increases exponentially and attains a reasonable rate ($\sim 10^{-10}$ cm^3 s^{-1}), which means that the destruction of ethanimine by the hydrogenation reaction also gradually increases and reaches a quasi-steady state. At the end of our simulation (after 1.1×10^6 years), we note an abundance of 1.27×10^{-12} for ethanimine, whereas the predicted abundance is $\sim 6.0 \times 10^{-11}$ from Quan et al. (2016).

C_2H_7N Isomeric Group

Trans-ethylamine, gauche-ethylamine, and dimethylamine belong to the C_2H_7N isomeric group (see Figure 4.8). Interestingly, no species of this isomeric group is detected in the ISM. However, the presence of ethylamine, which is the precursor of glycine, was traced in comet Wild 2 (Glavin et al., 2008). Ethylamine can exist in the form of two stable conformers: gauche and trans. An experiment by Hamada et al. (1986) shows that the trans conformer is slightly more stable than the gauche conformer. Our calculated values are also in line with this result. We obtain that the gauche conformer has 1.67 kJ/mol higher energy than the trans conformer. Hence, according to the enthalpy of formation and relative energies as shown in Table 4.2, trans-ethylamine has the least enthalpy of formation and is most stable among this isomeric group. In Figure 4.9, the enthalpy of formation of this isomeric group is depicted with the molecule number, and the enthalpy of formation is noted in Table 4.2. Compared to the experimentally measured enthalpies of formation, the G4 composite method overestimates it for ethylamine and dimethylamine.

In the case of the trans conformer of ethylamine, components "a" and "c" of dipole moments are more substantial, whereas, for the gauche form, the b-component is

found to be the strongest. For dimethylamine, also the b-component of the dipole moment dominates, and the "a" and "b" components have minor contributions. Based on the data available from our quantum chemical calculations, in Figure 4.10, we show the expected intensity ratio concerning the species having the least enthalpy of formation. Figure 4.10 depicts that the trans-ethylamine has the highest expected intensity ratio (~ 1) compared to the other two members (gauche-ethylamine has 0.97 and dimethylamine has 0.69) of this isomeric group, and thus trans-ethylamine has the highest probability of its astronomical detection from this isomeric group.

Ethylamine could be formed on the grain surface via two successive H additions of ethanimine. Our calculation reveals that the first step of this hydrogenation reaction has an activation barrier of 1846 K (R17). For the gas-phase hydrogenation reaction (G17), our calculated $\Delta G\ddagger$ parameter is found to be 9.98 kcal/mol. Since the second step of this reaction is radical $-$ radical, we assume that reaction R18 may be treated as a barrierless process. In the isothermal stage (see Figure 4.2), we have a peak abundance of 1.19×10^{-16} and 1.99×10^{-09} in the gas and ice phase, respectively. In the warm-up stage (see Figure 4.3), ice-phase abundance roughly remains unchanged up to 125 K, and then it starts to decrease sharply. Its gas-phase abundance is higher and has a peak abundance of 3.98×10^{-08}.

Ethanimine and ethylamine are more complex than methanimine and methylamine, respectively. Thus, the abundance of ethanimine/ethylamine would be less than methanimine/methylamine. But Figures 4.2 and 4.3 depict that this trend is not universal for all circumstances. It is because their formation is processed through totally different channels. Their destruction rates are also different. For example, the ice-phase formation of methanimine mainly occurs by successive hydrogenation reactions with HCN (reactions R4 to R7). In contrast, ethanimine appearance is primarily controlled by consecutive hydrogenation reactions with CH_3CN (reactions R14 and R15). Now, reactions R4 and R5 contain a much higher barrier than that of reaction R14. Since HCN is more abundant than CH_3CN, despite high barriers involved in forming methanimine, in the isothermal stage, most of the time, the ice-phase abundance of methanimine remains higher than in ethanimine. However, in the hot-core region, due to the lower activation barrier of reaction R14, ethanimine formation becomes more favorable. Methylamine is mainly formed from methanimine (by reactions R8 $-$ R10), whereas ethylamine is formed from ethanimine (by reactions R17 $-$ R18). Once again, the activation barrier engaged in methylamine formation (reaction R9) is higher than the barrier involved in forming ethylamine (reaction R17). Since very complex chemistry is going on, the abundances of these species should be compared very carefully.

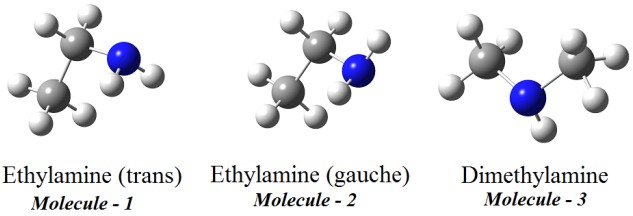

Figure 4.8: C_2H_7N isomers (Sil et al., 2018).

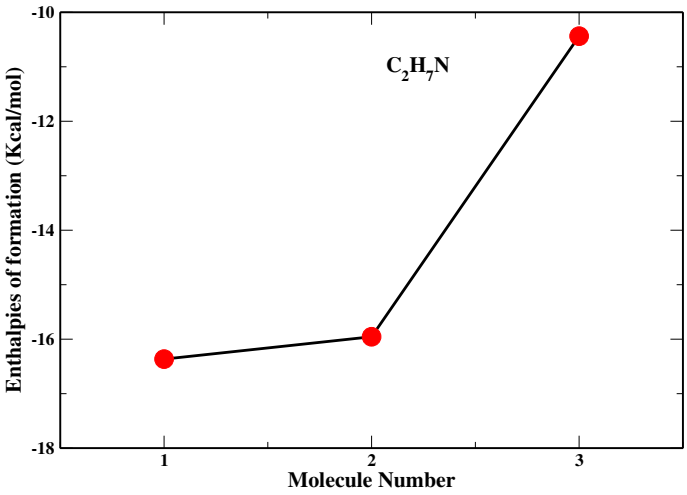

Figure 4.9: Enthalpy of formation of the C_2H_7N isomeric group (Sil et al., 2018).

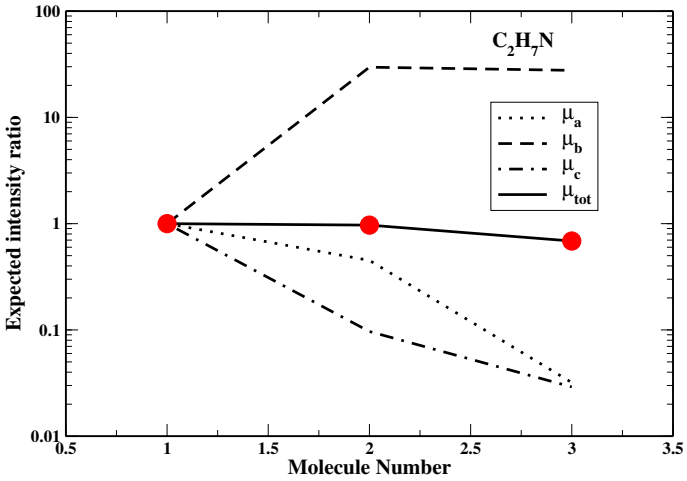

Figure 4.10: Expected intensity ratio of the C_2H_7N isomeric group by considering three components of the dipole moment and effective dipole moment of all the species (Sil et al., 2018).

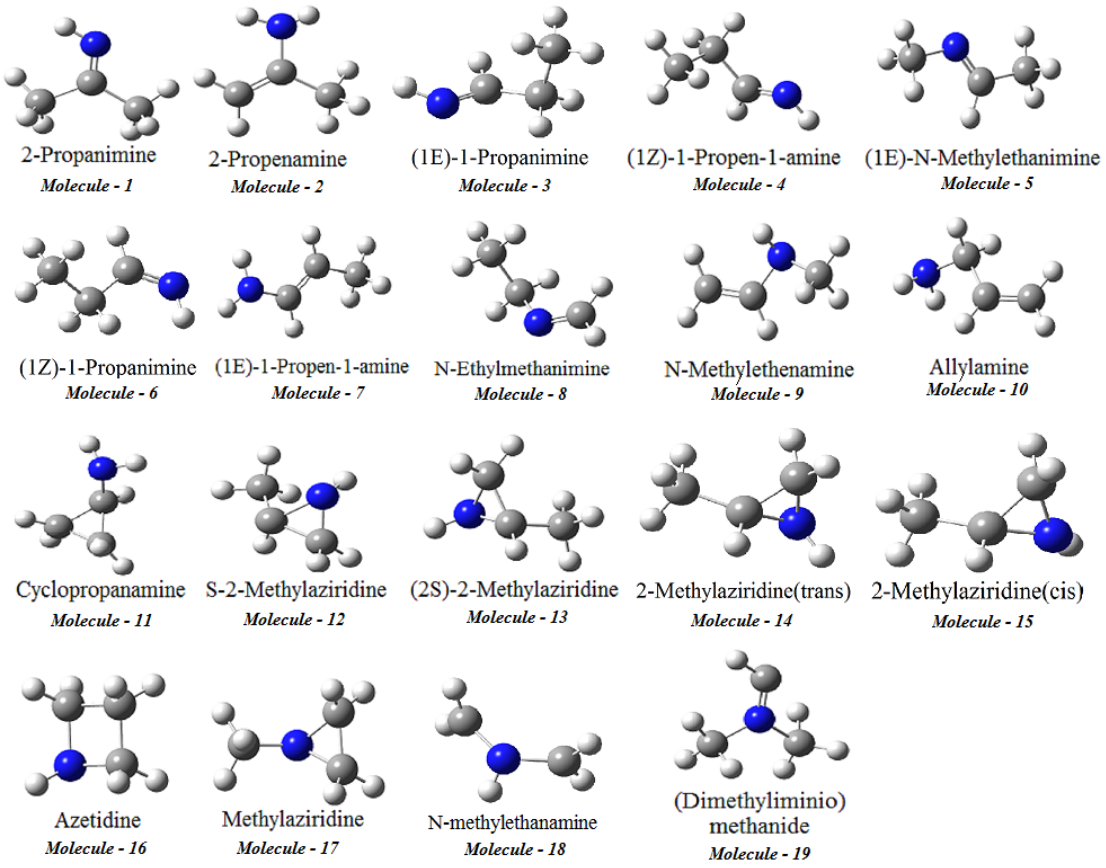

Figure 4.11: C_3H_7N isomers (Sil et al., 2018).

Altwegg et al. (2016) showed that in $67P/C-G$, relative abundance between methylamine and glycine is 1.0 ± 0.5, and the ethylamine-to-glycine ratio is 0.3 ± 0.2. Taking the maximum and minimum values from this observation, we can see that the methylamine-to-ethylamine ratio may vary in the range of $\sim 1-15$. We focus on the ice-phase evolution (at $T = 10$) to check the correlation (if any) between the cometary and interstellar ice. From our modeling results (see Figure 4.2b), we find that in the isothermal stage (at time 10^6 years), the methylamine-to-ethylamine ratio is ~ 17.7 in the ice phase is close to the observed value (Altwegg et al., 2016). It suggests that a more in-depth study is required to confirm this linkage between the interstellar and cometary origins of these molecules.

C_3H_7N Isomeric Group

Nineteen isomers (see Figure 4.11) belong to this isomeric group. In Table 4.2, we show the relative energies and enthalpy of formation of various isomers. Figure 4.12 depicts the enthalpy of formation ($\Delta_f H^O$) of this isomeric group. Only for cyclopropanamine, experimentally obtained enthalpy of formation is available, and this is in close agreement with our calculated enthalpies of formation with the DFT-B3LYP/6-31G(d,p) level of theory. 2-propanimine is the most stable isomer of this group, followed by 2-propenamine. The following species in this sequence is (1E)-1-propanimine. (1E)-1-propanimine has lower energy than that of the (1Z)-1-propanimine.

Though (dimethyliminio)methanide (molecule no. 19) is the least stable species in this isomeric group (containing the highest enthalpy of formation), our calculation listed in Table 4.4 shows that it possesses the highest effective electric dipole moment. (1Z)-1-propanimine (molecule no. 6) is found to have the second-highest effective dipole moment in this group. However, it is found that the a-type transitions of (1Z)-1-propanimine are the strongest among all the species of this group. Figure 4.13 shows the expected intensity ratio (by considering the three components of the dipole moment along with the effective dipole moment) concerning the most stable (and the species is having the least enthalpy of formation) isomer. Figure 4.13 shows that if the abundances of all these isomeric species are same, (dimethyliminio)methanide and (1Z)-1-propanimine would be the most probable candidates for the astronomical detection from this group. Since (dimethyliminio)methanide is not a very stable species, it does not have a high probability of detection. Thus, based on the stability, enthalpy of formation, and expected intensity ratio, (1Z)-1-propanimine is the most suitable species for future astronomical detection from this isomeric group. However, it is the reaction pathways that can ultimately decide the fate of this species.

Methanimine and ethanimine have already been observed in the ISM, and (1Z)-1-propanimine maybe the next probable candidate for astronomical detection. To the best of our knowledge, the astronomical searches of (1Z)-1-propanimine are yet to be reported in the literature. Hence, (1Z)-1-propanimine remains the best candidate for astronomical observation among all the isomers of the C_3H_7N isomeric group.

(1Z)-1-propanimine may be formed via two sequential H addition reactions on ice with propionitrile (CH_3CH_2CN), where propionitrile may be produced by the radical – radical barrierless interaction between C_2H_5 and CN. Instead of radical reactant CN, H_2CN may react with C_2H_5 to form propanimine directly by reaction R19. This reaction is assumed to be barrierless. We find that the first step (R21) of

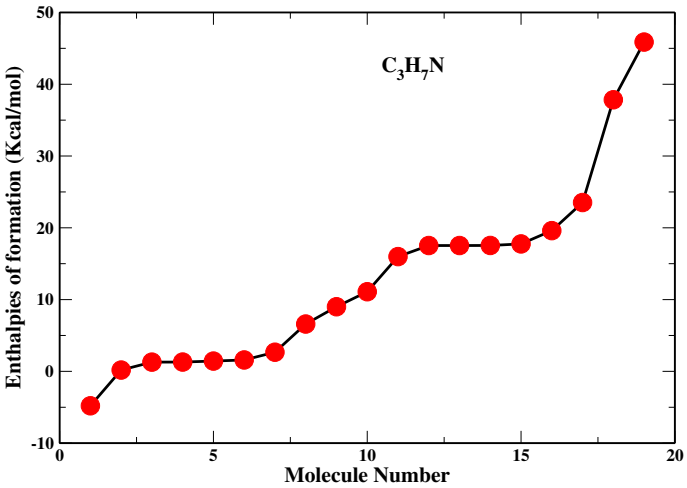

Figure 4.12: Enthalpy of formation of the C_3H_7N isomeric group (Sil et al., 2018).

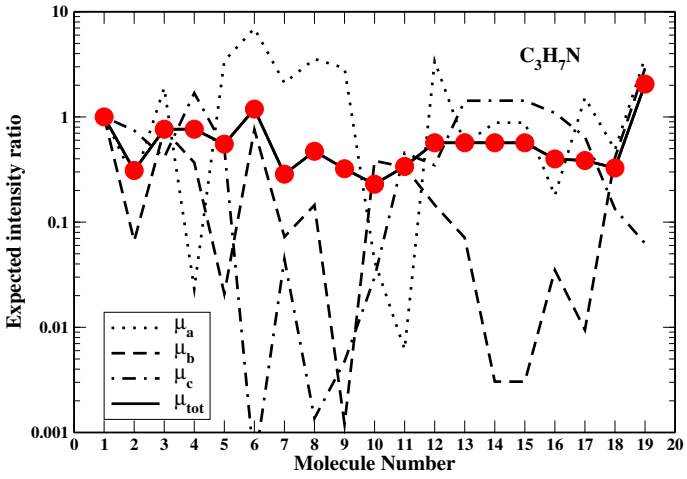

Figure 4.13: Expected intensity ratio of the C_3H_7N isomeric group by considering three components of the dipole moment and the effective dipole moment of all the species (Sil et al., 2018).

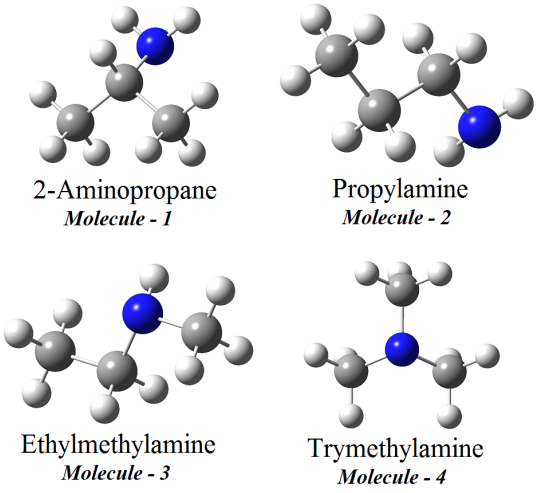

Figure 4.14: C_3H_9N isomers (Sil et al., 2018).

H addition with propionitrile has a barrier of 2712 K and the second step (R22) is a radical − radical barrierless interaction. For the gas-phase hydrogenation reaction (G21), our calculated $\Delta G‡$ parameter is 11.03 kcal/mol. In Figures 4.2 and 4.3, we show the time evolution of (1Z)-1-propanimine. These suggest that the production of (1Z)-1-propanimine is only favorable in the hot-core region. Here we obtain a peak gas-phase abundance of (1Z)-1-propanimine $\sim 2.20 \times 10^{-08}$ from our model.

C_3H_9N Isomeric Group

Four species (2-aminopropane, propylamine, ethylmethylamine, and trimethylamine) are considered (Figure 4.14) from this isomeric group. Methylamine is the most stable isomer of the CH_5N group, and ethylamine is the most stable isomer of the C_2H_7N group. In general, it is expected that the branched-chain molecules would be comparatively more stable than the other species of an isomeric group. Etim et al. (2017) showed that isopropyl cyanide, a branched-chain molecule, is the most stable within the C_4H_7N isomeric group. Tert-butyl cyanide, another branched-chain molecule, is the most stable species within the C_5H_9N isomeric group. Following a similar trend, we find that 2-aminopropane, a branched-chain molecule of the C_3H_9N isomeric group, is the most stable isomer. 2-aminopropane is found to be 2.51 kcal/mol more stable than propylamine. In Figure 4.15, we show the enthalpy of formation of these four species. Relative energy and enthalpy of formation of these four isomers are shown in Table 4.2 and arranged based on their enthalpy of

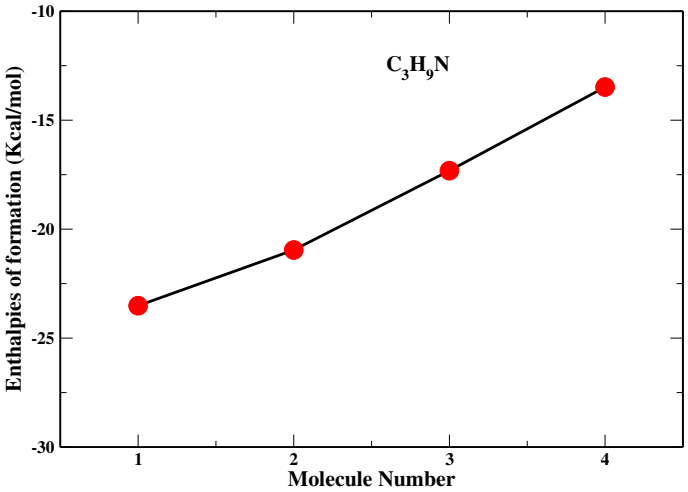

Figure 4.15: Enthalpy of formation of the C_3H_9N isomeric group (Sil et al., 2018).

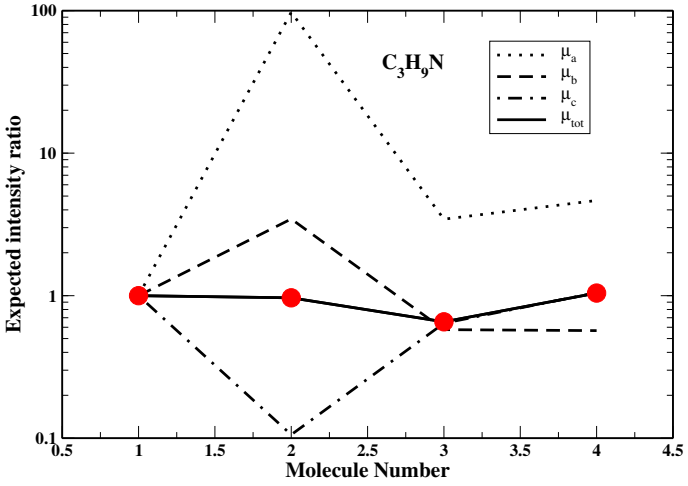

Figure 4.16: Expected intensity ratio of the C_3H_9N isomeric group by considering three components of the dipole moment and effective dipole moment of all the species (Sil et al., 2018).

formation. Theoretically calculated and experimentally obtained enthalpy of formation values have a similar trend. From Table 4.2, it is evident that the computed enthalpies of formation with the DFT-B3LYP/6-31G(d,p) level of theory appear to be comparatively closer to the experimental values than those of the G4 composite method. The expected intensity ratio concerning the species having the minimum enthalpy of formation is shown in Figure 4.16. Interestingly, though trimethylamine has the lowest total dipole moment value among this group, the rotational intensity is maximum because of its lower partition function. More interestingly, due to its unique structure, rotational constants A and B have the same value (8.75934 GHz). We also reconfirm this unique nature of trimethylamine (an oblate symmetric top species) using the G4 composite method and the HF/6-31G(3df) level of theory. Since the production of propanimine is not significantly higher, we do not prepare any reaction pathways to study the formation of species from this isomeric group.

From the above discussed results, we find that the imines (methanimine, ethanimine, and propanimine) and amines (methylamine and ethylamine) are efficiently produced in the ice phase. Depending on the barrier energy considered, Figure 4.3 depicts a nice trend of sublimation. For example, we adopt a BE of ethylamine and methylamine of 6480 K and 6584 K, respectively. Thus, ethylamine starts to sublime faster than methylamine. Similarly, methanimine, ethanimine, and propanimine having BEs 5534, 5580, and 6337 K, respectively, sublime sequentially.

4.1.3 Astrophysical implications

Methanimine is a crucial prebiotic molecule that is believed to be the precursor molecule for the formation of glycine. This species is already identified in the ISM. Also, in the upper atmosphere of Titan (the massive moon of Saturn; Vuitton et al., 2006), this is detected. The present atmosphere of Titan resembles the primeval atmosphere of the Earth and thus is thought to be important for abiotic synthesis. Our present study finds that methanimine may be further processed to form methylamine, which is yet to be observed in Titan's atmosphere. Modeling Titan's atmosphere is beyond the scope of this work. However, the inclusion of proposed pathways in the modeling of Titan atmosphere may come up with the higher mixing ratios of higher-order imines and amines in Titan's atmosphere.

We perform radiative transfer modeling (with both LTE and non-LTE consideration), which may be helpful for the future astronomical observation of ethylamine and propanimine in the ISM. For the calculation of the line parameters using an

Table 4.6: Line parameters of trans-ethylamine in the millimeter and submillimeter regime using ALMA (LTE) (Sil et al., 2018).

Frequency range (GHz)	Frequency (GHz)[a]	Transition (J′ k'_a k'_c v′ - J″ k''_a k''_c v″)	Intensity (K)
31 – 45 (ALMA Band 1)	31.4005744	5 1 4 0 – 5 0 5 0	0.0058
	33.0673762	2 0 2 1 – 1 0 1 1	0.0063
	34.9850027	6 1 5 0 – 6 0 6 0	0.008
	39.4293083	7 1 6 0 – 7 0 7 0	0.011
	44.8063428	8 1 7 0 – 8 0 8 0	0.015
67 – 90 (ALMA Band 2) and 84 – 116 (ALMA Band 3)	80.241995	5 1 5 1 – 4 1 4 1	0.098
	82.168784	5 0 5 1 – 4 0 4 1	0.106
	82.674301	5 2 4 1 – 4 2 3 1	0.088
	83.24287	5 2 3 1 – 4 2 2 1	0.089
	84.980785	5 1 4 1 – 4 1 3 1	0.107
	101.886754	6 1 5 1 – 5 1 4 1	0.169
	112.158369	7 1 7 1 – 6 1 6 1	0.222
	114.294235	7 0 7 1 – 6 0 6 1	0.234
	115.604884	7 2 6 1 – 6 2 5 1	0.211
	115.9771874	7 4 3 1 – 6 4 2 1	0.256
125 – 163 (ALMA Band 4)	145.871741	9 0 9 1 – 8 0 8 1	0.38
	149.11269	9 5 5 1 – 8 5 4 1 (9 5 4 1 – 8 5 3 1)	0.436
	152.224777	9 1 8 1 – 8 1 7 1	0.391
	159.753196	10 1 10 1 – 9 1 9 1	0.445
	161.496431	10 0 10 1 – 9 0 9 1	0.45
163 – 211 (ALMA Band 5)	182.3234429	11 5 7 0 – 10 5 6 0	0.684
	198.94447	12 5 8 1 – 11 5 7 1	0.767
	198.945801	12 5 7 1 – 11 5 6 1	0.768
	207.02715	13 1 13 1 – 12 1 12 1	0.64
	208.053547	13 0 13 1 – 12 0 12 1	0.65

Note:
[a] For the transitions with same J′ k'_a k'_c – J″ k''_a k''_c but having different vibrational state please see the cat file available at https://www.astro.uni-koeln.de/cdms/catalog.

Table 4.7: Line parameters of (1Z)-1-propanimine in the millimeter and submillimeter regime using ALMA (LTE) (Sil et al., 2018).

Frequency range (GHz)	Frequency (GHz)[a]	Transition (J' k'_a $k'_c v'$ - J'' k''_a k''_c v'')	Intensity (K)
31 – 45 (ALMA Band 1)	33.5198821	4 1 4 3 – 3 1 3 2	0.117
	33.7888724	4 0 4 5 – 3 0 3 4	0.136
	33.7897526	4 2 3 4 – 3 2 2 3	0.105
	34.0663468	4 1 3 4 – 3 1 2 3	0.123
	41.897946	5 1 5 6 – 4 1 4 5	0.261
	42.2302861	5 0 5 6 – 4 0 4 5	0.290
	42.2318919	5 3 3 5 – 4 3 1 5	0.326
	42.2361126	5 2 4 6 – 4 2 3 5	0.227
	42.5812455	5 1 4 6 – 4 1 3 5	0.270
67 – 90 (ALMA Band 2) and 84 – 116 (ALMA Band 3)	67.0236193	8 1 8 8 – 7 1 7 7	1.110
	67.5282969	8 0 8 8 – 7 0 7 7	2.252
	67.5717125	8 3 6 7 – 7 3 5 8	1.725
	68.117366	8 1 7 8 – 7 1 6 7	1.145
	75.3952267	9 1 9 9 – 8 1 8 8	1.510
	75.9707109	9 5 4 8 – 8 5 3 7	1.720
	75.9497207	9 0 9 10 – 8 2 6 9	1.440
	76.0013965	9 4 6 10 – 8 4 49	2.252
	76.0187663	9 3 6 9 – 8 3 5 9	2.244
	76.6257696	9 1 8 9 – 8 1 7 8	1.555
	83.7646502	10 11 0 10 – 9 1 9 9	1.955
	84.364287	10 0 10 9 – 9 1 8 9	2.000
	84.4134387	10 5 6 11 – 9 5 4 10	2.40
	84.4483753	10 4 6 9 – 9 4 5 10	4.650
	84.4661717	10 3 7 10 – 9 3 6 10	2.450
	84.5650434	10 2 8 10 – 9 2 7 9	1.870
	85.1318785	10 0 10 9 – 9 1 8 9	2.080
	92.1316784	11 1 11 11 – 10 1 10 10	2.420
	92.7713594	11 0 11 12 – 10 0 10 11	2.480
	92.8567065	11 5 6 10 – 10 5 6 9	3.150
	92.8959487	11 4 8 10 – 10 4 6 9	3.720
	93.0411029	11 2 9 11 – 10 2 8 10	3.720
	93.6354011	11 1 10 12 – 10 1 9 11	2.480
	100.4962033	12 1 12 11 – 11 1 11 12	2.900
	101.1702803	12 0 12 12 – 11 0 11 11	2.977
	101.3005235	12 5 8 13 – 11 5 6 12	3.925
	101.3444369	12 4 8 12 – 12 4 7 11	4.550
	101.5225577	12 2 10 11 – 12 2 9 12	2.800
	102.1359978	12 1 11 12 – 11 1 10 11	2.960
	109.7449013	13 5 9 13 – 12 5 7 12	4.703
	109.7938556	13 4 9 13 – 12 4 8 12	5.395
	110.0094549	13 2 11 13 – 12 2 10 12	3.300
	110.6333677	13 1 12 14 – 12 1 11 13	3.455
125 – 163 (ALMA Band 4)	126.6358855	15 5 10 15 – 14 5 10 14	6.200
	126.6960852	15 4 11 14 – 14 4 11 13	10.080
	133.9242154	16 1 16 15 – 15 0 15 16	4.730
	134.6750035	16 0 16 17 – 15 0 15 16	4.800
	135.148249	16 4 13 15 – 15 4 12 16	7.750
	143.6023263	17 4 13 17 – 16 4 12 16	8.350
	151.9783682	18 5 14 18 – 17 5 12 17	8.100
	152.0568371	18 4 15 17 – 17 4 14 18	8.750
	160.4277999	19 5 14 18 – 18 5 13 19	8.575
	160.5135369	19 4 15 19 – 18 4 14 19	9.200
163 – 211 (ALMA Band 5)	168.9718077	20 4 16 20 – 19 4 15 20	9.250
	168.878091	20 5 16 20 – 19 5 15 19	9.00
	177.3296583	21 5 16 20 – 20 5 16 19	9.350
	185.7821453	22 5 18 23 – 21 5 17 22	9.550
	185.8934615	22 4 18 22 – 21 4 17 22	8.350
	194.23659	23 5 19 22 – 22 5 17 22	10.520
	202.6910348	24 5 20 23 – 23 5 19 24	9.770

Note:
[a] For the transitions with the same J' k'_a k'_c – J'' k''_a k''_c but having different vibrational state, please see the catalog in the propanimine.tar.gz package provided in Sil et al. (2018).

Table 4.8: Non-LTE modeling line parameters of trans-ethylamine (Sil et al., 2018).

Frequency range (GHz)	Frequency (GHz)[a]	Transition (J′ k'_a k'_cv′ - J″ k''_a k''_c v″)	Intensity (K)
31 – 45 (ALMA Band 1)	31.4005744	5 1 4 0 – 5 0 5 0	0.0108
	33.06739330	2 0 2 0 – 1 0 1 0	0.0096
	34.98500270	6 1 5 0 – 6 0 6 0	0.0129
	39.42887460	7 1 6 1 – 7 0 7 1	0.0152
	44.80634280	8 1 7 0 – 8 0 8 0	0.0173
67 – 90 (ALMA Band 2) and 84 – 116 (ALMA Band 3)	80.24199500	5 1 5 0 – 4 1 4 0	0.0534
	82.16878400	5 0 5 0 – 4 0 4 0	0.0569
	82.67430100	5 2 4 0 – 4 2 3 0	0.0483
	83.2428700	5 2 3 1 – 4 2 2 1	0.0486
	84.98078500	5 1 4 1 – 4 1 3 1	0.0566
	98.30233700	6 0 6 0 – 5 0 5 0	0.0796
	101.886754	6 1 5 0 – 5 1 4 0	0.0806
	112.1583690	7 1 7 0 – 6 1 6 0	0.1016
	114.294235	7 0 7 0 – 6 0 6 0	0.1052
	115.604884	7 2 6 0 – 6 2 5 0	0.0996
125 – 163 (ALMA Band 4)	143.9269253	9 1 9 0 – 8 1 8 0	0.1586
	145.871741	9 0 9 0 – 8 0 8 0	0.1620
	148.397949	9 2 8 1 – 8 2 7 1	0.1598
	159.753196	10 1 10 0 – 9 1 9 0	0.1878
	161.49643100	10 0 10 0 – 9 0 9 0	0.1914
163 – 211 (ALMA Band 5)	192.561480	12 0 12 0 – 11 0 11 0	0.2432
	197.25631220	12 2 11 1 – 11 2 10 1	0.2436
	201.671390	12 1 11 0 – 11 1 10 0	0.2587
	203.166657	12 2 10 1 – 11 2 9 1	0.2534
	208.05354700	13 0 13 0 – 12 0 12 0	0.2565

Note:
[a] For the transitions with same J′ k'_a k'_c – J″ k''_a k''_c but having different vibrational state please see the cat file available at https://www.astro.uni-koeln.de/cdms/catalog.

Table 4.9: Non-LTE modeling line parameters of (1Z)-1-propanimine (Sil et al., 2018).

Frequency range (GHz)	Frequency (GHz)[a]	Transition (J′ k'_a k'_cv′ - J″ k''_a k''_c v″)	Intensity (K)
31 – 45 (ALMA Band 1)	33.51992460	4 1 4 5 – 3 1 3 4	0.1192
	33.78887240	4 0 4 5 – 3 0 3 4	0.1269
	41.89797460	5 1 5 6 – 4 1 4 5	0.1925
	42.25035000	5 2 3 6 – 4 2 2 5	0.1752
	42.58124550	5 1 4 6 – 4 1 3 5	0.1978
67 – 90 (ALMA Band 2) and 84 – 116 (ALMA Band 3)	76.62578210	9 1 8 10 – 8 1 7 9	0.6728
	83.76466100	10 1 10 11 – 9 1 9 10	0.7793
	84.36429660	10 0 10 11 – 9 0 9 10	0.7906
	84.56506570	10 2 8 11 – 9 2 7 10	0.7710
	85.13188840	10 1 9 1 – 9 1 8 10	0.8215
	93.63540110	11 1 10 12 – 10 1 9 11	0.9333
	100.49611750	12 1 12 13 – 11 1 11 12	0.9232
	101.17028780	12 0 12 13 – 11 0 11 12	0.9826
	102.13600470	12 1 11 13 – 11 1 10 12	0.9689
	109.56052950	13 0 13 14 – 12 0 12 13	0.9616
125 – 163 (ALMA Band 4)	125.51588020	8 2 7 9 – 7 1 6 8	0.0591
	126.31319130	15 0 15 16 – 14 0 14 15	0.6378
	127.00092650	15 2 13 16 – 14 2 12 15	0.3568
	127.61694790	15 1 14 15 – 14 1 13 14	0.3922
	134.67500350	16 0 16 17 – 15 0 15 16	0.3738
163 – 211 (ALMA Band 5)	175.64941420	9 3 7 10 – 8 2 6 9	0.09671
	175.80109580	9 3 6 10 – 8 2 7 9	0.09373
	184.02040330	10 3 8 11 – 9 2 7 10	0.09697
	184.25941520	10 3 7 10 – 9 2 8 9	0.09647
	207.19739490	8 4 5 9 – 7 3 4 8	0.09612

Note:
[a] For the transitions with same J′ k'_a k'_c – J″ k''_a k''_c but having different vibrational state, please see the catalog in the propanimine.tar.gz package provided in Sil et al. (2018).

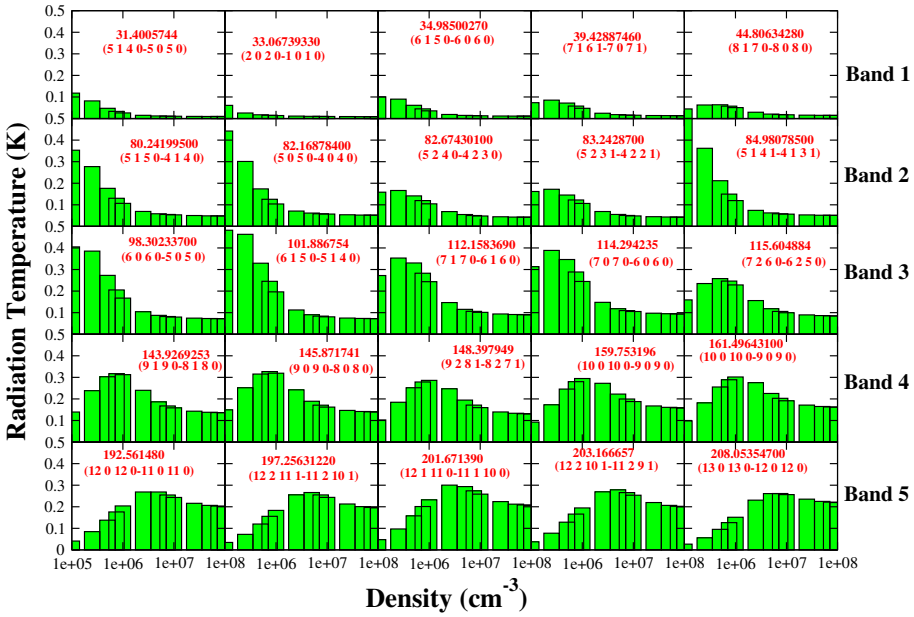

Figure 4.17: Density variation of the intensity of various transitions of ethylamine by considering a non-LTE approximation (Sil et al., 2018).

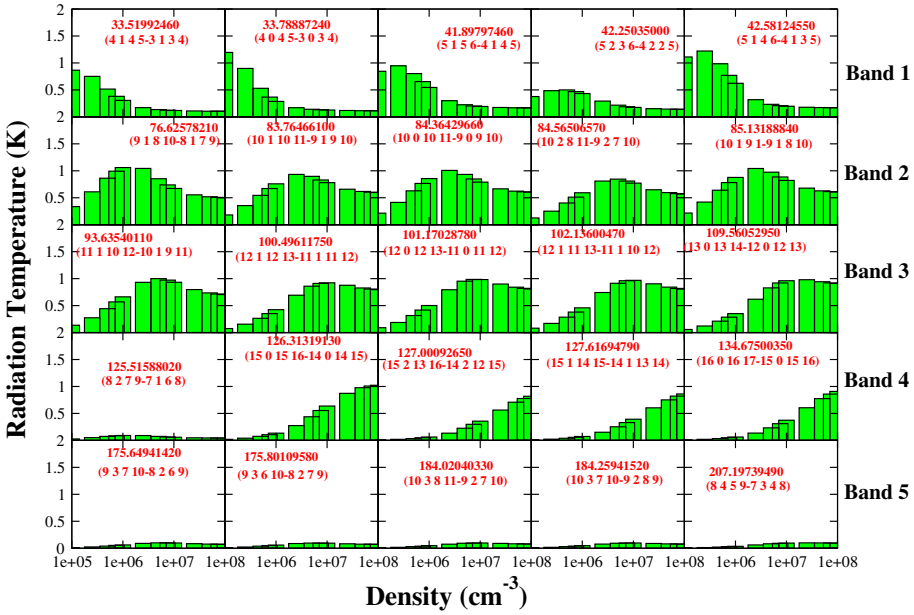

Figure 4.18: Density variation of the intensity of various transitions of propanimine by considering a non-LTE approximation (Sil et al., 2018).

LTE approximation, we use the CASSIS interactive spectrum analyzer[1]. In Table 4.6, we point out some of the most intense ethylamine transitions that falls in ALMA bands $1-5$. Required spectroscopic details for ethylamine are available in CDMS database[2]. Similarly, in Table 4.7, intense transitions of propanimine are shown. Required spectroscopic details for (1Z)-1-propanimine are obtained by including the experimentally obtained rotational and distortional constants in the SPCAT program (Pickett, 1991). For preparing these tables, we use a column density of $H_2 = 10^{23}$ cm^{-2}, $n_H = 10^7$ cm^{-3}, excitation temperature = 130 K, FWHM = 10 km s^{-1}, V_{LSR} = 64 km s^{-1}, source size = $3''$, abundance of ethylamine = 4.0×10^{-08}, and abundance of propanimine = 2×10^{-8}.

We also perform a non-LTE calculation using the RADEX program (van der Tak et al., 2007). The collisional data files for ethylamine and propanimine are unavailable. Thus, we prepare the collisional data file in the appropriate format from the spectral information available in JPL (for trans-ethylamine) and our calculation [for (1Z)-1-propanimine] propanimine.tar.gz. Altogether we consider transitions between 251 energy levels. Here, we assume H_2 as the colliding partner. We approximate the collisional rate of ethylamine and propanimine following the relation mentioned in Sharma & Chandra (2001) to estimate the line profile with non-LTE. Sharma & Chandra (2001) estimated the collisional rate coefficient for a downward transition of an asymmetric top molecule, cyclopropene, at temperature "T", by

$$C(J''K_a''K_c'' \rightarrow J'K_a'K_c') = [1 \times 10^{-11}/(2J''+1)]\sqrt{T/30}. \tag{4.7}$$

In Tables 4.8 and 4.9, we point out the most intense transitions of trans-ethylamine and (1Z)-1-propanimine, respectively, which fall within ALMA bands $1-5$. For the non-LTE calculations, we use a column density of ethylamine of 10^{15} cm^{-2} and a column density of propanimine of 5.0×10^{14} cm^{-2}, $n_H = 10^7$ cm^{-3}, excitation temperature = 130 K, $FWHM = 10$ km s^{-1}.

For the transitions pointed out in Tables 4.8 and 4.9, the density variation of ethylamine (Figure 4.17) and propanimine (Figure 4.18) is studied with the non-LTE consideration. Figures 4.17 and 4.18 would serve as a good starting point for observing ethylamine and propanimine in the ISM. It is to be noted that we use our estimated collisional rate in the absence of the measured or calculated collisional data file. Still, it is known that the non-LTE transitions are heavily dependent on collisional rates, and consideration of random rates may end up with some misleading results.

[1] http://cassis.irap.omp.eu

[2] https://www.astro.uni-koeln.de/cdms/catalog

4.1.4 Summary

In this work, the possibility of detecting various molecules which belong to six specific isomeric groups is examined. For this purpose, the chemical abundance, enthalpy of formation, optimized energy, and expected intensity ratio are used to shortlist some species that might be viable candidates for future astronomical detection in the ISM. Our modeling results suggest that ethylamine and propanimine are being produced efficiently in the hot-core condition. So we propose to observe these molecules in a hot molecular core. Furthermore, LTE and non-LTE models are employed to determine the most probable transitions of ethylamine and propanimine in the millimeter and submillimeter domains. Some spectroscopic data are provided to aid their identification. We also find a clue about the linkage between the interstellar and cometary chemical compositions.

4.2 Prebiotic molecules containing peptide-like bonds

Protein synthesis occurs through the peptide-bond ($-NH-C(=O)-$) formation (Goldman et al., 2010). Nitrogen is one of the most chemically active species in the ISM after hydrogen, oxygen, and carbon. N-bearing molecules are vital as they are actively involved in the formation of biomolecules. Therefore, it is essential to look for N-bearing species in various astrophysical sources. Looking around the high-mass star-forming regions is particularly important because the evolutionary history is comparatively poorly understood. CN is the first observed N-bearing species in space (McKellar, 1940). Since then, various N-bearing species are identified in numerous astronomical objects. Hot-core regions are unique laboratories of COMs. Forests of molecular lines are identified in several hot molecular cores (HMCs; e.g., Belloche et al., 2016; Garrod et al., 2017). Here, we focus on the observation of an HMC, G10 (Gorai et al., 2020b), which is located at a distance of 8.6 kpc (Sanna et al., 2014) with a luminosity 5×10^5 $L_\odot$ (Cesaroni et al., 2010).

Isocyanic acid (HNCO) is a simple molecule containing four biogenic elements (C, N, O, and H), making a peptide bond. HNCO was observed long ago toward the high-mass star-forming region Sgr B2 (Snyder & Buhl, 1972). In addition, it has been observed in various astronomical objects such as a translucent molecular cloud (Turner et al., 1999), a dense core (Marcelino et al., 2018), and the low-mass protostar IRAS $16293-2422$ (Bisschop et al., 2008). It was also previously detected in G10 (Wyrowski et al., 1999).

Formamide (NH_2CHO) is the simplest possible amide. It is a potential prebiotic molecule containing a peptide bond that can link with amino acids and form proteins. NH_2CHO is also a precursor of genetic and metabolic molecules (Saladino et al., 2012). This molecule is one of the key species for the formation of nucleobases and nucleobase analogs. NH_2CHO was observed for the first time toward the high-mass star-forming region, Sgr B2 (Rubin et al., 1971). Subsequently, it was identified in other hot-cores, such as Orion KL, $G327.3-0.6$, $G34-3+0.15$, NGC 6334 (Turner, 1991; Bøgelund et al., 2019), the solar-type low-mass protostar IRAS $16293-2422$ (Kahane et al., 2013), and in the shock of the prestellar core L1157-B1 (Codella et al., 2017). NH_2CHO was previously detected in G10 using millimeter and submillimeter wavelengths with Submillimeter Array (SMA) observation (Rolffs et al., 2011).

Methyl isocyanate (CH_3NCO) is another potential prebiotic molecule, which also has a peptide-like bond. It has been observed in the high-mass star-forming region Sgr B2 (Cernicharo et al., 2016) and the low-mass star-forming region IRAS

16293 − 2422 (Ligterink et al., 2017; Martín-Doménech et al., 2017). Gorai et al. (2020b) have reported the identification of CH_3NCO in G10 for the first time. HNCO has firmly been identified in G10, but NH_2CHO was tentatively detected (Rolffs et al., 2011). HNCO and NH_2CHO have recently been identified, but CH_3NCO has been tentatively identified in the 67P/C − G comet by the double-focusing mass spectrometer (DFMS) of the ROSINA experiment on ESA's Rosetta mission (Altwegg et al., 2017).

Here, detailed chemical modeling of three peptide-like bond containing molecules (HNCO, NH_2CHO, and CH_3NCO) is presented to aid their identification in G10 (Gorai et al., 2020b).

4.2.1 Chemical Modeling

To study the chemical evolution of three peptide-bond-related species, we use our gas-grain chemical network (Das et al., 2015a,b; Sil et al., 2018; Gorai et al., 2020b). Gas-phase pathways are mainly adopted from the UMIST database (McElroy et al., 2013), whereas ice-phase paths and BEs of the surface species are taken from the KIDA (Ruaud et al., 2016) unless otherwise stated. We consider that the diffusion energy of a species is 0.5 times its desorption energy and non-thermal desorption rate with a fiducial parameter of 0.01. A cosmic-ray rate of 1.3×10^{-17} s^{-1} is considered. For the formation and destruction reactions of these species, we mainly follow Quénard et al. (2018). In addition, following the recent study of Haupa et al. (2019), we exclusively include dual-cyclic H addition and abstraction reactions. These connect NH_2CHO, NH_2CO, and HNCO. We show the chemical linkages among HNCO, NH_2CHO, and CH_3NCO. Initial abundances of the model are provided in Table 4.10.

Physical condition of the adopted model

We consider a three-stage model to study the chemical evolution of these species (Garrod, 2013). This model is best suited because G10 is a high-mass star-forming region. The detailed considerations of each stage are discussed below.

First stage: In the first stage, we consider that the cloud collapses from a low total hydrogen density ($\rho_{min} = 10^3$ cm^{-3}) to a high value (ρ_{max}). The initial gas temperature (T_{gas}) is assumed to be 40 K, whereas the dust temperature is supposed to remain fixed at an initial ice temperature (T_{ice}). We consider a time interval of t_{coll} years to reach from ρ_{min} to ρ_{max}. Since the gas and dust are well coupled at

Table 4.10: Initial abundances with respect to total hydrogen nuclei (Gorai et al., 2020b).

Species	Abundance
H_2	5.00×10^{-1}
He	9.00×10^{-2}
C	7.30×10^{-5}
O	1.76×10^{-4}
N	2.14×10^{-5}
Cl	1.00×10^{-9}
Fe	3.00×10^{-9}
Mg	7.00×10^{-9}
Na	2.00×10^{-9}
S	8.00×10^{-8}
Si^+	8.00×10^{-9}
e^-	7.31×10^{-5}

the highest density, we consider $T_{gas} = T_{ice}$ at the highest density (ρ_{max}), i.e., at $t = t_{coll}$. From this stage onward, we assume that the temperature of the dust and the gas are the same. Thus, we consider a negative slope for T_{gas} for the collapsing stage. Throughout the first stage, the visual extinction parameter is considered to be constantly increasing from $A_V = A_{V\,min} = 10$ to finally at $A_{V\,max} = 200$ in $t = t_{coll}$.

Second stage: The second stage of the simulation corresponds to a warm-up stage. Since G10 is a high-mass star-forming region, we consider a moderate warm-up time-scale (t_w) 5×10^4 years (Garrod, 2013). Therefore, during this short period, the cloud temperature from T_{ice} can reach the highest hot-core temperature T_{max}. The density, temperature, and visual extinction parameter remain constant at ρ_{max}, T_{max}, and $A_{V\,max}$, respectively.

Third stage: This stage belongs to the post-warm-up time. Here, we consider a post-warm-up time scale (t_{pw}) of 10^5 years, so the total simulation time is $t_{tot} = t_{coll} + t_w + t_{pw}$. The parameters such as density and visual extinction are assumed to be the same as in the warm-up stage. The temperature of the cloud is kept at T_{max} throughout the last stage.

Binding energies of peptide-bond containing species

To study the BE and reaction pathways of three peptide-bond-like species HNCO, NH_2CHO, CH_3NCO, and their isomers/precursors, we use the GAUSSIAN 09 suite of programs (Frisch et al., 2013). To estimate the BEs of these species, we use the MP2/aug-cc-pVDZ level of theory. Our calculated BE values are given in Table

Table 4.11: Computed BEs (Gorai et al., 2020b).

Species	Optimized Structure	Calculated BE (K) using H_2O monomer	Average BE (K)	Scaled BE (K) (×1.416)	Calculated BE (K) using H_2O hexamer	Available BE (K) in literatures
CHNO						
HNCO	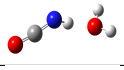	3308	3308	4684	6310, 5554	4400 ± 1320^a
HCNO	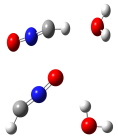	2640 2050	2345	3320	6046	2800^b
HOCN	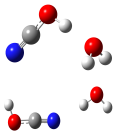	5936 2563	4250	6018	2153, 8404	2800^b
HONC	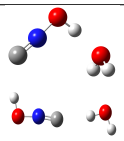	5874 2370	4122	5837	3387, 8727	2800^b
C_2NH_3O						
CH_3NCO	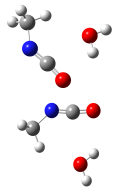	3627 2555	3091	4377	4309	4700 ± 1410^a
CH_3CNO	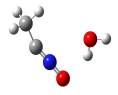	2786	2786	3945	—	—
CH_3OCN	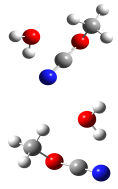	3534 3536	3535	5006	6530	—
CH_3ONC	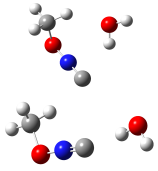	2939 2565	2752	3897	4652	—
CNH_3O						
NH_2CHO		3627 2880 5079	3862	5468	6602	6300 ± 1890^a

Note:
We use our calculated scaled BE values of monomers for astrochemical modeling.
[a] Wakelam et al. (2017).
[b] Quan et al. (2010).

4.11. For some cases, we find multiple probable sites for the adsorption and thus obtained multiple BE values. In that case, we take the average of the numerous BEs. Calculated BEs with a single water molecule are then scaled up by a factor of 1.416 (Das et al., 2018) to have a realistic estimation. Additionally, in Table 4.11, we present the BE values for some of these species with a hexamer configuration of water clusters. Since the BEs with the pentamer/hexamer configurations show minimum deviation (Das et al., 2018), one can use these BE values in the model without scaling. However, we cannot provide the BE values of all the species with a hexamer configuration and all the probable adsorption sites. Thus, we use BE values obtained with a single water molecule with appropriate scaling for the modeling.

Reaction dynamics of peptide-bond-like species

To form ice-phase HNCO, Quénard et al. (2018) considered the reaction between NH and CO. They considered an activation barrier of 4200 K for this reaction (Himmel et al., 2002). However, for the formation of its other isomers, no such reactions are available. Due to this reason, for the sake of completeness, here we run a quantum chemical calculation to check the reaction enthalpy of the following reactions:

$$\mathrm{NH + CO \rightarrow HNCO}, \tag{4.8}$$

$$\mathrm{CH + NO \rightarrow HCNO}, \tag{4.9}$$

$$\mathrm{CN + OH \rightarrow HOCN}, \tag{4.10}$$

$$\mathrm{CN + OH \rightarrow HONC}. \tag{4.11}$$

We find that the above four reactions are exothermic. Exothermicity values are given in Table 4.12. The activation barrier for the reaction between NH and CO was known to be 4200 K (Himmel et al., 2002), but for the others, it was unknown. The above reactions are mostly between radicals, and finding an actual TS is a difficult task. Instead, we calculate the reaction enthalpy of these four reactions. Based on the reaction enthalpies, we prepare the most probable reaction sequence in between these four reactions. Since the activation barrier of the first reaction was known to be 4200 K, we scale the activation barriers of the rest of the reactions. Though the reaction enthalpy (exothermicity values) is not directly related to the activation barrier of the reaction, it is eventually a better-educated approximation compared to using any other crude approximation. Scaled activation barriers are provided in Table 4.12.

Table 4.12: Calculated reaction enthalpies, type of reactions, and activation barriers (with ZPVE correction) of various reactions (Gorai et al., 2020b).

Reactions	**Reaction enthalpy (kcal/mol)**	**Types of reactions**	**Activation barrier (K)**
Ice-phase reactions			
$NH + CO \rightarrow HNCO$	−139.19	Exothermic	4200[a]
$CH + NO \rightarrow HCNO$	−124.62	Exothermic	4691
$CN + OH \rightarrow HOCN$	−120.35	Exothermic	4857
$CN + OH \rightarrow HONC$	−59.32	Exothermic	9855
$HNCO + H \rightarrow H_2NCO$	−31.35	Exothermic	1962
$H_2NCO + H \rightarrow NH_2CHO$	−92.76	Exothermic	0
$H_2NCO + H \rightarrow HNCO + H_2$	−73.15	Exothermic	0
$HCNO + H \rightarrow H_2CNO$	−57.29	Exothermic	1073
$H_2CNO + H \rightarrow HCNO + H_2$	−47.20	Exothermic	0
Gas-phase reactions			
$HNCO + O \rightarrow CO + HNO$	−23.70	Exothermic	...
$HNCO + O \rightarrow OH + OCN$	5.70	Endothermic	...
$HCNO + O \rightarrow CO + HNO$	−92.52	Exothermic	...
$HCNO + O \rightarrow OH + CNO$	0.064	Endothermic	...
$HOCN + O \rightarrow OH + OCN$	−22.90	Exothermic	...
$HONC + O \rightarrow OH + CNO$	−18.80	Exothermic	...

Note:
[a] Himmel et al. (2002)

Quénard et al. (2018) studied the peptide-bond-related molecules in the protostar IRAS 16293 − 2422 and the prestellar core L1554 by using a chemical model. Earlier, it was claimed that HNCO and NH_2CHO are chemically linked because NH_2CHO could be formed by the successive hydrogenation reactions of HNCO ($HNCO \rightarrow H_2NCO \rightarrow NH_2CHO$; Mendoza et al., 2014; López-Sepulcre et al., 2015; Song & Kästner, 2016; López-Sepulcre et al., 2019). The first step of this hydrogenation sequence has an activation barrier of 1962 K, and the second step is a radical − radical reaction and thus could be barrierless. However, recent experimental studies by Noble et al. (2015) and Fedoseev et al. (2015) questioned this fact. They opposed the formation of NH_2CHO by the reaction between H_2NCO and H; instead, they proposed that eventually, it would return to HNCO again ($H_2NCO + H \rightarrow HNCO + H_2$). Here, we consider only the formation of NH_2CHO in our ice-phase network. In order to continue a comparative study between the various isomers of HNCO, we are interested in checking the hydrogenation reactions with the various isomeric forms of HNCO. Thus, the reaction enthalpies of the following reactions are studied:

$$HNCO + H \rightarrow H_2NCO, \tag{4.12}$$

$$HCNO + H \rightarrow H_2CNO, \tag{4.13}$$

$$HOCN + H \rightarrow H_2OCN, \tag{4.14}$$

$$HONC + H \rightarrow H_2ONC. \tag{4.15}$$

However, we do not obtain a valid neutral structure for H_2OCN and H_2ONC, and thus we do not consider the last two hydrogenation reactions of this sequence. In Table 4.12, we summarize the obtained reaction enthalpies of reactions 4.12 and 4.13. Based on the obtained reaction enthalpy for the second reaction relative to the first reaction, we scale the activation barrier of the second reaction to 1073 K.

Recently, Haupa et al. (2019) proposed the successive H abstraction reactions to NH_2CHO for the formation of HNCO:

$$NH_2CHO + H \rightarrow H_2 + H_2NCO, \tag{4.16}$$

$$H_2NCO + H \rightarrow H_2 + HNCO. \tag{4.17}$$

They pointed out that reaction 4.16 has an activation barrier of $240 - 3130$ K depending on the level of theory used for the quantum chemical calculation. They found that reaction 4.17 is barrierless. This reaction is exciting as it might support the earlier claim of chemical linkage between HNCO and NH_2CHO. They also performed quantum chemical calculations for the H addition reactions to H_2NCO and HNCO:

$$H + H_2NCO \rightarrow NH_2CHO, \tag{4.18}$$

$$H + HNCO \rightarrow H_2NCO. \tag{4.19}$$

They found that reaction 4.18 is barrierless, whereas reaction 4.19 has an activation barrier of $2530 - 5050$ K, depending on the level of theory used for the computation.

For the calculation of the gas-phase reaction rate of these four reactions, we use

$$rate = \alpha\left(\frac{T}{300}\right)^{\beta} exp(-\gamma/T), \tag{4.20}$$

where α, β, and γ are the three constants of the reaction. We consider $\alpha = 10^{-10}$, $\beta = 0$ and $\gamma = 240 - 3130$ for reaction 4.16. For the reaction 4.17 and 4.18, we consider $\alpha = 10^{-10}$, $\beta = 0$, and $\gamma = 0$, and for reaction 4.19, we consider $\alpha = 10^{-10}$, $\beta = 0$, and $\gamma = 2530 - 5050$. Since a proper structure for H_2CNO is obtained, we consider the reaction $H + H_2CNO \rightarrow HCNO + H_2$ in both gas and ice phases.

Quénard et al. (2018) used the gas-phase destruction of HOCN, HCNO, and HONC by an oxygen atom. For all three destruction reactions, they considered an activation barrier of 195 K. However, Quan et al. (2010) considered the activation barriers of 2470 K, 195 K, and 3570 K, respectively, for these three destruction reactions by oxygen atoms, and these are the default in the UMIST 2012

network. Here, we consider the default destruction reactions as in UMIST 2012. The destruction of HNCO by the oxygen atom is not considered. To this effect, we calculate the reaction enthalpies for the reactions HNCO + O → CO + HNO and HNCO + O → OH + OCN. We find that the second reaction in this sequence is endothermic, whereas the first one is exothermic, and thus we do not consider the second one. The reaction HNCO + O → CO + HNO is very similar to the reaction HCNO + O → CO + HNO, for which a 195 K activation barrier is considered in UMIST 2012. Based on the exothermicity values between HCNO + O and HNCO + O, we use a scaling factor and obtain an activation barrier of 765 K for HNCO + O. Calculated reaction enthalpies and the activation barriers with ZPVE correction are noted in Table 4.12.

4.2.2 Modeling results

The observed abundances of HNCO, NH_2CHO, and CH_3NCO toward G10 (Gorai et al., 2020b) are shown in Table 4.13. The abundances are very sensitive to the physical parameters (T_{ice}, ρ_{max}, T_{max}, t_{coll}, and t_{pw}) and adopted rate constants. Here, we make an extensive effort to find out the simultaneous appearance of these three N-bearing species by varying the sensitive physical parameters and rate constants of some of the key reactions. More precisely, we prepare two models: Model A and Model B. The difference between the two models is highlighted in Table 4.14.

Results obtained with Model A

To constrain the best possible model, we explore the parameter space around which the modeling results agree with the observational results. To this effect, we run several cases by varying the initial dust temperature (T_{ice}) between 10 K and 25 K and ρ_{max} between 10^5 cm^{-3} and 10^7 cm^{-3} for Model A. Since G10 is a hot-core, a higher density ($10^6 - 10^7$ cm^{-3}) is preferable. G10 is extended by roughly 0.1 pc and has $\sim 10^3$ solar masses of matter (Cesaroni et al., 1994). From that estimation, the average density of the source is around 10^7 cm^{-3}. Interestingly, continuum temperatures vary between 19 K and 27 K from observational analysis (Gorai et al., 2020b). Based on the observational results as a preliminary guess, we use $\rho_{max} = 10^7$ cm^{-3} and $T_{ice} = 20$ K for Model A. Initially, we start with Model A with the rate constants of the gas-phase reactions available in the literature (Skouteris et al., 2017; Quénard et al., 2018; Haupa et al., 2019). Based on some preliminary iterations of our simulation, we vary the rate constants of some essential gas-phase

Table 4.13: Estimated rotational temperatures, column densities, and fractional abundances of the observed species (Gorai et al., 2020b).

Species	Rotational temperature (K)	Column density (cm^{-2})	Fractional abundance
HNCO	317 ± 25	1.37×10^{17}	1.02×10^{-8}
NH_2CHO	439 ± 100	3.88×10^{16}	2.87×10^{-9}
CH_3NCO	248 ± 19	1.20×10^{17}	8.88×10^{-9}

Note: Assuming the mean value of $N_{H_2} = 1.35 \times 10^{25}$ cm^{-2} as estimated in Table 4 of Gorai et al. (2020b).

reactions, which control the abundances of the three targeted species. We obtain an excellent correlation between these three species when the rate constants listed in Table 4.14 are used. Quénard et al. (2018) considered the reaction between HNCO and CH_3 in the ice phase to form the isomers CH_3NCO and CH_3OCN at the same rate. However, for the gas-phase formation of other isomers of CH_3NCO (CH_3CNO, CH_3OCN, CH_3ONC), Quénard et al. (2018) considered some rate coefficients of $\sim 10^{-20}$ and 5×10^{-11} cm^3 s^{-1}. Here, instead of the rate constant of 5×10^{-11} cm^3 s^{-1}, we consider 10^{-12} cm^3 s^{-1} for some gas-phase reactions and use a rate of 10^{-20} cm^3 s^{-1} for reactions as used in Quénard et al. (2018). We keep it as it was considered by Quénard et al. (2018) for the ice-phase formation reactions. To study the abundances of various isomers considered in the network, we choose our best-fitted parameters listed in Table 4.14 for Model A. Time evolution of the abundances of HNCO isomers, CH_3NCO isomers, and NH_2CHO is shown in Figures 4.19, 4.20, and 4.21, respectively. Results obtained with the best-fitted rate constants are shown separately in Figure 4.22, which clearly show a reasonable correlation among HNCO, CH_3NCO, and NH_2CHO around the age of $\sim 1.12 \times 10^6$ years. Parameter space obtained with the best-fitted rate constants after a suitable age position (1.12×10^6 years) is shown in Figure 4.23. For ease of understanding, abundances closer to the observed values are indicated with contours.

Among the other isomers of HNCO, HOCN is found to be significantly abundant. During the warm-up and post-warm-up stages, it attains a peak value of 4.8×10^{-9} for the best-fitted parameters of Model A. It is ~ 10 times lower than the lowest energy isomer, HNCO (peak abundance 4.13×10^{-8}). Similarly, among all the other isomers of CH_3NCO, the abundance of CH_3OCN is higher. It is because of the gas-phase formation of CH_3OCN by the reaction between CH_3 and HOCN. With the best-fitted parameters, we obtain a peak abundance of CH_3OCN as 6.1×10^{-10}, which is ~ 8 times lower than that of CH_3NCO (peak abundance 5.0×10^{-9}). We (Gorai et al., 2020b) report the identification of HNCO and CH_3NCO in G10. However,

Table 4.14: Key differences between the Model A and Model B (Gorai et al., 2020b).

Physical parameters	**Model A**	**Model B**
$\rho_{\rm max}$ (cm^{-3})	10^7	10^{5-7}
$T_{\rm max}$ (K)	200	$100-400$
t_{coll} (years)	10^6	10^{5-6}
t_w (years)	5×10^4	5×10^4
t_{pw} (years)	$(6.2-10)\times10^4$	10^5
T_{ice} (K)	$10-25$	20
	Gas-phase reactions parameterized	
	Gas-phase rate constants used in Model A and Model B	Rate constant used in literature
$NH_2 + H_2CO \rightarrow NH_2CHO + H$	$\alpha = 5.00\times10^{-12},\ \beta = -2.56,\ \gamma = 4.88$	$\alpha = 7.79\times10^{-15},\ \beta = -2.56,\ \gamma = 4.88$ (a)
$CH_3 + HNCO \rightarrow CH_3NCO + H$	$\alpha = 1.0\times10^{-12},\ \beta = 0,\ \gamma = 0$	$\alpha = 5\times10^{-11},\ \beta = 0,\ \gamma = 0$ (b)
$H + NH_2CHO \rightarrow H_2NCO + H$	$\alpha = 1\times10^{-10},\ \beta = 0,\ \gamma = 240$	$\alpha = -,\ \beta = -,\ \gamma = 240-3130$ (c)
$H + H_2NCO \rightarrow HNCO + H_2$	$\alpha = 1\times10^{-10},\ \beta = 0,\ \gamma = 0$	$\alpha = -,\ \beta = -,\ \gamma = 0$ (c)
$H + H_2NCO \rightarrow NH_2CHO$	$\alpha = 1\times10^{-10},\ \beta = 0,\ \gamma = 0$	$\alpha = -,\ \beta = -,\ \gamma = 0$ (c)
$H + HNCO \rightarrow H_2NCO$	$\alpha = 1\times10^{-10},\ \beta = 0,\ \gamma = 5050$	$\alpha = -,\ \beta = -,\ \gamma = 2530-5050$ (c)

References.
(a) Skouteris et al. (2017).
(b) Quénard et al. (2018).
(c) Haupa et al. (2019).

HOCN and CH_3OCN should also be considered as the potential candidates for future astronomical detection in G10, looking at their abundances. Cernicharo et al. (2016) predicted an upper limit of the column density of 6×10^{13} cm^{-2} for another isomer, CH_3CNO, in Orion. Here, we find its peak abundance to be 7.4×10^{-13}. Converting this peak abundance in terms of the column density, we have $\sim 10^{13}$ cm^{-2} (using a hydrogen column density of 1.35×10^{25} cm^{-2}), which is in line with the observed upper limit.

Results obtained with Model B

For Model B, we do not vary any rate constants. Instead, we keep it as it is obtained with the best-fitted Model A, noted in Table 4.14. To find out the best-fit physical parameters for Model B, we start with $T_{ice} = 20$ K and vary ρ_{max}. Figure 4.24 shows the variation of HNCO, CH_3NCO, and NH_2CHO abundance by considering a post-warm-up time (t_{pw}) of 10^5 years. Observed abundances are also marked in each panel. We find that the abundance of these three species is highly sensitive to the chosen collapsing time scale (t_{coll}) and the maximum density (ρ_{max}) achieved during the collapsing stage. As we increase ρ_{max}, abundance significantly decreases. Similarly, as we increase t_{coll}, abundance gradually reduces. Based on Figure 4.24, we find that $\rho_{max} = 10^7$ cm^{-3} and $T_{coll} \sim 2-3\times10^5$ years are most suitable for explaining the abundance of these three species simultaneously. We

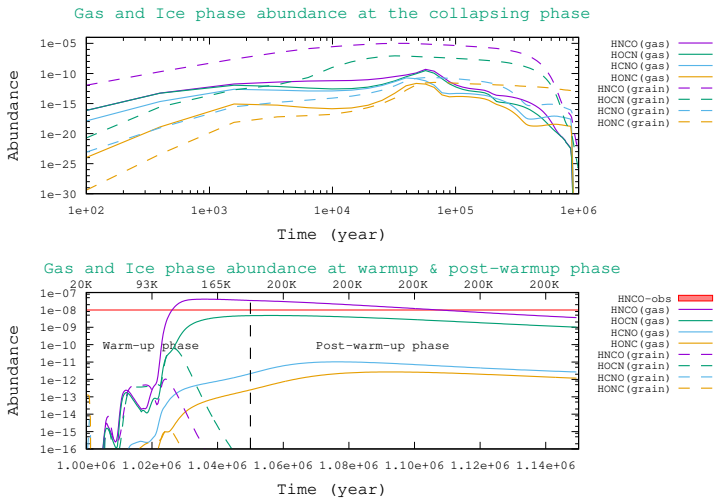

Figure 4.19: Chemical evolution of the peptide-bond-related molecule HNCO and corresponding isomers. This is shown for $\rho_{max} = 1.0 \times 10^7$ cm^{-3} and $T_{ice} = 20$ K by considering the best-fitted parameters with Model A. Red shaded lines represent the observed abundances obtained in G10 (Gorai et al., 2020b).

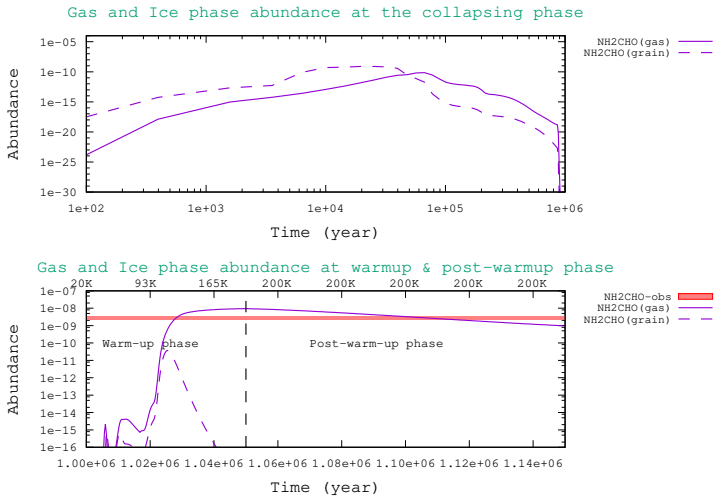

Figure 4.20: Chemical evolution of the peptide-bond-related molecule NH_2CHO. This is shown for $\rho_{max} = 1.0 \times 10^7$ cm^{-3} and $T_{ice} = 20$ K by considering the best-fitted parameters with Model A. Red shaded lines represent the observed abundances obtained in G10 (Gorai et al., 2020b).

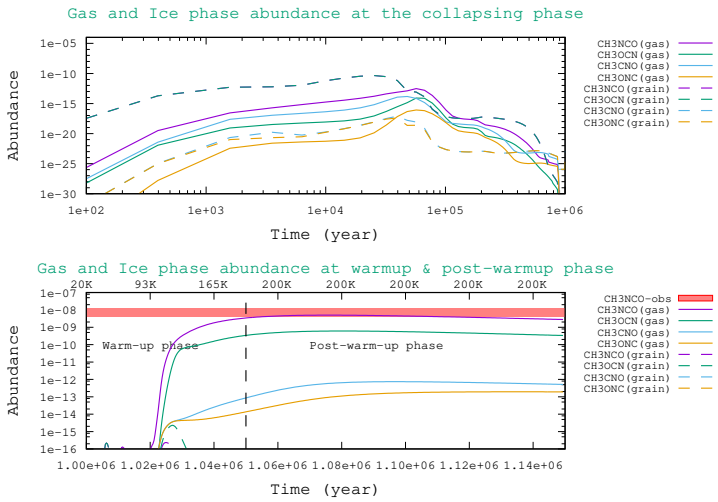

Figure 4.21: Chemical evolution of the peptide-bond-related molecule CH_3NCO and corresponding isomers. This is shown for $\rho_{max} = 1.0 \times 10^7$ cm^{-3} and $T_{ice} = 20$ K by considering the best-fitted parameters with Model A. Red shaded lines represent the observed abundances obtained in G10 (Gorai et al., 2020b).

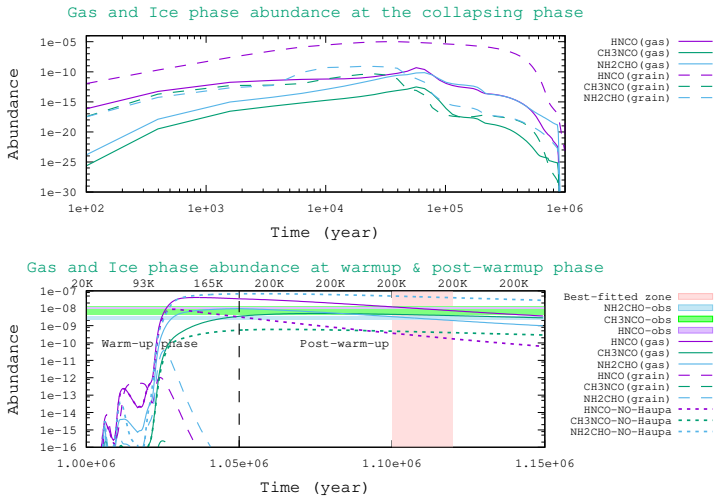

Figure 4.22: Chemical evolution of HNCO, CH_3NCO, and NH_2CHO during the three stages by considering the best-fit parameters of Model A. The best-fitted time zone is also highlighted. Abundance variation by avoiding Haupa et al. (2019) pathways in the gas phase is also shown (Gorai et al., 2020b).

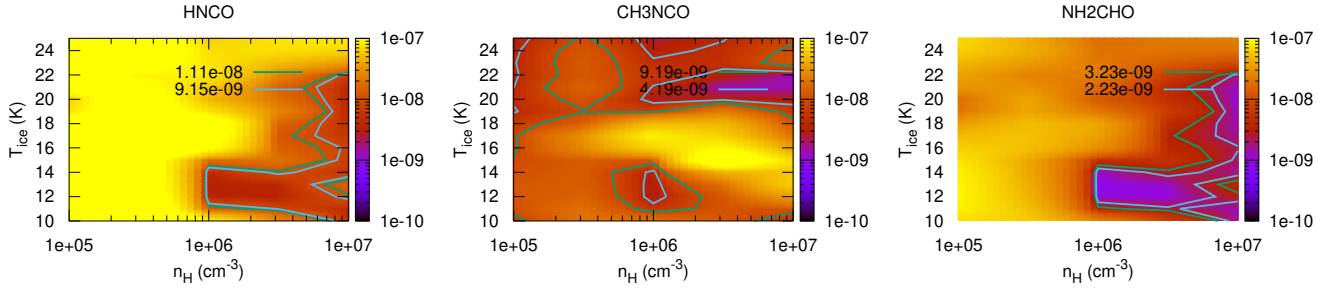

Figure 4.23: Parameter space obtained with Model A by considering the best-fitted parameters noted in Table 4.14 at an age position of 1.12×10^6 years. Color coding in the right side of the each panel represents the abundance with respect to H_2 (Gorai et al., 2020b).

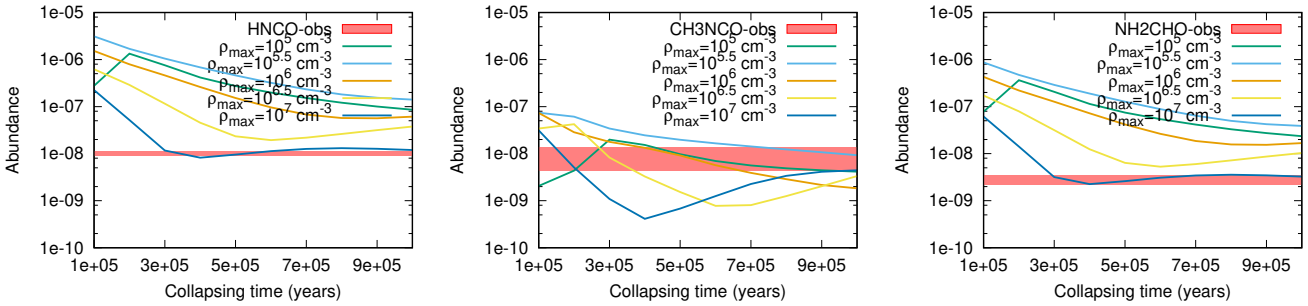

Figure 4.24: Abundances of HNCO, CH_3NCO, and NH_2CHO by considering different T_{coll} and ρ_{max} with Model B (Gorai et al., 2020b).

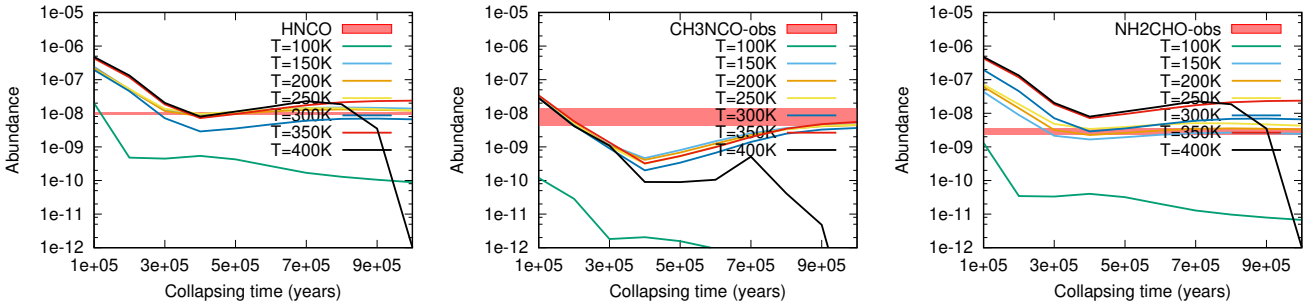

Figure 4.25: Abundances of HNCO, CH_3NCO, and NH_2CHO by considering $\rho_{max} = 10^7$ cm^{-3}, and different T_{max} and T_{coll} with Model B (Gorai et al., 2020b).

further vary T_{max} between 100 K and 400 K by considering $\rho_{max} = 10^7$ cm^{-3}. Figure 4.25 shows a strong increasing trend in the abundance profile with an increase in T_{max} from 100 K to 150 K. A suitable match is found when we use T_{max} = 200 K. In between T_{max} = 150 K and 350 K, the abundance profile shows moderate changes. Beyond 350 K, the abundances drastically decrease, while we consider a comparatively longer collapsing time scale. Thus, by considering all types of variation with Model B, we obtain a good fit among the three targeted N-bearing species using the parameters listed in Table 4.14. We find that our Model B with $T_{coll} = (2-3) \times 10^5$ years, $T_w = 5 \times 10^4$ years, and $T_{pw} = 10^5$ years can explain the observation of these three species simultaneously considering $\rho_{max} = 10^7$ cm^{-3}, T_{max} = 200 K, and T_{ice} = 20 K. The obtained lower timescale with Model B is very interesting because G10 is a high-mass star-forming region. The required gas-phase pathways to establish the linkage among these three species are summarized in Figure 4.26.

Chemical linkage between HNCO, NH_2CHO, *and* CH_3NCO

Earlier, it was proposed that HNCO and NH_2CHO are chemically linked. The successive hydrogenation reactions of HNCO were proposed for the formation of NH_2CHO. However, the validity of the second hydrogenation reaction was ruled out by the experimental study of Noble et al. (2015). Recently, a theoretical work

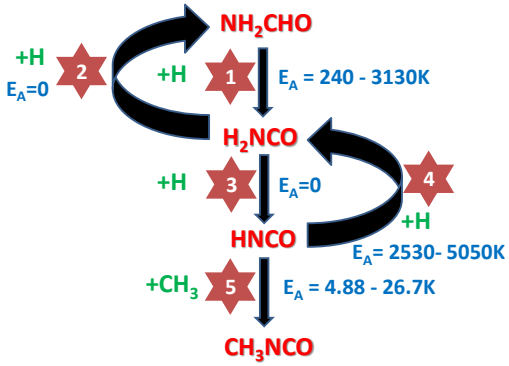

Figure 4.26: Chemical linkage between the three N-bearing molecules (Gorai et al., 2020b).

by Haupa et al. (2019) proposed dual-cyclic H addition and abstraction reactions to support the chemical linkage between HNCO and NH_2CHO. The chemical evolution of HNCO, NH_2CHO, and CH_3NCO with Model A is shown in Figure 4.22. Gradual enhancement in the abundance of ice-phase HNCO and its isomers arises because radicals become mobile enough to increase temperature. Beyond 80 K − 90 K, the diffusion timescale of the radicals becomes comparable to their desorption timescale, and thus they desorb back to the gas phase very quickly. Also, HNCO starts to sublimate beyond 90 K, resulting in a sharp decrease in the ice phase. The gas-phase production of CH_3NCO mainly occurs by the reaction between CH_3 and HNCO. The formation rate of CH_3NCO enhances during the later stages of the simulation. In the case of NH_2CHO, ice-phase production is sufficient in the collapsing stage, but gas-phase production is not adequate. A smooth transfer of NH_2CHO from the ice phase to the gas phase can occur in the warm-up period. The location of this transfer depends on the adopted BE of NH_2CHO. A major portion of NH_2CHO is formed by the gas-phase reaction between NH_2 and H_2CO in the warm-up and post-warm-up stage. Due to the increased temperature, the activation barrier for the hydrogen abstraction reaction of NH_2CHO (by reaction 4.16) becomes probable and thus produces HNCO by the barrierless reaction 4.17. To see the effects of adding the Haupa et al. (2019) pathways, we check with $\alpha = 0$ for the gas-phase reactions 4.16−4.19. Figure 4.22 shows the abundances of these three species by considering $\alpha = 0$ (marked as "NO-Haupa"). We notice that the abundance of gas-phase HNCO is significantly affected by the inclusion of the gas-phase pathways of Haupa et al. (2019). Consideration of reactions 4.16−4.19 shows more HNCO at the end, and an absence of these pathways (i.e., with $\alpha = 0$) reflects comparatively lower HNCO. In brief, we find that the pathways proposed by Haupa et al. (2019) are relevant for the gas-phase production of HNCO around the post-warm-up period. In the first stage, CH_3NCO is mainly formed on the grain surface by the reaction between CH_3 and OCN. CH_3NCO may also form by the reaction between CH_3 and HNCO (Quénard et al., 2018) in the ice phase. However, it is clear from the warm-up and post-warm-up stage that the major contribution of the gas-phase CH_3NCO is not coming from the ice phase. Instead, it is produced inside the gas phase itself. The gas-phase formation is efficient using the HNCO channel at the warm-up and post-warm-up stages.

4.2.3 Summary

From our chemical modeling results, we notice that the three N-bearing species are chemically linked. HNCO and NH_2CHO are chemically linked by dual-cyclic H addition and abstraction reactions proposed by Haupa et al. (2019) during the warm-up and post-warm-up stage. HNCO and CH_3NCO are also chemically related because HNCO reacts with CH_3 to form CH_3NCO (Figure 4.26). Our modeling results suggest that the abundances of HOCN and CH_3OCN are significantly higher and could be observed in G10.

4.3 Phosphorous-bearing species: precursor of biomolecules

Phosphorus (P) and its compounds play an essential role in the chemical evolution in galaxies. Phosphorus is a crucial element of life and is one of the main biogenic elements. However, its origin in the terrestrial system is yet to be fully understood. The ALMA and ESA probe Rosetta suggest that P-related species might have traveled from star-forming regions to the early Earth (e.g., Altwegg et al., 2016; Rivilla et al., 2020) through comets. The interstellar chemistry of P-bearing molecules has significant astrophysical relevance, and very little has been explored so far. P-bearing compounds are the major ingredients of any living system, where they carry out numerous biochemical functions. P-bearing molecules play a significant role in forming large biomolecules or living organisms. They store and transmit the genetic information in nucleic acids and work in nucleotides as precursors synthesize RNA and DNA (Maciá et al., 1997). Moreover, these molecules are the essential components of phospholipids (main characteristic features of cellular membranes; Maciá, 2005).

Phosphorus is relatively rare in the ISM. However, it is ubiquitous in various meteorites (Jarosewich, 1990; Lodders, 2003; Pasek, 2019). On an average, P is the 13th most abundant element in a typical meteoritic material and the 11th most abundant element in the Earth's crust (Maciá, 2005).

P^+ was identified with a cosmic abundance of $\sim 2 \times 10^{-7}$ in hot regions ($\sim$ 1200 K; Jura & York, 1978). PN, PO, HCP, CP, CCP, and PH_3 are observed in CSEs around evolved stars (Guelin et al., 1990; Agúndez et al., 2007, 2008; Agúndez et al., 2014; Tenenbaum et al., 2007; Halfen et al., 2008; Milam et al., 2008; Tenenbaum & Ziurys, 2008; De Beck et al., 2013; Ziurys et al., 2018). PN was detected in several star-forming regions (Turner & Bally, 1987; Ziurys, 1987; Turner et al., 1990; Caux et al., 2011; Yamaguchi et al., 2011; Fontani et al., 2016, 2019; Mininni et al., 2018). PN remained the only P-bearing species observed in the dense ISM for many years (Ziurys, 1987; Turner et al., 1990; Fontani et al., 2016). Rivilla et al. (2016) reported the first identification of PO toward W51 1e/2e and W3(OH), along with PN using the IRAM 30 m telescope. Thereafter, PO and PN were simultaneously observed in several low- and high-mass star-forming regions and the Galactic center (Lefloch et al., 2016; Rivilla et al., 2018, 2020; Bergner et al., 2019; Bernal et al., 2021).

Several studies (Millar et al., 1991; Charnley & Millar, 1994; Aota & Aikawa, 2012; Lefloch et al., 2016; Rivilla et al., 2016; Jiménez-Serra et al., 2018) reported their theoretical investigation on P-chemistry modeling. However, the study of the dense cloud region is not well constrained for P-chemistry. The significant uncer-

tainty lies in the depletion factor of the initial abundance of P. The complexity of gas-phase abundance within the gas and the exact depletion of different elements onto the grains are still uncertain (Jenkins, 2009). The chemical desorption of phosphine (PH_3) was recently studied by Nguyen et al. (2020). This study is indeed important in constraining the modeling parameters.

PH_3 is a relatively stable molecule that could hold a significant fraction of P in various astronomical environments. Scientists consider PH_3 to be a biosignature (Sousa-Silva et al., 2020). PH_3 was detected in the planets of our solar system containing a reducing atmosphere. PH_3 could be produced deep inside the reducing atmospheres of giant planets (Bregman et al., 1975; Tarrago et al., 1992) at high temperatures and pressures and dredged upward by the convection (Noll & Marley, 1997; Visscher et al., 2006). Very surprisingly, there is no such reducing atmosphere in Venus, but $\sim$ 20 ppb of PH_3 was inferred (Greaves et al., 2020). Such a high amount of PH_3 could not be explained with the steady-state chemical models, including the photochemical pathways. Greaves et al. (2020) also investigated the other abiotic routes for explaining this high abundance. But no suitable justification was found. They speculated some unknown photo or geo-chemical root of it. The possible reason behind its high abundance by some of the biological means could not be ruled out. This discovery initiated a series of debates. The presence of PH_3 in Venus's clouds could also not be explained by any abiotic mechanism (Bains et al., 2020). Villanueva et al. (2020) recently questioned the analysis and interpretation of the spectroscopic data used in Greaves et al. (2020). Snellen et al. (2020) also did not find any statistical evidence for PH_3 in the atmosphere of Venus.

PH_3 was tentatively observed (J = 1 $\rightarrow$ 0, 266.9 GHz) in the envelope of the carbon-rich stars IRC +10216 and CRL 2688 (Agúndez et al., 2008; Tenenbaum & Ziurys, 2008). Later, Agúndez et al. (2014) confirmed the presence of PH_3. They detected the J = 2 $\rightarrow$ 1 rotational transition of PH_3 (at 534 GHz) with a very high abundance toward IRC +10216 using the HIFI instrument onboard Herschel.

Chantzos et al. (2020) recently attempted to observe HCP (2–1), CP (2–1), PN (2–1), and PO (2–1) along the line of sight to the compact extragalactic quasar B0355+508 with the IRAM 30 m telescope. Unfortunately, they could not detect these transitions along this line of sight predicting 3σ upper limits. However, they successfully observed HNC (1–0), CN (1–0), and $C^{34}S$ (2–1) in absorption and ^{13}CO (1–0) in emission along the same line of sight.

Here, we implement various state-of-the-art chemical models to understand the PH_3 formation under different interstellar conditions such as diffuse cloud, interstel-

lar PDRs, and hot-core regions.

4.3.1 The chemical network of phosphorus

N and P have five electrons in the valance shell. Due to this reason, P-chemistry is sometimes considered analogous to N-chemistry. For example, successive hydrogenation of N yields NH_3, whereas for P it yields PH_3. However, the presence of NH_3 is ubiquitous in the ISM (Cheung et al., 1968; Wilson & Pauls, 1979; Keene et al., 1983; Mauersberger et al., 1988), but the presence of PH_3 is not so universal (Thorne et al., 1983). On the other hand, P-related chemistry can significantly differ from the N-related chemistry under the physical conditions prevailing in the different star-forming regions. In this work, we prepare an extensive network of P following the chemical pathways explained in Thorne et al. (1984); Adams et al. (1990); Millar et al. (1991); Fontani et al. (2016); Jiménez-Serra et al. (2018); Sousa-Silva et al. (2020); Rivilla et al. (2016); Chantzos et al. (2020). Charnley & Millar (1994) and Anicich (1993) differentiated the formation/destruction mechanism of PH_n (n=1, 2, 3) and their cationic species. Thorne et al. (1984) presented the reaction pathways for P, PO, P^+, PO^+, PH^+, HPO^+, and H_2PO^+. Furthermore, in a recent study, Chantzos et al. (2020) extended the gas-phase chemical network of PN and PO in accordance with Millar et al. (1987); Jiménez-Serra et al. (2018). We use the kinetic data of chemical reactions from the KIDA (Wakelam et al., 2015) and UMIST (McElroy et al., 2013) database. In Table 4.15, we show all the reactions considered in our P-network.

Table 4.15: Reaction pathways for P-chemistry (Sil et al., 2021).

Reaction Number (Type)	Reactions	Rate coefficient α	β	γ	References
	Gas-phase pathways				
R1 (IN)	$C^+ + P \rightarrow P^+ + C$	1.0×10^{-09}	0.0	0.0	McElroy et al. (2013)
R2 (IN)	$H^+ + P \rightarrow P^+ + H$	1.0×10^{-09}	0.0	0.0	McElroy et al. (2013)
R3 (IN)	$He^+ + P \rightarrow P^+ + He$	1.0×10^{-09}	0.0	0.0	McElroy et al. (2013)
R4 (IN)	$NH_3 + P^+ \rightarrow P + NH_3^+$	3.08×10^{-10}	−0.5	0.0	McElroy et al. (2013)
R5 (IN)	$Si + P^+ \rightarrow P + Si^+$	1.0×10^{-09}	0.0	0.0	McElroy et al. (2013)
R6 (CR)	$P + CRPHOT \rightarrow P^+ + e^-$	1.30×10^{-17}	0.0	750	McElroy et al. (2013)
R7 (PH)	$P + h\nu \rightarrow P^+ + e^-$	1.0×10^{-09}	0.0	2.7	McElroy et al. (2013)
R8 (ER)	$P^+ + e^- \rightarrow P + h\nu$	3.41×10^{-12}	-0.65	0.0	McElroy et al. (2013)
R9 (NR)	$P + CN \rightarrow PN + C$	3.0×10^{-10}	-	-	Jiménez-Serra et al. (2018)
R10 (NR)	$N + PH \rightarrow PN + H$	5.0×10^{-11}	0.0	0.0	Smith et al. (2004)
R11 (NR)	$N + PO \rightarrow PN + O$	3.0×10^{-11}	−0.6	0.0	Smith et al. (2004)
R12 (NR)	$N + PO \rightarrow P + NO$	2.55×10^{-12}	0.0	0.0	Millar et al. (1987)
R13 (NR)	$N + CP \rightarrow PN + C$	3.0×10^{-10}	-	-	Jiménez-Serra et al. (2018)
R14 (NR)	$C + PN^+ \rightarrow PN + C^+$	1.0×10^{-09}	0.0	0.0	McElroy et al. (2013)
R15 (DR)	$PN^+ + e^- \rightarrow P + N$	1.8×10^{-7}	−0.5	0.0	McElroy et al. (2013)
R16 (DR)	$HPN^+ + e^- \rightarrow PN + H$	1.0×10^{-7}	−0.5	0.0	Millar et al. (1991)
R17 (DR)	$HPN^+ + e^- \rightarrow P + NH$	1.0×10^{-7}	−0.5	0.0	McElroy et al. (2013)
R18 (DR)	$PNH_2^+ + e^- \rightarrow PN + H_2$	1.5×10^{-7}	−0.5	0.0	McElroy et al. (2013)
R19 (DR)	$PNH_3^+ + e^- \rightarrow PN + H_2$	1.5×10^{-7}	−0.5	0.0	McElroy et al. (2013)
R20 (CR)	$PN + CRPHOT \rightarrow P + N$	1.30×10^{-17}	0.0	250	McElroy et al. (2013)
R21 (IN)	$H^+ + PN \rightarrow PN^+ + H$	1.0×10^{-9}	−0.5	0.0	Millar et al. (1991)
R22 (IN)	$He^+ + PN \rightarrow P^+ + N + He$	1.0×10^{-9}	−0.5	0.0	Millar et al. (1991)
R23 (IN)	$H_3^+ + PN \rightarrow HPN^+ + H_2$	1.0×10^{-9}	−0.5	0.0	Millar et al. (1991)
R24 (IN)	$H_3O^+ + PN \rightarrow HPN^+ + H_2O$	1.0×10^{-9}	−0.5	0.0	Millar et al. (1991)
R25 (IN)	$HCO^+ + PN \rightarrow HPN^+ + CO$	1.0×10^{-9}	−0.5	0.0	Millar et al. (1991)
R26 (NR)	$N + PN \rightarrow P + N_2$	1.0×10^{-18}	0.0	0.0	Millar et al. (1987)
R27 (PH)	$PN + h\nu \rightarrow P + N$	5.0×10^{-12}	0.0	3.0	McElroy et al. (2013)
R28 (CR)	$HPO + CRPHOT \rightarrow PO + H$	1.30×10^{-17}	0.0	750	McElroy et al. (2013)
R29 (DR)	$HPO^+ + e^- \rightarrow PO + H$	1.50×10^{-7}	−0.5	0.0	Thorne et al. (1984)
R30 (DR)	$HPO^+ + e^- \rightarrow O + PH$	1.50×10^{-7}	−0.5	0.0	Millar et al. (1991)
R31 (DR)	$HPO^+ + e^- \rightarrow P + O + H$	1.00×10^{-7}	−0.5	0.0	McElroy et al. (2013)
R32 (DR)	$PO^+ + e^- \rightarrow P + O$	1.80×10^{-7}	−0.5	0.0	McElroy et al. (2013)
R33 (IN)	$H_2O + HPO^+ \rightarrow PO + H_3O^+$	3.40×10^{-10}	−0.5	0.0	McElroy et al. (2013)
R34 (IN)	$H_2O + P^+ \rightarrow PO^+ + H_2$	5.50×10^{-11}	−0.5	0.0	McElroy et al. (2013)
R35 (NR)	$O + HPO \rightarrow PO + OH$	3.80×10^{-11}	0.0	0.0	Smith et al. (2004)
R36 (NR)	$O + PH_2 \rightarrow PO + H_2$	4.0×10^{-11}	0.0	0.0	Millar et al. (1987)
R37 (NR)	$O + PH_2 \rightarrow H + HPO$	8.0×10^{-11}	0.0	0.0	Smith et al. (2004)
R38 (NR)	$O + PH \rightarrow PO + H$	1.0×10^{-10}	0.0	0.0	Smith et al. (2004)
R39 (NR)	$P + OH \rightarrow PO + H$	6.1×10^{-11}	−0.23	14.9	Jiménez-Serra et al. (2018)
R40 (NN)	$O_2 + P \rightarrow O + PO$	1.0×10^{-13}	0.0	0.0	McElroy et al. (2013)
R41 (NN)	$O_2 + PH_2^+ \rightarrow PO^+ + H_2O$	7.8×10^{-11}	0.0	0.0	McElroy et al. (2013)
R42 (IN)	$P^+ + CO_2 \rightarrow PO^+ + CO$	4.60×10^{-10}	0.0	0.0	McElroy et al. (2013)
R43 (IN)	$P^+ + O_2 \rightarrow PO^+ + O$	5.60×10^{-10}	0.0	0.0	McElroy et al. (2013)
R44 (IN)	$P^+ + OCS \rightarrow PO^+ + CS$	4.18×10^{-10}	0.0	0.0	McElroy et al. (2013)
R45 (PH)	$HPO + h\nu \rightarrow PO + H$	1.70×10^{-10}	0.0	5.3	McElroy et al. (2013)
R46 (CR)	$PO + CRPHOT \rightarrow P + O$	1.30×10^{-17}	0.0	250	McElroy et al. (2013)
R47 (IN)	$C^+ + PO \rightarrow PO^+ + C$	1.0×10^{-9}	−0.5	0.0	Thorne et al. (1984)
R48 (IN)	$H^+ + PO \rightarrow PO^+ + H$	1.0×10^{-9}	−0.5	0.0	Thorne et al. (1984)
R49 (IN)	$H_3^+ + PO \rightarrow HPO^+ + H_2$	1.0×10^{-9}	−0.5	0.0	Thorne et al. (1984)
R50 (IN)	$HCO^+ + PO \rightarrow HPO^+ + CO$	1.0×10^{-9}	−0.5	0.0	Thorne et al. (1984)
R51 (IN)	$He^+ + PO \rightarrow P^+ + O + He$	1.0×10^{-9}	−0.5	0.0	Thorne et al. (1984)
R52 (PH)	$PO + h\nu \rightarrow P + O$	3.0×10^{-10}	0.0	2.0	McElroy et al. (2013)
R53 (DR)	$PCH_2^+ + e^- \rightarrow HCP + H$	1.50×10^{-7}	−0.5	0.0	Millar et al. (1991)
R54 (CR)	$HCP + CRPHOT \rightarrow CP + H$	1.30×10^{-17}	0.0	750	McElroy et al. (2013)
R55 (IN)	$C^+ + HCP \rightarrow CCP^+ + H$	5.0×10^{-10}	0.0	0.0	Millar et al. (1991)
R56 (IN)	$C^+ + HCP \rightarrow HCP^+ + C$	5.0×10^{-10}	0.0	0.0	Millar et al. (1991)
R57 (IN)	$C + HCP^+ \rightarrow CCP^+ + H$	2.0×10^{-10}	0.0	0.0	McElroy et al. (2013)
R58 (IN)	$H^+ + HCP \rightarrow HCP^+ + H$	1.0×10^{-9}	0.0	0.0	Millar et al. (1991)
R59 (IN)	$H_3^+ + HCP \rightarrow PCH_2^+ + H_2$	1.0×10^{-9}	0.0	0.0	Millar et al. (1991)
R60 (IN)	$H_3O^+ + HCP \rightarrow PCH_2^+ + H_2O$	1.0×10^{-9}	0.0	0.0	Millar et al. (1991)
R61 (IN)	$HCO^+ + HCP \rightarrow PCH_2^+ + CO$	1.0×10^{-9}	0.0	0.0	Adams et al. (1990)
R62 (IN)	$He^+ + HCP \rightarrow P^+ + CH + He$	5.0×10^{-10}	0.0	0.0	Millar et al. (1991)
R63 (IN)	$He^+ + HCP \rightarrow PH + C^+ + He$	5.0×10^{-10}	0.0	0.0	Millar et al. (1991)
R64 (NR)	$O + HCP \rightarrow PH + CO$	3.61×10^{-13}	2.1	3080.0	Smith et al. (2004)
R65 (PH)	$HCP + h\nu \rightarrow CP + H$	5.48×10^{-10}	0.0	2.0	McElroy et al. (2013)
R66 (NR)	$CCP + O \rightarrow CO + CP$	6.0×10^{-12}	0.0	0.0	Smith et al. (2004)
R67 (IN)	$CCP + He^+ \rightarrow He + CP + C^+$	5.0×10^{-10}	−0.5	0.0	Millar et al. (1991)
R68 (IN)	$CCP + He^+ \rightarrow He + C_2 + P^+$	5.0×10^{-10}	−0.5	0.0	Millar et al. (1991)
R69 (DR)	$PCH_4^+ + e^- \rightarrow CP + C_3H$	7.5×10^{-8}	−0.5	0.0	McElroy et al. (2013)
R70 (DR)	$CCP^+ + e^- \rightarrow C + CP$	1.5×10^{-7}	−0.5	0.0	Millar et al. (1991)

Reaction Number (Type)	Reactions	Rate coefficient α	β	γ	References
R71 (DR)	$CCP^+ + e^- \rightarrow P + C_2$	1.5×10^{-7}	−0.5	0.0	Millar et al. (1991)
R72 (DR)	$PCH_2^+ + e^- \rightarrow CP + H_2$	1.50×10^{-7}	−0.5	0.0	Millar et al. (1991)
R73 (DR)	$HCP^+ + e^- \rightarrow CP + H$	1.50×10^{-7}	−0.5	0.0	Millar et al. (1991)
R74 (DR)	$HCP^+ + e^- \rightarrow P + CH$	1.50×10^{-7}	−0.5	0.0	Millar et al. (1991)
R75 (DR)	$CP^+ + e^- \rightarrow P + C$	1.00×10^{-7}	−0.5	0.0	McElroy et al. (2013)
R76 (NR)	$C + PH \rightarrow CP + H$	7.50×10^{-11}	0.0	0.0	Smith et al. (2004)
R77 (CR)	$CP + CRPHOT \rightarrow C + P$	1.30×10^{-17}	0.0	250	McElroy et al. (2013)
R78 (IN)	$C^+ + CP \rightarrow CP^+ + C$	1.0×10^{-9}	0.0	0.0	Millar et al. (1991)
R79 (IN)	$H^+ + CP \rightarrow CP^+ + H$	1.0×10^{-9}	0.0	0.0	Millar et al. (1991)
R80 (IN)	$H_3^+ + CP \rightarrow HCP^+ + H_2$	1.0×10^{-9}	0.0	0.0	Millar et al. (1991)
R81 (IN)	$H_2 + CP^+ \rightarrow HCP^+ + H$	1.0×10^{-9}	0.0	0.0	McElroy et al. (2013)
R82 (IN)	$H_3O^+ + CP \rightarrow HCP^+ + H_2O$	1.0×10^{-9}	0.0	0.0	Millar et al. (1991)
R83 (IN)	$HCO^+ + CP \rightarrow HCP^+ + CO$	1.0×10^{-9}	0.0	0.0	Adams et al. (1990)
R84 (IN)	$He^+ + CP \rightarrow P^+ + C + He$	5.0×10^{-10}	0.0	0.0	Millar et al. (1991)
R85 (IN)	$He^+ + CP \rightarrow P + C^+ + He$	5.0×10^{-10}	0.0	0.0	Millar et al. (1991)
R86 (NR)	$O + CP \rightarrow P + CO$	4.0×10^{-11}	0.0	0.0	Millar et al. (1991)
R87 (IN)	$O + CP^+ \rightarrow P^+ + CO$	2.0×10^{-10}	0.0	0.0	McElroy et al. (2013)
R88 (PH)	$CP + h\nu \rightarrow C + P$	1.0×10^{-9}	0.0	2.8	McElroy et al. (2013)
R89 (PH)	$C + P \rightarrow CP + h\nu$	1.41×10^{-18}	0.03	55.0	McElroy et al. (2013)
R90 (DR)	$PC_2H_3^+ + e^- \rightarrow PH + C_2H_2$	1.00×10^{-7}	−0.50	0.0	McElroy et al. (2013)
R91 (DR)	$PNH_2^+ + e^- \rightarrow PH + NH$	1.50×10^{-7}	−0.50	0.0	McElroy et al. (2013)
R92 (DR)	$PNH_3^+ + e^- \rightarrow PH + NH_2$	1.50×10^{-7}	−0.50	0.0	McElroy et al. (2013)
R93 (DR)	$PNH_2^+ + e^- \rightarrow P + NH_2$	1.50×10^{-7}	−0.50	0.0	McElroy et al. (2013)
R94 (DR)	$PNH_3^+ + e^- \rightarrow P + NH_3$	3.0×10^{-7}	−0.50	0.0	McElroy et al. (2013)
R95 (DR)	$PH_2^+ + e^- \rightarrow PH + H$	9.38×10^{-8}	−0.64	0.0	McElroy et al. (2013)
R96 (DR)	$PH_3^+ + e^- \rightarrow PH + H_2$	1.5×10^{-7}	−0.5	0.0	Millar et al. (1991)
R97 (DR)	$HPN^+ + e^- \rightarrow PH + N$	1.0×10^{-7}	−0.5	0.0	Millar et al. (1991)
R98 (DR)	$H_2PO^+ + e^- \rightarrow PH + OH$	1.5×10^{-7}	−0.5	0.0	McElroy et al. (2013)
R99 (DR)	$H_2PO^+ + e^- \rightarrow HPO + H$	1.5×10^{-7}	−0.5	0.0	McElroy et al. (2013)
R100 (IN)	$H_2O + PH_2^+ \rightarrow PH + H_3O^+$	1.62×10^{-10}	−0.5	0.0	Adams et al. (1990)
R101 (IN)	$NH_3 + PH^+ \rightarrow P + NH_4^+$	3.99×10^{-10}	−0.5	0.0	McElroy et al. (2013)
R102 (IN)	$NH_3 + PH^+ \rightarrow PNH_2^+ + H_2$	5.88×10^{-10}	−0.5	0.0	McElroy et al. (2013)
R103 (IN)	$NH_3 + PH^+ \rightarrow PNH_3^+ + H$	1.11×10^{-9}	−0.5	0.0	McElroy et al. (2013)
R104 (IN)	$NH_3 + P^+ \rightarrow PNH_2^+ + H$	2.67×10^{-10}	−0.5	0.0	McElroy et al. (2013)
R105 (IN)	$NH_3 + PH_2^+ \rightarrow PH + NH_4^+$	3.8×10^{-10}	−0.5	0.0	Adams et al. (1990)
R106 (IN)	$NH_3 + PH_2^+ \rightarrow PNH_3^+ + H_2$	1.62×10^{-9}	−0.5	0.0	McElroy et al. (2013)
R107 (NR)	$O + PH_2 \rightarrow PH + OH$	2.0×10^{-11}	0.0	0.0	Smith et al. (2004)
R108 (NR)	$C + HPO \rightarrow PH + CO$	4.0×10^{-11}	0.0	0.0	Millar et al. (1991)
R109 (CR)	$PH + CRPHOT \rightarrow P + H$	1.3×10^{-17}	0.0	250	McElroy et al. (2013)
R110 (IN)	$C^+ + PH \rightarrow PH^+ + C$	1.0×10^{-9}	0.0	0.0	Millar et al. (1991)
R111 (IN)	$H^+ + PH \rightarrow PH^+ + H$	1.0×10^{-9}	0.0	0.0	Millar et al. (1991)
R112 (IN)	$H_3^+ + P \rightarrow PH^+ + H_2$	1.0×10^{-9}	0.0	0.0	Adams et al. (1990)
R113 (IN)	$H_3^+ + PH \rightarrow PH_2^+ + H_2$	2.0×10^{-9}	0.0	0.0	Millar et al. (1991)
R114 (IN)	$HCO^+ + P \rightarrow PH^+ + CO$	1.0×10^{-9}	0.0	0.0	Adams et al. (1990)
R115 (IN)	$O + HCP^+ \rightarrow PH^+ + CO$	2.0×10^{-10}	0.0	0.0	Millar et al. (1991)
R116 (IN)	$O + HPO^+ \rightarrow PH^+ + O_2$	2.0×10^{-10}	0.0	0.0	Thorne et al. (1984)
R117 (IN)	$HCO^+ + PH \rightarrow PH_2^+ + CO$	1.0×10^{-9}	0.0	0.0	Millar et al. (1991)
R118 (IN)	$He^+ + PH \rightarrow P^+ + He + H$	1.0×10^{-9}	0.0	0.0	Millar et al. (1991)
R119 (IN)	$He^+ + HPO \rightarrow PH^+ + O + He$	5.0×10^{-10}	−0.5	0.0	Millar et al. (1991)
R120 (IN)	$He^+ + HPO \rightarrow PO^+ + H + He$	5.0×10^{-10}	−0.5	0.0	McElroy et al. (2013)
R121 (NR)	$H + PH \rightarrow P + H_2$	1.50×10^{-10}	0.0	416	Kaye & Strobel (1983)
R122 (IN)	$O + PH^+ \rightarrow PO^+ + H$	1.0×10^{-9}	0.0	0.0	Thorne et al. (1984)
R123 (IN)	$HCN + PH^+ \rightarrow HCNH^+ + P$	3.06×10^{-10}	−0.5	0.0	McElroy et al. (2013)
R124 (IN)	$O + PN^+ \rightarrow PO^+ + N$	2.0×10^{-10}	0.0	0.0	McElroy et al. (2013)
R125 (IN)	$OH + P^+ \rightarrow PO^+ + H$	5.0×10^{-10}	−0.5	0.0	McElroy et al. (2013)
R126 (IN)	$PH^+ + O_2 \rightarrow PO^+ + OH$	5.4×10^{-10}	0.0	0.0	Adams et al. (1990)
R127 (DR)	$PH^+ + e^- \rightarrow P + H$	1.0×10^{-7}	−0.5	0.0	Thorne et al. (1984)
R128 (PH)	$PH + h\nu \rightarrow P + H$	4.0×10^{-10}	0.0	1.5	McElroy et al. (2013)
R129 (DR)	$PH_3^+ + e^- \rightarrow H + PH_2$	1.5×10^{-7}	−0.5	0.0	McElroy et al. (2013)
R130 (DR)	$PH_2^+ + e^- \rightarrow P + H_2$	5.36×10^{-8}	−0.64	0.0	McElroy et al. (2013)
R131 (DR)	$PH_2^+ + e^- \rightarrow P + H + H$	5.23×10^{-7}	−0.64	0.0	McElroy et al. (2013)
R132 (IN)	$NH_3 + PH_3^+ \rightarrow PH_2 + NH_4^+$	2.3×10^{-9}	−0.5	0.0	Adams et al. (1990)
R133 (DR)	$PH_4^+ + e^- \rightarrow PH_2 + H_2$	1.50×10^{-7}	−0.5	0.0	Charnley & Millar (1994)
R134 (CR)	$PH_2 + CRPHOT \rightarrow PH + H$	1.3×10^{-17}	0.0	750.0	McElroy et al. (2013)
R135 (IN)	$H^+ + PH_2 \rightarrow PH_2^+ + H$	1.0×10^{-9}	0.0	0.0	Millar et al. (1991)
R136 (NR)	$H + PH_2 \rightarrow PH + H_2$	6.20×10^{-11}	0.0	318	Kaye & Strobel (1983)
R137 (IN)	$H_3^+ + PH_2 \rightarrow PH_3^+ + H_2$	2.0×10^{-9}	0.0	0.0	Millar et al. (1991)
R138 (IN)	$HCO^+ + PH_2 \rightarrow PH_3^+ + CO$	1.0×10^{-9}	0.0	0.0	Millar et al. (1991)
R139 (IN)	$He^+ + PH_2 \rightarrow P^+ + He + H_2$	1.0×10^{-9}	0.0	0.0	Millar et al. (1991)
R140 (IN)	$PH_2^+ + O_2 \rightarrow PO^+ + H_2O$	7.8×10^{-11}	0.0	0.0	Adams et al. (1990)
R141 (IN)	$H_2 + P^+ \rightarrow PH_2^+ + h\nu$	7.5×10^{-18}	−1.3	0.0	Adams et al. (1990)
R142 (PH)	$PH_2 + h\nu \rightarrow PH_2^+ + e^-$	1.73×10^{-10}	0.0	2.6	McElroy et al. (2013)
R143 (PH)	$PH_2 + h\nu \rightarrow PH + H$	2.11×10^{-10}	0.0	1.5	McElroy et al. (2013)
R144 (DR)	$PH_4^+ + e^- \rightarrow PH_3 + H$	1.50×10^{-7}	−0.5	0.0	Charnley & Millar (1994)
R145 (IN)	$PH_4^+ + NH_3 \rightarrow PH_3 + NH_4^+$	2.10×10^{-9}	0.0	0.0	Thorne et al. (1983)

Reaction Number (Type)	Reactions	Rate coefficient α	β	γ	References
R146 (NR)	$PH_2 + H \rightarrow PH_3$	3.7×10^{-10}	0.0	340	Kaye & Strobel (1983)
R147 (RA)	$H_2 + PH^+ \rightarrow PH_3^+ + h\nu$	2.40×10^{-17}	−1.4	0.0	Adams et al. (1990)
R148 (NR)	$H^+ + PH_3 \rightarrow PH_3^+ + H$	7.22×10^{-11}	0.0	886	Sousa-Silva et al. (2020)
R149 (NR)	$H + PH_3 \rightarrow PH_2 + H_2$	7.22×10^{-11}	0.0	886	Sousa-Silva et al. (2020)
R150 (RR)	$NH_2 + PH_3 \rightarrow PH_2 + NH_3$	1.50×10^{-12}	0.0	928	Kaye & Strobel (1983)
R151 (IN)	$H^+ + PH_3 \rightarrow PH_3^+ + H$	2.00×10^{-9}	0.0	0.0	Charnley & Millar (1994)
R152 (IN)	$He^+ + PH_3 \rightarrow PH_2^+ + H + He$	2.00×10^{-9}	0.0	0.0	Charnley & Millar (1994)
R153 (IN)	$C^+ + PH_3 \rightarrow PH_3^+ + C$	2.00×10^{-9}	0.0	0.0	Charnley & Millar (1994)
R154 (IN)	$H_3^+ + PH_3 \rightarrow PH_4^+ + H_2$	2.00×10^{-9}	0.0	0.0	Charnley & Millar (1994)
R155 (IN)	$HCO^+ + PH_3 \rightarrow PH_4^+ + CO$	2.00×10^{-9}	0.0	0.0	Charnley & Millar (1994)
R156 (IN)	$H_3O^+ + PH_3 \rightarrow PH_4^+ + H_2O$	2.00×10^{-9}	0.0	0.0	Charnley & Millar (1994)
R157 (IN)	$PH_3^+ + PH_3 \rightarrow PH_4^+ + PH_2$	1.10×10^{-9}	0.0	0.0	Smith et al. (1989)
R158 (PH)	$PH_3 + h\nu \rightarrow PH_2 + H$	9.23×10^{-10}	0.0	2.1	McElroy et al. (2013) [UMIST, following NH_3]
R159 (PH)	$PH_3 + h\nu \rightarrow PH + H_2$	2.76×10^{-10}	0.0	2.1	McElroy et al. (2013) [UMIST, following NH_3]
R160 (PH)	$PH_3 + h\nu \rightarrow PH_3^+ + e^-$	2.80×10^{-10}	0.0	3.1	McElroy et al. (2013) [UMIST, following NH_3]
R161 (NR)	$PH_3 + OH \rightarrow H_2O + PH_2$	2.71×10^{-11}	0.0	155	Sousa-Silva et al. (2020)
R162 (DR)	$PC_2H_2^+ + e^- \rightarrow CCP + H_2$	1.0×10^{-7}	−0.5	0.0	McElroy et al. (2013)
R163 (DR)	$PC_2H_3^+ + e^- \rightarrow CCP + H_2 + H$	1.0×10^{-7}	−0.5	0.0	McElroy et al. (2013)
R164 (DR)	$PC_2H_4^+ + e^- \rightarrow CCP + H_2 + H_2$	1.0×10^{-7}	−0.5	0.0	McElroy et al. (2013)
R165 (DR)	$PC_3H^+ + e^- \rightarrow CCP + CH$	1.0×10^{-7}	−0.5	0.0	McElroy et al. (2013)
R166 (DR)	$PC_4H^+ + e^- \rightarrow CCP + C_2H$	7.5×10^{-8}	−0.5	0.0	McElroy et al. (2013)
R167 (CR)	$CCP + CRPHOT \rightarrow C_2 + P$	1.3×10^{-17}	0.0	375.0	McElroy et al. (2013)
R168 (CR)	$CCP + CRPHOT \rightarrow CP + C$	1.3×10^{-17}	0.0	375.0	McElroy et al. (2013)
R169 (IN)	$C^+ + CCP \rightarrow CCP^+ + C$	5.0×10^{-10}	−0.5	0.0	McElroy et al. (2013)
R170 (IN)	$C^+ + CCP \rightarrow CP^+ + C_2$	5.0×10^{-10}	−0.5	0.0	McElroy et al. (2013)
R171 (IN)	$H^+ + CCP \rightarrow CCP^+ + H$	1.0×10^{-9}	−0.5	0.0	McElroy et al. (2013)
R172 (PH)	$CCP + h\nu \rightarrow C_2 + P$	1.0×10^{-10}	0.0	1.7	McElroy et al. (2013)
R173 (PH)	$CCP + h\nu \rightarrow CP + C$	1.0×10^{-9}	0.0	1.7	McElroy et al. (2013)
R174 (IN)	$C^+ + HPO \rightarrow HPO^+ + C$	1.0×10^{-9}	−0.5	0.0	McElroy et al. (2013)
R175 (IN)	$H^+ + HPO \rightarrow HPO^+ + H$	1.0×10^{-9}	−0.5	0.0	McElroy et al. (2013)
R176 (IN)	$H_2O + P^+ \rightarrow HPO^+ + H$	4.95×10^{-10}	−0.5	0.0	McElroy et al. (2013)
R177 (IN)	$H_2O + PH^+ \rightarrow HPO^+ + H_2$	7.44×10^{-10}	−0.5	0.0	McElroy et al. (2013)
R178 (IN)	$H_3O^+ + P \rightarrow HPO^+ + H_2$	1.00×10^{-9}	0.0	0.0	McElroy et al. (2013)
R179 (IN)	$H_2O + PH^+ \rightarrow H_2PO^+ + H$	2.04×10^{-10}	−0.5	0.0	McElroy et al. (2013)
R180 (IN)	$H_2O + PH^+ \rightarrow P + H_3O^+$	2.52×10^{-10}	−0.5	0.0	McElroy et al. (2013)
R181 (IN)	$H_2O + PH_2^+ \rightarrow H_2PO^+ + H_2$	3.28×10^{-10}	−0.5	0.0	McElroy et al. (2013)
R182 (IN)	$H_3^+ + HPO \rightarrow H_2PO^+ + H_2$	1.00×10^{-9}	−0.5	0.0	McElroy et al. (2013)
R183 (IN)	$H_3O^+ + HPO \rightarrow H_2PO^+ + H_2O$	1.00×10^{-9}	−0.5	0.0	McElroy et al. (2013)
R184 (IN)	$HCO^+ + HPO \rightarrow H_2PO^+ + CO$	1.00×10^{-9}	−0.5	0.0	McElroy et al. (2013)
R185 (IN)	$CH_3^+ + P \rightarrow PCH_2^+ + H$	1.0×10^{-9}	0.0	0.0	McElroy et al. (2013)
R186 (IN)	$CH_4 + P^+ \rightarrow PCH_2^+ + H_2$	9.6×10^{-10}	0.0	0.0	McElroy et al. (2013)
R187 (IN)	$H_2 + HCP^+ \rightarrow PCH_2^+ + H$	1.00×10^{-9}	0.0	0.0	McElroy et al. (2013)
R188 (DR)	$PCH_3^+ + e^- \rightarrow CP + H_2 + H$	1.5×10^{-7}	−0.5	0.0	McElroy et al. (2013)
R189 (DR)	$PCH_3^+ + e^- \rightarrow HCP + H_2$	1.5×10^{-7}	−0.5	0.0	McElroy et al. (2013)
R190 (DR)	$PCH_3^+ + e^- \rightarrow P + CH_3$	3.0×10^{-7}	−0.5	0.0	McElroy et al. (2013)
R191 (IN)	$CH_4 + PH^+ \rightarrow PCH_3^+ + H_2$	1.05×10^{-9}	0.0	0.0	McElroy et al. (2013)
R192 (IN)	$H^+ + CH_2PH \rightarrow PCH_3^+ + H$	1.00×10^{-9}	0.0	0.0	McElroy et al. (2013)
R193 (DR)	$PCH_4^+ + e^- \rightarrow CH_2PH + H_2 + H$	1.5×10^{-7}	−0.5	0.0	McElroy et al. (2013)
R194 (DR)	$PCH_4^+ + e^- \rightarrow HCP + H_2 + H$	1.5×10^{-7}	−0.5	0.0	McElroy et al. (2013)
R195 (DR)	$PCH_4^+ + e^- \rightarrow P + CH_4$	3.0×10^{-7}	−0.5	0.0	McElroy et al. (2013)
R196 (IN)	$CH_4 + PH^+ \rightarrow PCH_4^+ + H$	5.5×10^{-11}	0.0	0.0	McElroy et al. (2013)
R197 (IN)	$CH_4 + PH_2^+ \rightarrow PCH_4^+ + H_2$	1.1×10^{-9}	0.0	0.0	McElroy et al. (2013)
R198 (IN)	$H_3^+ + CH_2PH \rightarrow PCH_4^+ + H_2$	1.00×10^{-9}	0.0	0.0	McElroy et al. (2013)
R199 (IN)	$H_3O^+ + CH_2PH \rightarrow PCH_4^+ + H_2O$	1.00×10^{-9}	0.0	0.0	McElroy et al. (2013)
R200 (IN)	$HCO^+ + CH_2PH \rightarrow PCH_4^+ + CO$	1.00×10^{-9}	0.0	0.0	McElroy et al. (2013)
R201 (IN)	$H^+ + HC_2P \rightarrow HC_2P^+ + H$	1.00×10^{-9}	0.0	0.0	McElroy et al. (2013)
R202 (CR)	$HC_2P + CRPHOT \rightarrow CCP + H$	1.3×10^{-17}	0.0	750.0	McElroy et al. (2013)
R203 (DR)	$PC_2H_2^+ + e^- \rightarrow HC_2P + H$	1.0×10^{-7}	−0.5	0.0	McElroy et al. (2013)
R204 (DR)	$PC_2H_3^+ + e^- \rightarrow HC_2P + H_2$	1.0×10^{-7}	−0.5	0.0	McElroy et al. (2013)
R205 (DR)	$PC_2H_4^+ + e^- \rightarrow HC_2P + H_2 + H$	1.0×10^{-7}	−0.5	0.0	McElroy et al. (2013)
R206 (DR)	$PC_3H^+ + e^- \rightarrow HC_2P + C$	1.0×10^{-7}	−0.5	0.0	McElroy et al. (2013)
R207 (IN)	$C^+ + HC_2P \rightarrow CCP^+ + CH$	5.00×10^{-10}	0.0	0.0	McElroy et al. (2013)
R208 (IN)	$C^+ + HC_2P \rightarrow CP^+ + C_2H$	5.00×10^{-10}	0.0	0.0	McElroy et al. (2013)
R209 (IN)	$H_3^+ + HC_2P \rightarrow PC_2H_2^+ + H_2$	1.00×10^{-9}	0.0	0.0	McElroy et al. (2013)
R210 (IN)	$H_3O^+ + HC_2P \rightarrow PC_2H_2^+ + H_2O$	1.00×10^{-9}	0.0	0.0	McElroy et al. (2013)
R211 (IN)	$HCO^+ + HC_2P \rightarrow PC_2H_2^+ + CO$	1.00×10^{-9}	0.0	0.0	McElroy et al. (2013)
R212 (IN)	$He^+ + HC_2P \rightarrow CP^+ + CH + He$	5.00×10^{-10}	0.0	0.0	McElroy et al. (2013)
R213 (IN)	$He^+ + HC_2P \rightarrow CP + CH^+ + He$	5.00×10^{-10}	0.0	0.0	McElroy et al. (2013)
R214 (NN)	$O + HC_2P \rightarrow HCP + CO$	4.00×10^{-11}	0.0	0.0	McElroy et al. (2013)
R215 (PH)	$HC_2P + h\nu \rightarrow CCP + H$	5.48×10^{-10}	0.0	2.0	McElroy et al. (2013)
R216 (IN)	$H^+ + C_4P \rightarrow C_4P^+ + H$	1.00×10^{-9}	−0.5	0.0	McElroy et al. (2013)
R217 (CR)	$C_4P + CRPHOT \rightarrow C_3P + C$	1.3×10^{-17}	0.0	750.0	McElroy et al. (2013)
R218 (DR)	$PC_4H^+ + e^- \rightarrow C_4P + H$	7.50×10^{-8}	−0.5	0.0	McElroy et al. (2013)
R219 (IN)	$H_3^+ + C_4P \rightarrow PC_4H^+ + H_2$	1.00×10^{-9}	−0.5	0.0	McElroy et al. (2013)

Reaction Number (Type)	Reactions	Rate coefficient α	β	γ	References
R220 (IN)	$H_3O^+ + C_4P \rightarrow PC_4H^+ + H_2O$	1.00×10^{-9}	−0.5	0.0	McElroy et al. (2013)
R221 (IN)	$HCO^+ + C_4P \rightarrow PC_4H^+ + CO$	1.00×10^{-9}	−0.5	0.0	McElroy et al. (2013)
R222 (IN)	$He^+ + C_4P \rightarrow CCP^+ + C_2 + He$	5.00×10^{-10}	−0.5	0.0	McElroy et al. (2013)
R223 (IN)	$He^+ + C_4P \rightarrow CCP + C_2^+ + He$	5.00×10^{-10}	−0.5	0.0	McElroy et al. (2013)
R224 (NN)	$O + C_4P \rightarrow C_3P + CO$	1.00×10^{-11}	0.0	0.0	McElroy et al. (2013)
R225 (PH)	$C_4P + h\nu \rightarrow C_3 + CP$	5.48×10^{-10}	0.0	1.7	McElroy et al. (2013)
R226 (CR)	$C_3P + CRPHOT \rightarrow CCP + C$	1.3×10^{-17}	0.0	750.0	McElroy et al. (2013)
R227 (DR)	$C_4P^+ + e^- \rightarrow C_3P + C$	1.50×10^{-7}	−0.5	0.0	McElroy et al. (2013)
R228 (DR)	$PC_3H^+ + e^- \rightarrow C_3P + H$	1.00×10^{-7}	−0.5	0.0	McElroy et al. (2013)
R229 (DR)	$PC_4H^+ + e^- \rightarrow C_3P + CH$	7.50×10^{-8}	−0.5	0.0	McElroy et al. (2013)
R230 (IN)	$H_3^+ + C_3P \rightarrow PC_3H^+ + H_2$	1.00×10^{-9}	−0.5	0.0	McElroy et al. (2013)
R231 (IN)	$H_3O^+ + C_3P \rightarrow PC_3H^+ + H_2O$	1.00×10^{-9}	−0.5	0.0	McElroy et al. (2013)
R232 (IN)	$HCO^+ + C_3P \rightarrow PC_3H^+ + CO$	1.00×10^{-9}	−0.5	0.0	McElroy et al. (2013)
R233 (IN)	$He^+ + C_3P \rightarrow C_3^+ + P + He$	5.00×10^{-10}	−0.5	0.0	McElroy et al. (2013)
R234 (IN)	$He^+ + C_3P \rightarrow C_3 + P^+ + He$	5.00×10^{-10}	−0.5	0.0	McElroy et al. (2013)
R235 (NN)	$O + C_3P \rightarrow CCP + CO$	4.00×10^{-11}	0.0	0.0	McElroy et al. (2013)
R236 (PH)	$C_3P + h\nu \rightarrow C_2 + CP$	5.00×10^{-10}	0.0	1.8	McElroy et al. (2013)
R237 (CR)	$CH_2PH + CRPHOT \rightarrow HCP + H_2$	1.3×10^{-17}	0.0	750.0	McElroy et al. (2013)
R238 (IN)	$C^+ + CH_2PH \rightarrow HC_2P^+ + H_2$	1.00×10^{-9}	0.0	0.0	McElroy et al. (2013)
R239 (IN)	$He^+ + CH_2PH \rightarrow PH^+ + CH_2 + He$	5.00×10^{-10}	0.0	0.0	McElroy et al. (2013)
R240 (IN)	$He^+ + CH_2PH \rightarrow PH + CH_2^+ + He$	5.00×10^{-10}	0.0	0.0	McElroy et al. (2013)
R241 (NN)	$O + CH_2PH \rightarrow PH_2 + CO + H$	4.00×10^{-11}	0.0	0.0	McElroy et al. (2013)
R242 (PH)	$CH_2PH + h\nu \rightarrow CH_2 + PH$	9.54×10^{-10}	0.0	1.8	McElroy et al. (2013)
R243 (DR)	$PC_2H_2^+ + e^- \rightarrow P + C_2H_2$	1.00×10^{-7}	−0.5	0.0	McElroy et al. (2013)
R244 (IN)	$C_2H_2 + PH^+ \rightarrow PC_2H_2^+ + H$	1.30×10^{-9}	0.0	0.0	McElroy et al. (2013)
R245 (IN)	$C_2H_2 + PH_2^+ \rightarrow PC_2H_2^+ + H_2$	1.40×10^{-9}	0.0	0.0	McElroy et al. (2013)
R246 (IN)	$C_2H_2 + PH_3^+ \rightarrow PC_2H_3^+ + H_2$	5.80×10^{-10}	0.0	0.0	McElroy et al. (2013)
	Ice-phase/grain-surface pathways				
R1	$gH + gP \rightarrow gPH$	-	-	-	Chantzos et al. (2020)
R2	$gH + gPH \rightarrow gPH_2$	-	-	-	Chantzos et al. (2020)
R3	$gH + gPH_2 \rightarrow gPH_3$	-	-	-	Chantzos et al. (2020)
R4	$gH + gPH_3 \rightarrow gPH_2 + gH_2$	-	-	-	This work, Sousa-Silva et al. (2020)
R5	$gOH + gPH_3 \rightarrow gPH_2 + gH_2O$	-	-	-	This work, Sousa-Silva et al. (2020)
R6	$gPH_3 \rightarrow PH_3$	-	-	-	Chantzos et al. (2020)

Note:
CR refers to cosmic-rays, IN to ion − neutral reactions, NR to neutral − radical reactions, NN to neutral − neutral reactions, RR to radical − radical reactions, RA to radiative association reactions, ER to electronic recombination reactions for atomic ions, DR to dissociative recombination reactions for molecular ions, PH to photodissociation reactions, hν to a photon.
Grain surface species are denoted by the letter "g".

Table 4.16: Calculated BE (with MP2/aug-cc-pVDZ level of theory) and enthalpy of formation [with DFT-B3LYP/6-31G(d,p) level of theory] of P-bearing species (Sil et al., 2021).

Serial No.	Species	Astronomical status	Ground state	Binding Energy [Kelvin]						Enthalpy of formation [kJ/mol]	
				CO monomer	CH_3OH monomer	H_2O monomer	H_2O tetramer	H_2 monomer	Available[d]	Our calculated	Available[d]
1.	P	-	quartet	170	442	270	616[c]	107	1100	315.557[a], 310.202[b]	315.663[a], 316.5[b]
2.	P_2	not observed	singlet	378	904	494	1671	223	-	182.260[a], 180.434[b]	145.8[a]
3.	PN	observed	singlet	324	2560	2326	2838	399	1900	218.985[a], 217.974[b]	172.48[a], 171.487[b]
4.	PO	observed	doublet	703	4334	2818	4600	508	1900	13.483[a], 12.490[b]	-27.548[a], -27.344[b]
5.	HCP	observed	singlet	572	2122	1723	2468	132	2350	251.466[a], 250.054[b]	217.79[a], 216.363[b]
6.	CP	observed	doublet	300	1335	1126	1699[c]	165	1900	538.388[a], 540.696[b]	517.86[a], 520.162[b]
7.	CCP	observed	doublet	2181	3900	2701	2868	396	4300	660.424[a], 664.413[b]	-
8.	HPO	not observed	singlet	602	4097	2838	5434	521	2350	-38.035[a], -41.915[b]	-89.9[a], -93.7[b]
9.	PH	not observed	triplet	270	780	491	944[c]	134	1550	228.785[a], 227.878[b]	231.698[a], 230.752[b]
10.	PH_2	not observed	doublet	285	851	965	1226[c]	138	2000	128.872[a], 125.036[b]	139.333[a], 135.474[b]
11.	PH_3	observed	singlet	716	952	606	1672	545	-	12.934[a], 5.006[b]	13.4[a]

Note:
[a] Enthalpy of formation at T = 0 K and 1 atmosphere pressure.
[b] Enthalpy of formation at T = 298 K and 1 atmosphere pressure.
[c] Das et al. (2018).
[d] KIDA (http://kida.astrophy.u-bordeaux.fr).

4.3.2 The binding energy of P-bearing species

A continuous exchange of chemical ingredients within the gas and grain can determine the chemical complexity of the ISM. BEs of a species with a grain substrate are essential for constructing a chemical model. However, most COMs are primarily produced on the dust surface and further desorbed back to the gas phase (Requena-Torres et al., 2006). The major drawback in constraining this chemical process by astrochemical modeling is the lack of information about the interaction energy of the chemical species with the grain surface.

A sizable portion ($\sim 60 - 70\%$ of the surface coverage) of the icy interstellar layers may contain water molecules. That is why the BE of the interstellar species is usually expressed with the H_2O surface. However, the rest ($\sim 30 - 40\%$) of the grain mantle would comprise of other impurities such as CO_2, CO, and CH_3OH (Furuya & Persson, 2018). Keane et al. (2001) summarized the relative abundance of CO, CO_2, and CH_3OH concerning water ice could vary in the range of $0.4 - 15$, $0.17 - 21$, and $1.5 - 30$, respectively, in different lines of sight. So, the BE with these surface species is also required in the various evolutionary phases. Therefore, the surface coverage-dependent BEs are indeed needed to consider, which are not considered here.

The BEs of the interstellar species with the different substrates are unknown. Looking at these aspects, in Table 4.16, we report the BEs of some relevant P-bearing species by considering H_2O, CO, CH_3OH, and H_2 as a substrate. The computed BEs should have a range of values that depend on the position of the molecule on the ice (Das et al., 2018; Ferrero et al., 2020). Whenever we obtain different BE values at other binding sites, we exert the average of some of our calculations (see Table 4.16). In this work, we only consider the BE with water substrate for our simulation. BEs with the other substrates are provided for future usage. We perform all the BE calculations by the Gaussian 09 suite of programs (Frisch et al., 2013) using the formulae 2.1 and 2.2 mentioned earlier (see section 2.1.1). To find the optimized energy of all structures, we use the MP2/aug-cc-pVDZ level of theory (Dunning, 1989). We do not include the ZPVE and BSSE corrections. A fully optimized ground-state structure is verified as a stationary point (having nonimaginary frequency) by harmonic vibrational frequency analysis. The ground-state spin multiplicity of the species is also noted in Table 4.16.

Due to the similarities between the structures of NH_3 and PH_3, Chantzos et al. (2020) considered the BE of PH_3 same as NH_3. The BE of NH_3 is 5800 K, according to the KIDA. Since they also used this as BE of PH_3, they did not obtain much PH_3

by thermal desorption process in the cold regions. They pointed out that most of the PH_3 came to the gas phase by photo-desorption rather than thermal desorption from the colder region. Our calculation finds a noticeable decrease in the BE of PH_3, which could enable PH_3 to populate the gas phase by thermal desorption even at low temperatures. Das et al. (2018) noted BE of NH_3 with a c-hexamer configuration of water $\sim$ 5163 K in Table 2.10, whereas we find it $\sim$ 2395 K for PH_3. With significant ice constituents (monomer of CO, CH_3OH, H_2O, and H_2), our computed BE of PH_3 seems to be $<$ 1000 K. Sousa-Silva et al. (2020) noted that PH_3 has very low water solubility (at 17 °C only 22.8 ml of gaseous PH_3 dissolves in 100 ml of water), and it does not easily stick to aerosols. The recent claim of PH_3 in the Venusian atmosphere (Greaves et al., 2020) prompted us to determine the PH_3 BE considering some other species such as sulfuric acid (H_2SO_4) and Benzene (C_6H_6), which are the principal constituents of the Venus atmosphere. Our computed BE with H_2SO_4 and benzene is $\sim$ 2271 K and $\sim$ 3094 K, respectively. However, Snellen et al. (2020) and Villanueva et al. (2020) questioned the identification of Greaves et al. (2020). Table 4.16 also provides our calculated enthalpy of formation for several P-bearing species.

4.3.3 Chemical model

We use the reaction pathways shown in Table 4.15 to check the fate of the P-bearing species in various parts of the ISM (diffuse cloud, PDR, hot-core, and hot-corino). Here, we employ mainly two models using two different codes to study the chemical evolution of these species: a) the spectral synthesis code Cloudy (version 17.02, last described by Ferland et al., 2017) and b) the CMMC code (Sil et al., 2018, 2021; Das et al., 2019, 2021; Gorai et al., 2020b; Shimonishi et al., 2020).

Spectral synthesis code, Cloudy

We use a photoionization code, Cloudy, which simulates matter under a broad range of interstellar conditions. Using the Cloudy code, we check the fate of P-bearing species in the diffuse cloud and PDR environment.

Diffuse cloud model

Chantzos et al. (2020) prepared a diffuse cloud model to explain the observed abundance of HNC, CN, CS, and CO. We also employ a similar process to explain

Table 4.17: Initial elemental abundance for the diffuse cloud and PDR model considered in the CLOUDY code (Sil et al., 2021).

Element	Abundance	Element	Abundance
H	1.0	Si	3.2×10^{-5}
He	8.5×10^{-2}	Fe	3.2×10^{-5}
N	6.8×10^{-5}	Na	1.7×10^{-6}
O	4.9×10^{-4}	Mg	3.9×10^{-5}
C	2.7×10^{-4}	Cl	3.2×10^{-7}
S	1.3×10^{-5}	P	2.6×10^{-7}
		F	3.6×10^{-8}

the observed abundances of the four molecules and then look at the fate of the P-bearing molecules under similar circumstances. We consider the initial elemental abundance for this modeling as given in Chantzos et al. (2020). But in CLOUDY, only the atomic elemental abundance is allowed (no ionic or molecular form), so we use these abundances as the initial elemental abundance (see Table 4.17). For each calculation, we check whether the microphysics considered is time steady or not. We notice that the largest reaction timescale is much shorter than the typical lifetime ($\sim 10^7$ years) of the diffuse cloud. We use the grain size distribution, which is appropriate for the $R_V = 3.1$ extinction curve of Mathis et al. (1977). This grain size distribution is called "ISM" in CLOUDY. We use the anisotropic radiation field, which is appropriate for the ISM to specify the incident local ISRF. Additionally, we include the cosmic-ray microwave background with a redshift value of 1.52 (Wenger et al., 2000).

To check our model against the observed abundances, we first explain the observed abundance of CO, CN, CS, and HNC as obtained in Chantzos et al. (2020). For this, we use a parameter space for the formation of these species. Our parameter space consists of a density variation of $100 - 600$ cm^{-3} and a cosmic-ray ionization rate of H_2 (ζ_{H_2}) variation of $10^{-17} - 10^{-14}$ s^{-1}. We use a stopping criterion at different A_V values. The cases obtained by using stopping criterion $A_V = 1 - 5$ mag are given in Figure 4.27. The contours highlight the observed abundances of CO, CN, CS, and HNC of Chantzos et al. (2020) toward the cloud having a $V_{LSR} = -17$ km s^{-1}. Figure 4.28 shows the temperature variation at the end of the calculation for $A_V = 1 - 3$ mag. The parameter space also consists of the variation of n_H and ζ_{H_2}. Temperature variation is shown with the color bar.

From Figures 4.27 and 4.28, we see that the parameters that were adopted by Chantzos et al. (2020) for the diffuse cloud model (i.e., $\zeta_{H_2} = 1.7 \times 10^{-16}$ s^{-1}, $n_H = 300$ cm^{-3}, and $T_{gas} = 40$ K) can also reproduce the observed abundances of CO, CN, CS, and HNC with our model. Figure 4.29 shows the obtained abundances

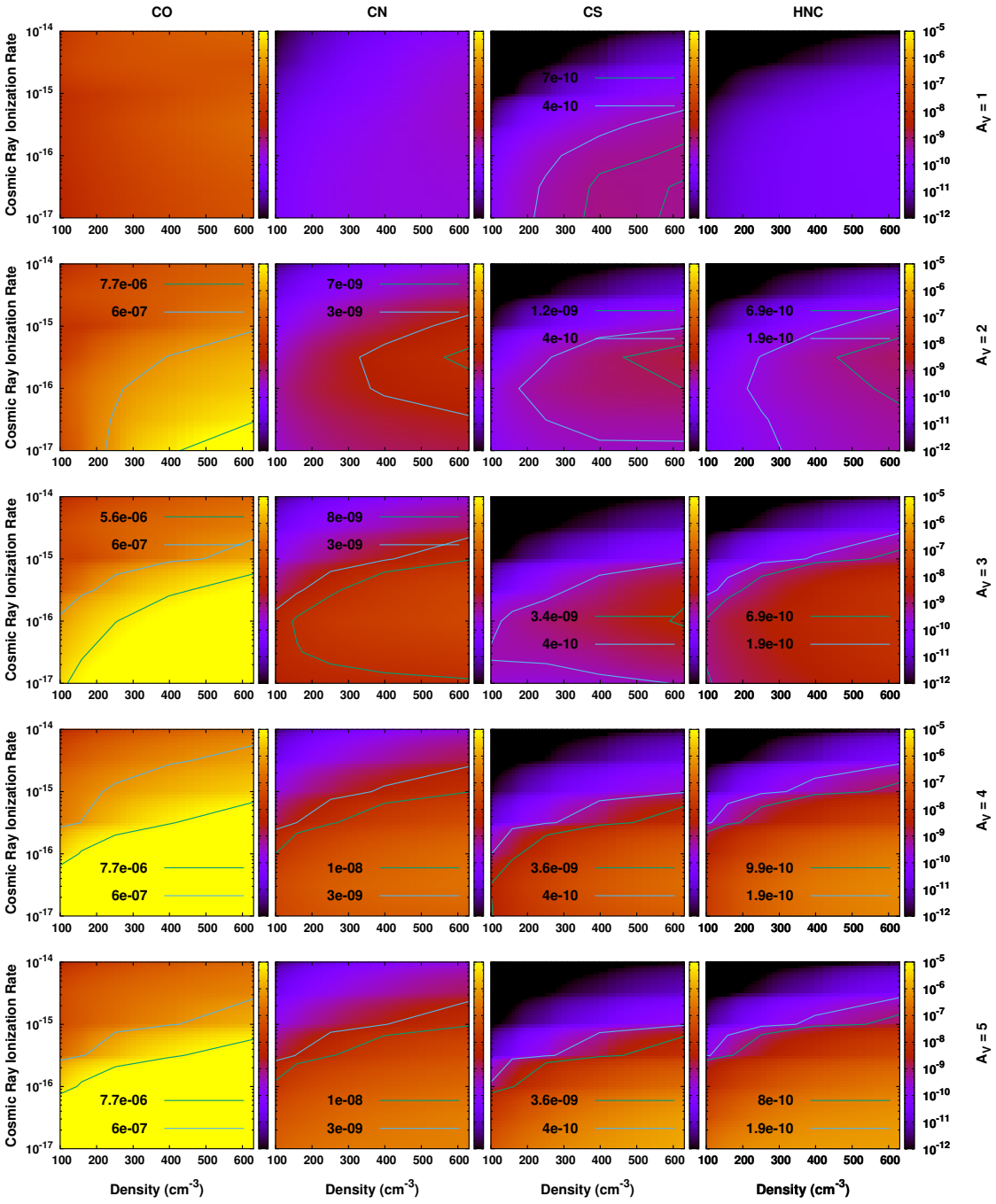

Figure 4.27: Parameter space of the abundances of CO, CN, CS, and HNC for $A_V = 1,\ 2,\ 3,\ 4,\ 5$ mag for the diffuse cloud model obtained with the CLOUDY code (Sil et al., 2021). The right side of each panel is marked with color-coded values of abundance concerning total hydrogen nuclei. The contours are highlighted around the previously observed abundance limit (Chantzos et al., 2020) toward the cloud with $v_{LSR} = -17$ km s^{-1}, including the inferred uncertainties.

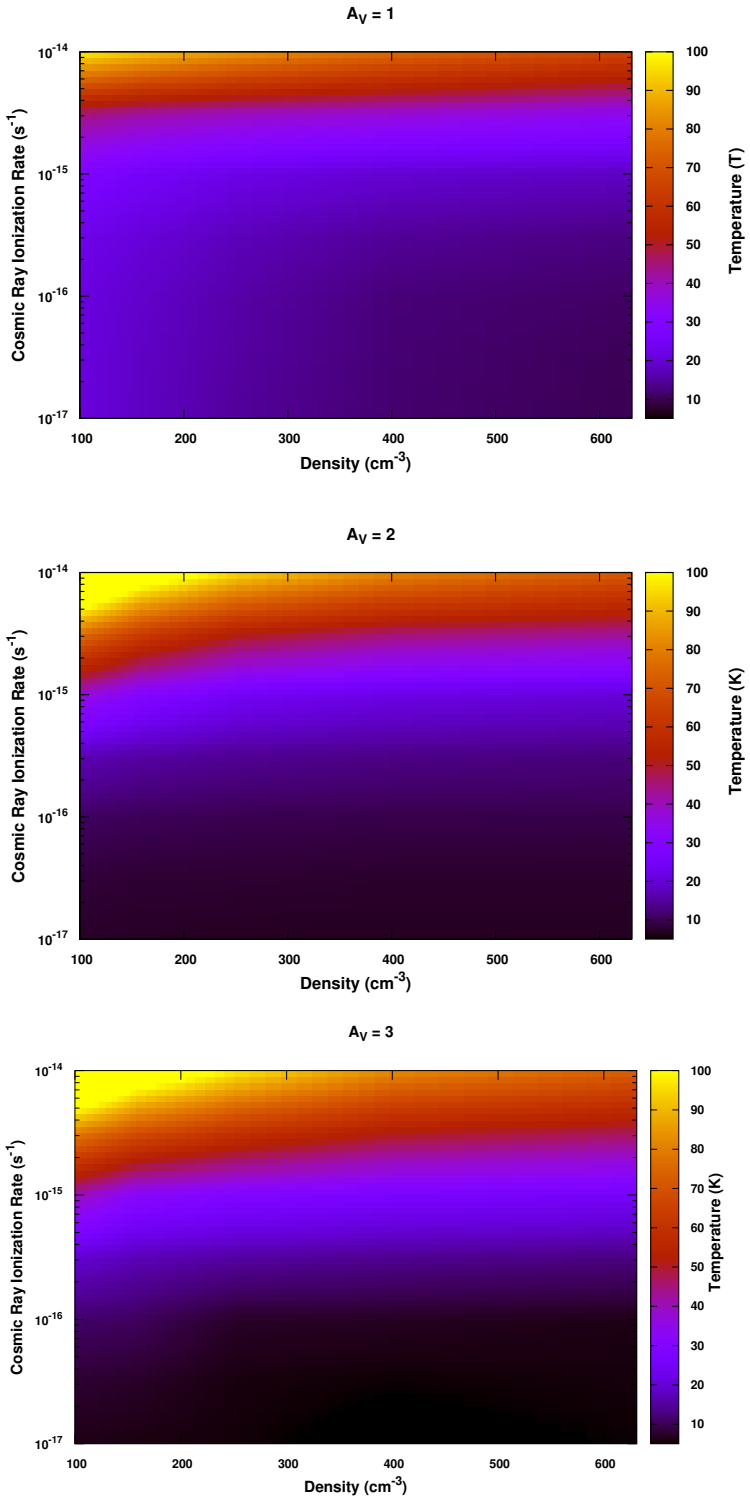

Figure 4.28: Parameter space of the temperature for A_V = 1, 2, 3 mag for the diffuse cloud model obtained with the CLOUDY code (Sil et al., 2021). The right side of each panel is marked with color-coded values of temperature.

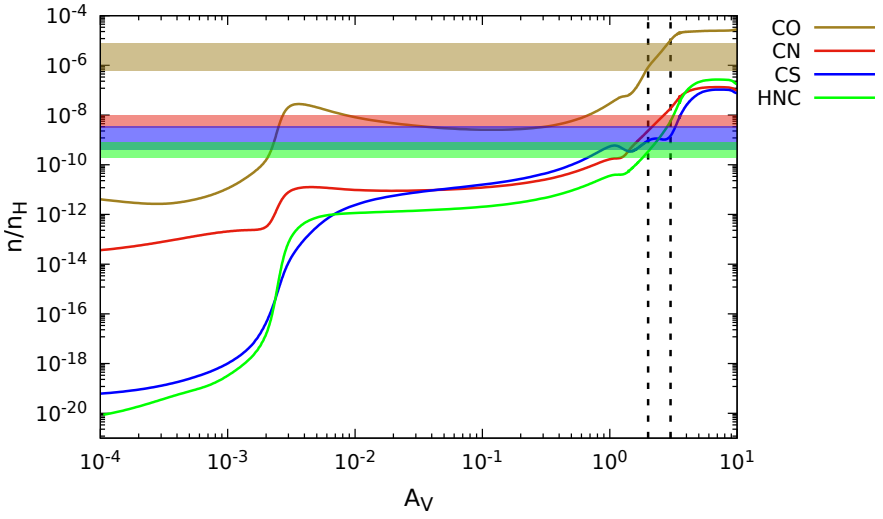

Figure 4.29: Chemical evolution of the abundances of CO, CN, CS, and HNC for the diffuse cloud model ($n_H = 300$ cm^{-3} and $\zeta = 1.7 \times 10^{-16}$ s^{-1}) with the CLOUDY code. The colored horizontal bands correspond to the observed abundances (Chantzos et al., 2020) toward the cloud with $v_{LSR} = -17$ km s^{-1}, including the inferred uncertainties (Sil et al., 2021). Here, the vertical dashed line indicates the visual extinction parameter of best agreement between observation and model results.

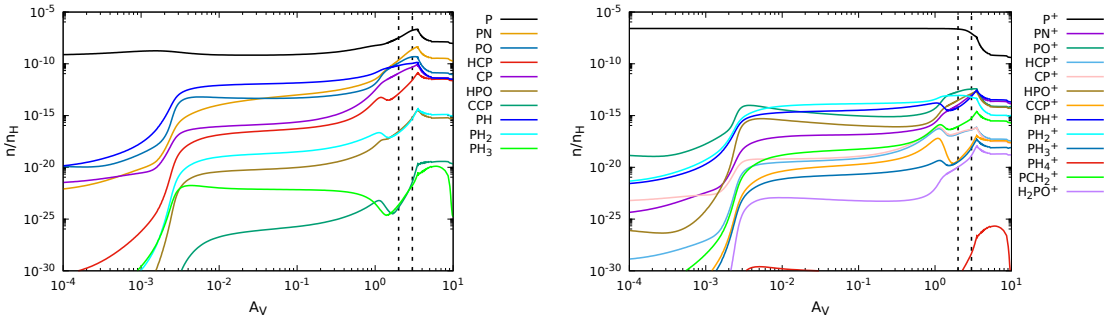

Figure 4.30: Chemical evolution of the abundances of neutral P-bearing species (left panel) and their corresponding cations (right panel) for the diffuse cloud model ($n_H = 300$ cm^{-3} and $\zeta = 1.7 \times 10^{-16}$ s^{-1}) with the CLOUDY code (Sil et al., 2021). Here, the vertical dashed line indicates the visual extinction parameter of the best agreement between observation and model results.

Table 4.18: Estimated column density and optical depth of the observed molecules for the diffuse cloud model obtained with the CLOUDY code (Sil et al., 2021).

Species	Transitions	E_{up} (K)	Frequency (GHz)	Optical Depth (τ)		Total Column Density (cm^{-2})	
				Model	Observation[a]	Model	Observation[a]
CN	$N = 1 - 0,\ J = 1/2 - 1/2,\ F = 3/2 - 1/2$	5.5	113.16867	0.256522	0.23 ± 0.07	1.47×10^{12}	$(0.87 \pm 0.28) \times 10^{13}$
HNC	$J = 1 - 0$	4.4	90.66357	0.33962	0.50 ± 0.10	2.11×10^{11}	$(0.69 \pm 0.16) \times 10^{12}$
$C^{34}S$	$J = 2 - 1$	6.9	96.41295	-	0.04 ± 0.02	-	$(1.64 \pm 0.82) \times 10^{11}$
^{13}CO	$J = 1 - 0$	5.3	110.20135	-	0.154 ± 0.004	-	$(3.98 \pm 0.16) \times 10^{14}$
HCP	$J = 2 - 1$	5.8	79.90329	2.56×10^{-6}	< 0.02	1.10×10^{8}	$< 2.27 \times 10^{12}$
PN	$J = 2 - 1$	6.8	93.97977	0.238015	< 0.02	1.62×10^{11}	$< 4.20 \times 10^{10}$
CP	$N = 2 - 1,\ J = 3/2 - 1/2,\ F = 2 - 1$	6.8	95.16416	4.92×10^{-4}	< 0.02	1.16×10^{10}	$< 1.26 \times 10^{12}$
PO	$J = 5/2 - 3/2,\ \Omega = 1/2,\ F = 3 - 2,\ e$	8.4	108.99845	0.0138432	< 0.02	9.08×10^{10}	$< 4.29 \times 10^{11}$
PO	$J = 5/2 - 3/2,\ \Omega = 1/2,\ F = 2 - 1,\ e$	8.4	109.04540	0.0125113	< 0.02	9.08×10^{10}	$< 6.70 \times 10^{11}$
PO	$J = 5/2 - 3/2,\ \Omega = 1/2,\ F = 3 - 2,\ f$	8.4	109.20620	0.0055508	< 0.02	9.08×10^{10}	$< 4.34 \times 10^{11}$
PO	$J = 5/2 - 3/2,\ \Omega = 1/2,\ F = 2 - 1,\ f$	8.4	109.28119	0.0182699	< 0.02	9.08×10^{10}	$< 6.69 \times 10^{11}$

Note: [a] Chantzos et al. (2020)

of the four molecules when we consider $n_H = 300$ cm^{-3} and $\zeta_{H_2} = 1.7 \times 10^{-16}$ s^{-1}. The X-axis shows the visual extinction of the cloud, and the Y-axis shows the abundance of n_H. Our results are in agreement with the observation between $A_V = 2$ and 3 mag. We highlight the best-suited zone by the black dashed curve. Thus, based on Figures 4.27, 4.28, and 4.29, we use $A_V = 2$ mag, $\zeta_{H_2} = 1.7 \times 10^{-16}$, and $n_H = 300$ cm^{-3} as the best-fitted parameters to explain the observed abundances of these species. This yields a $A_V/N(H) = 5.398 \times 10^{-22}$ mag cm^2 and dust to gas ratio of 6.594×10^{-3}. Table 4.18 compares our obtained optical depth and column densities with the observations. Obtained optical depths of CN and HNC are close to the observed values, but the column densities diverge by a few factors. This slight mismatch is because the CLOUDY model deals with steady-state values, but the column densities are time dependent in reality.

Figure 4.30 depicts the abundances of most of the P-bearing species considered in this study. The left panel shows the neutral P-bearing species, whereas the right panel shows the P-bearing ions. Interestingly, although we consider a neutral atomic abundance in our model, the abundance of P^+ is high owing to the strong cosmic-ray ionization and presence of a nonextinguished ISRF. The abundances of the comparatively larger P-bearing species are very low in the diffuse environment, and it would be pretty challenging to observe them. We notice that some simple neutral P-bearing species, such as PN, PO, HCP, CP, and PH are significantly more abundant than PH_3. The abundances of PO and PN appear to be comparable to each other (with PO/PN < 1 when $A_V \geq 2$). The obtained column densities for this case are listed in Table 4.18. There is an excellent agreement between the observed and the modeled optical depths of CN and HNC with the CLOUDY code.

In Figure 4.31, H, H_2, and N abundances are shown along with the major

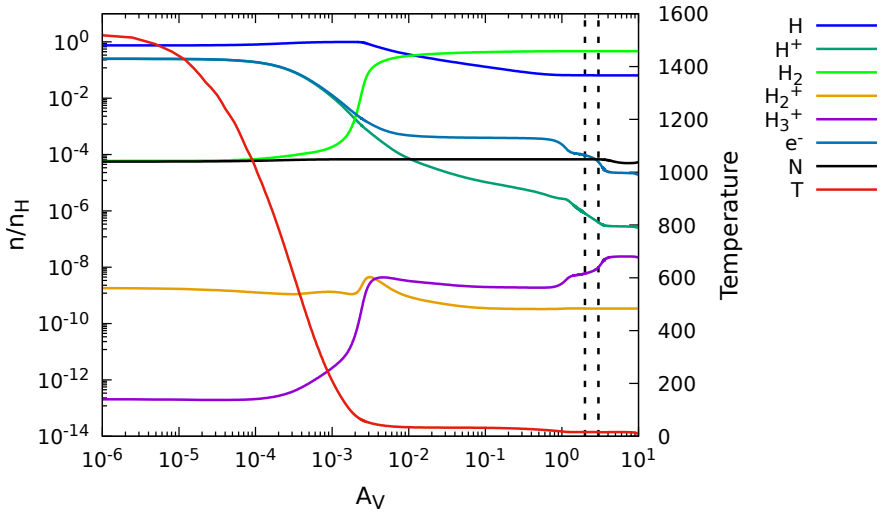

Figure 4.31: Abundance profiles of H, H^+, H_2, H_2^+, H_3^+, e^-, and N and temperature profile for the diffuse cloud model ($n_H = 300$ cm^{-3} and $\zeta = 1.7 \times 10^{-16}$ s^{-1}) with the CLOUDY code (Sil et al., 2021). The vertical dashed line indicates the visual extinction parameter of best agreement between observation and model results.

hydrogen-related ions, H^+, $H_2{}^+$, $H_3{}^+$. In CLOUDY, the cloud temperature is calculated self-consistently, depending on the known excitations. The primary source of such excitation is cosmic-ray ionization. Figure 4.31 depicts the gas temperature variation with A_V with the solid red curve. Deep inside the cloud, the temperature drops sufficiently and enhances the formation of molecular hydrogen. For $A_V = 2$ mag, we obtain a temperature of ~ 10 K when we use a cosmic-ray ionization rate of 1.7×10^{-16} s^{-1}. It is a little lower than that used in Chantzos et al. (2020).

PDR model

We use the CLOUDY code to explain the abundances of the P-bearing species in the PDRs. The CLOUDY code is capable of considering realistic physical conditions around this region. Röllig et al. (2007) included various PDR benchmark models, giving a range of physical conditions associated with PDR environments. We chose the F4 model. This model considers a constant gas temperature of 50 K and dust temperature of 20 K. A plane-parallel, semi-infinite cloud with total constant density of $10^{5.5}$ cm^{-3}, and standard UV field as $\chi = 10^5$ times the Draine (1978) field ($\chi = 1.71 G_0$) is considered. The cosmic-ray H ionization rate $\zeta = 5 \times 10^{-17}$ s^{-1}, the visual extinction $A_V = 6.289 \times 10^{-22} N_{H,tot}$, and a dust-to-gas ratio of 7.646×10^{-3}

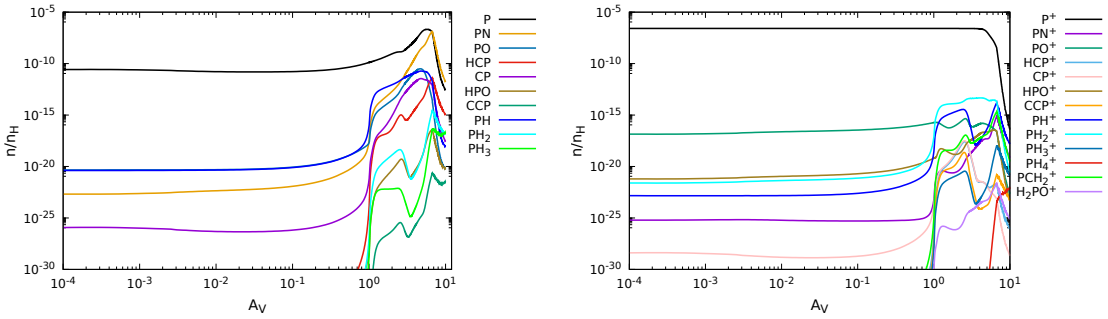

Figure 4.32: Chemical evolution of the abundances of important P-bearing species with the CLOUDY code considering Röllig et al. (2007) F4 PDR model (Sil et al., 2021).

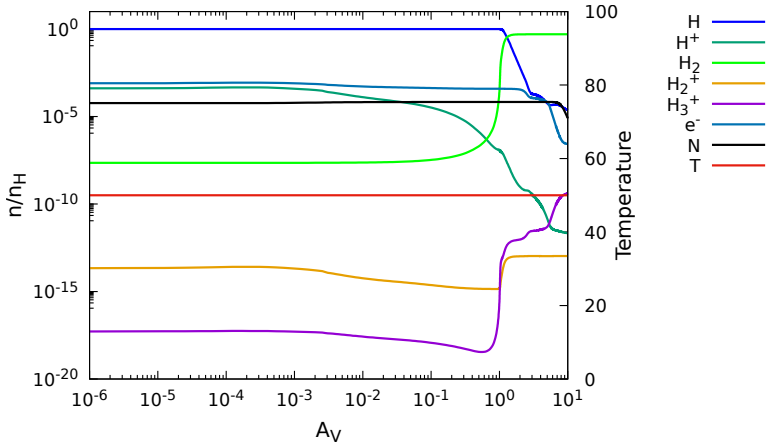

Figure 4.33: Abundance profiles of H, H^+, H_2, H_2^+, H_3^+, e^-, N, and temperature profile with the CLOUDY code considering the Röllig et al. (2007) F4 PDR model (Sil et al., 2021).

are assumed. We also consider these physical parameters and the initial elemental abundances as considered in our diffuse cloud model (Table 4.17). Figure 4.32 shows the abundances of important P-bearing species. In the diffuse cloud region (see Figure 4.30), we obtain PO and PN comparable abundances. However, for the PDR model, we find a very high abundance of PN compared to PO. Its peak abundance appears to be higher by several orders of magnitude than PO (i.e., PO/PN $<<$ 1). We use the photodestruction rate of PO and PN from Jiménez-Serra et al. (2018). The photodissociation rate of PO is estimated from the photodissociation rate of NO. Similarly, the photodissociation rate of PN is estimated from the photodissociation rate of N_2. These values reflect a higher photodissociation rate of PO (with $\alpha = 3 \times 10^{-10}$ s^{-1} and $\gamma = 2.0$) than PN (with $\alpha = 5 \times 10^{-12}$ s^{-1} and $\gamma = 3.0$). As in Jiménez-Serra et al. (2018), here, we also find that even if PN is photodissociated, it revert again via P + CN $\rightarrow$ PN + C owing to the presence of a large amount of atomic P in the gas phase. The rapid conversion of PO to PN by the reaction PO + N $\rightarrow$ PN + O is also crucial for maintaining a higher abundance of PN than PO.

It is not straightforward to relate the diffuse cloud region cases with the PDR because of different physical circumstances. In the diffuse cloud model, we obtain the peak abundances of PO and PN at $A_V = 2 - 3$ mag, whereas in the PDR model, we receive these peaks around $A_V = 6 - 7$ mag. In both cases, the PO/PN ratio is < 1, but this ratio seems to be $<<$ 1 for the PDR. Jiménez-Serra et al. (2018) also modeled the effect of intense UV photon illumination by varying the ISRF within ranges typical of PDRs. They showed for higher extinctions ($A_V = 7.5$ mag), and under high-UV radiation fields ($\chi = 10^4$ Habing) that the abundance of PN always remains above that of PO for both long-lived and short-lived collapse stages. Figure 4.33 shows H, H^+, H_2, $H_2{}^+$, $H_3{}^+$, N, and electrons abundances.

CMMC code

In the previous section, we implement CLOUDY code to study the chemical evolution of the P-bearing species in the diffuse cloud region. Comparatively larger P-bearing species are not very profuse in space, which creates a burden constraining the understanding of the P-bearing species of the ISM. The major drawback in the P-chemistry modeling is the uncertainty of the P depletion factor. The grain-surface chemistry plays a significant role in shaping the chemical complexity in these regions.

Since CLOUDY only considers the surface reactions of some key species, it would be impractical to apply the CLOUDY code in the dense cloud region. Thus, we use

Table 4.19: Initial elemental abundance for the diffuse cloud model considered in the CMMC code (Chantzos et al., 2020; Sil et al., 2021).

Element	Abundance	Element	Abundance
H	1.0	Si^+	3.2×10^{-5}
He	8.5×10^{-2}	Fe^+	3.2×10^{-5}
N	6.8×10^{-5}	Na^+	1.7×10^{-6}
O	4.9×10^{-4}	Mg^+	3.9×10^{-5}
C^+	2.7×10^{-4}	Cl^+	3.2×10^{-7}
S^+	1.3×10^{-5}	P^+	2.6×10^{-7}
		F^+	3.6×10^{-8}

our gas-grain CMMC code (Sil et al., 2018, 2021; Das et al., 2019, 2021; Gorai et al., 2020b) to explore the fate of P-bearing species in the denser region. In the next section, we first test our model for the diffuse region to validate our results and extend it for the more evolved stage.

Diffuse cloud model

We consider the initial elemental abundances for the diffuse cloud model as in Chantzos et al. (2020) (see Table 4.19). The dust-to-gas ratio of 0.01 is considered in our model. We consider a photodesorption rate of 3×10^{-3} molecules per incident UV photon for all the molecules. Öberg et al. (2007) experimentally derived this rate from the laboratory measurement of CO ice. Non-thermal desorption constant $a = 0.01$ and a cosmic-ray ionization rate of 1.7×10^{-16} s^{-1} are considered. We keep the gas and dust temperatures constant at 40 K and 20 K, respectively.

Figure 4.34 represents the results obtained with the CMMC code for the diffuse cloud region. Here, the solid curve in the figure represents the case when we consider $n_H = 100$ cm^{-3}, and the dotted curve represents the case when we consider $n_H = 500$ cm^{-3}. Thus, Figure 4.34 depicts that in the ranges of $A_V = 2 - 3$ mag and $n_H = 100 - 500$ cm^{-3}, we have a better agreement with the observed abundance.

Figure 4.35 shows the chemical evolution of the P-bearing species based on the obtained results. Here, we do not have a high abundance of PH_3 under this situation. This is because of the inclusion of the destruction pathways of PH_3 by H and OH in our network. The dashed green curve shows the PH_3 when we do not consider its destruction by H and OH in both the gas and ice phases. Interestingly, we have a couple of orders higher abundance of PH_3 in the absence of these destruction pathways. However, these destruction pathways are essential and need to consider before constraining the PH_3 abundance. The right panel of Figure 4.35 depicts that the abundance of P^+ remains constant for this case. Figure 4.36 shows

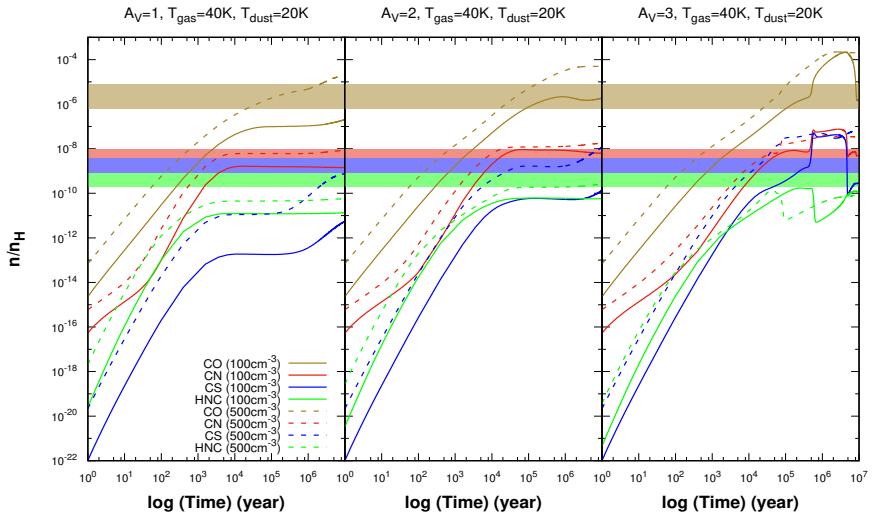

Figure 4.34: Time evolution of the abundances of CO, CN, CS, and HNC with the CMMC code for diffuse cloud. Observed abundances are also highlighted for better understanding. The solid curves represent the case with $n_H = 100$ cm^{-3} and dashed curves represent the case with $n_H = 500$ cm^{-3} (Sil et al., 2021).

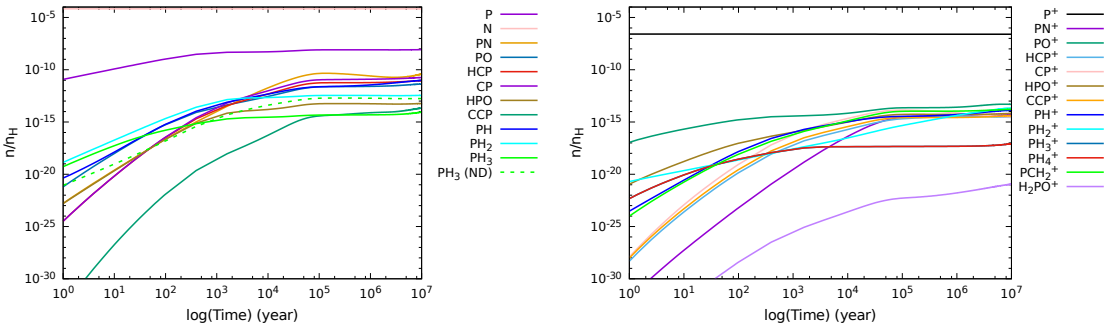

Figure 4.35: Chemical evolution of the P-bearing molecules for $A_V = 2$ mag, $n_H = 300$ cm^{-3}, $T_{gas} = 40$ K, and $T_{dust} = 20$ K with the CMMC code for diffuse cloud is shown. The evolution of the neutrals and radicals is shown in the left panel, whereas ions are shown in the right panel. Derived abundances of all the species are found to be $< 10^{-10}$ for such conditions (Sil et al., 2021).

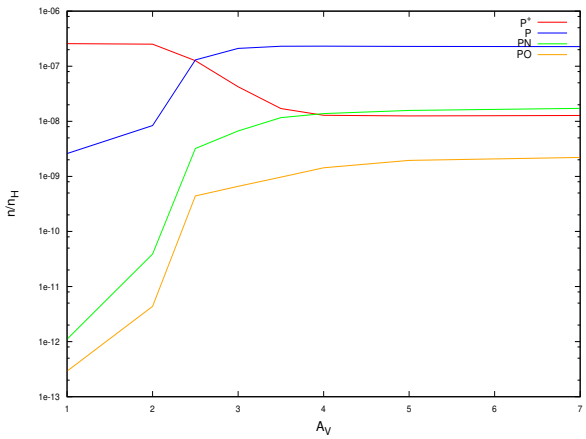

Figure 4.36: The final abundances of P^+, P, PO, and PN are shown with A_V with the CMMC code for diffuse cloud. The conversion of P^+ to P takes place in the range $A_V = 2 - 3$ mag. Beyond $A_V = 4$ mag no changes in the abundances of P^+ and P are obtained. The abundance ratio of PO and PN is found to be always < 1 (Sil et al., 2021).

the final abundance of P and P^+ with a variation of A_V. It shows that P^+-to-P conversion is possible between $A_V = 2$ and 3 mag and remains unchanged beyond $A_V > 4$ mag. For this case, we always get a higher peak abundance of PN compared to PO. At the end of the simulation, Chantzos et al. (2020) also obtain a comparatively higher abundance of PN than PO. With the CLOUDY code, in Figure 4.30, we also obtain PO/PN < 1. The major difference between the models using CMMC code or by Chantzos et al. (2020) and the CLOUDY code is the consideration of the physical conditions. The CLOUDY code considers physical conditions more realistically. Figure 4.31 (diffuse cloud results with CLOUDY) shows a substantial temperature variation with A_V, whereas in the case of the CMMC code, we assume a constant temperature ($T_{gas} = 40$ K and $T_{ice} = 20$ K) for all A_V. In the CMMC code, dust-to-gas ratio of ~ 0.01 is considered, whereas, in the diffuse cloud model using CLOUDY, it gives 6.594×10^{-3}.

Hot-core / Hot-corino model

Here, we consider a three-stage starless collapsing cloud model described in Gorai et al. (2020b). The first stage corresponds to an isothermal ($T_{dust} = T_{gas} = 10$ K) collapsing stage where density can increase from 3×10^3 cm^{-3} to 10^7 cm^{-3} and the visual extinction parameter (A_V) can increase from 2 to 200. The second stage

Table 4.20: Initial elemental abundance for the hot-core/corino model considered in the CMMC code (Wakelam & Herbst, 2008; Sil et al., 2021).

Element	**Abundance**	**Element**	**Abundance**
H_2	0.5	Fe^+	3.00×10^{-9}
He	1.40×10^{-1}	Na^+	2.00×10^{-9}
N	2.14×10^{-5}	Mg^+	7.00×10^{-9}
O	1.76×10^{-4}	Cl^+	1.00×10^{-9}
C^+	7.30×10^{-5}	P^+	2.00×10^{-10}
S^+	8.00×10^{-8}	F^+	6.68×10^{-9}
Si^+	8.00×10^{-9}	e^-	7.31×10^{-5}

corresponds to a warm-up stage where temperature rises from 10 to 200 K, keeping A_V constant at its maximum value in 5×10^4 years. The last stage is a post-warm-up stage where density, temperature, and visual extinction are constant at their respective highest values and continue for 10^5 years. Based on the timescale of the initial isothermal collapsing stage, we define the hot-core and hot-corino. In the hot-core case, we use an isothermal collapsing timescale $\sim 10^5$ years, whereas, for the hot-corino case a relatively longer timescale ($\sim 10^6$ years) is used. Thus, the total simulation timescale of 2.5×10^5 years and 1.15×10^6 years is considered for the hot-core and hot-corino cases, respectively. Table 4.20 shows the low metallic initial elemental abundance (Wakelam & Herbst, 2008), which is considered here.

Rivilla et al. (2016) reported the observed molecular abundance with an uncertainty of $\sim (0.5-5) \times 10^{-10}$ for PO and PN. The ratio between PO and PN is in the range of $1-5$. Figure 4.37 shows the variation of the peak abundance of PO and PN in the case of hot-core and hot-corino by considering various initial elemental P abundances. The peak abundances of PO and PN from our hot-core (left panel) model show a good match with the observation toward the massive star-forming region when an initial elemental P abundance (P^+ abundance) of $2 \times 10^{-10} - 2 \times 10^{-9}$ is considered.

The solid curve of Figure 4.37 represents the BE of the P-bearing species as it is in KIDA. The dashed curve represents our computed BE values (BE with water c-tetramer) of phosphorous (see the BE values in Table 4.16) and keeps all other BE values the same as in KIDA. We notice an increase in the peak abundances of PO and PN for the inclusion of our calculated BEs for the hot-corino case. We obtain that the peak abundance of PN increases, whereas it decreases for PO for the hot-core case. The peak abundance of PO is always more prominent than the peak abundance (beyond the isothermal stage) of PN in both cases. Variation of the PH_3 abundance is also shown, which is far below the derived upper limit for the C-rich

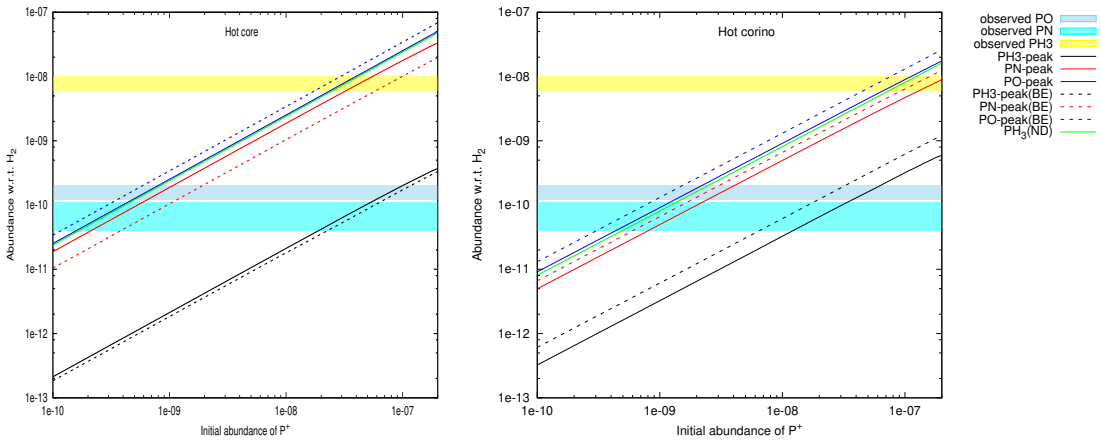

Figure 4.37: The observed abundances of PO and PN in the high-mass star-forming region W51 and W3(OH) (Rivilla et al., 2016) are shown along with our modeled peak abundances (taken beyond the isothermal stage) with hot-core (left panel) and hot-corino (right panel) cases using CMMC code (Sil et al., 2021). The peak abundance variation of the PH_3 is also shown with the initial abundance of P^+. PH_3 is yet to be observed in hot-core/corino. The obtained peak abundance of PH_3 is far below the observed limit of PH_3 in C-star envelope IRC +10216 (Agúndez et al., 2008; Agúndez et al., 2014). Peak abundances of PO, PN, and PH_3 are also shown with the dashed lines when the BE of the P-bearing species is considered from the tetramer configuration noted in Table 4.16. The solid green curve shows the peak abundance of PH_3 in the absence of its destruction by H and OH. We obtained a significantly higher peak abundance of PH_3 with the lack of these destruction pathways.

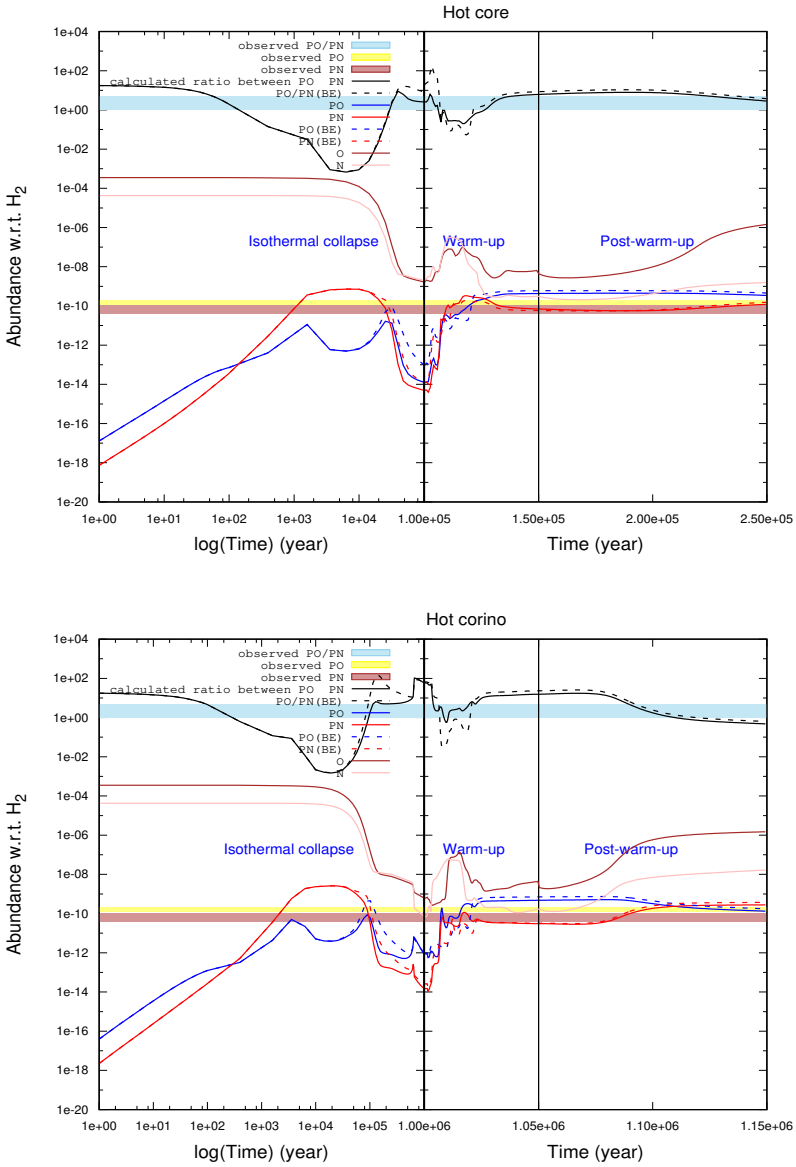

Figure 4.38: Abundance variation of PO, PN, and PO/PN ratio obtained using CMMC code by considering the initial elemental abundance of P^+ as 1.8×10^{-9} for hot-core and 5.6×10^{-9} for the hot-corino case (Sil et al., 2021). Solid lines represent the cases with the BEs from KIDA, and the dashed lines represent the values with the tetramer configuration of water. During the warm-up and post-warm-up stages, we have a good correlation with our results.

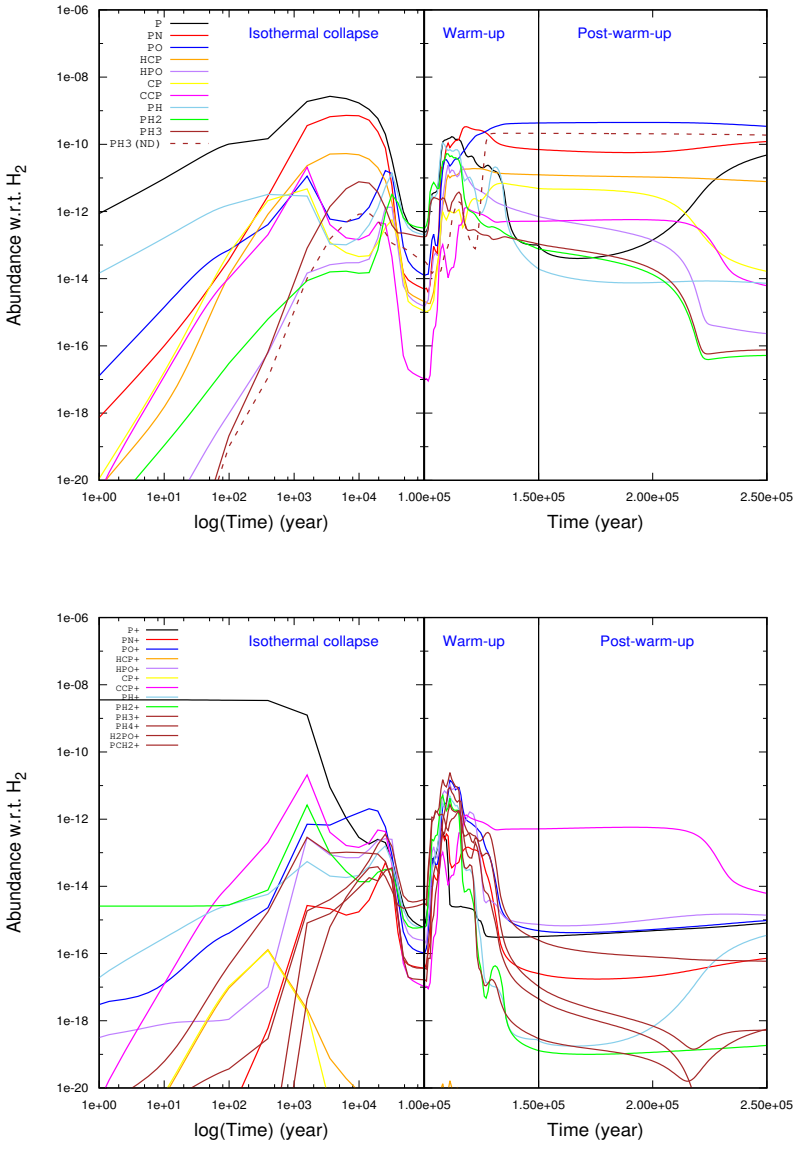

Figure 4.39: Abundance variations of most of the P-bearing neutral and ionic species are shown using CMMC code considering initial elemental abundance of P^+ as 1.8×10^{-9} and for the hot-core region (Sil et al., 2021). In the absence of the destruction of PH_3 by H and OH, PH_3 is highly abundant.

envelop (Agúndez et al., 2008; Agúndez et al., 2014). The changes in BE reflect a significant increase in the gas-phase abundance of PH_3 for the hot-corino case, but a marginal decrease in the peak abundance of PH_3 is obtained in the hot-core case. Additionally, in Figure 4.37, PH_3 abundance is shown with a solid green curve (with the BE of KIDA) when its destruction by H and OH is not included. It offers a significantly higher abundance of PH_3.

Unless otherwise stated, we always use a nonthermal desorption factor of $a = 0.01$. Additionally, we test with a reactive desorption factor of 0.023 (Nguyen et al., 2020) for PH_3, which yields a roughly 2.3 times higher abundance of PH_3 in our case.

The solid lines of Figure 4.38 show the time evolution of the abundances of PO and PN and PO/PN for the hot-core (top panel) and hot-corino (bottom panel) cases. The dashed lines represent the time evolution of the abundances of PO and PN and the ratio PO/PN by considering the BEs of P-bearing species with the tetramer configuration of water. Finally, we highlight the observed abundances and observed abundance ratio in the high-mass star-forming region (Rivilla et al., 2016) to better understand. For the hot-core case, we consider the initial P^+ abundance $\sim 1.8 \times 10^{-9}$, and for the hot-corino case, a comparatively higher initial abundance of P^+ ($\sim 5.6 \times 10^{-9}$) is considered to match the observational result. We obtain an exciting difference between the PO and PN abundances during the later stages of the simulation of the post-warm-up stage.

We obtain PO/PN > 1 in the late post-warm-up stage of the hot-core, whereas it shows an opposite trend in the hot-corino case. Thus, the higher abundance of PN in the hot-corino case happens as a result of the presence of a comparatively more elevated amount of atomic nitrogen (shown in Figure 4.38 with the pink curve) in this case. This high abundance of atomic nitrogen undergoes $PO + N \rightarrow PN + O$ and yields PO/PN < 1 in the hot-corino case. Also, the abundance of atomic P increases owing to the destruction of P-compounds. Our modeling results for hot-core (with PO/PN > 1) and hot-corino (with PO/PN < 1) agree well with the modeling results presented by Jiménez-Serra et al. (2018). The peak abundance of Figure 4.39 shows the time evolution of most of the P-bearing species with an initial P^+ abundance of 1.8×10^{-9}. Interestingly, P is mainly locked in PO and PN at the end of the simulation timescale.

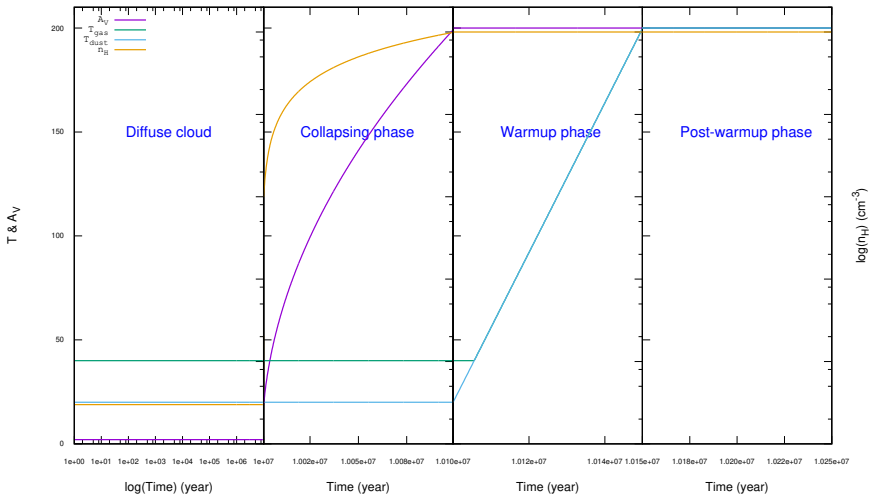

Figure 4.40: Four distinct stages considered for the simulation using CMMC code (Sil et al., 2021). In the first stage, the cloud remains in the diffuse stage for 10^7 years. It starts to collapse in the next step, which continues for 10^5 years. The collapsing stage is followed by a warm-up and post-warm-up stage, which continues for another 1.5×10^5 years.

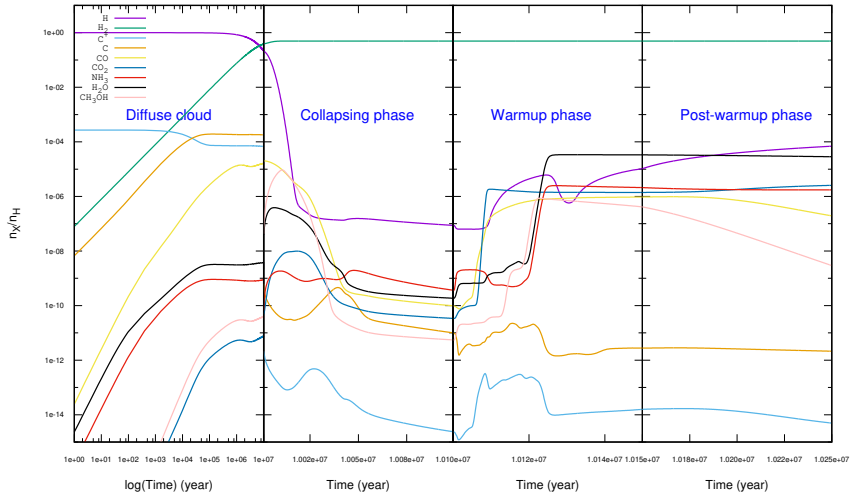

Figure 4.41: Time evolution of H, H_2, C^+, C, CO, CO_2, NH_3, H_2O, and CH_3OH obtained using CMMC code is shown (Sil et al., 2021). During the lifetime of the diffuse cloud H converts into H_2 and C^+ converts into C. During the collapsing stage, C atom is heavily depleted and converts into CO.

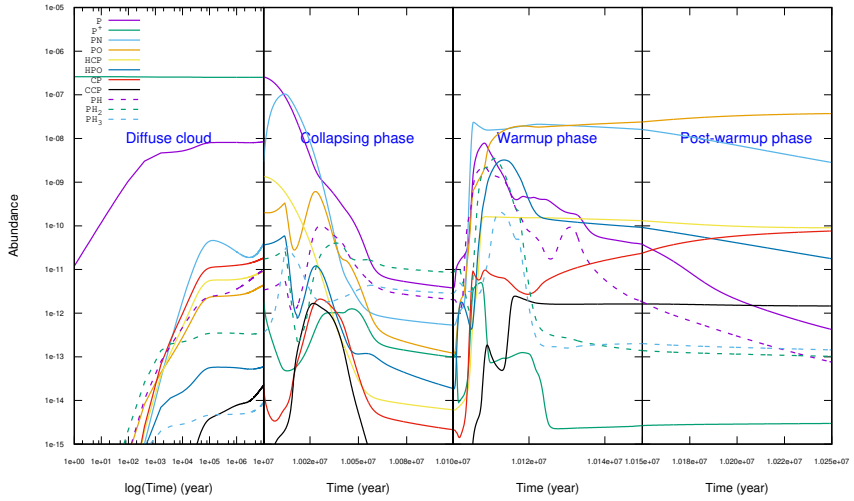

Figure 4.42: Time evolution of the abundances (concerning total hydrogen nuclei in all forms) of major P-bearing species using CMMC code is shown (Sil et al., 2021).

Diffuse to Dense cloud model

To avoid any ambiguity for considering the depletion factor, we consider that the diffuse cloud converts into a molecular cloud after a sufficient time. The adopted physical condition for this model is shown in Figure 4.40. It depicts that the total simulation time is divided into four steps. The first step is the diffuse stage, and it continues for the initial 10^7 years. The second step is the collapsing stage, whose span is for 10^5 years. Then, the warm-up stage starts after the collapsing stage, and it lasts for 5×10^4 years. Finally, the post-warm-up stage continues for another 10^5 years. In total, the simulation timescale is 1.025×10^7 years. Initial elemental abundance for this case is taken from Chantzos et al. (2020) (see Table 4.19). All the BEs are used from the KIDA. Figure 4.41 shows the time evolution of the H, H_2, C^+, C, and CO. Interestingly, most of the H atoms convert into H_2 during the lifetime of the diffuse cloud ($\sim 10^7$ years). Ionized carbon is converted into neutral carbon. During the collapsing stage, the conversion of C to CO takes place. Once CO has formed, it starts to deplete on the grain and forms COMs. In the warm-up stage, these CO and its related molecules are desorbed back to the gas phase. Figure 4.42 shows the chemical evolution of the notable P-bearing species. Figure 4.42 shows that in the warm-up stage we have very high abundances of PN and PO. The PH_3 abundance is also significantly higher ($\sim 10^{-10}$ concerning total H nuclei), comparable with Jiménez-Serra et al. (2018). At the end of the simulation, most of the P is locked as PO and PN.

4.3.4 An outline of our modeling results and a comparison with the earlier results

Table 4.21 shows the peak abundances of the significant P-bearing species obtained with the two model codes (Cloudy and CMMC). However, due to more realistic physical conditions, the Cloudy code is preferred for the diffuse cloud region. Both the diffuse cloud models with Cloudy and CMMC codes show higher abundance of PN than PO. Chantzos et al. (2020) also predicted a higher abundance of PN (4.8×10^{-11}) compared to PO (1.4×10^{-11}) in the diffuse cloud region. The abundances of PH_3 dramatically vary between the two models. This is because Cloudy does not consider the grain surface reactions for the formation of PH_3, whereas the grain chemistry is adequately considered in CMMC. Moreover, the adopted physical condition differs between the two models. We obtain a higher abundance of P-bearing species for our diffuse-dense model because of the consid-

eration of the initially high abundance of P^+ ($\sim 2.6 \times 10^{-7}$). In general, we obtain a nice trend with the peak abundance ratio between PO and PN. We find PO/PN ratio < 1 for the diffuse cloud region, $<< 1$ for the PDR, and > 1 for the hot-core/cornio (late warm-up stage) region. We have PO/PN > 1 for the hot-core and < 1 for the hot-corino in the late post-warm-up stage. We notice that the reaction $PO + N \rightarrow PN + O$ is mainly responsible for controlling this ratio.

Our diffuse cloud modeling results with the CLOUDY and CMMC code are in line with those obtained by Chantzos et al. (2020). The significant difference between our diffuse cloud model obtained with the CLOUDY code and the model presented in Chantzos et al. (2020) is in consideration of realistic physical conditions instead of just considering the constant temperature. In contrast, the diffuse cloud model obtained with the CMMC code adopts similar physical parameters to those considered in Chantzos et al. (2020). Since CLOUDY is not equipped with adequate surface chemistry treatment, we do not have a notable abundance of PH_3. Our CMMC results show lower PH_3 because of its destruction by H and OH.

Charnley & Millar (1994) studied the chemistry of P in hot molecular cores. They considered that the gas-phase P-chemistry in the hot-core starts from PH_3 release from the interstellar grains. In their case, PH_3 was gradually destroyed and transformed into P, PO, and PN. They noticed that the formation timescale of other P-bearing species is longer than those of the hot-core. We consider the in situ formation of PH_3 via chemical reaction on interstellar grains. Like Charnley & Millar (1994), in Figure 4.39, we also notice that at the end of the warm-up stage the abundances of most of the P-bearing species remain in the form of P, PO, and PN.

Rivilla et al. (2016) found that PO and PN are chemically associated and formed during the cold collapse stage by the gas-phase reactions. At the end of the collapsing stage, these two species are deposited to the interstellar grain. These again desorb back to the gas phase during the warm-up stage when the temperature is around 35 K. Our model result using CMMC code shown in Figure 4.38 reflects the similar behavior of PO and PN. In the isothermal collapsing stage, the gas-phase abundance of these two species offers a higher abundance, while at the end of this stage, these two are depleted to the grain. Once the temperature has become > 35 K in the warm-up stage, it desorbed back to the gas phase.

Table 4.21: Peak abundances of the P-bearing species under various physical conditions (Sil et al., 2021).

Species	**Cloudy output**		**CMMC output**[a]			
	Diffuse cloud (n/n_H) ($A_V = 2$, $n_H = 300$ **cm**$^{-3}$)	**PDR** (n/n_H) ($A_V = 5$, $T_{gas} = 50$ **K**, $T_{ice} = 20$ **K**, $n_H = 10^{5.5}$ **cm**$^{-3}$)	**Diffuse cloud** (n/n_H) ($A_V = 2$, $T_{gas} = 40$ **K**, $T_{ice} = 20$ **K**, $n_H = 300$ **cm**$^{-3}$)	**Hot-core** (n/n_{H_2}) (**initial P**$^+ \sim 1.8 \times 10^{-9}$)	**Hot-corino** (n/n_{H_2}) (**initial P**$^+ \sim 5.6 \times 10^{-9}$)	**Diffuse-Dense** (n/n_{H_2}) (**initial P**$^+ \sim 2.6 \times 10^{-7}$)
PN	3.33×10^{-10}	4.02×10^{-09}	4.6×10^{-11}	$1.7 \times 10^{-10}(2.9 \times 10^{-11})$	$1.4 \times 10^{-10}(8.0 \times 10^{-11})$	1.04×10^{-7}
PO	1.47×10^{-10}	2.60×10^{-11}	4.4×10^{-12}	$2.3 \times 10^{-10}(4.9 \times 10^{-11})$	$2.6 \times 10^{-10}(6.6 \times 10^{-11})$	3.7×10^{-8}
PH	1.13×10^{-10}	1.82×10^{-11}	9.6×10^{-12}	$5.5 \times 10^{-11}(1.5 \times 10^{-11})$	$6.5 \times 10^{-11}(8.9 \times 10^{-12})$	2.3×10^{-9}
PH_3	6.30×10^{-31}	1.16×10^{-22}	8.9×10^{-15}	$1.9 \times 10^{-12}(2.1 \times 10^{-10})$	$9.2 \times 10^{-12}(2.3 \times 10^{-10})$	2.0×10^{-10}
CP	2.03×10^{-11}	3.24×10^{-12}	1.8×10^{-11}	$3.5 \times 10^{-12}(6.7 \times 10^{-13})$	$3.1 \times 10^{-11}(3.2 \times 10^{-12})$	1.2×10^{-10}
HCP	1.38×10^{-13}	3.85×10^{-14}	9.1×10^{-12}	$9.5 \times 10^{-12}(3.7 \times 10^{-12})$	$3.5 \times 10^{-11}(4.3 \times 10^{-12})$	1.3×10^{-9}
HPO	4.43×10^{-17}	1.28×10^{-19}	5.9×10^{-14}	$1.2 \times 10^{-11}(1.6 \times 10^{-12})$	$1.5 \times 10^{-11}(9.8 \times 10^{-13})$	3.2×10^{-9}

Note:
[a] The bracketed values from the CMMC output denote the case when the destruction of PH_3 by H and OH are ignored.

Jiménez-Serra et al. (2018) constructed their model to explain the abundances of P-bearing species in a wide range of astrophysical conditions. They constructed a short-lived and long-lived chemical model depending on the time of the collapse. In the short-lived collapse, they stopped their calculations when the gas density reaches its maximum value. In the long-lived collapse, they considered some additional time after getting the final density. They noticed that the P and PN are the most abundant P-bearing species in the collapsing stage. Their maximum abundance is in the range $(5-10)\times10^{-10}$. From our hot-core model, in the collapsing stage (see Figure 4.39), we also obtain that P and PN remain the most abundant P-bearing species, and their peak abundance varies in the range $(7-27)\times10^{-10}$.

Jiménez-Serra et al. (2016) carried out a high-sensitivity observation toward the L1544 pre-stellar core. Unfortunately, they were not able to identify the PN transitions. However, they predicted an upper limit of $\sim 4.6\times10^{-13}$ for the abundance of PN. The first stage of Figure 4.39 represents the isothermal collapsing stage of a hot-core. At the end of the collapsing stage, we obtain a PN abundance of $\sim 5.4\times10^{-15}$, consistent with this upper limit.

Fontani et al. (2016) identified PN in various dense cores. These dense cores belong to various evolutionary stages (starless, with a protostellar object, and with ultracompact H II region) of intermediate- and high-mass stars. They obtained all the transitions of PN where the temperature is < 100 K, and line widths are < 5 km s^{-1}, suggesting that the origin of PN is the quiescent and cold region. The abundance of PN was not derived because of the lack of thermal dust continuum emission (at the millimeter/submillimeter regime for all these sources). Mininni et al. (2018) identified a few transitions of PN toward some of these sources (a sample of nine massive dense cores in different evolutionary stages). They calculated the H_2 total column densities of the sources and derived the abundances of PN. For the slightly warmer region $(25-30$ K), Fontani et al. (2016) and Mininni et al. (2018) obtained the abundances of PN of 10^{-11} and 5×10^{-12}, respectively. Figure 4.39 depicts that when the temperature is ~ 35 K in the warm-up stage, we have a little higher PN abundance $\sim 2.08\times10^{-11}$ with respect to H_2. This is because Mininni et al. (2018) found the excitation temperature of PN $\sim 5-30$ K. Since the average density ($\sim 10^{4-5}$ cm^{-3}) of their targeted regions are below the critical density (10^{5-6} cm^{-3}) of the PN, they suggested a subthermal excitation of PN. This is because the total hydrogen density can reach as high as 10^7 cm^{-3} in our isothermal stage. In the warm-up stage, we consider the same density. So, in our case, we have an average density, which is greater than the critical density of PN. So, a direct comparison between our model and the observation of Mininni et al. (2018) and Fontani et al.

Table 4.22: Summary of the obtained abundance ratio between PO and PN in different astrophysical environments (Sil et al., 2021).

References	Type of study	PDR	Diffuse cloud	Hot-core	Hot-corino	Shock	Comet	Other
This work	Modeling	$<< 1$	< 1	$\geq 1^{l}$	$\geq 1^{m}, \leq 1^{n}$	-	-	-
Bernal et al. (2021)	Observation	-	-	-	-	-	-	2.7^{a}
Rivilla et al. (2020)	Observation	-	-	-	-	-	$> 10^{b}$	1.7^{c}
Chantzos et al. (2020)	Modeling		< 1					
Bergner et al. (2019)	Observation	-	-	-	-	-	-	$(1-3)^{d}$
Rivilla et al. (2018)	Observation	-	-	-	-	-	-	$\sim 1.5^{e}$
Jiménez-Serra et al. (2018)	Modeling	$<< 1$	-	≥ 1	< 1	≤ 1	-	-
Lefloch et al. (2016)	Observation	-	-	-	-	$\approx 3^{f}$	-	-
Rivilla et al. (2016)	Observation	-	-	1.8^{g}, 3^{h}	-	-	-	-
Fontani et al. (2016)	Observation	-	-	-	-	-	-	$< (1.3-4.5)^{i}$
De Beck et al. (2013)	Observation	-	-	-	-	-	-	$0.17-2^{j}$
Aota & Aikawa (2012)	Modeling	-	-	-	-	$\sim (0.5-1.3)^{f,i}$	-	-
Tenenbaum et al. (2007)	Observation	-	-	-	-	-	-	2.2^{k}

Note:
[a] Orion-KL.
[b] 67P/C-G (Altwegg et al., 2016).
[c] Average over multiple positions and velocity components toward AFGL 5142.
[d] Class I low-mass protostar B1-a.
[e] G+0.693-0.03.
[f] L1157-B1.
[g] W51 e1/e2.
[h] W3(OH).
[i] Taking minimum and maximum values of upper limit of beam-averagd column densities of multiple sources.
[j] IK Tauri.
[k] VY Canis Majoris.
[l] For the late warm-up to post-warm-up stage of the hot-core model.
[m] During the late warm-up to the initial post-warm-up of hot-corino stage.
[n] During the late post warm-up stage.

(2016) would not be appropriate. Here, we refer to these observations to infer the enhancement of the PN abundance with an increase in temperature from 10 K to 35 K only.

After releasing to the gas phase, PH_3 can be destroyed rapidly (Jiménez-Serra et al., 2018). The gas-phase formation of PH_3 can continue by the reactions R144 and R145 of Table 4.15. These two reactions were considered in Jiménez-Serra et al. (2018) and were found to contribute marginally. Here, we have some additional destruction reactions of PH_3 by H (grain-phase reaction R4 and gas-phase reaction R149 of Table 4.15) and OH (grain-phase reaction R5 and gas-phase reaction R161 of Table 4.15), which yields a much lower PH_3 in the gas phase.

In Table 4.22, a summary of the PO/PN abundance ratio is listed in the different astrophysical environments, along with a comparison with the earlier literature (Tenenbaum et al., 2007; Aota & Aikawa, 2012; De Beck et al., 2013; Fontani et al., 2016; Lefloch et al., 2016; Rivilla et al., 2016, 2018, 2020; Jiménez-Serra et al., 2018; Bergner et al., 2019; Chantzos et al., 2020; Bernal et al., 2021). Our modeling results agree well with the observed (Rivilla et al., 2016) and modeled (Jiménez-Serra et al., 2018; Chantzos et al., 2020) PO/PN ratios.

4.3.5 IR spectroscopy of PH_3

Phosphine is an important reservoir of interstellar phosphorous (Charnley & Millar, 1994). Since it is of particular interest to astronomers, the IR vibrational spectra analysis of PH_3 could be helpful to the community. The vibrational spectra of PH_3 would be beneficial for future astronomical observations with the JWST. To precisely estimate the frequency and interpret the intensities, it is necessary to go beyond the harmonic approximation. The anharmonic calculations show a significant deviation from the harmonic calculations. Another advantage of the anharmonic analysis is that overtones and combination bands can also be analyzed with this. When anharmonicity is considered, its intensity vanishes at the harmonic level. Within the DFT approach, the standard B3LYP functional (Becke, 1993) is used in conjunction with the 6-311G(d,p) basis set to investigate the IR feature of PH_3. In addition, all DFT computations are performed employing the GAUSSIAN 09 suite of programs for quantum chemistry (Frisch et al., 2013). Figure 4.43 shows the calculated IR feature of the ice-phase PH_3. The PH_3 molecule is embedded in a continuum solvation field to represent local effects to mimic the ice features. The IEF variant of the PCM as a default SCRF method is employed with water as a solvent (Cancès et al., 1997; Tomasi et al., 2005). The implicit solvation model places the molecule of interest inside a cavity in a continuous homogeneous dielectric medium representing the solvent. The fundamental modes of vibration, along with the overtones and combination bands, are shown in Figure 4.43. Table 4.23 also notes down the wavenumbers (in cm^{-1}) and corresponding absorption coefficients (IR intensities in cm $molecule^{-1}$) of the fundamental bands, overtones, and combination bands.

A comparison between our computed spectra and those obtained experimentally by Turner et al. (2015) is shown in Table 4.23. The computed vibrational frequencies are often scaled to resemble the experimental results. This scaling factor varies with the choice of the basis sets and implemented method. The NIST database[3] noted some of the scaling factors, which are helpful to compare with the experimental values. Based on our method and the chosen basis set, we use a vibrational scaling factor of ~ 0.967. Puzzarini et al. (2014b) demonstrated that the best state-of-the-art theoretical estimation accuracy is about $5 - 10$ cm^{-1} and $10 - 20$ cm^{-1} for fundamental and nonfundamental transitions, respectively. This accuracy allows for reliable simulations of IR spectra supporting astronomical observations. The harmonic frequencies presented in Table 4.23 agree with the experimental values

[3] https://cccbdb.nist.gov/vibscalejust.asp

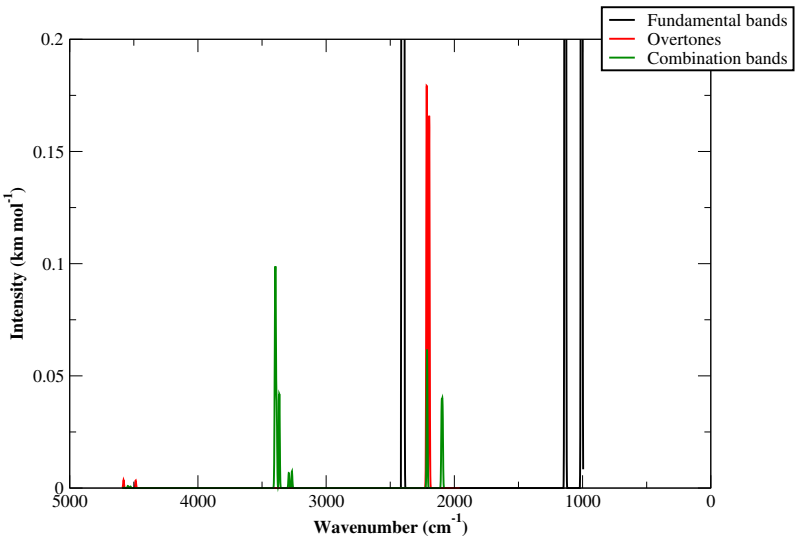

Figure 4.43: Ice-phase IR absorption spectra of PH_3 including the harmonic fundamental bands and anharmonic overtones and combination bands (Sil et al., 2021).

noted in Turner et al. (2015) within a limit of about $1 - 15$ cm^{-1} after scaling. Our calculated values agree well with the experimented values for the overtones and combination bands, even without scaling.

Figure 4.44 shows the IR feature of PH_3 in the presence of various impurities. H_2O molecules would cover a significant portion of the interstellar ice mantles in the dense interstellar region. Some other species, such as CO, CO_2, CH_4, NH_3, etc. (Boogert et al., 2015), can also constitute a sizable portion of the grain mantle. These molecules can influence the band profile of PH_3. We notice that the stretching of PH_3 around 2400 cm^{-1} is getting more robust in the presence of CO_2. H_2S and SO_2 are among the main components of Venusian atmospheres (Greaves et al., 2020; Sousa-Silva et al., 2020). It is important that a fundamental mode of SO_2 coincides with the bending-scissoring modes of PH_3 around $\sim 1000 - 1100$ cm^{-1}, which can blend the PH_3 transitions. Since H_2O is a major component of the interstellar dense cloud region, we check the effect of increasing concentration of H_2O on PH_3 separately in Figure 4.45. We notice that with increasing H_2O concentration, PH_3 fundamental bands are highly affected.

Table 4.23: Experimental and calculated IR data for PH_3 (Sil et al., 2021).

Assignment	**Frequency (cm^{-1})**					**Absorption Coefficients (cm $molecule^{-1}$)**		
	Experimental[a]	**Calculated**[b]		**Calculated**[b] × **0.967**		**Experimental**[a]	**Calculated**[b]	
		Harmonic	**Anharmonic**	**Harmonic**	**Anharmonic**		**Harmonic**	**Anharmonic**
Fundamental Bands								
ν_2 (bending)	982	1007.267	990.267	974.027	957.588	0.51×10^{-18}	5.40×10^{-18}	5.11×10^{-18}
ν_4 (scissoring)	1096	1134.859	1110.02	1097.409	1073.389	0.71×10^{-18}	2.78×10^{-18}	2.55×10^{-18}
scissoring		1134.967	1103.681	1097.513	1067.260		2.78×10^{-18}	2.58×10^{-18}
ν_1 (symmetric stretching)	2303	2396.887	2296.619	2317.790	2220.831	2.4×10^{-18}	7.82×10^{-18}	7.86×10^{-18}
ν_3 (asymmetric stretching)	2316	2401.893	2303.377	2322.630	2227.366	8.4×10^{-18}	1.38×10^{-17}	1.47×10^{-17}
asymmetric stretching		2405.153	2283.634	2325.783	2208.274		1.34×10^{-17}	1.45×10^{-17}
Overtones								
$2\nu_4$	2195		2213.024		2139.994			2.98×10^{-19}
$3\nu_2$	2905							
$2\nu_1$	4536		4540.981		4391.129			1.35×10^{-22}
Combination Bands								
$\nu_2 + \nu_4$	2067, 2083		2093.256		2024.178			2.86×10^{-20}
$\nu_1/\nu_3 + \nu_L$	2376, 2426, 2461							
$\nu_1 + \nu_2$	3288		3280.701		3172.438			6.50×10^{-22}
$\nu_1 + \nu_4$	3392		3391.715		3279.788			7.12×10^{-20}
$\nu_3 + \nu_4$	3405		3392.344		3280.397			5.67×10^{-20}
$\nu_1 + \nu_3$	4621		4523.242		4373.975			1.35×10^{-21}

Note:
[a] Turner et al. (2015).
[b] This work.

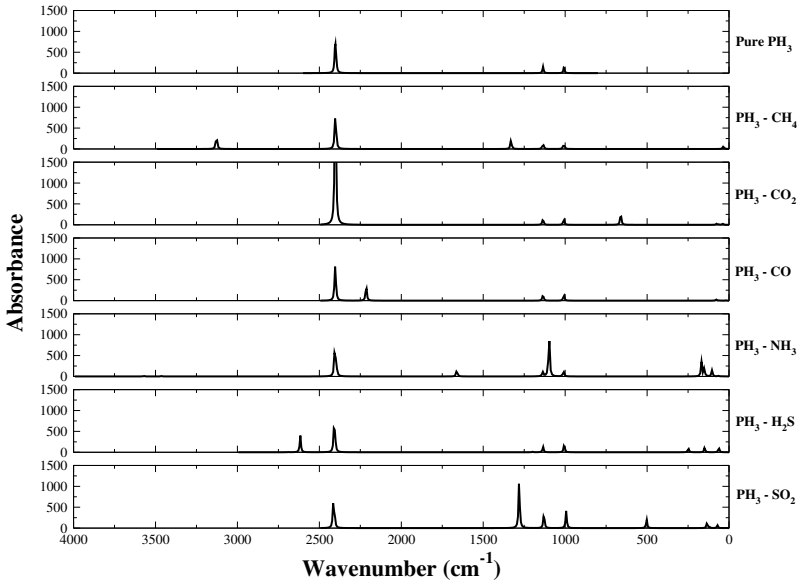

Figure 4.44: Comparison of ice-phase IR absorption spectra of pure PH_3 and mixture of PH_3 with other volatiles (CH_4, CO_2, CO, NH_3, H_2S, and SO_2) considering the harmonic fundamental bands (Sil et al., 2021).

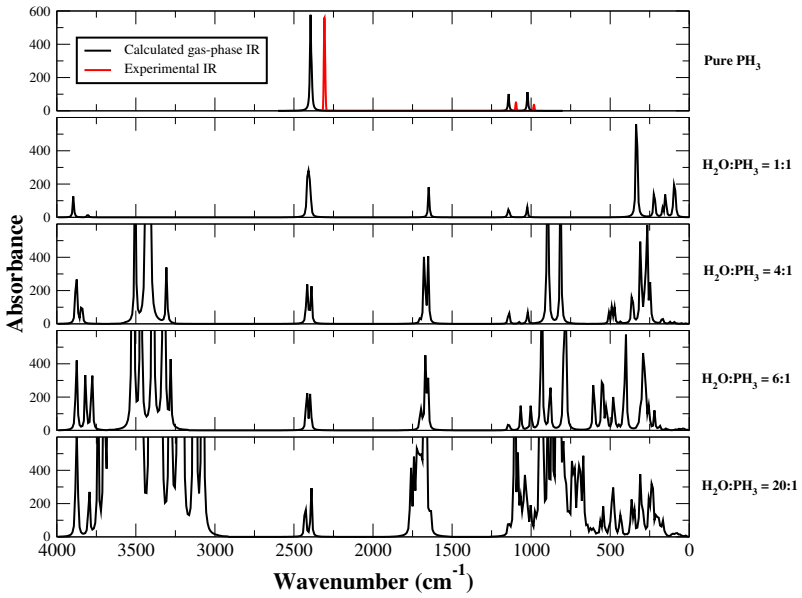

Figure 4.45: Gas-phase IR absorption spectra of PH_3 with increasing concentration of H_2O (Sil et al., 2021).

4.3.6 Summary

In this work, the abundance of the P-bearing species is examined under various interstellar circumstances. PH_3 abundance is low in the diffuse cloud region and PDR, whereas a detectable amount of PH_3 could be produced in the hot-core region. The abundance of PH_3 could be significantly affected by the destruction of H and OH. Without the inclusion of these pathways, any inference on the abundance of PH_3 in astrophysical environments would be inaccurate. The BE of PH_3 with water is found to be lower than that of NH_3. A good agreement between the calculated IR wavenumbers of PH_3 and the experimental feature of Turner et al. (2015) is seen. The stretching and bending-scissoring modes of PH_3 could be affected by the CO_2 and SO_2, respectively, in the ice. PH_3 fundamental bands are highly influenced by increasing H_2O concentration in the gas phase. We map the PO/PN abundance ratio, which is mainly governed by the reaction $PO + N \rightarrow PN + O$. A high abundance of atomic N in the diffuse clouds and PDRs compared to hot-cores yields PO/PN < 1 for the diffuse cloud region and $<< 1$ for the PDR. For the late warm-up to the post-warm-up part of the hot-core, we obtain PO/PN ≥ 1. We notice PO/PN ≥ 1 for the late warm-up to the initial post-warm-up stage for the hot-corino case, whereas it is ≤ 1 for the late post-warm-up stage.

Chapter 5

Summary, Conclusions and Future Plans

In this thesis, the synthesis of various simple and complex molecules is studied under different astrophysical conditions. The spectral properties of several species and the band profiles of interstellar ices in the presence of impurities are examined. Quantum chemical calculations using different theories are carried out to investigate various reactions, BEs, and various spectroscopic parameters of chemical species. Various physical conditions are prepared by varying density, temperature, and timescale of molecular clouds to study the time-dependent and depth-dependent chemical evolution of different exotic, simple, and complex species. The possibility of detecting several species in star-forming regions is discussed based on simple radiative transfer modeling.

The principal findings of this thesis are summarized below:

5.1 Summary and Conclusions

- Quantum-chemical calculations are performed for estimating BEs of different interstellar relevant species considering various substrates like water, methanol, carbon monoxide, hydrogen molecule.

- An exciting trend is noticed that BE of H_2 molecule always remains higher than H atom considering benzene, silica, and water cluster as substrates.

- The BEs of 100 interstellar species with the water tetramer as substrate are provided. The calculated BE values tend to converge to the experimental values with increasing cluster sizes of water molecules.

- The BEs of 95 interstellar species with H_2 monomer substrate are provided. Almost $\sim$ 10 times lower BE values are found than those considering H_2O tetramer as a substrate.

- These new BE values have significant consequences, such as locating the so-called snow lines of protoplanetary disks or obtaining the observed abundances toward hot cores and corinos or prestellar cores.

- A series of laboratory experiments and an extensive computational investigation are carried out to explain the effect of different amounts of representative impurities on the band strengths and absorption band features of interstellar ice. Based on the observational, experimental, and theoretical results, the most abundant contaminants are chosen to study their effects on four fundamental vibrational bands of pure water ice.

- The fate of noble gas hydride and hydroxyl cations are studied in the diffuse ISM and the Crab filamentary region. A wide range of parameter space and realistic chemical networks are involved in explaining the observational aspects suitably. Spectroscopic constants are calculated quantum chemically for the noble gas hydroxyl cations.

- Detectability of trans-ethylamine and (1Z)-1-propanimine as the most probable candidates from C_2H_7N and C_3H_7N aldimines and amines isomeric groups respectively are discussed based on the enthalpy of formation, chemical abundances, rotational transition along with the radiative transfer modeling. It is to be noted that interstellar chemistry is not controlled by thermodynamics alone. Instead, it depends on various kinetic parameters. We provide the spectroscopic parameters and the dipole moments that could provide guidance for future searches of these molecular species.

- Observed methylamine/ethylamine ratio is compared with that obtained from the chemical model in dark cloud condition. A good agreement is found between interstellar and cometary chemical compositions. However, a more in-depth study is required to understand whether the cometary chemical compositions are inherited from dense cloud conditions via protoplanetary disk or not.

- Three pre-biotic molecules, namely, HNCO, NH_2CHO, and CH_3NCO containing peptide-like bonds are investigated in a hot molecular core G10.47+0.03 and their chemical linkage is proposed.

- The abundances of important P-bearing species are modeled under various interstellar circumstances. For example, the PH_3 abundance is low in the diffuse cloud region and PDR, whereas a detectable amount of PH_3 can be

produced in the hot core region. The abundance of PH_3 can be significantly affected by the destruction of H and OH. Without the inclusion of these, any inference on the abundance of PH_3 in astrophysical environments would be inaccurate.

- The BE of PH_3 with water is found to be lower as compared to that of NH_3. A good agreement between the calculated IR wavenumbers of PH_3 and the experimental feature of Turner et al. (2015) is noticed. Thus, the stretching and bending-scissoring modes of PH_3 can be affected by the CO_2 and SO_2, respectively, in the ice. Furthermore, PH_3 fundamental bands are highly influenced by increasing H_2O concentration in the gas-phase.

- The PO/PN abundance ratio is mapped in different astrophysical environments and compared with the earlier studies. The ratio is found to be mainly governed by the reaction $PO + N \rightarrow PN + O$. A high abundance of atomic N in the diffuse clouds and PDRs compared to hot cores yields PO/PN < 1 for the diffuse cloud region and $<< 1$ for the PDR. For the late warm-up to the post-warm-up region of the hot core, we obtain PO/PN ≥ 1. For the hot corino case, we notice PO/PN ≥ 1 for the late warm-up to the initial post-warm-up stage, whereas it is ≤ 1 for the late post-warm-up stage. So, PO/PN ratio can be used as a tracer of different evolutionary stages of star formation.

5.2 Future Research Plans

Presently, I have started work related to the properties of complex interstellar species along with some noble-gas-related molecular ions and metallic compounds exposed to intense interstellar radiation environments (e.g., PDR, XDR, H II regions, plus the transition to dense molecular regions from diffuse regions). For this purpose, I am using the spectral synthesis code Cloudy (Ferland et al., 2017). I want to use this code to understand the more realistic physical and chemical properties for the particular environment.

Interstellar gas at low densities and low temperatures, of cosmic composition, left on its own will not generate extensive chemistry to produce useful tracer molecules. Instead, the chemistry must be driven by starlight, cosmic rays, grain catalysis, and gas dynamics. For example, diffuse clouds are readily penetrated by starlight, which is largely excluded from molecular clouds. Still, cosmic rays are almost unattenuated as they pass through such regions, and they drive much of the chemistry. Grain surfaces become essential drivers of complex chemistry in very dense regions of

massive star formation. The gas dynamics in regions such as stellar jets can inject energy and drive characteristic chemistry at the interface between the jet and the ambient gas. An interstellar shock arises when an external event – such as a collision of two interstellar clouds or the impact of a rapidly expanding H II region or SNR on a nearby cloud of cold neutral gas – drives a perturbation faster than the local sound speed.

Consequently, the kinetic energy of bulk motion is converted to internal thermal energy, and the shocked gas is heated and compressed. Such dynamic events are common in interstellar and circumstellar media and maybe detected spectroscopically. I am very much interested in carrying forward this type of investigation.

I want to model the properties of and the emission from COMs, star formation processes, shocked region, and the molecular emission from cometary knots in planetary nebulae (PNe). PNe is the end-stage of the life cycle of low- and intermediate-mass stars, consisting of the gas and dust ejected during previous stages of stellar evolution, surrounding a hot central star. My work would also focus on the modeling of the thermal emission from dust in supernova ejecta. The large amounts of dust observed in some high-redshift galaxies may have been produced by supernovae (SNe) from massive stars. In addition, core-collapse supernovae (CCSNe) play a vital role in the evolution of the ISM of galaxies.

Chapter A

X-ray ionization

A.1 Direct X-ray ionization

In Table 3.3, we have pointed out the direct X-ray ionization rates in reaction numbers 25-26 for Ar, 26-27 for Ne, and 17-18 for He. Rate constants are computed using the method discussed in the following.

We used the direct (or primary) ionization rate of species i at a certain depth z into the filament as:

$$\zeta_{\mathrm{XR}} = \zeta_{\mathrm{i,prim}} = \int_{\mathrm{E_{min}}}^{\mathrm{E_{max}}} \sigma_{\mathrm{i}}(\mathrm{E}) \frac{\mathrm{F(E,z)}}{\mathrm{E}} \mathrm{dE\ s^{-1}}\ , \tag{A.1}$$

where the integration bound is the spectral range of the emitted energy ($[E_{min},\ E_{max}] = [1, 10]$ keV (Meijerink & Spaans, 2005) for the entire X-ray rate calculations). The ionization cross section $\sigma_i(E)$ at energy E is calculated by using the eqn. A.2 and A.3 and the parameters provided in Table A.1. Verner & Yakovlev (1995) used a fitting procedure proposed by Kamrukov et al. (1983) for partial photoionization cross section $\sigma_{nl}(E)$ for different atoms and ions:

$$\sigma_i(E) = \sigma_{nl}(E) = \sigma_0 F(y),\ y = E/E_0, \tag{A.2}$$

$$F(y) = [(y-1)^2 + y_w^2] y^{-Q} \Big(1 + \sqrt{\frac{y}{y_a}}\Big)^{-P},\ Q = 5.5 + l - 0.5P, \tag{A.3}$$

where n is the principal quantum number of the shell, $l = 0, 1, 2$ (or s, p, d) is the subshell orbital quantum number, E is the photon energy in eV, σ_0=$\sigma_0(nl, Z, N)$, $E_0 = E_0(nl, Z, N)$, $y_w,\ y_a$, and P are the fitting parameters given in Table A.1 (Z and N are the atomic number and number of electrons, respectively). Verner & Yakovlev (1995) noticed that $F(y)$ is a "nearly universal" function for all species ($Z,\ N$) at a fixed shell nl.

The flux $F(E, z)$ in Equation (A.1) at depth z into the filament is given by

$$F(E, z) = F(E, z = 0) exp\big(-\sigma_{pa}(E) N_H\big), \tag{A.4}$$

where $N_H \sim 4.77 \times 10^{21}$ cm^{-2} is considered as the total column density of hydrogen nuclei and $F(E, z = 0) = 0.35$ erg cm^{-2} s^{-1} is considered as the flux at the surface of the cloud. The photoelectric absorption cross section per hydrogen nucleus, σ_{pa} used in Equation (A.4) is given by

$$\sigma_{pa}(E) = \sum_i A_i(total)\sigma_i(E), \tag{A.5}$$

where $A_i(total)$ is the total (gas and dust) elemental abundance used.

A.2 Secondary X-ray ionization

Part of the kinetic energy of fast photoelectrons is lost by ionizations. These secondary ionizations are far more important for H, H_2, and He than direct ionization. The energy carried away by the fast photoelectrons and Auger electrons is very efficient in ionizing the other species. For example, these electrons can readily ionize H, He, and H_2 and decay back to ground state by the removal of UV photons. These photons can trigger the induced chemistry and are very important for the chemical network. The secondary ionization rate per hydrogen molecule at depth z into the filament can be calculated using

$$\zeta_{H_2,XRPHOT} = \zeta_{i,sec} = \int_{E_{min}}^{E_{max}} \sigma_{pa}(E)F(E, z)\frac{E}{Wx(H_2)}dE \ s^{-1}, \tag{A.6}$$

where $x(H_2)$ is the fractional abundance of H_2 with respect to total hydrogen nuclei and W is the mean energy per ion pair. For our calculations, we considered x(H_2) $\sim 2 \times 10^{-4}$, which means that most of the hydrogen is in atomic form. Dalgarno et al. (1999) calculated W for pure ionized $H - He$ and $H_2 - He$ mixtures for E between 30 eV and 1 keV and parameterized W as

$$W = W_0(1 + Cx^{\alpha}), \tag{A.7}$$

where $x = 0.1$ is considered as the ionization fraction and W_0 is the value for neutral gas. W_0, C, and α are given in Table 4 of Dalgarno et al. (1999). We took those values (W_0 = 48.6 eV, C = 9.13, and α=0.807) only for pure He gas for 1 keV. Following Meijerink & Spaans (2005), we integrated over the range $1 - 10$ keV and W goes to a limiting value (42.69 eV). We considered the parameters for the 1 keV electron to determine the electron energy deposition, because these parameters do not change for higher energies. The X-ray photoionization rate then simplifies to,

$$\zeta_{H_2,XRPHOT} = \zeta_{i,sec} = \frac{1keV}{W(1keV)x(H_2)}\int_{E_{min}}^{E_{max}} \sigma_{pa}(E)F(E, z)dE \ s^{-1} \ . \tag{A.8}$$

The photon energy absorbed per hydrogen nucleus H_X is given by

$$H_X = \int_{E_{min}}^{E_{max}} \sigma_{pa}(E) F(E,z) dE. \tag{A.9}$$

Hence, the X-ray photoionization rate is given by

$$\zeta_{H_2,XRPHOT} = \zeta_{i,sec} = \frac{1keV}{W(1keV)x(H_2)} H_X \ s^{-1}. \tag{A.10}$$

Following Priestley et al. (2017), we multiplied $\zeta_{\mathrm{H_2,XRPHOT}}$ by $\frac{0.8}{1-\omega}$, where ω is the grain albedo (~ 0.5).

A.3 Electron-impact X-ray ionization

The electron-impact ionization rate (ζ_{XRSEC}) of other atoms or molecules can be calculated as a first approximation by

$$\zeta_{XRSEC} = \zeta_{H_2,XRPHOT} \times R_\sigma, \tag{A.11}$$

where R_σ is the ratio of electron-impact cross sections of that species to H_2 at a specific energy (Stäuber et al., 2005). For simplicity, here we assumed $\zeta_{\mathrm{H2,XRPHOT}} = \zeta_{\mathrm{H,XRPHOT}}$. Following Lennon et al. (1988), we determined the rate coefficients $\langle \sigma \mathrm{v} \rangle$ (cross sections at a given energy multiplied by electron velocity v at the same energy, evaluated over a Maxwellian velocity distribution) given by

$$\langle \sigma v \rangle = \Big(\frac{8kT}{\pi m}\Big)^{1/2} \int_{I/kT}^{\infty} \sigma(E) \Big(\frac{E}{kT}\Big) exp\Big(\frac{-E}{kT}\Big) d\Big(\frac{E}{kT}\Big), \tag{A.12}$$

where m is the electron mass. For the temperature range $I/10 \leq kT \leq 10I$, they fitted the rate coefficient with the following functional form,

$$\langle \sigma v \rangle = exp\Big(\frac{-I}{kT}\Big) \Big(\frac{kT}{I}\Big)^{1/2} \sum_{n=0}^{5} a_n \Big[log_{10}\Big(\frac{kT}{I}\Big)\Big]^n, \tag{A.13}$$

and for $kT > 10I$, they used the formula

$$\langle \sigma v \rangle = \Big(\frac{kT}{I}\Big)^{-1/2} \Big[\alpha ln\Big(\frac{kT}{I}\Big) + \sum_{n=0}^{2} \beta_n \Big(\frac{I}{kT}\Big)^n\Big]. \tag{A.14}$$

Following Lennon et al. (1988), the coefficients a_0, ..., a_5 and α, β_0, β_1, and β_2 are given in Table A.2. For T in K, I in eV, and $k = 0.8617 \times 10^{-4}$ eV K^{-1}, these

Table A.1: The parameters taken from Verner & Yakovlev (1995) for calculating ionization cross sections σ_i(E) (Das et al., 2020).

Species	E_0 **(eV)**	σ_0 **(cm^2)**	y_a	P
He I	0.2024×10^{1}	0.2578×10^{-14}	0.9648×10^{1}	0.6218×10^{1}
Ne I	0.3144×10^{3}	0.1664×10^{-16}	0.2042×10^{6}	0.8450×10^{0}
Ar I	0.1135×10^{4}	0.4280×10^{-17}	0.3285×10^{8}	0.7631×10^{0}

Table A.2: The parameters taken from Lennon et al. (1988) to calculate the rate coefficients $\langle \sigma v \rangle$ (Das et al., 2020).

Parameters	**Species**			
(cm^{3}s^{-1})	**H I**	**He I**	**Ne I**	**Ar I**
a_0	2.3743×10^{-08}	1.4999×10^{-08}	2.5262×10^{-08}	9.4727×10^{-08}
a_1	-3.6867×10^{-09}	5.6657×10^{-10}	1.6088×10^{-09}	1.4910×10^{-09}
a_2	-1.0366×10^{-08}	-6.0822×10^{-09}	1.5446×10^{-08}	-5.9294×10^{-08}
a_3	-3.8010×10^{-09}	-3.5594×10^{-09}	-3.5149×10^{-08}	1.7977×10^{08}
a_4	3.4159×10^{-09}	1.5529×10^{-09}	-1.0676×10^{-09}	1.2962×10^{-08}
a_5	1.6834×10^{-09}	1.3207×10^{-09}	1.2656×10^{-08}	-9.7203×10^{-09}
α	2.4617×10^{-08}	3.1373×10^{-08}	1.4653×10^{-07}	4.2289×10^{-07}
β_0	9.5987×10^{-08}	4.7094×10^{-08}	-1.8777×10^{-07}	-5.8297×10^{-07}
β_1	-9.2464×10^{-07}	-7.7361×10^{-07}	1.5661×10^{-08}	1.2344×10^{-06}
β_2	3.9974×10^{-06}	3.7367×10^{-06}	1.9135×10^{-06}	-7.2826×10^{-07}
$\langle \sigma v \rangle$	3.00×10^{-08}	2.53×10^{-08}	5.51×10^{-08}	1.66×10^{-07}

coefficients provide the rate $\langle \sigma v \rangle$ in cm^3 s^{-1}. Using Equations (A.12) and (A.13), we have determined $\langle \sigma v \rangle$ for Ar, Ne, and He. The obtained values are shown in the last row of Table A.2 and the calculated values of R_σ are 5.53, 1.84, and 0.84 for Ar, Ne, and He, respectively. All of the calculated values of different X-ray ionization rates of argon, neon, and helium are provided in Table A.3.

Table A.3: Calculated values of X-ray ionization rates (Das et al., 2020).

Species	ζ_{XR} **(s^{-1})**	ζ_{XRPHOT} **(s^{-1})**	ζ_{XRSEC} **(s^{-1})**
^{36}Ar	3.85×10^{-13}	1.67×10^{-10}	5.79×10^{-10}
^{38}Ar	1.53×10^{-12}	3.31×10^{-10}	1.14×10^{-9}
^{40}Ar	1.35×10^{-11}	4.57×10^{-11}	1.58×10^{-10}
^{20}Ne	2.47×10^{-17}	8.28×10^{-15}	9.52×10^{-15}
^{22}Ne	9.41×10^{-15}	7.27×10^{-13}	8.36×10^{-13}
He	1.31×10^{-19}	1.67×10^{-14}	8.76×10^{-15}

Chapter B

Glossary

A convenient list of covering units, constants, terms and acronyms used frequently in this thesis or in cited literature are provided here.

B.1 Units and constants

Symbol	Description	SI Units	CGS Units
Å	Angstrom	10^{-10} m	10^{-8} cm
μm	Micron	10^{-6} m	10^{-4} cm
G	Gravitational constant	6.673×10^{-11} N m^2 kg^{-2}	6.673×10^{-8} dyn cm^2 gm^{-2}
k_B	Boltzmann constant	1.3807×10^{-23} J/K	1.3807×10^{-16} erg/K
h	Planck's constant	6.6262×10^{-34} J s	6.6262×10^{-27} erg s
c	Speed of light	2.997925×10^{8} m s^{-1}	2.997925×10^{10} cm s^{-1}
eV	Electronvolt	1.602×10^{-19} J	1.602×10^{-12} erg
D	Debye	3.336×10^{-30} C m	10^{-18} esu cm
m_e	Electron mass	9.10956×10^{-31} kg	9.10956×10^{-28} gm
m_p	Proton mass	$1.6726231 \times 10^{-27}$ kg	$1.6726231 \times 10^{-24}$ gm
m_H	Hydrogen mass	1.673534×10^{-27} kg	1.673534×10^{-24} gm
u	Atomic mass unit	$1.6605402 \times 10^{-27}$ kg	$1.6605402 \times 10^{-24}$ gm
$E_\oplus$	Earth radius	6.378×10^{6} m	6.378×10^{8} cm
AU	Astronomical unit	1.4959×10^{11} m	1.4959×10^{13} cm
$R_\odot$	Solar radius	6.9599×10^{8} m	6.9599×10^{10} cm
ly	Light year	9.463×10^{15} m	9.463×10^{17}cm
pc	Parsec	3.085678×10^{16} m	3.085678×10^{18} cm
$L_\odot$	Solar luminosity	3.826×10^{26} J s^{-1}	3.826×10^{33} erg s^{-1}
$M_\oplus$	Mass of the Earth	5.977×10^{24} kg	5.977×10^{27} gm
$M_\odot$	Solar Mass	1.989×10^{30} kg	1.989×10^{33} gm
Jy	Jansky	1.00×10^{-26} W m^{-2} Hz^{-1}	1.00×10^{-23} erg sec^{-1} cm^{-2} Hz^{-1}

B.2 Acronyms

67P/C-G	67P/Churyumov-Gerasimenko
A_V	Visual extinction, measured in magnitudes (mag)
ab initio	Latin word for "from the beginning"
ALMA	Atacama Large Millimeter/submillimeter Array
APEX	Atacama Pathfinder Experiment
Ariel	Atmospheric Remote-sensing Infrared Exoplanet Large-survey
ASTE	Atacama Submillimeter Telescope Experiment
ASW	Amorphous Solid Water
BE	Binding Enegry
BSSE	Basis Set Superposition Error
CCSD(T)	Coupled Cluster Single-Double and perturbative Triple excitation
CDMS	The Cologne Database for Molecular Spectroscopy
CMB	Cosmic Microwave Background
CMMC	Chemical Model for Molecular Cloud
CP	Counterpoise
COMs	Complex Organic Molecules
CR	Cosmic Rays
CRESU	Cinétique de Réaction en Ecoulement Supersonique Uniforme (in French)
CSE	Circumstellar Envelop
CT	Classical Trajectory
DFT	Density Functional Theory
DFMS	Double Focusing Mass Spectrometer
ESA	European Space Agency
FTIR	Fourier Transform Infrared
ELT	Extremely Large Telescope
ESD	Electron-Stimulated Desorption
FTIR	Fourier Transform InfraRed
FWHM	Full Width at Half Maximum
GREAT	German REceiver for Astronomy at Terahertz Frequencies
HF	Hartree-Fock
HIFI	Heterodyne Instrument for the Far Infrared
HITRAN	High-resolution Transmission Molecular Absorption Database
HMC	Hot Molecular Core
HSO	Herschel Space Observatory
HST	Hubble Space Telescope
IR	Infrared
IRAM	Institute for Radio Astronomy in the Millimeter Range
IRTF	Infrared Telescope Facility
ISM	Interstellar Medium
ISO	Infrared Space Observatory
ISRF	Interstellar Radiation Field
ICSP	Indian Centre for Space Physics

IRC	Intrinsic Reaction Coordinate
JPL	Jet Propulsion Laboratory
JWST	James Webb Space Telescope
KIDA	KInetic Database for Astrochemistry
KMC	Kinetic Monte Carlo
LAMDA	Leiden Atomic and Molecular Database
LWS	Long Wavelength Spectrometer
LTE	Local Thermodynamic Equillibrium
MC	Monte Carlo
MCT	Mercury Cadmium Telluride
MP	Møller-Plesset perturbation
MD	Molecular Dynamics
NASA	National Aeronautics and Space Administration
NOEMA	Northern Extended Millimeter Array
NGC	New General Catalog
NIST	National Institute of Standards and Technology
PAC	Portable Astrochemistry Chamber
PACS	Photodetector Array Camera and Spectrometer
PAH	Polycyclic Aromatic Hydrocarbons
PCM	Polarizable Continuum Model
PDR	Photon-dominated/Photodissociation Region
QM/MM	Quantum Mechanics/Molecular Mechanics
QST	Quadratic Synchronous Transit
RAIRS	Reflection Absorption Infra-Red Spectroscopy
ROSINA	Rosetta Orbiter Spectrometer for Ion and Neutral Analysis
SB	Surface Brightness
SCRF	Self-consistent Reaction Field
SED	Spectral Energy Distribution
SIFT	Selected Ion Flow Tube
SMA	Submillimeter Array
SNR	Supernova remnant
SOFIA	The Stratospheric Observatory for Infrared Astronomy
SPIRE	Spectral and Photometric Imaging Receiver
STQN	Synchronous Transit-Guided Quasi-Newton
TPD	Temperature-Programmed Desorption
TS	Transition State
TST	Transition-State Theory
UHV	Ultra-High Vacuum
UDfA	UMIST Database for Astrochemistry
UV	Ultraviolet
VLA	Very Large Array
VUV	Vacuum Ultaviolet
XMM	X-ray Multi-Mirror Mission
XRISM	X-Ray Imaging and Spectroscopy Mission
YSO	Young Stellar Object
ZPVE	Zero Point Vibrational Energy

Bibliography

Abascal, J. L. F., Sanz, E., García Fernández, R., & Vega, C. 2005, JChPh, 122, 234511, doi: 10.1063/1.1931662

Abdoulanziz, A., Colboc, F., Little, D. A., et al. 2018, MNRAS, 479, 2415, doi: 10.1093/mnras/sty1549

Acharyya, K., Chakrabarti, S. K., & Chakrabarti, S. 2005, MNRAS, 361, 550, doi: 10.1111/j.1365-2966.2005.09195.x

Acharyya, K., Fuchs, G. W., Fraser, H. J., van Dishoeck, E. F., & Linnartz, H. 2007, A&A, 466, 1005, doi: 10.1051/0004-6361:20066272

Adams, N. G., McIntosh, B. J., & Smith, D. 1990, A&A, 232, 443

Agúndez, M., Cernicharo, J., Decin, L., Encrenaz, P., & Teyssier, D. 2014, ApJ, 790, L27, doi: 10.1088/2041-8205/790/2/127

Agúndez, M., Cernicharo, J., & Guélin, M. 2007, ApJL, 662, L91, doi: 10.1086/519561

Agúndez, M., Cernicharo, J., Pardo, J. R., Guélin, M., & Phillips, T. G. 2008, A&A, 485, L33, doi: 10.1051/0004-6361:200810193

Al-Halabi, A., Kleyn, A. W., van Dishoeck, E. F., & Kroes, G. J. 2002, JPCB, 106, 6515, doi: 10.1021/jp020007y

Al-Halabi, A., & van Dishoeck, E. F. 2007, MNRAS, 382, 1648, doi: 10.1111/j.1365-2966.2007.12415.x

Allamandola, L. J., Sandford, S. A., Tielens, A. G. G. M., & Herbst, T. M. 1992, ApJ, 399, 134, doi: 10.1086/171909

Allen, M., & Robinson, G. W. 1977, ApJ, 212, 396, doi: 10.1086/155059

ALMA Partnership, Brogan, C. L., Pérez, L. M., et al. 2015, ApJL, 808, L3, doi: 10.1088/2041-8205/808/1/L3

Altwegg, K., Balsiger, H., & Fuselier, S. A. 2019, ARA&A, 57, 113, doi: 10.1146/annurev-astro-091918-104409

Altwegg, K., Balsiger, H., Bar-Nun, A., et al. 2016, SciA, 2, e1600285, doi: 10.1126/sciadv.1600285

Altwegg, K., Balsiger, H., Berthelier, J. J., et al. 2017, MNRAS, 469, S130, doi: 10.1093/mnras/stx1415

Anicich, V. G. 1993, ApJS, 84, 215, doi: 10.1086/191752

Aota, T., & Aikawa, Y. 2012, ApJ, 761, 74, doi: 10.1088/0004-637X/761/1/74

Asplund, M., Grevesse, N., Sauval, A. J., & Scott, P. 2009, ARA&A, 47, 481, doi: 10.1146/annurev.astro.46.060407.145222

Avgul, N., Isirikyan, A., KIselev, A. V., Lygina, I., & Poshkus, D. 1957, Bulletin of the Academy of Sciences of the USSR, Division of chemical science, 6, 1334

Avgul, N., Kiselev, A., Lygina, I., & Poshkus, D. 1960, Russian Chemical Bulletin, 8, 1155

Baas, F., Grim, R. J. A., Geballe, T. R., Schutte, W., & Greenberg, J. M. 1988, in Dust in the Universe, ed. M. E. Bailey & D. A. Williams, 55–60

Bains, W., Petkowski, J. J., Seager, S., et al. 2020, arXiv e-prints, arXiv:2009.06499. https://arxiv.org/abs/2009.06499

Bak, B., & Skaarup, S. 1971, JMoSt, 10, 385, doi: 10.1016/0022-2860(71)85060-3

Bakes, E. L. O., & Tielens, A. G. G. M. 1998, ApJ, 499, 258, doi: 10.1086/305625

Balucani, N., Ceccarelli, C., & Taquet, V. 2015, MNRAS, 449, L16, doi: 10.1093/mnrasl/slv009

Barlow, M. J., Swinyard, B. M., Owen, P. J., et al. 2013, Sci, 342, 1343, doi: 10.1126/science.1243582

Barone, V., Biczysko, M., Bloino, J., et al. 2015, Journal of chemical theory and computation, 11, 4342

Barone, V., Biczysko, M., & Puzzarini, C. 2015a, Accounts of chemical research, 48, 1413

Barone, V., Latouche, C., Skouteris, D., et al. 2015, MNRAS, 453, L31, doi: 10.1093/mnrasl/slv094

Barrer, R. M. 1937, RSPSA, 161, 476, doi: 10.1098/rspa.1937.0157

Bates, D. R. 1983, ApJ, 270, 564, doi: 10.1086/161148

Bayet, E., Williams, D. A., Hartquist, T. W., & Viti, S. 2011, MNRAS, 414, 1583, doi: 10.1111/j.1365-2966.2011.18500.x

Becke, A. D. 1988, PhRvA, 38, 3098, doi: 10.1103/PhysRevA.38.3098

Becke, A. D. 1993, JChPh, 98, 5648, doi: 10.1063/1.464913

Bell, T. A., Roueff, E., Viti, S., & Williams, D. A. 2006, MNRAS, 371, 1865, doi: 10.1111/j.1365-2966.2006.10817.x

Bell, T. A., Viti, S., Williams, D. A., Crawford, I. A., & Price, R. J. 2005, MNRAS, 357, 961, doi: 10.1111/j.1365-2966.2005.08693.x

Belloche, A., Müller, H. S. P., Garrod, R. T., & Menten, K. M. 2016, A&A, 587, A91, doi: 10.1051/0004-6361/201527268

Benson, P. J., & Myers, P. C. 1989, ApJS, 71, 89, doi: 10.1086/191365

Bergin, E. A., & Tafalla, M. 2007, ARA&A, 45, 339, doi: 10.1146/annurev.astro.45.071206.100404

Bergner, J. B., Öberg, K. I., Walker, S., et al. 2019, ApJL, 884, L36, doi: 10.3847/2041-8213/ab48f9

Bernal, J. J., Koelemay, L. A., & Ziurys, L. M. 2021, ApJ, 906, 55, doi: 10.3847/1538-4357/abc87b

Bertoldi, F., & Draine, B. T. 1996, ApJ, 458, 222, doi: 10.1086/176805

Biczysko, M., Panek, P., Scalmani, G., Bloino, J., & Barone, V. 2010, Journal of chemical theory and computation, 6, 2115

Bieler, A., Altwegg, K., Balsiger, H., et al. 2015, Natur, 526, 678, doi: 10.1038/nature15707

Biham, O., Furman, I., Pirronello, V., & Vidali, G. 2001, ApJ, 553, 595, doi: 10.1086/320975

Bisschop, S. E., Fuchs, G. W., van Dishoeck, E. F., & Linnartz, H. 2007, A&A, 474, 1061, doi: 10.1051/0004-6361:20078210

Bisschop, S. E., Jørgensen, J. K., Bourke, T. L., Bottinelli, S., & van Dishoeck, E. F. 2008, A&A, 488, 959, doi: 10.1051/0004-6361:200809673

Black, J. H. 1978, ApJ, 222, 125, doi: 10.1086/156128

Black, J. H., & Dalgarno, A. 1977, ApJS, 34, 405, doi: 10.1086/190455

Black, J. H., Hartquist, T. W., & Dalgarno, A. 1978b, ApJ, 224, 448, doi: 10.1086/156392

Błasiak, B., Lee, H., & Cho, M. 2013, JChPh, 139, 044111, doi: 10.1063/1.4816041

Blum, J. 2018, SSRv, 214, 52, doi: 10.1007/s11214-018-0486-5

Bøgelund, E. G., McGuire, B. A., Hogerheijde, M. R., van Dishoeck, E. F., & Ligterink, N. F. W. 2019, A&A, 624, A82, doi: 10.1051/0004-6361/201833676

Bolina, A. S., Wolff, A. J., & Brown, W. A. 2005, JPCB, 109, 16836

Bonfanti, M., Martinazzo, R., Tantardini, G. F., & Ponti, A. 2007, The Journal of Physical Chemistry C, 111, 5825, doi: 10.1021/jp070616b

Boogert, A. C. A., Gerakines, P. A., & Whittet, D. C. B. 2015, Annual Review of Astronomy and Astrophysics, 53, 541, doi: 10.1146/annurev-astro-082214-122348

Boogert, A. C. A., Tielens, A. G. G. M., Ceccarelli, C., et al. 2000, A&A, 360, 683. https://arxiv.org/abs/astro-ph/0005030

Bouwman, J., Ludwig, W., Awad, Z., et al. 2007, A&A, 476, 995, doi: 10.1051/0004-6361:20078157

Boys, S. F., & Bernardi, F. 1970, MolPh, 19, 553, doi: 10.1080/00268977000101561

Bregman, J., Lester, D., & Rank, D. 1975, ApJ, 202, L55

Brinch, C., & Hogerheijde, M. R. 2011, LIME: Flexible, Non-LTE Line Excitation and Radiation Transfer Method for Millimeter and Far-infrared Wavelengths. http://ascl.net/1107.012

Brown, R. D., Godfry, P., & Winkler, D. A. 1980, Australian Journal of Chemistry, 33, 1

Brown, W. A. 2014, PCCP, 16, 3343, doi: 10.1039/C4CP90004A

Buch, V., & Czerminski, R. 1991, JChPh, 95, 6026, doi: 10.1063/1.461571

Burke, D. J., & Brown, W. A. 2010, PCCP, 12, 5947, doi: 10.1039/b917005g

Cancès, E., Mennucci, B., & Tomasi, J. 1997, JChPh, 107, 3032, doi: 10.1063/1.474659

Cappelli, C., Lipparini, F., Bloino, J., & Barone, V. 2011, JChPh, 135, 104505, doi: 10.1063/1.3630920

Caselli, P., & Ceccarelli, C. 2012, A&ARv, 20, 56, doi: 10.1007/s00159-012-0056-x

Caux, E., Kahane, C., Castets, A., et al. 2011, A&A, 532, A23, doi: 10.1051/0004-6361/201015399

Cazaux, S., & Tielens, A. G. G. M. 2002, ApJL, 575, L29, doi: 10.1086/342607

—. 2004, ApJ, 604, 222, doi: 10.1086/381775

Ceccarelli, C., Caselli, P., Bockelée-Morvan, D., et al. 2014, in Protostars and Planets VI, ed. H. Beuther, R. S. Klessen, C. P. Dullemond, & T. Henning, 859, doi: 10.2458/azu_uapress_9780816531240-ch037

Cernicharo, J. 2012, in EAS Publications Series, ed. C. Stehlé, C. Joblin, & L. d'Hendecourt, Vol. 58, 251–261, doi: 10.1051/eas/1258040

Cernicharo, J., Kisiel, Z., Tercero, B., et al. 2016, A&A, 587, L4, doi: 10.1051/0004-6361/201527531

Cesaroni, R., Churchwell, E., Hofner, P., Walmsley, C. M., & Kurtz, S. 1994, A&A, 288, 903

Cesaroni, R., Hofner, P., Araya, E., & Kurtz, S. 2010, A&A, 509, A50, doi: 10.1051/0004-6361/200912877

Chaabouni, H., Bergeron, H., Baouche, S., et al. 2012, A&A, 538, A128, doi: 10.1051/0004-6361/201117409

Chaabouni, H., Diana, S., Nguyen, T., & Dulieu, F. 2018, A&A, 612, A47, doi: 10.1051/0004-6361/201731006

Chakarov, D., & Kasemo, B. 1998, PhRvL, 81, 5181, doi: 10.1103/PhysRevLett.81.5181

Chakrabarti, S., & Chakrabarti, S. K. 2000a, A&A, 354, L6. https://arxiv.org/abs/astro-ph/0001079

Chakrabarti, S. K., & Chakrabarti, S. 2000b, Indian Journal of Physics Section B, 74B, 97. https://arxiv.org/abs/astro-ph/0003271

Chakrabarti, S. K., Das, A., Acharyya, K., & Chakrabarti, S. 2006a, A&A, 457, 167, doi: 10.1051/0004-6361:20065335

—. 2006b, Bulletin of the Astronomical Society of India, 34, 299. https://arxiv.org/abs/0806.4679

Chakrabarti, S. K., Majumdar, L., Das, A., & Chakrabarti, S. 2015, Ap&SS, 357, 90, doi: 10.1007/s10509-015-2239-1

Chang, Q., Cuppen, H. M., & Herbst, E. 2005, A&A, 434, 599, doi: 10.1051/0004-6361:20041842

—. 2007, A&A, 469, 973, doi: 10.1051/0004-6361:20077423

Chang, Q., & Herbst, E. 2012, ApJ, 759, 147, doi: 10.1088/0004-637X/759/2/147

Chang, Q., Zheng, X.-L., Zhang, X., et al. 2021, RAA, 21, 039, doi: 10.1088/1674-4527/21/2/39

Chantzos, J., Rivilla, V. M., Vasyunin, A., et al. 2020, A&A, 633, A54, doi: 10.1051/0004-6361/201936531

Charnley, S. B. 1997, MNRAS, 291, 455, doi: 10.1093/mnras/291.3.455

—. 1998, ApJL, 509, L121, doi: 10.1086/311764

—. 2001, ApJL, 562, L99, doi: 10.1086/324753

Charnley, S. B., Kress, M. E., Tielens, A. G. G. M., & Millar, T. J. 1995, ApJ, 448, 232, doi: 10.1086/175955

Charnley, S. B., & Millar, T. J. 1994, Monthly Notices of the Royal Astronomical Society, 270, 570, doi: 10.1093/mnras/270.3.570

Chastaing, D., Le Picard, S. D., Sims, I. R., & Smith, I. W. M. 2001, A&A, 365, 241, doi: 10.1051/0004-6361:20000026

Cheung, A. C., Rank, D. M., Townes, C. H., Thornton, D. D., & Welch, W. J. 1968, PhRvL, 21, 1701, doi: 10.1103/PhysRevLett.21.1701

Chiar, J. E., Gerakines, P. A., Whittet, D. C. B., et al. 1998, ApJ, 498, 716, doi: 10.1086/305569

Chiar, J. E., Whittet, D. C. B., Adamson, A. J., & Kerr, T. H. 1995, in Astronomical Society of the Pacific Conference Series, Vol. 73, From Gas to Stars to Dust, ed. M. R. Haas, J. A. Davidson, & E. F. Erickson, 75–78

Choi, J.-H., & Cho, M. 2011, JChPh, 134, 154513, doi: 10.1063/1.3580776

Chung, L. W., Sameera, W., Ramozzi, R., et al. 2015, ChRv, 115, 5678

Chyba, C., & Sagan, C. 1992, Natur, 355, 125, doi: 10.1038/355125a0

Chyba, C. F., & Sagan, C. 1997, in Comets and the Origin and Evolution of Life, 147–173

Chyba, C. F., Thomas, P. J., Brookshaw, L., & Sagan, C. 1990, Sci, 249, 366, doi: 10.1126/science.11538074

Codella, C., Ceccarelli, C., Caselli, P., et al. 2017, A&A, 605, L3, doi: 10.1051/0004-6361/201731249

Collings, M. P., Anderson, M. A., Chen, R., et al. 2004, MNRAS, 354, 1133, doi: 10.1111/j.1365-2966.2004.08272.x

Collings, M. P., Dever, J. W., & McCoustra, M. R. S. 2014, PCCP, 16, 3479, doi: 10.1039/C3CP54024C

Cooke, I. R., Fayolle, E. C., & Öberg, K. I. 2016, ApJ, 832, 5, doi: 10.3847/0004-637X/832/1/5

Corazzi, M. A., Brucato, J. R., Poggiali, G., et al. 2021, ApJ, 913, 128, doi: 10.3847/1538-4357/abf6d3

Cuppen, H. M., & Herbst, E. 2007, ApJ, 668, 294, doi: 10.1086/521014

Cuppen, H. M., & Hornekær, L. 2008, JChPh, 128, 174707, doi: 10.1063/1.2913238

Cuppen, H. M., Karssemeijer, L. J., & Lamberts, T. 2013, ChRv, 113, 8840, doi: 10.1021/cr400234a

Cuppen, H. M., van Dishoeck, E. F., Herbst, E., & Tielens, A. G. G. M. 2009, A&A, 508, 275, doi: 10.1051/0004-6361/200913119

Cuppen, H. M., Walsh, C., Lamberts, T., et al. 2017, SSRv, 212, 1, doi: 10.1007/s11214-016-0319-3

Curtiss, L. A., Raghavachari, K., Redfern, P. C., & Pople, J. A. 1997, JChPh, 106, 1063, doi: 10.1063/1.473182

Curtiss, L. A., Redfern, P. C., & Raghavachari, K. 2007, JChPh, 126, 084108, doi: 10.1063/1.2436888

Dalgarno, A., Yan, M., & Liu, W. 1999, ApJS, 125, 237, doi: 10.1086/313267

Dartois, E. 2005, SSRv, 119, 293, doi: 10.1007/s11214-005-8059-9

Das, A., Acharyya, K., Chakrabarti, S., & Chakrabarti, S. K. 2008a, A&A, 486, 209, doi: 10.1051/0004-6361:20078422

Das, A., Acharyya, K., & Chakrabarti, S. K. 2010, MNRAS, 409, 789, doi: 10.1111/j.1365-2966.2010.17343.x

Das, A., & Chakrabarti, S. K. 2011, MNRAS, 418, 545, doi: 10.1111/j.1365-2966.2011.19503.x

Das, A., Chakrabarti, S. K., Acharyya, K., & Chakrabarti, S. 2008b, NewA, 13, 457, doi: 10.1016/j.newast.2008.01.003

Das, A., Gorai, P., & Chakrabarti, S. K. 2019, A&A, 628, A73, doi: 10.1051/0004-6361/201834923

Das, A., Majumdar, L., Chakrabarti, S. K., & Chakrabarti, S. 2013b, NewA, 23, 118, doi: 10.1016/j.newast.2013.01.003

Das, A., Majumdar, L., Chakrabarti, S. K., & Sahu, D. 2015b, NewA, 35, 53, doi: 10.1016/j.newast.2014.07.006

Das, A., Majumdar, L., Sahu, D., et al. 2015a, ApJ, 808, 21, doi: 10.1088/0004-637X/808/1/21

Das, A., Sahu, D., Majumdar, L., & Chakrabarti, S. K. 2016, MNRAS, 455, 540, doi: 10.1093/mnras/stv2264

Das, A., Sil, M., Bhat, B., et al. 2020, ApJ, 902, 131, doi: 10.3847/1538-4357/abb5fe

Das, A., Sil, M., Ghosh, R., et al. 2021, Frontiers in Astronomy and Space Sciences, 8, 78, doi: 10.3389/fspas.2021.671622

Das, A., Sil, M., Gorai, P., Chakrabarti, S. i. K., & Loison, J. C. 2018, ApJS, 237, 9, doi: 10.3847/1538-4365/aac886

Davidson, K., & Fesen, R. A. 1985, ARA&A, 23, 119, doi: 10.1146/annurev.aa.23.090185.001003

Dawes, A., Mason, N. J., & Fraser, H. J. 2016, PCCP (Incorporating Faraday Transactions), 18, 1245, doi: 10.1039/C5CP05299H

De Beck, E., Kamiński, T., Patel, N. A., et al. 2013, A&A, 558, A132, doi: 10.1051/0004-6361/201321349

de Graauw, T., Whittet, D. C. B., Gerakines, P. A., et al. 1996, A&A, 315, L345

Demaison, J., Hüttner, W., Starck, B., et al. 1974, Atomic and Molecular Physics, 6

D'Hendecourt, L. B. 1986, Ultraviolet Photoprocessing and Infrared Spectroscopy of Laboratory Simulated Grain Mantles, ed. F. P. Israel, Vol. 124, 247, doi: 10.1007/978-94-009-4672-9_56

D'Hendecourt, L. B., & Jourdain de Muizon, M. 1989, A&A, 223, L5

Dohnálek, Z., Kimmel, G. A., Ayotte, P., Smith, R. S., & Kay, B. D. 2003, JChPh, 118, 364, doi: 10.1063/1.1525805

Draine, B. T. 1978, ApJS, 36, 595, doi: 10.1086/190513

—. 2003, ARA&A, 41, 241, doi: 10.1146/annurev.astro.41.011802.094840

—. 2011, Physics of the Interstellar and Intergalactic Medium

Dubernet, M. L., Alexander, M. H., Ba, Y. A., et al. 2013, A&A, 553, A50, doi: 10.1051/0004-6361/201220630

Duflot, D., Toubin, C., & Monnerville, M. 2021, FrASS, 8, 24, doi: 10.3389/fspas.2021.645243

Dulieu, F., Amiaud, L., Baouche, S., et al. 2005, CPL, 404, 187, doi: 10.1016/j.cplett.2005.01.044

Dulieu, F., Congiu, E., Noble, J., et al. 2013, NatSR, 3, 1338, doi: 10.1038/srep01338

Dunning, Thom H., J. 1989, JChPh, 90, 1007, doi: 10.1063/1.456153

Eddington, A. S. 1926, RSPSA, 111, 424, doi: 10.1098/rspa.1926.0076

—. 1937, The Observatory, 60, 99

Ehrenfreund, P., Boogert, A. C. A., Gerakines, P. A., Tielens, A. G. G. M., & van Dishoeck, E. F. 1997, A&A, 328, 649

Ehrenfreund, P., Breukers, R., D'Hendecourt, L., & Greenberg, J. M. 1992, A&A, 260, 431

Ehrenfreund, P., & Charnley, S. B. 2000, ARA&A, 38, 427, doi: 10.1146/annurev.astro.38.1.427

Ehrenfreund, P., & van Dishoeck, E. F. 1998, AdSpR, 21, 15, doi: 10.1016/S0273-1177(97)00827-2

Ehrenfreund, P., Fraser, H. J., Blum, J., et al. 2003, P&SS, 51, 473, doi: 10.1016/S0032-0633(03)00052-7

Eley, D. D. 1941, RSPSA, 178, 452, doi: 10.1098/rspa.1941.0067

Eley, D. D., & Rideal, E. K. 1940, Natur, 146, 401, doi: 10.1038/146401d0

Elsila, J. E., Dworkin, J. P., Bernstein, M. P., Martin, M. P., & Sandford, S. A. 2007, ApJ, 660, 911, doi: 10.1086/513141

Elsila, J. E., Glavin, D. P., & Dworkin, J. P. 2009, M&PS, 44, 1323, doi: 10.1111/j.1945-5100.2009.tb01224.x

Endres, C. P., Schlemmer, S., Schilke, P., Stutzki, J., & Müller, H. S. P. 2016, JMoSp, 327, 95, doi: 10.1016/j.jms.2016.03.005

Ercolano, B., & Koepferl, C. 2014, in The Labyrinth of Star Formation, Vol. 36, 63, doi: 10.1007/978-3-319-03041-8_11

Etim, E. E., Gorai, P., Das, A., & Arunan, E. 2017, European Physical Journal D, 71, 86, doi: 10.1140/epjd/e2017-70611-3

Eyring, H. 1935, JChPh, 3, 107, doi: 10.1063/1.1749604

Fedoseev, G., Ioppolo, S., Zhao, D., Lamberts, T., & Linnartz, H. 2015, MNRAS, 446, 439, doi: 10.1093/mnras/stu2028

Ferland, G. J., Korista, K. T., Verner, D. A., et al. 1998, PASP, 110, 761, doi: 10.1086/316190

Ferland, G. J., Porter, R. L., van Hoof, P. A. M., et al. 2013, RMxAA, 49, 137. https://arxiv.org/abs/1302.4485

Ferland, G. J., Chatzikos, M., Guzmán, F., et al. 2017, RMxAA, 53, 385. https://arxiv.org/abs/1705.10877

Ferrero, S., Zamirri, L., Ceccarelli, C., et al. 2020, ApJ, 904, 11, doi: 10.3847/1538-4357/abb953

Fischer, E., & Botskor, I. 1982, JMoSp, 91, 116, doi: 10.1016/0022-2852(82)90035-2

—. 1984, JMoSp, 104, 226, doi: 10.1016/0022-2852(84)90117-6

Fontani, F., Rivilla, V. M., Caselli, P., Vasyunin, A., & Palau, A. 2016, ApJL, 822, L30, doi: 10.3847/2041-8205/822/2/L30

Fontani, F., Rivilla, V. M., van der Tak, F. F. S., et al. 2019, MNRAS, 489, 4530, doi: 10.1093/mnras/stz2446

Fortenberry, R. C. 2019, Chem, 5, 1028, doi: https://doi.org/10.1016/j.chempr.2019.04.016

Fortenberry, R. C. 2020, MolAs, 18, 100062, doi: 10.1016/j.molap.2019.100062

Fortman, S. M., Neese, C. F., & De Lucia, F. C. 2014, ApJ, 782, 75, doi: 10.1088/0004-637X/782/2/75

Fourikis, N., Takagi, K., & Morimoto, M. 1974, ApJL, 191, L139, doi: 10.1086/181570

Fraser, H. J., Collings, M. P., McCoustra, M. R. S., & Williams, D. A. 2001, MNRAS, 327, 1165, doi: 10.1046/j.1365-8711.2001.04835.x

Fraser, M., & Boubert, D. 2019, ApJ, 871, 92, doi: 10.3847/1538-4357/aaf6b8

Frenkel', M. L., et al. 1994, Thermodynamics of organic compounds in the gas state, Vol. 1 (CRC press)

Frisch, M. J., Trucks, G. W., Schlegel, H. B., et al. 2013, Gaussian 09 Revision D.01

—. 2016, Gaussian 16 Revision A.03

Fuente, A., García-Burillo, S., Gerin, M., et al. 2005, ApJL, 619, L155, doi: 10.1086/427990

Fuente, A., Martin-Pintado, J., Cernicharo, J., & Bachiller, R. 1993, A&A, 276, 473

Furuya, K., & Persson, M. V. 2018, MNRAS, 476, 4994, doi: 10.1093/mnras/sty553

Galli, D., & Palla, F. 2013, ARA&A, 51, 163, doi: 10.1146/annurev-astro-082812-141029

García-Vázquez, R. M., Márquez-Mijares, M., Rubayo-Soneira, J., & Denis-Alpizar, O. 2019, A&A, 631, A86, doi: 10.1051/0004-6361/201935712

Garozzo, M., Fulvio, D., Kanuchova, Z., Palumbo, M. E., & Strazzulla, G. 2010, A&A, 509, A67, doi: 10.1051/0004-6361/200913040

Garrod, R., Park, I. H., Caselli, P., & Herbst, E. 2006a, FaDi, 133, 51, doi: 10.1039/b516202e

Garrod, R. T. 2013, ApJ, 765, 60, doi: 10.1088/0004-637X/765/1/60

Garrod, R. T., Belloche, A., Müller, H. S. P., & Menten, K. M. 2017, A&A, 601, A48, doi: 10.1051/0004-6361/201630254

Garrod, R. T., & Herbst, E. 2006b, A&A, 457, 927, doi: 10.1051/0004-6361:20065560

Garrod, R. T., & Pauly, T. 2011, ApJ, 735, 15, doi: 10.1088/0004-637X/735/1/15

Garrod, R. T., Wakelam, V., & Herbst, E. 2007, A&A, 467, 1103, doi: 10.1051/0004-6361:20066704

Garrod, R. T., Weaver, S. L. W., & Herbst, E. 2008, ApJ, 682, 283, doi: 10.1086/588035

Garrod, R. T., & Widicus Weaver, S. L. 2013b, ChRv, 113, 8939, doi: 10.1021/cr400147g

Gerakines, P. A., Schutte, W. A., Greenberg, J. M., & van Dishoeck, E. F. 1995, A&A, 296, 810. https://arxiv.org/abs/astro-ph/9409076

Gerakines, P. A., Whittet, D. C. B., Ehrenfreund, P., et al. 1999, ApJ, 522, 357, doi: 10.1086/307611

Ghio, E., Mattera, L., Salvo, C., Tommasini, F., & Valbusa, U. 1980, JChPh, 73, 556, doi: 10.1063/1.439855

Gibb, E. L., Whittet, D. C. B., Boogert, A. C. A., & Tielens, A. G. G. M. 2004, ApJS, 151, 35, doi: 10.1086/381182

Gillespie, D. T. 1976, JCoPh, 22, 403, doi: 10.1016/0021-9991(76)90041-3

Gillett, F. C., & Forrest, W. J. 1973, ApJ, 179, 483, doi: 10.1086/151888

Glassgold, A. E., & Langer, W. D. 1974, ApJ, 193, 73, doi: 10.1086/153130

—. 1975, ApJ, 197, 347, doi: 10.1086/153519

Glavin, D. P., Dworkin, J. P., & Sandford, S. A. 2008, M&PS, 43, 399, doi: 10.1111/j.1945-5100.2008.tb00629.x

Godfrey, P. D., Brown, R. D., Robinson, B. J., & Sinclair, M. W. 1973, ApJL, 13, 119

Goldman, N., Reed, E. J., Fried, L. E., William Kuo, I. F., & Maiti, A. 2010, Nature Chemistry, 2, 949, doi: 10.1038/nchem.827

Goldsmith, P. F., & Langer, W. D. 1999, ApJ, 517, 209, doi: 10.1086/307195

Gomez, H. L., Krause, O., Barlow, M. J., et al. 2012, ApJ, 760, 96, doi: 10.1088/0004-637X/760/1/96

Gorai, P. 2019, PhD thesis, University of Calcutta

Gorai, P., Bhat, B., Sil, M., et al. 2020b, ApJ, 895, 86, doi: 10.3847/1538-4357/ab8871

Gorai, P., Das, A., Das, A., et al. 2017a, ApJ, 836, 70, doi: 10.3847/1538-4357/836/1/70

Gorai, P., Das, A., Majumdar, L., et al. 2017b, MolAs, 6, 36, doi: 10.1016/j.molap.2017.01.004

Gorai, P., Sil, M., Das, A., et al. 2020a, ESC, 4, 920–946, doi: 10.1021/acsearthspacechem.0c00098

Gould, R. J., & Salpeter, E. E. 1963, ApJ, 138, 393, doi: 10.1086/147654

Graninger, D. M., Herbst, E., Öberg, K. I., & Vasyunin, A. I. 2014, ApJ, 787, 74, doi: 10.1088/0004-637X/787/1/74

Greaves, J. S., Richards, A. M. S., Bains, W., et al. 2020, Nature Astronomy, doi: 10.1038/s41550-020-1174-4

Grim, R. J. A., Baas, F., Geballe, T. R., Greenberg, J. M., & Schutte, W. A. 1991, A&A, 243, 473

Grimme, S. 2006, JChPh, 124, 034108, doi: 10.1063/1.2148954

Grimme, S., Antony, J., Ehrlich, S., & Krieg, H. 2010, JChPh, 132, 154104, doi: 10.1063/1.3382344

Guelin, M., Cernicharo, J., Paubert, G., & Turner, B. E. 1990, A&A, 230, L9

Guertler, J., Henning, T., Koempe, C., et al. 1996, in Astronomische Gesellschaft Abstract Series, Vol. 12, Astronomische Gesellschaft Abstract Series, 107

Güsten, R., Wiesemeyer, H., Neufeld, D., et al. 2019, Natur, 568, 357, doi: 10.1038/s41586-019-1090-x

Habing, H. J. 1968, BAN, 19, 421

Hadraoui, K., Cottin, H., Ivanovski, S. L., et al. 2019, A&A, 630, A32, doi: 10.1051/0004-6361/201935018

Hagen, W., Allamandola, L. J., & Greenberg, J. M. 1979, Ap&SS, 65, 215, doi: 10.1007/BF00643502

Hagen, W., Tielens, A. G. G. M., & Greenberg, J. M. 1981, CP, 56, 367, doi: 10.1016/0301-0104(81)80158-9

Halfen, D. T., Clouthier, D. J., & Ziurys, L. M. 2008, ApJL, 677, L101, doi: 10.1086/588024

Hama, T., & Watanabe, N. 2013, ChRv, 113, 8783, doi: 10.1021/cr4000978

Hama, T., Watanabe, N., Kouchi, A., & Yokoyama, M. 2011, ApJL, 738, L15, doi: 10.1088/2041-8205/738/1/L15

Hamada, Y., Tsuboi, M., Yamanouchi, K., & Kuchitzu, K. 1986, JMoSt, 146, 253, doi: 10.1016/0022-2860(86)80296-4

Hamilton, J. R., Faure, A., & Tennyson, J. 2016, MNRAS, 455, 3281, doi: 10.1093/mnras/stv2429

Han, S. S., & Lee, H. M. 2004, Carbon, 42, 2169, doi: https://doi.org/10.1016/j.carbon.2004.04.025

Harris, J., & Kasemo, B. 1981, SurSL, 105, L281, doi: 10.1016/0167-2584(81)90068-2

Harsono, D., Bjerkeli, P., van der Wiel, M. H. D., et al. 2018, NatAs, 2, 646, doi: 10.1038/s41550-018-0497-x

Hasegawa, T. I., & Herbst, E. 1993, MNRAS, 261, 83, doi: 10.1093/mnras/261.1.83

Hasegawa, T. I., Herbst, E., & Leung, C. M. 1992, ApJS, 82, 167, doi: 10.1086/191713

Haupa, K. A., Tarczay, G., & Lee, Y.-P. 2019, JAChS, 141, 11614

He, J., Acharyya, K., & Vidali, G. 2016b, ApJ, 825, 89, doi: 10.3847/0004-637X/825/2/89

He, J., Shi, J., Hopkins, T., Vidali, G., & Kaufman, M. J. 2015, ApJ, 801, 120, doi: 10.1088/0004-637X/801/2/120

Heays, A. N., Bosman, A. D., & van Dishoeck, E. F. 2017, A&A, 602, A105, doi: 10.1051/0004-6361/201628742

Heck, E. L., Flower, D. R., Le Bourlot, J., Pineau des Forets, G., & Roueff, E. 1993, MNRAS, 262, 795, doi: 10.1093/mnras/262.3.795

Hendricksen, D. K., & Harmony, M. D. 1969, JChPh, 51, 700, doi: 10.1063/1.1672059

Herbst, E. 2014, PCCP, 16, 3344, doi: 10.1039/C3CP54065K

Herbst, E., & Cuppen, H. M. 2006, Proceedings of the National Academy of Science, 103, 12257, doi: 10.1073/pnas.0601556103

Herbst, E., & van Dishoeck, E. F. 2009, ARA&A, 47, 427, doi: 10.1146/annurev-astro-082708-101654

Herbst, E., & Yates, John T., J. 2013, ChRv, 113, 8707, doi: 10.1021/cr400579y

Herzberg, G. 1966, Molecular spectra and molecular structure. Vol.3: Electronic spectra and electronic structure of polyatomic molecules

Hester, J. J. 2008, ARA&A, 46, 127, doi: 10.1146/annurev.astro.45.051806.110608

Heyer, M., & Dame, T. M. 2015, ARA&A, 53, 583, doi: 10.1146/annurev-astro-082214-122324

Himmel, H.-J., Junker, M., & Schnöckel, H. 2002, JChPh, 117, 3321, doi: 10.1063/1.1492276

Hincelin, U., Chang, Q., & Herbst, E. 2015, A&A, 574, A24, doi: 10.1051/0004-6361/201424807

Hogerheijde, M. R., & van der Tak, F. F. S. 2000, A&A, 362, 697. https://arxiv.org/abs/astro-ph/0008169

Hogness, T. R., & Lunn, E. G. 1925, Phys. Rev., 26, 786, doi: 10.1103/PhysRev.26.786

Hollenbach, D., & Salpeter, E. E. 1970, JChPh, 53, 79, doi: 10.1063/1.1673836

—. 1971, ApJ, 163, 155, doi: 10.1086/150754

Hollenbach, D. J., Takahashi, T., & Tielens, A. G. G. M. 1991, ApJ, 377, 192, doi: 10.1086/170347

Hollenbach, D. J., & Tielens, A. G. G. M. 1997, ARA&A, 35, 179, doi: 10.1146/annurev.astro.35.1.179

—. 1999, RvMP, 71, 173, doi: 10.1103/RevModPhys.71.173

Holtom, P. D., Bennett, C. J., Osamura, Y., Mason, N. J., & Kaiser, R. I. 2005, ApJ, 626, 940, doi: 10.1086/430106

Honig, B., & Karplus, M. 1971, Natur, 229, 558, doi: 10.1038/229558a0

Hornekær, L., Baurichter, A., Petrunin, V. V., et al. 2005, JChPh, 122, 124701, doi: 10.1063/1.1874934

Ikeda, M., Ohishi, M., Nummelin, A., et al. 2001, ApJ, 560, 792, doi: 10.1086/322957

Indriolo, N., Neufeld, D. A., Gerin, M., et al. 2012, ApJ, 758, 83, doi: 10.1088/0004-637x/758/2/83

Iqbal, W., & Wakelam, V. 2018, A&A, 615, A20, doi: 10.1051/0004-6361/201732486

Irvine, W. M., & Pollack, J. B. 1968, Icar, 8, 324, doi: 10.1016/0019-1035(68)90083-3

Jannuzi, B. T., Black, J. H., Lada, C. J., & van Dishoeck, E. F. 1988, ApJ, 332, 995, doi: 10.1086/166707

Jansen, D. J., van Dishoeck, E. F., Black, J. H., Spaans, M., & Sosin, C. 1995, A&A, 302, 223

Jansen, H. B., & Ros, P. 1969, CPL, 3, 140, doi: 10.1016/0009-2614(69)80118-1

Jarosewich, E. 1990, Meteoritics, 25, 323, doi: 10.1111/j.1945-5100.1990.tb00717.x

Jenkins, E. B. 2009, ApJ, 700, 1299, doi: 10.1088/0004-637X/700/2/1299

Jenniskens, P., & Blake, D. F. 1994, Science, 265, 753, doi: 10.1126/science.11539186

Jiménez-Serra, I., Viti, S., Quénard, D., & Holdship, J. 2018, ApJ, 862, 128, doi: 10.3847/1538-4357/aacdf2

Jiménez-Serra, I., Vasyunin, A. I., Caselli, P., et al. 2016, ApJL, 830, L6, doi: 10.3847/2041-8205/830/1/L6

Johnson, D. R., & Lovas, F. J. 1972, CPL, 15, 65, doi: 10.1016/0009-2614(72)87017-9

Jolly, W. L. 1984, Modern inorganic chemistry (McGraw-Hill College)

Jørgensen, J. K., Belloche, A., & Garrod, R. T. 2020, ARA&A, 58, 727, doi: 10.1146/annurev-astro-032620-021927

Jura, M. 1974, ApJ, 191, 375, doi: 10.1086/152975

—. 1975, ApJ, 197, 575, doi: 10.1086/153545

Jura, M., & York, D. G. 1978, ApJ, 219, 861, doi: 10.1086/155847

Kahane, C., Ceccarelli, C., Faure, A., & Caux, E. 2013, ApJL, 763, L38, doi: 10.1088/2041-8205/763/2/L38

Kaifu, N., Morimoto, M., Nagane, K., et al. 1974, ApJL, 191, L135, doi: 10.1086/181569

Kamrukov, A., Kozlov, N., Protasov, Y. S., & Chuvashev, S. 1983, Optics and Spectroscopy, 55, 9

Kaplan, D. L., Chatterjee, S., Gaensler, B. M., & Anderson, J. 2008, ApJ, 677, 1201, doi: 10.1086/529026

Karssemeijer, L. J., & Cuppen, H. M. 2014, A&A, 569, A107, doi: 10.1051/0004-6361/201424792

Katz, N., Furman, I., Biham, O., Pirronello, V., & Vidali, G. 1999, ApJ, 522, 305, doi: 10.1086/307642

Kaye, J. A., & Strobel, D. F. 1983, GeoRL, 10, 957, doi: 10.1029/GL010i010p00957

Keane, J. V., Tielens, A. G. G. M., Boogert, A. C. A., Schutte, W. A., & Whittet, D. C. B. 2001, A&A, 376, 254, doi: 10.1051/0004-6361:20010936

Keene, J., Blake, G. A., & Phillips, T. G. 1983, ApJL, 271, L27, doi: 10.1086/184086

Kennedy, G. M., & Kenyon, S. J. 2008, ApJ, 673, 502, doi: 10.1086/524130

Kessler, M., Steinz, J., Anderegg, M., et al. 1996, A&A, 315, L27

Kessler, M. F., Mueller, T. G., Leech, K., et al. 2003, The ISO Handbook, Volume I - Mission & Satellite Overview

Keto, E., & Caselli, P. 2008, ApJ, 683, 238, doi: 10.1086/589147

Kimber, H. J., Ennis, C. P., & Price, S. D. 2014, FaDi, 168, 167, doi: 10.1039/C3FD00130J

Kingdon, J. B., & Ferland, G. J. 1996, ApJS, 106, 205, doi: 10.1086/192335

Knacke, R. F., McCorkle, S., Puetter, R. C., Erickson, E. F., & Kraetschmer, W. 1982, ApJ, 260, 141, doi: 10.1086/160241

Knacke, R. F., & McCorkle, S. M. 1987, AJ, 94, 972, doi: 10.1086/114530

Köhler, M., Stepnik, B., Jones, A. P., et al. 2012, A&A, 548, A61, doi: 10.1051/0004-6361/201218975

Kuan, Y.-J., Charnley, S. B., Huang, H.-C., Tseng, W.-L., & Kisiel, Z. 2003, ApJ, 593, 848, doi: 10.1086/375637

Kvenvolden, K., Lawless, J., Pering, K., et al. 1970, Natur, 228, 923, doi: 10.1038/228923a0

Lacy, J. H., Carr, J. S., Evans, Neal J., I., et al. 1991, ApJ, 376, 556, doi: 10.1086/170304

Lacy, J. H., Faraji, H., Sandford, S. A., & Allamandola, L. J. 1998, ApJL, 501, L105, doi: 10.1086/311452

Lakard, B. 2003

Lamberts, T., & Kästner, J. 2017, ApJ, 846, 43, doi: 10.3847/1538-4357/aa8311

Langmuir, I. 1922, Trans. Faraday Soc., 17, 621, doi: 10.1039/TF9221700621

Le Bourlot, J., Pineau Des Forets, G., Roueff, E., & Flower, D. R. 1993, A&A, 267, 233

Le Petit, F., Roueff, E., & Herbst, E. 2004, A&A, 417, 993, doi: 10.1051/0004-6361:20035629

Lee, C., Yang, W., & Parr, R. G. 1988, PhRvB, 37, 785, doi: 10.1103/PhysRevB.37.785

Lee, H. H., Herbst, E., Pineau des Forets, G., Roueff, E., & Le Bourlot, J. 1996, A&A, 311, 690

Lee, J.-Y., Marti, K., Severinghaus, J. P., et al. 2006, GeCoA, 70, 4507, doi: 10.1016/j.gca.2006.06.1563

Lefloch, B., Vastel, C., Viti, S., et al. 2016, MNRAS, 462, 3937, doi: 10.1093/mnras/stw1918

Leger, A., Klein, J., de Cheveigne, S., et al. 1979, A&A, 79, 256

Lennon, M. A., Bell, K. L., Gilbody, H. B., et al. 1988, JPCRD, 17, 1285, doi: 10.1063/1.555809

Lepp, S., Stancil, P. C., & Dalgarno, A. 2002, Journal of Physics B Atomic Molecular Physics, 35, R57, doi: 10.1088/0953-4075/35/10/201

Leung, C. M., Herbst, E., & Huebner, W. F. 1984, ApJS, 56, 231, doi: 10.1086/190982

Licari, D., Baiardi, A., Biczysko, M., et al. 2015, Journal of computational chemistry, 36, 321, doi: 10.1002/jcc.23785

Ligterink, N. F. W., Coutens, A., Kofman, V., et al. 2017, MNRAS, 469, 2219, doi: 10.1093/mnras/stx890

Liu, B., & McLean, A. D. 1973, JChPh, 59, 4557, doi: 10.1063/1.1680654

Liu, X. W., Barlow, M. J., Dalgarno, A., et al. 1997, MNRAS, 290, L71, doi: 10.1093/mnras/290.4.L71

Lodders, K. 2003, ApJ, 591, 1220, doi: 10.1086/375492

Loh, E. D., Baldwin, J. A., Curtis, Z. K., et al. 2011, ApJS, 194, 30, doi: 10.1088/0067-0049/194/2/30

Loh, E. D., Baldwin, J. A., & Ferland, G. J. 2010, ApJL, 716, L9, doi: 10.1088/2041-8205/716/1/L9

Loh, E. D., Baldwin, J. A., Ferland, G. J., et al. 2012, MNRAS, 421, 789, doi: 10.1111/j.1365-2966.2011.20353.x

Loomis, R. A., Zaleski, D. P., Steber, A. L., et al. 2013, ApJL, 765, L9, doi: 10.1088/2041-8205/765/1/L9

López-Sepulcre, A., Balucani, N., Ceccarelli, C., et al. 2019, ESC, 3, 2122, doi: 10.1021/acsearthspacechem.9b00154

López-Sepulcre, A., Jaber, A. A., Mendoza, E., et al. 2015, MNRAS, 449, 2438, doi: 10.1093/mnras/stv377

Lord, S. D. 1992, A new software tool for computing Earth's atmospheric transmission of near-and far-infrared radiation, Vol. 103957 (Ames Research Center)

Lovas, F. J. 2004, JPCRD, 33, 177, doi: 10.1063/1.1633275

Lovas, F. J., Suenram, R. D., Johnson, D. R., Clark, F. O., & Tiemann, E. 1980, JChPh, 72, 4964, doi: 10.1063/1.439783

Luhman, K. L. 2012, ARA&A, 50, 65, doi: 10.1146/annurev-astro-081811-125528

Maciá, E. 2005, Chemical Society Reviews, 34, 691

Maciá, E., Hernández, M., & Oró, J. 1997, Origins of Life and Evolution of the Biosphere, 27, 459

Majumdar, L., Das, A., Chakrabarti, S. K., & Chakrabarti, S. 2012, Research in Astronomy and Astrophysics, 12, 1613, doi: 10.1088/1674-4527/12/12/003

—. 2013, NewA, 20, 15, doi: 10.1016/j.newast.2012.09.002

Majumdar, L., Gorai, P., Das, A., & Chakrabarti, S. K. 2015, Ap&SS, 360, 18, doi: 10.1007/s10509-015-2567-1

Maldoni, M. M., Egan, M. P., Smith, R. G., Robinson, G., & Wright, C. M. 2003, MNRAS, 345, 912, doi: 10.1046/j.1365-8711.2003.07013.x

Malfait, K., Waelkens, C., Waters, L. B. F. M., et al. 1998, A&A, 332, L25

Mantz, A. W., Maillard, J. P., Roh, W. B., & Narahari Rao, K. 1975, JMoSp, 57, 155, doi: 10.1016/0022-2852(75)90049-1

Marcelino, N., Agúndez, M., Cernicharo, J., Roueff, E., & Tafalla, M. 2018, A&A, 612, L10, doi: 10.1051/0004-6361/201833074

Marechal, Y. 1987, JChPh, 87, 6344, doi: 10.1063/1.453464

Margulès, L., Motiyenko, R. A., Guillemin, J. C., & Cernicharo, J. 2015, in 70th International Symposium on Molecular Spectroscopy, RI07, doi: 10.15278/isms.2015.RI07

Martín-Doménech, R., Rivilla, V. M., Jiménez-Serra, I., et al. 2017, MNRAS, 469, 2230, doi: 10.1093/mnras/stx915

Martinez, Oscar, J., Betts, N. B., Villano, S. M., et al. 2008, ApJ, 686, 1486, doi: 10.1086/591548

Mastrapa, R. M., Sandford, S. A., Roush, T. L., Cruikshank, D. P., & Dalle Ore, C. M. 2009, ApJ, 701, 1347, doi: 10.1088/0004-637X/701/2/1347

Mathis, J. S., Rumpl, W., & Nordsieck, K. H. 1977, ApJ, 217, 425, doi: 10.1086/155591

Mauersberger, R., Henkel, C., & Wilson, T. L. 1988, A&A, 205, 235

Max, J.-J., & Chapados, C. 2003, JChPh, 119, 5632, doi: 10.1063/1.1600438

—. 2004, JChPh, 120, 6625, doi: 10.1063/1.1649936

Mayo Greenberg, J. 2002, Surface Science, 500, 793, doi: 10.1016/S0039-6028(01)01555-2

McCall, B. J. 2006, RSPTA, 364, 2953, doi: 10.1098/rsta.2006.1876

McElroy, D., Walsh, C., Markwick, A. J., et al. 2013, A&A, 550, A36, doi: 10.1051/0004-6361/201220465

McGuire, B. A. 2018, ApJS, 239, 17, doi: 10.3847/1538-4365/aae5d2

McKee, C. F., & Ostriker, E. C. 2007, ARA&A, 45, 565, doi: 10.1146/annurev.astro.45.051806.110602

McKellar, A. 1940, PASP, 52, 187, doi: 10.1086/125159

McMillan, J. P., Fortman, S. M., Neese, C. F., & De Lucia, F. C. 2014, ApJ, 795, 56, doi: 10.1088/0004-637X/795/1/56

Mehrotra, S. C., Griffin, L. L., Britt, C. O., & Boggs, J. E. 1977, JMoSp, 64, 244, doi: 10.1016/0022-2852(77)90264-8

Meijerink, R., & Spaans, M. 2005, A&A, 436, 397, doi: 10.1051/0004-6361:20042398

Mendoza, E., Lefloch, B., López-Sepulcre, A., et al. 2014, MNRAS, 445, 151, doi: 10.1093/mnras/stu1718

Merrill, K. M., Russell, R. W., & Soifer, B. T. 1976, ApJ, 207, 763, doi: 10.1086/154545

Meshik, A., Mabry, J., Hohenberg, C., et al. 2007, Science, 318, 433, doi: 10.1126/science.1145528

Milam, S. N., Halfen, D. T., Tenenbaum, E. D., et al. 2008, ApJ, 684, 618, doi: 10.1086/589135

Millar, T. J., Bennett, A., & Herbst, E. 1987, Monthly Notices of the Royal Astronomical Society, 229, 41P, doi: 10.1093/mnras/229.1.41P

Millar, T. J., Herbst, E., & Charnley, S. B. 1991, ApJ, 369, 147, doi: 10.1086/169745

Mininni, C., Fontani, F., Rivilla, V. M., et al. 2018, MNRAS, 476, L39, doi: 10.1093/mnrasl/sly026

Minissale, M., & Dulieu, F. 2014, JChPh, 141, 014304, doi: 10.1063/1.4885847

Minissale, M., Dulieu, F., Cazaux, S., & Hocuk, S. 2016, A&A, 585, A24, doi: 10.1051/0004-6361/201525981

Møller, C., & Plesset, M. S. 1934, PhRv, 46, 618, doi: 10.1103/PhysRev.46.618

Molpeceres, G., & Kästner, J. 2020a, PCCP, 22, 7552, doi: 10.1039/D0CP00250J

—. 2021a, ApJ, 910, 55, doi: 10.3847/1538-4357/abe38c

Molpeceres, G., Zaverkin, V., & Kästner, J. 2020b, MNRAS, 499, 1373, doi: 10.1093/mnras/staa2891

Molpeceres, G., Zaverkin, V., Watanabe, N., & Kästner, J. 2021b, A&A, 648, A84, doi: 10.1051/0004-6361/202040023

Morales, S. B., Bennett, C. J., Le Picard, S. D., et al. 2011, ApJ, 742, 26, doi: 10.1088/0004-637X/742/1/26

Müller, H. S. P., Schlöder, F., Stutzki, J., & Winnewisser, G. 2005, Journal of Molecular Structure, 742, 215, doi: 10.1016/j.molstruc.2005.01.027

Müller, H. S. P., Thorwirth, S., Roth, D. A., & Winnewisser, G. 2001, A&A, 370, L49, doi: 10.1051/0004-6361:20010367

Müller, H. S. P., Muller, S., Schilke, P., et al. 2015, A&A, 582, L4, doi: 10.1051/0004-6361/201527254

Müller, H. S. P., Belloche, A., Xu, L.-H., et al. 2016, A&A, 587, A92, doi: 10.1051/0004-6361/201527470

Muralidharan, K., Deymier, P., Stimpfl, M., de Leeuw, N. H., & Drake, M. J. 2008, Icar, 198, 400, doi: 10.1016/j.icarus.2008.07.017

Nauta, K., & Miller, R. E. 2000, Sci, 287, 293, doi: 10.1126/science.287.5451.293

Nelson Jr, R. D., Lide Jr, D. R., & Maryott, A. A. 1967, Selected values of electric dipole moments for molecules in the gas phase, Tech. rep., National Standard Reference Data System

Neufeld, D. A., Goto, M., Geballe, T. R., et al. 2020, ApJ, 894, 37, doi: 10.3847/1538-4357/ab7191

Neufeld, D. A., & Wolfire, M. G. 2016, ApJ, 826, 183, doi: 10.3847/0004-637X/826/2/183

Nguyen, T., Oba, Y., Shimonishi, T., Kouchi, A., & Watanabe, N. 2020, ApJL, 898, L52, doi: 10.3847/2041-8213/aba695

Nguyen, T., Talbi, D., Congiu, E., et al. 2019, ESC, 3, 1196, doi: 10.1021/acsearthspacechem.9b00063

Noble, J. A., Congiu, E., Dulieu, F., & Fraser, H. J. 2012, MNRAS, 421, 768, doi: 10.1111/j.1365-2966.2011.20351.x

Noble, J. A., Theule, P., Congiu, E., et al. 2015, A&A, 576, A91, doi: 10.1051/0004-6361/201425403

Noll, K. S., & Marley, M. S. 1997, in Astronomical Society of the Pacific Conference Series, Vol. 119, Planets Beyond the Solar System and the Next Generation of Space Missions, ed. D. Soderblom, 115

Nuevo, M., Materese, C. K., & Sandford, S. A. 2014, ApJ, 793, 125, doi: 10.1088/0004-637X/793/2/125

Öberg, K. I. 2009, PhD thesis, Leiden Observatory, Leiden University, P.O. Box 9513, 2300 RA Leiden, The Netherlands

—. 2016, ChRv, 116, 9631. https://arxiv.org/abs/1609.03112

Öberg, K. I., & Bergin, E. A. 2021, PhR, 893, 1, doi: 10.1016/j.physrep.2020.09.004

Öberg, K. I., Boogert, A. C. A., Pontoppidan, K. M., et al. 2008, ApJ, 678, 1032, doi: 10.1086/533432

—. 2011, ApJ, 740, 109, doi: 10.1088/0004-637X/740/2/109

Öberg, K. I., Fuchs, G. W., Awad, Z., et al. 2007, ApJL, 662, L23, doi: 10.1086/519281

Öberg, K. I., Furuya, K., Loomis, R., et al. 2015, ApJ, 810, 112, doi: 10.1088/0004-637X/810/2/112

Öberg, K. I., van Broekhuizen, F., Fraser, H. J., et al. 2005, ApJL, 621, L33, doi: 10.1086/428901

Odutola, J. A., & Dyke, T. R. 1980, JChPh, 72, 5062, doi: 10.1063/1.439795

Ohishi, M., Suzuki, T., Hirota, T., Saito, M., & Kaifu, N. 2017, arXiv e-prints, arXiv:1708.06871. https://arxiv.org/abs/1708.06871

Ohno, K., Okimura, M., Akai, N., & Katsumoto, Y. 2005, Physical Chemistry Chemical Physics (Incorporating Faraday Transactions), 7, 3005, doi: 10.1039/B506641G

Olanrewaju, B. O., Herring-, Janine, C., Grieves, G. A., Aleksandrov, A., & Orlando, T. M. 2011, JPCA, 115, 5936, doi: 10.1021/jp110332v

Orient, O. J. 1977, CPL, 52, 264, doi: 10.1016/0009-2614(77)80538-1

Osmont, A., Catoire, L., Gökalp, I., & Yang, V. 2007, CoFl, 151, 262

Osterbrock, D. E., & Ferland, G. J. 2006, Astrophysics of Gaseous Nebulae and Active Galactic Nuclei, 2nd, University Science Books Mill Valley, CA

Owen, P. J., & Barlow, M. J. 2015, ApJ, 801, 141, doi: 10.1088/0004-637X/801/2/141

Pagani, L., Lesaffre, P., Roueff, E., et al. 2013, Philosophical Transactions of the Royal Society A: Mathematical, Physical and Engineering Sciences, 370, 5201, doi: 11.1098/rsta.2012.0027

Pagliai, M., Mancini, G., Carnimeo, I., De Mitri, N., & Barone, V. 2017, JCoCh, 38, 319

Palumbo, M. E. 2006, A&A, 453, 903, doi: 10.1051/0004-6361:20042382

Palumbo, M. E., Geballe, T. R., & Tielens, A. G. G. M. 1997, ApJ, 479, 839, doi: 10.1086/303905

Palumbo, M. E., Tielens, A. G. G. M., & Tokunaga, A. T. 1995, ApJ, 449, 674, doi: 10.1086/176088

Papajak, E., Leverentz, H. R., Zheng, J., & Truhlar, D. G. 2009, Journal of chemical theory and computation, 5, 1197

Parfenov, S. Y., Semenov, D. A., Sobolev, A. M., & Gray, M. D. 2016, MNRAS, 460, 2648, doi: 10.1093/mnras/stw1140

Pasek, M. A. 2019, Icar, 317, 59, doi: 10.1016/j.icarus.2018.07.011

Pearson, R., & Lovas, F. J. 1977, JChPh, 66, 4149, doi: 10.1063/1.434490

Peng, C., Ayala, P. Y., Schlegel, H. B., & Frisch, M. J. 1996, JCoCh, 17, 49

Peng, C., & Bernhard Schlegel, H. 1993, Israel Journal of Chemistry, 33, 449

Penteado, E. M., Walsh, C., & Cuppen, H. M. 2017, ApJ, 844, 71, doi: 10.3847/1538-4357/aa78f9

Pickett, H. M. 1991, Journal of Molecular Spectroscopy, 148, 371, doi: 10.1016/0022-2852(91)90393-0

Pickett, H. M., Poynter, R. L., Cohen, E. A., et al. 1998, JQSRT, 60, 883, doi: 10.1016/S0022-4073(98)00091-0

Pirronello, V., Liu, C., Roser, J. E., & Vidali, G. 1999, A&A, 344, 681

Pirronello, V., Liu, C., Shen, L., & Vidali, G. 1997, ApJL, 475, L69, doi: 10.1086/310464

Pontoppidan, K. M., Boogert, A. C. A., Fraser, H. J., et al. 2008, ApJ, 678, 1005, doi: 10.1086/533431

Pradzynski, C. C., Forck, R. M., Zeuch, T., Slavíček, P., & Buck, U. 2012, Science, 337, 1529, doi: 10.1126/science.1225468

Priestley, F. D., Barlow, M. J., & Viti, S. 2017, MNRAS, 472, 4444, doi: 10.1093/mnras/stx2327

Przybilla, N., Nieva, M.-F., & Butler, K. 2008, ApJL, 688, L103, doi: 10.1086/595618

Puzzarini, C. 2020, FrASS, 7, 19, doi: 10.3389/fspas.2020.00019

Puzzarini, C., Ali, A., Biczysko, M., & Barone, V. 2014a, ApJ, 792, 118, doi: 10.1088/0004-637X/792/2/118

Puzzarini, C., Biczysko, M., Bloino, J., & Barone, V. 2014b, ApJ, 785, 107, doi: 10.1088/0004-637X/785/2/107

Qasim, D., Fedoseev, G., Chuang, K. J., et al. 2020, NatAs, 4, 781, doi: 10.1038/s41550-020-1054-y

Quan, D., Herbst, E., Corby, J. F., Durr, A., & Hassel, G. 2016, ApJ, 824, 129, doi: 10.3847/0004-637X/824/2/129

Quan, D., Herbst, E., Osamura, Y., & Roueff, E. 2010, ApJ, 725, 2101, doi: 10.1088/0004-637X/725/2/2101

Quénard, D., Bottinelli, S., Caux, E., & Wakelam, V. 2018b, MNRAS, 477, 5312, doi: 10.1093/mnras/sty1004

Quénard, D., Jiménez-Serra, I., Viti, S., Holdship, J., & Coutens, A. 2018, MNRAS, 474, 2796, doi: 10.1093/mnras/stx2960

Raut, U., Famá, M., Teolis, B. D., & Baragiola, R. A. 2007, JChPh, 127, 204713, doi: 10.1063/1.2796166

Requena-Torres, M. A., Martín-Pintado, J., Rodríguez-Franco, A., et al. 2006, A&A, 455, 971, doi: 10.1051/0004-6361:20065190

Richardson, C. T., Baldwin, J. A., Ferland, G. J., et al. 2013, MNRAS, 430, 1257, doi: 10.1093/mnras/sts695

Rivilla, V. M., Fontani, F., Beltrán, M. T., et al. 2016, ApJ, 826, 161, doi: 10.3847/0004-637X/826/2/161

Rivilla, V. M., Jiménez-Serra, I., Zeng, S., et al. 2018, MNRAS, 475, L30, doi: 10.1093/mnrasl/slx208

Rivilla, V. M., Drozdovskaya, M. N., Altwegg, K., et al. 2020, MNRAS, 492, 1180, doi: 10.1093/mnras/stz3336

Roberge, W., & Dalgarno, A. 1982, ApJ, 255, 489, doi: 10.1086/159849

Roberts, H., & Millar, T. J. 2000, A&A, 361, 388

Rohatgi, A. 2020, Webplotdigitizer: Version 4.4. https://automeris.io/WebPlotDigitizer

Rolffs, R., Schilke, P., Zhang, Q., & Zapata, L. 2011, A&A, 536, A33, doi: 10.1051/0004-6361/201117112

Röllig, M., Hegmann, M., & Kegel, W. H. 2002, A&A, 392, 1081, doi: 10.1051/0004-6361:20020981

Röllig, M., Abel, N. P., Bell, T., et al. 2007, A&A, 467, 187, doi: 10.1051/0004-6361:20065918

Rothman, L. S. 2021, NatRP, 3, 302, doi: 10.1038/s42254-021-00309-2

Rothman, L. S., Gordon, I. E., Barbe, A., et al. 2009, JQSRT, 110, 533, doi: 10.1016/j.jqsrt.2009.02.013

Roueff, E., Alekseyev, A. B., & Le Bourlot, J. 2014, A&A, 566, A30, doi: 10.1051/0004-6361/201423652

Ruaud, M., Loison, J. C., Hickson, K. M., et al. 2015, MNRAS, 447, 4004, doi: 10.1093/mnras/stu2709

Ruaud, M., Wakelam, V., & Hersant, F. 2016, MNRAS, 459, 3756, doi: 10.1093/mnras/stw887

Rubin, M., Altwegg, K., van Dishoeck, E. F., & Schwehm, G. 2015, ApJL, 815, L11, doi: 10.1088/2041-8205/815/1/L11

Rubin, R. H., Swenson, G. W., J., Benson, R. C., Tigelaar, H. L., & Flygare, W. H. 1971, ApJL, 169, L39, doi: 10.1086/180810

Sahu, D., Das, A., Majumdar, L., & Chakrabarti, S. K. 2015, NewA, 38, 23, doi: 10.1016/j.newast.2014.12.011

Sahu, D., Liu, S.-Y., Das, A., Garai, P., & Wakelam, V. 2020, ApJ, 899, 65, doi: 10.3847/1538-4357/aba0a5

Saladino, R., Botta, G., Pino, S., G., C., & E., D. 2012, Chem Soc Rev, 41, 5526

Sameera, W. M. C., & Maseras, F. 2018, JCIM, 58, 1828, doi: 10.1021/acs.jcim.8b00332

Sameera, W. M. C., Senevirathne, B., Andersson, S., Maseras, F., & Nyman, G. 2017, JPCC, 121, 15223, doi: 10.1021/acs.jpcc.7b04105

Sandford, S. A., & Allamandola, L. J. 1993, ApJL, 409, L65, doi: 10.1086/186861

Sandford, S. A., Bernstein, M. P., Allamandola, L. J., Goorvitch, D., & Teixeira, T. C. V. S. 2001, ApJ, 548, 836, doi: 10.1086/319023

Sandford, S. A., Nuevo, M., Bera, P. P., & Lee, T. J. 2020, ChRv, 120, 4616, doi: 10.1021/acs.chemrev.9b00560

Sanna, A., Reid, M. J., Menten, K. M., et al. 2014, ApJ, 781, 108, doi: 10.1088/0004-637X/781/2/108

Sastry, K. V. L. N., & Curl, R. F., J. 1964, JChPh, 41, 77, doi: 10.1063/1.1725653

Savage, C., & Ziurys, L. M. 2004, ApJ, 616, 966, doi: 10.1086/424964

Schilke, P., Neufeld, D. A., Müller, H. S. P., et al. 2014, A&A, 566, A29, doi: 10.1051/0004-6361/201423727

Schöier, F. L., van der Tak, F. F. S., van Dishoeck, E. F., & Black, J. H. 2005, A&A, 432, 369, doi: 10.1051/0004-6361:20041729

Schutte, W. A., Gerakines, P. A., Geballe, T. R., van Dishoeck, E. F., & Greenberg, J. M. 1996, A&A, 309, 633

Schutte, W. A., Boogert, A. C. A., Tielens, A. G. G. M., et al. 1999, A&A, 343, 966

Semenov, D., Hersant, F., Wakelam, V., et al. 2010, A&A, 522, A42, doi: 10.1051/0004-6361/201015149

Senn, H. M., & Thiel, W. 2009, Angewandte Chemie International Edition, 48, 1198, doi: https://doi.org/10.1002/anie.200802019

Sharma, A. K., & Chandra, S. 2001, A&A, 376, 333, doi: 10.1051/0004-6361:20010873

Shaw, G., Ferland, G. J., Abel, N. P., Stancil, P. C., & van Hoof, P. A. M. 2005, ApJ, 624, 794, doi: 10.1086/429215

Shaw, G., Ferland, G. J., Srianand, R., & Abel, N. P. 2006, ApJ, 639, 941, doi: 10.1086/499221

Shi, J., Grieves, G. A., & Orlando, T. M. 2015, ApJ, 804, 24, doi: 10.1088/0004-637X/804/1/24

Shimonishi, T., Das, A., Sakai, N., et al. 2020, ApJ, 891, 164, doi: 10.3847/1538-4357/ab6e6b

Shimonishi, T., Nakatani, N., Furuya, K., & Hama, T. 2018, ApJ, 855, 27, doi: 10.3847/1538-4357/aaaa6a

Shu, F. H. 1977, ApJ, 214, 488, doi: 10.1086/155274

Shu, F. H., Adams, F. C., & Lizano, S. 1987, ARA&A, 25, 23, doi: 10.1146/annurev.aa.25.090187.000323

Shull, J. M., & van Steenberg, M. 1982, ApJS, 48, 95, doi: 10.1086/190769

Sil, M., Gorai, P., Das, A., et al. 2018, ApJ, 853, 139, doi: 10.3847/1538-4357/aa984d

Sil, M., Gorai, P., Das, A., Sahu, D., & Chakrabarti, S. K. 2017, European Physical Journal D, 71, 45, doi: 10.1140/epjd/e2017-70610-4

Sil, M., Srivastav, S., Bhat, B., et al. 2021, arXiv e-prints, arXiv:2105.14569. https://arxiv.org/abs/2105.14569

Sims, I. R., Queffelec, J.-L., Travers, D., et al. 1993, CPL, 211, 461, doi: 10.1016/0009-2614(93)87091-G

Skouteris, D., Vazart, F., Ceccarelli, C., et al. 2017, MNRAS, 468, L1, doi: 10.1093/mnrasl/slx012

Smith, D., McIntosh, B. J., & Adams, N. G. 1989, JChPh, 90, 6213, doi: 10.1063/1.456337

Smith, I. W. M. 2011, ARA&A, 49, 29, doi: 10.1146/annurev-astro-081710-102533

Smith, I. W. M., Herbst, E., & Chang, Q. 2004, Monthly Notices of the Royal Astronomical Society, 350, 323, doi: 10.1111/j.1365-2966.2004.07656.x

Snellen, I. A. G., Guzman-Ramirez, L., Hogerheijde, M. R., Hygate, A. P. S., & van der Tak, F. F. S. 2020, Re-analysis of the 267-GHz ALMA observations of Venus: No statistically significant detection of phosphine. https://arxiv.org/abs/2010.09761

Snow, T. P., & McCall, B. J. 2006, ARA&A, 44, 367, doi: 10.1146/annurev.astro.43.072103.150624

Snyder, L. E., & Buhl, D. 1972, ApJ, 177, 619, doi: 10.1086/151739

Soifer, B. T., Puetter, R. C., Russell, R. W., et al. 1979, ApJL, 232, L53, doi: 10.1086/183035

Song, L., Balakrishnan, N., Walker, K. M., et al. 2015, ApJ, 813, 96, doi: 10.1088/0004-637X/813/2/96

Song, L., & Kästner, J. 2016, PCCP, 18, 29278, doi: 10.1039/C6CP05727F

Sousa-Silva, C., Seager, S., Ranjan, S., et al. 2020, Astrobiology, 20, 235, doi: 10.1089/ast.2018.1954

Stäuber, P., Doty, S. D., van Dishoeck, E. F., & Benz, A. O. 2005, A&A, 440, 949, doi: 10.1051/0004-6361:20052889

Sternberg, A. 1995, Chemistry in Dense Photon Dominated Regions, ed. G. Winnewisser & G. C. Pelz, Vol. 459, 175, doi: 10.1007/BFb0102127

Sternberg, A., & Neufeld, D. A. 1999, ApJ, 516, 371, doi: 10.1086/307115

Suzuki, T., Ohishi, M., Hirota, T., et al. 2016, ApJ, 831, 114, doi: 10.3847/0004-637X/831/1/114

Takagi, K., & Kojima, T. 1973, ApJ, 181, L91, doi: 10.1086/181192

Tarrago, G., Lacome, N., Lévy, A., et al. 1992, JMoSp, 154, 30, doi: 10.1016/0022-2852(92)90026-K

Tenenbaum, E. D., Woolf, N. J., & Ziurys, L. M. 2007, ApJL, 666, L29, doi: 10.1086/521361

Tenenbaum, E. D., & Ziurys, L. M. 2008, ApJ, 680, L121, doi: 10.1086/589973

Tennyson, J., Yurchenko, S. N., Al-Refaie, A. F., et al. 2016, JMoSp, 327, 73, doi: 10.1016/j.jms.2016.05.002

Teyssier, D., Fossé, D., Gerin, M., et al. 2004, A&A, 417, 135, doi: 10.1051/0004-6361:20034534

Theis, R. A., & Fortenberry, R. C. 2016, MolAs, 2, 18, doi: 10.1016/j.molap.2015.12.001

Theis, R. A., Morgan, W. J., & Fortenberry, R. C. 2015, MNRAS, 446, 195, doi: 10.1093/mnras/stu1785

Theule, P., Borget, F., Mispelaer, F., et al. 2011, A&A, 534, A64, doi: 10.1051/0004-6361/201117494

Thorne, L. R., Anicich, V. G., & Huntress, W. T. 1983, CPL, 98, 162, doi: 10.1016/0009-2614(83)87120-6

Thorne, L. R., Anicich, V. G., Prasad, S. S., & Huntress, W. T., J. 1984, ApJ, 280, 139, doi: 10.1086/161977

Tielens, A. G. G. M. 2010, The Physics and Chemistry of the Interstellar Medium

—. 2013, RvMP, 85, 1021, doi: 10.1103/RevModPhys.85.1021

Tielens, A. G. G. M., & Hagen, W. 1982, A&A, 114, 245

Tielens, A. G. G. M., & Hollenbach, D. 1985, ApJ, 291, 747, doi: 10.1086/163112

Tomasi, J., Mennucci, B., & Cammi, R. 2005, ChRv, 105, 2999, doi: 10.1021/cr9904009

Tso, T. L., & Lee, E. K. 1985, JPhCh, 89, 1612

Turner, A. M., Abplanalp, M. J., Chen, S. Y., et al. 2015, Phys. Chem. Chem. Phys., 17, 27281, doi: 10.1039/C5CP02835C

Turner, B. E. 1991, ApJS, 76, 617, doi: 10.1086/191577

Turner, B. E., & Bally, J. 1987, ApJL, 321, L75, doi: 10.1086/185009

Turner, B. E., Terzieva, R., & Herbst, E. 1999, ApJ, 518, 699, doi: 10.1086/307300

Turner, B. E., Tsuji, T., Bally, J., Guelin, M., & Cernicharo, J. 1990, ApJ, 365, 569, doi: 10.1086/169511

van der Tak, F. 2011, in IAU Symposium, Vol. 280, The Molecular Universe, ed. J. Cernicharo & R. Bachiller, 449–460, doi: 10.1017/S1743921311025191

van der Tak, F. F. S., Black, J. H., Schöier, F. L., Jansen, D. J., & van Dishoeck, E. F. 2007, A&A, 468, 627, doi: 10.1051/0004-6361:20066820

van der Tak, F. F. S., Lique, F., Faure, A., Black, J. H., & van Dishoeck, E. F. 2020, Atoms, 8, 15, doi: 10.3390/atoms8020015

van Dishoeck, E. F. 1998a, FaDi, 109, 31, doi: 10.1039/a800815i

van Dishoeck, E. F. 2019, Proceedings of the International Astronomical Union, 15, 3–14, doi: 10.1017/S1743921319008792

van Dishoeck, E. F., Bergin, E. A., Lis, D. C., & Lunine, J. I. 2014, in Protostars and Planets VI, ed. H. Beuther, R. S. Klessen, C. P. Dullemond, & T. Henning, 835, doi: 10.2458/azu_uapress_9780816531240-ch036

van Dishoeck, E. F., & Black, J. H. 1986, ApJS, 62, 109, doi: 10.1086/191135

—. 1988, ApJ, 334, 771, doi: 10.1086/166877

—. 1989, ApJ, 340, 273, doi: 10.1086/167391

van Dishoeck, E. F., & Blake, G. A. 1998b, ARA&A, 36, 317, doi: 10.1146/annurev.astro.36.1.317

van Dishoeck, E. F., Blake, G. A., Draine, B. T., & Lunine, J. I. 1993, in Protostars and Planets III, ed. E. H. Levy & J. I. Lunine, 163

van Dishoeck, E. F., Blake, G. A., Jansen, D. J., & Groesbeck, T. D. 1995, ApJ, 447, 760, doi: 10.1086/175915

van Zadelhoff, G. J., Dullemond, C. P., van der Tak, F. F. S., et al. 2002, A&A, 395, 373, doi: 10.1051/0004-6361:20021226

Vasyunin, A. I., Caselli, P., Dulieu, F., & Jiménez-Serra, I. 2017, ApJ, 842, 33, doi: 10.3847/1538-4357/aa72ec

Vasyunin, A. I., & Herbst, E. 2013, ApJ, 769, 34, doi: 10.1088/0004-637X/769/1/34

Vasyunin, A. I., Semenov, D. A., Wiebe, D. S., & Henning, T. 2009, ApJ, 691, 1459, doi: 10.1088/0004-637X/691/2/1459

Verner, D. A., & Yakovlev, D. G. 1995, A&AS, 109, 125

Viala, Y. P. 1986, A&AS, 64, 391

Viala, Y. P., Roueff, E., & Abgrall, H. 1988, A&A, 190, 215

Viant, M. R., Cruzan, J. D., Lucas, D. D., et al. 1997, JPCA, 101, 9032, doi: 10.1021/jp970783j

Vidali, G., Ihm, G., Kim, H.-Y., & Cole, M. W. 1991, SurSR, 12, 135, doi: 10.1016/0167-5729(91)90012-M

Villanueva, G., Cordiner, M., Irwin, P., et al. 2020, No phosphine in the atmosphere of Venus. https://arxiv.org/abs/2010.14305

Villinger, H., Futrell, J. H., Howorka, F., Duric, N., & Lindinger, W. 1982, JChPh, 76, 3529, doi: 10.1063/1.443454

Visscher, C., Lodders, K., & Fegley, Bruce, J. 2006, ApJ, 648, 1181, doi: 10.1086/506245

Vuitton, V., Yelle, R. V., & Anicich, V. G. 2006, ApJL, 647, L175, doi: 10.1086/507467

Wakelam, V., & Herbst, E. 2008, ApJ, 680, 371, doi: 10.1086/587734

Wakelam, V., Loison, J. C., Mereau, R., & Ruaud, M. 2017, MolAs, 6, 22, doi: 10.1016/j.molap.2017.01.002

Wakelam, V., Smith, I. W. M., Herbst, E., et al. 2010, SSRv, 156, 13, doi: 10.1007/s11214-010-9712-5

Wakelam, V., Loison, J. C., Herbst, E., et al. 2015, ApJS, 217, 20, doi: 10.1088/0067-0049/217/2/20

Walmsley, C. M., Pineau des Forêts, G., & Flower, D. R. 1999, A&A, 342, 542

Ward, M. D., Hogg, I. A., & Price, S. D. 2012, MNRAS, 425, 1264, doi: 10.1111/j.1365-2966.2012.21520.x

Warshel, A., & Levitt, M. 1976, Journal of Molecular Biology, 103, 227, doi: https://doi.org/10.1016/0022-2836(76)90311-9

Weingartner, J. C., & Draine, B. T. 2001, ApJ, 548, 296, doi: 10.1086/318651

Wenger, M., Ochsenbein, F., Egret, D., et al. 2000, A&AS, 143, 9, doi: 10.1051/aas:2000332

Whittet, D. C. B. 2003, Dust in the galactic environment

Whittet, D. C. B., Bode, M. F., Longmore, A. J., et al. 1988, MNRAS, 233, 321, doi: 10.1093/mnras/233.2.321

Whittet, D. C. B., Schutte, W. A., Tielens, A. G. G. M., et al. 1996, A&A, 315, L357

Widicus Weaver, S. L. 2019, ARA&A, 57, 79, doi: 10.1146/annurev-astro-091918-104438

Wieler, R. 2002, RvMG, 47, 21, doi: 10.2138/rmg.2002.47.2

Williams, D., & Herbst, E. 2002, Surface Science, 500, 823, doi: 10.1016/S0039-6028(01)01538-2

Williams, J. P., & Cieza, L. A. 2011, ARA&A, 49, 67, doi: 10.1146/annurev-astro-081710-102548

Wilson, T. L., & Pauls, T. 1979, A&A, 73, L10

Wollrab, J. E., & Laurie, V. W. 1968, JChPh, 48, 5058, doi: 10.1063/1.1668177

Woon, D. E. 2002, ApJL, 571, L177, doi: 10.1086/341227

Wu, Y., Tepper, H. L., & Voth, G. A. 2006, JChPh, 124, 024503, doi: 10.1063/1.2136877

Wyrowski, F., Schilke, P., & Walmsley, C. M. 1999, A&A, 341, 882

Yamaguchi, T., Takano, S., Sakai, N., et al. 2011, PASJ, 63, L37, doi: 10.1093/pasj/63.5.L37

Zamirri, L., Casassa, S., Rimola, A., et al. 2018, MNRAS, 480, 1427, doi: 10.1093/mnras/sty1927

Ziurys, L. M. 1987, ApJL, 321, L81, doi: 10.1086/185010

Ziurys, L. M., Schmidt, D. R., & Bernal, J. J. 2018, ApJ, 856, 169, doi: 10.3847/1538-4357/aaafc6

Zubko, V. G., Mennella, V., Colangeli, L., & Bussoletti, E. 1996, MNRAS, 282, 1321, doi: 10.1093/mnras/282.4.1321